

Université des Sciences et Technologies de Lille

Travaux présentés par

Philippe GOLOUB

en vue de l'obtention de

L'HABILITATION A DIRIGER DES RECHERCHES EN SCIENCES PHYSIQUES

L'EXPERIENCE POLDER

OU

LA POLARIMETRIE COMME

ALTERNATIVE POUR LA TELEDETECTION DES

PARTICULES ATMOSPHERIQUES

Soutenance le 20 octobre 2000

devant le jury composé de :



M. J. PELON Directeur de Recherches au Service d'Aéronomie, Paris Rapporteurs

M.I. MISHCHENKO NASA research scientist, GISS, New York, USA

M. J.W. HOVENIER Professeur, Free University, Amsterdam, The Netherlands

M^{me}.A. FLOSSMAN Professeur à l'Université de Clermont-Ferrand Membres

M. D. TANRE Directeur de Recherches au LOA/USTL

M. M. HERMAN Professeur à l'USTL

M. J.L DEUZE Professeur à l'USTL

M. G. BROGNIEZ Professeur à l'USTL



D 030 176071 2

U.F.R de Physique Fondamentale

Laboratoire d'Optique Atmosphérique

Table des matières

Chapitre 1. Introduction.....
Chapitre 2. L'instrument POLDER.....
- POLDER in-flight calibration results (P. 1.1)	
- In-flight calibration of the POLDER polarized channels using the sunglint, (P. 1.2)	
Chapitre 3. Observation et caractérisation des nuages en lumière polarisée.....
- Analysis of the POLDER Airborne Polarization Measurements Performed over Clouds Covers (P 2.1)	
- Cloud Thermodynamic Phase Classification from the POLDER Spaceborne intrument (P. 2.2)	
- First Results of the POLDER « Earth Radiative Budget and Clouds » Operational Algorithms. POLDER-ADEOS (P. 2.3)	
- Cirrus Cloud properties deived from POLDER-1/ADEOS Polarized Radiances: First Validation using a Ground based Lidar Network (P. 2.4)	
- Comparison of POLDER phase to radar measurements (P. 2.5)	
- Global distribution of cloud top phase from POLDER/ADEOS (P. 2.6)	
- Observation of Horizontally Oriented Ice Crystals in Cirrus Clouds with POLDER/ADEOS (P. 2.7)	
- Ice crystal shapes in cirrus clouds derived from POLDER-1/ADEOS-1 (P. 2.8)	
- Cloud droplet effective radius from spaceborne polarization measurements (P. 2.9).	
Chapitre 4. Caractérisation des aérosols troposphériques.....
- Validation of the First Algorithm Applied for Deriving the Aerosol Properties Over the Ocean Using the POLDER/ADEOS Measurements (P. 3.1)	
- Characterization of aerosols over ocean from POLDER/ADEOS-1 (P. 3.2)	
- Estimate of the aerosols properties over the ocean with POLDER (P. 3.3)	
- Aerosol detection by TOMS and POLDER over oceanic regions (P. 3.4)	
- Remote sensing of aerosols over land surfaces from POLDER-ADEOS 1 measurements (P. 3.5)	
- Validation of POLDER aerosol index over land using ASTR-2 fires maps (P. 3.6)	
- Global observation of aerosol sources and transport from POLDER on ADEOS (P. 3.7)	
-	
Chapitre 5. Conclusions et perspectives.....

Chapitre 1

Introduction

Introduction

En raison de la possibilité d'une influence anthropique sur le climat, l'intérêt pour les sciences atmosphériques a considérablement augmenté au cours de ces dernières décennies. Des programmes de recherche internationaux et nationaux ont été mis en place afin de mieux comprendre les interactions aérosols-nuages-rayonnement, par nature complexes, et d'étudier leur influence sur le climat terrestre. En effet, le rayonnement solaire incident, non polarisé, est fortement affecté par la présence des gaz et des particules atmosphériques. La diffusion de ce rayonnement par ces différentes particules a très clairement un impact climatique. L'expression « particules atmosphériques » fait référence, dans notre travail, aux particules aérosols et aux particules nuageuses non précipitantes. Les particules aérosols (0.01 µm à quelques dizaines de micromètres) et nuageuses (quelques micromètres à quelques dizaines de micromètres) influencent directement le climat en diffusant et en absorbant le rayonnement solaire incident. Le mécanisme de diffusion vers l'espace de ce rayonnement produit, généralement, une augmentation de l'albédo planétaire et génère donc, dans la plupart des cas, un refroidissement de la surface en situation de ciel clair. D'autre part, les particules aérosols jouant le rôle de noyaux de condensation modifient les propriétés microphysiques des nuages en changeant la distribution en taille et la concentration des nuages en gouttelettes. Ceci a d'ailleurs un effet sur la durée de vie des nuages et leurs précipitations. Les aérosols industriels et ceux résultant de la combustion de biomasse sont des noyaux de condensation efficaces. Un nuage issu d'une masse d'air polluée contient davantage de gouttes plus petites et ces dernières sont de dimensions moindre ce qui a pour effet d'augmenter l'albédo du nuage.

En retour, les nuages influencent également les aérosols en constituant un puits important d'aérosols par dépôt humide. Les nuages selon leur altitude, leur composition et leur concentration en gouttes ou cristaux agissent de manière différente sur le rayonnement. Les nuages bas, constitués de gouttelettes d'eau sphériques, réfléchissent fortement le rayonnement solaire et ont donc pour effet de refroidir la planète. A l'inverse les cirrus, composés de cristaux de glace, sont généralement semi-transparents et affectent peu le rayonnement visible mais plutôt le rayonnement infrarouge.

La caractérisation, à l'échelle planétaire, des particules atmosphériques et l'estimation de leur impact climatique dépendent très largement de l'analyse du rayonnement qu'elles diffusent. La télédétection, cette capacité à percevoir et à étudier les objets à distance, est un domaine en pleine expansion depuis une trentaine d'années. A l'exception des molécules atmosphériques pour lesquelles la diffusion est simple à modéliser, la très grande variabilité de dimension, de forme, d'orientation, de composition chimique, de durée de résidence et d'abondance, rend difficile l'interprétation fine des mesures passives du rayonnement diffusé vers les capteurs satellitaires ou basés au sol, en terme de propriétés optiques et microphysiques. Il est maintenant possible de faire de telles études depuis l'espace, à une échelle globale et de façon opérationnelle et routinière. Jusqu'à très récemment de telles observations, de nature essentiellement passive, étaient limitées uniquement à l'aspect énergétique du rayonnement électromagnétique dans le spectre solaire et tellurique, et réalisées par la série d'instruments AVHRR (Advanced Very High Resolution Radiometre), TOMS (Total Ozone Mapping Spectrometer) et METEOSAT pour ne citer que les plus connus. Notons que, dans le passé, des versions satellitaires de polarimètres ont été utilisées

pour étudier les atmosphères planétaires, à l'exception de celle de la terre. On peut citer, néanmoins, l'instrument GOME en orbite sur ERS-2 depuis 1995, qui caractérise partiellement la polarisation du rayonnement. Ces mesures de polarisation, prévues initialement pour corriger les biais introduits par la polarisation instrumentale, ont cependant pu être exploitées pour déterminer l'altitude des nuages (Knibbe et al., 1995).

Une part importante des recherches expérimentales et théoriques réalisées au Laboratoire d'Optique Atmosphérique, de l'Université des Sciences et Technologies de Lille, porte sur l'exploitation des mesures de la polarisation pour caractériser les aérosols et les nuages de l'atmosphère terrestre. Des vols ballons des radiomètres RADIBAL (Herman et al., 1986), et PIRAT (Deuzé et al., 1989), ainsi que l'analyse d'expériences de polarimétrie réalisées à bord de la Navette spatiale Américaine (Egan 1993, Roger et al, 1994), ont permis d'obtenir dans les années 1980-1990, les premières observations stratosphériques et troposphériques en lumière polarisée. Parallèlement, des mesures passives réalisées au sol (Devaux et al., 1998) permettent de restituer les propriétés microphysiques des aérosols. Très récemment, l'expérience française POLDER (Deschamps et al., 1994), malheureusement écourtée à la suite d'une avarie de la plate-forme japonaise ADEOS-1, a démontré l'intérêt des mesures de polarisation, à l'échelle du globe, pour la télédétection des aérosols et des nuages. Le travail présenté ici en illustre certains aspects.

Ces résultats indiquent que la radio-polarimétrie peut-être considérée comme alternative et complémentaire à la radiométrie conventionnelle. La polarimétrie permet de connaître l'état de polarisation du rayonnement et fournit ainsi une information additionnelle à la mesure radiométrique qui est seulement sensible au flux d'énergie totale. Dans le cas de l'atmosphère, la mesure de polarisation fournit deux paramètres supplémentaires (composante polarisée et direction de polarisation) qui, de façon générale, permettent de mieux contraindre les procédures d'inversion restituant les propriétés optiques et microphysiques des particules aérosols ou des nuages. La composante polarisée du rayonnement, qui ne représente parfois que quelques pour cents du flux d'énergie diffusée et doit donc être mesurée avec précision, est très sensible aux propriétés microphysiques des particules diffusantes (propriétés angulaires remarquables en diffusion primaire) et également moins dégradée par les diffusions multiples.

La « gestation » du concept instrumental « POLDER » a débuté dans les années 1988-1989. En 1989, j'ai eu l'opportunité d'entrer au LOA, au tout début de cette aventure technique et scientifique. Dans le cadre de ma thèse (1990-1992), effectuée sous la direction de M Herman, j'ai développé le modèle radiométrique de l'imageur POLDER, ainsi que certains protocoles d'étalonnage en laboratoire et en orbite. J'ai également analysé les premières observations réalisées avec le simulateur aéroporté développé au LOA. Ensuite, dans le cadre de la préparation de la mission spatiale POLDER/ADEOS-1 prévue pour 1996, j'ai participé à l'élaboration de méthodes d'étalonnage en vol de l'instrument POLDER, ce qui représentait un travail original dans la mesure où le capteur ne disposait d'aucun système d'étalonnage embarqué. L'effort a porté sur la mise au point d'un méthode d'étalonnage interbande sur la réflexion spéculaire ainsi que sur le suivi en vol des paramètres du modèle radiométrique relatifs à la polarisation. Ce travail a été réalisé en collaboration avec M. Herman, JL. Deuzé, T. Bailleul, B. Toubbé et en relation avec le département qualité image (QTIS) du CNES. Il a donné lieu à 2 publications (Hagolle et al, 1999, Toubbé, 1999) .

Durant cette période d'intense activité à caractère plutôt « technique » et qui s'est achevée, pour ma part, après la mis à poste de POLDER, j'ai néanmoins réussi à poursuivre l'analyse des mesures aéroportées au-dessus des nuages, ce qui constituait un prolongement logique de mon travail de thèse. J'ai poursuivi, en collaboration avec M. Herman, l'étude de

l'altimétrie des nuages à partir des mesures de luminance bi-spectrale (443 et 865nm) (Goloub et al., 1994), mais surtout l'étude de la détection de la phase thermodynamique des nuages (Buriez et al, 1997), à l'aide des campagnes aéroportées qui se sont succédées jusqu'en 1995 (CLEOPATRA en 1991, ASTEX en 1992, EUCREX en 1994), méthodes mises en place dans la première génération d'algorithmes dans le segment sol POLDER.

Après la mise en orbite de la plate-forme ADEOS, à l'automne 1996, je me suis davantage impliqué dans l'analyse des premiers résultats de la phase des nuages, au niveau de l'amélioration de la méthode tout d'abord (Parol et al, 1999), (Goloub et al, 2000), puis dans sa validation à l'aide d'observations lidar au sol, en collaboration avec H. Chepfer du Laboratoire de Météorologie Dynamique, (Chepfer et al, 2000), à l'aide de données synoptiques et radar (Riedi et al., 2000) au cours du DEA puis de la thèse de J. Riedi que je dirige actuellement. Aujourd'hui, l'analyse géophysique des 8 mois de données POLDER (Riedi et al., 2000) est en cours ainsi que les comparaisons avec les climatologies pré-existantes telles que ISCCP (International Satellite Cloud Climatology Project) et également HIRS (High Infrared Resolution Sounders)

Dans le prolongement de ce travail, j'ai logiquement envisagé différentes applications. En effet la détermination de la phase thermodynamique constitue la première étape lorsque l'on s'intéresse aux propriétés microphysiques des particules constituant les nuages. Concernant la phase « *glace* », toujours en collaboration avec H. Chepfer et G. Brogniez, nous avons observé pour la première fois, à l'échelle globale, le phénomène de réflexion spéculaire sur les cristaux, traduisant l'orientation préférentielle de ces derniers. Le large champ de vue de POLDER (+/- 42°, +/- 51°) et la mesure de polarisation multispectrale rendent possible la détection de ce phénomène et permettent l'estimation de sa fréquence d'occurrence. Les distributions spatiale et temporelle de ce phénomène, et donc de l'orientation des cristaux à l'échelle du globe, ont pu être mises en évidence pour la première fois (Chepfer et al., 1999). Dans un deuxième temps, dans les situations où aucune orientation préférentielle n'est observée (distribution aléatoire dans l'espace), nous avons cherché à déterminer la « forme moyenne » des cristaux à l'aide d'une méthode simple basée sur la comparaison à des pré-calculs de transfert radiatifs réalisés pour quelques formes de cristaux habituellement considérés (colonnes et plaquettes hexagonales, polycristaux). Nous avons réalisé les cartographies à l'échelle globale sur les 8 mois de données POLDER (Chepfer et al., 2000). Ces résultats indiquent que la forme des particules composant le sommet des cirrus varie. Les polycristaux et les colonnes hexagonales dominent aux basses latitudes alors que les plaquettes hexagonales apparaissent plus fréquemment aux hautes latitudes. Ces résultats semblent compatibles avec les quelques études locales réalisées à partir de méthodes différentes, notamment à l'aide des mesures de l'instrument ATSR (Baran et al., 1999, 2000). La prochaine étape consiste à relier l'information microphysique obtenue, à savoir la forme moyenne, avec la thermodynamique et la dynamique atmosphérique.

Concernant la phase « *liquide* », la polarisation permet de déterminer, dans certaines conditions de visée, la distribution en taille des gouttelettes d'eau constituant le sommet du nuage. L'analyse des mesures obtenues lors des campagnes aéroportées m'avait permis de vérifier, compte tenu de la qualité de ces mesures, cette possibilité. Cette détermination a été réalisée sur les données satellitaires (Goloub et al, 1997 ; Bréon et Goloub, 1998). Les premières cartographies sont présentées dans Bréon et al., 1999. Les ordres de grandeurs retrouvés ainsi que les contrastes observés entre la taille des gouttes sur les océans et les continents sont cohérents avec les climatologies précédentes dérivées d'AVHRR (Han et al., 1994). La taille des gouttelettes systématiquement plus petite au-dessus des continents est une

indication supplémentaire de l'effet indirect des aérosols sur la formation des nuages (Bréon et Tanré, 2000).

La taille relativement modeste des équipes de recherche du LOA et la charge importante que représente la réalisation d'un projet tel que POLDER m'ont offert la possibilité d'aborder et de contribuer à différents sujets de recherches. Ma participation à plusieurs campagnes aéroportées m'a permis d'aborder l'étude des aérosols. Dans le cadre de la thèse de Thierry Elias (1997-2000), co-dirigée avec C. Devaux, j'ai abordé, simultanément à la mise en orbite de POLDER, l'analyse des observations polarimétriques depuis le sol réalisées par l'instrument RefPol (Reflectance-mètre Polarisé) et les photomètres automatiques du réseau AERONET. C'est alors, très naturellement, que je me suis impliqué dans la thématique «observations des aérosols» en prenant en charge la validation des résultats POLDER.

Au-dessus des océans, j'ai analysé les résultats du premier algorithme de restitutions de propriétés optiques des particules aérosols (épaisseur optique τ_a , coefficients d'Angström α , et indice de réfraction m) des aérosols (Deuzé et al., 1999), (Goloub et al, 1999). Ce travail de validation directe de τ_a et α a reposé intégralement sur les données du réseau international de photomètres automatiques AERONET (Holben et al., 1998). Mais la faiblesse, passagère, du réseau (pour sa partie américaine, notamment, de fin 1996 à mi 1997) couplée à la perte prématuée de la plate-forme ADEOS a limité fortement le nombre de données disponibles. Plus de 60% des données correspondent à des aérosols désertiques. Pendant la période de fonctionnement opérationnel de POLDER (novembre 1996-juin 1997), les principaux événements de «biomass burning» d'Amérique du sud, d'Asie et d'Indonésie n'ont pu être étudiés. Néanmoins, quelques sites urbains d'Europe du Nord ont fonctionné. Par contraste, aujourd'hui, depuis le lancement de la plate-forme américaine EOS (Earth Observing System), le nombre d'instruments opérationnels est de l'ordre d'une cinquantaine. L'analyse des résultats de l'algorithme, basé sur une approche utilisant une grille de pré-calculs de transfert radiatif a montré, à l'aide du jeu de données de validation disponible, une bonne restitution de l'épaisseur optique, mais une sous-estimation systématique du coefficient d'Angström (surestimation de la taille des particules). Une analyse plus détaillée de l'algorithme initial et des améliorations potentielles apportées par l'introduction de modèles d'aérosols plus réalistes (bimodal au lieu de monomodal) est présentée dans Deuzé et al., 2000.

L'intérêt de la comparaison avec le photomètre réside dans la cohérence physique entre les grandeurs mesurées par le photomètre (épaisseur optique spectrale, luminance diffuse) et dérivées de la mesure satellitaire. Lorsque les coïncidences sont peu nombreuses, il peut être avantageux comparer différents capteurs. Une comparaison a été réalisée entre POLDER et TOMS. Les informations obtenues sur les aérosols procèdent de mesures indépendantes, et, de plus, il n'y a plus cohérence entre les grandeurs déduites, épaisseur optique et exposant d'Angström pour POLDER et index aérosol pour TOMS. Selon plusieurs études, l'index aérosols TOMS déduit des mesures différentielles dans l'ultraviolet est bien corrélé à l'épaisseur optique (Torres et al., 1999 ; Hsu et al., 1999). Néanmoins, il dépend également de l'altitude de la couche d'aérosols qui peut donc être partiellement masquée par l'atmosphère moléculaire si les aérosols sont localisés dans les basses couches atmosphériques ainsi que de leur nature.

On comprend alors que la différence de sensibilité des instruments soit intéressante pour l'étude des aérosols. Cependant, elle complique l'interprétation de la comparaison directe entre les deux capteurs. Cette comparaison, réalisée en collaboration avec I. Chiapello sur plusieurs sites océaniques représentatifs des différents types d'aérosols, est présentée dans

(Chiapello et al., 2000). Les corrélations constatées sont bonnes dans la plupart des situations analysées. Néanmoins, POLDER témoigne d'une plus grande sensibilité à la présence d'aérosols dans des régions de mélange complexe en aérosols (sulfate/suie/poussière), telles que l'Asie et l'Amérique centrale.

Aujourd'hui, à l'exception notable de TOMS, les capteurs opérationnels (AVHRR, METEOSAT) permettent de dériver des informations sur les aérosols uniquement au-dessus des surfaces sombres, essentiellement océaniques (Stowe et al., 1992, Husar et al., 1997, Nakajima et al., 1998, Mishchenko et al., 1999). L'observation et la caractérisation des aérosols présents au-dessus des continents restent difficiles et imprécises. Au-dessus des continents, la contribution des aérosols à la luminance mesurée au niveau du capteur est généralement faible devant celle du sol. Jusqu'à présent, la caractérisation des aérosols (épaisseur optique) au-dessus des surfaces n'a pu se faire que dans des cas particuliers ; (i) surface sombre, végétation dense, (Kaufman, 1988, 1997), (ii) en présence de surfaces adjacentes contrastées (Dégradation de contraste, Tanré et al, 1988), ou bien encore, toujours par contraste, mais dans le domaine thermique cette fois par Legrand et al., 1989. Ces méthodes nécessitent la connaissance d'un modèle d'aérosol *a priori*. L'apport des mesures de TOMS dans le spectre UV est indéniable, mais la détection des aérosols absorbants et la détermination de leur épaisseur optique dépendent de l'altitude des aérosols et de leur nature. Dans ce contexte, POLDER offre de nouvelles possibilités, essentiellement liées à la mesure spectrale et directionnelle de la luminance polarisée (Leroy et al., 1997, Herman et al., 1997). La polarisation des surfaces tend à s'effacer devant celle de l'atmosphère. Néanmoins, la « lumière polarisée » générée par le sol n'est pas négligeable et doit être prise en compte (Nadal et al., 1999). L'index aérosols, défini dans Deuzé et al. (2000), permet de préciser certaines sources d'aérosols (Tanré et al , 2000). Là encore, la faiblesse du nombre de données photométriques et leur manque de représentativité rendent difficile l'estimation de la justesse de l'interprétation des produits POLDER. On constate, néanmoins, que POLDER est peu sensible aux aérosols désertiques constitués de particules de grande taille, non sphérique et générant peu de polarisation par diffusion. L'autre limitation, instrumentale cette fois, provient du faible écart entre les deux longueurs d'onde utilisées (670 et 865nm). On recherche actuellement à utiliser le canal à 443 nm pour augmenter le domaine de longueur d'onde et ainsi remonter à un paramètre de taille, mais il est nécessaire de réaliser des progrès au niveau de la correction du terme moléculaire prépondérant aux courtes longueurs d'onde.

Pour pallier le manque de mesures optiques depuis la surface, nous avons recherché des informations sur les sources principales de matière particulaire en suspension dans l'atmosphère. Les feux de biomasse (forêts, savanes, agriculture) émettent des quantités importantes de matière particulaire dans l'atmosphère. Ces points chauds de la surface peuvent être détectés de jour comme de nuit par des satellites équipés de détecteur moyen-infrarouge ou infrarouge. Le radiomètre ATSR-2 (Along Track Scanning Radiometer), embarqué sur la plate-forme européenne ERS-2, fournit depuis 1995 des mesures dans le visible, le proche infrarouge, le moyen infrarouge (1.6 et 3.7 μm) et l'infrarouge. Les mesures de nuit obtenues à 3.7 μm ont permis de réaliser la cartographie quotidienne des points chauds (Arino et al., 1995). A l'aide de ces cartes d'occurrence de feux de biomasse, nous avons pu interpréter correctement les valeurs élevées de l'index aérosols fourni par POLDER dans ces régions. La corrélation entre la distribution et le nombre de feux dans les zones de « biomass burning » et l'index POLDER est très satisfaisante (Goloub et al., 2000).

L'ensemble des travaux va maintenant être présenté en distinguant 3 parties. Je commencerai par faire une description de l'instrument POLDER et rappellerai brièvement son modèle radiométrique, ainsi que les méthodes mises en œuvre pour contrôler en orbite les paramètres instrumentaux (chapitre 2). Dans une seconde partie, je présenterai des résultats relatifs à l'observation et la caractérisation des nuages à l'aide de la polarisation (chapitre 3). Enfin, dans la dernière partie, je présenterai le travail de validation, concernant la caractérisation des aérosols troposphériques au-dessus des océans et des continents (chapitre 4). Chacune des trois parties est précédée d'une courte introduction.

Chapitre 2

L'instrument POLDER

Chapitre 2

L'instrument POLDER

L'instrument POLDER, imaginé au Laboratoire d'Optique Atmosphérique (LOA) est un instrument dédié à l'observation globale de la polarisation et la directionnalité du rayonnement solaire diffusé par le système terre-atmosphère. Le concept instrumental, rappelé ici, a été évalué à l'aide du simulateur aéroporté développé au LOA avec le soutien du Centre National d'Etudes Spatiales de Toulouse. Il a ensuite franchi les différentes phases de démonstration qui lui ont permis d'être sélectionné sur la plate-forme japonaise ADEOS-1. POLDER 1 /ADEOS 1, dont la durée de vie nominale était de 3 ans, a malheureusement cessé de fonctionner au bout de 8 mois, à la suite d'une panne du panneau solaire d'ADEOS.

L'originalité de POLDER, par rapport aux autres capteurs satellites, est sa capacité à caractériser complètement la composante électrique du rayonnement électromagnétique atteignant le capteur (intensité + état de polarisation linéaire) du spectre visible au spectre proche infrarouge, et son échantillonnage directionnel instantané rendu possible par son optique très large champ. POLDER restera un instrument innovant pour longtemps encore, car il est le premier radiomètre, en orbite autour de la terre, à caractériser complètement l'état de polarisation du rayonnement. La relève est en marche avec POLDER 2 en 2001 et PARASOL fin 2003. Le seul instrument américain polarisé est le scanner aéroporté RSP (Radiometer Scanning Polarimeter) développé au GISS (Goddard Institute of Space Studies) dont une version satellite, EOSP (Earth Observing System Polarimeter), serait prévue à l'horizon 2005.

Dans le cadre de ma thèse de 3^{ème} cycle (1990-1992), j'ai contribué au développement du modèle radiométrique et caractérisé les différents paramètres de ce modèle sur la version aéroportée développée au laboratoire. Ce modèle a été jugé suffisamment précis pour être repris, dans ces grandes lignes, dans la chaîne de traitement implantée dans le segment sol du CNES. J'ai également participé au développement de méthodes d'étalonnage en vol. Le grand champ de vue de l'instrument rendant difficile l'implantation d'un système d'étalonnage à bord du satellite, l'étalonnage de l'instrument repose sur une approche alternative profitant de certaines propriétés de l'atmosphère (claire ou nuageuse) et des surfaces terrestres. Dans cette première partie, le principe instrumental est rappelé et les méthodes d'étalonnage en vol, très spécifiques à POLDER, seront également présentées dans les articles (Hagolle et al, 1999 et Toubbé et al., 1999)

A) Principe instrumental

Rappelons le principe de l'instrument. POLDER est un polarimètre imageur CCD (Charge Coupled Device) grand champ (figure 1). L'avancée technologique dans le domaine des semi-conducteurs a permis, au cours de la décennie 1980, le développement des détecteurs CCD et a donné le jour à de nouveaux radiomètres tels que SPOT en 1986. Ce type de capteur fournit le même type de mesures qu'un scanner, mais en supprimant le balayage mécanique. POLDER est ainsi le premier radiomètre spatial équipé d'une matrice CCD (274x242 pixels). Il est également équipé d'une roue porte-filtres (filtres interférentiels par construction très stable en passage air-vide) qui présente 16 filtres devant la matrice CCD. À certaines longueurs d'onde, les filtres sont doublés de polariseur et, dans ce cas, le même filtre apparaît 3 fois avec des directions de polarisation décalées de 60°.

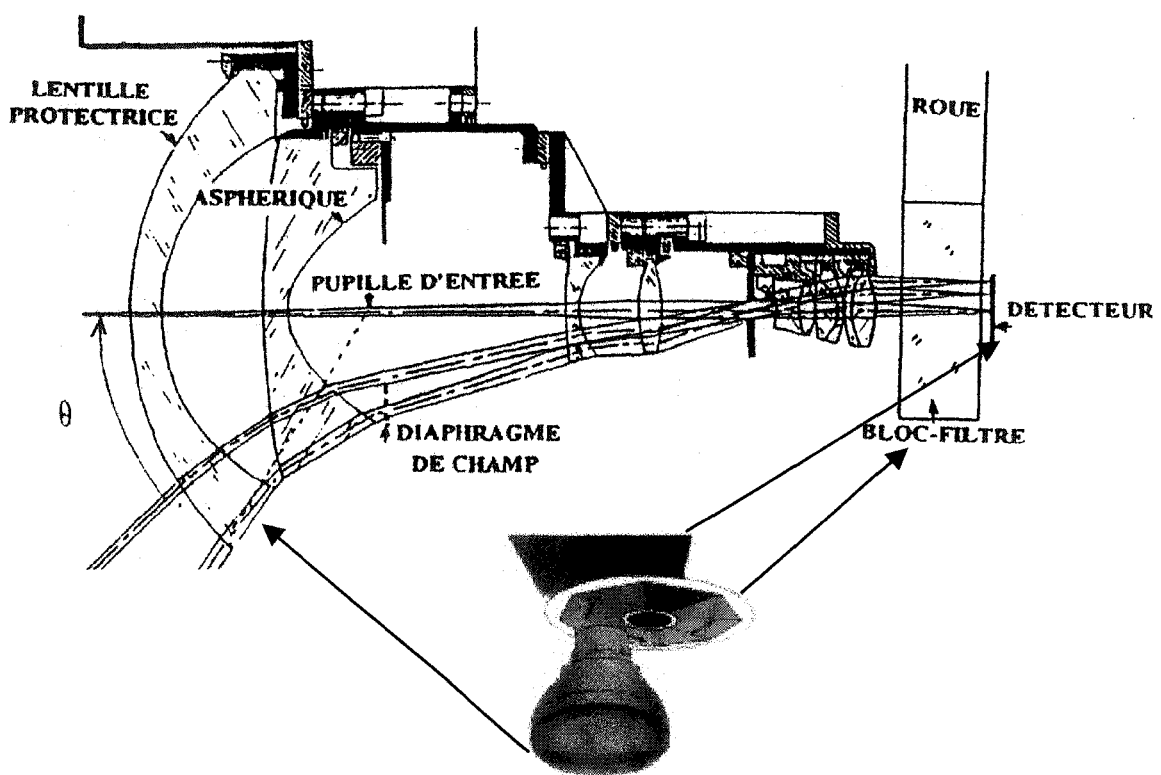


Figure 1 : Schéma de l'instrument.

Le système optique est composé d'un objectif télécentrique (figures 1 et 2) ce qui implique d'une part que les filtres sont traversés sous incidence normale et d'autre part que la pupille d'entrée asphérique compense la variation naturelle de la luminance en $\cos^4 \theta$. Cet objectif grand champ offre jusqu'à +/- 43° d'angle de visée le long de petit côté de la CCD, et +/- 51° selon le grand côté. La visée maximale, sur la diagonale de la matrice est de +/- 58°, ce qui, compte tenu de la rotundité de la terre, correspond, au sol, à +/- 70°, pour un satellite à 800km.

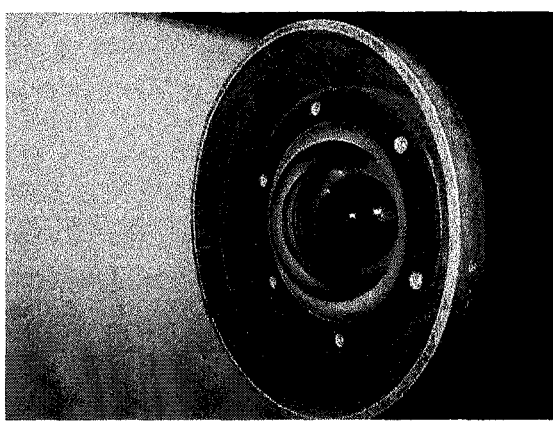


Figure 2a : Vue de l'objectif de POLDER (version aéroportée).

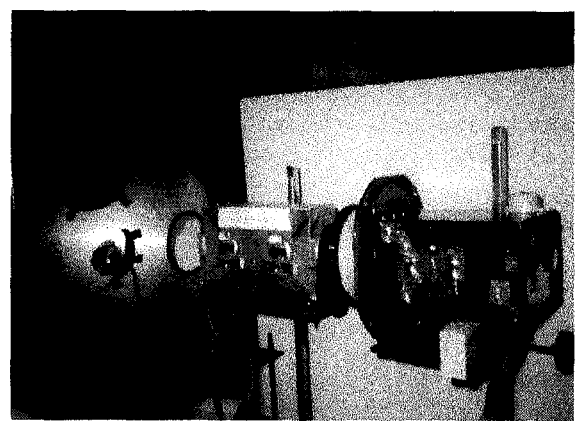


Figure 2b : POLDER (à droite) au cours d'un étalonnage en polarisation devant la sphère intégratrice (à gauche) et la boîte polarisante (au milieu).

Après avoir rappelé le concept instrumental, nous allons maintenant présenter, brièvement, le principe de la mesure ainsi que le modèle radiométrique.

B) Principe physique de la mesure

Illustrons simplement le principe de la mesure à l'aide de mesures acquises par le simulateur aéroporté au-dessus de la mer Méditerranée, pendant la campagne MEDIMAR en avril 1991. Les images de la figure 3 représentent les 3 voies polarisées à 865 nm. Elles correspondent respectivement à des directions du polaroïd de $+60^\circ$, 0° , -60° par rapport au petit côté de la matrice CCD. La tache intense observée sur les 3 images correspond au phénomène de « glitter » ou encore réflexion spéculaire du soleil sur le dioptrre air-eau. L'intensité de cette tache dépend principalement de l'angle solaire et de l'agitation de la surface (vent). Par réflexion sur la surface de l'eau, le rayonnement solaire incident non polarisé se polarise fortement perpendiculairement au plan d'incidence solaire.

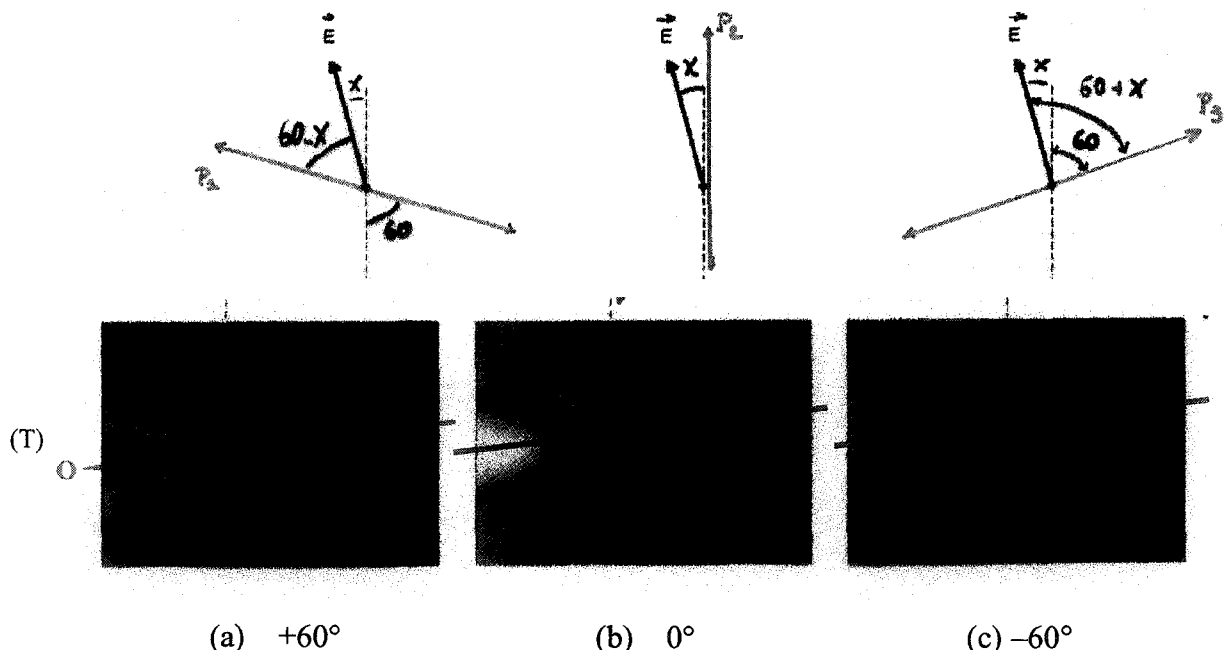


Figure 3 : Images associées aux 3 voies polarisées du canal 865 nm acquises pendant le survol de la Méditerranée.

Sur la figure 3, \vec{E} représente le vecteur champ électrique qui, dans le cas de la réflexion du soleil sur l'eau, est perpendiculaire au plan d'incidence (plan solaire). L'angle entre \vec{E} et la direction de l'axe passant du polariseur central (P_2) est noté χ . Si l'on représente l'évolution spatiale du signal sur les 3 voies, selon la radiale (T) placée dans le plan solaire, nous observons les signaux reportés sur la figure 4.

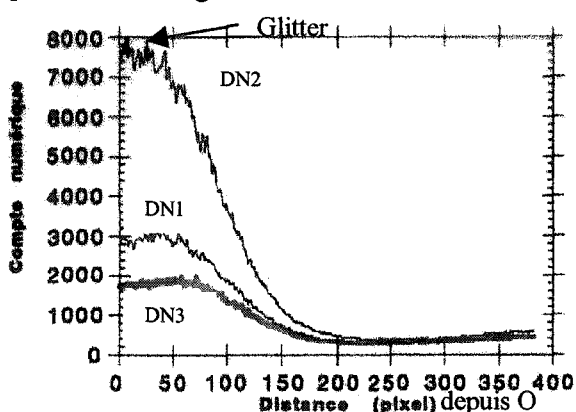


Figure 4 : Signaux mesurés sur les 3 voies polarisées du canal 865 nm (radiale (T))

La loi de Malus permet d'interpréter simplement les signaux observés et donne pour les 3 voies polarisées

$$\begin{aligned} DN_1 &= A \left(\frac{L_{nat}}{2} + L_{pol} \cdot \cos^2(60 - \chi) \right) \\ DN_2 &= A \left(\frac{L_{nat}}{2} + L_{pol} \cdot \cos^2 \chi \right) \\ DN_3 &= A \left(\frac{L_{nat}}{2} + L_{pol} \cdot \cos^2(60 + \chi) \right) \end{aligned} \quad (1)$$

L_{nat}, L_{pol} étant respectivement la composante naturelle et polarisée de la luminance totale L .

Le coefficient d'étalonnage A permet de traduire la sortie instrumentale, exprimée en compte numérique DN, en grandeur énergétique exprimée en luminance normalisée. On observe que le signal est maximum dans la tache du glitter sur la voie 2 car c'est pour cette voie que la projection du champ électrique sur la direction de l'axe passant du polariseur est maximale. La projection est plus faible sur la voie 1 et devient minimum sur la voie 3 pour laquelle le champ électrique de l'onde réfléchie sur le dioptre air-eau est presque perpendiculaire à la direction du polariseur. La combinaison des signaux DN_1, DN_2 et DN_3 et la connaissance de A permettent alors de déterminer la luminance polarisée L_{pol} , la luminance totale L ($L_{nat} + L_{pol}$) et la direction de polarisation χ . Dans la modélisation instrumentale et la modélisation du transfert radiatif, on préfère décrire le rayonnement par les paramètres de Stokes L, Q, U qui présentent l'avantage d'être des grandeurs additives ce qui n'est pas le cas de L, L_{pol} et χ .

C) Modèle radiométrique

Dans la pratique, on utilise le formalisme de Müller qui est mieux adapté aux paramètres de Stokes. Je résume, ci-après, en quelques mots le modèle radiométrique de l'imageur, en commençant par le cas de la mesure en lumière naturelle.

1. Modèle en lumière naturelle.

On montre que, pour une voie polarisé a ($a=1,2,3$), le signal numérique DN, fourni par l'instrument pour le détecteur élémentaire de coordonnées l,p et pour une luminance en entrée L_{lp} , est donné par

$$DN_{lp}^a = AT^a g_{lp}^a p_{(\theta)} \left(1 + \eta \epsilon_{(\theta)} \cdot \cos 2\alpha_a \right) L_{lp} \quad (2)$$

Le premier paramètre A, apparaissant dans cette modélisation et déjà cité plus haut, est le coefficient d'étalonnage absolu qui permet de convertir la sortie numérique DN en flux d'énergie incident (luminance).

Nous allons illustrer, très qualitativement, la signification des autres paramètres. Plaçons pour cela le capteur devant une sphère intégrante telle que celle présentée sur la figure 2b. Les images obtenues dans les trois voies polarisées d'une même longueur d'onde sont représentées sur les figures 5a,b,c.

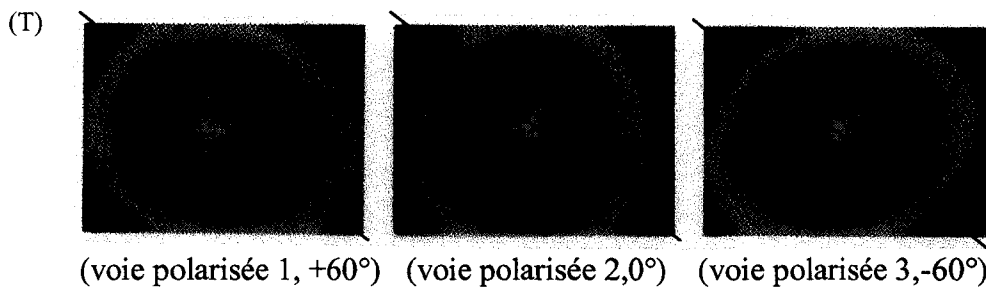


Figure 5 : Images obtenues pour 3 voies polarisées pour un éclairement incident non polarisé ($Q=U=0$) généré par la sphère intégratrice.

Une coupe diagonale, (T), réalisée sur ces 3 images, montre que les trois voies ne se superposent pas, même si l'éclairement qu'elles reçoivent est identique (Figure 6a).

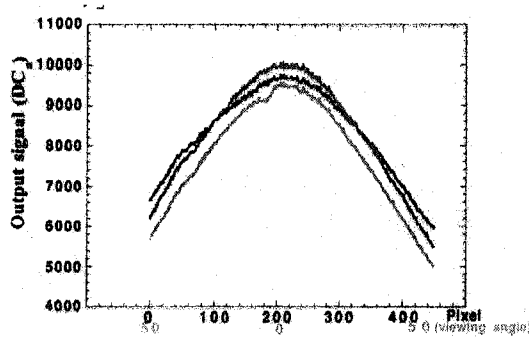


Figure 6a : Coupe sur les 3 voies polarisées

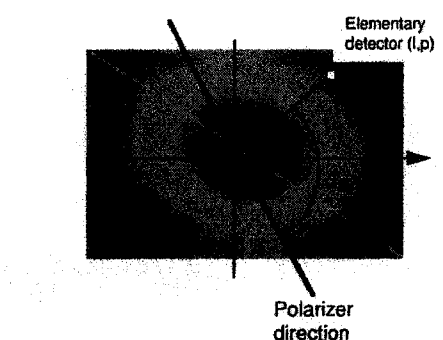


Figure 6b : Définition de l'angle α_a

La variation basse fréquence spatiale observée sur les 3 voies correspond à la variation de transmission, $p(\theta)$, de l'objectif en fonction de l'inclinaison, θ , du rayon incident par rapport à l'axe optique. Cette variation rend compte également de la polarisation intrinsèque de l'objectif, $\epsilon(\theta)$, créée par la traversée des différentes lentilles. Le terme $p(\theta) \cdot (1 + \eta \epsilon \cos 2\alpha_a)$, où η est l'efficacité des polaroïds, modélise l'ensemble de ces deux effets. L'objectif télescéntrique n'est pas parfait et son imperfection doit être caractérisée et prise en compte dans les corrections radiométriques. La figure 7 représente la polarisation induite par la traversée de l'objectif à 865 nm.

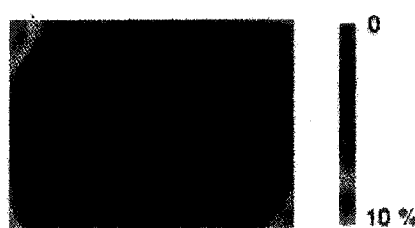


Figure 7 : Image de la polarisation induite par l'objectif à 865nm (version aéroportée de Polder).

Les variations de hautes fréquences spatiales, qui apparaissent également, sont liées à la sensibilité inter-détecteur. Chaque détecteur possède sa propre réponse qui doit également être mesurée. Ce terme est noté g_{lp} .

Au centre du champ ($\theta=0^\circ$), les signaux des 3 voies diffèrent jusqu'à 10%. Cet écart de transmission moyenne au centre du champ ne peut être attribué à la polarisation induite par l'objectif, cette dernière étant nulle en incidence normale. Elle s'interprète par des différences de transmission moyenne entre les trois blocs filtre-polariseur. Les rapports entre les transmissions moyennes, notés T_a , sont également mesurés avec précision et pris en compte dans les corrections radiométriques appliquées aux images.

Le dernier paramètre η , correspond à l'efficacité des polaroïds. Il est souvent proche de l'unité. Il est mesuré par ailleurs et également introduit dans l'algorithme de correction radiométrique.

2. Modèle en lumière Polarisée.

La généralisation du modèle au cas d'un rayonnement partiellement polarisé, représenté par ses paramètres de Stokes (L, Q, U), s'exprime à l'aide de 3 équations ($a=1,2,3$) de la forme

$$DN_{lp}^a = AT^a g_{lp}^a p_{(θ)} \left(p_{1,(θ)} L_{lp} + p_{2,(θ)} Q_{lp} + p_{3,(θ)} U_{lp} \right) \quad (3)$$

avec

$$p_{1,(θ)} = 1 + \eta \epsilon_{(θ)} \cdot \cos 2\alpha_a, \quad p_{2,(θ)} = \epsilon_{(θ)} + \eta \cdot \cos 2\alpha_a \quad \text{et} \quad p_{3,(θ)} = \eta \cdot \sin 2\alpha_a \quad (4)$$

Finalement, le modèle peut s'écrire, pour chaque détecteur élémentaire (l,p) de la matrice CCD, sous la forme matricielle suivante

$$\begin{pmatrix} DN_{lp}^1 \\ DN_{lp}^2 \\ DN_{lp}^3 \end{pmatrix} = [M] \begin{pmatrix} L_{lp} \\ Q_{lp} \\ U_{lp} \end{pmatrix} \quad (5)$$

où M est la matrice de transfert de l'instrument qui dépend des différents paramètres listés ci-dessus. Les corrections radiométriques se ramènent donc à connaître $[M]$ en chaque détecteur et à l'inverser pour en déduire les paramètres de Stokes incident. L'ensemble de ces paramètres est caractérisé en laboratoire avant le lancement.

Le très grand champ de vue de l'instrument rend très difficile et coûteux le développement de dispositifs d'étalonnage à bord du satellite. Il a donc été décidé de contrôler l'étalonnage à l'aide de méthodes utilisant des visées remarquables à la surface terrestre ou dans l'atmosphère (diffusion moléculaire, nuages, glitter océanique, sites désertiques,...). En ce sens, POLDER ouvre une nouvelle ère, car la richesse de ses observations lui offre la possibilité de suivre précisément en vol pratiquement tous les paramètres du modèle radiométrique.

D) Etalonnage en vol

Profitons de l'une des toutes premières images acquises par POLDER pour introduire les cibles remarquables utilisées pour suivre en vol les paramètres du modèle radiométrique. La figure 8 présente un exemple d'image obtenue à l'aide de POLDER1/ADEOS.

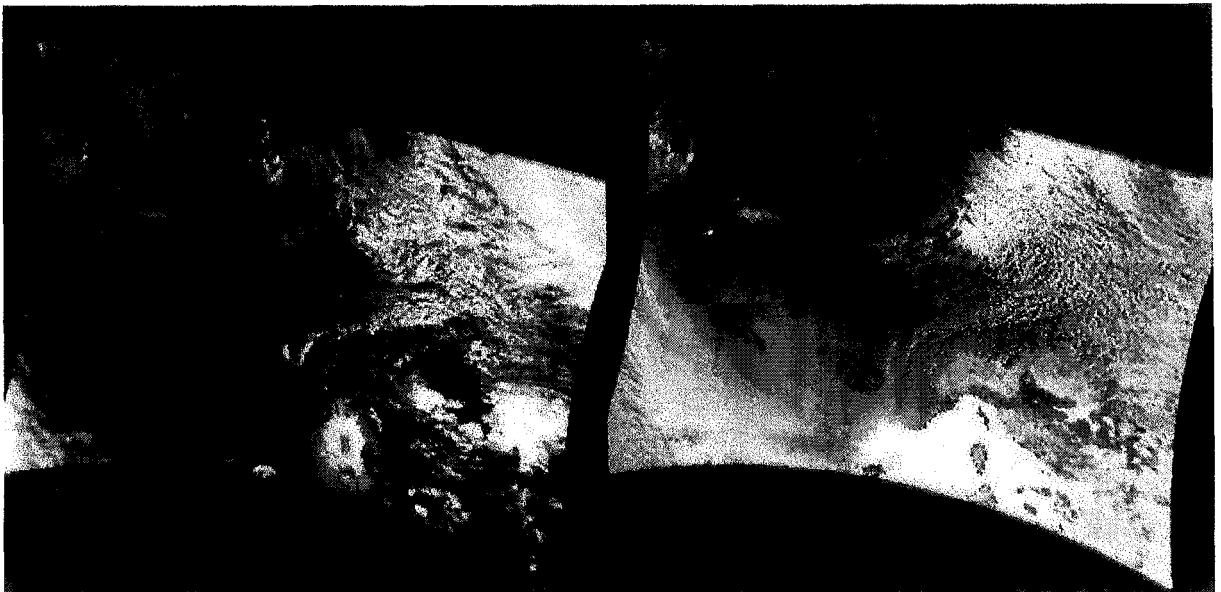


Figure 8 : Exemples d'images obtenues par POLDER. L'image (a) correspond à une image en luminance totale. L'image (b) correspond à la même scène observée en lumière polarisée. Les dimensions de l'image sont 2400km x 1800km, avec une résolution spatiale au sol de 6.2 km x 6.2 km. Les deux images résultent d'une composition colorée des canaux 443(bleu), 670 (vert) et 865nm (rouge).

Sur l'image en luminance totale, on distingue clairement les terres émergées et l'océan. On constate, au contraire, que ce contraste s'atténue fortement sur l'image en luminance polarisée. Ceci indique que la polarisation est plus caractéristique de l'atmosphère que de la surface. Les fortes valeurs de luminance et de polarisation observées sur la Méditerranée, près de la Corse, correspondent à la réflexion du soleil sur l'eau (« glitter ») déjà mentionnée (figure 3). La couleur blanche-jaunâtre s'explique par la neutralité spectrale de la réflexion de Fresnel. Cette propriété remarquable est utilisée pour contrôler l'étalonnage inter-bande de POLDER. L'étalonnage absolu, c'est-à-dire la détermination du coefficient A du modèle radiométrique, est réalisé, en vol, par visée océanique en conditions de ciel très pur. Dans ce cas, l'essentiel du signal provient de la diffusion moléculaire que l'on sait bien modéliser. Cependant, cet étalonnage ne peut être réalisé qu'aux courtes longueurs d'onde ($\lambda < 565\text{nm}$) pour lesquelles la diffusion moléculaire est suffisamment intense. L'étalonnage des plus grandes longueurs d'onde se fait, alors, par report de l'étalonnage « courte longueur d'onde » vers les grandes longueurs, au moyen d'un coefficient d'étalonnage inter-bande déterminé par une autre méthode. En l'absence d'atmosphère diffusante, la tache du glitter serait effectivement « blanche » dans le spectre considéré ici. Cependant, l'atténuation et la diffusion du rayonnement solaire par les molécules et les particules atmosphériques altèrent la neutralité spectrale du signal mesuré par le capteur. Afin de profiter de cette cible intrinsèquement blanche pour reporter l'étalonnage, il est nécessaire de corriger les mesures obtenus au niveau du satellite de l'effet de ces diffusions atmosphériques. Ceci est possible, sans aucune mesure exogène, grâce à la capacité directionnelle de POLDER (figure 9).

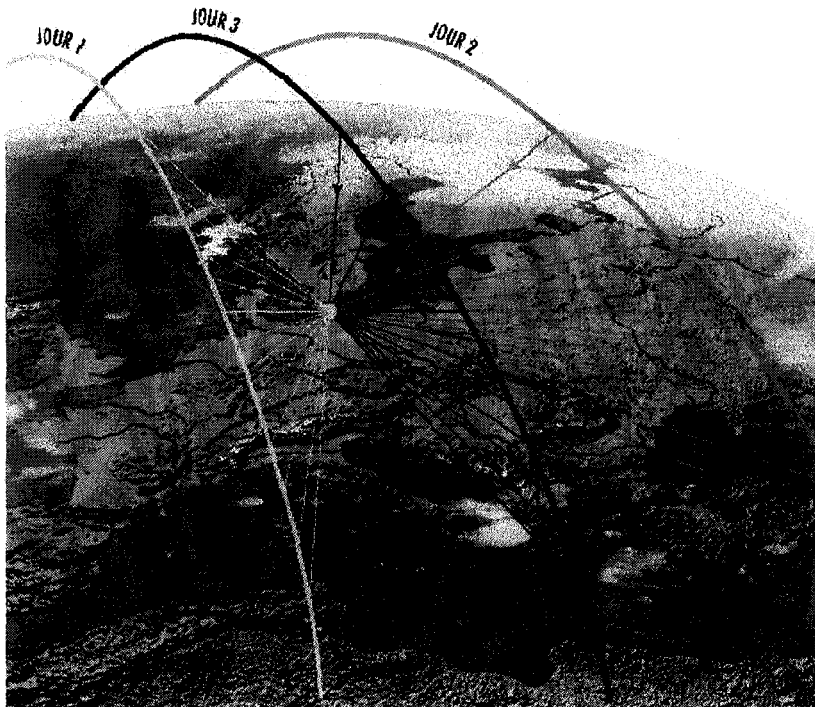


Figure 9 : Illustration des capacités directionnelles de POLDER. Un même point au sol (nord de l'Allemagne, sur la mer Baltique) est vu sous plusieurs directions de visée au cours de la même orbite. Son objectif grand champ permet à POLDER d'observer un même point au sol sous, au maximum, 14 directions d'observation distinctes et de façon quasi-instantanée (20s).

En effet, si un point particulier de la surface ou de l'atmosphère peut être observé dans les conditions spéculaires, quelques secondes plus tard, le même point de la surface ou la même colonne atmosphérique sera observé dans des conditions de visées proches de la rétrodiffusion pour lesquelles le signal observé est essentiellement d'origine atmosphérique. C'est à partir des ces visées « atmosphériques » que la contribution atmosphérique est estimée et corrigée, ensuite, dans la direction d'observation spéculaire afin de s'approcher, le plus possible, du signal spéculaire intrinsèquement « blanc » qui permettra de reporter l'étalonnage aux grandes longueurs d'onde (**P.1.1**).

La rayonnement solaire réflechi sur l'eau est fortement polarisé (maximale dans les conditions de Brewster pour une surface parfaitement plane). Cette seconde propriété est également utilisée pour suivre l'étalonnage en polarisation pour les fortes valeurs de la polarisation. Dans ce cas, c'est le paramètre η du modèle qui peut-être déterminé en vol. Pour les mêmes raisons que précédemment, il importe de caractériser l'atmosphère en dehors des visées « glitter » pour en corriger l'effet dans la direction du glitter. La mise au point de la méthode et sa validation sur des mesures aéroportées sont présentées dans la publication **P. 1.2** et ses performances en orbite dans **P. 1.1**.

Les masses nuageuses présentes au-dessus du nord-est de l'Europe polarisent également la lumière, mais à un niveau nettement moindre. D'autres nuages, visibles au-dessus de la mer Adriatique, apparaissent beaucoup plus sombres en polarisation. Dans cette géométrie, les nuages génèrent par diffusion un rayonnement très faiblement polarisé. Il est alors possible de s'en servir pour contrôler les performances de l'instrument à bas niveau de polarisation. Les paramètres T^a et la polarisation de l'objectif ϵ peuvent ainsi être suivi en vol, à l'aide d'observation nuageuse, pour des géométries d'observations particulières. Les figures 10a et

10b sont, à l'instar de la figure 8, des compositions colorées d'images acquises pendant la campagne ACE-2 (Aerosols and Clouds Experiment) à la fin du mois de juin 1997, au large des Canaries.

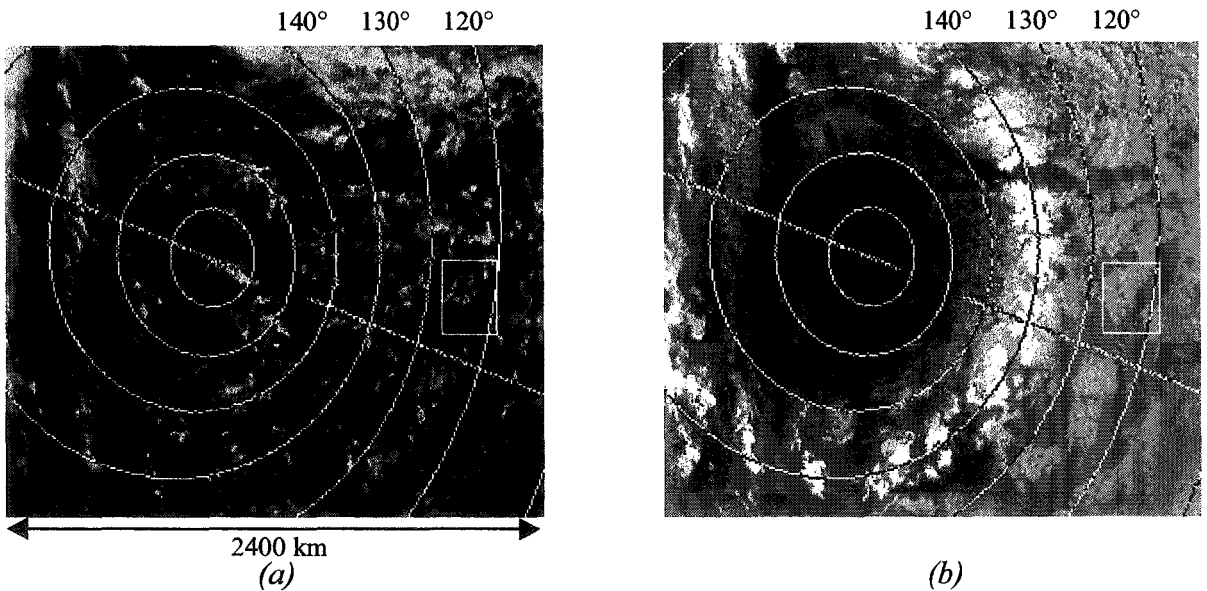


Figure 10 : Images POLDER/ADEOS du 26 juin 1996. (a) luminance totale, (b) luminance polarisée. Orbite 8437, séquence 44. Les lignes circulaires blanches indiquent les angles de diffusion par pas de 10° . Le plus petit rayon correspond à un angle de diffusion de 170° . La ligne droite matérialise le plan principal solaire.

La figure 11 représente un zoom des images acquises par le simulateur aéroporté POLDER survolant à 4.5 km d'altitude le banc de nuages délimité par le rectangle blanc sur la figure 10.

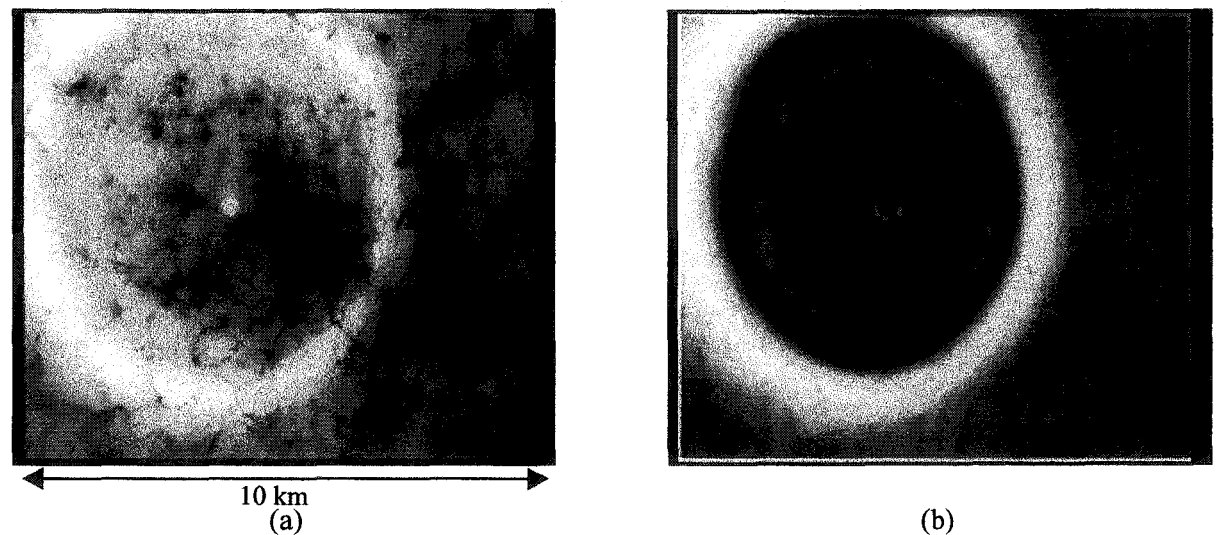


Figure 11 : Images acquises par le simulateur POLDER aéroporté le 26 juin dans la zone ACE-2 ($\text{Lat}=29.5^\circ\text{N}$, $\text{Lon}=16.9^\circ\text{W}$). (a) image en luminance totale à 865nm, (b) image en luminance polarisée. L'altitude de l'avion est 4500 m.

On distingue sur les figures 10 et 11 un anneau polarisé vers 140° (c'est l'arc-en-ciel). Dans l'exemple présenté, le contraste angulaire en luminance est suffisant (nuage fin) pour que l'anneau soit également observable. En présence de particules diffusantes de forme sphérique, il est, par contre, toujours observable en polarisation. En dehors de cette géométrie d'observation bien particulière, nous constatons que les nuages polarisent peu, voire pas du tout.

tout, constituant ainsi une source intense de lumière naturelle permettant de contrôler en orbite les paramètres T^a et ϵ dans les 3 canaux polarisées de POLDER. L'accumulation d'observations nuageuses dans la géométrie adéquate permet de déterminer en orbite les coefficients T^a et de re-générer à partir d'observations géophysiques une image ϵ similaire à celle présentée sur la figure 7. Cependant, dans le canal à 443nm, les méthodes restent moins précisent à cause de la contribution parasite des molécules de l'atmosphère libre qui se trouve au-dessus des nuages observés. Notons que les propriétés polarisantes des nuages sont directement reliées à leurs propriétés microphysiques. Ce point particulier sera abordé en détail dans le chapitre 3 de ce document.

Enfin, la polarisation « bleue » observée au-dessus de l'océan Atlantique indique une forte composante polarisée dans le canal 443nm. La diffusion par les molécules (diffusion « Rayleigh ») polarise également le rayonnement solaire incident. Cette propriété peut également être utilisée pour contrôler l'étalonnage absolu et la polarisation.

Pour terminer, un mot sur la précision de relocalisation. La relocalisation géographique est d'un pixel, soit près de 6.2 km. Les écarts de localisation entre les 3 voies polarisées d'une même longueur d'onde et entre deux longueurs d'onde sont de l'ordre de 1/10 de pixel, soit 600m et les écarts entre les différentes directions de l'ordre de 2/10 de pixel.

Les précisions radiométriques sont, quant à elles, présentées dans les articles qui suivent (**P. 1-1 et P. 1-2**)

Publications relatives au chapitre 2.

P. 1.1 Hagolle O , P. Goloub , P.Y. Deschamps, T.Bailleul, J.L. Deuzé, M. Herman, J.C.. Buriez, X. Briottet. "POLDER in-flight calibration results ", *IEEE Transactions on Geosci. Em.Sensing*, Vol 37, N 3, May 1999, pp 1550-1566.

P. 1.2 Toubbé B., T Bailleul, JL Deuzé, P Goloub, O. Hagolle and M. Herman "In-flight calibration of the POLDER polarized channels using the sunglint", *IEEE Transactions on Geosci. Em.Sensing*, Vol 37, N 1, January 1999, pp 513-525.

Contrats

Goloub P., Deuzé J.L., Herman M, "Etude du modèle radiométrique de POLDER". Rapport contrat CNES n° 833-2-91-0094, 1992.

Goloub P., Deuzé J.L., Herman M., "POLDER interband calibration, using the sunglint". Rapport de contrat CNES n° 833-2-91-0151, 1992.

Goloub P, M Herman, O Hagolle, 1996: "Etalonnage en vol de l'instrument POLDER. Suivi de la polarisation". Rapport contrat CNES n° 95/1956/00., 1996.

P. 1.1.

POLDER in-flight calibration results

Results of POLDER In-Flight Calibration

Olivier Hagolle, Philippe Goloub, Pierre-Yves Deschamps, Hélène Cosnefroy, Xavier Briottet, Thierry Bailleul, Jean-Marc Nicolas, Frédéric Parol, Bruno Lafrance, and Maurice Herman

Abstract—POLDER is a CNES instrument on board NASDA's ADEOS polar orbiting satellite, which was successfully launched in August 1996. On October 30, 1996, POLDER entered its nominal acquisition phase and worked perfectly until ADEOS's early end of service on June 30, 1997. POLDER is a multispectral imaging radiometer/polarimeter designed to collect global and repetitive observations of the solar radiation reflected by the earth/atmosphere system, with a wide field of view (2400 km) and a moderate geometric resolution (6 km). The instrument concept is based on telecentric optics, on a rotating wheel carrying 15 spectral filters and polarizers, and on a bidimensional charge coupled device (CCD) detector array. In addition to the classical measurement and mapping characteristics of a narrow-band imaging radiometer, POLDER has a unique ability to measure polarized reflectances using three polarizers (for three of its eight spectral bands, 443 to 910 nm) and to observe target reflectances from 13 different viewing directions during a single satellite pass.

One of POLDER's original features is that its in-flight radiometric calibration does not rely on any on-board device. Many calibration methods using well-characterized calibration targets have been developed to achieve a very high calibration accuracy. This paper presents the various methods implemented in the in-flight calibration plan and the results obtained during the instrument calibration phase: absolute calibration over molecular scattering, interband calibration over sunglint and clouds, multi-angular calibration over deserts and clouds, intercalibration with Ocean Color and Temperature Scanner (OCTS), and water vapor channels calibration over sunglint using meteorological analysis. A brief description of the algorithm and of the performances of each method is given.

Index Terms—Atmosphere, calibration, in-flight, optical remote sensing, vicarious.

ACRONYMS

ADEOS	Advanced Earth Observing Satellite.
ATSR2	Along Track Scanning Radiometer-2.
BRDF	Bidirectional reflectance distribution function.
ECMWF	European Center for Mean-Range Weather Forecast.
ERS2	European Remote-Sensing Satellite 2.
LUT	Look-up table.
MISR	Multiangle Imaging Spectro-Radiometer.

Manuscript received April 16, 1998; revised January 25, 1999. The results presented in this paper were obtained using data from CNES's POLDER on board NASDA's ADEOS. The ECMWF meteorological data was provided by Meteo France.

O. Hagolle and B. Lafrance are with the Centre National d'Etudes Spatiales (CNES), 31055 Toulouse Cedex France (e-mail: Olivier.Hagolle@cnes.fr).

P. Goloub, P.-Y. Deschamps, T. Bailleul, J.-M. Nicolas, F. Parol, and M. Herman are with the Université des Sciences et Technologies de Lille, Laboratoire d'Optique Atmosphérique, Lille, France.

H. Cosnefroy and X. Briottet are with the Office National d'Etudes et Recherches Aerospatiales, Département d'Optique Théorique et Appliquée, Toulouse, France.

Publisher Item Identifier S 0196-2892(99)03569-X.

MODIS	Moderate-Resolution Imaging Radiometer.
OCTS	Ocean Color and Temperature Scanner.
POLDER	Polarization and directionality of earth reflectances.
SeaWiFS	Sea-Viewing Wide Field-of-View Sensor.
SPOT	Satellite pour l'Observation de la Terre (earth observing satellite).
SOS	Successive orders of scattering.
TOA	Top of atmosphere.

I. INTRODUCTION

RADIOMETRIC calibration accuracy is one of the major elements contributing to the quality of the measurements obtained with optical remote sensing instruments. This radiometric calibration can be obtained through preflight measurements in optical laboratories, but the accuracy of these measurements is not perfect (precise radiance calibration is a difficult subject, and extraterrestrial solar irradiance is not perfectly known). Moreover, the instruments are subject to degradation after launch because of the aging of the optics or of the outgassing which occurs when the instrument leaves the atmosphere. To cope with this problem, many spaceborne instruments are equipped with on-board calibration devices. SPOT satellites [22] have an inner lamp and an optical fiber system to observe the sun. Actually, the inner lamp is used only for multitemporal monitoring of the instrument sensitivity and for detector normalization. The solar observations are affected by a difficult preflight calibration of the system itself and by a slow degradation of the optical fibers. SPOT calibration relies now mainly on natural targets. OCTS on board ADEOS is also equipped with inner lamps and a solar observation system: but the OCTS calibration provided by these devices is not very accurate because of degradation of the lamps after the launch and of nonuniformity in the mirror which allows observation of the sun. These problems lead to the decision of using natural targets for OCTS calibration [26]. ATSR2 on board ERS2 is also equipped with a visible sun-observing calibration device which is operationally used but needs to be completed by multitemporal calibration over desert sites to correct a drift of the solar calibration signal [34]. Many future instruments have also based their calibration mainly on on-board devices, such as SeaWiFS, MODIS, and MISR on-board EOS AM-1, but are also developing vicarious methods in order to verify the on-board device [33].

The POLDER project team has decided to avoid the development of an on-board calibration system. Past experiences of on-board calibration devices in CNES with SPOT satellites have failed to provide accurate results, and vicarious

TABLE I
SPECTRAL BAND CHARACTERISTICS FOR THE POLDER INSTRUMENT ABOARD THE ADEOS-1 SATELLITE. THIS TABLE DIFFERS FROM THE FIGURES PREVIOUSLY PUBLISHED IN [9], WHICH WERE BASED ON EARLY BUDGETS

POLDER band	443	443	490	565	670	763	765	865	910
Central Wavelength (nm)	444.5	444.9	492.2	564.5	670.2	763.3	763.1	860.8	907.7
Band Width (nm)	20	20	20	20	20	10	40	40	20
Polarization	Yes	No	No	No	Yes	No	No	Yes	No
Saturation level (normalized radiance)	1.1	0.97	0.75	0.48	1.1	1.1	1.1	1.1	1.1

methods using natural targets were necessary to obtain the required absolute calibration. Moreover, the implementation of a calibration system in POLDER compact design would have been expensive and hazardous in case of failure, and it was difficult to build a device that could have covered the entire POLDER bidimensional field of view. To compensate for the lack of an on-board calibrating source, lots of effort has been invested in the development of a very stable instrument [1], in an exhaustive and accurate preflight calibration [3], and in the adaptation and enhancement of calibration methods over natural targets.

Such methods have been intensively used to calibrate AVHRR/NOAA or METEOSAT and have achieved good results [24], [36], [38] using natural targets such as molecular scattering over ocean for absolute calibration, high altitude clouds, or ocean sunglint for interband calibration and desert sites. The POLDER calibration plan adapts all these methods to make use of the multidirectional and polarization measurements of the instrument. New calibration methods have also been introduced to characterize the POLDER sensitivity to polarization [43].

II. THE POLDER INSTRUMENT ON ADEOS

The POLDER radiometer design consists of three principal components: a charge coupled device (CCD) matrix detector, a rotating wheel carrying the polarizers and spectral filters, and a wide field of view (FOV) telecentric optics [9], [21]. The optics has a focal length of 3.57 mm, opening to f/4.5 with a maximum FOV of 114°.

The CCD sensor array is composed of 242 × 274 independent sensitive areas. The total array detection unit size is 6.5 × 8.8 mm², which corresponds to along-track and cross-track field-of-view of ±43° and ±51°, respectively, and to a diagonal FOV of ±57°. The spectral sensitivity of the CCD array extends between 400 and 1050 nm.

The rotating wheel, which rotates steadily with a period of 4.9 s, carries the interference filters and polarizers that select the spectral band and polarization direction. It carries 16 slots, including an opaque filter to estimate the CCD detector dark current. The remaining 15 slots carry six unpolarized and nine polarized filters (three polarization directions for three different wavelengths). Thus, POLDER acquires measurements in nine bands, three of which are polarized. POLDER filters have been designed to avoid any spectral variation of the filters when passing from air to vacuum (filters are made with an ion-assisted deposition technology). This characteristic is the

key for an accurate in-flight calibration, since the sensitivity of the bands measured before launch is still valid after launch.

A. Spectral Bands

POLDER has nine spectral bands ranging from 443 nm. Two of these spectral bands are centered on molecular absorption bands: 763 (O₂) and 910 (H₂O). The nine bands are defined by their central wavelength, spectral width and polarization capability. The saturation levels are given in Table I in terms of normalized radiance, i.e., the maximum spectral radiance divided by the solar spectral irradiance at nadir and multiplied by π . The saturation level in reflectance is subsequently obtained by dividing the value given in Table I by $\cos \theta_s$, where θ_s is the solar zenith angle. Owing to the significant noise requirements for ocean color measurements, the 443 nm channel had to be split into a polarized band (three filters: 443P) and an unpolarized band (one filter: 443NP).

B. Polarization Measurements

For three of the nine spectral bands (443, 670, and 763 nm), a polarizer is added to the filters in order to assess the degree of linear polarization and the polarization direction. These parameters are derived by combining measurements in three channels with the same spectral filters but with polarizer axes turned by steps of 60°. The three polarization measurements in a spectral band are successive and have a total time lag of 0.6 s between the first and the third measurement. In order to compensate for spacecraft motion during the lag and to register the three measurements, a wedge prism is used in each polarizing assembly. As a consequence, the matrix image is translated in the image plane to offset the satellite motion, and the three polarization measurements are collocated.

C. Spatial Resolution

The ground size or resolution of a POLDER-measured image from ADEOS is 6 × 7 km² at nadir. Due to the earth curvature, the pixel size depends slightly on the viewing angle, leading to an increase of 21% for an incidence angle of 60°.

D. Data Acquisition

The POLDER instrument is in imaging mode on the sun-synchronous part of the ADEOS orbit only. Data acquisition starts at the time when the solar zenith angle on the earth surface at the sat-

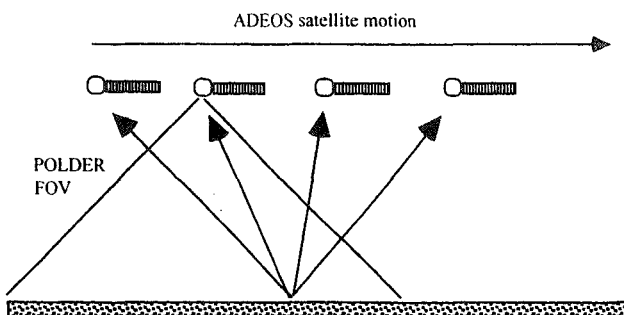


Fig. 1. POLDER multidirectional viewing principle. Owing to its bidimensional wide field of view, POLDER has the ability of looking at the same point on the ground from different viewing angles during a single orbit.

nadir is smaller than 75° and stops, in the south, when it is larger than 75° . The 16-filter sequence is repeated every 19.6 s. During this interval, a given point on the surface, initially at nadir viewing, moves by about 9° relative to the satellite (Fig. 1). The point remains within the POLDER field of view. As the satellite passes over a target, about 12 (up to 14) directional radiance measurements (for each spectral band) are performed aiming at the point. Therefore, POLDER successive observations allow the measurement of the bidirectional reflectance properties of any target within the instrument swath.

ADEOS is on a sun synchronous orbit at an altitude of 797 km. Thanks to POLDER's very wide field of view, each point on the earth is observed by POLDER every day, except near the equator where one point is only observed four days out of five. Combining all the viewing directions obtained during a one-week period, a very complete sampling of any target's BRDF can be obtained.

III. PREFLIGHT CALIBRATION

A. Radiometric Model

The aim of the radiometric model of the instrument is to give a synthetic but totally representative description of the physics of the instrument. It characterizes completely the response to the incoming polarized light for each pixel of the CCD matrix, in each spectral band. This model has been described in Hagolle *et al.* [15], as well as the inversion of the Stokes parameters. Since polarization is not the purpose of this paper, we present here the simplified POLDER radiometric model, which can be used to retrieve the first Stokes parameter, once all the polarization effects have been removed. Let I , the normalized total radiance, be defined as

$$I = \pi \cdot \text{radiane/solar irradiance.}$$

The Stokes parameters are expressed in normalized radiance units, because accurate calibration of normalized radiances is easier than direct calibration of radiances. A unique solar spectral irradiance profile has been adopted by POLDER project (the solar spectrum recommended by the World Meteorological Organization [41]), and POLDER in-flight absolute calibration is, in fact, a relative calibration to this solar irradiance profile.

The radiometric model can be written

$$DN_{lp}^k = A^k \cdot R_{lp}^k I_{lp}^k \quad (1)$$

where

- l, p line and column numbers of the CCD array;
- k spectral band number;
- DN_{lp}^k digital number measured by the elementary detector (l, p) with a quantization over 12 bits;
- I_{lp}^k normalized radiance observed by (l, p) ;
- A^k absolute calibration coefficient, which accounts for the conversion of normalized radiance units into digital numbers;
- R_{lp}^k multiangular calibration coefficient: it corresponds to sensitivity variations within the instrument field of view, coming either from the elementary detectors or from the optics.

7)

This parameter is not easy to measure in-flight and has been split into three terms, and a different in-flight calibration method is used for each term. This is explained in Section IV-B.

B. Preflight Calibration

POLDER preflight calibration [3] gives rise to two main difficulties: 1) the calibration of a bidimensional very wide field of view and 2) the characterization of the polarization sensitivity in the whole field of view. The accuracy of preflight calibrations relies on the following important hardware.

- *Two Integrating Spheres:* A large integrating sphere for the calibration measurements and a transfer integrating sphere in order to check the air/vacuum stability of the absolute calibration, to control the stability of the reference radiometer and to determine the large integrating sphere nonuniformity.
- A polarizing system which enables the generation of different polarization rates and directions. It is made up of two parallel glass plates which can be oriented around two axes.
- A reference radiometer fitted with filters identical to POLDER ones. The radiometer is used for absolute calibration and has been calibrated with each of the filters in L.C.I.E. (Laboratoire Central des Industries Electriques). This calibration has been operated against a spectrally calibrated source: a standard incandescent lamp and a BaSO₄ plate with a good uniformity, and a standard radiometer. The estimated accuracy of this calibration is $\pm 3.5\%$.
- A monochromator to measure the spectral response of the instrument; the rotation of the grating is synchronous with the instrument imaging cycle, and the emission stability of the lamp is checked all along the measurement. The stability of the response over several measurements is better than 1% and the variation of the center of the spectral profile is less than 0.3 nm.

The evaluated accuracy of the preflight absolute calibration is 5%. The relative calibration performances are divided in two parts: the high spatial frequency is determined with an

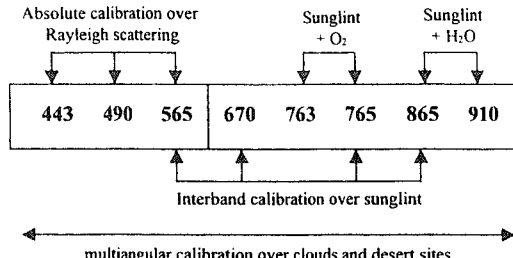


Fig. 2. Schematic view of the nominal calibration methods.

uncertainty of 0.1%, while the low spatial frequencies are obtained with an uncertainty of 1% (because of residual errors in integrating sphere nonuniformity correction). Absolute calibration and thus spectral responses of the filters did not vary when measurements were made in a vacuum chamber. Preflight calibration was also successfully compared to OCTS calibration through a round robin of both projects' calibrating radiometers [29]. However, it was foreseen that because of the ultraviolet irradiation of the external lenses, a slight decrease in the sensitivity of POLDER blue spectral bands could occur (10% maximum for 443 nm band after three years, but less than 1% for 670). From all these arguments, it appears that POLDER calibration should only vary slightly after launch but needs to be monitored in-flight to comply with its strict calibration requirements.

IV. INFLIGHT RADIOMETRICAL CALIBRATION: NOMINAL METHODS

In order to ensure good in-flight radiometric performances, each calibration parameter of the radiometric model can be measured and monitored using various in-flight calibration methods. Absolute calibration methods (Section IV-A) aim to measure the A^k parameter, while multiangular calibration methods (Section IV-B) measure the $p^k(\theta)$ and $g^k p$ parameters. Polarization calibration methods are presented in Goloub *et al.* [13] and Toubb   *et al.* [43].

Among the various calibration methods that were considered in the preliminary studies for POLDER in-flight calibration, one method for each parameter was chosen as the nominal method (the one having the best error budget). The other methods are used as validation methods to control the results of the nominal methods. This chapter details the procedure, the error budget computed before launch, and the in-flight results for each nominal method. A schematic view of the nominal calibration methods is given in Fig. 2.

A. Absolute Calibration

POLDER absolute calibration is achieved through an absolute calibration of the "blue" spectral bands (443P, 443, 490, 565) using the well-characterized Rayleigh scattering signal over ocean. This absolute calibration is then transferred to the other wavelengths through interband calibration using the specular reflection of the sun over the ocean.

1) Absolute Calibration over Rayleigh Scattering:

a) *Method:* The scattering of light by the air molecules (Rayleigh scattering) over ocean is a bright and well-

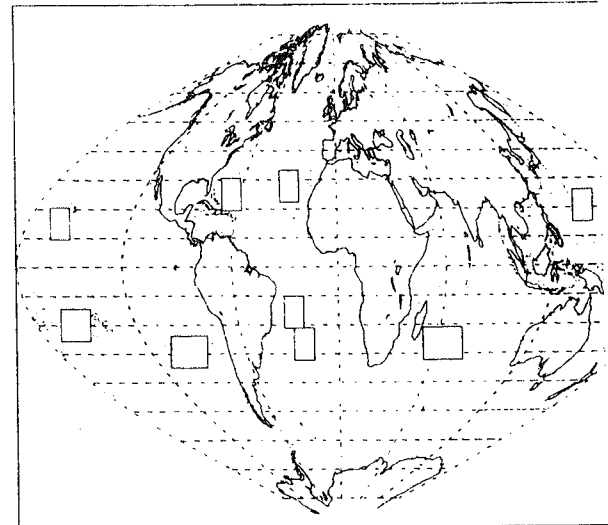


Fig. 3. The boxes on the map are the zones with low chlorophyll concentration where the calibration points for the Rayleigh method are chosen.

characterized target in the lower POLDER spectral (443P to 565 spectral bands). For given viewing and angles, the Rayleigh scattering can be accurately predicted by radiative transfer codes, and the radiance observed over the ocean depends mainly on water-leaving radiance, foam presence, and aerosol amount. The uncertainty that comes from the parameters can be reduced through a strict selection of pixels used for calibration. The calibration points are selected among POLDER data according to criteria defined to minimize the nonmolecular contribution to the measured signal. They are chosen inside oligotrophic geographic areas having an average well-known weak and stable chlorophyll content (oligotrophic waters), with no clouds, a low wind speed, and a low atmospheric optical thickness. (Fig. 3 shows the geographical zones.

Cloudy pixels are eliminated using a cloud screening on the 865-nm radiance, and meteorological data (ECMWF) are used to select zones with a low wind speed ($<5 \text{ ms}^{-1}$). The aerosol content is estimated using the channel 865 nm: the observations with a normalized radiance under 0.002 (subtraction of Rayleigh scattering contribution) are selected for calibration.

Our calibration method is derived from Vermote *et al.*. The preflight/in-flight variation of the calibration coefficient is obtained through the formula

$$\Delta A^k = \frac{A_{\text{in-flight}}^k}{A_{\text{preflight}}^k} = \frac{MI^{k, oz}}{I^k(v_w) + T^{k, 865} \cdot (MI^{865} - I^{865})}$$

where

- $MI^{k, oz}$ is the normalized radiance measured by POLDER (level 1 product with preflight calibration) in a band k among {443, 490, 565}. This radiance has been corrected for ozone absorption as described in Appendix;

- $I^k(v_w)$ is the radiance that would be observed above a pure molecular atmosphere. It is a function of geometric conditions, chlorophyll concentration, and wind speed v_w . The LUT's are obtained with the SOS code.

TABLE II
MARINE REFLECTANCES USED FOR RAYLEIGH CALIBRATION

Spectral Band	Chlorophyll concentration : 0.17 mg/m ³	Chlorophyll concentration : 0.035 mg/m ³
443	0.0212	0.0344
490	0.0174	0.0193
565	0.0052	0.0037

Two “extreme” chlorophyll contents ($0.035 \text{ mg} \cdot \text{m}^{-3}$ and $0.17 \text{ mg} \cdot \text{m}^{-3}$) are systematically considered for these areas, and the associated water reflectance (Table II) is estimated using the Morel model [23] updated by using new pure water absorption coefficients [27];

- $T^k, 865$ is a unitless LUT, function of the viewing geometry, which expresses the ratio between the aerosol contribution in spectral band k and aerosol contribution at 865 nm. This LUT is computed with SOS for two aerosol models [32]: a coastal model with 70% humidity (C70) and a marine model with 98% humidity (M98). These models consist of a mixture of sea-salt component and continental component with a log-normal distribution. M98 is an open-sea aerosol model with more sea-salt components than C70, and with a flatter spectral dependence.

b) *Error budget:* The main error sources for the theoretical error budget are listed below.

- TOMS measures the ozone amount with an accuracy of 10 Dobson units. The resulting uncertainty on the calibration coefficient is of 0.5% on 565-nm channel, and far less for 490- and 443-nm channels.
- The wind speed modifies the sunglint geometry and the contribution of the photons scattered by the atmosphere after their reflection over the sea-surface. The uncertainty on wind speed (ECMWF meteorological data) is 2 m/s and induces a 0.5 to 1.5% calibration error on the three channels.
- The surface pressure (meteorological data) is accurately known. (Its bias is estimated under 1 hPa.) This leads to a 0.1% uncertainty on the three channels.
- Aerosol amounts and properties cannot be obtained from external data, but 865 channel is used to discard turbid atmospheres or to estimate aerosol contribution on clear ones. For this error budget, simulations were performed with an aerosol model different from the one used as reference for computing the LUT. These simulations show that the impact of the aerosol model on calibration coefficients is always under 1%. Calibration errors in the 865-nm band also result in some errors in the aerosol correction: a 5% error for 865-nm calibration induces a 1% error on 565 and less for 443 and 490.
- The water-leaving radiance is the main uncertainty for the channel 443. According to bio-optical models and if assumptions on phytoplankton concentrations are globally verified, an error of 50% on the chlorophyll concentration leads to an uncertainty on calibration coefficient up to 2% for 443 nm channel.

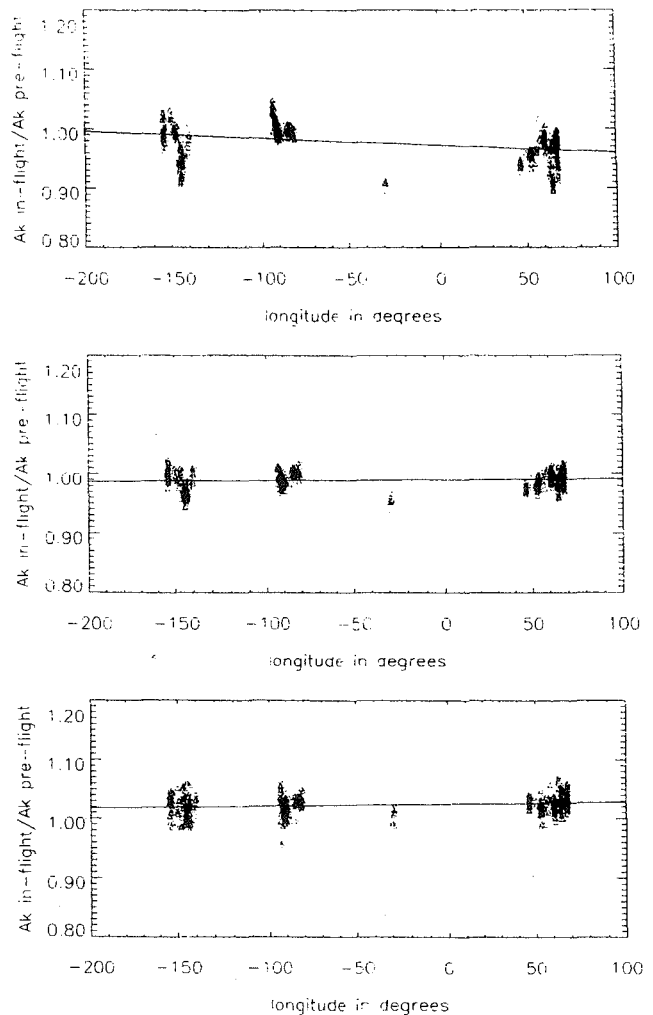
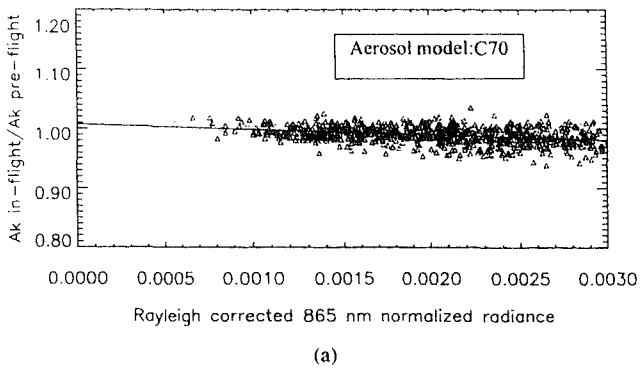


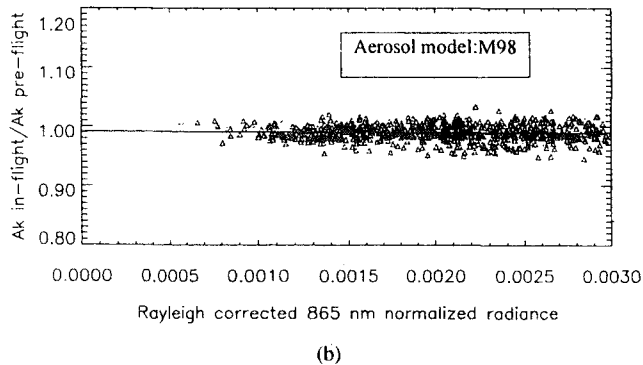
Fig. 4. Absolute calibration elementary results for Rayleigh scattering method as a function of the longitude (with C70 aerosol model and a chlorophyll concentration of $0.035 \text{ mg} \cdot \text{m}^{-3}$). Each grey level corresponds to a different location or date of acquisition of the calibration points. All dates are within the first week of November. For 443 nm, the dispersion of the results inside a given site is lower than the dispersion from one site to another. This fact is related to the high variability of water-leaving radiances as a function of chlorophyll concentration. From top to bottom, Rayleigh scattering is 443 nm, 490 nm, 565 nm.

All these uncertainties lead to a 4% maximal error for 443 and 3% for 490 and 565 channels.

c) *Results:* For each selected calibration point, an elementary calibration result ΔA^k is computed for channels 443, 490, and 565: using all the POLDER level 1 products obtained during one week (100 orbits), more than 200 000 elementary results are collected. It is interesting to analyze how the individual measurements vary with the various parameters of the algorithm. Fig. 4 shows that channel 443 is far more sensitive to the variations of chlorophyll concentration with the calibration sites (4% standard deviation for 443) than channels 490 and 565, because water reflectance variation as a function of the chlorophyll content is high at 443 nm and lower around 500 nm. Fig. 5 shows that the estimated calibration coefficients do not depend on the aerosol amount determined with POLDER 865 nm measurements, when the proper aerosol model is used. According to the aerosol model



(a)



(b)

Fig. 5. Absolute calibration elementary results for Rayleigh scattering method, as a function of the Rayleigh corrected 865 nm radiance, for two different aerosol models (a) C70 and (b) M98 (modeled radiances simulated with a chlorophyll concentration of $0.035 \text{ mg} \cdot \text{m}^{-3}$). The 865-nm radiance is used to determine the effect of the aerosols in the calibrated band. Calibration coefficient and 865-nm radiance are correlated in (a) but not in (b): M98 is likely the most frequent aerosol model in this data set. The Rayleigh method for both plots is 490 nm.

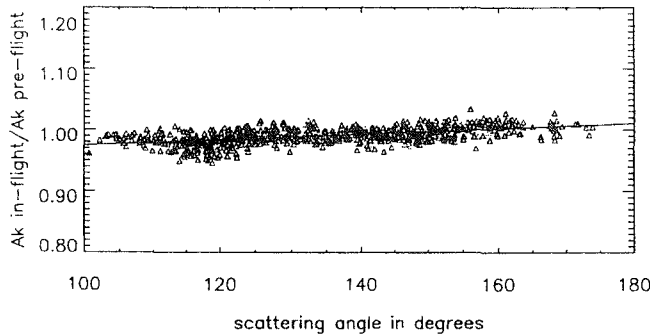


Fig. 6. Absolute calibration elementary results for Rayleigh scattering method as a function of the scattering angle (with C70 aerosol model and a chlorophyll concentration of $0.035 \text{ mg} \cdot \text{m}^{-3}$). Here, a correlation exists between the calibration elementary results and the scattering angle. This correlation appears also for the 443-nm spectral band and could be related to directional effects in water-leaving radiances (considered as Lambertian in the algorithm). The Rayleigh scattering is 490 nm.

used in the simulations, the A^k values differ by 1.5% for 565 and by less than 1% for 490 and 443. Finally, calibration coefficients almost linearly depend on the scattering angle (Fig. 6): some effects might not be perfectly modeled, such as directional variations of water-leaving radiance (assumed to be Lambertian). Many more parameters have been studied, such as wind speed, ozone amount, or geometric conditions, but the estimated absolute calibration is not correlated to any of them.

To determine the in-flight calibration coefficients, the elementary results collected during one week are averaged. Simulations are performed using each “extreme” chlorophyll content and both aerosol models, and this is done for sets of one week of data, leading to 12 calibration results. $A^k(\text{in-flight})/A^k(\text{preflight})$ ratio is the mean value of the results (Table III). The zero-peak dispersion of the average results is 4% for 443, 2% for 490, and 3% for 565. The dispersion for 443 is related to the impact of water-leaving radiance: the thresholds imposed both on the contribution of aerosols at 865 nm and on the wind speed (smaller than 5 m/s) prevent the effect of these parameters on calibration coefficients from being greater than 2%. The uncertainty on oceanic water reflectance seems to be greater than expected in this band.

However, the Rayleigh scattering method is an efficient method for the absolute calibration of optical instruments without using *in-situ* measurements. This method provides calibration coefficients with a 3–4% uncertainty for specific bands 490 and 565, but a better knowledge of the cartography of water-leaving radiance at 443 nm is required to obtain the same results for 443. Of course, the use of oligotrophic waters is not the ideal case for the calibration of 443 channel since water-leaving radiance is high. But it is not easy to find zones away from the coasts with high and stable chlorophyll concentrations. Another way of enhancing the results is to use *in-situ* measurements: Fougne *et al.* [11] have acquired *in-situ* data of water-leaving radiances, using SIMBAD instrument quasi-simultaneously with POLDER acquisitions.

2) Interband Calibration over Sunlight: This method uses the specular reflection of the sun (sunlight) on the sea-surface to transfer the calibration of 565 to the spectral bands 670, 765, 865, and 910 (Fig. 2). The sunlight is spectrally flat and has a high radiance that limits the influence of other parameters such as water leaving radiance or aerosols. The sunlight radiance depends mainly on the sea-surface roughness, which is related to the wind speed. For a mirror-like sea-surface, the sunlight radiance would be very high in the exact sun direction and very low outside of it, whereas an aging sea-surface scatters a lower radiance in a wider cone. 565-nm radiance is used to estimate the sea-surface roughness (via a radiative transfer code). The surface roughness is then used to estimate the radiance for 670, 765, and 865 nm spectral bands. The calibration of 763- and 910-nm channels requires ancillary information to evaluate the high atmospheric absorption: surface pressure (for 763) and atmospheric water vapor content (for 910) derived from ECMWF analysis. The sunlight method can also be used to calibrate 443 and 490 nm spectral bands with a reduced accuracy, just to verify that the results are consistent with the Rayleigh scattering results.

a) Calibration of 670-, 765-, and 865-nm spectral bands:

i) Method: The radiance measured in 565, 670, 765, and 865 spectral bands is first corrected for molecular absorption as described in the Appendix. Then, the sunlight radiance observed by POLDER in each spectral band k within the 765–865 nm range is estimated at the top of atmosphere (TOA) and compared to the real POLDER measurement.

TABLE III

ABSOLUTE CALIBRATION RESULTS ΔA^k OBTAINED WITH THE NOMINAL IN-FLIGHT CALIBRATION METHODS. SUNGLINT CALIBRATION IS AN INTERBAND CALIBRATION METHOD AND THUS NEEDS A REFERENCE (565) TO BECOME AN ABSOLUTE CALIBRATION METHOD. THE ΔA^k OBTAINED WITH RAYLEIGH SCATTERING FOR 565 IS COPIED IN ITALIC IN THE SUNGLINT COLUMN. RESULTS REPORTED IN "IN-FLIGHT" COLUMN ARE OPERATIONALLY USED IN POLDER LEVEL 1 PRODUCTS

Spectral band	Pre-Flight	Rayleigh Scattering	Sunglint	In-Flight V2.0
443	1.00	0.95		0.97
490	1.00	0.99		0.99
565	1.00	1.035	<i>1.035</i>	1.035
670	1.00		1.03	1.03
763	1.00		1.025	1.025
765	1.00		1.035	1.035
865	1.00		1.05	1.05
910	1.00		1.025	1.05

Equation (3) shows the different parameters that control the TOA normalized radiance I_{spe}^k in the specular direction

$$I_{\text{spe}}^k = I_m^k + I_a^k + (I_g + I_w^k + I_f) T_m^k \cdot T_a^k. \quad (3)$$

I_g is the normalized radiance of the sunglint with no atmosphere, I_m^k is the radiance of the light scattered by the molecules, I_a^k corresponds to aerosols scattering, T_m^k and T_a^k are the scattering transmission of the molecules and aerosols, and the water-leaving radiance I_w^k and the foam radiance I_f are modeled by Lambertian contributions [19]. (Actually, the scattering transmission factors are not exactly the same when applied to sunglint highly directional target, or to a quite Lambertian target like foam, but the equation has been simplified for better clarity).

I_g depends on the viewing geometry and on the surface roughness (related to wind speed), but not on the spectral band [8]. However, because I_m^k is not negligible in comparison to I_g , the TOA reflectances depend on the spectral bands and this dependence varies with the sea-surface roughness. An estimate of surface roughness is thus necessary to perform the interband calibration.

Equation (3) is just an approximation limited to single scattering. To accurately compute the sunglint radiance I_{spe}^k observed by POLDER, (4) is used, for which all the terms are obtained using LUT's obtained through radiative transfer simulations.

A first LUT is used to estimate the wind speed from the 565-nm radiance. The LUT is computed assuming the atmosphere is purely molecular, and using the SOS method [10], which takes into account multiple scattering in the atmosphere and multiple reflections on the sea-surface. The sea-surface is represented by a Lambertian contribution (the water-leaving radiance), and by the Cox and Munk model which relates the wind speed to the sea-surface roughness. The simulations are made for a dense grid of geometrical conditions, and for 15 different wind speeds (from 1 to 15 m/s). The first step of the methods seeks the wind speed v_w that corresponds to a radiance equal to the one measured at 565 nm. The obtained wind speed may be not very accurate and is just an indicator of the sea-surface roughness.

Then the radiance for the bands 670, 765, and 865 is estimated using (4)

$$I_{\text{spe}}^k = I_{\text{PMA}}^k(v_w) + \Delta I^k(I_{\text{PMA}}^k(v_w), MI_{\text{atm}}^{670}, MI_{\text{atm}}^{865}). \quad (4)$$

The first term of (4) is the sunglint radiance $I_{\text{PMA}}^k(v_w)$ that would be observed with a pure molecular atmosphere (PMA) with no aerosol and a surface wind-speed v_w . A second LUT is used to derive the PMA radiance in spectral band k from the wind speed.

The second term of (4) is an empirical correction of the first term. ΔI^k accounts for the effect of atmospheric aerosols on the sunglint radiance, through the use of an empirical model obtained by mean squares minimization. This model depends on the POLDER measurements MI_{atm}^{670} and MI_{atm}^{865} in a viewing direction outside the sunglint, and on the sunglint radiance $I_{\text{PMA}}^k(v_w)$. MI_{atm}^{865} gives information on the optical depth of aerosols, and combined with MI_{atm}^{670} , on the Angstrom coefficient α which accounts for the spectral variation of aerosol optical depth.

The coefficients of the model of the aerosol effect are derived statistically through a mean square minimization of the difference between the two parts of (4). A regression is performed for each node of a very dense grid of viewing geometry (sunglint and off-sunglint viewing and solar angles), and each regression is obtained from simulations with the SOS method, performed for a large set of aerosol models [six Shettle and Fenn models [32]: C70, C90, C98 (coastal models) and M70, M90, M98 (maritime models)] [14], [32], optical thickness (four values: 0.025, 0.05, 0.075, 0.1) and wind speeds (2, 5, 10, 15). These simulations apply not only to the exact specular direction, but also to a small cone around this direction.

ii) Error Budget: Various error sources limit the accuracy of the interband calibration method. The error budget presented below is computed with simulated data for $k = 865$ nm (budget for 670 would be even better); the reported errors are averaged over 96 cases (six aerosol models, four aerosol optical thickness, and four wind speeds) for solar zenith angles between 20 and 40°. This error budget has been computed for the exact specular direction, but other simulations have shown that the accuracy remains stable for an angular distance to

the specular point lower than 3°. The residual rms error after regression over 96 simulation cases is about 0.1%.

Instrumental Errors:

Noise: The effect of instrumental noise is completely negligible, since more than 1000 calibration points are averaged to compute each absolute calibration coefficient.

Calibration errors: An error in the absolute calibration of the 565 channel introduces an error on the estimated surface roughness and therefore on the PMA estimation of the sunglint radiance. If we have an absolute calibration bias of 3% for 565, simulations show that the bias for 865 is also 3%, leading to no error on the interband calibration (this is not true if 443 is used as a reference). Errors on the initial calibration of 670 and 865 impact on the estimation of the aerosol influence. Given an error (ΔA^{670} , ΔA^{865})₁, applying the interband calibration method gives a smaller new error (ΔA^{670} , ΔA^{865})₂ and the process needs to be iterated. Final errors are below 0.5%.

Geophysical Errors:

Foam Contribution: To evaluate the influence of foam radiance, the coefficients are applied on two different data sets, one with foam scattering and one without. The error budget was made assuming that foam scattering is spectrally flat, and the impact on the budget is negligible. Some new studies have shown that the foam might not be spectrally flat, so we discarded calibration points having a wind speed higher than 5 m/s.

Chlorophyll Concentration: To estimate the impact of a realistic error on the chlorophyll concentration, the coefficients calculated with the radiance of sea water with a chlorophyll concentration of 0.05 mg/m³ (water-leaving normalized radiance of 0.0042 for 565), were applied to a simulation with a water leaving radiance associated to a chlorophyll concentration of 0.10 mg/m³. The resulting error is 0.3%.

Atmospheric Pressure: The coefficients are calculated for the standard atmospheric pressure at sea level. They were applied on simulations calculated with a higher pressure (10 hPa, more than the expected rms error on the ECMWF meteorological data). Impact of this error is about 0.1%.

Gaseous Absorption: An uncertainty of 20% on water vapor amount has no impact on the method, but an uncertainty of 5% on ozone amount induces an error on the gaseous transmission, which leads to an error on I_{spe}^{565} of less than 0.1%.

Aerosol Model: The coefficients a_m^k obtained by fitting various aerosol models were applied to simulations performed with a unique coastal aerosol model. The resulting error is about 0.1%.

The total error budget gives an interband calibration accuracy better than 1%, and an absolute calibration error of 3.5% for 865 assuming 565 nm absolute calibration is accurate to 3%.

b) Calibration of 763- and 910-nm spectral bands: 763 and 910 channels are centered on gaseous absorption bands: oxygen A-Band and 910-nm water vapor absorption band, respectively. The absolute calibration of the 763-nm (re-

spectively, 910-nm) band can be derived from the absolute calibration of the 765-nm (respectively, 865-nm) band and the sunglint, provided the atmospheric gaseous absorption is known.

i) Calibration of 763-nm band: Owing to the fact that the O₂ proportion is constant within the atmosphere, the atmospheric absorption can be related to the atmospheric pressure level in clear sky conditions. Based on line-by-line simulations (using the spectroscopic data from HITRAN96 database), a polynomial model is derived that links the O₂ transmission at 763 nm to the sea-surface pressure and to the air temperature factor. The atmospheric pressure is obtained with ECMWF analysis, and the O₂ transmission derived through this model, $T_{O_2}^{\text{ECMWF}}$, is compared to that derived from the POLDER measurements, $T_{O_2}^{763}$. From the two equations in the Appendix, $T_{O_2}^{763}$ can be written as

$$T_{O_2}^{763} = \frac{(1 - A) \frac{MI^{763}}{MI^{765}}}{1 - A \frac{MI^{763}}{MI^{765}}} \frac{T_{O_3}^{765} \cdot T_{H_2O}^{765}}{T_{O_3}^{763} \cdot T_{H_2O}^{763}}$$

where MI^{763} and MI^{765} are the POLDER radiance measured at 763 nm and 765 nm, respectively, where the other parameters are described in the Appendix. Finally, the variation of the absolute calibration coefficient at 763 nm is expressed as

$$\Delta A^{763} = \frac{A_{\text{in-flight}}^{763}}{A_{\text{preflight}}^{763}} = \frac{T_{O_2}^{763}}{T_{O_2}^{\text{ECMWF}}}.$$

Since the 765-nm band is involved in the computation of $T_{O_2}^{763}$, it may be necessary to iterate the method in case of a large variation of the calibration coefficient of this band.

The error sources of this interband calibration are small: they mainly come from the aerosol scattering, (but we still select only low aerosol contents using an off-sun measurement at 865 nm), from the accuracy of the sun pressure (less than 1 hPa of bias), and from the quality of the absorption corrections. However, the main error for 763 nm comes from the 765-nm absolute calibration error. But, as 763 nm is never used alone but always in conjunction with the 765-nm band to determine apparent pressure [37], POLDER data users are only interested by 763/765 interband calibration that should be better than 1%.

ii) Calibration of 910-nm band: This band is calibrated in a similar way as 763-nm band, replacing surface pressure by vertical profiles of atmospheric water vapor content, as it has been shown that total water vapor absorption does not depend only on the total water vapor amount but also on its vertical distribution. Derivation of water vapor absorption from the vertical profile is described in Bouffies *et al.* [2].

These vertical profiles are obtained from ECMWF analyses every 6 h and interpolated to the date of acquisition. Although the data are known to be inaccurate over the oceans where radiosoundings are very sparse, some studies [25] have shown that they are globally unbiased. The corresponding error should therefore be reduced to 1.5% by accumulating a large number of calibration points. The 910 and 865 spectral bands are as close as 763 and 765, but effects of spectral variations

the target between both wavelengths are very low thanks to the use of sunglint.

Because of their high altitude (above water vapor), stratospheric aerosols could induce some errors in the estimation of the total water vapor absorption, but POLDER was calibrated in a period of very low stratospheric aerosol content. The amount of tropospheric aerosols is limited by using only the pixels which have a 865-nm radiance in an off-sunglint viewing direction under 0.005 (after correction of the molecular scattering contribution). As shown in [40], 6S simulations show that the total impact of aerosols on the error budget is less than 0.3%.

The choice of this sunglint method is arguable because of radiosoundings scarcity in the open ocean, but it combines two advantages: spectral variation of surface reflectance is far better known than that of any land surface, and the effects of aerosols are lower because selecting clear atmospheres is easier. Total error budget for this calibration method is estimated to 1.6%. Vesperini *et al.* [40] have carried out a validation of the calibration of band 910 by comparing water vapor content derived from POLDER to water vapor measured by radiosoundings.

c) *Results:* The sunglint interband calibration uses the same kind of target as the molecular scattering method: very clear ocean scenes with a very low aerosol optical thickness. Of course, a third selection criterion has been added: the viewing direction of the calibration point must be within a cone of 3° of radius, centered on the specular direction [$\theta_s = \theta_v, j = 180^\circ$ (Fig. 14)]. For higher values, the dispersion of the results increases quickly, indicating that the geometrical modeling of the sunglint is less accurate. The off-sunglint 865-nm maximal radiance threshold (0.005 in normalized radiance units) is a little higher than for calibration over molecular scattering.

The dispersion of the elementary results (Fig. 7) is very low, except for 910 nm because of the dispersion of meteorological data. A complete analysis of the elementary measurements does not show any significant dependency of the elementary results on any of the algorithm parameters. For example, the correlation between the measured calibration coefficient and the aerosol normalized radiance (Fig. 8) is very low, indicating that the aerosol scattering has been properly corrected. Some correlation was found, however, between A865 and the atmospheric water vapor amount. The correlation disappeared when we decided not to correct for the absorption by water vapor continuum (the existence of this continuum of absorption in the near infrared is questionable). To prevent any impact of this parameter on calibration accuracy, only low water vapor contents have been selected.

To determine the in-flight calibration coefficients, the elementary results collected during one week are averaged. Averaged results have been obtained for the five channels over five periods of one week distributed during the whole life of the instrument. The results given in Table III are obtained after having calibrated the 565 reference band over Rayleigh scattering. Fig. 8 shows that the dispersion of the averaged results is small and Fig. 9 shows that interband calibration does not evolve with time.

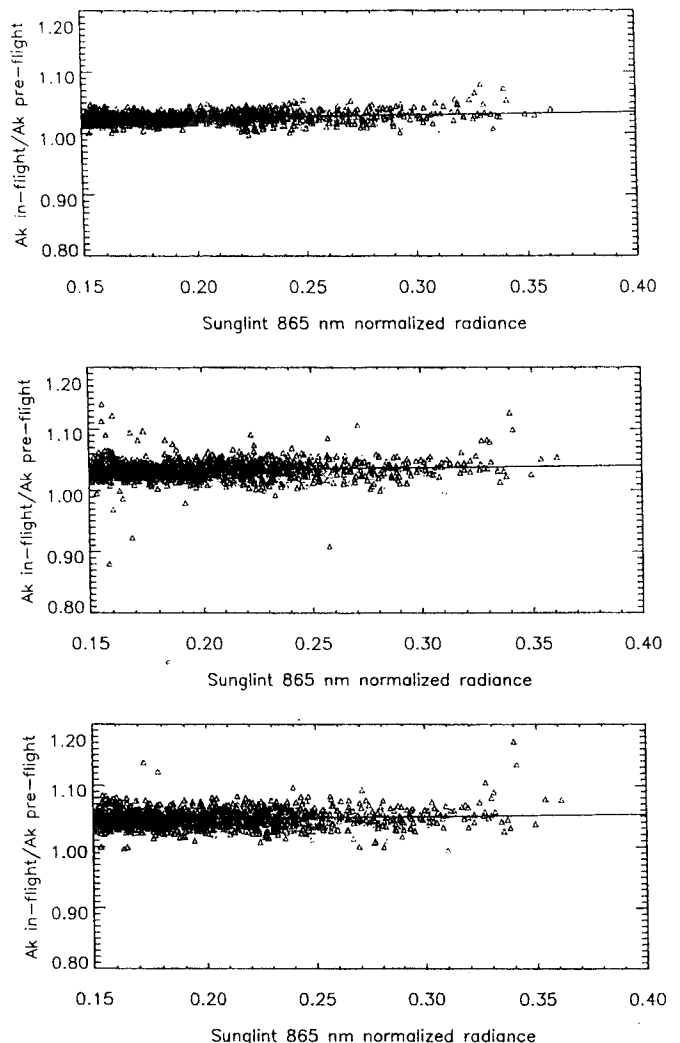


Fig. 7. Absolute calibration elementary results for sunglint interband method as a function of sunglint 865-nm radiance (for all the calibration points selected during the first week of November 1996). Standard deviation is very low for 670-nm calibration (0.8%) and increases slightly when spectral distance to 565 reference band increases (1.5% for 865 nm). The curves show no correlation between calibration results and sunglint radiance at 865 nm. From top to bottom, the Sunlight method is 670 nm, 765 nm, and 865 nm.

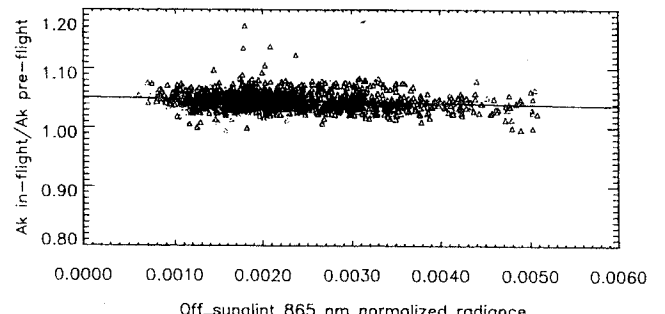


Fig. 8. Absolute calibration elementary results for sunglint interband method as a function of the Rayleigh corrected 865-nm radiance in an off-sunglint direction (for all the calibration points selected during the first week of November 1996). Correlation with the aerosol content is very small: this validates the aerosol effect correction. The Sunlight method is 865 nm.

The results obtained for the 910-nm spectral band show a rather high dispersion (4%) which comes from the limited accuracy of the water vapor information from ECMWF data.

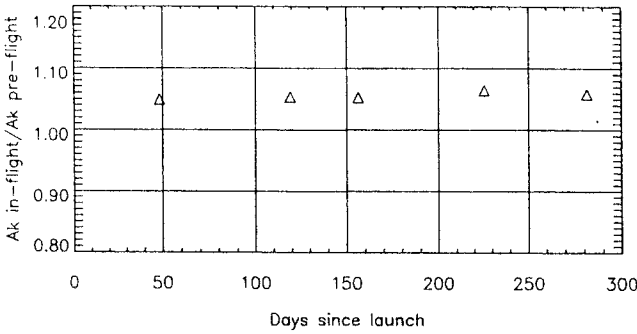


Fig. 9. Absolute calibration averaged results for sunglint interband method as a function of time: each point is the average of all the elementary results obtained with one week of POLDER data (100 orbits). The dispersion of the results is very low and the curve shows no drift during the whole life of POLDER instrument. The Sunglint method (averaged results) is 865 nm.

The results obtained in the other spectral bands are excellent and a great confidence can be given to this calibration method.

The same calibration method can be applied using 443P instead of 565 as the reference band. This leads to a degraded calibration performance because of water-leaving radiance uncertainty and because of the higher spectral distance between 443P and the near infrared spectral bands. However, this method enabled us to check 443P/565 interband calibration with an independent method. Assuming $\Delta A^k(565) = 1.035$ (as obtained with Rayleigh scattering method), the interband calibration gives 0.96 for 443P, very close to 0.95 obtained with Rayleigh scattering method (Table V).

B. Multiangular Calibration

Multiangular calibration is defined as the process of estimating the sensitivity variations at different points of POLDER wide field of view. Usually, the multiangular calibration methods consist in having the instrument look at a spatially uniform landscape, which can be an internal source (VGT/SPOT4, SPOT) or natural targets such as snow fields (SPOT). For a wide field-of-view instrument (2400 km * 1800 km), a continuous uniform landscape does not exist. As POLDER is not equipped with an on-board calibration device, new methods have been defined to simulate a spatially uniform landscape.

However, no method was found able to completely calibrate the sensitivity differences for all POLDER detectors. Different methods are used to calibrate the low spatial frequencies and the high spatial frequencies of the multiangular calibration coefficients. This explains why multiangular calibration coefficients R_{lp}^k in the radiometric model have been split into three terms:

$$R_{lp}^k = p^k(\theta) \cdot gmf_{lp}^k \cdot ghf_{lp}^k. \quad (7)$$

- $p^k(\theta)$ expresses the low-frequency variations of the optic transmission which decreases slightly when the viewing angle θ increases (Fig. 10). Its measurement is performed over desert sites as described below and the targeted accuracy is 1%. Desert sites are neither uniform enough nor frequent enough to be used for high frequency.



Fig. 10. Typical response on a radial section of the CCD ($p^k \cdot gmf_{lp}^k$). The smooth line represents the low-frequency variation of multiangular calibration p^k .

TABLE IV
CENTER LOCATIONS OF THE DESERT SITES (LONGITUDE > 0 FOR EAST LO

Site Name	Latitude (°)	Longitude (°)
Arabia1	18.88	46.76
Arabia2	20.13	50.96
Arabia3	28.92	43.73
Sudan1	21.74	28.22
Niger1	19.67	9.81
Niger2	21.37	10.59
Niger3	21.57	7.96
Egypt1	27.12	26.10
Libya1	24.42	13.35
Libya2	25.05	20.48
Libya3	23.15	23.10
Libya4	28.55	23.39
Algeria1	23.80	-0.40
Algeria2	26.09	-1.38
Algeria3	30.32	7.66
Algeria4	30.04	5.59
Algeria5	31.02	2.23
Mali1	19.12	-4.85
Mauritania1	19.40	-9.30
Mauritania2	20.85	-8.78

- ghf_{lp}^k refers to high-frequency variations of the sensitivity of the elementary detectors. It is measured over clouds. Its targeted accuracy is 0.1%. Of course clouds are Lambertian targets, and their BRDF depends on the type of cloud: the low-frequency variation of the multiangular calibration cannot be estimated by this method.
- gmf_{lp}^k refers to low-frequency variations in the sensitivity of the elementary detectors that cannot be modeled by a polynomial function of the viewing angle. The targeted accuracy is 1%. Since this parameter is mainly linked to the heterogeneity in the CCD matrix, it is expected not to vary after launch, and preflight calibration is used for this parameter. However, calibration over desert sites can be used to detect an unlikely large variation.

TABLE V

COMPARISON OF THE NOMINAL IN-FLIGHT ABSOLUTE CALIBRATION RESULTS ΔA^k WITH THE VALIDATION METHOD RESULTS. VALUES IN ITALIC INDICATE THAT THE CORRESPONDING BAND IS USED AS A REFERENCE FOR AN INTERBAND METHOD. ITALIC VALUE IS COPIED FROM "IN-FLIGHT" COLUMN

Spectral band	OCTS (pre-flight)	OCTS (in-flight)	Sunglint	Clouds	ATSR-2	In-Flight (Used in level 1)
443	0.96	0.955	0.96	1.01		0.97
490	0.92	0.975	0.98	1.02		0.99
565	1.045	1.01	1.035		1.06	1.035
670	1.01	1.09		1.03	1.035	1.03
765	1.01	1.12				1.035
865	0.98	1.28			1.00	1.05

1) *Low-Frequency Multiangular Calibration over Desert Sites:* Stable desert areas of the Sahara and Saudi Arabia can potentially be used as calibration test sites in the solar reflected spectrum. Such sites have already been used to monitor the calibration temporal drifts of the AVHRR [18], [30], [36], ATSR-2 [34], Meteosat [5], [24], and HRV/SPOT sensors [17]. They can also be used to estimate the multiangular calibration of wide field of view sensors equipped with CCD arrays such as POLDER. This requires a good characterization of the directional variations of their top-of-atmosphere reflectances, to account for the variations of the solar or viewing configurations between measurements.

a) *Method:* A procedure has been defined to select 100 \times 100 km² desert areas in North Africa and Saudi Arabia [6] using a spatial uniformity criterion in Meteosat-4 visible data. Twenty such sites (Table IV) meet this criterion within 3%. The temporal stability of the spatially averaged reflectance of each selected site has been investigated at seasonal and hourly time scales with multitemporal series of Meteosat-4 data. It was found that the temporal variations of an 8–15% typical peak-to-peak amplitude (in relative value) were mostly controlled by directional effects. Once the directional effects are removed, the residual root mean square variations, representative of random temporal variability, are in the order of 1–2% in relative values.

Second, a field experiment [7] took place in February–March 1993 to characterize the BRDF of four desert sites (Algeria 2, Algeria 3, Algeria 4, and Algeria 5). The purpose of this experiment was to measure the BRDF of the sites to use them as a reference for multiangular calibration of optical sensors. Bidirectional measurements of the surface reflectance (and also polarization) were collected in three different planes (principal, perpendicular, and 45°) at four wavelengths: 450, 650, 850, and 1650 nm. Then, the surface reflectance measurements have been adjusted against an empirical model of BRDF defined as

$$\rho_{TOA}^k(\theta_s, \theta_v, \varphi) = a^k + \theta_s \theta_v \frac{\cos \theta_s \cos \theta_v}{\cos \theta_s + \cos \theta_v} \cdot (b^k \cos \varphi + \theta_s \theta_v (c^k + d^k \cos^4 \varphi)) \quad (8)$$

where $(\theta_s, \theta_v, \varphi)$ are, respectively, the solar zenith angle, the viewing zenith angle, and the difference of solar and viewing azimuth angles, and where the coefficients a^k , b^k , c^k , and d^k are determined by a least square regression (more details about

this model are included in [7]). A spectral linear interpolation is then performed to adapt the model to POLDER spectral bands.

The TOA surface reflectance ρ^* in each spectral band is then estimated by decoupling the absorption and scattering effects

$$\rho_{TOA}^k(\theta_s, \theta_v, \varphi) = T_g(\theta_s, \theta_v) \rho_{surf+atm}^k(\theta_s, \theta_v, \varphi). \quad (9)$$

$\rho_{surf+atm}^k(\theta_s, \theta_v, \varphi)$ is computed with the SOS code [10] with as inputs i) the atmospheric optical thickness in the POLDER bands (derived from the barometric pressure for the Rayleigh scattering and, for the aerosols, from the extinction measurements during the field campaign), ii) an aerosol model (a Junge size distribution associated with the Angstrom coefficient derived from the extinction measurements, and a standard refractive index of the aerosols chosen to be that of silica) and iii) the BRDF measured during the field campaign. The gaseous absorption T_g is derived from a climatology of absorbing gas concentrations for ozone, and oxygen and water vapor absorption are estimated using POLDER 763 and 910 spectral bands as explained in the Appendix.

To obtain an experimental error budget, the retrieved BRDF has been compared to the reflectance measurements made by AVHRR in channel 1 for the four desert sites (Algeria 2, Algeria 3, Algeria 4, and Algeria 5) [7]. The AVHRR instrument is used as a reference, since its only detector does not introduce calibration variation within the field of view. Using the revolution symmetry of the polynomial function $p(\theta)$, this comparison gives a zero-peak error of 1% for high sun zenith angles (50–60°) that correspond to the range observed during the field campaign. Unfortunately, this budget does not apply to 443-nm band, which is not covered by AVHRR channel 1.

Once the BRDF of each site is obtained for POLDER spectral bands, it is possible to perform POLDER multiangular calibration. After discarding cloudy acquisitions, selected POLDER data are averaged over the site surface (15 \times 15 POLDER pixels), and an estimation of the evolution of calibration coefficients is performed for each viewing direction using the following formula:

$$\Delta(Ap(\theta))^k = \frac{A_{in-flight}^k \cdot p_{in-flight}^k(\theta)}{A_{preflight}^k \cdot p_{preflight}^k(\theta)} = \frac{M \rho^k}{\rho_{TOA}^k(\theta_s, \theta_v, \varphi)} \quad (10)$$

where $M\rho^k$ is the reflectance measured by POLDER and comes from the level 1 product obtained with preflight calibration, $p_{\text{preflight}}^k(\theta)$ is low frequency preflight calibration, and $p_{\text{in-flight}}^k(\theta)$ is the in-flight calibration. Of course, during a clear day, up to 12 different satellite viewing angles θ (Fig. 14) are obtained for a given desert site. $\Delta(Ap(\theta))^k$ is computed for each reference site as a function of the viewing angle and a polynomial fit is performed to estimate the low-frequency polynomial $p^k(\theta)$. Even if absolute calibration coefficients are present in the above equation, it is not possible to derive an accurate absolute calibration from this method, since absolute calibration was not the aim of the *in-situ* campaign. However, if EOS had worked longer, this method could have been used to verify multitemporal calibration, i.e., variations of absolute calibration with time.

b) Results: The data have been acquired during four weeks in November 1996, and a second set during the two first weeks in January 1997. More than 650 images have been used on the 20 desert sites to perform the multiangular calibration. For each image, the areas corresponding to the reference sites are extracted and then automatic tests are used to discard clouds. Six tests were used but the most efficient are:

- a spectral index computed between bands 865P and 443P (desert TOA reflectance increases with the wavelength whereas clouds are whiter);
- statistics on the spatial uniformity of the measurements inside each desert site.

Since only four of the 20 selected desert sites have been characterized with *in-situ* measurements, the nominal method was to use the four Algerian sites for calibration and those having a similar behavior among the others. In Fig. 11(a), the results obtained on one of the Algerian sites (Algeria 2) are plotted. These sites have been affected by bad weather during November, 1996, and only a small amount of cloud-free data has been collected, but moreover, the results have a great standard deviation. Multiangular calibration seems to be correct (except for 443), but the forecast accuracy of 1.5% cannot be achieved with this data set. For 443 spectral band, multiangular calibration seems to be correct up to 45°. For higher viewing angles, the calibration seems to decrease, but it is difficult to prove that the error comes from POLDER multiangular calibration: the data in this zone were only collected with two cloud-free acquisitions (one clear day gives 12 different viewing directions).

In Fig. 11(b), the multiangular calibration results obtained for site Niger 2 are plotted. Even if this site was not among the sites characterized with *in-situ* data, the standard deviation of multiangular calibration results is lower than for Algeria, ranging from 2.3% in band 443 to 0.8% for 865. The errors decrease when the wavelength increases, as do the directional effects of the desert site. Once again, the results indicate a good multiangular calibration for all spectral bands except 443, but it is still difficult to conclude if it comes from the inaccuracy of the BRDF model in this band or from multiangular calibration.

As a conclusion, this multiangular calibration method confirms the quality of the preflight multiangular calibration and the temporal stability of the instrument, except for spectral

band 443: in this case, multiangular calibration may have evolved after launch. But since confidence in 443 nm reflectance is low, preflight calibration of this parameter is still in the level 1 product. The BRDF's of the 20 desert sites are now being characterized using POLDER data in order to use it to cross calibrate POLDER with other optical sensors (Section V-C).

2) High-Frequency Multiangular Calibration over Clouds: Changes after launch in the high-frequency multiangular calibration of POLDER might occur for two reasons: i) if elementary sensitivities of the detectors in the CCD array change because of temperature variation or because of vacuum transition or ii) if particles of dust are deposited on the optics after the last preflight calibration, or if they move in the field-of-view (POLDER pupil dimension is around 0.4 mm at the center of the external lens). However, the POLDER CCD array is thermally controlled and air vacuum transition was tested before launch without showing any significant variation; the first cause of variation is unlikely.

In order to determine this high-frequency multiangular in-flight calibration with an accuracy around 0.1%, a method has been developed using cloud observations. For each elementary detector of the CCD array, and for each channel, the method consists in averaging all the cloud observations performed by the detector. The procedure assumes that a very high number of cloud observations is collected for each elementary detector, the high-frequency variations of the average of all the measurements will characterize the sensitivity variations within the array, and only the low frequencies will be affected by artifacts of cloud anisotropy.

This calibration method has been experimented with NOAA/AVHRR band 1 raw data using the fact that one line of an AVHRR product is obtained with a single detector. 300 lines of AVHRR data have been used. The data have been processed as if each line was acquired with 2048 different detectors having exactly the same sensitivity. The observed high frequencies variations would then be only artifacts. AVHRR cloud detection is performed by a simple threshold on the normalized radiance ($I > 0.25$), since the procedure does not require a precise cloud mask. For each column number of AVHRR data, all the cloud measurements are averaged and the standard deviation of the averages is computed: the obtained accuracy is under 0.3%.

The same method has been used for POLDER. In this case, the only difficulty is related to the amount of data necessary for the calibration: the required number of cloud measurements is 15(channels) × 66 308(detectors) × 15 000(measurements). This requires the use of three entire weeks of POLDER data (there are only 120 measurements per orbit for a given POLDER detector in one spectral band and only one half of them are clouds). In order to estimate the accuracy of the results, two sets of three weeks have been used to obtain two results with independent data sets. The difference between the results of the two data sets has a standard deviation around 0.2%, which indicates that the results obtained from the whole six weeks of data have a precision better than 0.2%. The difference between preflight and in-flight data is between 0.3% and 0.1%, depending on the spectral bands. A few dust parti-

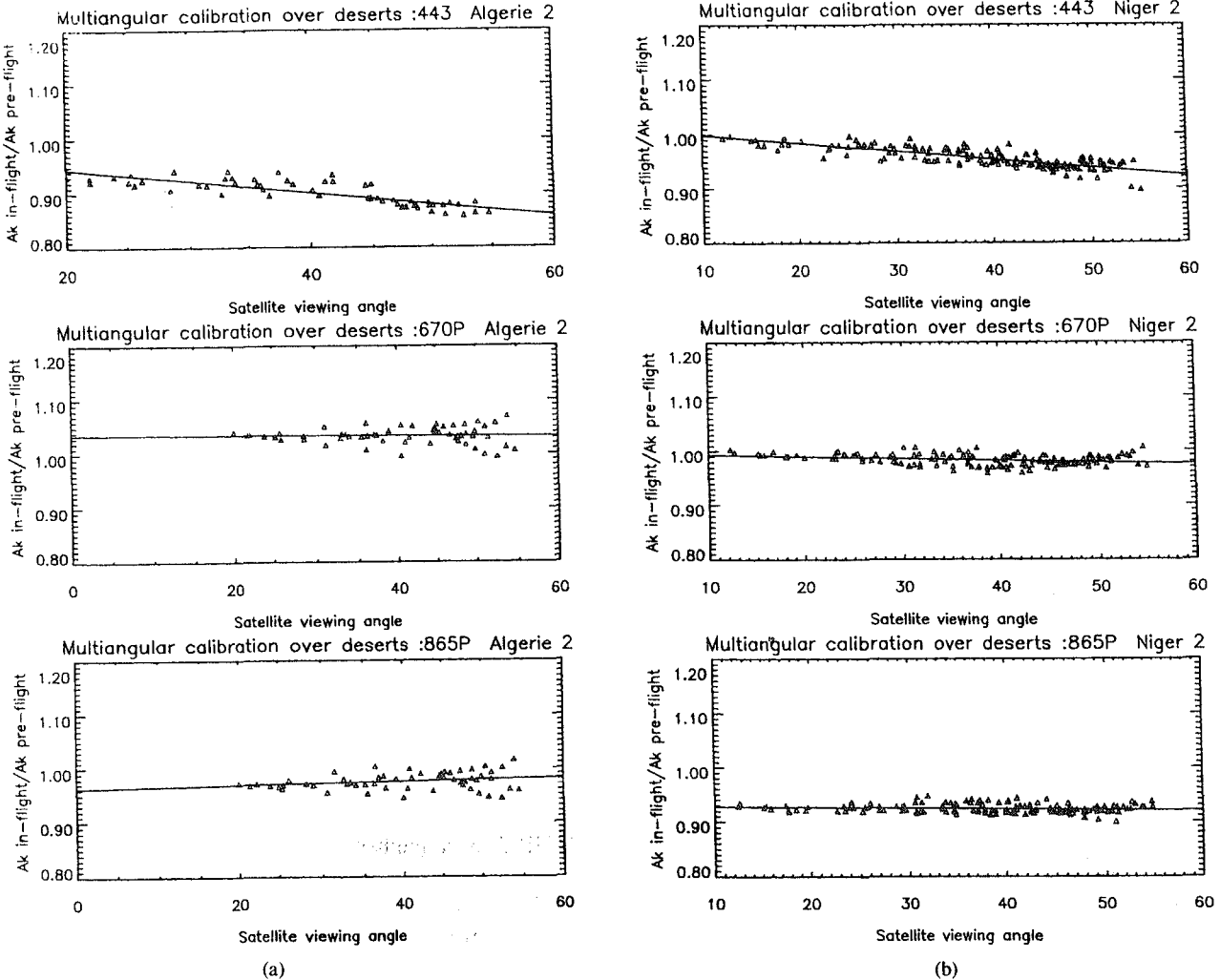


Fig. 11. Multiangular calibration of POLDER over desert sites as a function of satellite viewing angle θ : (a) Algeria 2 site: the number of cloud-free acquisitions during November, 1996, was low over this site, and dispersion of the results is rather high for the remaining points. A variation of POLDER multiangular calibration may be possible for 443 nm band. (b) Niger 2 site: the number of cloud-free acquisitions during November, 1996, was much higher than for Algeria 2, and the dispersion of the results is also lower, but the BRDF model was not measured on this site. A variation of POLDER multiangular calibration might be possible for 443-nm band, whereas the two other bands seem to be correctly calibrated.

effects have been noticed with differences of about 1%, and some differences are linked to the disappearing of artifacts in the preflight calibration.

The coefficients determined by this method are now implemented in POLDER level 1 processing.

V. IN-FLIGHT RADIOMETRICAL CALIBRATION: VALIDATION

In this chapter are presented three additional calibration methods that were used to validate the results of POLDER in-flight calibration nominal methods. These independent calibration methods are based on different atmospheric models or different calibration sources (including on-board sources for POLDER/ATSR2 cross calibration) in order to verify that the nominal methods are not biased.

A. Interband Calibration Using Clouds

Starting from level 1 data calibrated with the nominal methods, we use the 670-nm radiance measurements as a

reference for the estimation of 443-nm and 490-nm absolute calibration coefficients (565 is usually saturated over high reflective clouds). The calibration pixels are selected when their reflectance is over 0.8, when the cloud top apparent pressure deduced from the band ratio 763/765 [4] is under 250 hPa, and when the clouds are uniform enough. Data are corrected for ozone absorption using TOMS data.

Simulations of TOA radiances above convective clouds have been performed using a discrete ordinate method: they are arranged in look-up tables calculated for 443-, 490-, and 670-nm channels. They correspond to three different ice particles (hexagonal plates or columns with a radius 20–60 μm , assumed to be dominant in the highest layers of cumulonimbus), to a cloud top altitude of 10 or 15 km, to a dense grid of observation angles, and to scattering cloud optical thickness between 20 and 200.

For a given altitude and ice particle model, the first step of the procedure finds the scattering optical thickness δ_{est} that corresponds to the observed radiance at 670 nm. Then the

LUT at 443 and 490 are used to estimate the radiances in these bands, assuming the cloud optical thickness does not vary between 443 and 670 nm.

The new estimated calibration coefficient is obtained from the initial coefficient A^k and from measured MI^k and estimated radiance $CI^k(\delta_{\text{est}})$ by

$$A_{\text{in-flight}}^k = A_{\text{preflight}}^k \times \frac{MI^k}{CI^k(\delta_{\text{est}})}. \quad (11)$$

The average results derived from 12 POLDER orbits in November 1996, are reported in Table V. The standard deviation is below 0.8% for the 443 and 490 channels. Changing the cloud top altitude from 15 to 10 km results in an increase of 1% in the calibration coefficient, and the choice of the particle model does not introduce more than 0.5% of variation. The results do not depend on the cloud reflectance, meaning that the selected clouds are thick enough so that the radiance of the surface and of the atmospheric layer below the cloud does not impact on the calibration. The interband calibration results over clouds do not agree perfectly with the results obtained with the nominal methods: the discrepancy at 443 nm is about 6% (only 3% at 490) and has still not been explained in spite of comprehensive verifications.

B. Cross Calibration Between POLDER and OCTS

OCTS is a NASDA radiometer which flew on board ADEOS. Its nadir resolution is around 800 m, the swath is 1400 km wide, and acquisitions are made with eight visible and near infrared bands and four thermal infrared bands. OCTS scanning mechanism is based on a rotating mirror with a maximum scanning angle of 40°, and ten detectors per spectral band are used to collect simultaneously ten lines across-track. Since POLDER and OCTS are on the same platform and share six spectral bands (443, 490, 565, 670, 765, and 865), it is possible to compare the radiance of targets observed at the same instant with the same viewing and solar angles and in nearly identical spectral bands. Simultaneous acquisitions of POLDER and OCTS data have been used in order to cross calibrate both sensors.

In order to enhance the accuracy of the cross calibration, the targets are chosen so that they have a quite high normalized radiance (more than 0.2), a very low polarization rate (polarization sensitivity is not corrected for OCTS), and a good spatial uniformity to avoid possible registration errors between the two sensors: a POLDER pixel is used for cross calibration if the standard deviation of the OCTS measurements inside it is less than 1% of the radiance. The targets corresponding to these criteria are mostly clouds, which also have the advantage of being quite spectrally flat.

Table V gives the absolute calibration derived considering OCTS preflight calibration as a reference (this preflight calibration was still used in the OCTS level 1B products with software ID 3.7). Agreement with the POLDER in-flight method stays within a 7% margin. The same computation has been made using the in-flight calibration of OCTS that is used to produce the version 3.0 ocean color products. This calibration is in fact called “algorithm tuning parameters” by

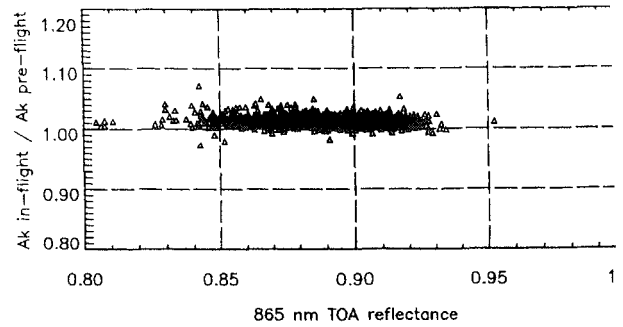


Fig. 12. Absolute calibration elementary results for clouds interband me as a function of the cloud 865-nm reflectance. The interband calibration clouds is 443 nm.

the OCTS calibration team: it was obtained for all spec bands by comparing *in-situ* chlorophyll-a data with OCTS [26], and its aim was not to perfectly calibrate OCTS data to obtain the best ocean color products. One can note the agreement is good for 443 and 490 and gets worse the wavelength increases (22% for 865 nm band). This probably be explained by OCTS in-flight calibration of 8 nm band with a Rayleigh method that uses very low radian in the near-infrared bands over ocean.

C. Cross Calibration Between POLDER and ATSR2

ATSR-2 is a multispectral scanner on board the ER satellite launched in 1995. It is based on a conical scann mechanism which allows the acquisition of the same sce from two viewing angles during a single pass: a forward alk track view (viewing zenith angle around 60°) and a nadir vi ATSR-2 has four infrared channels and three visible/ne infrared channels very close to POLDER spectral bands: 5 660, and 870 nm. ATSR-2 is calibrated using an on-bo diffuser monitored by a photodiode, and using desert sites measure the drift of the on-board calibration system [34]. successful cross-calibration between both instruments would be a good validation of both sensor's absolute calibration and also a partial validation of POLDER multiangular calibration

Since POLDER and ATSR-2-acquisitions of the same sce are not simultaneous, the cross calibration target must be stable with time, uniform to avoid geometrical registration problem and its BRDF has to be known: the desert site Sudan 1 has been used for this cross calibration. Thanks to its bidirectional capabilities, POLDER is able to obtain a dense sampling of the viewing conditions over one site. Each month, a BRDF model of the desert site is derived from all the cloud-free ATSR2 measurement is then compared to the interpolation of the BRDF model of the same month for ATSR2 viewing conditions. Cloud detection for POLDER data is described in Section IV-B, and for ATSR-2 in Smith *et al.* [32]. POLDER data are corrected for gaseous absorption as described in the Appendix and ATSR-2 data are corrected for ozone absorptio using TOMS data. Of course, aerosols above the desert site can cause some variability in the results, but by accumulating enough data, the results should not be biased.

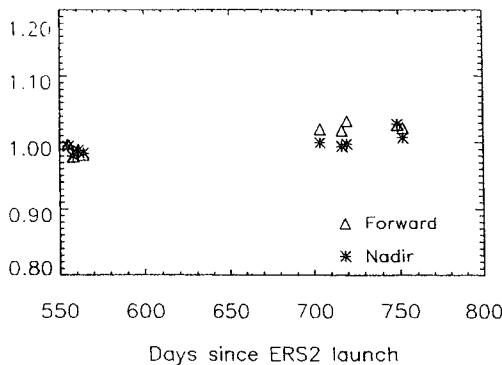


Fig. 13. Ratio of the reflectances at 670 nm measured by ATSR2 and POLDER over a desert site (Sudan 1) from November 1996 to May 1997 with the same viewing angles. Stars indicate that the data have been acquired with nadir viewing, whereas triangles correspond to a forward viewing. In most of the cases, triangles and stars overlap when acquired the same day, and this provides a validation of POLDER multiangular calibration.

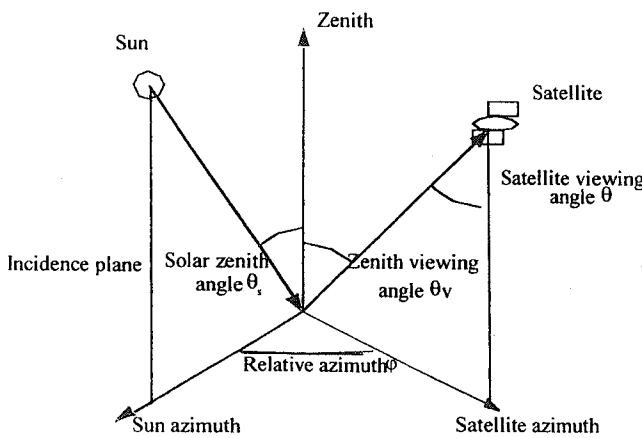


Fig. 14. Definition of the various angles used to characterize the geometry of satellite acquisitions.

The results are quite good (Table V): the agreement between the radiance measured by ATSR-2 and the BRDF derived from POLDER is better than 6% for 565, 1% for 670, but degrades to 5% for 865. The agreement between the directional variations of POLDER BRDF and ATSR-2 reflectances is also very satisfactory and validates partially POLDER multiangular calibration in these spectral bands (Fig. 13).

VI. CONCLUSION

A new calibration approach has been developed for POLDER based on the design of a very stable instrument, on an exhaustive preflight calibration of the instrument, and on the development of many in-flight operational calibration methods using natural targets. The result is very satisfactory since the in-flight absolute calibration has shown that:

- **POLDER Instrument is Stable:** All in-flight absolute calibration coefficients differ from preflight coefficients by less than 5%, and multiangular calibration did not evolve after launch (except maybe for 443);
- in-flight calibration methods (except POLDER/OCTS cross calibration) agree within a margin of 4% for all the spectral bands but 443.

This calibration process is efficient to provide a correct absolute calibration within a few months (five months were necessary for POLDER 1, but this delay will be reduced with POLDER 2). It is less expensive than developing an on-board calibration device, and more reliable than using *in-situ* measurement campaigns which are subject to weather conditions and provide very few calibration points, maximizing the impact of random error sources. However, all these methods are perfectly suited to POLDER measurements and could not be easily applied to other instruments that do not provide multidirectional measurements (for aerosol detection in sunglint calibration method) or O₂ pressure (for cloud altitude determination in interband calibration using clouds). Such accuracy also could not be achieved without a good characterization and correction of POLDER polarization sensitivity, since our calibration targets (Rayleigh scattering and sunglint) have a high polarization rate.

Still, some uncertainty exists in the calibration of the 443-nm channels, with a discrepancy of 6% between the Rayleigh and the cloud methods that has not yet been explained in spite of intensive verifications.

APPENDIX CORRECTIONS FOR GASEOUS ABSORPTION

Ozone absorption is removed by computing the transmissions $T_{O_3}^k$ as functions of $m \cdot U_{O_3}$, where m is the air mass factor and U_{O_3} is the column amount of ozone measured by TOMS. The water vapor transmission $T_{H_2O}^k$ is modeled as a function of the ratio of 910- and 865-nm normalized radiances (MI^{910}/MI^{865}). The parameterizations of ozone and water vapor transmissions are derived from simulations using a line-by-line model.

For the oxygen absorption in the 763 and 765 spectral bands, the normalized radiance MI^* that would be measured if there was no absorption is assumed to be the same in both channels (which is really true for sunglint targets). The normalized radiances measured by POLDER (MI^{763} and MI^{765}) can be expressed as a function of MI^* as follows:

$$MI^{763} = MI^* \cdot T_{O_2}^{763} \cdot T_{H_2O}^{763} \cdot T_{O_3}^{763} \quad (A1)$$

$$MI^{765} = A \cdot MI^{763} + (1 - A) \cdot MI^* \cdot T_{H_2O}^{765} \cdot T_{O_3}^{765} \quad (A2)$$

In this formula, the constant A may be considered as the percentage of the 765 spectral band where oxygen lines are located. Its value is derived from line-by-line simulations and is close to 0.3. The oxygen transmittance $T_{O_2}^{763}$ and the normalized radiance without absorption MI^* can be derived by combining (A1) and (A2).

ACKNOWLEDGMENT

The authors are grateful to H. Oaku (NASDA/EORC) for supplying OCTS data, to D. L. Smith in the Rutherford Appleton Laboratory, U.K. for providing ATSR-2 extractions over site Sudan 1, and to all the persons in CNES who helped

the authors exploiting the huge amount of POLDER data used to provide the above results: C. Gélis, P. Théron, A. Meygret, P. Soulé, J. M. Laherrère, A. Guerry, and S. Lafont.

REFERENCES

- [1] Y. Andre, J. M. Laherrère, T. Bret-Dibat, M. Jouret, J. M. Martinuzzi, and J. Perbos, "Instrumental concept and performances of the POLDER instrument," in *SPIE Proc. Infrared Spaceborne Remote Sensing III*, San Diego, CA, July 1995, vol. 2553.
- [2] S. Bouffiès, D. Tanré, F. M. Bréon, and P. Dubuisson, "Atmospheric water vapor estimate by a differential absorption technique with the POLDER instrument," *J. Geophys. Res.*, vol. 102, pp. 3831–3841, 1997.
- [3] T. Bret-Dibat, Y. André, and J. M. Laherrère, "Preflight calibration of the POLDER instrument," in *SPIE Proc. Remote Sensing and Reconstruction for Three Dimensional Objects and Scenes*, San Diego, CA, July 1995, vol. 2572.
- [4] J. C. Buriez, C. Vanbauce, F. Parol, P. Goloub, M. Herman, B. Bonnel, Y. Fouquart, P. Couvert, and G. Sèze, "Cloud detection and derivation of cloud properties from POLDER," *Int. J. Remote Sens.*, vol. 18, no. 13, pp. 2785–2813, 1997.
- [5] F. Cabot, G. Dedieu, and P. Maisongrande, "Monitoring NOAA/AVHRR and Meteosat shortwave bands and calibration over stable areas," in *Proc. 6th ISPRS Int. Symp. Physics, "Measurements and signatures in remote sensing," Val d'Isère, France, Jan. 17–21, 1994*, pp. 41–46.
- [6] H. Cosnefroy, M. Leroy, and X. Briottet, "Selection and characterization of Saharan and Arabian desert sites for the calibration of optical satellite sensors," *Remote Sens. Environ.*, vol. 58, no. 1, pp. 101–114, 1996.
- [7] H. Cosnefroy, X. Briottet, M. Leroy, P. Lecomte, and R. Santer, "A field experiment in Sahara for the calibration of optical satellite sensors," *Int. J. Remote Sens.*, vol. 18, no. 16, pp. 3337–3359, 1997.
- [8] C. Cox and W. Munk, "Slopes of the sea surface deduced from photographs of sun glitter," *Bull. Scripps Inst. Ocean.*, vol. 6, pp. 401–488, 1985.
- [9] P.-Y. Deschamps, F. M. Bréon, M. Leroy, A. Podaïre, A. Bricaud, J. C. Buriez, and G. Sèze, "The POLDER mission: Instrument characteristics and scientific objectives," *IEEE Trans. Geosci. Remote Sensing*, vol. 32, pp. 598–615, 1994.
- [10] J.-L. Deuzé, M. Herman, and R. Santer, "Fourier series expansion of the transfer equation in the atmosphere ocean system," *J. Quant. Spectrosc. Radiat. Transfer*, vol. 41, pp. 483–494, 1989.
- [11] B. Fougnie, P.-Y. Deschamps, and R. Frouin, "Vicarious calibration of the POLDER ocean color spectral bands using *in situ* measurements," *IEEE Trans. Geosci. Remote Sensing*, this issue, pp. 1567–1574.
- [12] B. Fougnie and P. Y. Deschamps, "Observation et modélisation de la signature spectrale de l'écumé de mer," in *Proc. 7th Int. Colloq. Physical Measurements and Signatures in Remote Sensing*, Apr. 7 and 11, 1997, pp. 227–234.
- [13] P. Goloub, B. Toubbe, M. Herman, T. Bailleul, O. Hagolle, J. M. Martinuzzi, and B. Rougé, "In-flight polarization calibration of POLDER," in *Proc. EUROPTO Advanced and Next-Generation Satellites*, 1996, vol. 2957, pp. 299–310.
- [14] H.-R. Gordon and M. Wang, "Retrieval of water leaving radiance and aerosol optical thickness over the oceans with Seawifs: A preliminary algorithm," *Appl. Opt.*, vol. 33, pp. 443–452, 1994.
- [15] O. Hagolle, A. Guerry, L. Cunin, B. Millet, J. Perbos, J.-M. Laherrère, T. Bret-Dibat, and L. Poutier, "POLDER Level 1 processing algorithms," in *SPIE Aerosense Proc. Algorithms for Multispectral and Hyperspectral Imagery II*, Orlando, FL, 1996, pp. 308–319.
- [16] O. Hagolle, A. Guerry, L. Cunin, B. Millet, J. Perbos, J.-M. Laherrère, and T. Bret-Dibat, "POLDER level 1 processing algorithms," *SPIE Proc.*, vol. 2758, pp. 308–319, 1996.
- [17] P. Henry, M. Dinguirard, and M. Bodilis, "Spot multitemporal calibration over stable desert areas," in *SPIE Int. Symp. Aerospace and Remote Sensing, Tech. Conf. 1938*, Orlando, FL, Apr. 12–16, 1993, pp. 67–76.
- [18] B.-N. Holben, Y.-J. Kaufman, and J.-D. Kendall, "NOAA.11 AVHRR visible and near-infrared in-flight calibration," *Int. J. Remote Sens.*, vol. 11, pp. 1511–1519, 1990.
- [19] P. Koepke, "Effective reflectance of oceanic white caps," *Appl. Opt.*, vol. 20, p. 34, 1984.
- [20] J. M. Laherrère, L. Poutier, T. Bret-Dibat, O. Hagolle, C. Baqué, P. Moyer, and E. Verges, "POLDER on-ground stray light analysis, calibration and correction," *EUROPTO SPIE Proc.*, vol. 3221, pp. 132–140.
- [21] A. Lifermann, J.-L. Counil, J.-M. Martinuzzi, and J. Perbos, "General outlines of the POLDER experiment," in *SPIE Proc. Symp. Satellite Remote Sensing II*, Paris, France, Sept. 1995, pp. 245–252.
- [22] A. Meygret, O. Hagolle, P. Henry, M. Dinguirard, P. Hazane, R. S and J.-L. Deuzé, "SPOT 3: First in-flight calibration results," in *IGARSS'94*, Pasadena, CA, 1994.
- [23] A. Morel, "Optical modeling of the upper ocean in relation biogenous matter content (case I waters)," *J. Geophys. Res.*, vol. C9, pp. 10 749–10 768, Sept. 15, 1988.
- [24] C. Moulin, C. E. Lambert, J. Poitou, and F. Dulac, "Long (1983–1994) calibration of the Meteosat solar (VIS) channel using and ocean targets," *Int. J. Remote Sens.*, vol. 17, no. 6, pp. 1183–1196.
- [25] A.-P. McNally and M. Vesperini, "Variational analysis of hru information from TOVS radiances," EUMETSAT/ECMWF Res. 1.
- [26] OCTS Team: M. Shimada *et al.*, "A CAL/VAL report on the Version 3 products," Feb. 98, NASDA Intern. Rep.
- [27] R. M. Pope and E. S. Fry, "Absorption spectrum (380–700nm) of water—II: Integrating cavity measurements," *Appl. Opt.*, vol. 36, pp. 8710, 1997.
- [28] L.-S. Rothman, C.-P. Rinsland, A. Goldman, S.-T. Massie, D.-F. Wards, J.-M. Flaud, A. Perrin, C. Camy-Peyret, V. Dana, J.-Y. Mandl, Schroeder, A. McCann, R.-R. Gamache, R.-B. Wattson, K. Yoshida, Chance, K. Jucks, L.-R. Brown, V. Nemtchinov, and P. Varanasi, HITRAN molecular spectroscopic database and HAWKS (HIT Atmospheric Workstation): 1996 Edition," *J. Quant. Spectrosc. Radiat. Transfer*, 1998.
- [29] F. Sakuma, T. Bret-Dibat, H. Sakate, A. Ono, J. Perbos, J. M. Martinuzzi, K. Imaoka, H. Oaku, T. Moriyama, Y. Miyachi, and Tange, "POLDER-OCTS preflight cross calibration using round radiometers," in *SPIE Proc. Infrared Spaceborne Remote Sensing*, San Diego, CA, July 1995, vol. 2553.
- [30] R. Santer, M. Asmani, E. Vermote, and M. Sharman, "In-flight calibration of channels 1 and 2 of AVHRR using desertic sites and clouds," *Proc. 5th ISPRS Int. Symp. Physics on Measurements and Signatures in Remote Sensing*, Courchevel, France, 1991, pp. 65–68.
- [31] M. Schwindling, P.-Y. Deschamps, and R. Frouin, "Verification of aerosol models for satellite ocean color remote sensing," *J. Geophys. Res.*, pp. 24 919–24 935, 1998.
- [32] E. Shettle and R. Fenn, "Models for the aerosols of the lower atmosphere and the effects of humidity variations on their optical properties," AGFL-TR-79-0214, Sept. 20, 1979.
- [33] P.-N. Slater, S.-F. Biggar, K.-J. Thome, D.-I. Gellman, and P.-R. Sp, "Vicarious radiometric calibrations of EOS sensors," *Amer. Meteorol. Soc. J.*, 1996.
- [34] D.-L. Smith, P.-D. Read, and C.-T. Mutlow, "The calibration of visible/infrared channels of the along-track-scanning-radiometer (ATSR2)," in *EUROPTO Proc. Sensors, Systems, and Next Generation Satellites*, London, Brittany, Sept. 97, vol. 3221, pp. 53–62.
- [35] K. Starnes, S. C. Tsay, W. Wiscombe, and K. Jayaweera, "Numerically stable algorithm for discrete ordinate method radiative transfer multiple scattering and emitting layered media," *Appl. Opt.*, vol. 37, pp. 2502–2509, 1998.
- [36] W. F. Staylor, "Degradation rates of the AVHRR visible channel for 6, 7 and 9 spacecraft," *J. Atmos. Ocean. Technol.*, vol. 7, pp. 411–419, 1990.
- [37] C. Vanbauce, J.-C. Buriez, F. Parol, B. Bonnel, G. Sèze, and P. Couvert, "Apparent pressure derived from ADEOS-POLDER observations in oxygen A-band over ocean," *Geophys. Res. Lett.*, 1998.
- [38] E. Vermote and Y.-J. Kaufman, "Absolute calibration of AVHRR visible and near infrared using ocean and cloud views," *Int. J. Remote Sens.*, vol. 16, no. 13, pp. 2317–2340, 1995.
- [39] E. Vermote, R. Santer, P. Y. Deschamps, and M. Herman, "In-flight calibration of large field of view sensors at short wavelengths using Rayleigh scattering," *Int. J. Remote Sens.*, vol. 13, no. 18, pp. 3409–3429.
- [40] E. Vermote, D. Tanré, J. L. Deuzé, M. Herman, and J. J. Morcrette, "Second simulation of the satellite signal in the solar spectrum, 6S: overview," *IEEE Trans. Geosci. Remote Sensing*, vol. 35, pp. 675–686, May 1997.
- [41] M. Vesperini, F. M. Bréon, and D. Tanré, "Atmospheric water vapor content from POLDER spaceborne measurements," this issue, 1613–1619.
- [42] C. Wehrli, "Extraterrestrial solar spectrum," Publ. no. 615 Physikalisch-Meteorologisches Observatorium, World Radiation Center, Davos, Switzerland, 1985.
- [43] B. Toubbé, T. Bailleul, J. L. Deuzé, Ph. Goloub, O. Hagolle, and M. Herman, "In flight calibration of the POLDER instrument using the sun glitter," *IEEE Trans. Geosci. Remote Sensing*, vol. 37, pp. 513–525, June 1999.

Olivier Hagolle, for a photograph and biography, see p. 525 of the January 1999 issue of this TRANSACTIONS.

Philippe Goloub, for a photograph and biography, see p. 525 of the January 1999 issue of this TRANSACTIONS.

Pierre-Yves Deschamps received the Ph.D. degree in 1977 in atmospheric physics from the Université de Lille, France.

Since then, he has been a Researcher at the Centre National de la Recherche Scientifique, working at the Laboratoire d'Etudes et de Recherches en Télédétection Spatiale and at the Laboratoire d'Optique Atmosphérique. He conducts research in atmospheric satellite remote techniques to retrieve various biophysical parameters for use in climate change studies.

Hélène Cosnefroy, photograph and biography not available at the time of publication.

Xavier Briottet received the Ph.D. degree in electronics from Ecole National Supérieure de l'Aéronautique et de l'Espace, Toulouse, France, in 1986.

Since 1986, his primary research interest in the remote sensing domain are in vicarious calibration using Rayleigh scattering and desert sites and in multiresolution problems.

Thierry Bailleul, for a photograph and biography, see p. 525 of the January 1999 issue of this TRANSACTIONS.

Jean-Marc Nicolas graduated from the Institut National des Télécommunications in 1992.

He has been working at the Laboratoire d'Optique Atmosphérique, Lille, France, since 1994, where he began to participate in the POLDER experiment as a Computer Scientist. He is interested in both atmospheric correction over ocean and calibration/validation activities for POLDER.



Frédéric Parol was born in 1963. He studied at the University of Lille, France, and received the M.S. degree in physics in 1986 and the Ph.D. degree in atmospheric physics in 1990.

He is currently an Assistant Professor of physics at the University of Lille and a Researcher employed at the Laboratoire d'Optique Atmosphérique, Lille, France. He participated in the development of the first POLDER "Earth Radiation Budget and Clouds" processing line and he was especially in charge of the "Molecular absorption correction" and "Cloud pressure" algorithms. He has been a member of the International POLDER Science Working Team (IPSWT) since 1994. His work covers theoretical and experimental research in atmospheric science, radiative transfer, and remote sensing. His major areas of activity concern remote sensing of cloud properties, interaction between clouds and radiation, and the influence of clouds on climate.

Bruno Lafrance received the Ph.D. degree in atmospheric physics from the Université des Sciences et Technologies de Lille, Laboratoire d'Optique Atmosphérique, Lille, France, in 1997. His dissertation focused on the stratospheric aerosol correction for the POLDER data processing and the formation of polarized light in the atmosphere.

He is currently with the Center National d'Etudes Spatiales, Toulouse, France. He works on the interband calibration of POLDER and vegetation over thick clouds.

Maurice Herman, for a photograph and biography, see p. 525 of the January 1999 issue of this TRANSACTIONS.

In-flight calibration of the POLDER polarized channels using the sun-glint

In-Flight Calibration of the POLDER Polarized Channels Using the Sun's Glitter

Bébé Toubbé, Thierry Bailleul, Jean Luc Deuzé, Philippe Goloub, Olivier Hagolle, and Maurice Herman

Abstract—The spaceborne sensor Polarization and Directionality of the Earth Reflectances (POLDER), launched on the Japanese platform Advanced Earth Observation Satellite (ADEOS) on August 17, 1996, is a new instrument devoted to multispectral observations of the directionality and polarization of the solar radiation reflected by the earth-atmosphere system. Polarization measurements are performed in three channels, centered at 443, 670, and 865 nm. As POLDER has no onboard calibration system, in-flight calibration methods have been developed. We address in this paper the calibration of the polarization measurements. The method uses the sunlight reflected within the sun's glitter. While the radiance of the sun's glitter depends strongly on the sea surface roughness, its intrinsic degree of polarization depends only on the observation geometry, which is specially convenient for calibration purposes. However, the degree of polarization measured at the satellite level is affected by the atmosphere. The proposed calibration scheme allows us to take into account the influence of the atmosphere on the degree of polarization measured in some viewing direction within the glitter pattern by using the radiance measured in the same viewing direction and in another direction far from the glitter. The expected accuracy is about 0.5% in the near-infrared channel 865 nm and about 2% in the visible channels, in terms of percent polarization. The method has been applied successfully to measurements achieved over ocean areas with the airborne version of the POLDER instrument.

Index Terms—Atmospheric correction, polarization of the sun glint, polarized light, remote sensing.

I. INTRODUCTION

THE SPACEBORNE sensor Polarization and Directionality of the Earth Reflectances (POLDER) is a new instrument devoted to the earth observation by providing multispectral observations of the directionality and polarization of the solar radiation reflected by the earth-atmosphere system. The instrument concept and the objectives of the experiment are described in [3].

The POLDER instrument is based on a charge coupled device (CCD) matrix array detector, a rotating filter wheel, and a wide field of view optics, for both along-track and cross-track

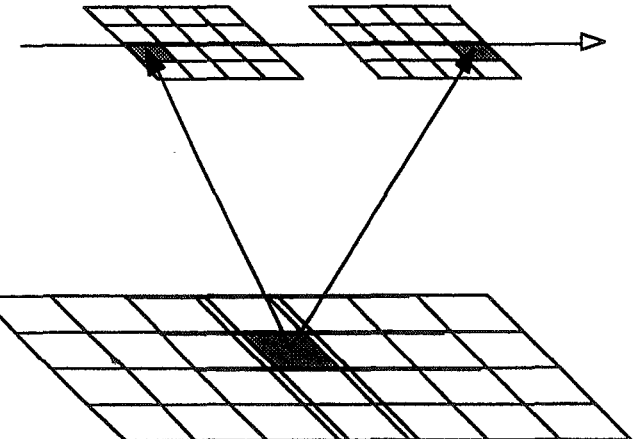


Fig. 1. Bidimensional ground areas imaged on the POLDER CCD matrix, for successive POLDER positions, overlap. As a result, convenient ground pixels may be viewed successively within the glitter pattern and out from the glitter.

viewing directions, with a maximum 114° field of view. The POLDER sensor possesses the original capability of observing the same terrestrial target from different viewing angles during the same orbit (see Fig. 1). Within some viewing directions, the radiance is measured in nine channels, ranging from 443 to 910 nm, and the polarized radiance is measured in three channels, centered at 443, 670, and 865 nm.

The objectives of the POLDER mission consist mainly in mapping atmospheric aerosol and water vapor, assessing cloud properties, improving earth radiation budget estimates, characterizing land surface properties and vegetation cover, and estimating ocean color and its role in the carbon cycle. Concerning the contribution of the polarization measurements, they are expected to provide better characterization of the terrestrial aerosols over cloud-free areas because the small aerosol particles are known to generate significant polarized light when scattering solar radiation [5]. Over cloudy areas, the polarized light should allow us to estimate the cloud top pressure and differentiate cirrus clouds from liquid clouds, from their different polarization signatures [6].

The success of the POLDER mission will depend strongly on the reliability of the calibration. As there is no internal system for onboard calibration of POLDER after launch, methods have to be developed to calibrate the instrument while in flight. We describe here the in-flight calibration method of the polarization measurements. The polarization data are assessed by using the polarization of the sun's glitter. The main characteristics of the glitter are well known (see, e.g., [2],

Manuscript received October 21, 1997; revised May 7, 1998. This work was supported by the Centre National d'Etudes Spatiales (CNES). The MEDIMAR campaign was supported by the Programme National de Télédétection Spatiale (PNTS). The data processing was supported by the Conseil Régional Nord-Pas de Calais and the Fond de la Recherche et de la Technologie.

B. Toubbé, J. L. Deuzé, P. Goloub, and M. Herman are with the Laboratoire d'Optique Atmosphérique, Université des Sciences et Technologies de Lille, 59655 Villeneuve d'Ascq Cedex, France (e-mail: herman@loa.univ-lille1.fr).

T. Bailleul is with URBA 2000, Lille, France.

O. Hagolle is with the Centre National d'Etudes Spatiales, 31055 Toulouse Cedex, France.

Publisher Item Identifier S 0196-2892(99)00327-7.

[11], [10], [15]). As shown by [2], the radiance is governed by the amount of wave facets that mirror the incident sun direction within the viewing direction. As a result, the radiance within the glitter pattern is very sensitive to the sea surface roughness that is controlled by the wind speed. The degree of polarization of the light reflected by some wave facet, however, depends only on the reflection angle according to the corresponding Fresnel's coefficients, so that the intrinsic degree of polarization of the glitter depends only on the viewing geometry. This is especially interesting for calibration purposes: measurements performed within the sun's glitter will exhibit known polarization ratios to be compared with the retrieved ones. Of course, when seen from the top of the atmosphere, the characteristics of the sun's glitter are perturbed by the influence of the atmosphere. The method consists in correcting this perturbing effect by using other POLDER measurements.

In Section II, we first describe the atmosphere-ocean model used to develop the calibration method. Then Section III presents how the POLDER measurements are used for performing the needed correction. The validation of the method is carried out in Section IV by using measurements obtained in the spring of 1991 over the Mediterranean Sea with the airborne simulator of POLDER. Finally, the error budget of the method is discussed in Section V.

II. ATMOSPHERE-OCEAN SYSTEM MODELING

Let us consider the atmosphere-ocean system consisting in a plane parallel atmosphere with inhomogeneous mixing of aerosols and molecules, bounded by the rough sea surface. The foam reflectance and the water-leaving radiance are accounted for by the way of Lambertian diffuse reflection at the bottom of the system.

To determine the upwelling radiance and its degree of polarization at top of the atmosphere (TOA), the Stokes' vector equation of radiative transfer [1] is solved according to the successive orders of scattering (SOS) scheme described by [4]. This code decomposes in Fourier series the radiative field, the atmosphere phase matrix, and the sea surface reflection matrix corresponding to the lower boundary condition. The forthcoming numerical simulations have been achieved by using exponential vertical density profiles for molecules and aerosols, with respective scale heights of 8 and 2 km; the resulting inhomogeneous atmosphere was subdivided in 26 homogeneous sublayers.

Numerical simulations of the radiation field in the coupled atmosphere-ocean system show that the resulting polarized radiance is nearly linearly polarized, which means Stokes' parameter $V = 0$, with the direction of the polarized vibration nearly parallel or perpendicular to the sun-target-satellite plane. Therefore, in what follows, we will no more consider the direction of the polarized vibration and the polarized radiance $\tilde{L} = (I, Q, U, V)$, will be characterized by the radiance $L = I$ and the polarized radiance $L^{\text{pol}} = \sqrt{Q^2 + U^2}$, or, equivalently, by the corresponding reflectance ρ , and polarized reflectance ρ^{pol} , according to

$$\rho = \pi L / (E \cos \theta_s); \quad \rho^{\text{pol}} = \pi L^{\text{pol}} / (E \cos \theta_s) \quad (1)$$

where E is the irradiance of the sun beam and θ_s is the solar zenith angle.

To account for the sea surface roughness, we use the isotropic form of the model of Cox and Munk. The slope distribution of the wave facets is simulated by an isotropic Gaussian law whose width depends on the wind speed. The resulting total reflectance and polarized reflectance ρ_g and ρ are [2]

$$\rho_g(\theta_s, \phi_s, \theta_v, \phi_v) = \frac{R(\Omega)}{4\pi\sigma^2 \cos \theta_s \cos \theta_v \cos^4 \theta_n} \cdot \exp\left(-\frac{tg^2 \theta_n}{\sigma^2}\right) \quad (2)$$

and

$$\rho^{\text{pol}}(\theta_s, \phi_s, \theta_v, \phi_v) = \frac{R^{\text{pol}}(\Omega)}{4\pi\sigma^2 \cos \theta_s \cos \theta_v \cos^4 \theta_n} \cdot \exp\left(-\frac{tg^2 \theta_n}{\sigma^2}\right). \quad (3)$$

In these equations, (θ_s, ϕ_s) are the solar zenith and azimuth angles, respectively—we will put $\phi_s = 0$, with the solar azimuth as the origin— (θ_v, ϕ_v) are the viewing zenith and azimuth angles, respectively, θ_n is the slope of the wave facets that mirror the incident direction (θ_s, ϕ_s) into the reflected direction (θ_v, ϕ_v) , Ω is the corresponding angle of incidence of the sun beam on the wave facets, and

$$\sigma^2 = 0.003 + 0.0512v^2$$

where v is the wind speed at the sea surface, in $\text{m} \cdot \text{s}^{-1}$; $R(\Omega)$ and $R^{\text{pol}}(\Omega)$ are the Fresnel's reflection coefficient and polarized reflection coefficient, i.e.,

$$R(\Omega) = (r_l^2 + r_r^2)/2; \quad R^{\text{pol}}(\Omega) = (r_l^2 - r_r^2)/2$$

with

$$r_l(\Omega) = \frac{m \cos \Omega - \cos \Omega'}{m \cos \Omega + \cos \Omega'} \quad (4)$$

and

$$r_r(\Omega) = \frac{m \cos \Omega' - \cos \Omega}{m \cos \Omega' + \cos \Omega} \quad (5)$$

where m is the refractive index of the sea water (here $m = 1.33$) and Ω' is the refraction angle for the angle of incidence Ω .

The estimates of the water-leaving radiance here correspond to waters classified as "Morel's case I" [9], consisting of oceanic waters without terrigenous influx and resuspended sediment from the continental shelf. The water-leaving radiance is modeled by a Lambertian diffuse reflection ρ_w that depends on the assumed mean pigment concentration according to the model of [9]. ρ_w is nearly null at 670 nm and completely null in the near-infrared channel at 865 nm. It contributes significantly to the signal only in the visible channel at 443 nm.

Finally, the contribution of the ocean whitecaps is modeled as well by an isotropic Lambertian reflectance ρ_f . The foam intrinsic reflectance is modeled as 0.22 independent of wavelength and, according to [8],

$$\rho_f = 0.22W \quad \text{with} \quad W = 2.95 \cdot 10^{-6} v^{3.52}$$

where W is the fraction of the sea surface covered by whitecaps.

Let L and L^{pol} stand for the radiance and polarized radiance at TOA in some viewing direction within the glitter pattern; ρ and ρ^{pol} stand for the corresponding reflectances, according to (1). They are approximately in the form

$$\rho \cong (\rho_g + \rho_w + \rho_f) e^{-M\delta} + \rho_m + \rho_a \quad (7)$$

and

$$\rho^{\text{pol}} \cong \rho_g^{\text{pol}} e^{-M\delta} + \rho_m^{\text{pol}} + \rho_a^{\text{pol}} \quad (8)$$

with

$$P = \rho^{\text{pol}} / \rho \quad (9)$$

for the degree of polarization at TOA. In these equations, ρ_m and ρ_m^{pol} correspond to the molecular scattering, ρ_a and ρ_a^{pol} to the aerosol scattering, ρ_w to the water-leaving radiance, and ρ_f to the foam; M is the air mass factor, and δ is the total optical thickness of the atmosphere. In (8), it is assumed that the foam and sea water contributions have no polarized components. The linearly polarized components from the glitter and the atmosphere are nearly either parallel or perpendicular to the scattering plane (i.e., the sun-target-satellite plane) and are considered as, respectively, negative or positive. Of course, different coupling terms between these contributions exist. They are taken into account by exact calculations, as provided by the SOS code.

Further, Fig. 12 displays a typical example of the directional patterns of the reflectance and degree of polarization of the atmosphere-ocean system, as observed by POLDER from an aircraft. Note that each image pixel corresponds to a different observation geometry. Pixels viewed under some given viewing angle θ_v are along a circle centered on the POLDER matrix center, and pixels viewed under some given azimuth ϕ_v are along a straight line through the POLDER matrix center. The observation wavelength is $\lambda = 850$ nm, the solar zenith angle and the wind speed are, respectively, about $\theta_s = 40^\circ$ and $v = 4$ m/s. Satellite measurements exhibit very similar patterns, except for slight changes in the relation between the image pixel and the corresponding solar and viewing zenith angles at ground level, due to the earth curvature.

The reflected light is mainly localized around the specular direction, that is, the direction where all light would be reflected by a perfectly flat oceanic surface. The glitter appears as an oval blob, with a decreasing intensity from the core to the rims, with a large degree of polarization, because the corresponding angles of incidence are not far from the Brewster's angle. We plan to select polarization measurements within the glitter blob, with leading contributions of the glitter terms in (7) and (8). The degree of polarization P of the incoming light in these directions must be near from the intrinsic degree of polarization of the glitter P_g , i.e., $\rho_g^{\text{pol}} / \rho_g$. As P_g may be predicted from the observation geometry, by assuming that the departure ($P - P_g$) due to the other terms of (7) and (8) may be estimated from other POLDER measurements, we will obtain the degree of polarization to be compared with the measured one for calibration purposes.

III. CALIBRATION METHOD

A. Principle

As shown by (7)-(9), the degree of polarization measured at the TOA within the glitter pattern depends partly on surface and atmospheric effects. By selecting images acquired with wind speeds lower than about 10 m/s, the foam contribution should be negligible, with $\rho_f < 0.001$ according to (6), compared with typical glitter reflectances $\rho_g \approx 0.20-0.60$. Similarly, the water-leaving radiance is quite small at 670 and 865 nm, so that in these POLDER channels the degree of polarization at TOA is approximately

$$P \cong \frac{\rho_g P_g e^{-M\delta} + \rho_m P_m + \rho_a P_a}{\rho_g e^{-M\delta} + \rho_m + \rho_a} \quad (10)$$

where the molecular terms are known. Equation (10) shows that the estimate of the degree of polarization at TOA needs some knowledge of the sun glitter magnitude and of the aerosol properties. The 443-nm channel will require further study concerning the sea water contribution.

Clearly, given the large radiance of the sun's glitter, ρ_g is the leading term in (7). Therefore, the radiance ρ measured in the same direction as P , say, the calibration direction, should give some insight about the ρ_g terms in (10). Concerning the aerosols, it is known that the path radiance measured above dark surfaces, as waters at 865 nm, is strongly correlated to the aerosol loading (see, e.g., [7]). Let ρ_{atm} stand for the radiance measured in some viewing direction outside from the glitter pattern, say, the atmospheric direction; we will look for using ρ_{atm} as an indicator of the aerosol contribution in (10). As POLDER enables us to see the same target in 13 different directions, the radiance will be measured nearly simultaneously in the glitter and far from the glitter region, and these measurements will be used to account, respectively, for the surface and aerosol influences in the measured degree of polarization.

B. Feasibility

To illustrate this possibility, let us consider numerical simulations of POLDER observations over oceanic targets. The calculations are carried out at 443 and 865 nm for different solar zenith angles ranging from 20 to 60°, four different surface wind speeds, $v = 2, 5, 10$, and 15 m/s, and four different aerosol loadings characterized by the aerosol optical thickness δ_a at 865 nm, $\delta_a = 0.05, 0.10, 0.15$, and 0.20. For simplicity, the water-leaving radiance and the foam reflectance are neglected. The calculations are conducted for different aerosol models, consisting in spherical particles with real refractive index m and with size distribution in the form

$$n(r) = \frac{1}{\sqrt{2\pi}\sigma r} \exp\left(-\frac{\ln^2(r/\bar{r})}{2\sigma^2}\right). \quad (11)$$

For a first guess, we consider seven aerosol models: three models with $m = 1.33$ corresponding to large maritime aerosols and four models with $m = 1.50$ to change the physical properties of the particles. The model parameters are given in Table I. They were adjusted to provide Angström coefficient

TABLE I

CHARACTERISTICS OF THE SEVEN AEROSOL MODELS USED AS DATABASE FOR THE FAISABILITY STUDY OF THE METHOD. \bar{r} AND σ ARE THE MODAL RADIUS AND STANDARD DEVIATION OF THE AEROSOL DISTRIBUTION (11), RESPECTIVELY; α IS THE RESULTING ANGSTROM COEFFICIENT

Refractive index	1.33			1.50			
model number	1	2	3	4	5	6	7
$\bar{r} (\mu\text{m})$	0.5	0.33	0.25	0.45	0.3	0.2	0.27
σ	1.52	1.5	1.5	1.47	1.47	1.5	1.36
α	0	0.52	1	0	0.5	1	1.5

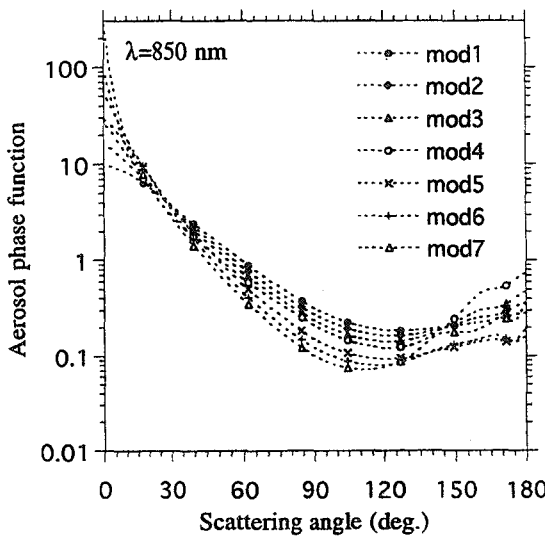


Fig. 2. Phase functions of the aerosol models described in Table I, for $\lambda = 865 \text{ nm}$.

α , ranging from zero to 1.5 ($\alpha = \ln(\delta(\lambda)/\delta(\lambda'))/\ln(\lambda'/\lambda)$, with $\lambda = 670 \text{ nm}$ and $\lambda' = 865 \text{ nm}$).

The phase function and the degree of linear polarization for single scattering of the models, at $\lambda = 865 \text{ nm}$, are shown in Figs. 2 and 3, respectively. Note that the polarization characteristics of the models differ largely, which allows us to test whether this aerosol property has a small influence on the retrieval of the glitter polarization.

For simplicity, let us restrict to just observations in the exact specular direction that are representative of the problem. The degree of polarization calculated in this calibration direction for the different conditions (θ_s, δ_a, v , aerosol model) is reported in Figs. 4 and 5, for $\lambda = 865 \text{ nm}$ and 443 nm , respectively, as a function of P_g in the same direction. As P_g depends only on the viewing geometry, it depends only on θ_s in these simulations.

Figs. 4 and 5 show that P may depart largely from P_g . The discrepancies are larger at 443 nm , where the larger influence of the molecular scattering reduces the glitter contribution in the measurements. We intend to predict from radiance measurements of POLDER the departure

$$\Delta P = P - P_g. \quad (12)$$

Let us consider measurements at $\lambda = 865 \text{ nm}$.

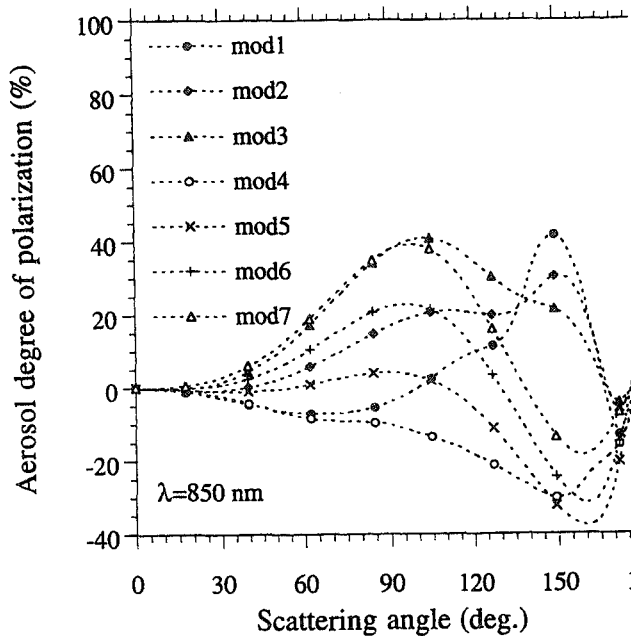


Fig. 3. Degree of polarization for single scattering of the aerosol models described in Table I, for $\lambda = 865 \text{ nm}$.

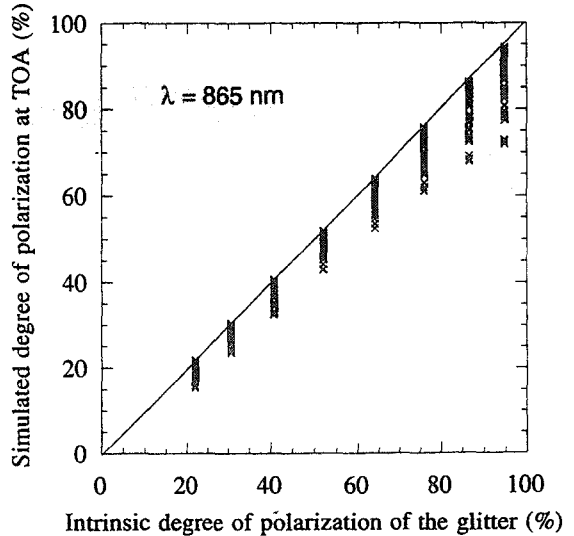


Fig. 4. Degree of polarization at TOA in the specular direction P is compared with the intrinsic degree of polarization of the glitter in the same view direction P_g . Numerical simulations. The discrepancy $(P - P_g)$ illustrates atmospheric influence. Different surface wind speeds, aerosol loadings, aerosol models, and solar zenith angles are considered. The observation wavelength is $\lambda = 865 \text{ nm}$.

First, let us examine how ΔP varies as a function of sea surface condition, with the aerosol component unchanged. When reporting (10) in (12), it comes after transformation

$$\frac{\Delta P}{P_g} \approx -\frac{\rho_a \left(1 - \frac{P_a}{P_g}\right) + \rho_m \left(1 - \frac{P_m}{P_g}\right)}{\rho_g e^{-M\delta} + \rho_m + \rho_a} \approx -\frac{K}{\rho} \quad (13)$$

where ρ is the reflectance in the considered calibration direction. Fig. 6 shows some examples of $\Delta P/P_g$ as a function of the reflectance ρ in the specular direction, for the same con-

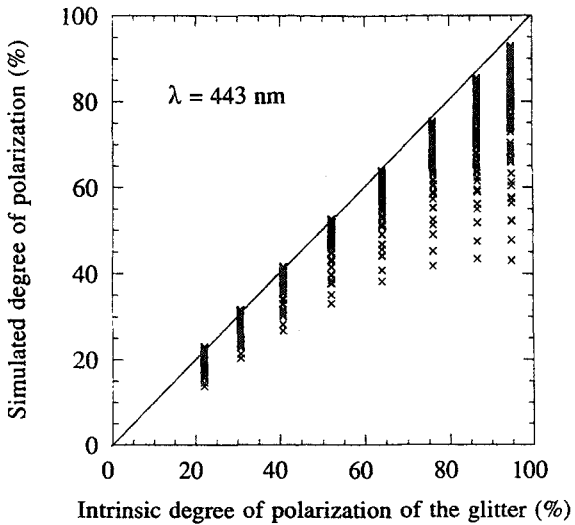


Fig. 5. Same legend as Fig. 4, but for $\lambda = 443 \text{ nm}$.

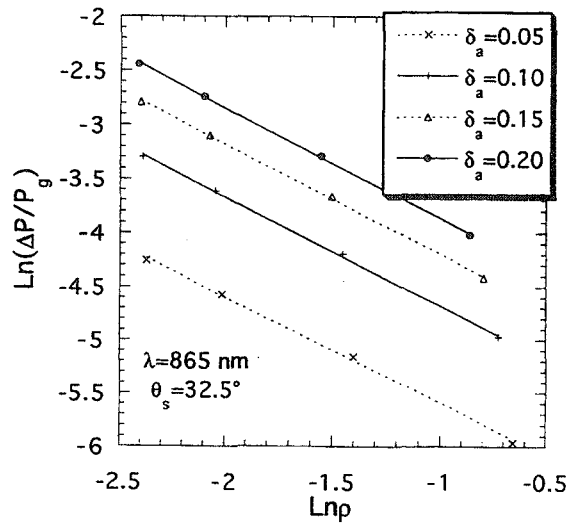


Fig. 6. Discrepancy $(P - P_g)$ between the polarization ratio at TOA and the intrinsic glitter one, in the specular direction, as a function of the reflectance at TOA in the same direction ρ ; $\lambda = 865 \text{ nm}$. Here, the solar zenith angle and the aerosol model are fixed and the wind speed and the aerosol loading are varied. The reflectance depends mainly on the sea surface wind speed, while the polarization ratio at TOA depends on the aerosol component. Similar figures, for other aerosol models, solar zenith angles, and observation wavelengths show that $((P - P_g) \approx P_g/\rho)$.

tions. The results are qualitatively consistent with (13). Within the ranges of aerosol characteristics and solar zenith angles, the calculations provide approximately $\Delta P/P_g \cong -K\rho^\beta$, where $\beta = -1.10 \pm 0.10$.

Let us put $\beta = -1.10$, that is

$$\frac{\Delta P}{P_g} \cong -K\rho^\beta \quad \text{with } \beta = -1.10 \quad (14a)$$

and, then, examine whether the aerosol influence on K is correlated with the atmospheric reflectance at TOA, say, ρ_{atm} , in directions outside the glitter pattern.

According to (13), K is approximately in the form $\rho_a(1 - P_a/P_g) + \rho_m(1 - P_m/P_g)$, so that the correlation

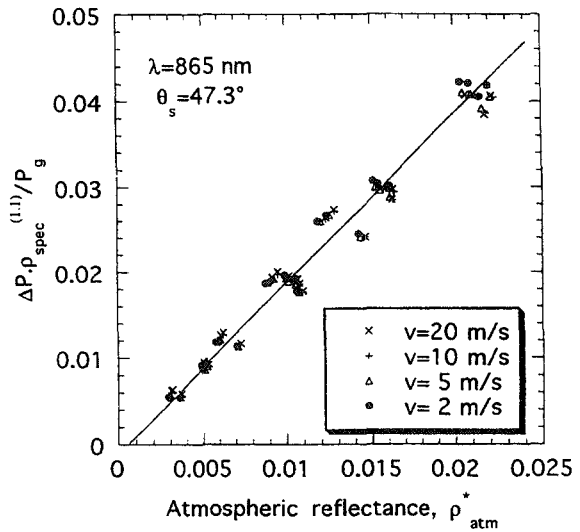


Fig. 7. Correlation between the normalized discrepancy $\rho^{1.10}(P - P_g)/P_g$ and the reflectance in some viewing direction outside the glitter pattern, corrected from the molecular contribution ρ_{atm}^* . The correlation depends on the solar zenith angle, which is fixed in the figure, but it is nearly independent on the sea surface wind speed (four values), aerosol model (seven models) or aerosol loading (four optical thicknesses).

between ρ_{atm} and K clearly depends on the calibration direction within the glitter, say, $(\theta_{\text{glitt}}, \phi_{\text{glitt}})$, on the atmospheric direction, say, $(\theta_{\text{atm}}, \phi_{\text{atm}})$, and on the solar zenith angle at the observed point θ_s . Whatever θ_s , let us again restrict to just the specular direction as the calibration one, and, for simplicity, let us choose arbitrarily the atmospheric direction within the antispecular half-plane with $\theta_{\text{atm}} = 21^\circ$, which is nearly always obtained within the 14 simultaneous directions of POLDER. Moreover, for better linearity, let us correct the atmospheric reflectance for the molecular contribution according to $\rho_{\text{atm}}^* = \rho_{\text{atm}} - \rho_{\text{atm}}^m$, where ρ_{atm}^m is obtained by neglecting the aerosol component in the calculations.

For $\theta_s = 47.3^\circ$ as an example, Fig. 7 shows how $\rho^{1.10}\Delta P/P_g$ varies as a function of ρ_{atm}^* . Similar results are obtained for other solar zenith angles, but the correlation is better when θ_s is close to the Brewster angle. This is consistent with (13) since the expected influence of the aerosols on K , i.e., $\rho_a(1 - P_a/P_g)$, must be reduced when P_g is large. In any case, Fig. 7 suggests that, given the sea surface condition, we may look for a linear relationship between the corrected atmospheric path radiance ρ_{atm}^* and the departure ΔP due to the aerosol influence.

At $\lambda = 670$ and 443 nm , ΔP exhibits similar behaviors. Whatever the polarized channel, however, the best information on the aerosols and the sea surface condition are expected from the measurements at 865 nm , where the water-leaving radiance is null and the influence of molecular scattering is minimum. Therefore, according to the previous analysis, we will search to derive the degree of polarization P at TOA, in some viewing direction of the glitter pattern, from

$$\Delta P = P - P_g = P_g(a_0 + a_1(\rho^{865})^\beta + a_2(\rho^{865})\rho_{\text{atm}}^{*865}), \quad \beta = -1.10 \quad (14b)$$

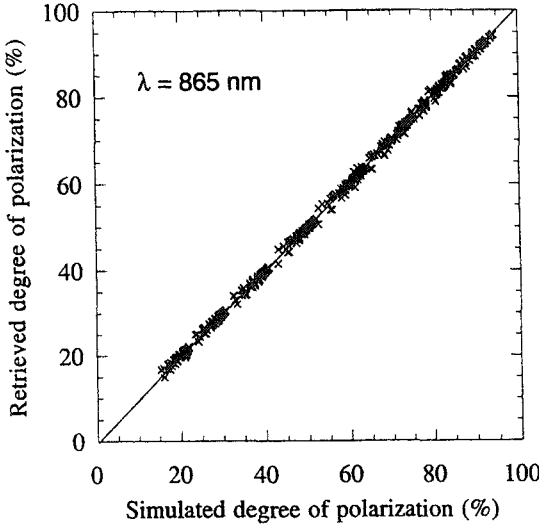


Fig. 8. Direct calculations of the degree of polarization at TOA in the specular direction are compared with their retrieval according to (14b) from the reflectances in the calibration and atmospheric directions. Different solar zenith angles, sea surface wind speeds (4), aerosol models (7), and aerosol loadings (4) are considered. The calculations are for $\lambda = 865$ nm.

where ρ^{865} and ρ_{atm}^{*865} stand, respectively, for the reflectance in the calibration direction and the corrected reflectance in the atmospheric direction at 865 nm. In (14b), given the wavelength, a_0, a_1, a_2 depend only on $\theta_s, \theta_{\text{glitt}}, \phi_{\text{glitt}}, \theta_{\text{atm}}, \phi_{\text{atm}}$ and have to be adjusted through numerical simulations of the radiances and degree of polarization for a set of experimental conditions and aerosol models. A more general polynomial formula will be looked for later.

C. Results

Given θ_s , considering the specular direction as the calibration one and by using the atmospheric direction indicated previously, the reflectances and polarization ratios at 443 and 865 nm were calculated for the previous set of conditions (four wind speeds, four aerosol optical thicknesses, and seven aerosol models). Then, the coefficients a_0, a_1, a_2 were adjusted to minimize the standard deviation between the $4 \times 4 \times 7$ direct calculations of P and their estimates from ρ^{865} and ρ_{atm}^{*865} according to (14b); a_0, a_1, a_2 depend only on θ_s and no more on the surface conditions and aerosol properties. Finally, the degrees of polarization retrieved from (14b) are compared with their direct calculations in Figs. 8 and 9, for 865 and 443 nm, respectively. Comparison of these figures with Figs. 4 and 5 shows the efficiency of the correction scheme.

In Fig. 8, the standard deviation is $\Delta P \approx \pm 0.5\%$; the largest errors, which correspond to large wind speeds and/or to large aerosol contents, are no more than $\Delta P \approx \pm 2\%$. The least-squares fit to the relationship between the retrieved and calculated degrees of polarization, say, $P_{\text{retr}} = aP_{\text{calc}} + b$, gives $a = 0.9995, b = 0.02$ with correlation coefficient $r = 0.9997$; note that the leading term in (14a) is the a_2 term (about 95% of the P estimate).

Let us now consider the case of calibration directions different from the specular one. In order to determine the glitter area convenient for calibration, the method was applied

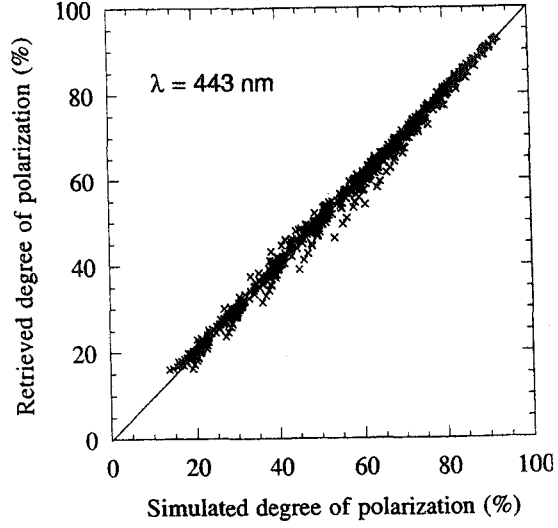


Fig. 9. Same legend as Fig. 8, but for $\lambda = 443$ nm.

systematically to a set of calibrations directions such th

$$\theta_s - 20^\circ < \theta_{\text{glitt}} < \theta_s + 20^\circ \quad \text{and} \quad -40^\circ < \phi_{\text{glitt}} <$$

Whatever θ_s and $\theta_{\text{glit}}, \phi_{\text{glit}}$, we used the same atmosph direction as previously. For each direction $\theta_{\text{glit}}, \phi_{\text{glit}}$ coefficients were adjusted and the resulting standard dev was estimated. An example of result is shown in Fig. the format of the POLDER images. Retrieval of P $\Delta P \approx \pm 1\%$ is possible for a large set of points aroun specular point. Examination of these points shows that correspond grossly, in the Cox and Munk model, to facets with inclination $\theta_n < 6^\circ$, which provides a s geometrical test for selecting the image pixels to be use

As an example, for the case of $v = 5$ m/s, $\theta_s = 40^\circ$: specular point, with an optical thickness $\delta_a = 0.14$ at 86 of the aerosol model 1 of Table I, the method was appli all the image pixels corresponding to $\theta_n < 6^\circ$. The r compare well, in Fig. 11, with the direct calculations c degree of polarization within the glitter pattern.

IV. VALIDATION OF THE METHOD

A. Data

To test the method on experimental data, we used images acquired by the airborne simulator of POLDER sea surfaces during the French Mediterranean campaign M IMAR, organized by INSU (Institut National des Sci de l'Univers) in March and April 1991. Oceanographic experiments conducted during this campaign were perfo aboard the oceanic vessel SUROIT. The airborne simulator POLDER was flown five times over the Mediterranean from March 28 to April 4, 1991, aboard the ARAT (Avio Recherches Atmosphériques et de Télédétection), at a altitude of 4500 m. During these flights, the simulator equipped only with five filters, centered at 450, 500, 670, and 850 nm, with polarization measurements perfo

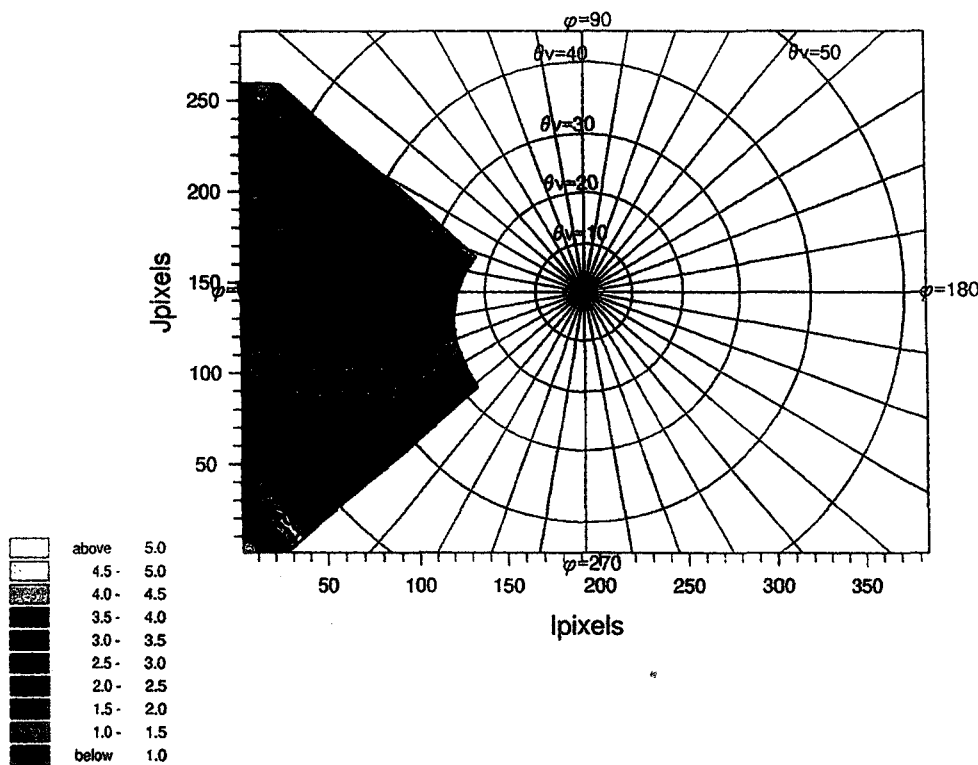


Fig. 10. Error in the retrieval of the polarization ratio at TOA, as a function of the viewing direction within the glitter pattern. Results are presented in the format of a POLDER image. Given the image pixel, the mean quadratic error corresponding to the different wind speeds, aerosol models, and aerosol loadings considered is reported, in terms of percent polarization. The calculations are for $\lambda = 865 \text{ nm}$ and $\theta_s = 43.6^\circ$. Concentric circles indicate the viewing zenith angle. Isolines corresponding to constant values of wave facet slope θ_n are also indicated.

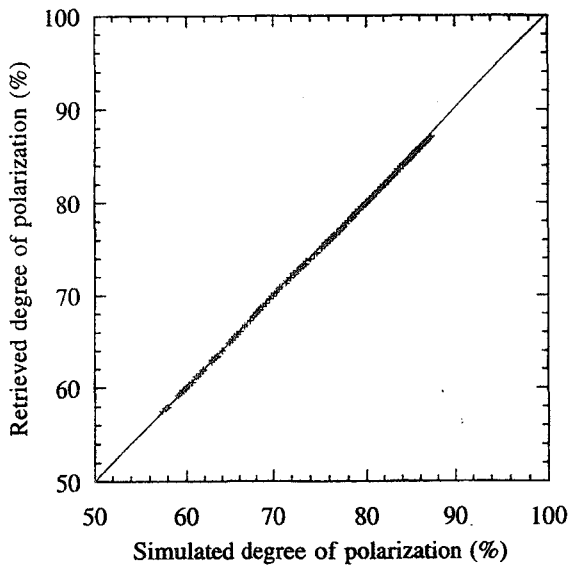


Fig. 11. Solar zenith angle, the sea surface wind speed, and the aerosol component are fixed (see text). Direct calculations of the degree of polarization at TOA, in different directions within the glitter pattern, are compared with their retrieval according to (15) from the reflectances in the calibration and atmospheric directions. The viewing directions have been selected according to a threshold on the corresponding wave facet slopes: $\theta_n < 6^\circ$.

in the 450- and 850-nm channels. In parallel with the flights of POLDER, ground-based measurements of the aerosol spectral optical thickness were performed with instruments located on the SUROIT. Moreover, the surface wind speed was measured when the ARAT overpassed the SUROIT.

TABLE II
CHARACTERISTICS OF THE POLDER FLIGHTS OF THE MEDIMAR CAMPAIGN USED FOR THE VALIDATION OF THE METHOD: θ_s IS THE SOLAR ZENITH ANGLE, v IS THE WIND SPEED, AND δ_a IS THE AEROSOL OPTICAL THICKNESS AT 850 nm, MEASURED ABOARD THE OCEANOGRAPHIC VESSEL SUROIT AT THE POLDER OVERPASS

	March 31	April 1	April 2
$v(\text{m/s})$	7	14.5	4
$\delta_a(850 \text{ nm})$	0.14	0.11	0.14
$\theta_s (\text{°})$	46	38	40

We have selected three POLDER flights that were performed with small cloud amounts: on March 31, April 1, and April 2, 1991. The prevailing surface wind speed, solar zenith angle, and aerosol optical thickness at 850 nm when POLDER overpassed the SUROIT have been reported in Table II. Note that two of these flights offer the advantage of low wind speed and, thus, negligible whitecaps and high glitter reflectance.

B. Results

Examination of the results shows that, for our present study, the POLDER images acquired all along a flight exhibit negligible differences. Therefore, for each flight, we will restrict to typical measurement sequences acquired in the vicinity of the SUROIT. We will present the results obtained for the 850-nm channel only. In the 450-nm channel, the measurements are very noisy. Moreover, because of the uncertainty on the prevailing water-leaving reflectance over

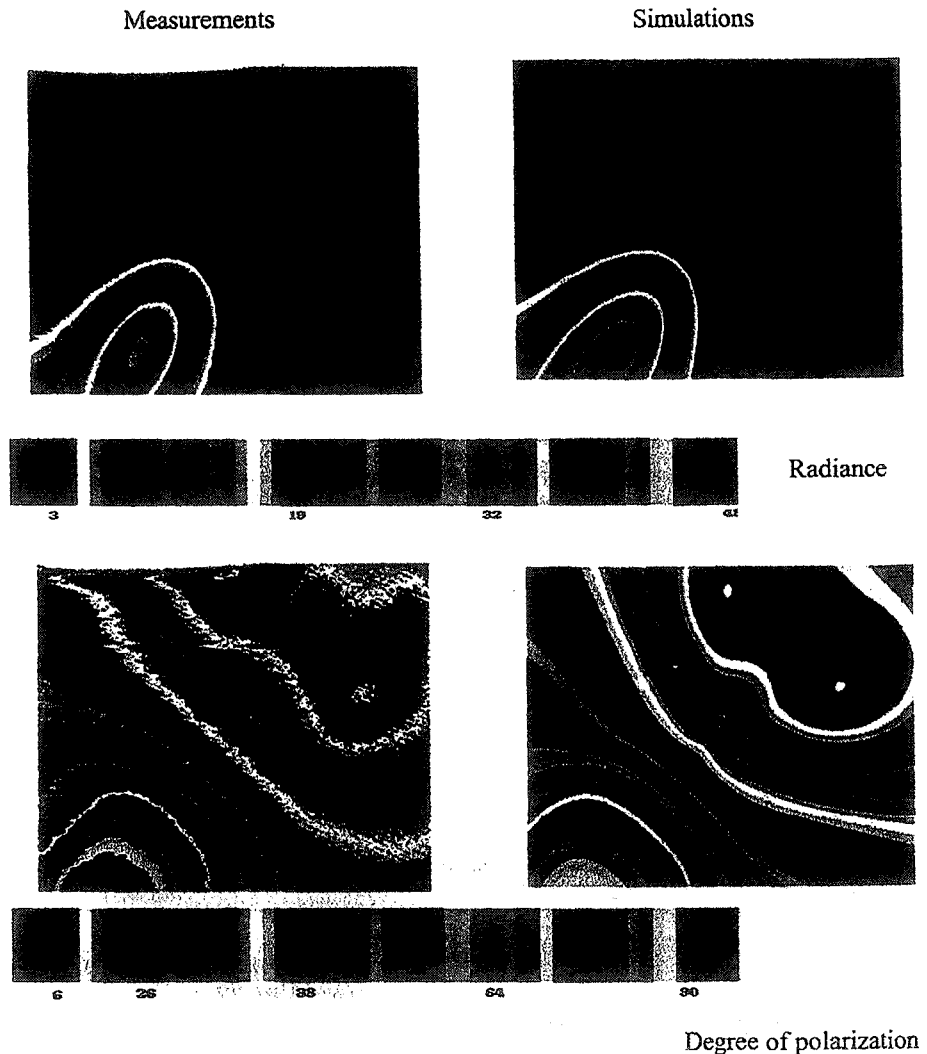


Fig. 12. Upper left and lower left: bidirectional measurements of the radiance and degree of polarization performed by the airborne version of POLDER over the Mediterranean sea, at 4500-m altitude at $\lambda = 850$ nm, on April 2, 1991; the solar zenith angle is 40° . The glitter pattern is localized in the lower left corner of the POLDER image, exhibiting large radiance and degree of polarization. Upper right and lower right: numerical simulation of the POLDER observations. The sea surface wind speed and aerosol optical thickness used in the calculations correspond to ground-based measurements. Better fit could be obtained by adjusting these parameters and the aerosol model.

this nearly coastal area, the agreement between the simulated and measured degree of polarization depends partly on the assumed figure for ρ_w , so that the validation is not convincing. On account of the aircraft altitude, calculations related to these measurements will be conducted with 57% of the molecular atmosphere under and 43% above the sensor. By considering that tropospheric aerosols are generally encountered within the very first kilometers of the atmosphere, all of the aerosol layer will be assumed to be under the sensor, with homogeneous mixing of aerosol and molecules in this lower layer.

For the flight of April 2, 1991, Fig. 12 shows the radiance and degree of polarization measured in the 850-nm channel. The experimental data have been smoothed on 3×3 pixel areas to reduce the radiometric noise. The measurements are compared with numerical simulations based on the *in-situ* measurements of the wind speed and aerosol optical thickness. The aerosol model was determined by simply adjusting the parameters of a log-normal distribution of spherical particles with

refractive index 1.33 to fit the measured Angström coefficient. Fig. 12 shows that measurements and numerical simulations exhibit very similar patterns. Of course, because the POLDER simulator was calibrated in the laboratory just before after the campaign, we are confident in the polarization and the validation here consists in controlling that the degree of polarization retrieved by the algorithm agrees with measured one.

Then, to apply the calibration scheme to these images, a_0, a_1, a_2 coefficients were adjusted from numerical simulations. The calculations were conducted for the same wind speeds and aerosol optical thicknesses as previously, but for different aerosol models. According to the ground-based measurements, the Angström coefficient of the aerosol particles observed during the MEDIMAR campaign was about 1.5, which is larger than typical Angström coefficients of maritime aerosols. As the measurements were carried out no farther than about 100 km from the coast, a component of smaller continental

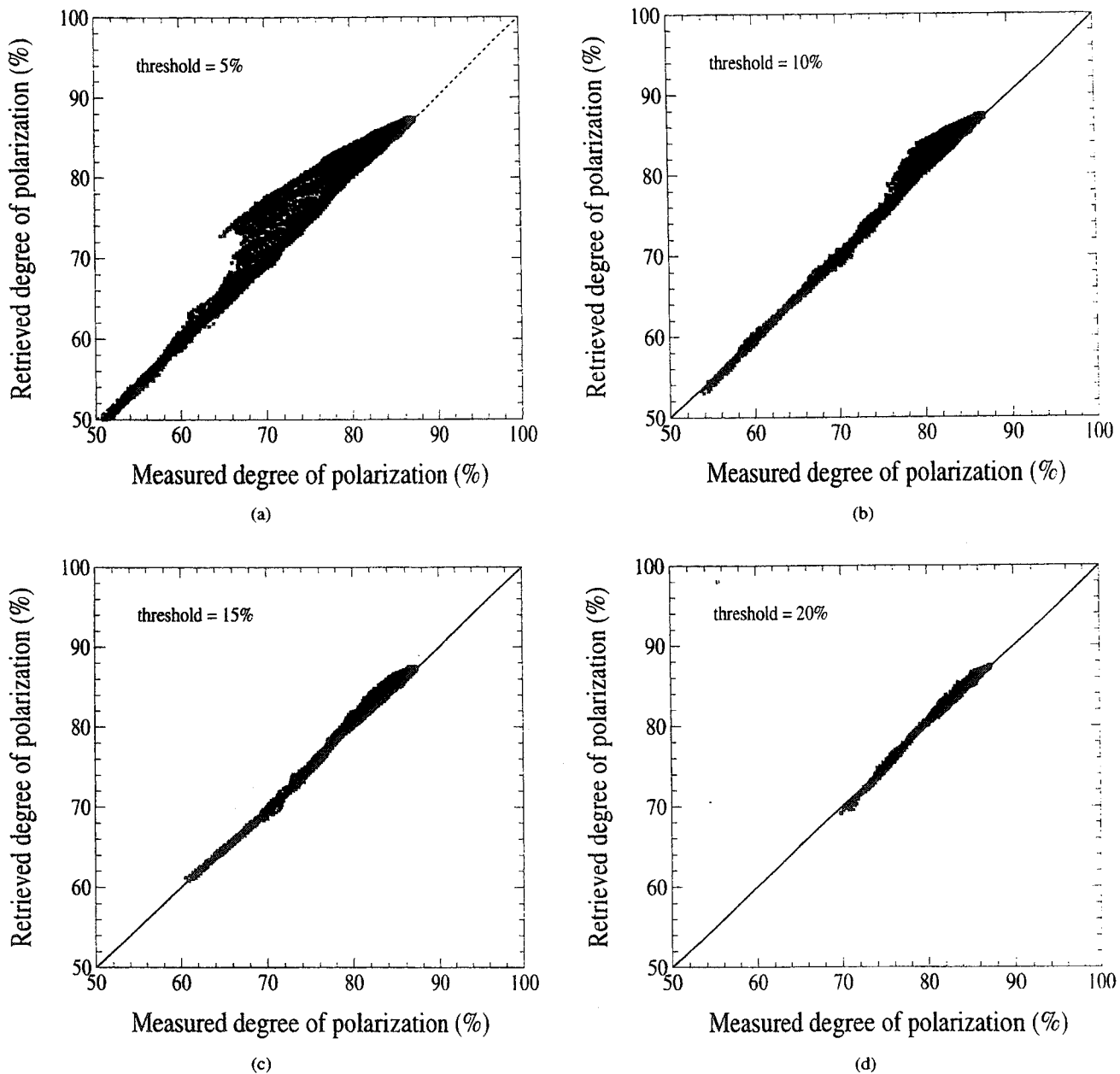


Fig. 13. Measurements of the degree of polarization in different directions within the glitter pattern, at the aircraft level, are compared with their retrieval according to (15) from the reflectances in the calibration and atmospheric directions. Measurements are selected according to different thresholds on the reflectance in the calibration direction: 0.05, 0.10, 0.15, and 0.20 in Fig. 13(a)–(d), respectively. The last two thresholds correspond approximately to $\theta_n < 9^\circ$ and $\theta_n < 7^\circ$. April 2, 1991, flight; $\lambda = 850$ nm.

aerosols probably prevailed. Therefore, the database of Table I was enlarged by four supplementary aerosol models with Angström coefficients ranging from 1.2 to two. As θ_s does not vary through a POLDER image for aircraft observations, the calculations were conducted only for the solar zenith angles of Table II. Finally, the atmospheric direction was fixed arbitrarily as previously; we assumed that the aerosol properties did not change within a POLDER image (about 9 km at sea level), and, whatever the considered calibration direction within the POLDER image, we used the atmospheric direction corresponding to $\theta_{\text{atm}} = 21^\circ$ in the antispecular half plane. To summarize, for each flight, $4 \times 4 \times 11$ calculations of the corrected reflectance in the fixed direction $(\theta_{\text{atm}}, \phi_{\text{atm}})$

and of the reflectance and degree of polarization in a set of directions $(\theta_{\text{glitt}}, \phi_{\text{glitt}})$ within the glitter pattern were performed, for $\lambda = 850$ nm, from which the coefficients were adjusted; given θ_s, a_0, a_1, a_2 depend only on $(\theta_{\text{glitt}}, \phi_{\text{glitt}})$.

In Section III, we proposed to limit the calibration area from geometric considerations. Another possibility consists in selecting the pixels to be used by some convenient threshold on their radiance to eliminate pixels for which the direct glitter contribution is too small. Let us consider the April 2 flight, the observations of which compare well with numerical simulations based on the correlative measurements of the aerosol optical thickness and wind speed. For one image of this flight, Fig. 13(a)–(d) compare the degree of polarization

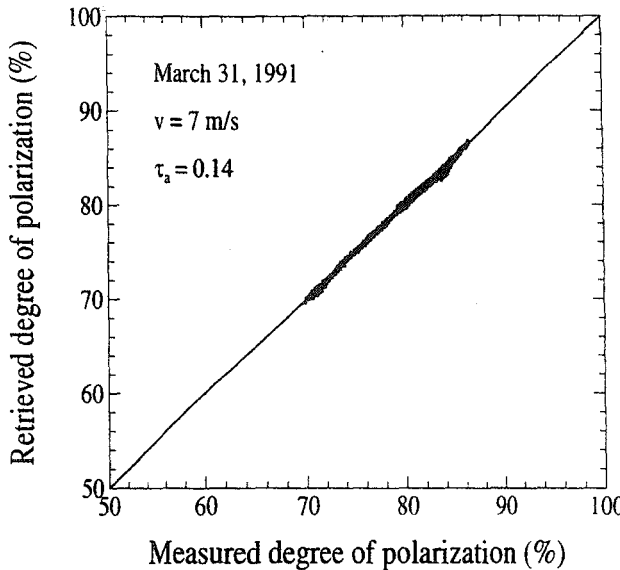


Fig. 14. Typical comparison between measurements and retrieval of the degree of polarization in different directions within the glitter pattern, at the aircraft level. The POLDER image corresponds to the flight of March 31, 1991. The wind speed and aerosol loading measured aboard the SUROIT are indicated.

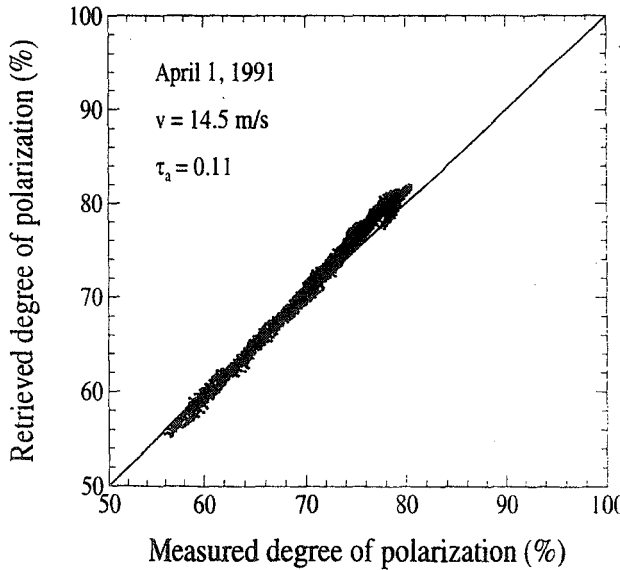


Fig. 15. Same legend as Fig. 14, but for a picture acquired on April 1, 1991.

retrieved from (15) with the measurements, for four different thresholds on ρ : 0.05, 0.1, 0.15, and 0.2. The 0.15 and 0.20 thresholds seem correct. By neglecting the small atmospheric effect, which is small at this wavelength, according to (2), these thresholds correspond approximately to $\theta_n < 9^\circ$ and $\theta_n < 7^\circ$, which confirms the selectivity of the proposed test.

Finally, Figs. 14–16 present results obtained for POLDER images acquired during the flights of March 31, April 1, and April 2, respectively. On March 31 and April 2, the results are quite good and agree within about 1% polarization. On account of the large wind speed prevailing on April 1, the results are more scattered in Fig. 15, which shows that, for calibration purposes, images acquired with wind speeds lower than about 10 m/s are preferred.

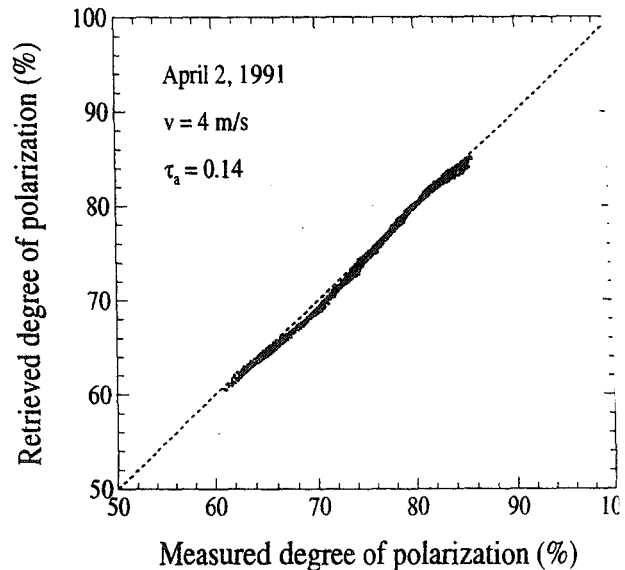


Fig. 16. Same legend as Fig. 14, but for a picture acquired on April 2, 1991.

TABLE III
CHARACTERISTICS OF THE SIX AEROSOL MODELS USED AS DATABASE FOR 1 SATELLITE VERSION OF THE METHOD. \bar{r} AND σ ARE THE MODAL RADIUS AND STANDARD DEVIATION, RESPECTIVELY, OF THE AEROSOL SIZE DISTRIBUTION

Relative humidity	Tropospheric model		Maritime model	
	σ	$\bar{r} (\mu\text{m})$	σ	$\bar{r} (\mu\text{m})$
70%	0.806	0.02846	0.921	0.2041
90%	0.806	0.03884	0.921	0.3803
98%	0.806	0.04751	0.921	0.6024

V. ERROR BUDGET OF THE SATELLITE VERSION OF THE METHOD

A. Satellite Version of the Method

The calibration method that will be applied to the satellite measurements corresponds to the main previous considerations, except for some minor points.

To improve the accuracy of the method, the polynomial development of ΔP has been taken into the form

$$\begin{aligned} \Delta P &= P - P_g \\ &= P_g [a_0 + \rho^\beta (a_1 + a_2 \rho_{\text{atm}}^* + a_3 \rho + a_4 \rho_{\text{atm}}^* \rho \\ &\quad + a_5 \rho_{\text{atm}}^{*2} + a_6 \rho^2)] \end{aligned} \quad (1)$$

where $\beta = -1.10$; whatever the calibrated channel, ρ and ρ_{atm}^* correspond to measurements in the near-infrared channel 865 nm.

Because the aerosol properties may vary within the glitter area, as seen from the Japanese platform Advanced Earth Observation Satellite (ADEOS) orbit, the calibration will be performed by using for ρ and ρ_{atm}^* the measurements corresponding to the same ground pixel, so that $(\theta_{\text{atm}}, \phi_{\text{atm}})$ will depend on $(\theta_{\text{glitt}}, \phi_{\text{glitt}})$ and on the POLDER position.

TABLE IV

ERROR BUDGET OF THE CALIBRATION METHOD, IN TERMS OF PERCENT POLARIZATION, FOR THE THREE POLDER POLARIZED CHANNELS AS A FUNCTION OF SOLAR ZENITH ANGLE. THE RESULTING ERROR IS THE QUADRATIC SUM OF THE FIVE ERROR SOURCES

θ_s	443 nm		670 nm		865 nm	
	40°	60°	40°	60°	40°	60°
Method error	0.56	0.70	0.36	0.86	0.16	0.72
Calibration error (at 865nm)	0.10	0.15	0.10	0.15	0.10	0.15
Foam reflectance error	0.10	0.00	0.05	0.00	0.02	0.00
Water-leaving radiance error	0.90	0.00	0.00	0.00	0.00	0.00
Atmospheric pressure error	0.02	0.04	0.001	0.009	0.017	0.014
Mean quadratic error	1.07	0.72	0.37	0.87	0.19	0.73

on its orbit. The coefficients of (16), therefore, have been calculated for different values of the five geometric parameters, i.e., $a_i(\theta_s, \theta_{\text{glitt}}, \phi_{\text{glitt}}, \theta_{\text{atm}}, \phi_{\text{atm}})$. Note that numerical tests show that, given θ_s and $(\theta_{\text{glitt}}, \phi_{\text{glitt}})$, the accuracy of the method does not vary with $(\theta_{\text{atm}}, \phi_{\text{atm}})$, provided that the atmospheric direction is well outside the glitter. We will use for $(\theta_{\text{atm}}, \phi_{\text{atm}})$ the viewing direction furthest from the calibration one.

The numerical simulations of P , ρ , and ρ_{atm}^* from which the coefficients in (16) have been adjusted correspond again to four different wind speeds, four different aerosol loading, and a set of aerosol models, as follows.

- 1) For the surface wind speed, we have used as previously $v = 2, 5, 10$, and 15 m/s in the model of Cox and Munk, but, given v , we have taken into account the corresponding foam contribution by the way of its Lambertian reflectance, according to the model of [8], that is, $\rho_f = 0.0, 0.19, 10^{-3}, 2.15, 10^{-3}$, and $8.95, 10^{-3}$, respectively, for $v = 2, 5, 10$, and 15 m/s .
- 2) As the aerosol optical thickness is generally quite low over the open ocean [12], we considered only $\delta_a = 0.025, 0.050, 0.075$, and 0.100 at 865 nm . To assess that the POLDER images used for calibration correspond effectively to low aerosol loading, a convenient threshold, $\rho_{\text{atm}}^* \cos \theta_s < 0.005$, will be used.
- 3) The aerosol database used for the simulations consists in six aerosol models retained from the models of [13] and [14]. We retained the tropospheric model and a mixture of 99% of the tropospheric model and 1% of the maritime model, for 70, 90, and 98% of relative humidity; the refractive indexes of the tropospheric and maritime models as a function of the humidity level are given in [14], and their standard deviation and mode radii are given in Table III.
- 4) Finally, we have taken into account the sea water contribution by the way of the Lambertian reflectance ρ_w corresponding to a chlorophyll pigment concentration of 0.05 mg/m^3 , according to the model of [9], that is, $\rho_w = 0.00, 0.00048$, and 0.026 , respectively, at $\lambda = 865, 670$, and 443 nm .

The test for selecting pixels to be used for the calibration is $\theta_n < 6^\circ$, as shown previously.

B. Error Budget

The error budget of the calibration has been estimated by using the previous satellite version of the method. We identified the following as the main error sources:

- 1) method error, due to the different approximations;
- 2) errors on ρ and ρ_{atm}^* , due to the radiometric calibration of POLDER;
- 3) errors on ρ_w and ρ_f , that are derived from models;
- 4) error on the molecular contribution; the numerical simulations from which $a_i(\theta_s, \theta_{\text{glitt}}, \phi_{\text{glitt}}, \theta_{\text{atm}}, \phi_{\text{atm}})$ are derived are performed for a standard 1013-hPa pressure at sea level.

The method error is defined by the mean standard deviation between the calculated and retrieved degrees of polarization for the different situations. It results principally from the differences between the exact discrepancies ΔP , depending on the considered aerosol model, and the standard calculation of ΔP by the way of (16).

Concerning the accuracy on the POLDER radiometric calibration, we have considered 3% error according to the POLDER project estimate [3]. The influence of this error has been estimated by calculating ΔP from (16) with the correct coefficients but with reflectances ρ and ρ_{atm}^* both differing by $\pm 3\%$ from the calculated figures.

Similarly, to estimate the influences of the uncertainties on ρ_w , ρ_f , and the molecular optical thickness, we have calculated ΔP from (16) with the correct coefficients but with reflectances ρ and ρ_{atm}^* calculated by assuming, respectively, 0.10 mg/m^3 (instead of 0.05 mg/m^3) for the chlorophyll pigment concentration, $\pm 50\%$ variation of the nominal whitecap reflectance, and $\pm 2\%$ variation of δ_m .

Table IV adds the error budget for the three POLDER polarized channels, for $\theta_s = 40^\circ$ and 60° , which is the range in which the method should be applied. For too small values of θ_s , the accuracy of the method decreases, as indicated previously, and for too large values, because the sea surface reflection coefficient increases, saturation of the POLDER channels may appear at low wind speeds. Table IV gives the mean result of the estimates corresponding to the $(4 \times 4 \times 11)$ different cases. At 443 nm , the uncertainty on the water reflectance is important; it seems useful to control

the results of the ocean color algorithm when processing the polarization calibration. The uncertainty on the foam reflectance is not negligible; it seems better to process the calibration with images acquired with low wind speeds, say, $v < 5$ to 7 m/s. The principal source of error is the method itself. Note that, to control the validity of this estimate, (16) was used also with reflectances ρ and ρ_{atm}^* calculated for a lot of aerosol models different from those of the database; the mean discrepancies are similar to the figures of Table IV.

Finally, the accuracy of the calibration is about 1%, in terms of degree of polarization.

VI. CONCLUSION

The previous study indicates that the sun's glitter provides a valuable target for in-flight calibration of polarization measurements. The method is especially convenient for POLDER, whose multidirectional capability allows us to characterize the aerosol component prevailing on the ground pixel precisely used for the calibration.

The calibration method suggested and presented in this paper is mainly suited for some favorable conditions. To expect good accuracy on the calibration, the solar elevation should be preferably about 45°, corresponding to large intrinsic glitter degree of polarization. For these large values of the glitter contribution, the aerosol particle type effect is minor compared to the wind speed and the aerosol optical thickness effects.

The setting-up of a suitable algorithm requires caution about the composition of the reference aerosol database. The optical and physical properties of the aerosol particle types should be close to those of particle types really present in the atmosphere. As measurements will be achieved over the ocean, it is reasonable to choose marine aerosol particle types. Measurements obtained far from ocean coasts should be chosen for the calibration, so that problems related to dust carrying would be avoided. Moreover, in the upper ocean, diffusely reflected water is generally stable, so this area will be favorable for 443-nm calibration. Finally, the bias coming from whitecap reflectance should be sorted out by restricting the wind speed at 7 m/s.

The expected accuracy of the calibration is about 1%, in terms of degree of polarization. To improve the accuracy, the aerosol polarization should probably be taken into account, which should need a more elaborate iterative process.

ACKNOWLEDGMENT

The authors are indebted to C. Verwaerde and Y. Balois for their work in assembling the POLDER instrument and to L. Gonzalez and F. Lemire for processing the airborne POLDER raw data.

REFERENCES

- [1] S. Chandrasekhar, *Radiative Transfer*. Oxford, U.K.: Oxford Univ. Press, 1950.
- [2] C. Cox and W. Munk, "Measurement of the roughness of the sea surface from photographs of the sun's glitter," *J. Opt. Soc. Amer.*, vol. 44, pp. 838-850, 1954.
- [3] P. Y. Deschamps, F. M. Bréon, M. Leroy, A. Podaire, A. Bricaud, J. C. Buriez, and G. Sèze, "The POLDER mission: Instrument characteristics and scientific objectives," *IEEE Trans. Geosci. Remote Sensing*, vol. 32, pp. 598-615, Mar. 1994.
- [4] J. L. Deuzé, M. Herman, and R. Santer, "Fourier series expansion transfer equation in the atmosphere-ocean system," *J. Quant. Spectr. Radiat. Transf.*, vol. 41, no. 6, pp. 483-494, 1988.
- [5] J. L. Deuzé, F. M. Bréon, P. Y. Deschamps, C. Devaux, M. Herma Podaire, and J. L. Roujean, "Analysis of the POLDER (POLarization Directionality of Earth's Reflectances) airborne instrument observations over land surfaces," *Remote Sens. Environ.*, vol. 44, pp. 137-154, 1993.
- [6] P. Goloub, J. L. Deuzé, M. Herman, and Y. Fouquart, "Analysis of the POLDER polarization measurements performed over cloud cover," *IEEE Trans. Geosci. Remote Sens.*, vol. 32, pp. 78-88, Jan. 1994.
- [7] Y. Kaufman, "Aerosol optical thickness and atmospheric path radiance," *J. Geophys. Res.*, vol. 98, no. D2, pp. 2677-2692, 1993.
- [8] P. Koepke, "Effective reflectance of the oceanic whitecaps," *Appl. Opt.*, vol. 23, pp. 1816-1824, 1984.
- [9] A. Morel, "Optical modeling of the upper ocean in relation to biogenous matter content (Case I waters)," *J. Geophys. Res.*, vol. 93, no. C9, pp. 10749-10768, 1988.
- [10] T. Nakajima and M. Tanaka, "Effect of wind-generated waves on transfer of solar radiation in the atmosphere-ocean system," *J. Quant. Spectrosc. Radiat. Transf.*, vol. 29, pp. 521-537, 1983.
- [11] G. N. Plass, G. W. Kattawar, and J. A. Guinn, "Radiance distribution over a ruffled sea: Contributions from glitter, sky and ocean," *Appl. Opt.*, vol. 15, no. 12, pp. 3161-3165, 1976.
- [12] M. Schwindling, "Modèles et mesures pour l'observation spatiale de la couleur de l'océan: Diffusion atmosphérique par les aérosols: réflexion de surface par l'éclume," *Thèse de l'Université des Sciences et Technologies de Lille, Spécialité "Lasers. Molécules, Rayonnement atmosphérique"*, Sept., 15, 1995.
- [13] E. P. Shettle and R. W. Fenn, "Models of the atmospheric aerosols: their optical properties," in *AGARD Conf. Proc. 183, Opt. Propag. Atmos., Electromagn. Wave Propagat. Panel Symp.*, Lyngby, Denmark, Oct. 27-31, 1975. AGARD-CP-183, ADA028-615, 1976.
- [14] ———, "Models of the aerosols of the lower atmosphere and the effect of humidity variations on their optical properties," *AFGL TR-79-02 ADA 085951*, 1979.
- [15] T. Takashima and K. Masuda, "Degree of polarization and radiance of the upwelling radiation from an atmosphere-ocean system," *Appl. Opt.*, vol. 24, pp. 2423-2429, 1985.



Bébé Toubbé received the M.S. degree in physics in 1992 and the Ph.D. degree in atmospheric optics in 1996 from the University of Lille, Lille, France. She was with the Laboratoire d'Optique Atmosphérique, University of Lille, from 1992 to 1997, where her research activities focused on radiative polarization. She is currently Postdoctoral Fellow in the Centre d'Application et de Recherche en Teledetection (CARTEL), Sherbrooke, P.Q., Canada. Her research interests include remote sensing of aerosols over land surfaces and oceans and calibration of spaceborne instruments.

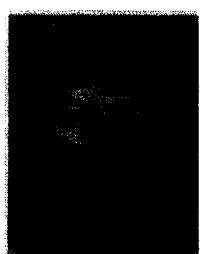


Thierry Baileul received the diplôme d'ingénieur degree from the Ecole des Hautes Etudes Industrielles de Lille, Lille, France, in 1988. He was an Engineer in computer science for the Ecole de Pilotage Amaury de la Grange, la Motte au Bois, France, from 1989 to 1993. Then he was with the Université des Sciences et Techniques de Lille and the Laboratoire d'Optique Atmosphérique, University of Lille, from 1994 to 1997. During this period, he was involved in research activities concerning the POLDER mission, in particular, the development of the algorithms for the in-flight calibration of the POLDER instrument. He is currently an Engineer with URBA 2000, Lille.



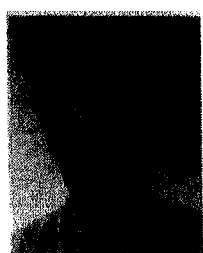
Jean Luc Deuzé received the M.S. degree in physics in 1970 and the Ph.D. degree in atmospheric optics in 1974 from the University of Lille, Lille, France.

He is currently a Professor of Physics at the University of Lille and a Researcher at the Laboratoire d'Optique Atmosphérique, University of Lille. His research activities include radiative transfer modeling within the atmosphere and the inversion of the sky radiance measurements for aerosol monitoring. He is also involved in field campaigns to monitor aerosols (Airborne POLDER flights) and estimate the radiance at the sensor level (SPOT calibration, atmospheric corrections). One of his main interests is in exploiting polarization data to retrieve aerosol properties for climate investigations. Within the POLDER project, he is in charge of the inversion schemes for getting aerosol characteristics over both ocean and land surfaces.



Philippe Goloub received the Ph.D. degree in atmospheric physics in 1992.

He is currently an Assistant Professor of physics and a Researcher with the Laboratoire d'Optique Atmosphérique, University of Lille, Lille, France. He is a member of the POLDER science team. His main interests include exploiting polarization measurements to retrieve aerosol and cloud microphysical properties. He also contributes to the definition and validation of different vicarious in-flight calibration algorithms for the POLDER instrument.



Olivier Hagolle received a degree from the Ecole Supérieure d'Electricité, Paris, France, in 1990.

He has been with the Image Quality and Processing Division, French Space Agency (CNES), Toulouse, since 1990. From 1990 to 1993, he successively designed a simulator of satellite optical images and was in charge of SPOT 3 image quality assessment. Since 1994, he has been in charge of POLDER image quality and calibration.



Maurice Herman received a degree in physics in 1962 and the Ph.D. degree in physics in 1968 from the University of Lille, Lille, France.

He is currently a Professor at the Université des Sciences et Technologies, Lille. His experiment is principally in the area of aerosol remote sensing. His research activities include radiative transfer and atmospheric signal modeling, planetary atmosphere studies from analysis of telescopic observations, ground-based and balloon-borne remote sensing of aerosols, with special emphasis on polarization.

Chapitre 3

Observation et caractérisation des nuages en lumière polarisée

Observation et caractérisation des nuages en lumière polarisée

Les nuages ont une part importante dans le cycle de l'eau dans l'atmosphère. On peut dire qu'ils concrétisent et révèlent certaines propriétés de l'atmosphère où ils se développent. Il existe une très grande variabilité dans les types de nuages. Certains sont composés de gouttelettes d'eau à l'état liquide (dimension effective < 50 µm), d'autres de cristaux de glace (quelques centaines de micromètres). Selon les quantités de vapeur d'eau, de noyaux de condensation ou de congélation disponibles et les propriétés thermodynamiques de l'atmosphère, les caractéristiques des nuages (altitude, phase de l'eau, concentration et distribution en taille des gouttelettes ou des cristaux, forme et orientation pour les cristaux) varient, ainsi que leur impact radiatif. Le suivi continu depuis l'espace de leur couverture, de leurs propriétés optiques et microphysiques est indispensable et constitue l'un des objectifs de nombreuses missions d'observation spatiale.

Lorsque l'on cherche à étudier les nuages, la première difficulté consiste à les détecter correctement, notamment au-dessus des continents où les surfaces peuvent être tout aussi réfléchissantes. Différentes techniques opérationnelles ont été développées pour le traitement des données d'imageurs tels que AVHRR et METEOSAT. Elles sont basées sur des algorithmes de seuillage des radiométries visible et infrarouge. Notons, cependant, que la détection des nuages fin semi-transparents reste difficile à l'aide des informations recueillies par ces instruments (Rossow et al., 1985). Jusqu'à ce jour, seul le sondeur infrarouge haute résolution HIRS (Wylie et al., 1994, Jin et al., 1996) est sensible aux nuages élevés de très faible épaisseur.

En supposant la détection nuageuse réalisée, on cherche ensuite à déterminer les propriétés microphysiques des particules nuageuses. Cela implique dans une première étape la détection de la phase de l'eau (liquide ou solide) constituant ces particules. La phase de l'eau est un paramètre important du bilan énergétique terrestre. Les techniques classiques et opérationnelles de détection de phase reposent sur un seuillage en température appliqué sur la température de brillance déduite des mesures infrarouge (Rossow et al, 1989 ; 1991 ; 1993). Dans le cas du seuillage en température, le choix de la valeur du seuil est délicat. La température ne constitue pas un critère fiable pour déterminer la phase de l'eau. Par exemple, le phénomène de surfusion (Curran et al., 1982, Heymsfield, 1991) existe et permet à l'eau, si l'air n'est pas pollué, de se maintenir à l'état liquide jusqu'à des températures très basses de l'ordre de -35°C voire -40°C. Des mesures réalisées en laboratoire indiquent qu'à des températures inférieures à -40°C l'eau existe uniquement sous forme solide.

D'autres techniques, n'utilisant pas directement un seuil en température, ont également été développées. Elles reposent sur une classification à partir de l'imagerie multispectrale infrarouge utilisant 2 canaux à 11 et 12 µm (Inoue, 1987 ; 1989), et plus récemment 3 canaux 8, 11 et 12 microns pour MODIS (Baum et al., 2000) ou encore 3.7, 11 et 12µm (Hutchinson et al., 1997, Key et al., 2000). Ces techniques, utilisables de nuit comme de jour, peuvent être complétées, de jour, par des mesures de réflectance dans le visible et moyen infrarouge (1.6 µm) (King et al., 1992). Elles sont toutes basées sur des différences d'absorption entre l'eau liquide et la glace, comme l'illustre la figure 1 qui montre la partie imaginaire de l'indice de réfraction pour la glace et pour l'eau dans les domaines spectraux mentionnés ci-dessus.

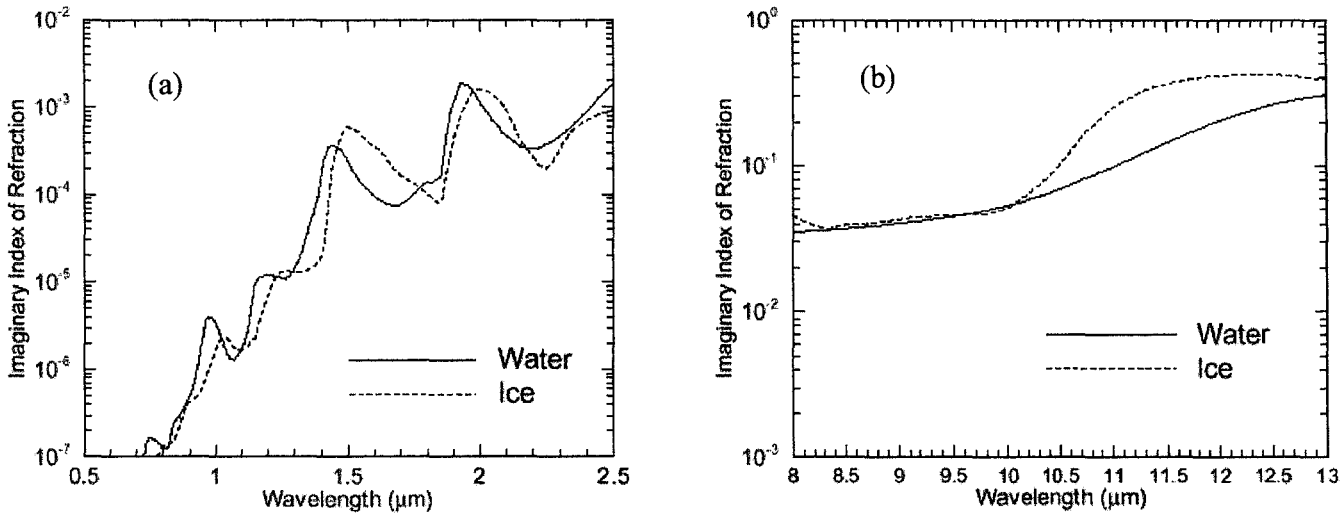


Figure 1 : Indice de réfraction (partie imaginaire) de l'eau en phase liquide et solide.

On constate que les nuages de glace et liquide réagissent différemment au rayonnement solaire et tellurique. Par exemple, entre 10 et 11 μm , l'absorption du rayonnement est plus importante dans un nuage de glace que dans un nuage liquide de même contenu en eau.

Dans le moyen infrarouge, des différences d'absorption apparaissent également (figure 1a). Si l'on dispose d'une résolution spectrale suffisante, il est possible de préciser la phase de l'eau en utilisant par exemple deux canaux à 1.5 et 1.6 μm . En effet, dans cette petite plage spectrale, les comportements spectraux de l'eau et de la glace sont très différents. Cette méthode est utilisée pour le spectromètre Schiamachy, (Knapp et al., 2000).

Dans le spectre visible et proche infrarouge ($\lambda < 0.865\mu\text{m}$), la différence d'indice entre l'eau et la glace est trop faible pour pouvoir être utilisable. Néanmoins, une autre approche est possible à condition, tout d'abord, de pouvoir observer le nuage sous plusieurs visées.

Qui n'a jamais vu un arc-en-ciel (figure 2a) ou un halo (figure 2b) ?

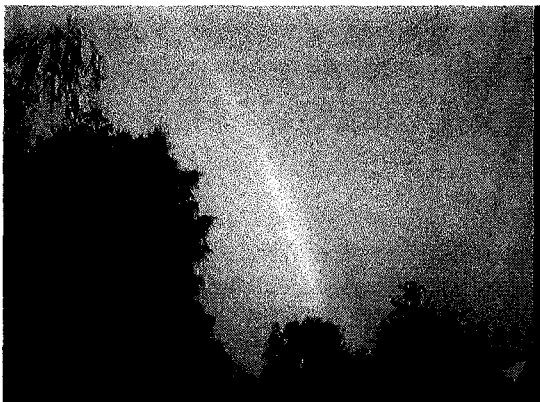


Figure 2a : Arc-en-ciel observé à Lille, le 13 juin 1998. Ce phénomène optique traduit la présence de gouttelettes d'eau (pluie) dans l'atmosphère. (Photographie P. Goloub).

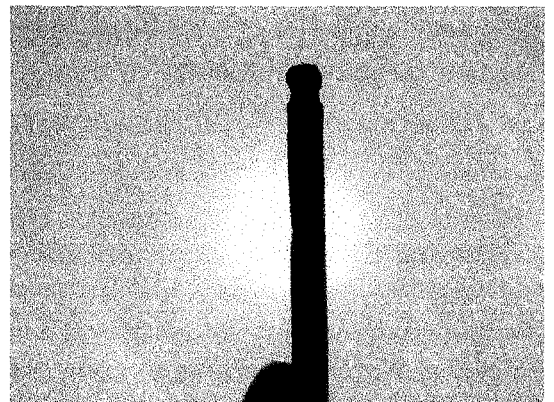


Figure 2b : Halo à 22° observé à Lille, le 8 juin 2000. Ce phénomène optique traduit la présence de cristaux de forme hexagonale dans l'atmosphère. (Photographie P. Goloub).

L'observation visuelle (optique) directe de ces phénomènes renseigne sur la forme cristalline des particules nuageuse et par la même sur l'état thermodynamique de l'eau.

L'observation satellitaire considérée ici ne permet pas, bien évidemment, d'observer le phénomène du halo, caractéristique de certains types de cristaux de glace de forme hexagonale plate, car il est trop proche du soleil. Le phénomène de l'arc-en-ciel lui, peut l'être, à condition de pouvoir regarder à environ 140° de la direction du soleil, mais ne présente pas toujours un contraste angulaire suffisant pour être observé en luminance.

La seconde condition suppose que l'on mesure également l'état de polarisation de la lumière diffusée. En présence de nuages en phase liquide, l'observation en lumière polarisée, montre systématiquement le phénomène de l'arc-en-ciel spécifique aux gouttelettes d'eau de forme sphérique. Ce phénomène correspond à l'accumulation de lumière, par réflexion interne dans la goutte d'eau de forme sphérique, dans une direction bien particulière. C'est justement ce phénomène de réflexion sur le dioptre eau-air qui polarise partiellement la lumière solaire se réfractant dans la goutte. Dès que la forme du diffusant s'écarte de la sphère, l'arc-en-ciel disparaît et l'indicatrice de diffusion en lumière naturelle comme en lumière polarisée se modifie dans son ensemble, ce qui permet de séparer « optiquement » les diffusants de forme sphérique de tous les autres. *Pour résumer, la détection de phase est équivalente à une détection de forme.* En effet, au cours du changement d'état l'eau cristallise dans un réseau cubique, puis des directions privilégiées de croissance apparaissent suivant les conditions de température et d'humidité. La phase glace correspond donc à des particules dont la forme diffère de la forme sphérique.

Les toutes premières mesures de polarisation ont été réalisées à l'aide d'un polarimètre embarqué sur un avion et fonctionnant dans le moyen infrarouge par Coffeen et Hansen 1971, 1979. Des exemples sont présentés sur la figure 3. On y a représenté le taux de polarisation ($100 \times L_p / L$) en fonction de l'angle de phase qui est l'angle supplémentaire de l'angle de diffusion.

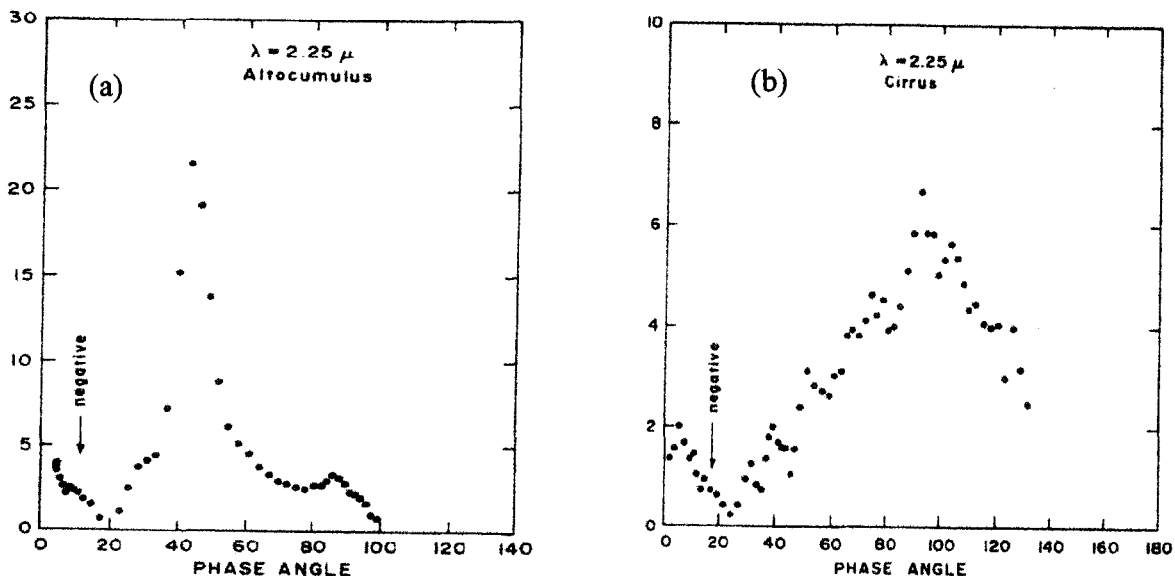


Figure 3 : Taux de polarisation mesurés par Coffeen et Hansen au début des années 1970 au-dessus d'un AltoCumulus (a) et d'un cirrus (b) à $2.25 \mu\text{m}$.

Plus tard, en 1985, l'expérience ballon PIRAT réalisée par M. Herman et JL Deuzé a permis également d'obtenir des mesures de polarisation en atmosphère claire et nuageuse au-dessus de l'océan et des terres.

Signalons également, qu'au cours de la décennie 80, des mesures en lumière polarisée ont été réalisées à bord de la navette spatiale (Egan et al., 1985 ; Roger et al., 1994). Elles ont fourni des mesures de polarisation, mais sans échantillonnage angulaire.

Un peu plus tard, dans les années 1990-1991, la première version aéroportée de POLDER a permis d'obtenir les premières images en lumière polarisée au-dessus de zones partiellement nuageuses, comme l'illustrent les images présentées ci-dessous.

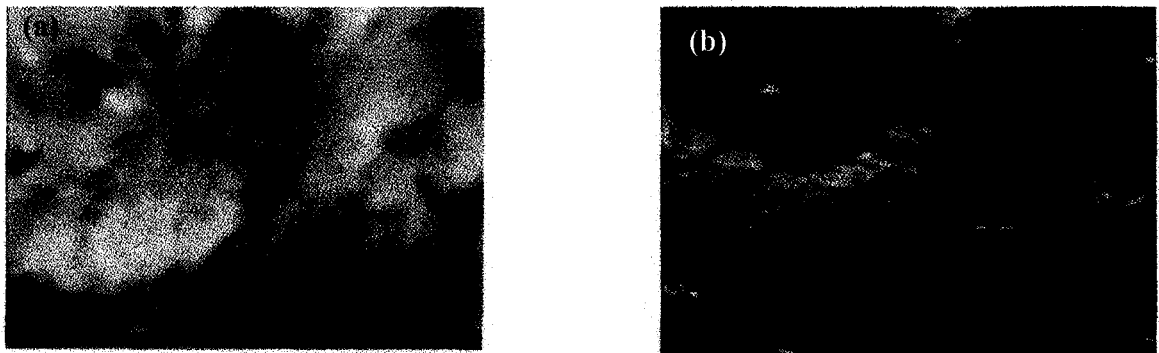


Figure 4 : Images en luminance totale (a) et polarisée (b) dans le proche infrarouge (865nm) acquises pendant la campagne MEDIMAR en mars 1991. L'altitude de vol est d'environ 4000m.

Cette scène présente un nuage hétérogène (un strato-cumulus) dans une partie du champ de l'instrument. Sur l'image en lumière polarisée (figure 4b), la présence d'un demi-arc de polarisation plus importante traduit la présence de gouttelettes nuageuses sphériques (phase liquide). Nous avons représenté, pour les pixels nuageux, les luminances polarisées obtenues en fonction de l'angle de diffusion sur la figure 5.

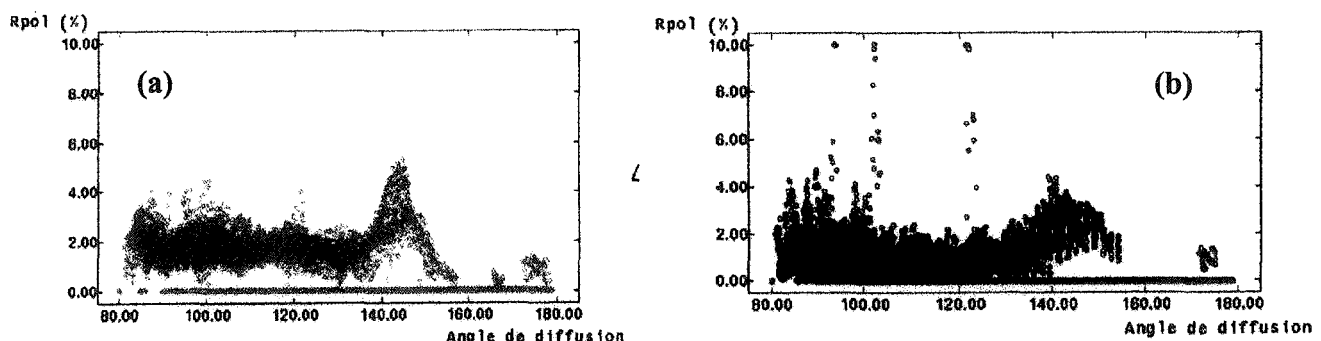


Figure 5 : Diagramme de luminance polarisée en fonction de l'angle de diffusion pour les longueurs d'onde 443 nm (a) et 865 nm (b) pour les images de la figure 4.

Le maximum de polarisation observé vers 140° , à 443 nm comme à 865 nm, correspond au phénomène d'arc-en-ciel caractéristique des diffusants sphériques d'indice de réfraction 1.33 (eau liquide). On observe dans les deux canaux une forte dispersion des mesures. Cette dispersion est liée à l'hétérogénéité du couvert nuageux qui, compte contenu des erreurs de recalage des voies polarisées sur le simulateur aéroporté (voir chapitre 2), introduit une polarisation apparente qui s'ajoute à la polarisation des nuages. Cette effet est plus important à 865 nm car le niveau de polarisation propre du système (atmosphère+nuage) y est plus

faible qu'à 443nm. En effet, à 865nm c'est essentiellement le nuage qui contribue à la polarisation, alors qu'à 443 nm, la diffusion due aux molécules situées au-dessus du nuage contribuant largement à des angles de diffusion proches de 90°, s'ajoute à celle du nuage. Cette contribution moléculaire, observable sur la figure 5a est d'ailleurs utilisée pour estimer l'altitude des nuages (Goloub et al., 1994, P. 2.1).

Ces premiers résultats qualitatifs issus de la version aéroportée, illustrent la capacité de POLDER à mesurer le rayonnement solaire diffusé par les nuages dans le visible et le proche infrarouge dans différentes géométries de visée. Sa capacité d'analyse angulaire lui permet de sonder les « indicatrices de diffusion » des nuages observés dans une gamme d'angle de diffusion variable et pouvant couvrir l'intervalle 60°- 180° avec, pour la version satellitaire, un pas angulaire moyen de l'ordre de 3 à 4°. De plus, il réalise ces observations en lumière polarisée. La fraction de lumière polarisée ne représente que quelques pour cents de l'énergie totale arrivant au niveau du satellite (figure 6). La théorie et l'expérience ont montré que ces indicatrices de diffusion en polarisation étaient très sensibles à la forme des particules, notamment entre les diffusants de forme sphérique associés aux gouttes d'eau donc à la phase liquide, et les particules non sphériques associées aux cristaux et donc à la phase glace (Goloub et al., 1994, P. 2.1). Elles indiquent également que les indicatrices de diffusion en polarisation se déforment beaucoup moins, sous l'effet des diffusions multiples, que les indicatrices de diffusion en lumière naturelle.

La méthode de détection de la phase à l'aide des mesures de polarisation, illustrée par les figures 3 à 5, est décrite dans les publications P. 2.2 et P. 2.3.

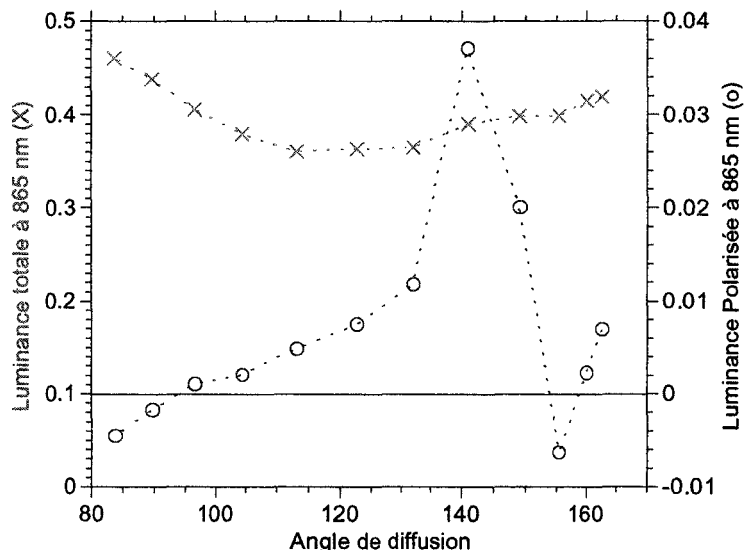


Figure 6 : Exemple d'échantillonage angulaire des luminances totale et polarisée réalisé par POLDER dans le cas d'un pixel appartenant à une scène nuageuse.

Notre travail a consisté ensuite à estimer la fiabilité de la détection de phase réalisée par POLDER. La première piste de validation envisagée a consisté à comparer la phase et la classification nuageuse déduite des canaux visible et infrarouge de METEOSAT. La méthode de classification par nuées dynamiques appliquée aux données METEOSAT est basée sur la radiométrie visible et infrarouge. Il s'agit d'une technique de classification par seuillage dans un espace à 4 dimensions composé des luminances des canaux visible et infrarouge ainsi que

des variances spatiales associées (Sèze et Desbois, 1987). Elle permet de classifier les nuages en classe d'altitude. Les résultats sont présentés dans la publication P. 2.3. On notera que 95 % des nuages appartenant au type « nuage bas » sont bien déclarés « liquide » par POLDER. Les classes de nuages « haut » sont plus délicates à interpréter car POLDER détecte pour certaines classes beaucoup de nuages liquides. Pour les nuages hauts, nous avons donc recherché d'autres moyens de valider la phase. Nous avons utilisé les mesures *lidar* conjointes à des radiosondages afin de préciser la température thermodynamique des cirrus sélectionnés pour cette étude. Cette étude indique que plus de 95% des nuages dont la température est inférieure à -40° sont correctement identifiés comme nuages de glace par POLDER (P. 2.4). Cette étude étant limitée au cas de cirrus peu épais et seuls dans l'atmosphère, nous avons cherché ensuite à tirer profit des mesures radar réalisées sur le site d'ARM aux USA (P. 2.5). Le radar 35GHz utilisé est, a priori, moins sensible aux nuages peu denses, mais il permet d'envisager des situations de nuages multicouches avec des nuages de glace coiffant des nuages bas ou moyens en phase liquide. Comme pour les lidars, l'association de radiosondages permet de déterminer la température thermodynamique du sommet du nuage. Là encore, le taux de reconnaissance de la phase glace est très bon.

Enfin, nous avons utilisé les relevés synoptiques disponibles au-dessus des continents pendant la vie de POLDER. Les résultats indiquent une cohérence de 96% entre la phase glace et l'observation de nuages élevés.

Une première comparaison « climatologique » entre les distributions zonales des nuages « hauts » selon ISCCP et en phase glace selon POLDER a été réalisée et est présentée dans Riedi et al., 2000 (P. 2.6).

La phase déterminée, on peut alors s'intéresser aux propriétés microphysiques des nuages, plus précisément des particules constituant le sommet des nuages.

Commençons par les nuages composés de cristaux de glace. Les cristaux sont caractérisés, par leur taille, par leur forme ainsi que leur orientation dans l'espace. En 1998, Chepfer et collègues ont observé, sur les images du simulateur aéroporté POLDER, le phénomène de réflexion spéculaire sur les cirrus. Ce phénomène traduit l'orientation préférentielle des cristaux dans un plan. Angulairement très localisé et, par nature, polarisé, il est détectable à l'aide des observations en lumière polarisée. La détection et la quantification de ce phénomène ont été réalisées à l'échelle globale sur les 8 mois de données. La démarche et les résultats sont présentés dans la publication P. 2.7.

Dans une seconde étape, nous avons réalisé une « cartographie » des formes des cristaux orientés aléatoirement dans l'espace et estimé leurs fréquences d'occurrence. Pour cela, nous avons considéré 3 modèles microphysiques distincts (polycristaux, colonnes hexagonales, plaquettes hexagonales) et pour chaque observation POLDER correspondant à un nuage en phase glace ne présentant pas de pic spéculaire, nous avons recherché le modèle restituant le plus fidèlement l'observation en terme de luminance polarisée. Ces tests sont effectués pour certaines géométries de visée et d'azimut présentant le maximum de sensibilité à la forme. Les résultats présentés dans la publication P. 2.8 indiquent que la forme varie beaucoup spatialement. Néanmoins, les polycristaux et les colonnes à base hexagonale sont observés plus fréquemment aux basses latitudes, alors que les plaquettes hexagonales le sont aux hautes latitudes. La prochaine étape consistera à interpréter ces distributions au regard de l'état dynamique et thermodynamique de l'atmosphère.

Parallèlement à ces travaux, nous avons cherché à déterminer les propriétés microphysiques (rayon ou diamètre effectif) des gouttelettes d'eau. Nous présentons, tout d'abord, des résultats obtenus à l'aide des mesures du simulateur aéroporté pendant la campagne EUCREX

en 1994. La figure 7 montre le diagramme directionnelle de la lumière polarisée mesurée au cours du survol d'un banc de strato-cumulus.

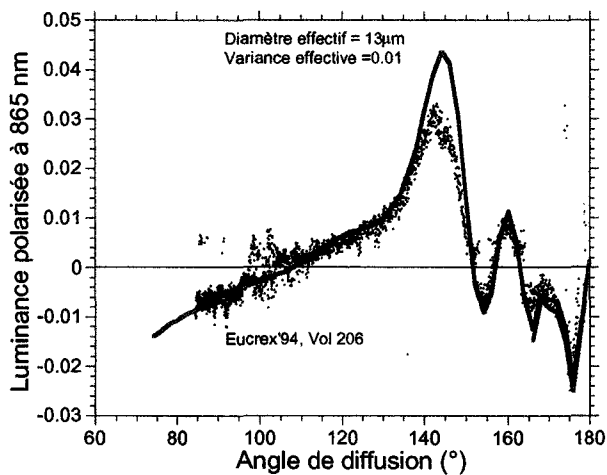


Figure 7 : Signature polarisée obtenue (en point noir) à 865 nm durant l'expérience EUCREX'94. La modélisation est représentée par la ligne continue.

La distribution dimensionnelle des gouttelettes (définie ici par le diamètre effectif et la variance effective), restituant au mieux la position du point neutre, des arcs et leur amplitude, à l'exception de l'arc primaire, correspond à une distribution en taille de diamètre effectif $13\mu\text{m}$ avec une variance de 0.01. Ceci indique que le sommet du nuage est constitué de gouttelettes très "monodispersées". Une validation de ce résultat est apportée par des mesures in-situ réalisées à l'aide d'un "Forward Scattering Spectrometer Probe" (Brenguier et al., 1996; Pawlowska et al., 1996). La figure 8 illustre la variation verticale du diamètre effectif des gouttelettes nuageuses déduite du FSSP.

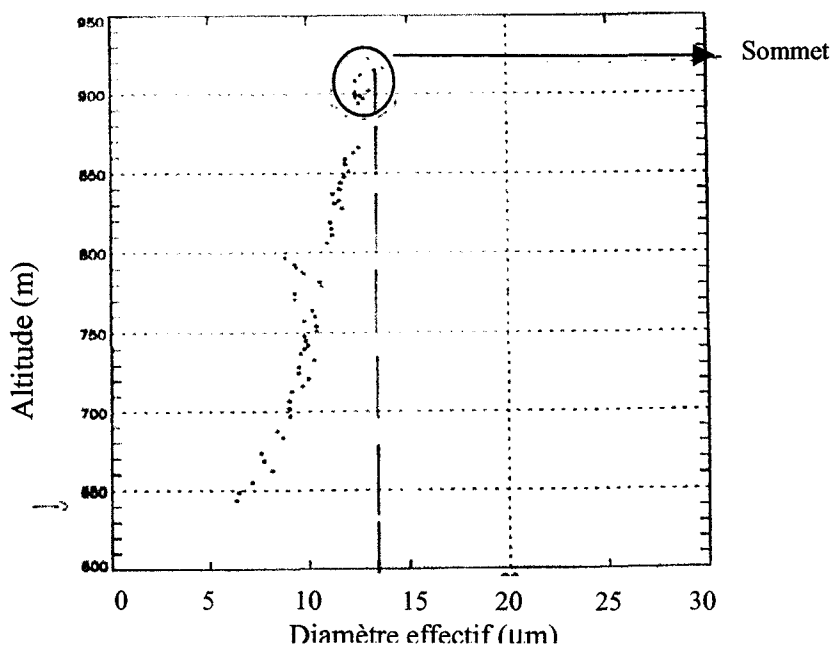


Figure 8 : Diamètre effectif des gouttelettes nuageuses mesuré in-situ par le FSSP pendant EUCREX'94.

Au sommet du nuage le diamètre effectif est de l'ordre de $12 \mu\text{m}$, ce qui est compatible avec le diamètre déduit de la mesure de polarisation.

Dès la réception des premières données POLDER/ADEOS, nous avons développé un algorithme assez simple de détermination du rayon effectif des gouttelettes nuageuses (Goloub et al., 1997). Les images présentées sur les figures 9a et 9b correspondent respectivement à la réflectance à 865 nm mesurée par POLDER au-dessus de la France un jour de Novembre 1996 et au rayon effectif des gouttes déduit de la mesure de polarisation.

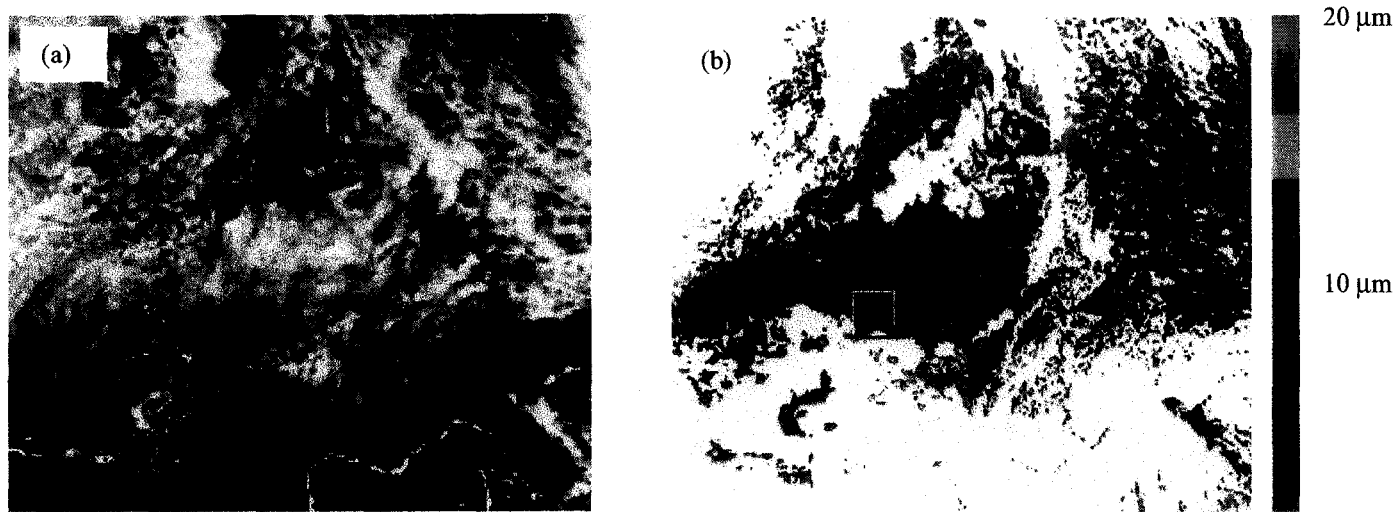


Figure 9 : Image en luminance à 865 nm au-dessus de la France (a) et image correspondante en rayon effectif des particules au sommet des nuages (b), d'après Goloub et al., 1997.

On a représenté, sur la figure 10, les luminances polarisées relatives aux pixels contenus dans une zone carrée de $100 \text{ km} \times 100 \text{ km}$ repérée sur la figure 9b.

measurements

— Simulation with $\text{Reff}=5\text{micron}$

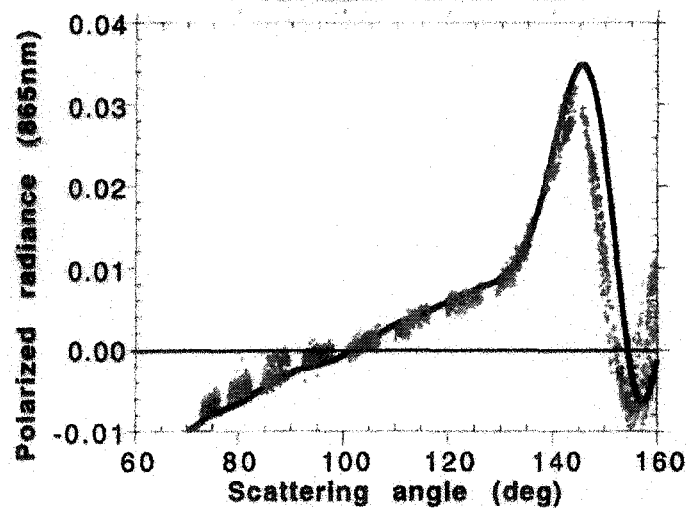


Figure 10 : Polarisation mesurée à 865 nm pour un ensemble de pixels contenus dans une zone d'environ $100 \times 100 \text{ km}$. Le calcul pour une distribution de gouttes de rayon effectif $5 \mu\text{m}$ est superposé. L'épaisseur optique du nuage utilisée pour le calcul est égale à 10.

La prise en compte d'un ensemble suffisant de pixels voisins permet d'améliorer l'échantillonnage angulaire de la luminance polarisée de la scène nuageuse considérée et, par conséquent, de mieux ajuster la distribution en taille des gouttelettes.

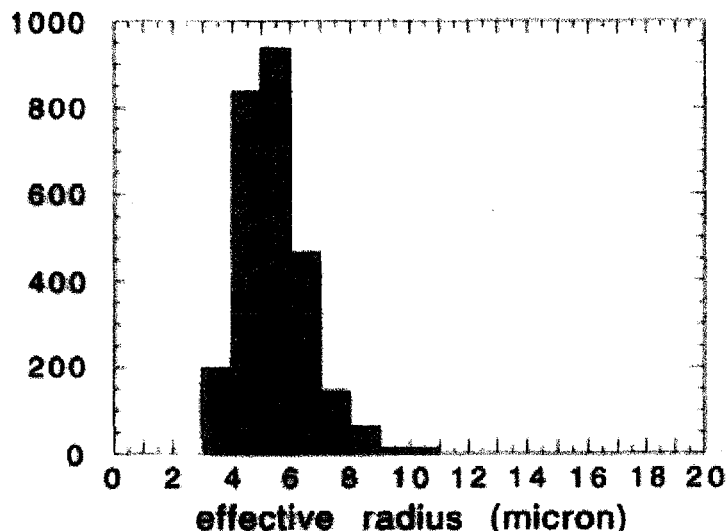


Figure 11 : Histogramme du rayon effectif retrouvé sur une zone plus large contenant la zone précédente. Le rayon effectif moyen des gouttes est de l'ordre de 6 µm.

La méthodologie a ensuite été améliorée en utilisant comme contrainte le respect de la positions des arcs aux trois longueurs d'onde polarisées (Bréon et Goloub, 1998, P. 2.9), et appliquée à l'échelle globale. Nous présentons sur la figure 12 une carte globale du rayon effectif des gouttelettes déduite à l'aide de cet algorithme.

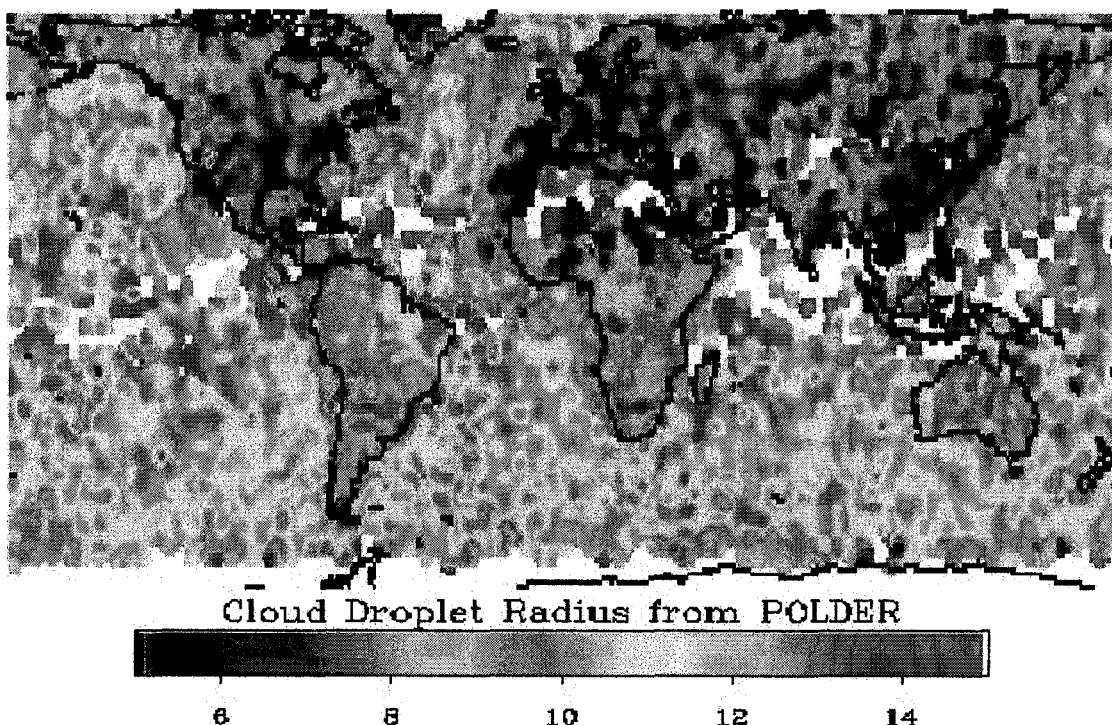


Figure 12 : Moyenne sur trois mois (mars-avril-mai) du rayon effectif des gouttes (d'après Bréon et al., 1999).

Les ordres de grandeurs trouvés sont compatibles avec les résultats obtenus à partir d'AVHRR et publiés par Han et collègues en 1994. La taille effective des gouttelettes d'eau apparaît plus petite au-dessus des régions moins continentales moins humides et plus polluées qu'au-dessus des océans. Le contraste entre l'hémisphère nord où se trouvent l'essentiel des sources de pollution atmosphérique et l'hémisphère sud est également très net.

L'ensemble de ces travaux est présenté dans les publications dont la liste est donnée ci-après.

P. 2.1 Goloub P, JL Deuzé, M Herman and Y Fouquart "Analysis of the POLDER Airborne Polarization Measurements Performed over Clouds Covers", IEEE Transactions on Geoscience and Remote Sensing, Vol 32, N 1, January 1994, p78-87.

P. 2. 2 Goloub P., M. Herman, H. Chepfer, J. Riedi, G. Brogniez' P. Couvert, G. Séze, Cloud Thermodynamical Phase Classification from the POLDER Spaceborne intrument, Journal of Geophysical Research, VOL 105., NO. D11, Pages 14747-14759, 2000.

P. 2.3 Parol F., J.C Buriez, C. Vanbause, P. Couvert, G. Sèze, P. Goloub, and S. Cheinet, "First Results of the POLDER « Earth Radiative Budget and Clouds » Operational Algorithms. POLDER-ADEOS ", IEEE Transactions on Geoscience and Remote Sensing, vol. 37, pp. 1597-1612, 1999.

P. 2.4 Chepfer H., P. Goloub, J. Spinhirne, P. H. Flamant, M Lavorato, L. Sauvage, Brogniez, and J. Pelon, "Cirrus Cloud properties deived from POLDER-1/ADEOS Polarized Radiances: First Validation using a Ground based Lidar Network", J. Applied. Meteor, VOL 39, Pages 154-168, 2000.

P. 2.5 Riedi J., P., Goloub, R. Marchand, 2000, « Comparison of POLDER phase to radar measurements », submitted to Geophys. Res. Lett. 2000.

P. 2.6 Riedi J., M. Doutriaux-Boucher, P. Goloub, P., Couvert, 1999, « Global distribution of cloud top phase from POLDER/ADEOS 1 », Geophys. Res. Lett., VOL 27, N 12, Pages 1707-1710, 2000.

P. 2.7 Chepfer H., G. Brogniez, P. Goloub, F. M. Bréon, P. H. Flamant, "Observation of Horizontally Oriented Ice Crystals in Cirrus Clouds with POLDER/ADEOS ", J. Quant. Spec. Rad. Transfer, Special Issue, Light Scattering by nonspherical particles'98, Vol. 63, 521-543, Sept/Dec 1999.

P. 2.8 Chepfer H., P. Goloub, J. Riedi, J.F. De Haan, J.W. Hovenier, P.H Flamant, Ice crystal shapes in cirrus clouds derived from POLDER-1/ADEOS-1, to appear in Journal of Geophysical Research, 2000.

P. 2.9 Bréon, F.M., and P. Goloub, "Cloud droplet effective radius from spaceborne polarization measurements", Geophys. Res. Letts, Vol. 25, N 11, PAGES 1879-1882, 1998.

Analysis of the POLDER Airborne Polarization Measurements Performed over Clouds Covers

Analysis of the POLDER Polarization Measurements Performed Over Cloud Covers

Phillippe Goloub, Jean Luc Deuzé, Maurice Herman, and Yves Fouquart

Abstract—The POLDER instrument is designed to provide wide field of view bidimensional images in polarized light. During campaigns of the airborne version of the instrument, images of homogeneous cloud fields were acquired in polarized bands centered at 450 and 850 nm. The polarization of these images is analyzed. The bidirectional polarization distribution function measured in the 850 nm band is shown to make evident the liquid phase of the cloud droplets, by the large characteristic polarization of the cloudbows detected in backward scattering directions. The sensitivity of this feature to cloud parameters is discussed. On the contrary, for observation directions at about 90°–100° from the Sun, the cloud polarization is negligible. In these directions, the polarized light observed in the 450 nm band is characteristic of the molecular scattering about the cloud, which allows to derive the cloud top altitude. The feasibility of the method is analyzed and is tested on cloud pictures acquired at different altitudes above cloud fields.

I. INTRODUCTION

THE POLDER instrument is a radiometer designed to measure the directionality and polarization of the sunlight scattered by the ground-atmosphere system [1]. The instrument concept consists of imaging bidimensional pictures of the site on a CCD detector matrix, through a wide field of view telecentric optics. A given ground pixel thus may be observed with different viewing angles in consecutive pictures acquired while the sensor overflies the experimental site. The spectral analysis of the radiance is provided by a filter wheel. In some spectral bands, 3 filters are equipped with analyzers rotated by 60° and the polarization is deduced from combination of the 3 images. POLDER, that has been selected to fly on the Japanese ADEOS payload, is now in phase C study by the Centre National d'Etudes Spatiales (CNES).

The long-term scientific objectives of the experiment concern remote sensing of aerosols, ocean color, and vegetation, and the estimation of the cloud impact on the terrestrial short-wave radiative budget [2]. Concerning clouds, the POLDER observations should be useful in two respects. Observation of the cloud bidirectional reflectance distribution function (BRDF) should provide better estimate of their radiative impact and better understanding of their radiative properties as a function of their morphology. The cloud bidirectional polarization distribution function (BPDF) is expected to be useful for cloud altimetry, by the way of the molecular

scattering as the barometric signal, and for determination of the cloud phase, ice, or liquid by the way of the cloud particle polarization signature. We will restrict here to the polarization aspects of cloud observations.

The interest of polarized measurements for cloud studies has been outlined long ago (see e.g. [3]). First, polarization measurements from space should be able to provide cloud altimetry by the way of molecular scattering. For this purpose, measurements have to be performed at short wavelengths (say, $\lambda < 500$ nm) and for observation geometries corresponding to scattering angles near from $\Theta = 90^\circ$. In these conditions, molecules are very efficient for scattering polarized light. Then, by considering that the ground and most of the aerosols are screened by the cloud and by neglecting or correcting the cloud contribution, the amount of polarized light should yield the optical thickness of the atmosphere above the cloud, i.e., the cloud top altitude.

On the other hand, the angular polarization signature of clouds, as measured at near infrared wavelengths, could help for discriminating between liquid and solid phases of the cloud particles. Liquid cloud droplets should be evidenced by the characteristic polarization feature of the rainbow, exhibited by spherical particles for scattering angles near from 140° . Conversely, theoretical studies of scattering by crystalline particles with different geometries (prisms, cylinders, hexagonal crystals, spheroids; see e.g., [4]–[7]) all show that the rainbow characteristic disappears as soon as the scattering particles depart from spherical geometry. The lack of this characteristic feature in cloud polarization signature, therefore, should be indicative of the presence of ice crystals. More generally, cirrus clouds could exhibit their own characteristic signature. As shown by Masuda and Takashima [8], for example, the degrees of linear polarization calculated for randomly oriented hexagonal ice crystals are very similar for column and plate shaped crystals, as are quite similar to the degrees of linear polarization calculated by Mishchenko and Travis, [9] for randomly oriented prolate and oblate spheroids. This point, however, has to be ascertained from observations because the actual ice crystal geometries are probably very variable.

II. PRINCIPLE

The investigation of the interest of polarized measurements for cloud studies, airborne or balloon-borne experiments were flown long ago (see e.g., [3] and [10]). As outlined previously, however, polarization is really informative when obtained for different viewing conditions. Because these previous experiments consisted in cloud scannings by narrow field of view

Manuscript received November 19, 1992; revised July 7, 1993. This work was supported by the Centre National d'Etudes Spatiales and the Center National de la Recherche Scientifique.

The authors are with the Laboratoire d'Optique Atmosphérique, URACRNS713, Université des Sciences et Technologies de Lille, U.F.R. de Physique, Adex, France.

IEEE Log Number 9213366.

polarimeters, they were not easy and practically valid only when performed over horizontally homogeneous cloud fields.

Conversely, for preparatory studies of the POLDER experiment, an airborne simulator of the instrument has been developed and experimental campaigns have been conducted. Cloud fields were observed occasionally and polarization measurements were performed in spectral bands centered at 450 and 850 nm. These bidimensional POLDER pictures benefit from the ability to observe any cloud pixel with different viewing conditions, according to the sensor displacement during the successive acquisitions, or to acquire the entire BRDF and BPDF from one single picture, when overflying homogeneous cloud fields. The purpose of this paper is to describe these measurements and to investigate the possibility of cloud altitude retrieval from Rayleigh scattering barometry.

No cirrus clouds were present during these flights, or detectable because of the aircraft maximum altitude, but all the observations exhibited the characteristic cloudbow polarization in backward scattering directions. This supports the possibility to identify liquid cloud droplets from this feature, whose the sensitivity to cloud parameters is discussed.

On the contrary, for directions at about 90° – 100° from the Sun, the observed polarization was negligible in the 850 nm channel but not in the 450 nm one. Mie theory calculations confirm that the cloud polarization (as observed at 850 nm because of the λ^{-4} dependence of the Rayleigh scattering) is fairly low in this range of scattering angles. The polarized light in the 450 nm band is therefore characteristic of the molecular scattering above the cloud. A simple scheme to derive the cloud top pressure from the polarization measurements in the two channels is proposed. The results are compared with observations and of the sensitivity of the method to different error sources is analyzed.

III. DESCRIPTION OF THE DATA

A. Experimental Campaigns

The present cloud observations were obtained occasionally during the various campaigns of the POLDER airborne simulator.

POLDER was first flown aboard the French Avion de Recherches Atmosphériques (ARAT) for campaigns devoted to land surfaces observations, in the Southern of France during the Summer of 1990 (La CRAU and LANDES 90 campaigns) and for a campaign devoted to the ocean color, over the Mediterranean Sea in the Summer of 1991 (MEDIMAR campaign). Then, it was flown aboard the Falcon of DLR for a campaign specifically designed to cloud observations, over the Alps in late 1991 (CLEOPATRA campaign). Finally, POLDER was flown again aboard the ARAT, over the Atlantic Ocean, during the ASTEX-SOFIA campaign in the Summer of 1992. Table I sums up some characteristic points concerning these different acquisitions.

B. Flight Conditions—BRDF Acquisitions

The POLDER instrument includes a matrix array CCD of 288×384 detectors with dimensions $23 \times 23 \mu\text{m}$, in the focal plane of a wide field of view optics with 3.565 mm

TABLE I
SOME CHARACTERISTICS OF THE PRINCIPAL POLDER CAMPAIGNS
FOR POLARIZED BAND AND NP FOR NON-POLARIZED BAND

Campaign	Spectral band	Aircraft	Flight Lev (km)
CRAU 90	550P, 650P, 850P	ARAT	6 km
MEDIMAR 91	450P, 500NP, 570NP, 670NP, 850P	ARAT	4.5 km
CLEOPATRA 91	450P, 500NP, 570NP, 670NP, 850P	FALCON	Variable: 11 km
SOPHIA- ASTEX 92	450P, 763NP, 765NP, 850P, 910NP	ARAT	3.5 km

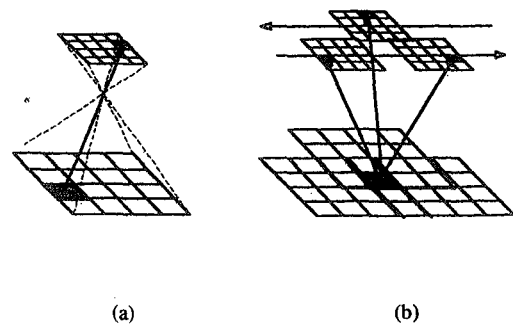


Fig. 1.

focal length. This provides an angular coverage with view angles θ_v of $\pm 42^\circ$ in the along track direction and $\pm 15^\circ$ in the crosstrack direction, or inversely depending of the orientation with respect to the aircraft (Fig. 1(a)). For a altitude of 5000 m above the ground or the cloud to example, the foot print is approximately 9.3×12.3 km and resulting image is partitioned in 288×384 identical g or cloud pixels with 32×32 m dimensions.

During the aircraft displacement, the radiance from a ground or cloud pixel is measured for different viewing angles. For land observations, the flight plans consisted in successive parallel runs (Fig. 1(b)), which allowed to sample the BRDF and BPDF of each ground pixel. For the cloud observations here reported, because of the expected changes in the structure between successive runs, we only flew simple over the cloud cover, at nearly constant altitudes (from 6000 m to 6000 m with the ARAT, until 11000 m for the Falcon). These results are reported in Table I. On one occasion, during the CLEOPATRA, the same extended cloud was overflown by the Falcon at different altitudes.

Given these conditions, we have restricted our analysis to the average gross features of the BPDF of cloud scenes, which looked rather homogeneous within the POLDER footprint. The average BPDF, then, will be derived from one single picture. The different pictures acquired along the flight run can be used for testing the cloud homogeneity and/or for averaging the cloud properties.

C. Polarization and Spectral Analysis

The filter wheel of the airborne simulator has 10 filter positions. One blind position is used for the measurement of the darkness current. The system therefore allows measurements in 3 polarized spectral bands, or in 2 polarized and 3 unpolarized bands, etc. For cloud studies in polarized light, the best seems to measure polarization in the shortest and largest POLDER wavelength bands, 450 and 850 nm, as it was retained for the CLEOPATRA campaign. The spectral bands and polarization configurations used for the different campaigns are indicated in Table I.

A measurement sequence consists of these 9 spectral polarized images. They are acquired in 3.7 s, which is the period of the filter wheel. The time interval between two consecutive sequences is 11 s. During a sequence acquisition, the aircraft displacement is about 370 m, or about 120 m between the images of a polarized band. Within the sequence time interval, variations in the cloud structure are assumed to be negligible. Then, by processing the 9 images, the spectral and polarization properties of the cloud cover may be retrieved.

D. Data Processing

Because most clouds exhibit significant structure variations at 100 m scale, lengths, polarization, and multispectral measurements necessitate correct image registration.

For land observations, the processing of the POLDER data has been elaborated [11]. However, registration of the data within a 1 pixel accuracy requires that the POLDER attitude with respect to the aircraft inertial system should be estimated, from known landmarks selected in the pictures. As this is not possible over cloud fields, the data processing of cloudy scenes was simplified as follows.

Step 1: The raw data in the 9 channels of each sequence were first corrected from dark current and from the optics transfer function. For unpolarized spectral bands, within the appropriate calibration factor, this correction step provides directly the radiance or the reflectance in entrance of the instrument.

Step 2: In the polarized bands, the 3 images were then corrected for the aircraft translation. Change in the aircraft attitude was neglected and the images were just translated, within 1 pixel, in order to minimize the contrasts between the 3 images.

Step 3: To smooth the residual registration errors, the results were averaged with a 5×5 pixel window.

Step 4: Finally, the entrance radiance and polarization were deduced from the averaged data.

As confirmed simulations and observations over terrestrial targets, we considered that the light linearly polarized. The entrance radiance is then given by $(L_1 + L_2 + L_3)/3$ where L_i ($i = 1, 2, 3$) are the 3 polarized measurements calculated from (2), and the entrance polarized radiance (i.e., the polarized part of the radiance), from $(\sum_i 2(L'_i - L_i + 1)^2/9)^{1/2}$; the direction of the polarized vibration (say, the angle ξ between the polarized vibration and some convenient reference) may be deduced too from the L_i . The calibration factor is such that the results reported here are expressed in terms of normalized

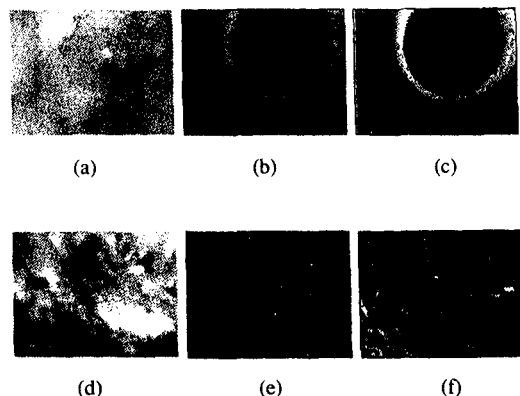


Fig. 2. POLDER pictures obtained during CLEOPATRA, on October 18, 1991, over an extended homogeneous cloud field. (a) Shown is the observations with full POLDER resolution, in one filter of the 850 nm spectral band. (b) Shown is the reflectance derived from the 3 component images of the 850 nm band, with smoothing processing (see text). The 256 gray levels correspond to reflectances ranging from 0.5 to 1.3. (c) and (d) shown are the polarized reflectances, derived in the 850 and 450 nm bands, respectively. (e) and (f) shown are synthetic images of (c) and (d), respectively, corresponding to plane parallel clouds underlying the molecular atmosphere.

radiances, ρ , and normalized polarized radiances, ρ_P , as

$$\rho = \pi L / (\cos \theta_s E_s) \quad \rho_P = \pi L_P / (\cos \theta_s E_s) \quad (1)$$

where L is the radiance, θ_s the solar zenith angle, and E_s the solar irradiance at the top of the atmosphere. The degree of linear polarization is defined as

$$P = \rho_P / \rho.$$

Note that the characterization of the polarized light is provided by (ρ, ρ_P, ξ) , or, equivalently, by its Stokes parameters (ρ, ρ_Q, ρ_U) , with

$$\rho_Q = \rho_P \cdot \cos 2\xi; \rho_U = \rho_P \cdot \sin 2\xi. \quad (2)$$

As an example, Fig. 2 shows a cloud picture acquired on October 18, 1991 during the CLEOPATRA campaign, with the aircraft at about 8000 m above the cloud top. Image (a) shows the measurements in one of the polarized channels of the 850 nm band, i.e., with the best resolution of POLDER, just corrected from the optics transfer function (Step 1). Image (b) shows the total reflectance in the 850 nm band as derived when processing the 3 polarized images as explained previously. We see that the cloud structure is well preserved by the 5×5 pixel smoothing process. The other features are discussed below.

The POLDER calibration was performed in laboratory. The calibration in absolute reflectance, ρ , was derived from secondary standards. The estimated accuracy is about 5%. The NED ρ corresponding to the radiometric noise is about 0.003. The calibration in polarization was checked by illuminating POLDER with a plane-parallel-glasses transmission calibrator, providing entrance polarization ratios P ranging from 0 to 0.30 with $\Delta P = \pm 0.002$. The accuracy on P , however, is generally limited by the radiometric noise. The corresponding NED P varies with P and ρ . When reducing the radiometric noise by the averaging 5×5 pixel window, and for the typical reflectances of the clouds here examined, the inaccuracy on P is about $\Delta P = \pm 0.005$, for the case of entrance unpolarized light.

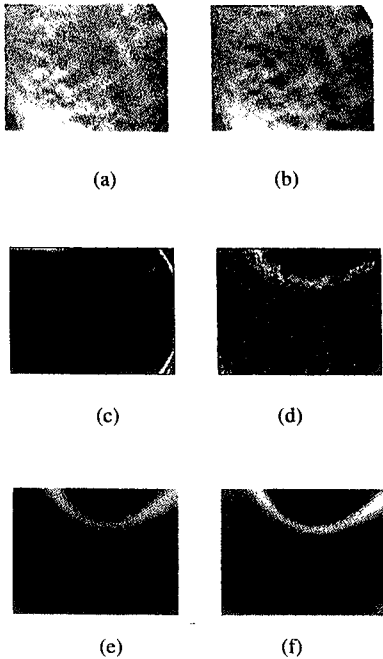


Fig. 3. POLDER observations over a thin stratocumulus, during ASTEX ((a), (b), (c)) and over a heterogeneous cloud, during MEDIMAR ((d), (e), (f)). Processed images of polarized bands (see text). (a) and (d) display the reflectance in the 850 nm bands; (b) and (e) the polarized reflectance in the 850 nm band; (c) and (f) the polarized reflectance in the 450 nm band.

IV. CLOUD POLARIZATION FEATURES

A. Qualitative Results

Fig. 2(c) and 2(d) show the polarized reflectances measured above the cloud field in the 850 nm and 450 nm bands, respectively. We look at the polarized reflectance rather than at the polarization ratio because the polarized reflectance is known to be formed in the upper cloud layer [12] and to be less sensitive to the cloud optical thickness or to the properties of the underlying ground.

The most significant feature in these images are the highly polarized arches. The flight direction here was nearly parallel to the sun incident plane, with the antispecular direction (i.e., scattering angle 180°, or zero phase angle) near the top of the pictures, and these highly polarized features correspond to viewing directions (θ_v, ϕ_v) such that the scattering angle Θ is near from 140° (i.e., $\cos \Theta = \cos \theta_s \cos \theta_v + \sin \theta_s \sin \theta_v \cos \phi_v$). This is the angular position of the primary rainbow of large spherical particles, which confirms that the cloud particles are large cloud droplets. The same feature was repeatedly observed over all the cloud fields encountered during the campaigns. As examples, Fig. 3 shows cloud pictures obtained, respectively, over a thin stratocumulus, during ASTEX (Figs. 3(a), (b), (c)) and over a much more heterogeneous cloud, during MEDIMAR (Figs. 3(d), (e), (f)); Figs. 3(b) and 3(e) display the polarized reflectances in the 850 nm band, Figs. 3(c) and 3(f), in the 450 nm one. The rainbow signature was a permanent characteristic of these low, very probably liquid clouds, and in the case of thin clouds as for Fig. 3(f), secondary cloudbows were even discernable for scattering angles larger than 140°.

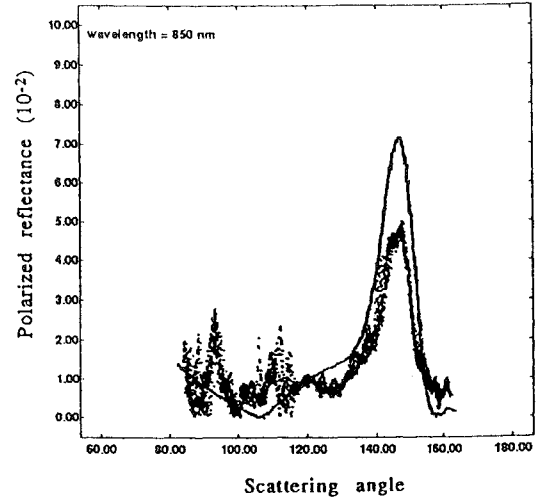


Fig. 4. Data points: polarized reflectances measured in the 850 nm over the cloud of Fig. 2; ρ_P is reported only for viewing directions in the solar incident plane, as a function of the scattering angle Θ . Cor curve: polarized reflectances calculated, for the same geometry, for parallel cloud with optical thickness $\delta = 15$ and with Deirmendjian's C1 for the droplet size distribution.

In other viewing directions, the polarized reflectance is rather low. Let us restrict for the moment to the 850 nm band that is more convenient for observing the internal cloud polarization since molecular scattering is negligible. A second characteristic observation is that cloud polarization at $\lambda = 850$ nm tends to vanish for scattering angles near 100°. To make it clearer, for the case of Fig. 2(c), the polarized reflectance ρ_P (here defined as a positive quantity, according to (1)) and the angle ξ between the polarized vibration and the scattering plane (i.e., the plane formed by the Sun and the viewing directions) have been reported in Figs. 5, respectively, as a function of Θ . For clarity, we considered pixels corresponding to viewing directions very close to the solar incident plane (i.e., nearly the central column of Fig. 2(c)). Because of the radiometric noise and the registration errors (see later), zero polarization is not attained, but its minimum is near $\Theta = 90^\circ - 110^\circ$. In Fig. 5, the agreement between the observed and measured polarization directions is rather bad for $\Theta = 100^\circ - 130^\circ$. Clearly, it is difficult to measure ξ near from zero-polarization points because the polarized measurements, then, are very close and the $\Delta\xi$ resulting from the radiometric noise quite large. Figure 5, however, shows that the polarized vibration is perpendicular to the scattering plane in backward scattering directions and parallel to the scattering plane in forward scattering directions, and this change in the direction of the electric field component goes through zero by continuity.

B. Polarization Modeling

Quantitative analysis of these results needs numerical calculations of the cloud polarization. In a first approximation, for cloud pictures like that of Fig. 2, it seems reasonable to investigate the mean BPDF over the whole POLDER footprint, regardless of small scale features and assuming plane parallel geometry. We therefore simulated POLDER polarization

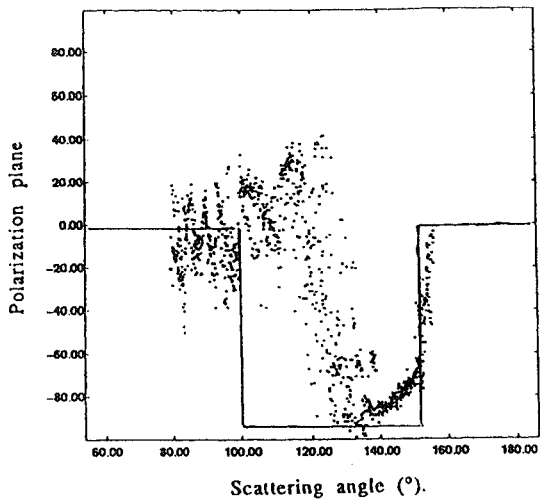


Fig. 5. Same legend as Fig. 4, but for the angle ξ between the polarized vibration and the scattering plane (i.e., here, the solar incident plane).

TABLE II
SIZE DISTRIBUTION PARAMETERS WITH THE SIZE DISTRIBUTION
GIVEN BY $n(r) = ar^\alpha \exp(-br^\gamma)$.

	α	b	γ	a
C1	6.0	1.5	1.0	2.37
C2	8.0	0.0415	3.0	$1.08 \cdot 10^{-2}$
C3	8.0	0.333	3.0	5.55
Cumulus	3.0	0.5	1.0	2.604
Altocstratus	5.0	1.11	1.0	6.28
Stratocumulus	5.0	0.8	1.0	0.437
Stratus	3.0	0.667	1.0	8.24

measurements above plane parallel clouds. Calculations were performed with a code, provided by C. E. Siewert [13], of the Generalized Spherical Harmonics Solution (GSHS) of the radiative transfer problem in polarized light [14].

The polarized reflectance was calculated for different cloud optical thicknesses δ , and for different size distribution functions of the cloud droplets $n(r)$. Table II indicates the models used in the calculations and the corresponding cloud type, according to Deirmendjian's classification [15]. The corresponding size distributions are shown in Fig. 6. Calculations were performed by neglecting molecular scattering above and within the cloud and by assuming zero reflectance of the underlying ground.

The calculations confirm that the polarized light has negligible ellipticity and may be considered as linearly polarized, with direction along the major axis of the ellipse. To state how the polarized reflectance varies according to the cloud properties: i) Fig. 7 shows how ρ_P varies as a function of the cloud optical thickness δ , for the case of the cloud model C1 (for comparison, Fig. 8 shows the behavior of the corresponding total reflectance), ii) and Fig. 9 shows how ρ_P varies as a function of the cloud model, for a constant cloud optical thickness $\delta = 15$. The solar zenith angle is 60° . For simplicity, the results are shown for viewing directions within the solar incident plane. They are reported versus Θ . Because of the symmetry exhibited by the solar incident plane, ξ is exactly

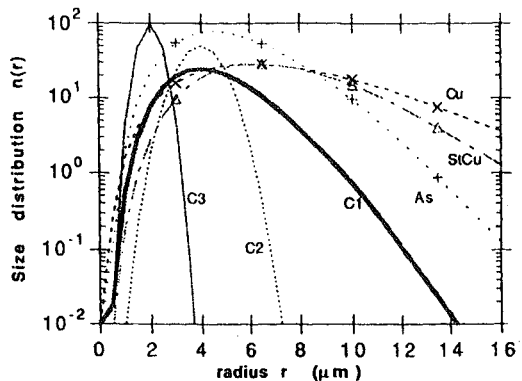


Fig. 6. Cloud droplet size distributions used for the calculations.

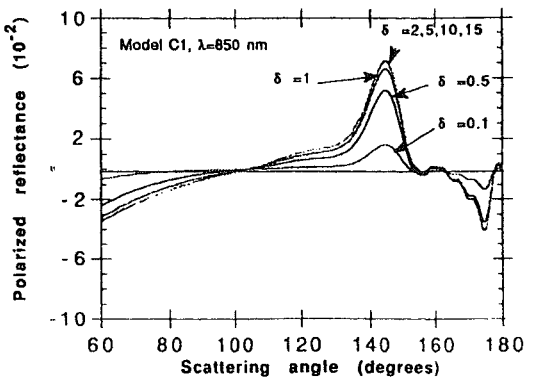


Fig. 7. Calculations of the polarized reflectance reflected by a plane parallel cloud overlying a non reflecting ground, for different optical thicknesses δ of the cloud (noted δ_N in the Figure). The solar zenith angle is 60° ; the observation direction is within the solar principal plane. The polarized reflectance is reported, as a function of the scattering angle Θ , as positive when the polarized vibration is perpendicular to the solar plane and negative when parallel (say ρ_{P*}). The cloud droplet size distribution is the Deirmendjian's model C1; the observation wavelength is $\lambda = 850$ nm. The molecular scattering is neglected.

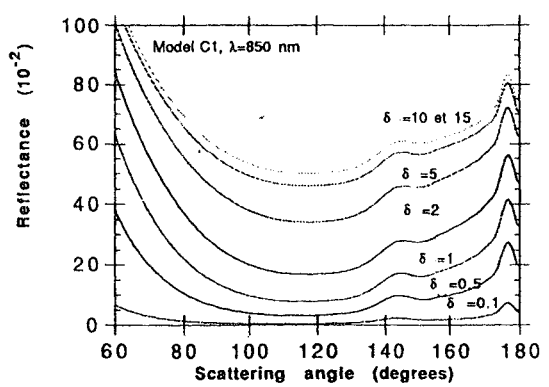


Fig. 8. Same legend as Fig. 7, but for the total reflectance.

either 0° or 90° , and we reported here the algebraic polarized reflectance, say ρ_{P*} , that is ρ_p as negative for $\xi = 0^\circ$ and as positive for $\xi = 90^\circ$.

As suggested previously, Fig. 7 shows that because the polarized light is formed in the very upper cloud layer the polarized light scattered by the cloud no more depends on the cloud thickness as soon as the optical thickness is larger than

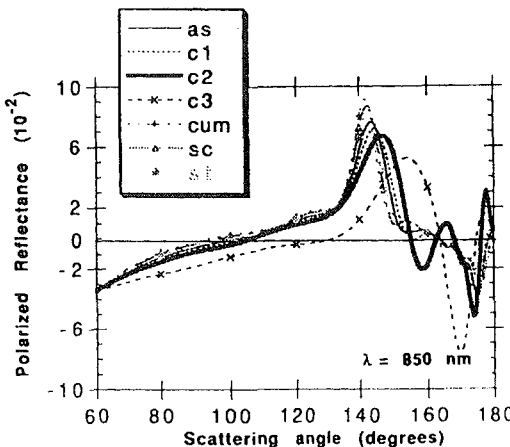


Fig. 9. Same legend as Fig. 7, but ρ_P is reported for a constant cloud optical thickness ($\delta = 15$), for different cloud droplet size distributions (see Table II).

1. Clearly, the total reflectance, and therefore the polarization ratio, are much more dependent on δ . The polarized light reflected by cloud fields, when located above land surfaces, should no more depend on the underlying ground properties because the polarized light reflected by most terrestrial surfaces (bare soils, vegetative canopies, etc.) and by clouds, when illuminated by the direct sunbeam, are of the same order of magnitude; their contribution should therefore be negligible when overlayed by a rather thin cloud. The same is probably not true for oceanic observations. In this case, the sea surface reflection may give a large amount of polarized light, and, as shown by Masuda and Takashima [8], cloud thicknesses much larger than 1 then may be needed to mask the "ground" contribution.

Fig. 9 shows that the primary rainbow near $\Theta = 140^\circ$ and the less intense cloudbow near 175° are features that are nearly insensitive to the cloud droplet dimensions. Similarly, all cloud models exhibit zero polarization for scattering angle near from 100° . Only very small size spectrum as corresponding to models C2 and C3 show departures from these characteristics.

C. Comparison

From such calculations, given the solar zenith angle and the flight direction, polarized POLDER pictures over plane parallel clouds may be simulated.

For the geometric conditions of Fig. 2, (e) shows the synthetic POLDER picture in polarized light obtained by this way, when assuming a cloud model C1 with an optical thickness $\delta = 15$. The corresponding values of ρ_P and ξ for viewing directions in the solar incident plane have been reported as continuous curves in Figs. 4 and 5. Finally, to compare the results over the entire POLDER picture, we just plotted, in Figs. 10 and 11, respectively, the observed and the simulated polarized reflectances for all the pixels of the image, as a function of the corresponding scattering angle Θ .

Fig. 11 shows that the representation is specially convenient. Moreover, we reported in Fig. 11 calculations of ρ_P for the same cloud, but for different solar zenith angles. It is

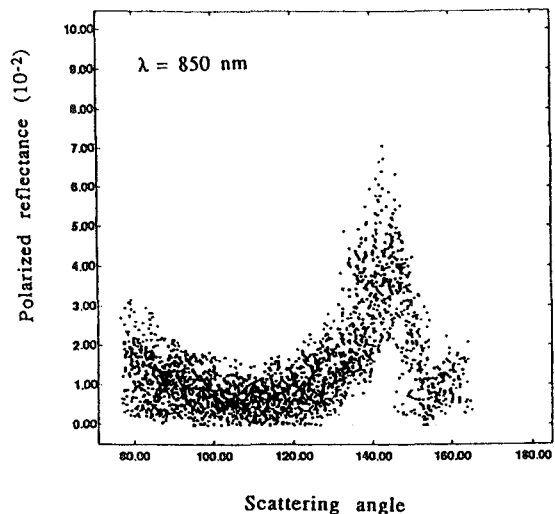


Fig. 10. Polarized reflectance ρ_P , measured over cloud field of Fig. 2 850 nm band; ρ_P has been plotted vs the scattering angle Θ , for all the pixels of the image. Cloud observations conducted during CLEOPATRA, on 19, 1991, at about 11 000 m altitude, with mean solar zenith angle θ_s :

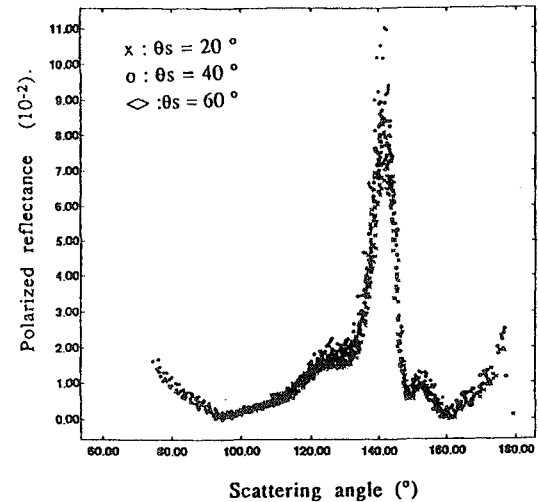


Fig. 11. Polarized reflectance ρ_P , calculated for the same geometry ($\theta_s = 60^\circ$) and observation wavelength as in Fig. 10, for a plane parallel cloud with optical thickness $\delta = 15$ and with Deirmendjian's model for the droplet size distribution. The polarized reflectances calculated for the same cloud but for other solar zenith angles ($\theta_s = 20^\circ, 40^\circ$) are indicated by different labels.

noteworthy that the entire bidirectional polarized reflectance distribution function of a plane parallel cloud may practically be displayed by a simple bidimensional plot, as a function of the scattering angle Θ . This comes from the fact that polarized light is mainly formed by the single scattering process. In approximation, for sufficient optical thickness of the layer, we have

$$\rho_P = \frac{p(\Theta)P(\Theta)}{4(\cos \theta_s + \cos \theta_v)}$$

where $p(\Theta)$ and $P(\Theta)$ are the phase function and polarization ratio for single scattering of the cloud particles, which shows that the polarized light is mainly governed by Θ . The 1

influence of single scattering explains also that calculated values of ξ (not presented here) are always near from 0° or 90° , since single scattering by spherical particles gives polarization either parallel or perpendicular to the scattering plane.

The reasonable agreement between Figs. 10 and 11 confirms that polarimetric measurements indicate average particle sizes with dimensions typical of known magnitudes for liquid cloud droplets. In some conditions, the measurements displayed clearly secondary cloudbows that could correspond to smaller cloud droplets in the uppermost entrainment layer of the cloud. Despite the large dispersion of the results, the observations confirm also that most clouds exhibit, near 90° – 100° scattering angle, negligible polarization, which may be useful for the purpose of estimating the cloud top pressure as will be seen now.

V. CLOUD ALTIMETRY FROM RAYLEIGH SCATTERING

A. Multiband Polarization Observations

Let us then consider the spectral aspect of polarization measurements over cloud fields. We will limit our discussion to data acquired during the CLEOPATRA campaign, because of the reasonable altitude above the clouds allowed by the Falcon of DLR, thus providing sufficient effect of the molecular scattering layer between the cloud and the aircraft.

As shown previously (Fig. 2(c) and 2(d), for example) the rainbow features are very similar in the 450 and 850 nm spectral bands of POLDER, but in other viewing directions, specially around $\Theta = 90^\circ$, the polarized reflectance is clearly larger at 450 nm than 850 nm. This effect is present in all sequences of all flights. It results from the increasing influence of the intervening molecular layer at shorter wavelengths. Of course, nothing similar do appear in the reflectance images where the spectral effect varies largely as a function of the underlying ground properties.

On October 21, 1991, because of the large extension of the cloud field, the Falcon was able to overfly the cloud at different altitudes, including a first run near the top, at about 3.5 km. Fig. 12 shows ρ_P versus Θ in the 450 nm channel, derived from 3 pictures obtained at about 3.5 km (cloud top), 7.3 km and 11.3 km, with mean solar zenith angle $\theta_s = 60^\circ$. For clarity, the ρ_P measurements have been reported only for pixels near from the solar incident plane. Within the range of scattering angles 80° – 100° , where population by molecular scattering is large, the polarized reflectance increases with the aircraft altitude, i.e., with the thickness of the intervening molecular atmosphere. By contrast, the polarized reflectance at 850 nm is practically unchanged, in accordance with the λ^{-4} dependence of the molecular scattering efficiency. These observations confirm that differences in the polarized reflectance observed at 450 and 850 nm above clouds mainly correspond to molecular scattering, from which the cloud top altitude could be estimated.

To test this possibility, let us consider that the polarized light measured at 450 nm around $\Theta = 90^\circ$ corresponds only to light scattered by the molecular layer, since cloud contribution

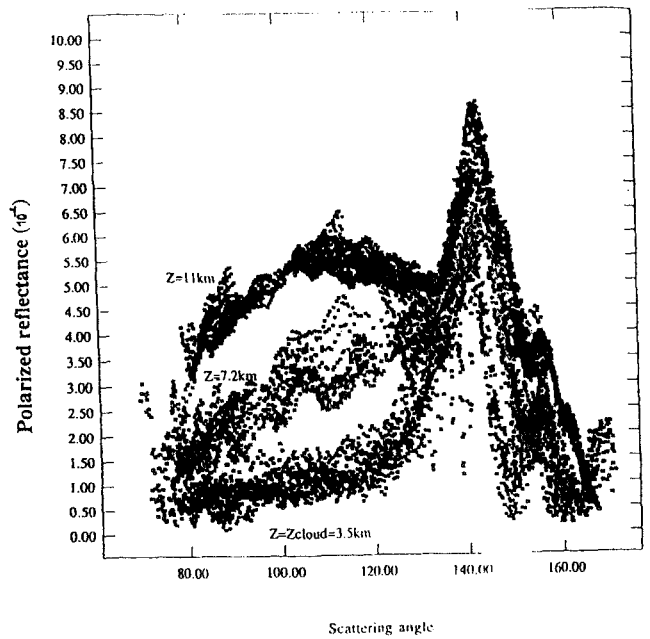


Fig. 12. Polarized reflectance ρ_P , in the 450 channel, vs the scattering angle Θ . Cloud observations conducted during CLEOPATRA, on October 21, 1991, with mean solar zenith angle $\theta_s = 60^\circ$. For clarity, only pixels near from the solar incident plane have been reported. The different labels correspond to measurements performed at about 3.5 km (cloud top), 7.3 km and 11.3 km.

is negligible in this direction. Let $\Delta\delta_m(\lambda)$ be the optical thickness of the molecular layer; because $\Delta\delta_m(\lambda)$ is small, single scattering approximation of ρ_P , or $\rho_{m,P}$, is valid and therefore

$$\begin{aligned} \rho_{m,P}(\lambda) &= \Delta\delta_m(\lambda) \frac{p_m(\Theta)P_m(\Theta)}{4 \cos \theta_v \cos \theta_s} \\ &= \frac{3\Delta\delta_m(\lambda)}{16 \cos \theta_s \cos \theta_v} (1 - \cos^2 \Theta). \end{aligned} \quad (4)$$

When calculating $\rho_{m,P}$, the mean polarized reflectances measured around $\Theta = 90^\circ$ from Fig. 12, the derived estimates of $\Delta\delta_m$ are, respectively, $\Delta\delta_m = 0.071$ for $z_A = 7.3$ km and $\Delta\delta_m = 0.098$ for $z_A = 11.3$ km. Given the altitude of the aircraft z_A , the altitude of the cloud top z_C , derived from these measurements according to

$$\Delta\delta_m = \delta_{0,m} (\exp(-z_C/H) - \exp(-z_a/H)) \quad (5)$$

where $\delta_{0,m}$ is the total Rayleigh optical thickness and H the atmospheric scale height, are, respectively, 2.5 km and 2.9 km (with $\delta_{0,m} = 0.216$ at $\lambda = 450$ nm and $H = 8$ km), that is, respectively, 1 km and 0.6 km lower than the observed altitude $z_C = 3.5$ km.

To extend the method to observation directions other than 90° —which is important for enlarging the applicability of the method in satellite pictures—we must account for the cloud contribution to the polarized light. Let us assume that the polarized light reflected by the cloud does not depend on the wavelength because of the large dimension of the cloud droplets and that the light resulting from multiple interactions between the cloud and the molecular layer exhibits negligible

polarization. The expected polarized reflectance will be then

$$\hat{\rho}_P(\lambda) \approx \hat{\rho}_{m,P}(\lambda) + \exp\left(-\frac{\delta_m(\lambda)}{\cos \theta_s} - \frac{\Delta\delta_m(\lambda)}{\cos \theta_v}\right) \hat{\rho}_{c,P} \quad (6)$$

where δ_m is the optical thickness of all molecules above the cloud and $\rho_{c,P}$ stands for the polarized light at the top of the cloud when directly illuminated by the solar beam; the exponential term accounts for the attenuation by the overlying molecular layer. Note that (6) is written in terms of the reduced 2 terms Stokes' matrix $\rho = (\rho_Q, \rho_U)$ which are additive, while the simple absolute polarized reflectances may not be, when for example the molecular and cloud components are polarized at right angles.

To simplify (6), as δ_m and $\rho_{m,P}$ are negligible at $\lambda = 850$ nm, let us consider that $\rho_P(\lambda = 850)$ provides directly $\rho_{c,P}$, and let us neglect the transmission effect. Then, (6) reduces to

$$\begin{aligned} \hat{\rho}_P(\lambda = 450 \text{ nm}) - \hat{\rho}_P(\lambda = 850 \text{ nm}) \\ \approx \hat{\rho}_{m,P}(\lambda = 450 \text{ nm}). \end{aligned} \quad (7)$$

We note that molecular scattering gives polarization perpendicular to the scattering plane, i.e., $\xi_m = 90^\circ$ or $\rho_{m,U} = 0$ (cf. (2)). The ρ_Q term of (7), therefore, has only to be considered; it provides all the polarized reflectance ρ_P , so that according to (4) it comes

$$\begin{aligned} \Delta\delta_m(\lambda = 450 \text{ nm}) &= \frac{16 \cos \theta_s \cos \theta_v}{3(1 - \cos^2 \Theta)} \\ &\left\{ [\cos 2\xi \cdot \rho_P]_{(\lambda=450 \text{ nm})} - [\cos 2\xi \cdot \rho_P]_{(\lambda=850 \text{ nm})} \right\} \end{aligned} \quad (8)$$

from which $\Delta\delta_m$ and the cloud-top altitude may be derived.

To assess the validity of these approximations, the POLDER measurements at 450 and 850 nm were simulated by the GSHS code, taking into account the molecular scattering at 850 nm, the multiple scattering within the free atmosphere and within the cloud and the spectral variation of the cloud droplet scattering, derived from Mie theory. We only neglected the influence of molecules mixed with cloud droplets, i.e., we considered a homogeneous cloud. These assumptions are reasonable since the effective cloud optical depth which the polarized light comes from $\delta \approx 2$ should correspond only to 40 m for a typical cloud scattering coefficient 50 km^{-1} .

The calculations were made for different cloud models and for different pressures of the cloud top within a standard atmosphere. We considered satellite measurements (i.e., $\Delta\delta_m = \delta_m$). The cloud optical thickness and the solar zenith angle were fixed ($\delta = 15$ at 850 nm, $\theta_s = 60^\circ$) and the measurements were simulated for viewing directions within the whole POLDER pictures. They were reported in (8) and the derived δ_m were converted in cloud top pressures.

The results are shown in Fig. 13 as a function of the scattering angle; we restricted Θ range of 80° to 100° where the molecular polarization is large enough compared to that of the cloud. Some improvements (systematic correction of $\rho_{m,P}$ for multiple molecular scattering and iteration between (6) and (8) to take into account transmission effect) could reduce the dispersion, but the principal limitation is probably the spectral

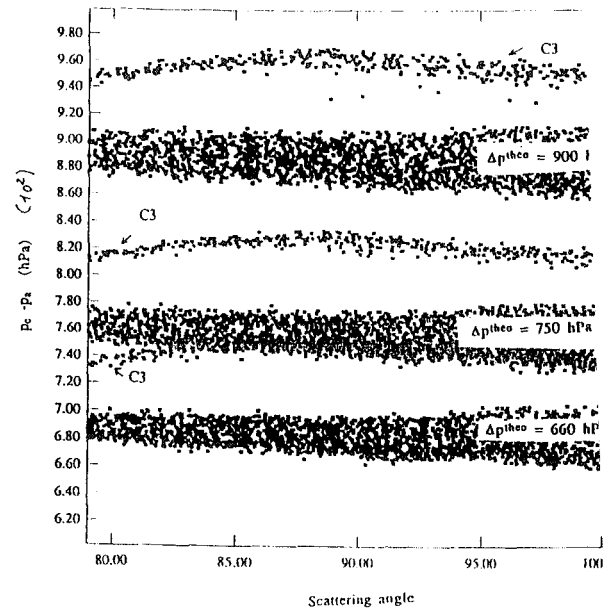


Fig. 13. Simulations of the cloud top pressure derived from PC measurements at 450 and 850 nm, over plane parallel cloud, by us proposed approximate inversion method (see text). Measurements have simulated by the GSHS code, with different assumed models of the droplets and pressures of the cloud top, for viewing directions with whole POLDER images. The assumed differences between the cloud and the aircraft pressures, Δp^{theo} , are indicated. The retrieved pressure differences, $p_C - p_A$, have been plotted with different labels according to assumed droplet model vs the scattering angle Θ corresponding to the v direction. Results are restricted to directions where molecular scattering is large enough. The results are nearly similar, within 20 hPa, for all models except model C3, for which the cloud top pressure is underestimated by about 50 hPa.

variation of the cloud polarization, which introduces increasing errors for backward scattering directions, for all cloud models and, in the case of very small particles (C3). Fig. 13 shows that the crude approximation (8) gives, however, correct results for pressure errors no more than 20 hPa for most cloud models, while the systematic error increases to 50 hPa for the very small particles of model C3.

The method was then applied to CLEOPATRA images in order to minimize possible errors due to small scale variations in $\rho_{c,P}$, the POLDER pictures in the 2 channels were transferred for superposition; the resulting variation of Θ , for the same cloud pixel as seen in the two channels, is negligible. $\Delta\delta_m(\lambda = 450 \text{ nm})$ derived from (8) were converted into pressure differences DP between the aircraft and the cloud top, according to

$$\Delta P = P_C - P_A = P_0 \cdot \Delta\delta_m / \delta_{0,m}$$

where P_0 is the standard pressure at sea level.

As an example, Fig. 14 shows the results for the case of the CLEOPATRA picture of Fig. 2. The continuous curve shows the average result and we indicated the expected pressure difference, according to the altitudes z_C and z_A . Fig. 14 is representative of the scatter in the ΔP estimates obtained for all the pictures that we analyzed. In the case of the cloud picture of Fig. 12, we only reported in Fig. 15 the average

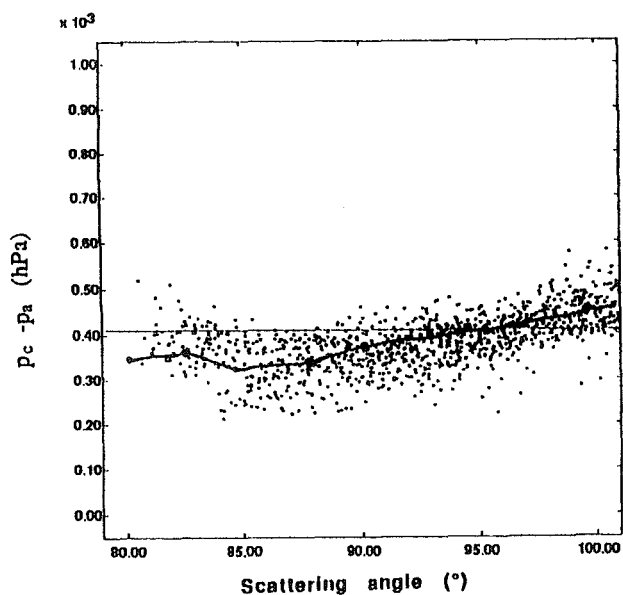


Fig. 14. Estimates of pressure differences between the cloud top and aircraft levels, derived from the POLDER observations of CLEOPATRA, on October 18, 1991. The inversion has been applied only to image pixels corresponding to scattering angles Θ ranging from 80° to 100° , and results have been reported vs Θ . The continuous curve is the average result. The expected pressure difference (400 hPa) is indicated.

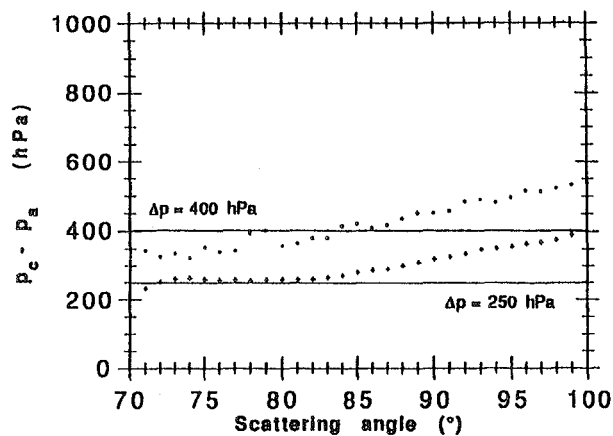


Fig. 15. Same legend as Fig. 14, but for CLEOPATRA observations on October 21, 1991, performed at 2 different altitudes above the same cloud. The average results only have been reported.

estimates, as a function of Θ , for the 2 altitudes of the aircraft ($z_A = 7.2$ and 11 km) above the cloud top ($z_C = 3.5$ km).

Polarization provides the correct order of magnitude and Figs. 14 and 15 suggest that cloud altimetry derived by this way could be valid. There is, however, a large dispersion in the estimates and some apparent systematic discrepancy as a function of the viewing direction.

B. Discussion

The scatter in the results of Fig. 14 comes partly from the simplifying assumptions of the method, from probable

departures from the assumed plane geometry and maybe from horizontal variations in the particle dimension. According to Fig. 13, however, the method error should be quite small, at least for large enough cloud droplet dimensions. On the other hand, Fig. 11 shows that polarized light is not sensitive to variations in θ_s and θ_v , so that it is expected that polarized light should not be affected by small departures from plane parallel geometry resulting from the cloud top roughness. It seems therefore very likely that most of the scatter comes from the quality of the measurements, as seen in Figs. 4 and 12.

The measurement method of polarization by POLDER, using differences between successive images, entails reduction in the large influence of radiometric noise and registration errors on the estimated polarized light. It may be shown that the radiometric noise, say $\Delta\rho$, leads to a measured polarized reflectance, ρ_P^{est} , in the form

$$(\rho_P^{\text{est}})^2 = (\rho_P)^2 + \frac{4}{3} \Delta\rho \cdot \rho_P + \frac{4}{3} (\Delta\rho)^2. \quad (10)$$

The noise equivalent $\Delta\rho$ of the airborne instrument, however, is only 5.10^{-4} , which does not explain the observed dispersion nor the residual polarization, of the order of 0.005, near zero polarization directions. The present principal limitation, therefore, is probably the image superposition, which introduces an apparent polarization into an otherwise unpolarized scene if the scene exhibits reflectance variations at small scales. This defect out to be reduced in the satellite version of POLDER, whose filters will be equipped by prisms for better superposition of the images. This point deserves further study in the airborne version. Improved processing of the data has to be searched for, specially by looking for image registration within better accuracy than the present 1 pixel. Note, however, that during CLEOPATRA condensation occurred on the optics and on the filters, which resulted in small localized defects that could not be corrected by post- and pre-flight calibrations. The pictures acquired during the ASTEX campaign prove to exhibit much smaller dispersion; but they were performed from altitudes too low to permit validation of the altimetry method.

In any case, the fact that the dispersion level of the data, about 100 hPa in Fig. 14, did not mask anticipated results. May be more serious in the second defect in Figs. 14 and 15, where the estimated pressure increases systematically for observation directions corresponding to backward scattering. Because the residual aerosol layer, above 3.5 km, is expected to have negligible influence, the only explanation suggested by the present modeling would be the existence of very small cloud droplets in the upper entrainment cloud layer, whose spectral dependence should have been included (6). Indication of such particles might be the secondary cloudbows clearly observed in the ASTEX pictures (Fig. 3(c)), but probably discernable also in the CLEOPATRA measurements of Fig. 12. Apart from the possible interest of this detection for cloud studies, this should require that some correction term in (7) and (8), accounting for the spectral variation of the cloud contribution, be derived from the bidirectional polarization signature at 850 nm.

Finally, concerning the application of this method to satellite data, the influence of the stratospheric aerosols on the polarized light has to be considered. The influence of the background stratospheric aerosol layer is very probably negligible. The polarizing properties of these particles, as observed from balloon-borne experiments [16], correspond to spherical hydrated sulfuric acid particles, with $\sigma = 1.35$ and $r_m = 0.3 \mu\text{m}$ as parameters of the lognormal size distribution convenient for these particles. When using these data in Mie theory calculations, the predicted difference $\Delta\rho_P$ between the polarized reflectance of these particles in the POLDER channels 443 and 865 nm, around $\Theta = 90^\circ$, is typically $\Delta\rho_P = 0.025\delta_{\text{aer}}(1020 \text{ nm})$, where the optical thickness of the aerosol layer is estimated at $\lambda = 1020 \text{ nm}$, i.e., the SAGE II aerosol channel. The SAGE II data show that, in the post El Chinon period from 1985 to 1989 for example, $\delta_{\text{aer}}(1020 \text{ nm})$ was smaller than 0.005 [17]. The resulting perturbation of these aerosols should have been smaller than $\Delta\rho_P = 10^{-4}$, corresponding to no more than 1 or 2 hPa as the systematic error in the derived cloud top pressure.

After major volcanic events like the El Chinon or Pinatubo ones, however, during some months, the optical thickness of the resulting stratospheric aerosol layer is known to be possibly 50 to 100 times larger than the background values. Because, in these conditions, the particle dimensions are somewhat larger than in the background ones (typically, $r_m = 0.45 \mu\text{m}$, from balloon-borne observations performed two months after the Pinatubo event), the differential polarizing effects is somewhat reduced, but could entail systematic errors about 50 hPa. During such periods, therefore, the POLDER measurements would probably benefit from systematic corrections based on stratospheric data, as provided by SAGE II/III instruments or by systematic balloon soundings of the stratosphere.

VI. CONCLUSION

The POLDER airborne instrument was able to measure on different occasions the bidirectional polarization distribution function of low cloud fields. Over all these clouds, polarized observations made it clear that the characteristic rainbow of spherical cloud droplets is very probably a good indicator of the presence of a liquid phase. It is noteworthy that the POLDER capability to provide bidimensional pictures makes this feature recognizable whatever the cloud field heterogeneity. Simulations show that the BPDF of homogeneous cloud fields is specially simple in terms of polarized reflectances defined by only the scattering angle and by the polarization of the upper cloud droplets.

The observations confirmed that difference in the polarized reflectance at 450 and 850 nm above clouds mainly corresponds to the residual molecular atmosphere scattering, that may be used as a barometer to estimate the cloud top pressure. Simulations indicate that because of the small effective cloud depth concerned by the formation of polarized light the method should lead to a well defined cloud top pressure (typically $\pm 100 \text{ hPa}$). The simple scheme proposed for the retrieval of the cloud top pressure should be efficient

provided the upper cloud layer is formed of large droplets.

The present observations, however, suggest that very particles near the cloud top might necessitate more extensive treatment. We no more examined the case of heterogeneous cloud fields, which is clearly a much more complicated problem. Although, the present lack of cirrus cloud observations prevents a definitive conclusion concerning the possibility of identifying ice clouds from polarimetry, future PC campaigns have been planned to determine this possibility.

ACKNOWLEDGMENT

The authors are very grateful to Pr. C. Siewert who provided his GSHS code, to F. Parol, Y. Balois and C. Verwaerde who conducted the different campaigns, L. Gonzalez and F. Lemire who processed the PC data.

REFERENCES

- [1] P. Y. Deschamps, M. Herman, A. Podaire, M. Leroy, M. Laporte, P. Vermande, "A spatial instrument for the observation of polarization and directionality of Earth reflectances: POLDER," in *Proc. ICPOL 90*, Washington, D.C., 1990.
- [2] F. M. Bréon, A. Bricaud, J. C. Buriez *et al.*, "The POLDER 1 Instrument characteristics and scientific objectives," *IEEE Trans. Remote Sens.*, (to be published).
- [3] D. L. Coffeen, and J. E. Hansen, "Airborne infrared polarimeter," in *Proc. 8th Internat. Symp. Remote Sensing Environment*. Oct. 1972.
- [4] Q. Cai and K. N. Liou, "Polarized light scattering by hexagonal crystals: Theory," *Ap. Optics*, vol. 21, pp. 3569-3580, 1982.
- [5] Y. Takano and K. Jayaweera, "Scattering phase matrix for hexagonal crystals computed from ray optics," *Ap. Optics*, vol. 24, pp. 3254-3261, 1985.
- [6] J. De Haan, "Effects of aerosols on the brightness and polarization of cloudless planetary atmospheres," M.S. thesis, Free University Amsterdam, Holland, The Netherlands, 1987.
- [7] G. Brogniez, "Contribution à l'étude des propriétés optiques et radiatives des cirrus," Thèse d'état, Université des Sciences et Technologies de Lille, 1992.
- [8] K. Masuda and T. Takashima, "Feasibility study of derivation of information using polarimetric measurements from satellite," *J. Remote Sens. Environ.*, vol. 39, pp. 45-59, 1992.
- [9] M. I. Mishchenko and L. D. Travis, "Light scattering by size distributions of nonspherical particles of size comparable to a wavelength," To appear in *Atmospheric Propagation and Remote Sensing*, vol. II, A. Kohnle and W. B. Miller Eds., Proc. SPIE, 1968, (to be published).
- [10] J. L. Deuzé, C. Devaux, M. Herman, R. Santer, J. Y. Balois, L. Gonzalez, P. Lecomte, and C. Verwaerde, "Photopolarimetric observations of aerosols and clouds from balloon," *Remote Sens. Environ.*, vol. 27, pp. 93-109, 1989.
- [11] J. L. Deuzé, F. M. Bréon, J. L. Roujean, P. Y. Deschamps, C. Devaux, and M. Herman, "Preliminary results of POLDER overland flights," *Remote Sens. Environ.*, (to be published).
- [12] J. E. Hansen and L. D. Travis, "Light scattering in planetary atmospheres," *Space Sci. Rev.*, vol. 16, pp. 527-610, 1974.
- [13] R. D. M. Garcia and C. E. Siewert, "A generalized spherical harmonic solution for radiative transfer models that include polarization effects," *J. Quant. Spec. Rad. Transfer*, vol. 36, pp. 401-423, 1986.
- [14] C. E. Siewert, *Astrophysical J.*, vol. 245, pp. 1080-1086, 1986.
- [15] Diermendjian, *Electromagnetic Scattering on Spherical Polydisperse Particles*, New York: Elsevier, 1969.
- [16] M. Herman, J. Y. Balois, L. Gonzalez, P. Lecomte, J. Lenoble, R. Santer, and C. Verwaerde, "Stratospheric aerosol observations from a balloon-borne polarimetric experiment," *Appl. Opt.*, vol. 15, pp. 3573-3582, 1986.
- [17] C. Brogniez and J. Lenoble, "Analysis of 5-Year aerosol data from the Stratospheric Aerosol and Gas Experiment," *J. Geophys. Res.*, vol. 96, pp. 15,479-15,497, 1991.



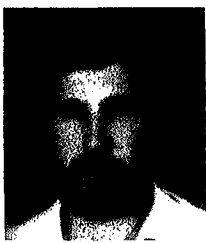
Philippe Goloub received the Ph.D. degree in atmospheric optics from the University of Lille, France.

He is currently working in the ScaRaB team at Laboratoire de Météorologie Dynamique (Paris), before joining the Laboratoire d'Optique Atmosphérique (Lille) to work in the POLDER team, on aerosols remote sensing problems. His works concern the development of the French instrument POLDER.



Maurice Herman received all degrees in physics, in 1962, and the Ph.D. degree in physics, in 1968, from the University of Lille.

He is currently Professor at the Université des Sciences et Technologies of Lille. His experiments are principally in the area of aerosol remote sensing. His research activities include radiative transfer and atmospheric signal modeling, planetary atmosphere studies from analysis of telescopic observations, ground-based and balloon-borne remote sensing of aerosols, with special emphasis about polarization.



Jean-Luc Deuzé received the M.S. degree in physics in 1970 and the Ph.D. degree in atmospheric optics in 1974 from the Université de Lille, France.

He is currently a Professor of Physics at the Université de Lille and a Researcher at the Laboratoire d'Optique Atmosphérique. His research activities focus on radiative transfer modeling within the atmosphere and the inversion of sky radiance measurements for aerosol monitoring. He is also involved in field campaigns to monitor aerosols. One of his main interests is in exploiting polarization data to retrieve aerosol properties for climate investigations. Within the POLDER project he is in charge of the inversion retrievals to obtain aerosol characteristics over both ocean and land surfaces.



Yves Fouquart received a scholarship at University of Lille, where he became Assistant Professor in 1968 and Full Professor in 1983. His Ph.D. degree, received in 1975, was on the spectral properties of radiation reflected by scattering planetary atmospheres.

He is author or co-author of 32 publications. His major areas of activity concern: radiative transfer modeling for numerical climate models, theoretical and experimental (satellite, surface-based, and airborne, *in situ*) study of clouds and radiation interactions, dynamics of boundary layer clouds, experimental and theoretical work on desert aerosols, use of ERBE data to validate GCMs.

Dr. Fouquart was a Member of the Joint Scientific Committee for the World Climate Programme from 1986 to 1993 and co-chaired the IRC/JSC working group on Intercomparison of Radiation Codes for Climate Models (ICRCCM). He is presently Co-investigator of EUCREX (European Cloud and Radiation Experiment).

Cloud Thermodynamic Phase Classification from the POLDER Spaceborne instrument

Journal of Climate

CLOUD THERMODYNAMIC PHASE CLASSIFICATION FROM THE POLDER SPACEBORNE INSTRUMENT

P.Goloub⁽¹⁾, M. Herman⁽¹⁾, H. Chepfer⁽²⁾, J. Riedi⁽¹⁾, G. Brogniez⁽¹⁾, P. Couvert⁽³⁾, G. Séze⁽⁴⁾

- (1) Laboratoire d'Optique Atmosphérique, Université des Sciences et Technologies de Lille. 59655 Villeneuve d'Ascq Cedex. France, Phone (33) 03 20 43 47 66 Fax: (33) 03 20 43 43 42 E-mail: goloub@loaser.univ-lille1.fr
- (2) Laboratoire de Météorologie Dynamique, Ecole Polytechnique, 91128 Palaiseau. France
- (3) Laboratoire des Sciences du Climat et de l'Environnement, CEA, 91191 Gif sur Yvette. France
- (4) Laboratoire de Météorologie Dynamique, CNRS, Université P. et M. Curie, Jussieu, 75252 Paris

Université des Sciences et Technologies de Lille
Laboratoire d'Optique Atmosphérique

Abstract.

Cloud phase recognition is important for cloud studies. Ice crystals correspond to physical process and properties that differ from those of liquid water drops. The angular polarization signature is a good mean to discriminate between spherical and non-spherical particles (liquid and ice phase respectively). POLDER (POLarization and Directionality of the Earth Reflectance) has been launched on the Japanese ADEOS (ADvanced Earth Observing System) platform in August 1996. Due to its multi-directional, multispectral and multi-polarization capabilities, this new radiometer gives useful information on the clouds and on their influence on the radiation in the short-wave range. The POLDER bi-directional observation capability provides the polarization signatures within a large range of scattering angles in three spectral bands centered on 0.443, 0.670 and 0.865 μm with a spatial resolution of 6.2 km \times 6.2 km. These original features allow to obtain some information both on cloud thermodynamic phase and even on the cloud microphysics (size/shape). According to POLDER airborne observations, liquid cloud droplets exhibit the very specific polarization features of the rainbow for scattering angles near 140°. Conversely, theoretical studies of scattering by various crystalline particles and also airborne measurements show that the rainbow characteristics disappear as soon as the particles depart from the spherical shape. In the paper, the POLDER algorithm for cloud phase classification is presented as well as the physical principle of this algorithm. Results derived from POLDER spaceborne version are also presented and compared with lidar ground-based observations and satellite cloud classification. This cloud phase classification method is shown to be reliable. The major limitation appears when thin cirrus clouds overlap liquid cloud layer. In that case, if the cirrus optical thickness is smaller than two, liquid phase may be retrieved. Otherwise, ice phase is correctly detected as long as cloud detection works.

1. Introduction

Clouds are a strong modulator of the shortwave and longwave component of the earth's radiation budget (Ramanathan, 1987; 1989). The importance of clouds and radiation in studies of the earth's climate has been demonstrated from both observations (Ramanathan 1989) and modeling (Cess et al., 1989). Knowledge of cloud properties (cloud cover, optical thickness, altitude, thermodynamical *phase*, water vapor, microphysics properties) and their variations in space and time are crucial for studies of global climate change. Thus remote sensing of the optical, microphysical and physical properties of clouds is important for improvement of earth's climate system understanding.

POLDER (Deschamps et al., 1994) is a sensor that provides new information for improving our knowledge of

clouds, radiation and climate interactions.

In this paper we intend to describe how cloud thermodynamic phase classification can be derived from POLDER. Cloud phase is an important property of clouds. Cirrus clouds have been recognized to have a great influence on weather and climate through their effect on the radiative energy budget in the atmosphere (Liou 1986). Cloud cover estimate over both land and ocean needs improvements. Even though cirrus clouds cover nearly 20 to 30 % of the terrestrial surface (Warren et al., 1988), their influence on the radiation budget is still poorly known. Moreover, the estimate of global coverage of cirrus cloud is still poorly known. It is ranging between 20% and 60% of the globe depending on the sensor used to detect ice clouds (Wylie et al, 1998).

Usual techniques for "thermodynamical phase retrieval" are based on infrared measurements. Threshold on brightness temperature or bispectral methods is then used to select cold clouds that are assumed to be composed of ice particles (Han et al. 1994, Nakajima and Nakajima 1995). Future sensor such as MODIS will combine 1.37, 1.64 μm and thermal infrared channels (King et al, 1992). The potential of polarization measurements of the upward radiation to derive cloud information has been studied recently with the POLDER airborne simulator during several airborne campaigns (Goloub et al., 1994, Brogniez et al. 1995, Chepfer et al. 1997, 1998, Bréon and Goloub, 1998). Cloud polarimetric observations over a large range of scattering angles make possible the distinction between spherical (liquid) and non-spherical particles (ice). The satellite version of POLDER provided polarization measurements at a global scale from October 1996 to June 1997. POLDER data are described in section 2. The third section is devoted to the presentation of cloud polarization features. Then, the algorithm used to retrieve the cloud phase is described and comparisons with ground-based lidar measurements and cloud classifications are presented and discussed in section 5. Finally, examples of monthly ice and liquid occurrence frequency maps are presented and discussed.

2. POLDER data

POLDER is an optical sensor launched on the ADEOS platform in August 1996. It provided continuous measurements of the Earth spectral, directional and polarized signatures before the ADEOS platform unexpectedly failed at the end of June 1997. The same instrument will be launched on ADEOS-2 in 2001.

Thanks to its optical design (CCD bidimensional matrix and a wide field of view lens), the POLDER instrument acquires up to 14 successive measurements over a given target as the satellite goes along its orbit. This allows an evaluation of the target directional signature. An other original feature of POLDER is its capability to measure the polarization state of the radiance field.

For cloud study, the main interests of the polarization measurement are in the remote sensing of thermodynamical phase and top pressure (Goloub et al., 1994; Buriez et al., 1997) and microphysics properties (Bréon and Goloub, 1998; Chepfer et al., 1998). POLDER has 8 spectral bands from 0.443 μm to 0.910 μm . Polarization measurements are performed in three of these bands (0.443, 670 and 0.865 μm). These specific bands are equipped with three polarizers in order to determine completely the characteristics of the radiation field (radiance and linear polarization state) in term of Stokes' vector components I, Q and U (Hagolle et al., 1999). The normalized total radiance, L , and polarized radiance, L_p , are defined as follows,

$$L = \frac{\pi \cdot I}{E_s} \quad (1)$$

$$L_p = \frac{\pi \cdot \sqrt{Q^2 + U^2}}{E_s} \quad (2)$$

where I is the radiance, $\sqrt{Q^2 + U^2}$ the polarized radiance and E_s the solar irradiance.

Here, we preferentially used the algebraic normalized polarized radiance defined by $L_p = L^\perp - L^//$ where L^\perp and $L^//$ are the normalized radiance components respectively perpendicular and parallel to the scattering plane. Positive polarized radiance means electric vibration perpendicular to the scattering plane and negative means vibration

parallel to the scattering plane. Calculations and observations are presented in terms of algebraic polarized radiance. The POLDER data full spatial resolution is 6.2 km x 6.2 km (Level 1 products). However, operational cloud-products (Buriez et al., 1997, Parol et al., 1999) are averaged on a 60 km x 60 km spatial resolution (Level 2 products).

3. Cloud polarization features

When considering the solar radiation reflected by clouds observed from a satellite, the polarized component of the upward radiance is mainly formed in the upper cloud layer. About 80 % of the single scattered radiation reflected from the cloud layer arise from the upper 100 m layer. Calculations show that the polarized component, L_p , is saturated for cloud optical thickness greater than 2 (Goloub et al., 1994). By contrast, the total normalized radiance L and the polarization degree (ratio of L_p over L), are more dependent on τ (Hansen, 1971).

The interesting quantity is therefore the polarized radiance L_p that is less sensitive than polarization degree to multiple scattering effect, so that the polarization features, corresponding to single scattering, are preserved in L_p . According to single scattering approximation, the polarized radiance can be written as follows

$$L_p = \frac{1 - \exp[-\tau(1/\cos\theta_s + 1/\cos\theta_v)]}{4(\cos\theta_s + \cos\theta_v)} q(\Theta) \quad (3)$$

In case of large enough optical thickness ($\tau > 2$), the polarized radiance can be written as follows

$$L_p = \frac{\cos\theta_s}{4(\cos\theta_s + \cos\theta_v)} q(\Theta) \quad (4)$$

where $q(\Theta)$ is the polarized phase function that depends on cloud microphysics properties (shape/size) and refractive index. The others quantities θ_s , θ_v are respectively the sun zenith angle and viewing angle and Θ is the scattering angle that is referred to the incident solar direction. Looking at (4) we immediately note that the product of the polarized radiance L_p by $(\cos\theta_s + \cos\theta_v)/\cos\theta_s$ will be mainly governed by the scattering angle Θ . Conservative scattering is assumed and effect of atmospheric gaseous is neglected.

The cloud thermodynamical phase depends of the local thermodynamic conditions and presence of impurities within the atmosphere. Frequently, above seven or eight km, clouds are composed of ice crystals or of mixed liquid and ice particles. In particular thermodynamical conditions, supercooled water droplets may be observed (Curran et al., 1982). Ice particles are microphysically, and thus radiatively, quite different from water droplets. The intent of the three following sub-sections is to describe the main polarization features of water droplets (sect. 3.1), ice clouds (sect. 3.2) and multilayered clouds (sect.3.3).

3.1. Water droplet clouds

According to in-situ measurements, the radius of liquid-phase water droplets ranges from 0.5 to 50 μm (Hansen 1971, Paltridge 1974, Stephens et al., 1978). This size range has been confirmed by lidar observation (Platt et al., 1987), and more recently by FSSP (Forward Scattering Spectrometer Probe) measurements (Pawlowska and Brenguier, 1996). According to global climatology of cloud top droplet size, which is based on 3.7 μm AVHRR channel, the effective radius, r_{eff} , ranges from 5 to 25 μm (Han et al., 1994; Rossow et al., 1996). Global mean value of the effective radius is about 11 μm over the ocean and 8 μm over the continent.

Given the cloud size-distribution, the optical properties (for example the polarized phase function $q(\Theta)$) are derived from standard Mie theory. A convenient analytical size distribution, proportional to the droplet number concentration, is given by (5),

$$n(r) \propto r^\alpha \cdot \exp(-\beta \cdot r) \quad (5)$$

with

$$\alpha = \frac{1-3\sigma_{eff}}{\sigma_{eff}} \text{ and } \beta = \frac{1}{r_{eff} \sigma_{eff}}$$

where r_{eff} is the effective radius of the size distribution and σ_{eff} the effective variance distribution. Typical values of r_{eff} range from 5 μm to 15 μm and σ_{eff} varies from 0.01 (narrow size distribution) to 0.1 (broad size distribution). The refractive index for water droplet is almost constant within the POLDER spectral range.

The radiative transfer calculations of solar radiation in a plane-parallel water clouds may be performed by different techniques (Hansen, 1971), given the single scattering phase matrix for the considered wavelength, corresponding to the assumed water droplets size distribution. Calculations have been performed with the radiative transfer code GHSPOL (General Spherical Harmonic with POLarization, Garcia and Siewert, 1986). To study the sensitivity of the polarized radiance to cloud microphysical properties, for cloud optical thickness $\tau=10$ and surface albedo equals to 0, calculations have been performed for several size distributions of the cloud droplets that correspond to three different values of the effective radius r_{eff} for the same effective variance σ_{eff} (Figure 1) and for the same r_{eff} to different several values of σ_{eff} (Figure 2).

The ‘polarization’ of cloud water droplet exhibits a strong maximum at about 140° from the incoming incident direction. In the geometric optic approximation, this is generated by the first internal reflection within the droplets. This maximum, the Primary Rainbow (PR), is highly polarized which makes it easily detectable. The position of the PR depends slightly on the particle effective radius, r_{eff} . The intensity of the PR peak is increasing with the radius. Another noticeable property is the zero of polarization, the Neutral Point (NP). Its angular position ranges from 75° to 130° depending on r_{eff} . Calculations have shown that the neutral point position is sensitive to the effective radius and increases when the radius decreases (Figure 1).

For narrow size distributions, several bows (succession of secondary polarization peaks and neutral points) occur (Supernumerary Bows), beyond 150°, mainly depending on σ_{eff} and r_{eff} (Figure 2). On the contrary, if the size distribution is broad no supernumerary exists. These properties can be used, in some cases, to retrieve water droplet size distribution (Bréon and Goloub, 1998).

These theoretical features have been confirmed by measurements obtained with the POLDER airborne simulator used during several field campaigns Cleopatra'91 (Meischner, 1993), Astex'92 (Weill et al., 1995), and Eucrex '94 (Raschke et al., 1996).

The Astex campaign took place in region of the Azores in June 1992. During Astex'92 an homogeneous stratocumulus cloud layer above Atlantic Ocean was overflowed at an altitude of 3.5 km. An example of the corresponding directional polarized radiance measured at 0.865 μm is shown in figure 3. A second example, from the Cleopatra'91, is plotted on figure 4. In that case, POLDER overflowed an altostratus cloud layer over land at an altitude of about 10 km. Cloud top altitude was about 3.5 km. Typical spatial resolution was about 40 m. Typical polarization patterns, such as primary rainbow and supernumerary bows indicating narrow droplet size distribution are clearly observed in these airborne data.

3. 2. Ice particles.

Unlike water clouds, cirrus clouds are composed of ice crystals with extremely large variability in shape, size and density depending on temperature and humidity in cloud. From balloon experiment, Miloshevitch and Heymsfield (1996) have shown ice crystal replicas that represent the qualitative microphysical properties in a vertical profile through a cirrus which illustrates the diversity and complexity of ice crystals, with shape and size depending on temperature and humidity in cloud. More recent observations (Heymsfield et al., 1997, 1998; Lawson et al., 1998) based on aircraft optical probes and replicator techniques for midlatitude, tropical, and contrail cirrus, reveal that these clouds are largely composed of bullet rosettes, solid and hollow columns, plates, aggregates, with sizes ranging from a

few micrometers to 1000 μm . Some observations (Lawson et al., 1998) have shown that particles ranging from 50 to 200 μm are mostly columns or rosettes while particles larger than 200 μm are usually bullet rosettes. Heterogeneous nucleation via freezing of previously condensed supercooled water droplets could lead to spheroidal shapes. However, other observations providing high resolution replicas suggest that particles smaller than 20 μm are often plates and columns, combined with irregular and spheroidal shapes. More recently, a cloud particle imager (Lawson et al., 1998) has provided information of ice particles within Arctic cirrus. In that case, smaller particles appear to have smooth edges, but depart from exact spherical shape.

According to the present knowledge on cloud ice microphysics, the assumption that ice clouds are composed of non-spherical particles is quite credible.

To study the sensitivity of the polarization signature to the shape of ice cloud particles, different ice crystals have been used. Because in nature, ice crystals growth in hexagonal structure, the hexagonal shape is commonly used to simulate ice crystals properties: hexagonal columnar or plated monocrystalline particles (e.g. Brogniez 1988; Takano and Liou 1989), and polycrystalline particles (Macke et al. 1996), both randomly oriented in space. For such particles, computations of optical properties are based on a ray-tracing method supplemented by calculations of the Fraunhofer diffraction. These hexagonal crystals are described by their aspect ratio $Q = L/D$, where L and D are the length and the diameter of the crystal, respectively, and by R_{eq} , the radius of an equivalent spherical particle with the same volume. These calculations are valid only in the geometrical optic approximation, i.e. radius R_{eq} greater than 15 μm for visible wavelengths. In the present study, we consider three types of hexagonal monocrystals: plate ($Q = 0.05$), compact ($Q = 1$), and columnar ($Q = 2.50$). Polycrystalline particles (Macke et al., 1996) have also been considered. For all these crystals presented above, the radius R_{eq} is equal to 20 μm .

In the case of randomly oriented particles, the radiative transfer code used to compute polarized radiance is an adding-doubling code (De Hann et al. 1986), taking into account the molecular and the aerosol scattering, and the Earth's surface albedo. The optical properties of the ideal cirrus ice crystals are introduced in this code, and Stokes vectors of the upwelling radiance in the viewing direction relatively to the incident one are then computed (Figure 5). The radiative transfer computations show that the main features, within the range of scattering angle that can be observed by the radiometer POLDER, are (i) positive polarization, (ii) general decrease of the polarization for increasing scattering angle, (iii) neutral point for scattering angle about 160° which may shift slightly depending on the cloud microphysics (Masuda and Takashima, 1992).

According to airborne observations acquired during the EUCREX (EUropean Cloud and Radiation Experiment) experiment in April 1994, polarized measurements allow the characterization of cirrus clouds. An homogeneous cirrus cloud layer above Atlantic Ocean was overflowed at an altitude of 11 km. An example of directional polarized radiance measured at 0.865 μm is plotted in Figure 6. As for water droplet clouds, the observations agree well with radiative transfer simulations and clearly demonstrate the difference between directional polarization features associated to liquid (Figures 1 to 4) and ice phase (Figures 5 and 6).

3. 3. Multilayered cloud.

Ice clouds are often located above thick water clouds. In that case the polarized radiance will mainly depend on the upper cirrus optical thickness. In order to study the sensitivity of the polarized signal to the ice cloud optical thickness, we have simulated an atmosphere composed of 2 layers: (i) the lower layer corresponds to a water cloud (spherical particles) with an optical thickness of 15, (ii) the upper layer is composed of ice hexagonal particles randomly oriented in space with an optical thickness ranging from 0.25 to 4.

Figure 7, shows the resulting bi-directional polarized radiance as it could be measured with POLDER. This figure clearly shows that the intensity of the primary rainbow peak ($\Theta \sim 140^\circ$) decreases when the cirrus cloud optical thickness increases. Moreover the positive slope corresponding to liquid cloud for $\Theta < 110^\circ$ disappears only when the ice cloud optical thickness is larger than 2.

Based on these simulations, clear discrimination between ice and liquid cloud derived from polarized observations

needs cirrus optical thickness higher than 2, in the case of multilayered clouds. Otherwise ice phase should be correctly identified. The principle of cloud phase retrieval is presented in the next section.

4. Principle of cloud phase classification algorithm.

In the POLDER cloud analysis, the cloud detection and the derivation of its properties (cloud optical thickness and albedo, cloud top pressures, cloud phase) are separated. Cloud detection is based on visible and near-infrared measurements. Sequential tests are applied to each individual pixel as described by Buriez (1997). The first one is based on the apparent pressure which is related to oxygen transmission that is derived from the ratio between radiances measured in the 0.763 and 0.765 μm channels (Fischer et al., 1991, Parol et al., 1994b). The second test is based on the comparison of the measured reflectance with clear sky reference. The third test is a polarization test performed in the 0.443 μm band where the polarized radiance is proportional to the cloud top pressure. The last test makes use of polarization information in the 0.865 μm channel where water droplet primary rainbow can be detected. Combination of the 4 previous tests defines the cloud flag. If the pixel is flagged as "cloudy" then the cloud phase detection is applied.

According to the previous considerations on cloud polarization characteristics (sect. 3), confirmed by airborne data, the polarized component of the light reflected by cloud exhibits quite different features for ice and liquid phases. This is illustrated on Figure 8, where both total and polarized radiance images are presented. Figure 8 is a three color composite (Blue: 0.443 μm ; Green: 0.670 μm ; Red: 0.865 μm) of the radiance measured by POLDER over a 1600x2200 km^2 area located across the Atlantic Ocean. The black/white lines overlaid on the images indicate the scattering angle in 10° increments as well as the solar principal plane. The top figure shows the total radiance and is similar to what would be observed with an instrument without polarization capabilities. The bottom figure displays for the same area, the polarized component of the total radiance. The white band along the 140° scattering angle line, corresponds to a maximum in the polarized radiance, which is characteristic of water droplets with radius larger than the wavelength. This feature is an unambiguous indication of liquid water droplets. For the same scattering angle, a dark/brown zone (low polarization) when associated to cloudy pixels, indicates the presence of ice particles alone in the atmosphere or overlapping low-level clouds, as can be seen here in Figure 8b near the sun principal plane.

The algorithm consists in three tests on the polarized radiance at 865nm, using three specific angular ranges. As molecular contribution is rather weak at this wavelength, it is neglected. For scattering angle Θ within 60°-140°, the angular slope is positive for water droplet and negative for ice particles (Figure 9). For scattering angle Θ within 140°-180°, the angular slope is negative both for water droplet and ice particles, but the standard deviation, σ , of the least square fit is typically 10 times larger for liquid than for ice. Thus, the slope, a , and the standard deviation, σ (6), of the least-square fit are used to make discrimination between 'ice' and 'liquid' phase.

$$\sigma = \sqrt{\frac{1}{N_{dir}} \sum_1^{N_{dir}} (L_{pol}^{meas} - a.\Theta - b)^2} \quad (6)$$

where N_{dir} is the number of available direction in the corresponding angles range.

On the typical signatures presented in Figure 9, the slopes are also different within the 140°-180° range, however, the standard deviation appears to be a better parameter. Finally, if the particular 135°-145° range is completely observable, presence or lack of the primary rainbow can be detected using simple threshold on L_p . Thresholds on 'slope', a , and 'standard deviation', σ , have been checked by comparing to Meteosat cloud classification derived from the "Dynamic Clustering Method", (Sèze and Desbois, 1987). Cloud classification have been applied to Meteosat data acquired in coincidence with POLDER. We have selected "high-thick-and homogeneous" cloud in the Meteosat data for ice test and "low/middle-level" clouds for liquid test. For these two classes, we have plotted on Figures 10 and 11 the histograms for slope in the 60-140° range and for standard deviation in the 140-180° one. We clearly observe that the two thermodynamical phases are well separated and that

ice is well defined. More than 80% of "high-thick-homogeneous" cloud cases have a negative slope and 95% of "low/middle" level have a positive slope. We also observe that 80% of "high-thick-homogeneous" clouds have a 'standard deviation' smaller than 10^{-5} and more than 90 % of "low/middle-level" clouds have a 'standard deviation' greater than 10^{-5} .

Combination of the 'slope' and 'standard deviation' tests with the result of the test on the primary rainbow gives the cloud thermodynamical phase index.

Note that the POLDER angular coverage, in term of available scattering angles, depends on the latitude and the season. The most complete POLDER angular sampling can give access to a large range of scattering angles. In some cases, only one or two of the three angular ranges are available.

5. Accuracy of the thermodynamical phase retrieval.

The quality of the POLDER thermodynamical phase retrieval is difficult to assess because present phase retrieval algorithms are mainly based on infrared measurement that can not lead unambiguously to the cloud phase. Current methodologies for retrieving cloud-top phase are based mainly on infrared measurements or bispectral methods (Inoue 1985; Saunders and Kriebel, 1988; Nakajima and King, 1990) using a threshold on the brightness temperature difference between AVHRR channels 4 and 5. Multispectral techniques based on near-infrared (0.75 and 1.64 μm) and infrared (11 μm) measurements have been shown to be reliable to make cloud phase discrimination (King et al., 1992). In this context, polarimetric observations from which cloud-top phase is derived are original. In the paper, we have checked the validity of POLDER against ground-based lidar observations and cloud classification applied to METEOSAT data.

5.1 Validation against ground-based lidar network.

The comparison between POLDER and lidar ground-based observations concern only cases high-level clouds with temperature lower than 233 K and where no low-level liquid cloud were present (Chepfer et al., 1998). The different spatial resolution of lidar and POLDER were taken into account by selecting spatially homogenous areas and temporally stable cloud layers.

Within the whole available POLDER dataset matching the lidar observations, 148 cases correspond to cloudy observations performed at several places mainly in Paris (France), ARM sites (USA and Pacific Ocean) and Buenos Aires (Argentina). When the cirrus optical thickness is not too large, cloud top altitude can be inferred from Lidar measurements. Then the use of simultaneous radiosounding yields the cloud top temperature. Among these dataset, 32 cases correspond to cirrus temperature lower to 233 K. The analysis shows that most of these cases (95%) are declared as "ice" cloud by POLDER (Chepfer et al., 1998). We assume that only ice phase is present when the temperature is lower than 233K which is the temperature at which water spontaneously solidify. Among the same dataset, 32 others cases corresponding to cloud top temperature within the range 233 to 253 K are declared respectively "ice" (69%), "liquid" (6%) and "mixed phase"(25%) by POLDER. Within the rest of the data, associated to temperature greater than 253 K, 30% are declared 'ice', 20% 'mixed' and 50% 'liquid'. Despite the comparatively limited number of matching data, the results indicate that when temperature is lower than 233 K, ice phase is clearly identified by polarimetric measurements. When the temperature is greater than 233 K, POLDER retrievals exhibit sometimes ice phase, but occurrence of liquid water increases when the temperature increases.

The results of this study does not demonstrate rigorously the validity of the cloud thermodynamical phase retrieval. Nevertheless, the thermodynamical phase inferred from POLDER is a first attempt to derive cloud phase from polarized observations. In the future, the POLDER-2/ADEOS-2 thermodynamical phase retrieval will be certainly more completely validated by comparisons with (i) the growing ground-based lidar network that will allow to increase the number of validation data, (ii) lidar depolarization measurements giving the particles shape, (iii) other passive spaceborne instrument like MODIS in 1999, (iv) lidar in space (PICASSO-CENA in 2003) that will provide global thermodynamical phase retrieval from linear depolarization measurements.

5.2 Comparison with cloud classification.

The POLDER thermodynamical phase retrieval was compared also with statistical cloud classifications resulting from visible (0.4-1.1 μ m) and infrared (10-12 μ m) METEOSAT measurements. The comparison is preliminary, because it was temporally and spatially restricted to one Meteosat image in coincidence with three POLDER orbits, and only restricted to oceanic observations. "The Dynamic Clustering method" (Séze and Desbois, 1987), based on statistical properties of visible and infrared radiances, has been applied to the METEOSAT data acquired the 10 November 1996. For the main METEOSAT "cloud types", occurrence frequencies of ice-phase and liquid phase derived from POLDER are presented in table 1.

The "very thin cloud" type exhibits mostly ice-phase (~70%) according to polarimetric signature. The 30% of liquid clouds can be explained by the fact that this cloud type includes not only very thin cirrus but also thin edges of liquid clouds.

The low-level, middle-level and multilayered classes are essentially composed of liquid clouds. The occurrence of ice cloud in these classes is marginal and minimum for the low-level clouds (4%). This occurrence is doubled when considering middle-level clouds class (10%) and increases again up to 22% in the case of multilayered clouds. These results are understandable, when considering that the higher clouds are located in the atmosphere, the higher the probability for ice phase is. An other reason is that, as explained in sect 3.3, in the case of relatively thin cirrus overlapping low/middle-level clouds, the polarized signature of the lower layer cloud (liquid) is still observable from satellite and can bias the thermodynamical phase retrieval by favorising liquid phase.

Comparison between "cirrus" class and thermodynamical phase occurrence indicates that about 62 % of this class are considered as ice clouds and 38% as liquid clouds. The non-negligible part of this cloud class considered as composed of liquid is somewhat surprising result. Three reasons may be put forward; the first one is that cirrus clouds may be composed of spherical ice particles, but this is not in agreement with most in-situ observations. The second reason is that mono-spectral infrared measurements cannot yield unambiguously the cloud thermodynamical phase. The presence of liquid water at low temperature (supercooled water) may also explain this results. When investigating in details the "cirrus" class, especially when focusing on "thick cirrus", we surprisingly observed that 55 % of this subclass is composed of liquid water. One possible explanation is that "thick cirrus" may correspond in some cases to multilayered systems, with ice in the upper layer. In this case and for upper cloud optical thickness smaller than two, as explained previously, the algorithm may retrieve liquid water.

The last class presented is the high-level cloud class. The cloud classification method distinguishes two separate classes: high-level, thick and heterogeneous clouds on one hand and high-level, thick and homogeneous, respectively on the other hand. The results of the phase occurrence for these two classes are distinguished in table 1. First, let us consider with the "high-level, thick and homogeneous" class. In more than 80% of the cases, these clouds are considered as composed of ice particles according to polarimetric observations. As explained in sect. 4, this particular class was used to check the different thresholds in the algorithm and histograms shown in Figures 10 and 11 indicate unambiguous ice phase retrieval. For the second class, called "high-level thick and heterogeneous" clouds, the available observations exhibit a completely opposite trend. Most of these clouds are detected as composed of liquid water (87%) which is surprising when compared to the previous class. One possible interpretation is that this class corresponds to multiple cloud layers (convective cloud with relatively thin cirrus layers in the upper layer). However, this result requires a further investigation (more METEOSAT data and synergy with other sensors/techniques), which is out of the scope of the present paper.

6. Example of geographical distribution of cloud thermodynamical phase.

We present finally one example of geographical phase distribution as derived from POLDER. Its major features are briefly commented and qualitatively compared with general features previously derived from other independent sensors/techniques (Rossow et al., 1996, Doutriaux-Boucher et al., 1998, Wylie et al, 1997, Liao et al., 1995).

Figures 12 and 13 are the maps of the occurrence frequency for ice and liquid phase, respectively, for February 1997 (boreal winter). The spatial resolution for these maps is the standard POLDER level 2 cloud-product resolution, which is about 60km x 60 km. Occurrence frequency of ice (resp. liquid) cloud, is defined by the number

of observed ice (resp. liquid) clouds over the number of cloudy observations. The number of cloudy observations for the period, is presented in figures 14; some areas, such as Sahara, Arabia or India, are very often cloud-free.

The average occurrences for February have been derived from these maps. Over land and ocean, respectively, we find 39% and 27% of ice phase occurrence frequency, and 61% and 73% for the liquid water cloud. The repartition between ice and liquid clouds at global scale is about 30 % for ice clouds and 70% for liquid water clouds. It can be noted that ice phase is much more frequent over land than over ocean which is in agreement with previous climatologies of cloud types distributions.

Figures 11 and 12, show that liquid water clouds are more frequent in the Southern Hemisphere, while ice clouds occur much more frequently in the Northern Hemisphere. The Inter Tropical Convergence Zone (ITCZ) is a region where ice phase is frequently observed (Indonesia, Eastern Pacific, West Africa), which is essentially due to cumulonimbus convection injecting water vapor and ice particles into the upper atmosphere. Contrarily, in the Southern Hemisphere, Eastern Pacific off south America, Atlantic ocean off south Africa and Indian Ocean exhibit weak ice clouds occurrence frequencies but large occurrence of liquid water clouds. For instance, stratocumulus clouds are very present off Angola coasts and are generally detected as liquid water clouds according to polarimetric measurements. Same frequent detection occurrence of liquid water clouds is observed off West South American coasts.

Other regions where, according to POLDER, ice phase is observed frequently are North Asia, Russian Federation, North Europe and West North America, which is also qualitatively consistent with other observations such as ISCCP (Rossow et al., 1996) and climatologies of SAGE data (Liao et al., 1995), HIRS data (Wylie et al., 1997) and synoptic reports (Hahn et al., 1998). Preliminary comparisons between 'ice' phase and ISCCP high-level clouds occurrences are currently investigated (Riedi et al., 1999a) and show some differences that can be very likely attributed to POLDER cloud detection weakness (thin cirrus) and to the degraded spatial resolution of the phase product with respect to the sensor resolution.

7. Conclusions

Cloud thermodynamical phase retrieval based on near-infrared polarimetric measurements is a new method. An improved algorithm is described here. The algorithm takes advantage of the measured polarized radiance at $0.865 \mu\text{m}$. Both theoretical and experimental studies show that polarized signatures of water droplets and ice particles are quite different and thus can be used to discriminate between solid and liquid phase. Satellite cloud thermodynamic phase retrieval is somewhat difficult to validate. Two attempts have been performed. One original approach, which is based on ground-based lidar network. It shows that such observations are very useful for the thermodynamical phase retrieval, even if a moderate amount of data were available and linear depolarization was not measured. This first but important result clearly indicates the direction of future works. Extension of the ground-based lidar network is, clearly, essential for cirrus cloud studies. Finally, future spaceborne lidar with depolarization measurements will be quite useful for this purpose.

Preliminary comparisons with cloud classification derived from METEOSAT data show that liquid cloud ("low/middle-level" classes) are correctly identified by POLDER. However, some disagreements occur when considering the "cirrus" class. A non negligible part of this class are detected as "liquid" clouds. Here may appear the major limitation of the polarimetric method, assuming Meteosat classification is right: thin cirrus overlapping low/middle-level clouds can be interpreted as liquid water cloud. Two other limitations are (i) the efficiency of the POLDER cloud detection itself, based on visible and near infrared channels, which is unable to detect very thin, (ii) the degraded spatial resolution of the operational POLDER cloud-products. Full resolution ($6.2\text{km} \times 6.2 \text{ km}$) should improve cloud phase detection, which is known to depend on the sensitivity and size of the sensor field of view. Complementary studies are going on in progress (i) comparison with synoptic weather reports over the whole POLDER operational period, (ii) comparison with radar observations (Riedi et al., 1999b). In that case, the effect of multiple cloud layers could be studied. The use of multispectral-spectral method with OCTS (Ocean Color and Thermal Scanner) sensor also on the ADEOS satellite or other visible-thermal sensors will be also useful to better understand ice phase retrieval.

ACKNOWLEDGMENT

The authors are very grateful to NASDA and CNES who provided the POLDER data. De Haan and J.W. Hovenier for providing adding-doubling RT code and A. Macke for providing polycrystals scattering properties.

<i>Type of cloud</i>	<i>Ice occurrence (%)</i>	<i>Liquid occurrence(%)</i>
Very thin cloud	69	31
Low-level cloud	4	96
Middle-level cloud	10	90
Multilayered cloud	22	78
Cirrus	62	38
High-Thick- Homogeneous cloud	80	20
High-Thick - Heterogeneous cloud	13	87

Table 1 : Occurrence frequency of ice and liquid phase as derived from POLDER versus METEOSAT cloud type.

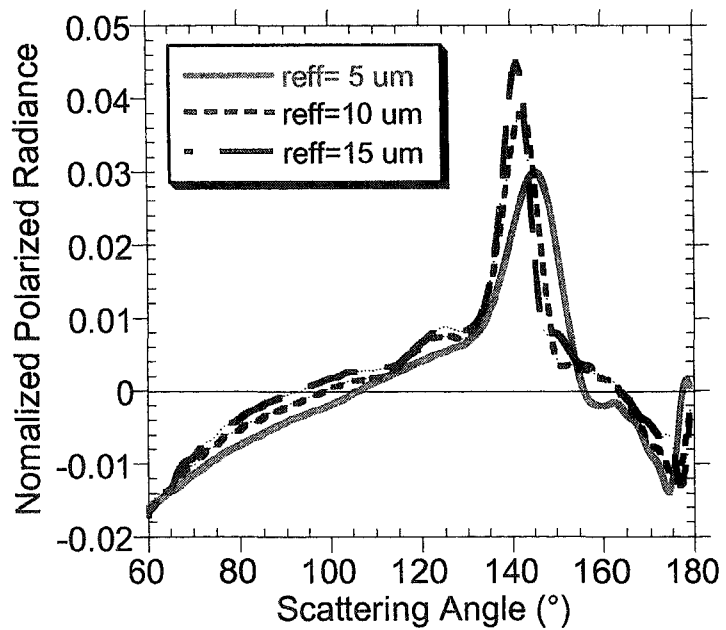


Figure 1 : Simulated normalized polarized radiance for water droplets cloud (liquid phase) for 3 size distributions ($\sigma_{\text{eff}}=0.1$), $r_{\text{eff}}=5, 10, 15 \mu\text{m}$, $\theta_s=60^\circ$, $\tau=10$.

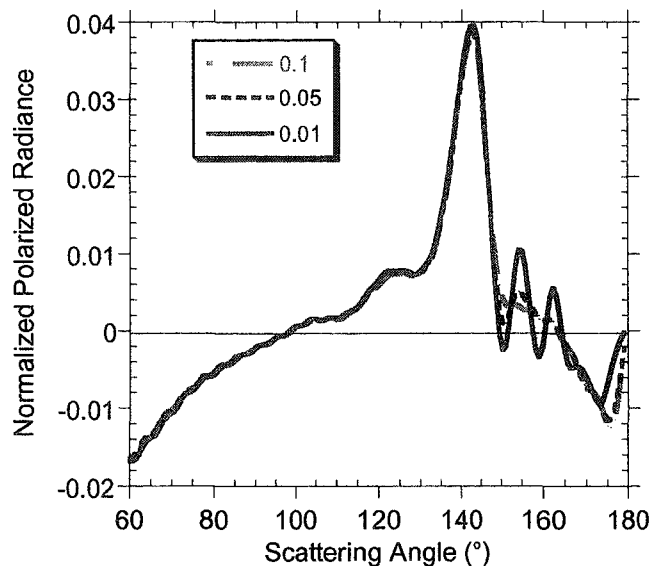


Figure 2 : Simulated normalized polarized radiance for water droplets cloud (liquid phase) for 3 size distributions ($r_{\text{eff}}=10 \mu\text{m}$), $\sigma_{\text{eff}}=0.01, 0.05, 0.10$, for $\tau=10$. This figure shows the effect of the σ_{eff} parameter on the polarization features.

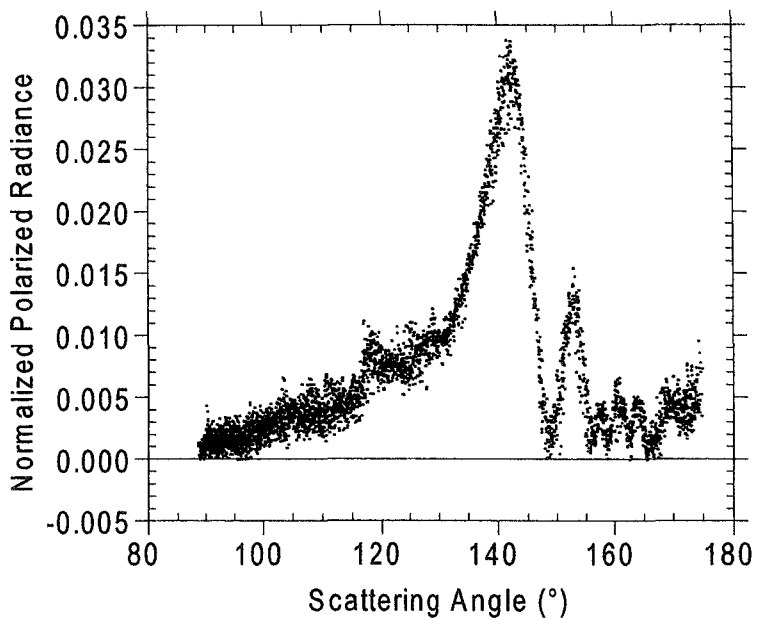


Figure 3 : Normalized polarized radiance measured at $0.865 \mu\text{m}$ over a stratocumulus cloud during POLDER airborne experiment (Astex'92). The altitude of the aircraft is 3.5 km.

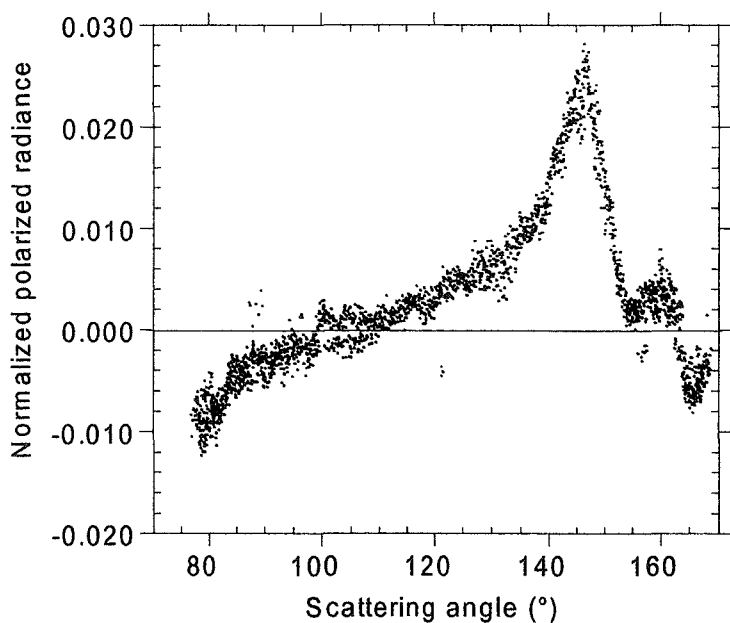


Figure 4 : Normalized polarized radiance measured at $0.865 \mu\text{m}$ over an altocumulus cloud during POLDER airborne experiment (CLEOPATRA, 1991). The altitude of the aircraft is 11 km

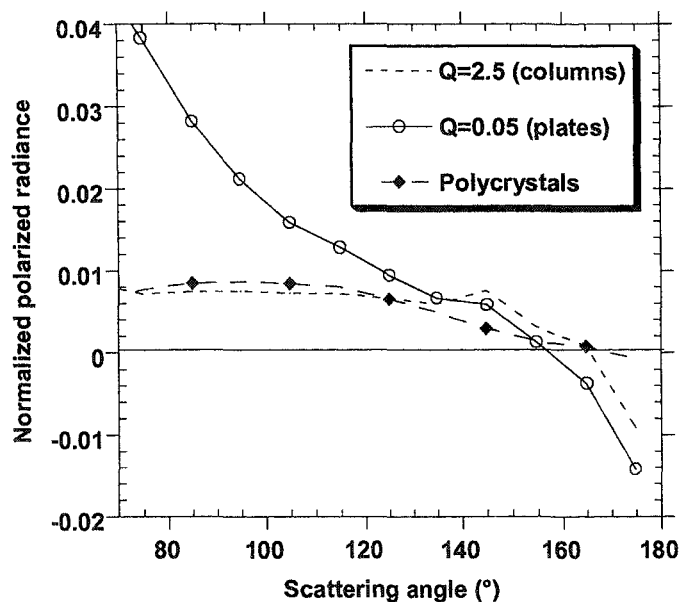


Figure 5 : Simulated normalized polarized radiance for cloud composed of crystals (ice phase) for 3 size particles shapes. Sun zenith angle, θ_s , is 55° , $\tau=2$ at $0.865 \mu\text{m}$.

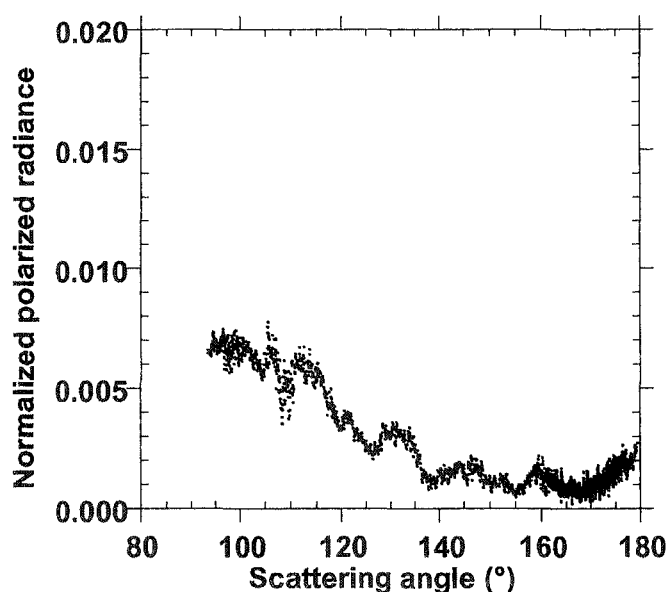


Figure 6 : Normalized polarized radiance measured at $0.865 \mu\text{m}$ over a cirrus cloud during POLDER airborne experiment EUCREX'94.

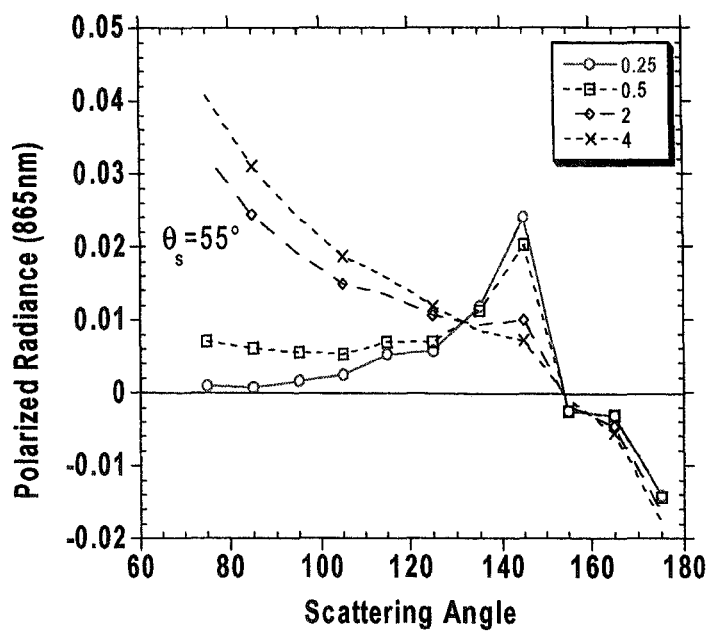


Figure 7 : Bidirectional polarized radiance simulated for a two cloud layer system. The lower layer is a liquid cloud (spherical particles, and $\tau=15$). The upper layer is composed of hexagonal particles with various optical thicknesses ($\tau = 0.25$ to 4).

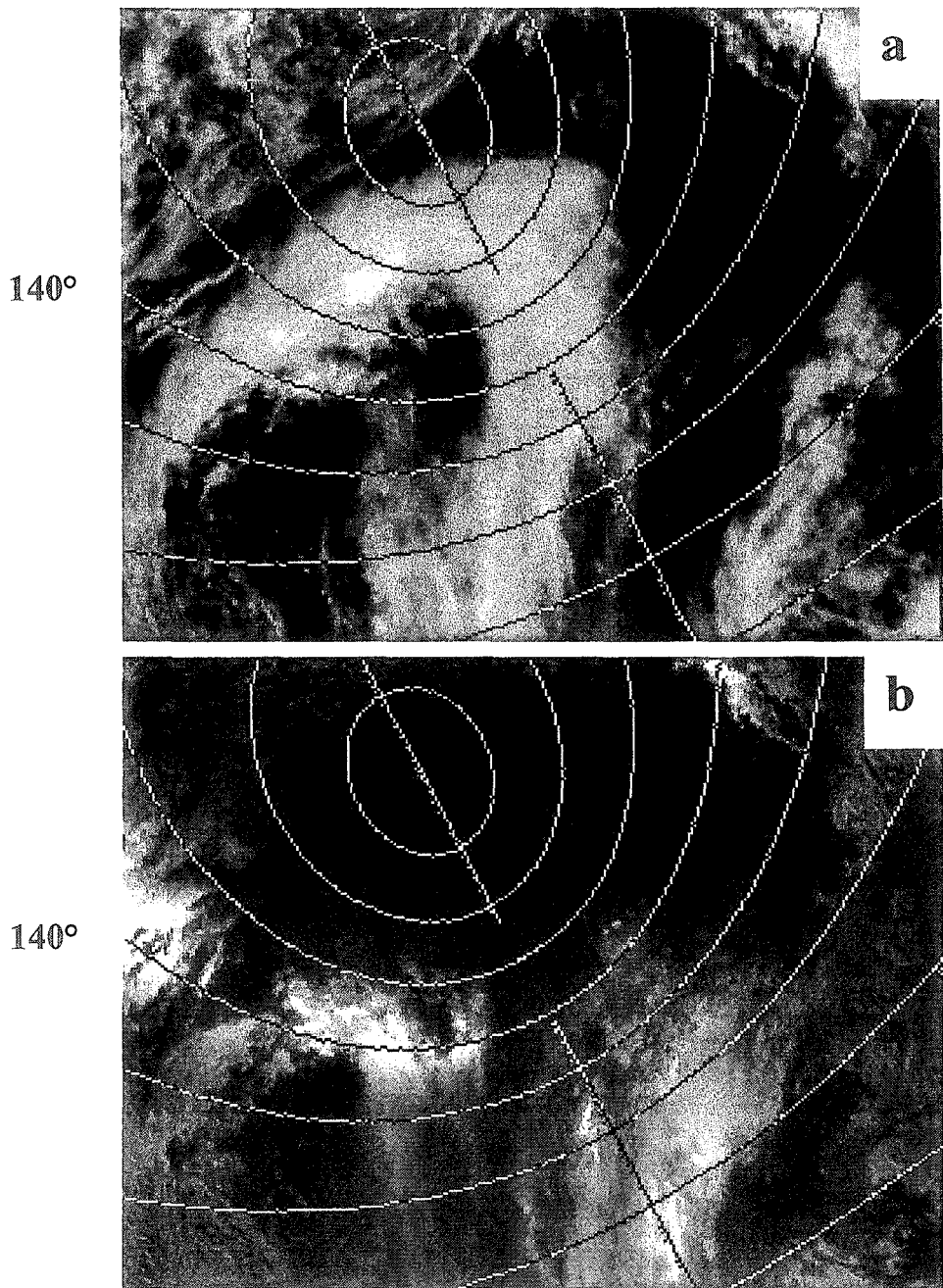


Figure 8 : Illustration of the cloud thermodynamical phase recognition. These images are a three color composite (Blue : $0.443\text{ }\mu\text{m}$; Green : $0.670\text{ }\mu\text{m}$; Red: $0.865\text{ }\mu\text{m}$) of the radiance measured by the instrument CCD detector over a $1600\times 2200\text{ km}^2$ area located over Atlantic Ocean. The black/white lines overlaid on the figure indicate the scattering angle in 10° increment as well as the principal plane. The top image (a) shows the total radiance and is similar to what would be observed with an instrument without polarization capabilities. The bottom image (b) corresponds to the exact same area, but displays the perpendicular component of the polarized radiance. For each spectral band, the scale varies from 0 to 0.80 in radiance, and from 0 to 0.08 in polarized radiance.

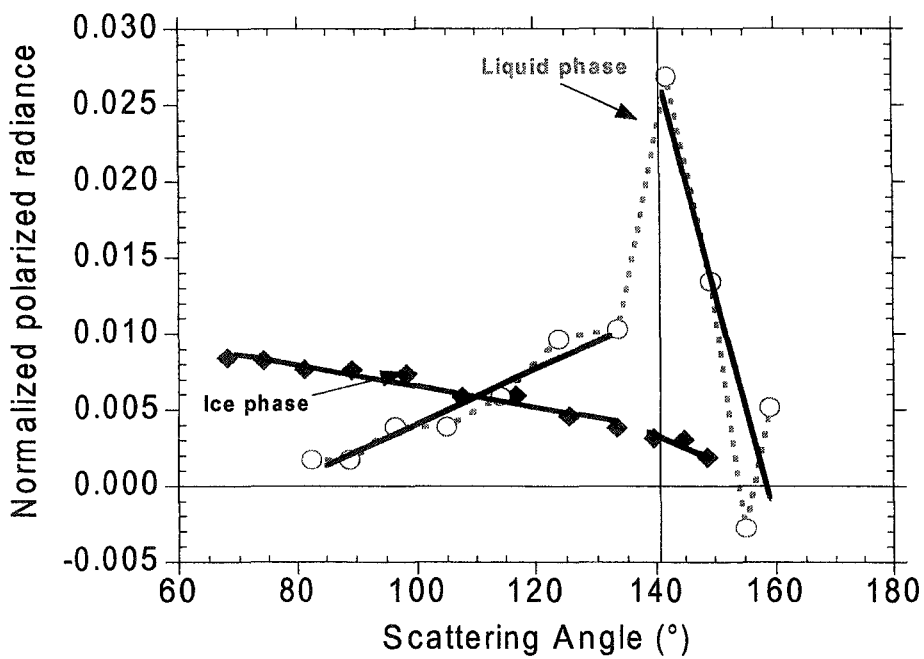


Figure 9 : Examples of directional polarization samples at $0.865 \mu\text{m}$ measured by POLDER over Lille (North of France), for cirrus cloud and liquid cloud. Solid lines correpond to linear fit of mesurements for the two scattering angle ranges 60° - 140° and 140° - 180° .

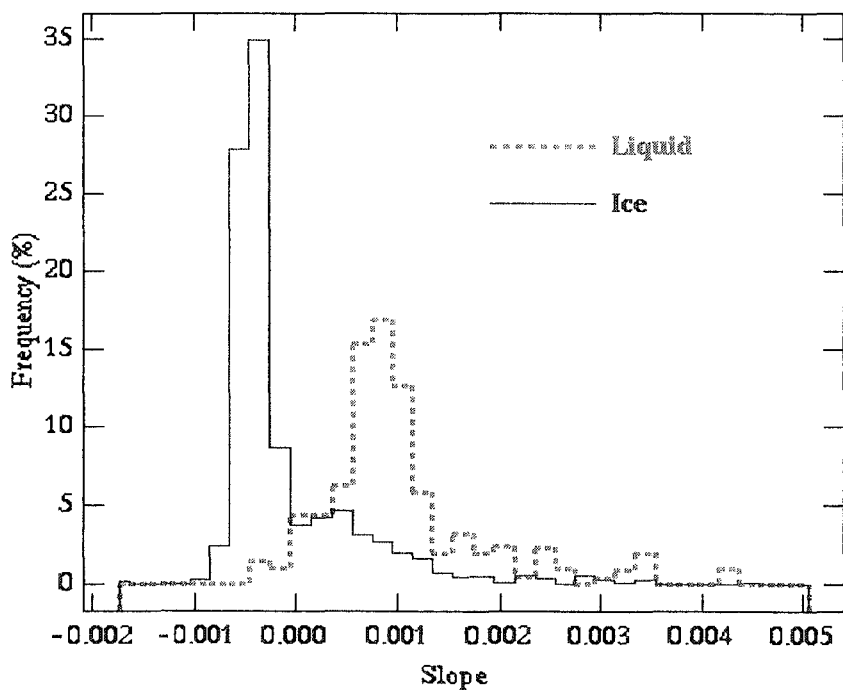


Figure 10 : Slope histogram for the 60 - 140° scattering angle range (orbit 3108, 10 Novembre 1996).

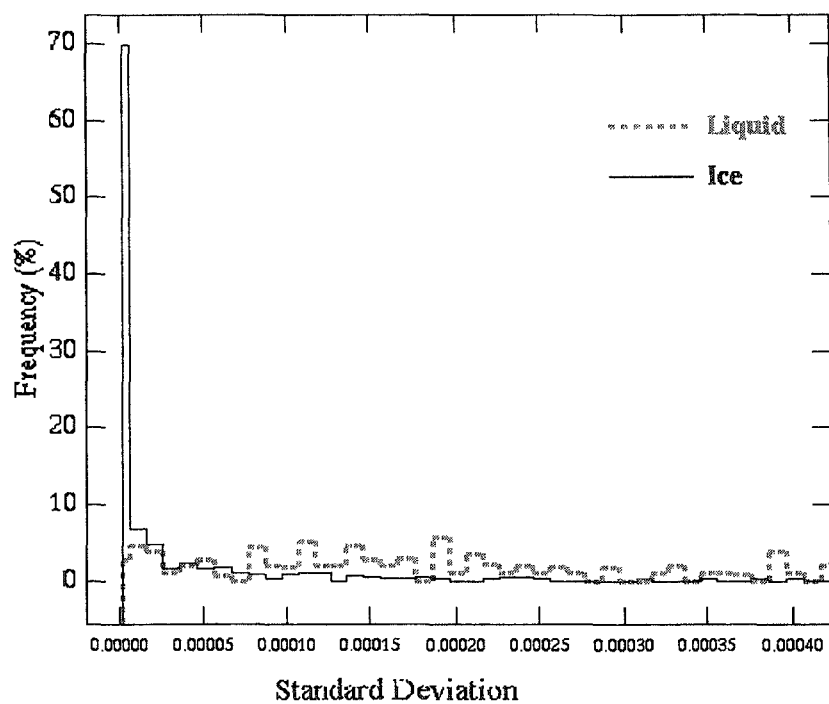


Figure 11 : Standard deviation histogram for the 140-180° scattering angle range (orbit 3108, 10 Novembre 1996).

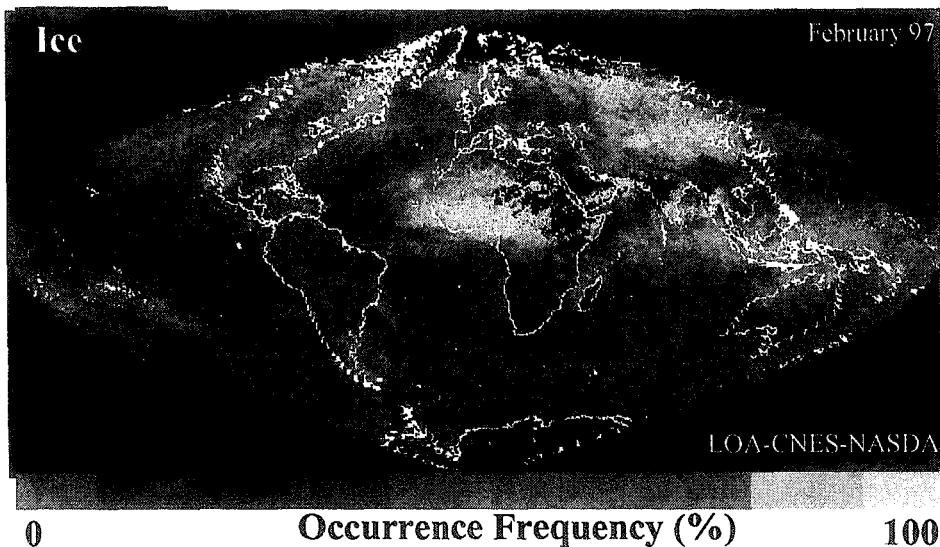


Figure 12

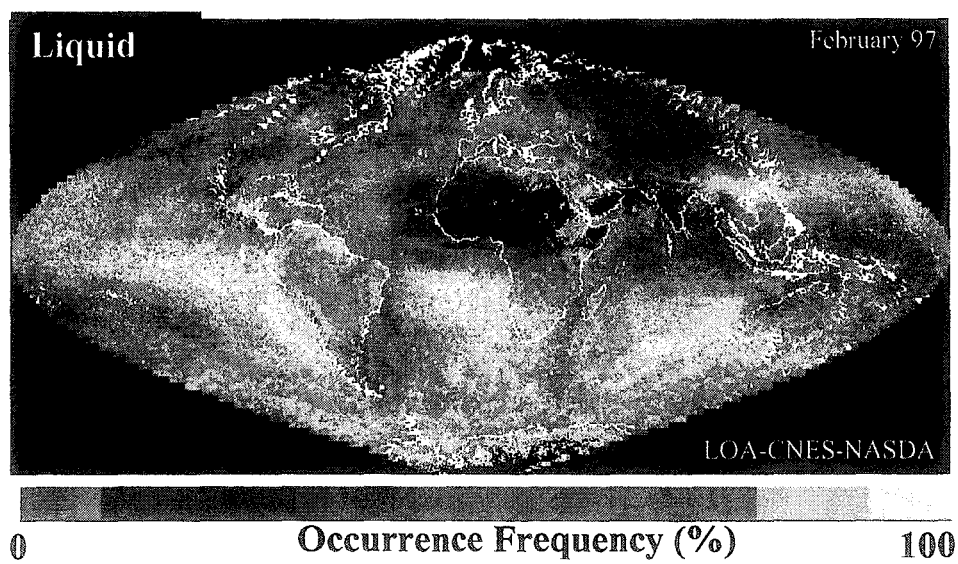


Figure 13

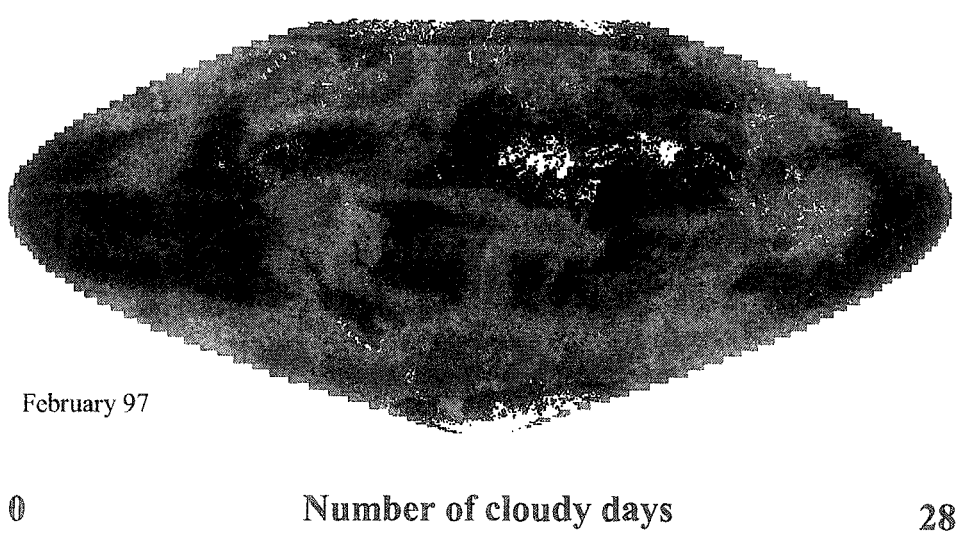


Figure 14

REFERENCES

- Bréon, F.M., and S. Colzy, 1999 "Cloud detection from the spaceborne POLDER instrument and validation against surface synoptic observations", *J. Appl. Meteor.*, in press
- Bréon, F.M., and P. Goloub, "Cloud droplet effective radius from spaceborne polarization measurements", *Geophys. Res. Letts.*, Vol. 25, N 11, PAGES 1879-1882, 1998.
- Brogniez, G., 1988: Light scattering by finite hexagonal ice crystals arbitrarily oriented in space. Proceedings of the International Radiation Symposium, J. F. Gelyn and J. Lenoble, Eds., A. Deepak, Publishing, Lille, France, 18-24 August, 64-67.
- Brogniez, G., J. C.. Buriez, V. Giraud, and C. Vanbauce, 1995 : « Determination of effective emittance and radiatively equivalent microphysical model of cirrus from ground-based and satellite observations during the International Cirrus Experiment : the 18 october 1989 case study » *Mon. Wea. Rev.*, 123, 1025-1036.
- Buriez J. C., C. Vanbauce, F. Parol, P. Goloub, M. Herman, B. Bonnel, Y. Fouquart, P. Couvert, G. Sèze, 1997: "Cloud detection and derivation of cloud properties from POLDER ", *Int. J. Em. Sens.*, 18, 2785-2813.
- Cess, R.D., G.L. Potter, J.P. Blanchet, G.J. Boer, S.J. Ghan, J.T. Kiehl, H. Le Treut, Z.X. Li, X.Z. Liang, J.F.B. Mitchell, J.J. Morcrette, D.A. Randall, M.R. Riches, E. Roeckner, U. Schlese, A. Slingo, K.E. Taylor, W.M. Washington, R.T. Wetherald, I. Yagai, 1989: Interpretation of cloud-climate feedback as produced by 14 atmospheric general circulation models. *Science* 245, 513-516
- Cess et al., "Intercomparison and interpretation of climate feedback processes in 19 atmospheric general circulation models," *J. Geophys. Res.*, vol. 95, pp.16601-1661, 1990.
- Cess et al., "Cloud feedback in atmospheric general circulation models: An update," *J. Geophys. Res.*, vol. 101, pp. 12791-12794, 1996.
- Chepfer H., G. Brogniez, Y. Fouquart, "Cirrus clouds microphysical properties deduced from POLDER observations", *J. of Quant. Spectr. and Rad. Transfer*, 30, 375-390, 1998.
- Chepfer H., P. Goloub, L. Sauvage, P. H. Flamant, Brogniez, J. Spinhirne, M Lavorato, S. Asano," Validation of POLDER/ADEOS data using ground-based lidar network : preliminary results for semi-transparent and cirrus clouds. semi-transparent Clouds", *Phys. and Chem. of the Earth*, Vol. 24, 3, pp 203-206, 1999.
- Chepfer H., P. Goloub, J. Spinhirne, P. H. Flamant, M Lavorato, L. Sauvage, Brogniez, and J. Pelon, "Cirrus Cloud properties deived from POLDER-1/ADEOS Polarized Radiances: First Validation using a Ground based Lidar Network", *J. Applied. Meteor.*, 1999 (in press).
- Chepfer H., G. Brogniez, P. Goloub, F. M. Bréon, Pierre H. Flamant, "Cloud Ice Crystals Horizontally Oriented in Space Observed with POLDER1/ADEOS", *J.Quant.Spec.Rad.Transfer*, Special Issue, Light Scattering by nonspherical particles'98, Vol. 63, 521-543, September/December 1999.
- Chepfer, H., G. Brogniez, V. Trouillet, J. Pelon, P. H. Flamant, and F. Albers, 1999: Remote sensing of cirrus radiative parameters during EUCREX'94. Part 1: Observations and analysis at the regional scale, *Mon. Wea. Rev.*, vol 127., pp 504-518.
- Curran R.J and M. L. C. Wu, "Skylab near infrared observations of clouds indicating supercooled liquid water droplets". *J. Atmos. Sci.*, Vol 39, pp. 635-647, 1982.
- De Haan, J. F., P. B. Bosma, and J. W. Hovenier, 1986 : "The adding method for multiple scattering calculations of polarized light." *Astron. Astrophys.*,183, 371-391.
- Deschamps, P-Y., F-M. Bréon, M. Leroy, A. Podaire, A. Brickaud, J-C. Buriez, and G. Sèze, 1994 : "The POLDER Mission : Instrument Characteristics and Scientific Objectives " *IEEE*, 32, 598-615.
- Doutriaux-Boucher M., G. Séze, Significant changes between the ISCCP C and D cloud climatologies. *Geophys. Res. Letts.*, Vol 25, N 22, PAGES 4193-4196, 1998.
- Fischer, J. and Grassl, H., 1991, Detection of cloud -top height from backscattered radiances within the Oxygen A band. Part 1: Theoretical study. *Journal of Applied Meteorology*, 30, 1245-1259.
- Gao, B.C, A.F.H. Goetz, and W.J. Wiscombe, 1993: Cirrus cloud detection from airborne imaging spectrometer data using the 1.38 mm water vapor bands. *Geophys. Res. Letts.*, 20, 301-304.
- Garcia, R.D.M., and C.E.Siewert, 1986. A generalized spherical harmonics solution for radiative transfer models that include polarization effects. *J.Quant.Spec.Rad.Transfer*, 36, p401-423.
- Goloub P, JL Deuzé, M Herman and Y Fouquart, Analysis of the POLDER Airborne Polarization Measurements Performed over Clouds Covers, *IEEE Trans. Geosci. and Remote Sensing*, vol. 32, pp. 78-87, 1994.
- Hagolle, Ph.Goloub , P.Y. Deschamps, T.Bailleul, JM Nicolas, Y Fouquart, A Meygret, J.L. Deuzé, M. Herman, F Parol, FM Bréon, 1999. "POLDER in-flight calibration results", *IEEE Trans. Geosci. and Remote Sensing*, vol. 37,

- pp. 1550-1566, 1999.
- Hahn, C.J, and S.G. Warren, 1998 : Extended Edited Synoptic Cloud Reports from ships and Land Stations Over the globe, 1952-1996. NDP026C, Carbon Dioxide Information Analysis Center, Oak Ridge National Laboratory, Oak Ridge, TN.
- Han, Q., W.B. Rossow, and A.A. Lacis, 1994: "Near-global survey of effective droplet radii in liquid water clouds using ISCCP data", *J. Climate*, 7, 465-497.
- Hansen, J.E. and L.D. Travis, 1974. Light scattering in planetary atmospheres. *Space Science Reviews*, 16, 527-610.
- Hansen J. E., 1971 : "Multiple scattering of polarized light in planetary atmospheres. Part I. The Doubling Method." *J. Atmos. Sci.*, 28, 120-125.
- Heymsfield A. J., 1975a : "Cirrus uncinus generating cells and the evolution of cirriform clouds. Part 1 : Aircraft observations of the growth of the ice phase." *J. Atm. Sci.*, 32, 799-807.
- Heymsfield A. J., 1993 : "Microphysical Structure of Stratiform and Cirrus Clouds." *Aerosol Cloud - Climate Interactions. P. V. Hobbs, Ed.*, 54 in the International Geophysics Series, 233pp.
- Inoue T., 1985, On the temperature and effective emissivity determination of semi-transparent cirrus clouds by bi-spectral measurements in the 10 micron window region. *Journal of Meteorological Society of Japan*, 63, 88-99.
- Jin, Y., W.B. Rossow, D.P. Wylie, 1996: Comparison of the climatologies of high level clouds from HIRS and ISCCP., *J. Climate*, 9, 2850-2879.
- King M.D, Y. Kaufman, W.P. Menzel, D. Tanré, 1992, Remote sensing of Cloud, Aerosol, and Water vapour properties from Moderate Resolution Imaging Spectrometer (MODIS), *IEEE Transactions on Geoscience and Remote sensing*, Vol 30., N 1, January 1992.
- Lawson R.P, A. J. Heymsfield, S. Aulencbach, T.L. Jensen, 1998: "Shapes, sizes and light scattering properties of ice crystals cirrus and a persistent contrail during SUCESS". *Geophys. Res. Letter*, 25, 1331-1334.
- Lawson R.P, 1998: "A comparison of Ice Crystal Observations using a New Cloud Particles Imager Probe in Arctic Cirrus and Decaying Anvil in Texas", in *Cirrus, OSA Technical Digest (Optical Society of America, Washington DC, 1998)*, pp.113-115
- Liao, X., W.B. Rossow, D. Rind, 1995a : Comparison between SAGE II and ISCCP high-level clouds, 1 Global and zonal amounts., *J.Geophys.Res.*, 100, 1121-1135.
- Liou, K. N., 1986 : Review. Influence of cirrus clouds on weather and climate processes : A global perspective. *Mon. Wea. Rev.*, 114, 1167 - 1199.
- Macke, A., J. Mueller, and E. Raschke, 1996: Single scattering properties of atmospheric ice crystals. *J. Atmos. Sci.*, 53, 2813-2825.
- Masuda, K. and T.Takashima, 1992. Feasability study of derivation of cirrus information using polarimetric measurements from satellite. *Remote Sens. Environ.*, 39, 45-59.
- Meischner, P., M. Hagen, T. Hauf, D. Heinmann, H. Höller, U. Schumann, W. Jaeschke, W. Mauser and H.R. Pruppacher, 1993: The Field Project CLEOPATRA, May-July 1992 in Southern Germany, *Bull. Amer. Meteorol. Soc.* 74, 401-412.
- Miloshevich, L. M., and A. J. Heymsfield, 1996: A balloon-borne cloud particle replicator for measuring vertical profiles of cloud microphysics : Instrument design and performance. Proceeding of the International Conference of Cloud and Precipitation., Zurich, 354-360.
- Nakajima T., M.D. King, J.D. Spinhirne, and L.F. Radke: "Determination of the optical thickness and effective radius of clouds from reflected solar radiation measurements". Part II: Marine stratocumulus observations", *J. Atmos. Sci*, vol 48, pp. 728-750, 1991.
- Nakajima T., M.D. King: "Determination of the optical thickness and effective radius of clouds from reflected solar radiation measurements. Part I Theory", *J. Atmos. Sci*, vol 47, pp. 1878-1893, 1989.
- Nakajima, T.Y., and T. Nakajima, 1995: "Wide-area determination of cloud microphysical properties from NOAA AVHRR measurements for FIRE and ASTEX regions", *J. Atmos. Sci.*, 52, 4043-4059.
- Masuda K. and T. Takashima, 1992: "Feasibility study of derivation of cirrus information using polarimetric measurements from satellite." *Rem.Sens. Environ.*, 39, 45-59.
- Miloshevich L. M., and A. J. Heymsfield, 1997: "A balloon-borne continuous cloud particle replicator for measuring vertical profiles of cloud microphysics properties: Instrument design and performance and collection efficiency analysis." *J. Atmos. Oc. Tech.*, 753-768.
- Paltridge, G.W, 1974, Infrared emissivity, short wave albedo, and microphysics os stratiform water clouds. *J. Geophys. Research.*, 1979. 4053-4058
- Parol, F., P. Goloub, M. Herman, J.C. Buriez, 1994, Cloud altimetry and water phase retrieval from POLDER

- instrument during EUCREX'94. In Atmospheric Sensing and Modelling, edited by R. P. Santer, Proceedings of SPIE, 2311, 171-181.
- Parol F., J.C Buriez, C. Vanbauce, P. Couvert, G. Sèze, P. Goloub, and S. Cheinet, "Information content on clouds from POLDER-ADEOS", IEEE Transactions on Geoscience and Remote Sensing, vol. 37, pp. 1597-1612, 1999.
- Pavlowska, H and JL Brenguier, 1996 : A study of the micro-physical structure of stratocumulus cloud, Proceeding of the ICCP 1996.
- Pilewskie P. and S. Twomey, 1987 : "Discrimination of ice from water clouds by optical remote sensing", *Atmos.Res.*, vol. 21, pp.113-122.
- Platt, C. M. R., and T. Takashima, 1987: Retrieval of water clouds properties from carbon dioxide lidar soundings, *Appl. Opt.*, 26, 1257-1263.
- Platt C. M. R., 1978 : "Lidar backscatter from horizontal ice crystal plates." *J. Appl. Meteor.*, 17, 482 - 488.
- Ramanathan V., 1987: "the role of the earth radiation budget studies in climate and general circulation research." *J. Geophys.Res.*, 92, 4075-4095.
- Ramanathan V , R.D. Cess, E.F. Harrison, P. Minnis, B.R. Barkstrom, E. Ahmad, and D. Hartmann, "Cloud radiative forcing and climate: Results from the Earth Radiation Budget Experiment," *Science.*, vol. 243, pp. 57-63, 1989.
- Ramanathan, V., B.R. Barkstrom, and E.F. Harrison, 1989: Climate and the earth's radiation budget. *Physics Today* , 22-32.
- Raschke, E., 1996 : European Cloud and Radiation Experiment (EUCREX). Final report on the project, EV5V-CT 920130 EUCREX-2, 154pp (available from GKSS Research Center; D-2054, Geesthacht, Germany.)
- Riedi J., M. Doutriaux-Boucher, P., Goloub, P., Couvert, Global distribution of cloud top phase from POLDER/ADEOS 1, *Geophys. Res. Lett.* 1999a (to appear).
- Riedi J., P. Goloub, R. Marchand, H. Chepfer, Cloud Thermodynamic Phase from POLDER/ADEOS: comparison with Millimeter Wave Radar Measurements and Synoptic Weather Reports, paper presented at Remote Sensing of Clouds and the Atmosphere conference, EOS/SPIE Symposium on Remote Sensing, Florence, Italy, 20-24 September 1999b.
- Rossow W.B, A.W Walker, D.E. Beuschel and M. Roiter, " International Satellite Cloud Climatology Project (ISCPP). Documentation of New Cloud Datasets," WMO/TD-No. 737, World Meteorological Organization, 115p, 1996.
- Sassen K., 1991 : "The polarization lidar technique for cloud research : A review and current assessment." *Bull. Amer. Meteor.Soc.*, 72, 1848-1866.
- Saunders, R. W. and Kriebel, K.T., 1988, An improved method for detecting clear sky and cloudy radiances from AVHRR data. *Int. Journ. Rem. Sens.* 9, 123-150.
- Sèze G. and M. Desbois, "Cloud cover analysis in satellite imagery using spatial and temporal characteristics of the data," *J. Climate Appl. Meteor.*, vol. 26, 287-303, 1987.
- Stephens, G. L., 1978: Radiation profiles in extended water clouds. I Theory. *J. Atmos. Sci.*, 35, 2111-2122.
- Stephens, G. L., G.W. Paltridge, and C.M.R. Platt, 1978: Radiation profiles in extended water clouds. Observations. *J. Atmos. Sci.*, 35, 2133-2141.
- Takano Y., K.N Liou, « Solar Radiative transfer in cirrus clouds. Part 1 : single scattering and optical properties of hexagonal ice crystals. » *J. Atmos. Sci.* 46,3-19.
- Warren S.G., C.J. Hahn, J. London., R.M. Chervin, R. Jenne, 1988: NCAR Tech. Note. TN-317 STR, 212p
- Weill. A, Baudin, F. Dupuis, H., Eynard, L., Frangi, J.P., Gerard, E. Durand, P. Benech, B., Dessens, J., Druihet, A., Rechou, A., Flamant, P., Elouragini, S., Valentin, R., R., Seze, G., Pelon, J., Flamand, C., Brenguier, J.L., Planton, S., Rolland, J., Brisson, A., Le Borgne, P., Marsouin, A, Moreau, T, Katsaros, K, Monis,R., Queffeulou, P., Tournadre, J., Taylor, P. K., Kent, E., Pascal, R, Schibler, P. P. Parol, F., Descloitres, J., Balois, JY.,Andre., Mand Charpentier, M., 1995, SOFIA 1992 experiment during ASTEX, *The Global Atmosphere and Ocean System*, 3, 355-395.
- Wylie D.P., P. Wang, 1997: Comparison of cloud frequency data from HIRS and SAGE II. *J. Geophys. Res.* 102, 29893-29900.
- Wylie D.P, 1998: "Cirrus and Weather: A satellite Perspective", in *Cirrus, OSA Technical Digest (Optical Society of America, Washington DC, 1998)*, pp.66-69.

**First Results of the POLDER «Earth Radiative Budget and Clouds»
Operational Algorithms. POLDER-ADEOS**

First Results of the POLDER “Earth Radiation Budget and Clouds” Operational Algorithm

Frédéric Parol, Jean-Claude Buriez, Claudine Vanbause, Pierre Couvert,
Geneviève Sèze, Philippe Goloub, and Sylvain Cheinet

Abstract— The POLDER instrument is devoted to global observations of the solar radiation reflected by the earth-atmosphere system. Algorithms of the “Earth Radiation Budget and Clouds” processing line implemented at the French Space Center are applied to ADEOS-POLDER data. First results on derived cloud properties are presented from POLDER level 2 data of 10 November 1996 and level 3 products of June 1997.

A good correlation is observed between the POLDER cloud detection algorithm and the Dynamical Clustering Method applied to METEOSAT data. The multidirectional capability of POLDER appears useful to check schemes of cloud optical thickness retrieval. As expected, a water droplet model is suitable for liquid water clouds and inadequate for ice clouds. That indirectly validates our algorithm of cloud phase recognition. An apparent pressure is derived from O₂-absorption measurements and a Rayleigh cloud pressure from polarization observations. For overcast conditions, the apparent pressure is larger (by more than 100 hPa) than the Rayleigh pressure chiefly due to the photon penetration effect. For partly cloudy conditions, it can be larger or weaker depending on the surface reflectivity.

Preliminary comparisons between POLDER and ISCCP monthly mean products outline some differences resulting in part from the original characteristics of POLDER.

Index Terms—Clouds, polarization, remote sensing.

I. INTRODUCTION

HUMAN activities are increasing the atmospheric concentrations of both greenhouse gases and anthropogenic aerosols, which tend, respectively, to warm and to cool the earth-atmosphere system [22], [11]. Global climate models (GCM's) endeavor to project what the future has in store for the earth, but the large range of possible scenarios mainly comes from the little understood in the climate sensitivity to such perturbations [22]. A major uncertainty in the determination of this sensitivity is the misunderstanding in the feedbacks associated with cloudiness changes and the

Manuscript received April 2, 1998; revised November 18, 1998. This work was supported by CNES, European Economic Community, Région Nord-Pas De Calais, and Préfecture du Nord through EFR. Meteorological data have been provided by Météo-France. METEOSAT data have been provided by the Centre de Météorologie Spatiale in Lannion. Currently updated information about POLDER project is available from <http://polder@www-projet.cnes.fr:8060>.

F. Parol, J.-C. Buriez, C. Vanbause, P. Goloub, and S. Cheinet are with the Laboratoire d'Optique Atmosphérique, URA CNRS 713, Université des Sciences et Technologies de Lille, UFR de Physique, 59655 Villeneuve d'Ascq Cedex, France (e-mail: fred@loa.univ-lille1.fr).

P. Couvert is with the Laboratoire des Sciences du Climat et de l'Environnement, Centre d'Etudes de Saclay, 91191 Gif-sur-Yvette, France.

G. Sèze is with the Laboratoire de Météorologie Dynamique, CNRS, Université P. et M. Curie, Jussieu, 75252 Paris Cedex 05, France.

Publisher Item Identifier S 0196-2892(99)03575-5.

difficulty of GCM's to correctly account for cloud-radiation-climate interactions [8], [9], [36]. Indeed, cloud-radiation interactions are really complex and depend on numerous physical parameters such as the cloud macrophysical and microphysical characteristics but also the atmospheric and terrestrial environment. Consequently, GCM's need realistic representation of clouds and their effects on radiation balance at global scale as well as at regional scale. It is essential to correctly simulate the present forcing of clouds on radiation but especially to model what the future forcing of clouds will be. Global observations of cloud properties and global measurements of the effects of clouds on radiation are essential to achieve this objective.

The most comprehensive way to obtain global cloud observations is by means of satellite-based measurements, even if field experiments and ground-based measurements remain essential to support the satellite observations. Satellites can directly observe not only the spatial and temporal variabilities of clouds [33] but also their effects on earth's radiation budget (ERB) at the top of the atmosphere [30], [20]. Since the first satellite images were used [1], satellite observations of clouds and satellite derivation of cloud properties have been widely developed and investigated (see [32] for an almost exhaustive historical summary of cloud algorithms).

POLDER (POLARization and Directionality of the Earth's Reflectances) is a component of a series of new sensors that may provide key information for improving our knowledge of clouds, radiation, and climate interactions. POLDER is a CNES (the French Space Agency) instrument which was on board the Japanese ADEOS (ADVanced Earth Observing Satellite) polar orbiting platform, successfully launched in August 1996. In November 1996, POLDER entered into its nominal acquisition phase and functioned perfectly until ADEOS early end of service in June 1997. POLDER is a multispectral imaging radiometer-polarimeter designed to provide global and repetitive observations of the solar radiation reflected by the earth-atmosphere system [13]. The instrument concept is based on a wide field of view (~2200 km) telecentric optics, a rotating wheel carrying spectral filters and polarizers, and a charged coupled device (CCD) array of (242 × 274) detectors that induces a moderate spatial resolution of 6.2 km. As the ADEOS satellite passes over a scene, up to 14 successive measurements are acquired in eight narrow spectral bands located between 443 and 910 nm. The POLDER level 1 products routinely processed by CNES consist of calibrated radiances and Stokes parameters at full spatial resolution. The

level 2 and 3 products are split into three processing lines which are the "ERB, water vapor, and clouds" (hereafter noted as "ERB & clouds"), the "Ocean color and aerosols over the ocean," and the "Land surfaces and aerosols over land" lines. For different reasons put forward in [7], all of the results of the "ERB & clouds" processing line are averaged at the "super-pixel" scale that typically corresponds to (9×9) pixels. The spatial resolution of the super-pixel ($0.5^\circ \times 0.5^\circ$ at the equator, i.e., $\sim 50 \text{ km} \times 50 \text{ km}$) appears suitable both for comparison with ISCCP (International Satellite Cloud Climatology Project, [33]) products and for use in connection with ERB instruments like ScaRaB (Scanner for the Earth Radiation Budget) [23] and CERES (Cloud and the Earth's Radiant Energy System) [45].

The "ERB & clouds" thematic interest takes advantage of the multispectral, multidirectional, and multipolarization capabilities of POLDER to derive useful information on clouds and their effects on short-wave radiation [7]. This paper deals with one of the main goals of the "ERB & clouds" line which is the derivation of cloud properties, such as cloud amount, cloud optical thickness, cloud pressure, and cloud thermodynamic phase at global scale. The atmospheric water vapor content is presented in a companion paper in this issue [43]. Similarly to many "cloud algorithms" [32], the "ERB & clouds" processing line uses two basic steps: the cloud detection phase and the cloud properties derivation phase. The first step is crucial since it controls further processing and it has a major impact on determining other products. Particular attention is therefore given to the cloud detection algorithm of the "ERB & clouds" line; it is a threshold method employing several sequential tests for the presence of clouds. The adjustments of the different tests involved in the algorithm are presented in the next section. The so-derived POLDER pixel identification is compared to a cloud classification applied to METEOSAT data and based on the Dynamical Clustering Method [37]. The following sections present the others cloud properties, cloud optical thickness, cloud pressure, and cloud phase, respectively. The original contribution of POLDER regarding these products is emphasized. The discussions are supported by the analysis of POLDER data acquired on November 10, 1996, especially along three ADEOS orbits over the Atlantic Ocean (orbit numbers 3107–3109), i.e., in the METEOSAT field of view (see Fig. 1). At the end of a validation period foreseen in July 1998, the complete set of POLDER data will be processed by CNES and level 2 and 3 products will be made available to the scientific community. For the moment, the only available monthly synthesis of the "ERB & clouds" line is for June 1997. Section VI presents the global monthly means of POLDER-derived cloud properties and compares them to the ISCCP products. Finally, Section VII summarizes the results and concludes.

II. CLOUD AMOUNT: THE CLOUD DETECTION ALGORITHM

The physical principles of the POLDER cloud detection algorithm are extensively developed in [7]. They were based on the analysis of measurements performed by the airborne simulator of POLDER. Since then, POLDER has flown aboard ADEOS, and some adjustments and improvements have been



Fig. 1. Image constructed from 670 nm reflectance measured by POLDER on November 10, 1996 along three ADEOS paths (orbit numbers 3107–3109) over the Atlantic Ocean. Clouds appear as light shades against a darker ocean or land background.

brought to the algorithm. First, this section briefly covers different threshold tests used in the algorithm and presents methodology used to adjust the different threshold values. This consists mainly in analyzing the coherence of results from various tests involved in the algorithm. The validation of the cloud identification is emphasized through comparison with the results of the Dynamical Clustering Method applied to METEOSAT satellite observation [37].

The cloud detection algorithm of the "ERB & clouds" line mainly based on a series of sequential threshold tests applied to each individual pixel (6.2 km) and for every viewing direction. Some of these tests use the spectral reflectance defined as $R_\lambda = \pi L_\lambda / (\cos \theta_s E_\lambda)$, where L_λ is the measured spectral radiance, θ_s is the solar zenith angle, and E_λ is the spectral averaged solar irradiance at the top of the atmosphere. These tests aim at detecting clouds, and a pixel is declared cloudy when one of these tests proves positive.

- 1) An "apparent" pressure P_{app} is derived from the ratio of reflectance measured in the channels centered at 763 and 765 nm (see Section IV). The pixel is labeled

cloudy if P_{app} is markedly lower than the sea-surface pressure P_{surface} . The threshold applied to $P_{\text{surface}} - P_{\text{app}}$ depends on the ratio between the molecular and the total reflectance at 765 nm, R_{mol}/R^* [42].

- 2) A pixel is declared cloudy if the measured reflectance at wavelength λ , R_λ ($\lambda = 865$ nm over ocean and $\lambda = 443$ nm over land) is significantly larger than its clear-sky estimate R_λ^{clear} . Over ocean, a large threshold value (15%) is chosen in order to avoid classifying aerosols as clouds. The same value is chosen over land, but the spatial variability is taken into account.
- 3) For scattering angles less than 140° , the molecular optical thickness τ_{443} of the atmospheric layer above the observed surface (cloud or sea-surface) is directly derived from the polarized reflectance at 443 nm. It is compared to the total molecular optical thickness of the atmosphere $\tau_{443}^{\text{clear}}$. If the $\tau_{443}^{\text{clear}} - \tau_{443}$ difference is above threshold, the pixel is rejected as cloud contaminated. In [7] the threshold was set to a constant value. In the new version of the algorithm, it varies as a linear function of the air-mass factor.
- 4) The polarized radiance at 865 nm presents different features for clear-sky and for cloud conditions specifically in the rainbow direction (see Section V). A pixel is identified as cloud-contaminated if the actual polarized radiance is outside the expected range for clear-sky conditions. This range is now defined as a function of the scattering angle.

If all of the previous tests prove negative, two more tests are added in order to identify the clear pixels.

- 5) A pixel that has not been declared cloudy is labeled as clear if $R_\lambda - R_\lambda^{\text{clear}}$ ($\lambda = 865$ nm over ocean and $\lambda = 443$ nm over land) is small enough (<2%).
- 6) Finally, a pixel is expected to be clear if its reflectance exhibits a large spectral variability. Practically, following [5] the R_{865}/R_{443} ratio was found to be a better indicator than the R_{865}/R_{670} ratio initially considered in [7]. Over ocean, a pixel is declared as cloud-free if the R_{865}/R_{443} ratio is less than 0.4. Over land surface, this ratio has to be more than 1.2.

The different thresholds presented above have been adjusted according to the following philosophy. When adjusting the four first tests, the reflectance threshold test, $R_\lambda - R_\lambda^{\text{clear}} < 2\%$ is considered as a reference test. Indeed, all the pixels that satisfy this test for all the viewing directions are expected to be clear. Consequently, the reflectance threshold test is used as an indicator of the relevance of the different "cloud" thresholds. At this stage, the philosophy of the cloud detection algorithm is to adjust the "cloud" thresholds in order to make sure that all the four tests prove negative when the pixel is clear. When detecting the cloud-free pixels, a similar approach is adopted. Pixels are expected to be "cloudy" if the reflectance threshold test, $R_\lambda - R_\lambda^{\text{clear}} > 15\%$, is satisfied whatever the direction of view. The spectral variability thresholds are thus adjusted in such a way that practically no cloudy pixel is declared as clear. Illustration of this methodology can be found in [38].

If a POLDER pixel does not satisfy at least one of the six tests described above, it remains unclassified for a given viewing direction. However, if this pixel is labeled as clear (or cloudy) in some viewing directions and undetermined in all the other ones, then it is labeled as clear (or cloudy) for all the directions. If the pixel remains undetermined, it is then relabeled as clear or cloudy depending on the classification of the neighboring pixels and the spatial variability of R_{670} . Afterwards, when all of the elementary pixels are identified as cloud-free or cloudy, the cloud cover is computed at the super-pixel scale ($\sim 9 \times 9$ pixels), direction by direction. An example of so-derived global distribution of the monthly mean cloud cover retrieved from ADEOS/POLDER data is presented in Section VI.

A first validation of the POLDER cloud identification algorithm goes through a comparison with the results of the Dynamical Clustering Method [37] applied to METEOSAT data acquired every 30 min between 7 and 14 UTC from October 30 to November 10, 1996. The spatial resolution of the METEOSAT data is 5 km at nadir. The Dynamical Clustering Method uses two spectral parameters, the infrared and visible radiances and two structural parameters, the local spatial standard deviation of the visible and infrared radiances (computed for 3×3 neighboring pixels). These data are processed following [29] for five latitudinal regions over ocean and six regions over land. The result is a set of cloud type classifications valid between 7 and 14 UTC for the October 30–November 10, 1996 period. From this set, any ADEOS-POLDER path in the METEOSAT field of view can be simulated with a time lag of ± 15 min.

The POLDER and METEOSAT cloud covers are compared for the three ADEOS paths (orbit numbers 3107–3109) on November 10 (Fig. 1). The proportion of clear (overcast) pixels is 28% (49%) in the METEOSAT classification and 34% (53%) in the POLDER one. The smaller clear pixel percentage in the METEOSAT classification is compensated by a larger percentage of partially covered pixels (small cumulus, cloud edges, very thin cirrus) than in the POLDER cloud classification. Note that "partly" does not have the same meaning for METEOSAT and POLDER pixels. In the former, it is used for METEOSAT pixels that are expected to be partly covered by clouds. In the latter, it is used for POLDER pixels that are labeled as cloudy for some viewing directions and clear for the others. The co-occurrence matrix obtained from the pixel-to-pixel comparison of the two classifications (Table I) shows that 76% of the pixels belong to the same class and only 1.7% belong to opposite classes (clear/overcast or overcast/cloudy). The percentage of pixels declared clear by POLDER but declared cloud-contaminated by METEOSAT (9%) is larger than the opposite case (3%). Only 13% of these anomalous pixels are overcast in the first case, and 17% in the second case. Tables II and III, respectively, give the distribution of the METEOSAT cloud types for each of the three POLDER classes and the distribution of the three POLDER classes for each of the METEOSAT cloud types. The overcast cloud types (low, middle, multilayer, cirrus, high thick clouds) have at least 85% of their pixels belonging to the overcast class in the POLDER classification and less than

TABLE I
CO-OCCURRENCE MATRIX OBTAINED FROM THE PIXEL-TO-PIXEL
COMPARISON OF METEOSAT AND POLDER IDENTIFICATION
FOR THE 3 POLDER-ADEOS PATHS OF FIG. 1

METEOSAT	POLDER		
	Clear	Partly	Overcast
Clear	25.1%	2.5%	0.5%
Partly	7.9%	6.6%	8.0%
Overcast	1.2%	3.9%	44.3%

TABLE II
DISTRIBUTION OF THE METEOSAT CLOUD TYPES IN EACH OF THE THREE
POLDER CLASSES FOR THE THREE POLDER-ADEOS PATHS OF FIG. 1

METEOSAT Cloud types	POLDER classes		
	Clear	Partly	Overcast
28.1% clear	89%	9%	2%
9.6% nearly clear	46%	28%	26%
7.0% thin edges	40%	38%	22%
5.9% partly cloudy	12%	21%	68%
9.2% low clouds	2%	3%	96%
7.4% middle clouds	3%	6%	91%
5.8% multi-layers	3%	13%	85%
4.2% thin cirrus clouds	11%	32%	57%
11.5% cirrus clouds	2%	10%	89%
11.3% high thick clouds	0%	0%	100%

3% of them are classified as clear. An exception is the thin cirrus class. For the partly cloudy types, the percentage of clear POLDER pixels decreases as the subpixel cloud cover is expected to increase. Study of the spatial neighboring of these partially covered METEOSAT pixels shows that when they are declared clear by POLDER, the percentage of clear METEOSAT pixels in the neighboring is larger than in the other cases.

The cloud cover derived from POLDER compares well with the METEOSAT cloud classification on an instantaneous basis and at the pixel scale. The percentage of full agreement between POLDER and METEOSAT (76%) is close to the 81% which is found by comparing the METEOSAT classification with itself by introducing a shift of one pixel. However, in this last case, only 0.2% of the pixels are classified in opposite categories against 1.7% in the POLDER-METEOSAT comparison. This discrepancy between POLDER and METEOSAT classifications comes from the differences both in the observations and the algorithms. The METEOSAT algorithm is very sensitive to a very small spatial variability of radiance values close to surface ones. In the POLDER scheme, thresholds have

been set up to avoid the inclusion of "false clouds" such as Saharan dust. When the apparent pressure threshold and the reflectance threshold is decreased, the percentage of clear POLDER pixels declared clear by METEOSAT increases, the percentage of clear METEOSAT pixels declared cloudy by POLDER increases, too. This comparison appears encouraging though there are some discrepancies especially for the partly cloudy and the thin cloud cases.

One has to keep in mind that the aim of the "ERE clouds" processing line is to derive cloud properties and not to detect surface parameters. Consequently, the cloud detection algorithm is very different from a cloud-clearing algorithm. The previous discussion highlights that broken cloudiness as well as thin cloud cover are sometimes classified as clear by the POLDER pixel identification scheme. In fact, one verifies that the different thresholds of the POLDER algorithm have been adjusted in such a manner that questionable cloud cases as well as thick aerosol layers are rejected as clear. Generally speaking, it seemed to the authors that it was preferable to allocate to an entire POLDER pixel some mean cloud properties corresponding only to a small fraction of the pixels. However, this philosophy may have some impact on the final results, as illustrated in Section VI.

III. CLOUD OPTICAL THICKNESS

Cloud optical thickness is directly related to the ice/water content and is thus a key parameter in cloud modeling. It can be derived from bidirectional reflectance measurements. However, this needs some assumptions both on cloud microphysics and on cloud morphology and spatial distribution. Cloud fields are commonly viewed as a single and homogeneous plane parallel layer composed of prescribed particles despite possible large effects due to both cloud heterogeneities (e.g., [2, 10]) and different particles [28]. Unlike the usual scanning radiometers, POLDER provides up to 14 quasi-simultaneous reflectance measurements of a geographical target. While it is always possible to find a cloud model that satisfies one single bidirectional observation of a given target, it is not so easy to fulfill the complete set of 14 observations. Consequently, POLDER not only allows the determination of cloud optical thickness under some hypotheses, but it also enables us to test the validity of these hypotheses.

A cloud water droplet model is used in our algorithm that operationally derives cloud optical thickness from ADEOS-POLDER data [7]. The cloudy pixels are assumed fully covered by a plane-parallel layer composed of liquid water droplets with an effective radius of $10 \mu\text{m}$ and an effective variance of 0.15 [18]. In these conditions, the optical thickness is the only cloud property that is allowed to vary. This model is similar to the one used in the first ISCCP analysis [33]. The uncertainties due to the use of this model have been discussed in [32].

An example of global distribution of the monthly mean cloud optical thickness retrieved from ADEOS-POLDER data is presented in Section VI. The purpose here is to illustrate the ability to test the cloud model used. To do that, for the cloudy situations observed over ocean during three ADEOS

TABLE III

DISTRIBUTION OF THE THREE POLDER CLASSES IN EACH OF THE METEOSAT CLOUD TYPES FOR THE THREE POLDER-ADEOS PATHS OF FIG. 1

POLDER classes	METEOSAT cloud types									
	Clear	Nearly clear	Thin edges	Partly cloudy	Low clouds	Middle clouds	Multi- layers	Thin cirrus	Cirrus clouds	High Thick
	34.2% Clear	73%	13%	8%	2%	0%	1%	0%	1%	1%
13.0% Partly	19%	21%	20%	9%	2%	4%	6%	10%	8%	0%
52.8% Overcast	1%	5%	3%	8%	17%	13%	9%	5%	19%	21%

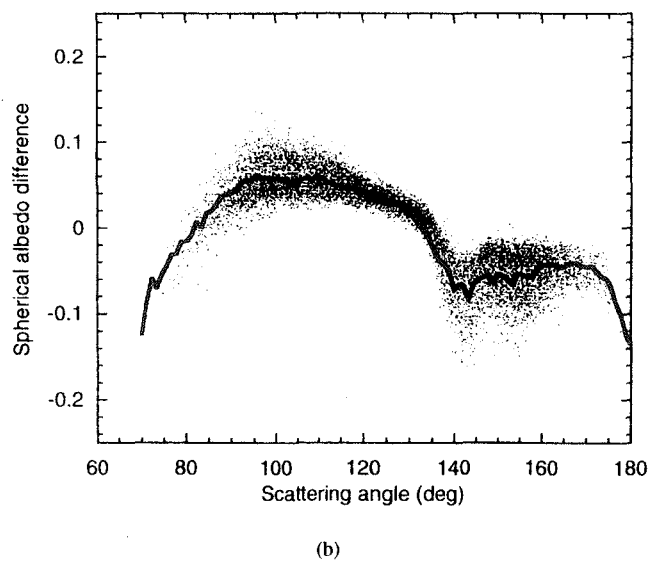
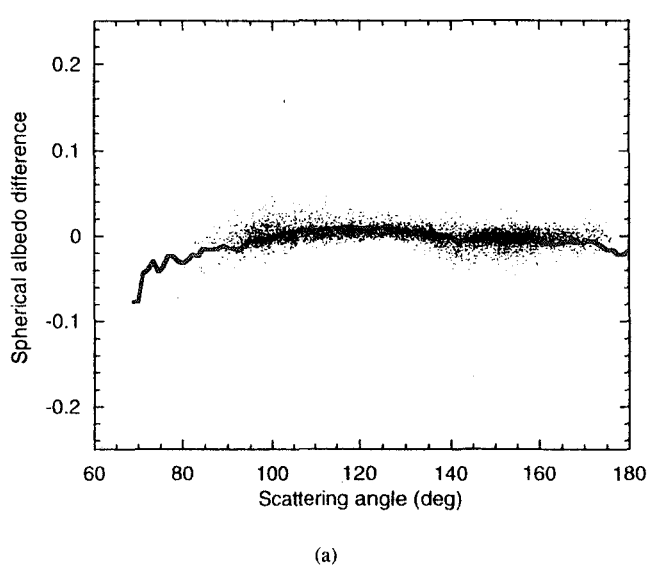


Fig. 2. Differences between the "directional" values of cloud spherical albedo and their mean value as a function of scattering angle for (a) liquid water clouds and (b) ice clouds. The wavelength is 670 nm. The POLDER data corresponds to ADEOS orbits 3107–3109.

overpasses (orbit numbers 3107–3109), we make use of the $N(\leq 14)$ "directional" values of cloud optical thickness, given in the "ERB & clouds" products. Since the retrieval is based on the standard cloud droplet model, these N values are expected to be close to one another in the case of liquid water clouds and dispersed in the case of ice clouds. By another way, for each cloudy pixel the thermodynamic phase is identified following the method described in Section V. We thus select the super-pixels only composed of pixels for which the phase is found liquid and the super-pixels for which the phase is ice whatever the pixel. For every superpixel observed under at least seven directions, we calculate the difference between each of the "directional" values of optical thickness and their mean value. More precisely, we make use of a representation, introduced in the ISCCP scheme, that is equivalent in radiative energy amount. Indeed, the variability of the cloud properties we are interested in is important according to their contribution to the earth radiation budget. Additionally, as the basic measurements are radiances, the precision of the calculated differences is more easily interpretable in energy rather than in optical thickness. Practically, the calculated parameter is the cloud spherical albedo (over a black surface) which is a one-to-one function of the optical thickness (see [34, Fig. 3.13]).

These cloud spherical albedo differences are reported as a function of scattering angle for the selected liquid water clouds in Fig. 2(a). On average, the liquid water clouds appear well represented by the standard droplet model. The absolute difference of retrieved spherical albedo is typically 0.01. Only about ten superpixels, located near a depression off Iceland, notably depart from this good behavior; the large spherical albedo differences are certainly due to shortcomings in the cloud phase detection for these ambiguous multilayered cloud systems. The spherical albedo difference averaged over the 2278 superpixels classified as liquid water clouds remains very close to zero for all the scattering angles larger than 90°. The values of scattering angle around 80° correspond to large values of the solar and/or the viewing zenith angle, which may induce a serious weakness of the plane-parallel approximation [25]. However, note that the abrupt decrease of the spherical albedo difference near 70° corresponds to the

ambiguous cases mentioned above and must not be considered as representative of the liquid water clouds.

The spherical albedo differences calculated for the superpixels classified as ice clouds are reported in Fig. 2(b). As expected, it clearly appears that the liquid water droplet model is not suitable for ice clouds. The difference of retrieved spherical albedo often reaches values as large as ± 0.1 . The value of the spherical albedo difference averaged over the 1197 superpixels varies by 0.12 when the scattering angle varies from 100° to about 140° . The minimum observed near 140° is related to the peak of the phase function of the water droplet model in the rainbow direction. A smoother phase function would give a better agreement in the treatment of ice clouds.

However, the standard water droplet model which is used in the POLDER operational algorithm—a cloud droplet radius of $10 \mu\text{m}$ —is in good agreement with mean values retrieved from near-infrared radiance observations over low-level clouds: about $11\text{--}12 \mu\text{m}$ in maritime clouds and $8\text{--}9 \mu\text{m}$ in continental clouds [17]. On the opposite, many studies have shown that the single-scattering properties of ice cloud particles differ substantially from those of liquid water spheres (see [28] and references therein). For that reason, an ice fractal polycrystal model, which is expected to be representative of irregularly shaped and randomly oriented ice particles, was introduced in the treatment of cold clouds in the recent ISCCP re-analysis [34]. On the other hand, the analysis of airborne POLDER data acquired during the EUCREX'94 (European Cloud and Radiation Experiment) campaign confirmed that the standard water droplet model is suitable for stratocumulus and the ice polycrystal model is more adequate for cirrus clouds [14].

Thus, the POLDER bidirectional reflectance measurements appear useful to check the schemes of cloud optical thickness retrieval. In the near future, different cloud particle models will be investigated in order to minimize the angular variability of the cloud spherical albedo.

IV. CLOUD PRESSURE

Together with cloud optical thickness, one of the most important cloud properties with respect to global climate changes is cloud height. Several techniques for deriving cloud altitude from satellite have already been developed, generally using radiances in the $15 \mu\text{m}$ CO₂ band (e.g., [40], [27]) or in the atmospheric windows (e.g., [31], [26]). Two different methods were developed to retrieve cloud pressure from ADEOS-POLDER data [7]. Here we present the first comparison between these two cloud pressures, respectively, derived from absorption measurements in the oxygen A-band and from spectral polarization measurements.

The algorithm of derivation of the “apparent pressure” P_{app} is extensively described in [7]. It is based on a differential absorption technique using the radiances measured in the POLDER narrow-band and wide-band channels centered on the oxygen A-band. In this algorithm, P_{app} is calculated both for clear and for cloudy conditions (cf., Section II; see also [42]). Here we consider only the cloudy conditions. The atmosphere is assumed to behave as a pure absorbing medium

overlying a perfect reflector located at pressure P_{app} . Because all scattering effects are neglected, P_{app} is not the cloud pressure; it is somewhat of a mean pressure, between bottom and the top of a single cloud or of a multilayer cloud system. This difference between P_{app} and the cloud pressure can be amplified when the ground influence is negligible. A correction for this effect, proposed in [7], is to be validated and is not considered here.

Another retrieved cloud pressure is the so-called “Rayleigh cloud pressure,” P_{Ray} , derived from polarization measurements at 443 nm. At this wavelength, the polarized reflectance is mainly related to the atmospheric molecular optical thickness above the observed cloud, at least for scattering angles ranging from 80° and 120° and outside the sunglint direction. A correction is introduced to remove the small contamination by the cloud layer itself as explained in [7]. The pressure P is then directly proportional to the retrieved molecular optical thickness. That pressure is thus expected to be close to the cloud top pressure, at least when the whole signal comes from the molecules situated above the cloud, that needs overcast conditions.

Fig. 3 compares the Rayleigh cloud pressure to that derived from O₂ absorption for the clouds observed during the three selected ADEOS overpasses. As expected, P_{app} is almost always larger than P_{Ray} for overcast conditions [Fig. 3(a) and (b)]. The mean difference is 140 hPa for the 2776 oceanic superpixels and 209 hPa for the 219 continental ones. A comparable difference was observed for optically thick clouds between P_{app} and the cloud top pressure derived from brightness temperature measured in the $11\text{-}\mu\text{m}$ channel of METEOSAT [42]. These differences are thought to be chiefly due to the photon penetration effect that strongly affects the retrieval of the pressure from O₂ absorption measurements. This effect is known to be more negligible as the volume scattering coefficient is larger [46]. That is the case of maritime stratocumulus clouds for which P_{app} is much closer to P_{Ray} [see the range 900–1000 hPa in Fig. 3(a)].

The comparison between P_{app} and P_{Ray} appears more complex for the partly cloudy superpixels [Fig. 3(c) and (d)]. The difference $P_{\text{app}} - P_{\text{Ray}}$ remains positive over land but is very often negative over ocean. The mean difference is 22 hPa for the 711 continental superpixels but -32 hPa for the 3462 oceanic ones. When the cloud cover tends toward zero, the retrieved pressures do not tend necessarily to the surface pressure P_{surface} . The Rayleigh pressure tends to P_{surface} only if there is no additional polarization by the surface. The apparent pressure tends to P_{surface} only if all of the reflected light comes from the surface. Practically, P_{app} is close to P_{surface} for highly reflecting surfaces but can be as weak as 500 hPa for dark surfaces such as the ocean outside the regions of the solar specular reflection [42]. Therefore, for partly cloudy pixels, P_{Ray} is generally larger than the actual cloud top pressure and P_{app} is weaker or larger than the cloud mean pressure depending on whether the surface is dark or bright. That explains that $P_{\text{app}} - P_{\text{Ray}}$ is generally positive for partly cloudy superpixels over land [Fig. 3(d)] but is now negative and now positive over ocean depending on the relative contribution of the cloud in the observed reflectance [Fig. 3(c)].

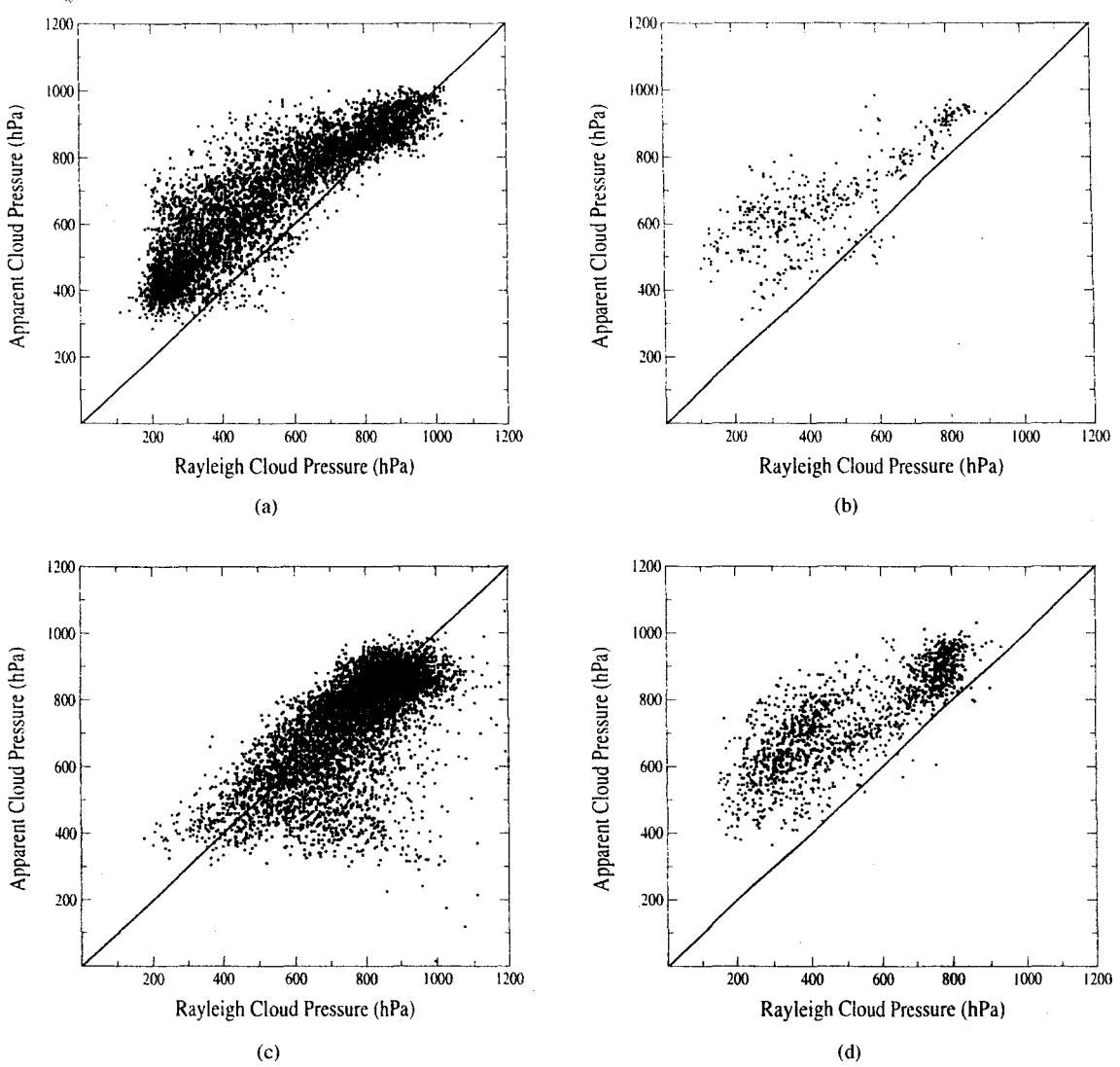


Fig. 3. Apparent cloud pressure derived from O_2 absorption versus Rayleigh cloud pressure derived from polarization at 443 nm, for overcast conditions over (a) ocean and (b) land and for partly cloudy conditions over (c) ocean and (d) land. POLDER data correspond to ADEOS orbits 3107–3109.

V. CLOUD THERMODYNAMIC PHASE

An improved algorithm for remotely determining the cloud-top thermodynamic phase is described hereafter. The algorithm utilizes near-infrared polarized reflectance over a large range of scattering angles in order to discriminate between ice and liquid water phases. Indeed, theoretical as well as experimental studies have shown that polarized signatures of water droplets and ice particles are quite different [15], [16], [6], [35], [12].

Considering a cloudy system observed from satellite, the polarized component of the upward radiance is mainly formed in the upper cloud layer [15]. Around 80% of the single-scattered radiation reflected by the cloud arises from the upper hundred meters of the layer. In studying cloud polarization, the physical interesting quantity is the polarized reflectance PR_λ , which is less sensitive to multiple scattering effects than the total reflectance [19]. Thus, the polarization features, mainly governed by single scattering, are preserved in PR_λ .

For a large enough optical thickness ($\tau > 1$), the polarized reflectance PR_λ roughly varies as the cloud polarized phase

function, which depends on cloud microphysics properties (shape/size) and refractive index.

In most cases, cloud water droplets are expected to have a particle effective radius ranging between 5 μm and 15 μm . Fig. 4(a) and (b) presents, respectively, theoretical simulations and observations of the main polarization features for scattering angles that can be observed by POLDER. The light scattering by cloud water droplets exhibits a strong maximum about 140° from the incoming direction. This peak, the so-called primary rainbow, is highly polarized which makes it easily detectable. The maximum and the width of the peak are dependent on the droplet size distribution [15]. Another noticeable property is the neutral point, which is located between 75° and 120° according to droplet size. For narrow size distributions, several supernumerary bows appear [16]. On the contrary, if the size distribution is relatively broad, no supernumerary bow appears. In some cases these properties are used to retrieve the effective radius of liquid water droplets [4]. The last polarization feature that can be observed is the glory, which is centered on the backscattering peak (scattering

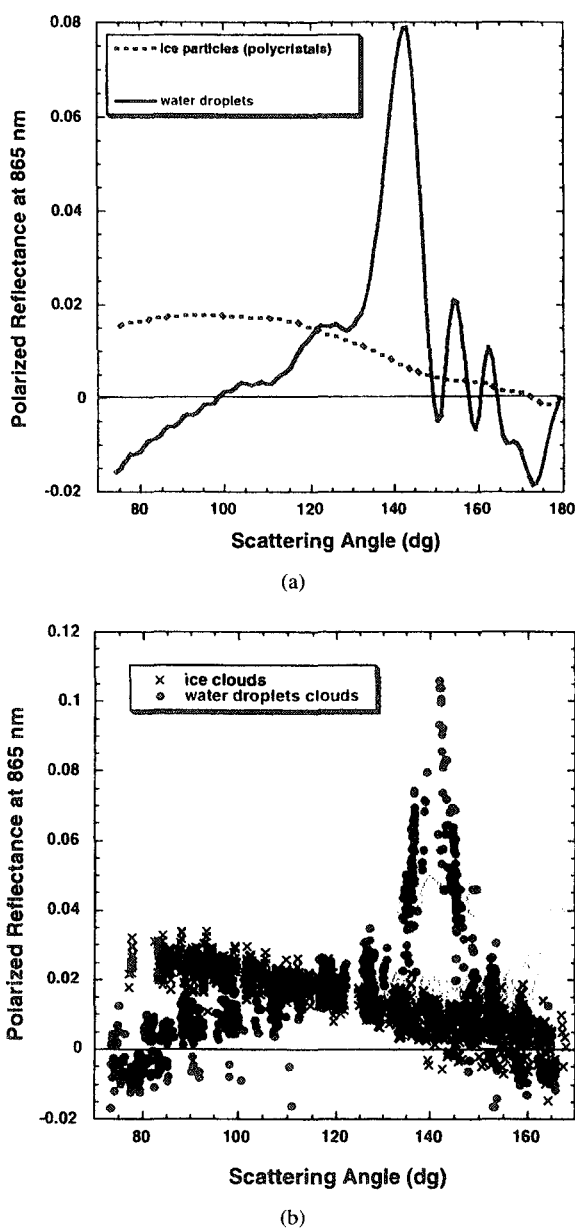


Fig. 4. Polarized reflectance at 865 nm as a function of scattering angle. (a) corresponds to simulation in the solar principal plane for polycrystals randomly oriented in space (dashed line) and water spheres of effective radius of $10 \mu\text{m}$ (solid line). In both cases cloud optical thickness is two. The sun zenithal angle is 55° . (b) is an example of polarized reflectance measured by POLDER over cirrus cloud (crosses) and over liquid water cloud (full circle) on November 10, 1996.

angle equal to 180°). This is a typical characteristic of water spheres [41].

Unlike water clouds, cirrus clouds are mainly composed of ice crystals with extremely large variabilities in shape and size [21]. Diversity and complexity of ice crystal shape and size depend on temperature and humidity in cloud. For scattering angles that can be observed from space, radiative transfer computations [6], [12] performed for randomly oriented hexagonal particles [Fig. 4(a)] and observations [Fig. 4(b)] show different important features: i) a generally positive polarization (vibration perpendicular to the scattering plane), ii) a decreasing of the polarization for increasing scattering

angles (i.e. negative slope), and iii) a neutral point around 160° .

Since [7], preliminary analysis of polarized reflecta acquired by ADEOS-POLDER has highlighted a possible way to recognize the cloud thermodynamic phase. The pre operational algorithm is described hereafter. Two spe angular ranges are considered. For scattering angles sm than 110° , the direction of the polarization plane with res to the scattering plane is predominately 90° (positive polar component and negative slope) for ice clouds and 0° (negative polarization and positive slope) for liquid water clouds. larger scattering angles (around 140°) the two cloud types positively polarize the radiation, but the polarized reflect is ten times higher for liquid water clouds than for ice clouds. The POLDER angular coverage in term of available scattering angles depends on the latitude and the season. most complete POLDER angular sampling can give access to these two angular ranges. In some cases, one or both angular domains can be not sampled. The phase detection is based on tests performed in the two scattering angle domains at 865 nm. At this wavelength, the molecular contribution is rather weak and is corrected for by using the Rayleigh cloud top pressure (see Section IV).

The algorithmic principle and results are illustrated in Fig. 5. First, examine the 670-nm reflectance image [Fig. 5(a)] acquired over France on November 10, 1996. The size of selected area is about $1000 \text{ km} \times 1000 \text{ km}$. Clouds cover a large part of the scene. Now, examine the corresponding polarized reflectance images at 865 nm for scattering angles around 100° [Fig. 5(b)] and for scattering angles around 140° [Fig. 5(c)]. In Fig. 5(b) black pixels correspond to negative polarization near 100° . This characterizes the "liquid" phase. The same pixels exhibit large polarized reflectance around 140° [Fig. 5(c)]. A combination of the polarization information in these two scattering angle domains leads to label the pixels as "liquid" [Fig. 5(d)]. On the other hand, gray pixels [Fig. 5(b)] correspond to relatively high positive polarization around 100° and to very small (<0.01) polarization around 140° [dark pixels in Fig. 5(c)]. The corresponding pixels are labeled "ice" [Fig. 5(d)]. The processing of the POLDER level 1 data thus allows the determination of cloud phase at global scale. Each cloudy "superpixel" of the level 2 POLDER product is finally identified as "liquid," "ice," "mixed" or else "undetermined."

VI. MONTHLY MEAN CLOUD PROPERTIES

The level 2 POLDER "ERB & clouds" products contain for each orbit the retrieved cloud property parameters (cloud cover, cloud pressures, optical thickness, . . .) with their full directional properties and their angular averaging as nondirectional parameters [7]. In level 3 processing, most of the latter, coming from up to 420 orbits, are averaged on a global coverage scale to provide monthly mean climatologies and associated temporal dispersions. For each pixel, the number of daily POLDER observations extend from at most one between 30° N and 30° S to up to 14 close to the poles. For the June 1997 POLDER data presented here, the number of average

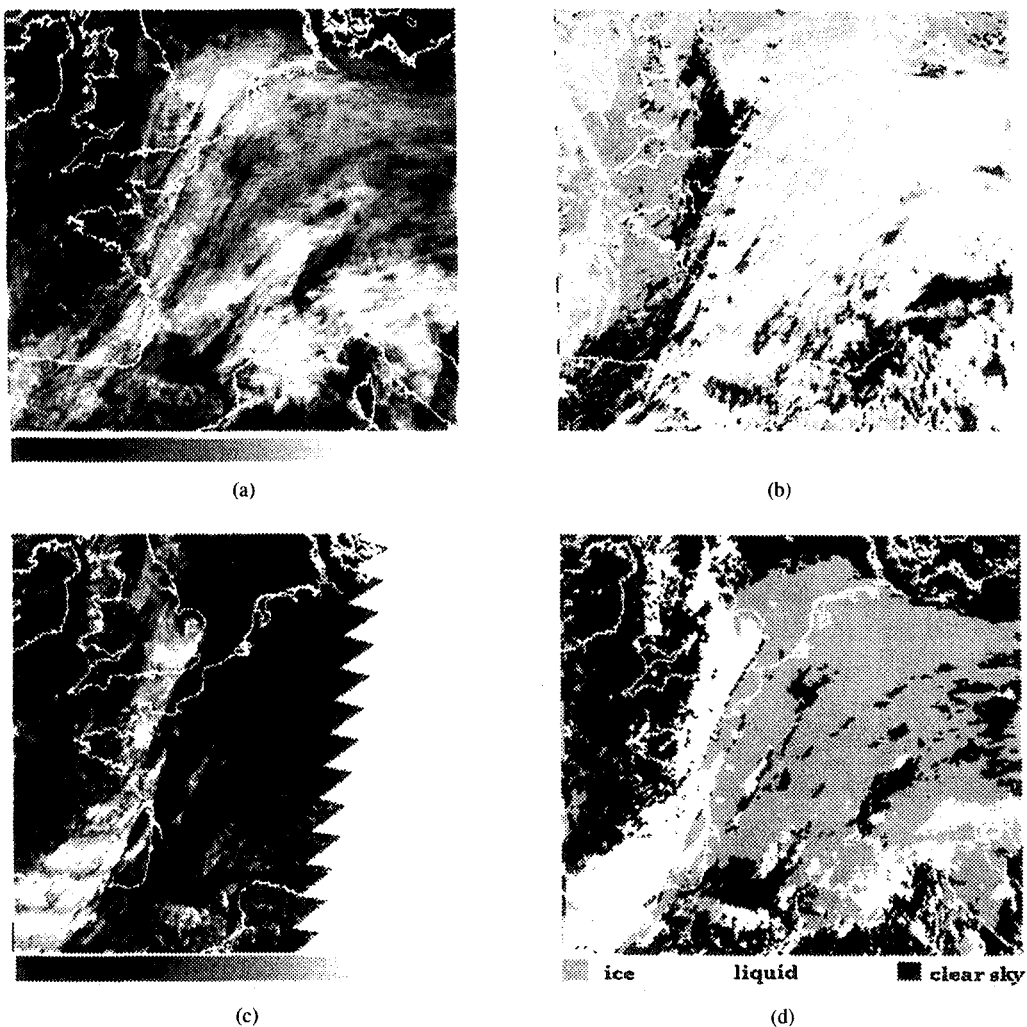


Fig. 5. Illustration of the cloud thermodynamic phase recognition. (a) Reflectance image in the 670-nm band acquired over France on November 10, 1996. Reflectance dynamic ranges from 0–0.9. (b) Polarized reflectance at 865 nm for scattering angles close to 100° . Black pixels indicate negative polarization ($-0.04 < PR < 0$). Gray levels are for positive polarization up to 0.02. (c) Same as (b), but for scattering angles near 140° . Polarized reflectance ranges from 0–0.07. (d) Thermodynamic phase index (black is for clear sky, light gray for liquid, and dark gray for ice). This resulting image is a combination of information contained in (b) and (c).

observations used to construct these climatologies lies, in most cases and depending on cloud cover and latitude, from 15 up to more than 150 observations.

As quoted in Section I, "ERB & clouds" products are averaged at a $\sim 50 \times 50 \text{ km}^2$ scale which corresponds, except very near the poles, to 9×9 aggregates of elementary POLDER equal area pixels. This low-resolution grid has been constructed in direct relationship with the equal area ISCCP grid, in such a way that each ISCCP cell contains an integer number of these "superpixels" (namely 5×5 , between 80° N and 80° S).

As an example of the first available "ERB & clouds" level 3 monthly synthesis, we present here the June 1997 climatology of four selected parameters (cloud cover, optical thickness, O_2 apparent cloud pressure, and Rayleigh cloud pressure) and make a first comparison to interannual means of ISCCP monthly mean data. For this, we have used both C2 (1983–1991) [33] and D2 (1987, 1989–1993) [34] data interpolated at 10:30 a.m. local time, but we will concentrate on the latter, as the most recent reprocessing of the archives.

More exactly, we reprocess the D2-level data from ISCCP-D1 data by weighting the cloud optical thickness and cloud pressures by the cloud cover to obtain monthly means coherent with POLDER processing.

In the following, all comparisons of POLDER and ISCCP data are restricted to the 60° N – 60° S latitude band because of the large snow and sea-ice occurrence near the pole. Furthermore, for all statistical studies, the POLDER observations have been averaged at the ISCCP cell resolution.

A. Cloud Cover

The POLDER cloud cover for June 1997 is presented in Fig. 6. All the large cloud structures associated with the main climate processes are easily identified and their location is coherent with what we would expect for the month of June: the intertropical convergence zone (ITCZ) along the 10° N parallel, large clear-sky area over the deserts of Sahara, South-West Africa, and Australia, subtropical zones of heavy cloud cover west of Peru, Angola, California, and over the northern Pacific. We note, however, an abnormal overcast area around

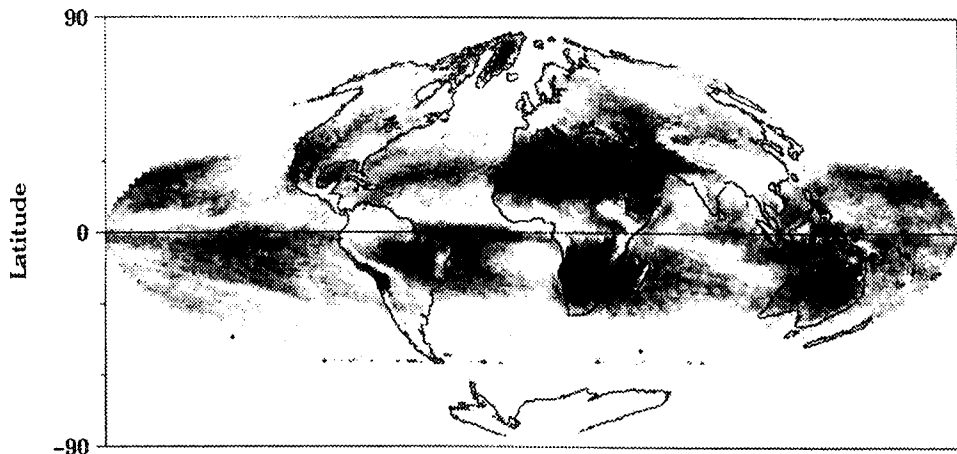


Fig. 6. POLDER level 3 monthly synthesis of cloud cover for June 1997. Coverage ranges from zero (black) to one (white) over a light gray background.

TABLE IV
GLOBAL MEANS OF ISCCP C&D AND POLDER CLOUD COVERS. FOR THE D DATA SET,
MIN AND MAX GIVE THE INTERANNUAL DISPERSION AMONG THE SIX PROCESSED YEARS

	C	D			POLDER
	Mean	Min	Mean	Max	Mean
All cells	0.63	0.65	0.66	0.68	0.58
Over ocean	0.68	0.68	0.70	0.72	0.63
Over land	0.50	0.56	0.58	0.61	0.48

the North Pole corresponding, as it will be confirmed later, to a faulty cloud detection over sea ice.

Crude statistics of this cloud cover (Table IV) show that POLDER data underestimate the global cloud amount by 8% (5%) when compared with ISCCP D2 (C2) interannual mean data sets. When comparing these cloud covers at pixel scale, we see that POLDER is always weaker over ocean, but close to the C2 data set over land.

A more detailed view of these statistics in terms of cloud cover distribution (Fig. 7) shows that, for POLDER and ISCCP D2 data sets, 20% of the cells have a cloud cover higher than 0.8. However, 34% of POLDER cells have a cloud cover lower than 0.5, whereas this percentage drops to 20% for ISCCP-D2 climatology. A closer look at the POLDER (respectively, ISCCP-D2) cloud covers shows that, over ocean, 22% (respectively, 30%) of the cells have a coverage higher than 0.8, while 28% (15%) of cells have a coverage less than 0.5. Over land, these percentages become 8% (10%) for POLDER (ISCCP) cells with a coverage higher than 0.8 and 48% (32%) for cells with a coverage lower than 0.5.

Over land, in the 60° N–60° S latitude range, the increase of cloud coverage observed between the C2 data set and the D2 reprocessing is mainly due to the lower brightness temperature threshold used to separate clear and cloudy cells [34]. We may thus presume that the POLDER underestimation of cloud cover over land comes from a weaker detection of thin cirrus, as it is typically observed over the Saharan desert. This can

be extended for ocean observations and is coherent with the precautions included in the cloud detection algorithms to avoid aerosol contamination (see Section II).

Finally, we have checked the coherence between POLDER cloud cover and ISCCP reprocessed climatologies at the pixel scale by looking at the cloud cover differences (δCC) with POLDER. Over ocean, δCC is weaker than 0.1 for 62% of the pixels while over land, this is observed for only 49% of the pixels. When the tolerance threshold is set to $\delta CC < 0.2$, these percentages reach 86% over ocean and 79% over land. That shows a good coherence at a global coverage scale despite the fact that i) we compare June 1997 to a six-year interannual mean and ii) POLDER has a daily global coverage, while ISCCP climatologies use multisensor data.

B. Cloud Optical Thickness

In both level 2 (with full directional properties) and level 3 processings, spatial and angular, then temporal averageings of optical thickness have been performed separately in terms of linear means and energy equivalent means (see Section III). Both sets of information are given in “ERB & clouds” POLDER products as in ISCCP products, but we will concentrate here on the latter.

The POLDER energy averaged optical thickness for June 1997 is presented in Fig. 8. Besides the values much larger than 15 at high latitudes which are obviously due to the large reflectivity of sea-ice areas detected as overcast pixels, the

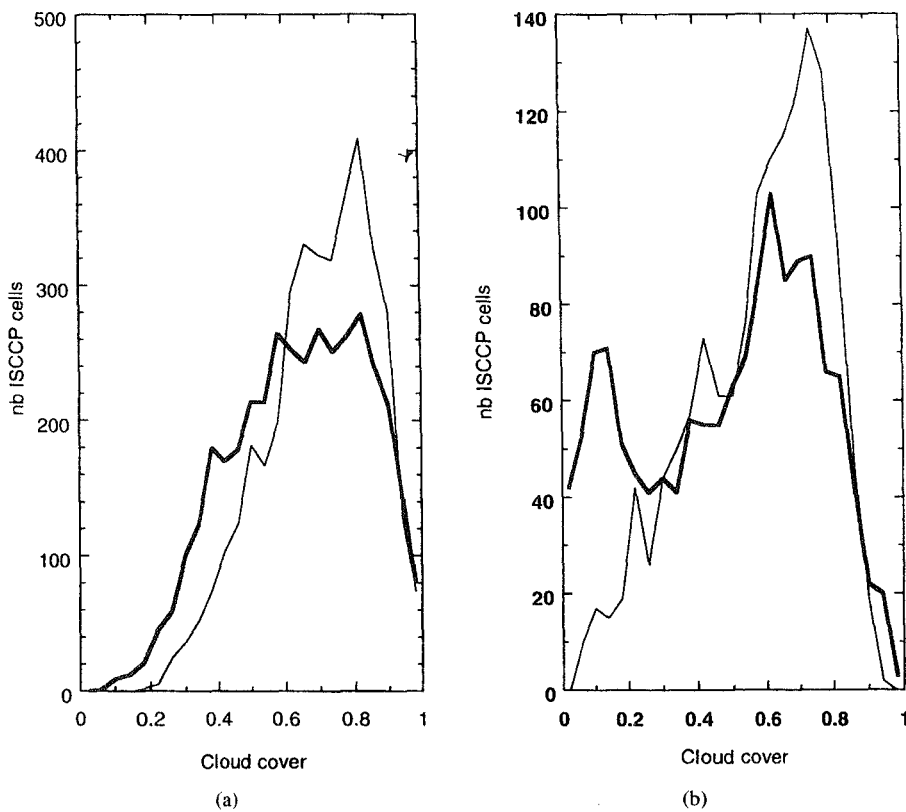


Fig. 7. Comparison of POLDER (thick solid line) and ISCCP D2 (thin solid line) cloud cover distributions (a) over ocean and (b) over land. The count axis corresponds to the number of ISCCP equal area grid cells in 4% bins.

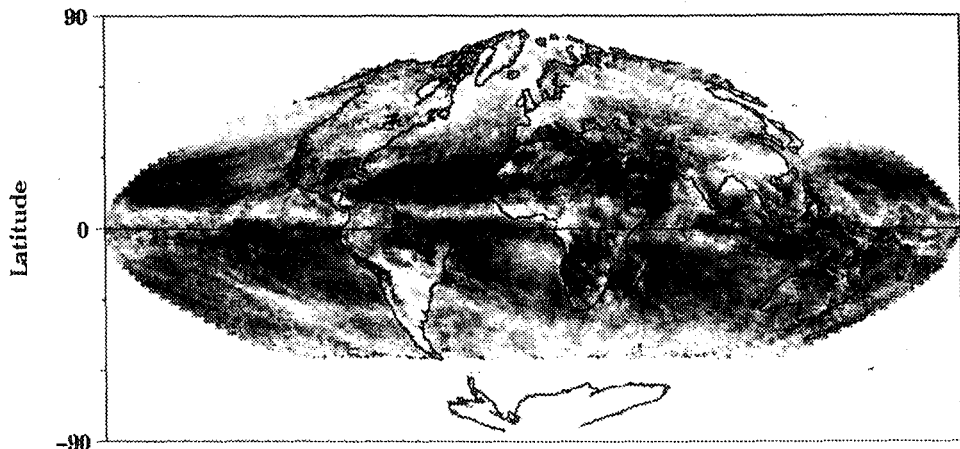


Fig. 8. POLDER level 3 monthly synthesis of cloud optical thickness (energy means) for June 1997. The scale ranges from zero (black) to 15 (white) over a light gray background.

observed optical thickness is coherent with the above-observed cloud structures and their expected regional reflectivity characteristics: high mean values all along the ITCZ, over midlatitude depression areas and for frequent thick enough cirrus banks as seen over the Sahara.

The statistical distribution of all the retrieved optical thicknesses between 60° N and 60° S is presented in Fig. 9 along with the corresponding ISCCP data. The pixel values (coded in equivalent energy amount) have been averaged, with cloud cover weighting, at the ISCCP cell scale and then converted to corresponding optical thickness for presentation. We observe

a noticeable spreading of the POLDER distribution (4.66 ± 0.64) toward higher optical thickness values, compared to ISCCP (3.91 ± 0.58). At this stage of a first comparison, we may think of different grounds for this discrepancy. First, ISCCP and POLDER present differences in the optical thickness retrieval methods as well as in the measurements. Another would be the effect of the POLDER cloud detection algorithm thresholds on thin cirrus and small or broken clouds at the subpixel scale, compared to the ISCCP rate of detection. Since optical depth averaging is only done for nonzero cloud cover, the statistical effect may be far from negligible, even for

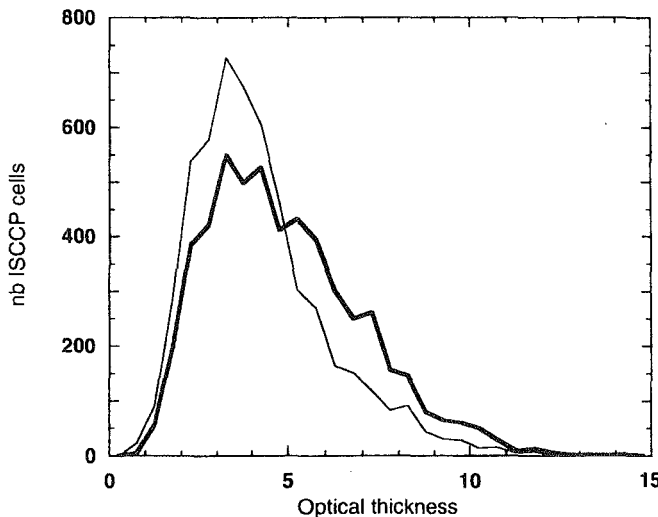


Fig. 9. Comparison of POLDER (thick solid line) and ISCCP (thin solid line) optical thickness distributions. The count axis corresponds to the number of ISCCP equal area grid cells in 0.5 bins.

energy means, and would lead toward the observed spreading over higher optical thickness values. Given the importance of optical thickness as a cloud characteristic, more precise studies are clearly needed, in particular with June 1997 ISCCP data when available.

C. Cloud Pressure

As explained in Section IV, two different POLDER cloud pressures (P_{app} and P_{Ray}) have been defined, using two different physical principles. We may thus expect to attain different characteristics of the usually complex cloud structures.

The POLDER mean “apparent” cloud pressure P_{app} for June 1997 is presented in Fig. 10. The abnormally high values around the pole are in fact surface pressures of snow and sea-ice, as mentioned above. The main climatic trends of cloud top heights are easily recognizable: large areas of dense low cloud structures on subtropical west sides of main continents and the southern Indian Ocean, high cloud accumulation all along the ITCZ and over high altitude continental zones. However, but not surprisingly (see Section IV), P_{app} appears systematically lower than the expected cloud “top” pressure.

This is clearly confirmed by a global statistical comparison of this retrieved pressure against ISCCP pressures (Table V). For the latter, we have chosen to confront POLDER pressures to both “adjusted cloud top pressure” (noted P78, following ISCCP D2 notation [34]) and “nonadjusted cloud top pressure” (P79). When averaged, P_{app} appears very close to the uncorrected P79 pressure but significantly higher than P78.

Pressure distributions over all ICCP cells (Fig. 11) furnish further hints. First, P_{app} and P78 present a very similar shape of distribution which shows, more or less clearly, three expected structures: the concentration of large strato-cumulus decks with high pressure values, thick high-level clouds on the other end of the histogram, and a majority of middle/multilayered cloud structures in between. Second, there is an overall shift of 139 hPa between P_{app} and P78, the latter being expected to be close to the top cloud pressure.

This overall value is probably a complex statistical mixing two main radiative processes: photon penetration inside cloud layers and transparency of thin upper layer to lower cloud layers or surface reflectivity (see Section IV and [42]).

The POLDER mean “Rayleigh pressure” P_{Ray} for Jt 1997, presented in Fig. 12, is expected to be closer to top cloud pressure (Section IV). Indeed, all the main climatic trends of known cloud top heights are enhanced when compared to P_{app} : geographic extension of the high-level clouds particularly over land, and clear higher mean values of cloud pressure. We note, however, an abnormal amount of large (>900 hPa) pressure values which are currently under investigation.

When P_{Ray} is compared to ISCCP cloud top pressure P78 (Table V and Fig. 13) we observe a shift of 78 hPa toward high pressure values, whereas the general trends of pressure distribution are comparable. Given the very different radiative physics involved in the retrieval of these two cloud pressures (brightness temperature in one case and polarization visible reflectivity in the other), a detailed comparison is beyond the scope of this paper. However, when exploring the lower pressure end of the distribution (Fig. 3) at the pixel scale, we observe that (22%) (16%) (36%) of (all)(ocean)(land) ISCCP P78 pixels have a cloud top pressure weaker than 400 hPa, while the corresponding percentages drop to (5%) (4%) (7%) for P_{Ray} . As observed for P_{app} , one part of this lack of high pressures is due to the POLDER misdetection of thin cirrus, particularly over land; another part may be interpreted as a transparency effect of the polarization due to molecular scattering underneath high rather thin cloud layers; further studies are nonetheless needed to confirm such a statement.

At the present state of the validation, the comparison presented above for three of the main cloud properties is encouraging and lead to rather coherent hints regarding the observed discrepancies. However, this preliminary study limited to a single month and any conclusive statement should wait until the whole eight months of level 3 POLDER data are processed.

VII. SUMMARY AND CONCLUSION

First results on the derivation of cloud properties from ADEOS-POLDER have been presented in this paper. The original contribution of POLDER has been emphasized for each cloud property investigated. Particular attention was given to POLDER level 2 data of November 10, 1996 and level 3 products of June 1997.

A first key result is a good correlation between the POLDER cloud detection algorithm and the Dynamical Clustering Method [37] applied to METEOSAT data. Some discrepancies appear for broken cloudiness and very thin cirrus cloud cases. However, we think that it is preferable to not allocate to an entire POLDER pixel ($6.2 \text{ km} \times 6.2 \text{ km}$) cloud properties that correspond only to a small fraction of the pixel. This choice can explain why our cloud cover appears to be weaker (typically by 0.08) than the ISCCP climatological values.

Cloud optical thickness was derived from bidirectional reflectances by using the standard water droplet model with

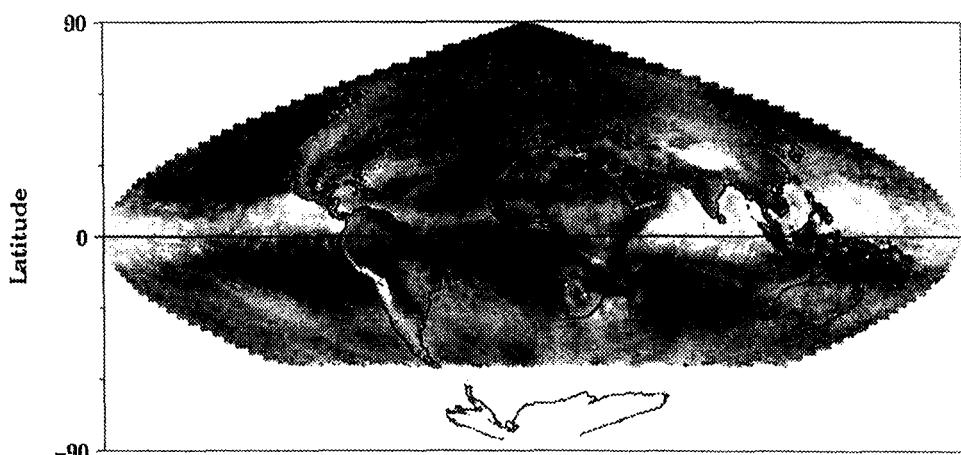


Fig. 10. POLDER level 3 monthly synthesis of apparent O₂ pressure (P_{app}) for June 1997. Pressure ranges from 200 hPa (white) to 1000 hPa (black).

TABLE V

GLOBAL MEANS AND STANDARD DEVIATIONS (hPa) OF ISCCP P78 AND P79 (SEE TEXT) AND POLDER P_{app} AND P_{Ray} PRESSURE DISTRIBUTIONS

	P78	P79	P_{app}	P_{Ray}
All cells	565 ± 131	670 ± 103	704 ± 108	643 ± 135
Over ocean	545 ± 132	660 ± 105	700 ± 116	668 ± 137
Over land	605 ± 117	685 ± 94	717 ± 87	585 ± 136

an effective radius of 10 μm . The multidirectional capability of POLDER is demonstrated to be useful to check schemes of cloud optical thickness retrieval. As expected, the standard water droplet model is suitable for liquid water clouds and inadequate for ice clouds. This statement indirectly validates our algorithm of cloud thermodynamic phase recognition, since it was used to select these two types of clouds. The next "ERB & clouds" algorithm planned for POLDER2 on ADEOS2 (end of 2000) should begin with the cloud phase detection; then the more adequate particle models should be used to derive the cloud optical thickness. For this purpose, different ice crystal models will be analyzed and validated in the very near future.

Two POLDER cloud pressures are derived by two different ways: the O₂-apparent pressure is derived from absorption measurements in the oxygen-A band, while the Rayleigh cloud pressure makes use of spectral polarization observations. On average, the apparent pressure is weaker (typically by 60 hPa) than the Rayleigh pressure. For overcast conditions, the Rayleigh pressure is expected to be close to the cloud top pressure; the O₂-apparent pressure is larger by more than 100 hPa chiefly due to the photon penetration effect inside the cloud layers. For partly cloudy conditions, the difference between the two retrieved pressures can be now negative now positive depending on the importance of the surface reflectivity.

Comparisons between POLDER and ISCCP monthly mean products were performed for the month of June. However, they are still only preliminary since the ISCCP data are not yet

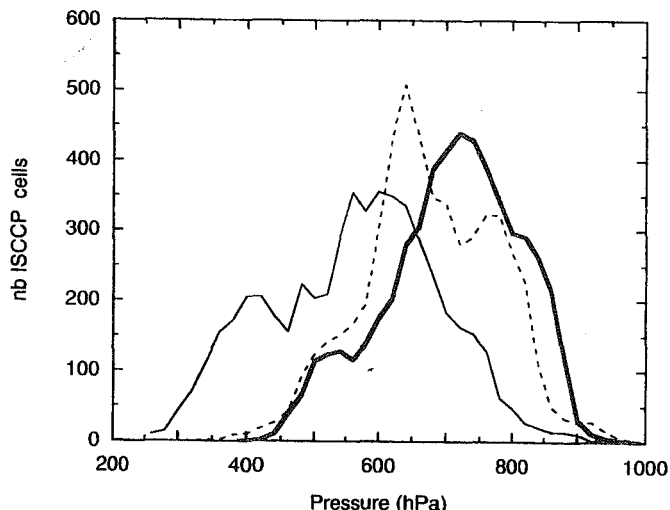


Fig. 11. Comparison of P_{app} (thick solid line), ISCCP P78 pressure (thin solid line) and P79 pressure (dotted line) distributions. The count axis corresponds to the number of ISCCP equal area grid cells in 20 hPa bins.

available for the period of the ADEOS-POLDER acquisition (November 1996–June 1997). Overall, the agreement is rather good. Differences between POLDER and ISCCP cloud optical thickness and cloud pressure certainly result for a large part from differences in the cloud detection schemes. They also result from the original characteristics of the POLDER instrument, which is complementary to usual satellite radiometers.

The multispectral multipolarization and multidirectional capabilities of POLDER thus appear useful for cloud studies.

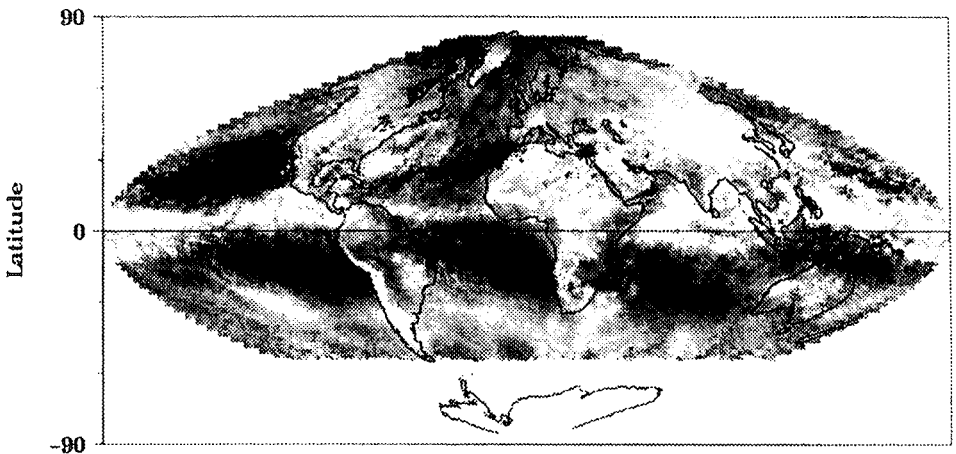


Fig. 12. As in Fig. 10 for POLDER "Rayleigh" pressure (P_{Ray}).

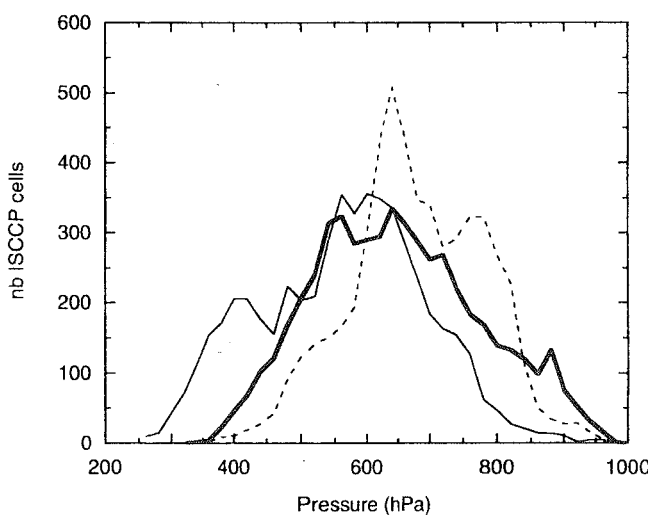


Fig. 13. As in Fig. 11 for P_{Ray} (thick solid line).

Moreover, POLDER allows observing a large sampling of the BRDF (up to 14 quasi-simultaneous radiance measurements) of any scene. Hence, it makes possible the construction of angular directional models directly correlated with the retrieved cloud properties. This item is important in view of the high remaining uncertainty when inverting radiances to fluxes in the Earth Radiation Budget Experiment (ERBE) project, which is simply due to the use of limited and sometimes incorrect angular directional models [3], [2]. In the recent Tropical Rainfall Measuring Mission (TRMM) [39] and near-future Earth Observing System (EOS) projects [44], this fundamental problem is expected to be improved by combining broadband CERES measurements [45] with the use of narrow-band moderate spatial resolution cloud imagers like Moderate Resolution Imaging Spectrometer (MODIS) [24] and Visible and Infrared Scanner (VIRS).

ACKNOWLEDGMENT

The authors wish to thank A. Lifermann for her comments on the manuscript. They also gratefully acknowledge Dr. I. Melnikova and two anonymous referees for their very helpful comments and suggestions.

REFERENCES

- [1] A. Arking, "Latitudinal distribution of cloud cover from TIRO photographs," *Science*, vol. 143, pp. 569–572, 1964.
- [2] D. G. Baldwin and J. A. Coakley, Jr., "Consistency of Earth radi budget experiment bidirectional models and the observed anisotrop reflected sunlight," *J. Geophys. Res.*, vol. 96, pp. 5195–5207, 1991.
- [3] B. R. Barkstrom, E. F. Harrison, and R. B. Lee, "Earth radiation budget experiment. Preliminary seasonal results," *EOS*, vol. 71, pp. 297–299, 1990.
- [4] F. M. Bréon and P. Goloub, "Cloud droplet effective radius from spaceborne polarization measurements," *Geophys. Res. Lett.*, vol. 25, pp. 1879–1992, 1998.
- [5] F. M. Bréon and S. Colzy, "Cloud detection from the spaceborne POLDER Instrument and validation against synoptic observations," *Appl. Meteorol.*, to be published.
- [6] G. Brogniez, "Light scattering by finite hexagonal crystals arbitrarily oriented in space," in *Proc. IRS'88*, J. L. Lenoble, J. F. Geleyn, and Deepak, Eds., Hampton, VA, 1988, p. 64.
- [7] J.-C. Buriez, C. Vanbaucq, F. Parol, P. Goloub, M. Herman, B. Bor, Y. Fouquart, P. Couvert, and G. Sèze, "Cloud detection and derivation of cloud properties from POLDER," *Int. J. Remote Sens.*, vol. 18, pp. 2785–2813, 1997.
- [8] R. D. Cess *et al.*, "Intercomparison and interpretation of climate feedback processes in 19 atmospheric general circulation models," *J. Geophys. Res.*, vol. 95, pp. 16601–16610, 1990.
- [9] ———, "Cloud feedback in atmospheric general circulation models: update," *J. Geophys. Res.*, vol. 101, pp. 12791–12794, 1996.
- [10] L. H. Chambers and B. A. Wielicki, "Accuracy of independent parameter approximation for satellite estimates of oceanic boundary layer cloud optical depth," *J. Geophys. Res.*, vol. 102, pp. 1779–1794, 1997.
- [11] R. J. Charlson, S. E. Schwartz, J. M. Hales, R. D. Cess, J. A. Coakley Jr., J. E. Hansen, and D. J. Hofmann, "Climate forcing by anthropogenic aerosols," *Science*, vol. 255, pp. 423–430, 1992.
- [12] H. Chepfer, G. Brogniez, L. Sauvage, P. H. Flamant, V. Trouillet, and J. Pelon, "Remote sensing of cirrus radiative parameters during EUCREX'94. Case study of Apr. 17, 1994. Part 1: Microphysical modelization," *Mon. Wea. Rev.*, vol. 127, pp. 504–519, 1999.
- [13] P. Y. Deschamps, F. M. Breon, M. Leroy, A. Podaire, A. Bricaud, J. Buriez, and G. Sèze, "The POLDER mission: Instrument characteristics and scientific objectives," *IEEE Trans. Geosci. Remote Sensing*, vol. 32, pp. 598–615, 1994.
- [14] J. Descloitres, J.-C. Buriez, F. Parol, and Y. Fouquart, "POLDER observations of cloud bidirectional reflectances compared to a planar parallel model using the ISCCP cloud phase functions," *J. Geophys. Res.*, vol. 103, pp. 11411–11418, 1998.
- [15] P. Goloub, J.-L. Deuzé, M. Herman, and Y. Fouquart, "Analysis of the POLDER polarization measurements performed over cloud cover," *IEEE Trans. Geosci. Remote Sensing*, vol. 32, pp. 78–88, 1994.
- [16] P. Goloub, H. Chepfer, M. Herman, G. Brogniez, and F. Parol, "Use of polarization for clouds study," in *Proc. SPIE*, 1997, vol. 3121, pp. 330–341.
- [17] Q. Han, W. B. Rossow, and A. A. Lacis, "Near-global survey of effective droplet radii in liquid water clouds using ISCCP data," *J. Climate*, vol. 7, pp. 465–497, 1994.

- [18] J. E. Hansen and L. D. Travis, "Light scattering in planetary atmospheres," *Space Sci. Rev.*, vol. 16, pp. 527–610, 1974.
- [19] J. E. Hansen, "Multiple scattering of polarized light in planetary atmospheres. Part II. Sunlight reflected by terrestrial water clouds," *J. Atmos. Sci.*, vol. 28, pp. 1400–1426, 1971.
- [20] E. F. Harrison, P. Minnis, B. R. Barkstrom, V. Ramanathan, R. D. Cess, and G. G. Gibson, "Seasonal variations of cloud radiative forcing derived from the Earth radiation budget experiment," *J. Geophys. Res.*, vol. 95, pp. 18687–18703, 1990.
- [21] A. J. Heymsfield, "Cirrus unicinus generating celles and evolution of cirriform clouds. Part I: Aircraft observations of the growth of the ice phase," *J. Atmos. Sci.*, vol. 32, pp. 799–807, 1975.
- [22] J. T. Houghton, G. J. Jenkins, and J. J. Ephraums, Eds., "Climate change: The IPCC scientific assessment," in *World Meteorological Organization/United Nations Environment Programme*. Cambridge, U.K.: Cambridge Univ. Press, 1990, p. 364.
- [23] R. S. Kandel, J. L. Monge, M. Viollier, L. A. Pakhomov, V. I. Adasko, R. G. Reitenbach, E. Raschke, and R. Stuhlmann, "The ScaRaB project: Earth radiation budget observations from the Meteor satellites," *World Space Congress (Washington)-COSPAR Symp. A.2-S. Adv. Space Res.*, vol. 14, no. 1, pp. 47–54, 1994.
- [24] M. D. King, Y. J. Kaufman, W. P. Menzel, and D. Tanré, "Remote sensing of cloud, aerosol, and water vapor properties from the moderate resolution imaging spectrometer (MODIS)," *IEEE Trans. Geosci. Remote Sensing*, vol. 30, pp. 2–27, Jan. 1992.
- [25] T. Kobayashi, "Effects due to cloud geometry on biases in the albedo derived from radiance measurements," *J. Climate*, vol. 6, pp. 120–128, 1993.
- [26] X. Lin and J. A. Coakley, "Retrieval of properties for semitransparent clouds from multispectral infrared imagery data," *J. Geophys. Res.*, vol. 98, pp. 18501–18514, 1993.
- [27] W. P. Menzel, D. P. Wylie, and K. L. Strabala, "Seasonal and diurnal changes in cirrus clouds in four years of observations with the VAS," *J. Appl. Meteorol.*, vol. 31, pp. 370–385, 1992.
- [28] M. I. Mishchenko, W. B. Rossow, A. Macke, and A. A. Lacis, "Sensitivity of cirrus cloud albedo, bidirectional reflectance and optical thickness retrieval accuracy to ice particle shape," *J. Geophys. Res.*, vol. 101, pp. 16973–16985, 1996.
- [29] J. L. Raffaelli and G. Sèze, "Cloud type separation using local correlation between visible and infrared satellite images," in *Passive Infrared Remote sensing of clouds and the atmosphere III*, *Proc. SPIE*, vol. 2578, pp. 61–67, 1995.
- [30] V. Ramanathan, R. D. Cess, E. F. Harrison, P. Minnis, B. R. Barkstrom, E. Ahmad, and D. Hartmann, "Cloud radiative forcing and climate: Results from the Earth radiation budget experiment," *Science*, vol. 243, pp. 57–63, 1989.
- [31] D. W. Reynolds and T. H. Vonder Harr, "A bi-spectral method for cloud parameter determination," *Mon. Wea. Rev.*, vol. 105, pp. 446–457, 1977.
- [32] W. B. Rossow, L. C. Garder, and A. A. Lacis, "Global, seasonal cloud variations from satellite radiance measurements. Part I: Sensitivity of analysis," *J. Climate*, vol. 2, pp. 419–458, 1989.
- [33] W. B. Rossow and R. A. Schiffer, "ISCCP cloud data products," *Bull. Amer. Meteorol. Soc.*, vol. 6, pp. 2394–2418, 1991.
- [34] W. B. Rossow, A. W. Walker, D. E. Beuschel, and M. D. Roiter, "International satellite cloud climatology project (ISCCP). Documentation of new cloud datasets," WMO/TD 737, World Meteorolog. Org., 1996, p. 115.
- [35] L. Sauvage, H. Chepfer, V. Trouillet, P. H. Flamant, G. Brogniez, J. Pelon, and F. Albers, "Remote sensing of cirrus radiative parameters during EUCREX'94. Case study of Apr. 17, 1994. Part 1: Observations," *Mon. Wea. Rev.*, vol. 127, pp. 486–503, 1999.
- [36] C. A. Senior and J. F. B. Mitchell, "Carbon dioxide and climate: The impact of cloud parameterization," *J. Climate*, vol. 6, pp. 393–418, 1993.
- [37] G. Sèze and M. Desbois, "Cloud cover analysis in satellite imagery using spatial and temporal characteristics of the data," *J. Climate Appl. Meteorol.*, vol. 26, pp. 287–303, 1987.
- [38] G. Sèze, C. Vanbauce, J.-C. Buriez, F. Parol, and P. Couvert, "Comparison of the POLDER cloud detection over ocean with a METEOSAT cloud classification," in *Proc. AMS'98*, Paris, France, May 25–29, 1998, pp. 500–503.
- [39] J. Simpson, R. F. Adler, and G. R. North, "A proposed tropical rainfall measuring mission (TRMM) satellite," *Bull. Amer. Meteorol. Soc.*, vol. 69, pp. 278–295, 1988.
- [40] W. L. Smith and C. M. R. Platt, "Comparison of satellite-deduced cloud heights with indications from radiosonde and ground-based measurements," *J. Appl. Meteor.*, vol. 17, pp. 1796–1802, 1978.
- [41] J. D. Spinhirne and T. Nakajima, "Glory of clouds in the near-infrared," *Appl. Opt.*, vol. 33, pp. 4652–4662, 1994.
- [42] C. Vanbauce, J. C. Buriez, F. Parol, B. Bonnel, G. Sèze, and P. Couvert, "Apparent pressure derived from ADEOS-POLDER observations in the oxygen A-band over ocean," *Geophys. Res. Lett.*, vol. 25, pp. 3159–3162, 1998.
- [43] M. Vesperini, F. M. Bréon, and D. Tanré, "Atmospheric water vapor content from POLDER spaceborne measurements," this issue, pp. 1613–1619.
- [44] B. A. Wielicki, R. D. Cess, M. D. King, D. A. Randall, and E. F. Harrison, "Mission to Planet Earth: Role of clouds and radiation in climate," *Bull. Amer. Meteorol. Soc.*, vol. 76, pp. 2125–2152, 1995.
- [45] B. A. Wielicki and B. R. Barkstrom, "Cloud and the Earth's radiant energy system (CERES): An Earth observing system experiment," in *2nd Symp. Global Change Studies*, New Orleans, LA, Amer. Meteorol. Soc., 1991, pp. 11–16.
- [46] M. C. Wu, "Remote sensing of cloud-top pressure using reflected solar radiation in the oxygen-A band," *J. Clim. Appl. Meteorol.*, vol. 24, pp. 539–546, 1985.

Frédéric Parol, for a photograph and biography, see this issue, p. 1566.



Jean-Claude Buriez received the M.S. degree in physics in 1968 and the "Doctorat d'Etat" in physics in 1981, both from the University of Lille, France.

He is currently a Professor of physics at the University of Lille and a Researcher at the Laboratoire d'Optique Atmosphérique. Before 1981, he worked on radiative transfer theory of inhomogeneous scattering atmospheres to analyze planetary spectra. Since then his research has focused on the remote sensing of cloud properties using space- and ground-based instruments. His scientific interests include the influence of clouds on radiation in climate modeling. He is in charge of the inversion of POLDER measurements for cloud and radiative budget analysis.



Claudine Vanbauce received the M.Sc. degree in physics in 1988 and the Ph.D. degree in atmospheric physics from the University of Lille, France, in 1992 for studies about remote sensing of fog.

During 1993, she worked on a Centre National d'Etudes Spatiales (CNES) Post-Doctoral subject devoted to the possibility of detection and classification of clouds from multispectral and multiangular POLDER data. She is currently an Assistant Professor of physic and a Researcher employed at the Laboratoire d'Optique Atmosphérique, Lille, France. She participated in the POLDER "ERB & Clouds" line algorithms development and in the validation of associated products.



Pierre Couvert received the "Doctorat de 3ième cycle" in nuclear physics in 1974 and the "Doctorat d'Etat" in 1982.

From 1974 to 1993, he worked mainly at the Laboratoire National Saturen, Saclay, France, as a member of the Nuclear Physics Department of the Commissariat à l'Energie Atomique. From 1982 to 1984, he spent two sabbatical years at TRIUMF, Vancouver, B.C., Canada. His domain of research was mainly devoted to nucleon scattering and meson production in nuclei. In 1994, he turned to earth sciences by joining the Laboratoire des Sciences du Climat et de l'Environnement of Saclay as a Researcher and Member of the POLDER project. In charge of the technical aspects of the "Earth Radiation Budget and Clouds" POLDER data processing line with the Centre National d'Etude Spatiale, Toulouse, he participates in the validation of the first POLDER data with the scientific team of the Laboratoire d'Optique Atmosphérique, Lille.



Geneviève Sèze received the Ph.D. degree in computer science from the University of Paris VI, France, in 1977.

In 1978, she joined the Laboratoire de Météorologie Dynamique (LMD) of the Centre National de la Recherche Scientifique. In 1985 and 1986, she was a Visiting Scientist at the Goddard Institute for Space Studies, New York, where she also collaborated with the International Satellite Cloud Climatology Program (ISCCP) team. In November 1989, she was selected as a member of the First ISCCP Regional Experiment (FIRE) Science Team. At LMD, she conducts research on cloud cover analyses from satellite observation and the validation of Global Circulation Model cloud cover. She participates in the definition and development of future space missions dedicated to cloud cover analyses. For the POLDER project, she is in charge of the analysis and the validation of the cloud cover.

Philippe Goloub, for photograph and biography, see p. 525 of the January 1999 issue of this TRANSACTIONS.

Sylvain Cheinet graduated from Ecole Polytechnique, Palaiseau, France, in 1994. In 1998, he received the M.S. degree in atmospheric physics from the University of Lille, France, where he participated in the exploit of POLDER products with the working group "Earth Radiation Budget Clouds" of the Laboratoire d'Optique Atmosphérique. He is currently pursuing the Ph.D. degree in the Laboratoire de Météorologie Dynamique (working group: Modélisation Du Climat), whose topic is to determine the influence of cloud parameterization in the General Circulation Model of the LMD.

**Cirrus Cloud properties deived from POLDER-1/ADEOS Polarized
Radiances: First Validation using a Ground based Lidar Network**

Cirrus Cloud Properties Derived from POLDER-1/ADEOS Polarized Radiances: First Validation Using a Ground-Based Lidar Network

HÉLÈNE CHEPFER,* PHILIPPE GOLOUB,⁺ JAMES SPINHIRNE,[#] PIERRE H. FLAMANT,* MARIO LAVORATO,[@]
LAURENT SAUVAGE,* GÉRARD BROGNIEZ,⁺ AND JACQUES PELO[&]

* Laboratoire de Météorologie Dynamique, École Polytechnique, Palaiseau, France
+ Laboratoire d'Optique Atmosphérique, Université Lille 1, Villeneuve d'Ascq, France

NASA Goddard Space Flight Center, Greenbelt, Maryland
@ CEILAP, Villa Martelli, Argentina
& Service d'Aéronomie, Université Paris 6, Paris, France

(Manuscript received 26 October 1998, in final form 21 April 1999)

ABSTRACT

Bidirectional polarized reflectances measured with the POLDER-1 instrument on board *Advanced Earth Observing Satellite-1* have been used to infer cloud altitude and thermodynamical phase (ice/liquid) at a global scale. This paper presents a validation of these properties for cirrus clouds. The validation presented here is based on comparisons between POLDER-1 retrievals and measurements collected with a ground-based lidar network. The scale differences between POLDER measurements and lidar data are treated by selecting homogeneous and stable cloud layers.

These comparisons show that the cloud altitude retrieval with POLDER is valid for optically thick cloud, and nonvalid for semitransparent and thin cirrus clouds. The limitations of the cloud altitude retrieval method are analyzed by using both comparisons between POLDER and lidar and simulations of the bidirectional polarized reflectances performed with a radiative transfer code to assess a threshold of validity of the POLDER retrieval method. The comparisons of lidar and POLDER data show that the cloud thermodynamical phase (ice/liquid) retrieval is satisfactory, and examples of cloud thermodynamical phase retrieval are presented as a function of cloud temperatures.

1. Introduction

The occurrence of cirrus clouds inferred from satellite data is usually larger than 50% at mid- and tropical latitudes. These high clouds have a major influence on the earth-atmosphere energy budget through a combination of factors including large coverage, both in space and time, and low temperature. They influence the energy balance through effects on incoming solar radiation and outgoing infrared radiation (Liou 1986). At the present time, the impact of cirrus clouds on climate change is accepted in a broad sense but still needs to be asserted more quantitatively (Hansen et al. 1984). Among the missing quantities are the key radiative properties, that is, optical depth and microphysical characteristics, as well as structural parameters, for example, height, geometrical thickness, and geographical coverage. The ice crystal size in cirrus cloud is variable, and the particle shape can be complex. In situ measurements can be used to observe cirrus cloud composition, but it requires high

altitude aircraft because of the high altitude of cirrus clouds. In addition, semitransparency makes high clouds difficult to detect in satellite data and gives an inherent difficulty to discriminate between ice and liquid water.

At the present time, cloud parameters on a global scale are derived from observations by space-based radiometers (in sun-synchronous or geostationary orbit). Recently, the French space agency Centre National d'Études Spatiales developed a new radiometer, the POLDER (Polarization and Directionality of the Earth's Reflectances; Deschamps et al. 1994). POLDER was launched in August 1996 on board the Japanese heliosynchronous *Advanced Earth Observing Satellite-1* (ADEOS-1) (1030 LST) orbiting at 796-km altitude. The inclination is 98.59°, and the orbit period is 100 min.

POLDER-1 data inversion algorithms are currently under validation. As part of this ongoing effort, we focus our current research on cirrus clouds, with special attention paid to two parameters that can be inferred from polarized radiances: cloud height and discrimination between ice and liquid water (i.e., thermodynamical phase). The validation is conducted by comparison with contemporary lidar measurements. The current validation involves a lidar network of four ground-based stations distributed over different latitudes in the two hemi-

Corresponding author address: Dr. Hélène Chepfer, Laboratoire de Météorologie Dynamique, École Polytechnique, 91128 Palaiseau CEDEX, France.

E-mail: chepfer@lmd.polytechnique.fr

TABLE 1. POLDER cloud products deduced from polarized measurements.

Cloud parameter inferred from polarized data	Inversion method	POLDER-1 measurements
Height	Rayleigh pressure method (Goloub et al. 1994)	Bidirectional polarized reflectances at 443 and 864 nm
Thermodynamical phase	Absence or presence of rainbow $\Theta = 140^\circ$ (Goloub et al. 1994) Particle shape signature for scattering angles lower than 110°	Bidirectional polarized reflectances at 864 nm around 140° Bidirectional polarized reflectances at 864 nm for scattering angles lower than 110°

spheres. Lidars can detect subvisible cirrus clouds, and they are well suited to retrieve cloud boundaries (height) with high accuracy (tens to hundred of meters) and properties such as the optical depth and backscattering phase function. This latter parameter provides information on the cloud particle microphysics, while lidar linear depolarization ratio (Sassen 1991) provides relevant information on cloud phase. Prior to the current work, POLDER radiometer data have been used in conjunction with backscatter lidar data in the framework of an airborne experiment (Sauvage et al. 1999; Chepfer et al. 1999).

Section 2 addresses the mean features and capabilities of POLDER-1 on *ADEOS-1*. Section 3 is dedicated to the POLDER data inversion techniques used to derive the cloud information to be validated. Section 4 presents the lidar network and lidar data. The implemented procedure to conduct a reliable comparison between POLDER-1 and lidar is discussed in section 5. Sections 6 and 7 present the results of the comparisons for cloud height and cloud phase, respectively.

2. POLDER radiometer on *ADEOS-1*

The POLDER instrument was designed to collect accurate observations of the polarized and directional solar radiation reflected by the earth-atmosphere system (Deschamps et al. 1994). The data collected by POLDER-1 are currently used to address several key scientific objectives related to climate change: 1) cloud climatology, or description, and earth radiative budget (Buriez et al. 1997), 2) atmospheric aerosols and earth radiative budget (Herman et al. 1997), 3) atmospheric water vapor amount and atmospheric branch of the hydrological cycle (Vesperini et al. 1999), 4) ground reflectances and surface cover change (Leroy et al. 1997), and 5) ocean color. Considering the most important cloud parameters relevant to the earth radiative budget, the polarization measurement capability of the new radiometer is used in the current paper to infer the height and thermodynamical phase of cirrus clouds. The first radiometer POLDER-1 was operational for 8 months, from 1 November 1996 to 30 June 1997. A follow-on POLDER-2 should be launched on *ADEOS-2* in the summer of 2000.

The POLDER instrument concept is based on a

charged coupled device (CCD) matrix array detector, rotating filter wheel, and wide field-of-view optics both alongtrack and cross-track directions with a maximum field of view of 114° (Deschamps et al. 1994). The POLDER cross-track swath is about 2200 km, allowing for near-complete daily coverage of the globe. The CCD matrix is 242×74 pixels, with pixel resolution at nadir equaling $6 \text{ km} \times 7 \text{ km}$. An atmospheric target can be observed several times in different perspectives (14 at maximum). The viewing direction will respond to scattering angles between 70° and 180° , depending on the solar zenith angle and *ADEOS* positioning with respect to the target.

The reflectance measurements are taken in eight different wavelength bands: 443 (20), 490 (20), 565 (20), 670 (20), 763 (10), 765 (40), 865 (40), and 910 nm (10), where the first number is the wavelength of band center and the second one the bandwidth. Two of these channels, that is, 443, 670, and 865 nm, measure the state of polarization of the reflected solar radiation. The potential of polarization measurements for atmospheric applications was pointed out by Hansen (1971) and van de Hulst (1981), and more recently by Herremans et al. (1997). The state of polarization of the scattered radiation is sensitive to the shape of the scatterers and is particularly relevant for the study of ice clouds. In this study we used the POLDER-1 measurements in two polarized channels: 443 and 865 nm.

3. Inversion method for POLDER data

The POLDER cloud algorithms are presented in Buriez et al. (1997). The main output of the data inversion process are the (i) cloud-top height, (ii) cloud phase, (iii) cloud optical depth (using an a priori microphysical model for a given cloud type). As stated before, the present study focuses on the validation of the quantities inferred from polarized radiance measurements, that is, cloud-top height using the so-called Rayleigh pressure method, and cloud phase (Table 1; Goloub et al. 1994).

The Rayleigh pressure method is based on an accurate determination of the integrated air column above a cloud using the polarized radiances at 443 and 864 nm. It relies on three basic properties: (i) the intensity of the Rayleigh scattering by molecules is a significant contribution at 443 nm, but it is weak at 864 nm; (ii) the scatter-

intensity by ice crystals is about the same in the two channels, and (iii) the first orders of scattering provide the main contribution to POLDER polarized radiances.

Let us assume that the polarized light reflected by the cloud does not depend on the wavelength, because of the large dimension of the cloud droplets or ice crystals, and that the light resulting from multiple interactions between the cloud and the molecular layer exhibits negligible polarization. The expected polarized radiance L_p will be

$$L_p = L_{p,m} + L_{p,c} \exp\left[-\delta_m\left(\frac{1}{\cos\theta_s} + \frac{1}{\cos\theta_v}\right)\right], \quad (1)$$

where δ_m is the optical thickness of all molecules above the cloud, $L_{p,m}$ stands for the polarized light due to molecular scattering, and $L_{p,c}$ stands for the polarized light at the top of the cloud when directly illuminated by the solar beam; the exponential term accounts for the attenuation by the overlying molecular layer. To simplify (1), as δ_m and $L_{p,m}$ are negligible at $\lambda = 864$ nm, let us consider that L_p ($\lambda = 864$ nm) directly provides $L_{p,c}$, and let us neglect the transmission effect, which is justified for high-level clouds. Then, (1) reduces to

$$L_p^{443} - L_p^{864} \approx L_{p,m}^{443}. \quad (2)$$

Let $\delta_m(\lambda)$ be the optical thickness of the molecular layer; because $\delta_m(\lambda)$ is small, single scattering approximation of $L_{p,m}$ is valid in first approximation and therefore

$$\begin{aligned} L_{p,m}^{443} &= \delta_{0,m}^{443} \left(\frac{p}{p_0} \right) \frac{P_m(\Theta)P_m(\Theta)}{\cos\theta_v} \\ &= \left(\frac{p}{p_0} \right) \frac{3\delta_{0,m}^{443}(1 - \cos^2\Theta)}{16 \cos\theta_v}, \end{aligned} \quad (3)$$

where $\delta_{0,m}^{443}$ is the total Rayleigh optical thickness, and p_m and P_m are, respectively, the molecule's phase function and polarization ratio. Equation (3) shows that the polarized light is mainly governed by the scattering angle Θ . The cloud-top pressure and surface pressures are, respectively, p and p_0 . As a consequence, the difference between 443 and 864 nm will account for the molecular contribution above the cloud. Following (3) the cloud-top pressure is

$$p = C \frac{\cos\theta_v}{(1 - \cos^2\Theta)} (L_p^{443} - L_p^{864}) \quad (4)$$

with the constant C equal to 2.45×10^4 hPa.

The retrieved pressure is the average of the values calculated for all scattering angles ranging between 80° and 120° . The single scattering approach used for the Rayleigh model should be enough for high-level cloud observations since in that case the molecular layer above the cloud is very thin.

Cloud thermodynamical phase is inferred from polarized radiation measurements at 864 nm. The molecular contribution to the scattered radiation is weaker in this channel when compared with other available chan-

nels. An underlying assumption is that the polarized reflectance at this wavelength is mainly due to cloud particles. Discrimination between ice particles and water droplets is based on sensitivity of the normalized polarized radiance to scatterer shape (Goloub et al. 1994; Mishchenko and Travis 1997; Chepfer et al. 1998) as displayed in Fig. 1. The polarized radiance L_p is defined as

$$L_p = \sqrt{Q^2 + U^2 + V^2}, \quad (5)$$

where Q , U , and V are the Stokes parameters at the top of the atmosphere. The normalized polarized radiance $L_{n,p} = \pi L_p/E_s$, where E_s is the incident light at the top of the atmosphere. The normalized polarized radiance $L_{n,p}$ is linked to the bidirectional polarized reflectance ρ_p as $\rho_p = L_{n,p}/\mu_s$. The polarized radiance $L_{n,p}$ at 864 nm reflected by a cloud composed of spherical particles or hexagonal plates randomly oriented in space has been simulated using an adding-doubling radiative transfer code (de Haan et al. 1986). The scattering matrices are computed using Mie theory for water droplets ($r_e = 20 \mu\text{m}$) and a ray-tracing code accounting for the Fraunhofer diffraction in the forward direction for ice crystals (aspect ratio $Q = 0.05$; $r_e = 20 \mu\text{m}$; Brogniez 1988; Chepfer 1997). In Fig. 1, the scattering angles range from 70° to 175° , the limited number of cross (ice plates) and dot (spheres) points represent each POLDER observation (11 in the current case), the solar zenith angle $\theta_s = 55^\circ$, and cloud optical depth $\delta = 2$.

Figure 1 shows two ranges of scattering angles suitable to discriminate between ice and liquid water: (i) between 130° and 140° , where a strong peak corresponds to the rainbow phenomena for liquid water cloud, and the normalized polarized radiance displays a smooth behavior for ice plates; and (ii) between 70° and 120° where the slopes are quite different—positive for droplets and negative for ice plates. The sensitivity of the polarized radiance to the crystal habit (hexagonal plates, columns, polycrystals, etc.) has been studied in Chepfer et al. (1998). In practice, the information contained in the two scattering angle ranges are complementary, since normally POLDER cannot observe the full range of scattering angles depending on the respective orientations of the sun and satellite track. In practice, the use of any of these two ranges of scattering angles can discriminate the cloud thermodynamical phase for most of the actual POLDER viewing geometry.

4. Lidar network and dataset

The current validation of cirrus cloud-top height and thermodynamical phase takes advantage of lidar measurements conducted at different sites during the POLDER-1 operational phase.

a. The lidar network

The ground-based lidar network involves four geographically diverse sites: two are located in the Northern

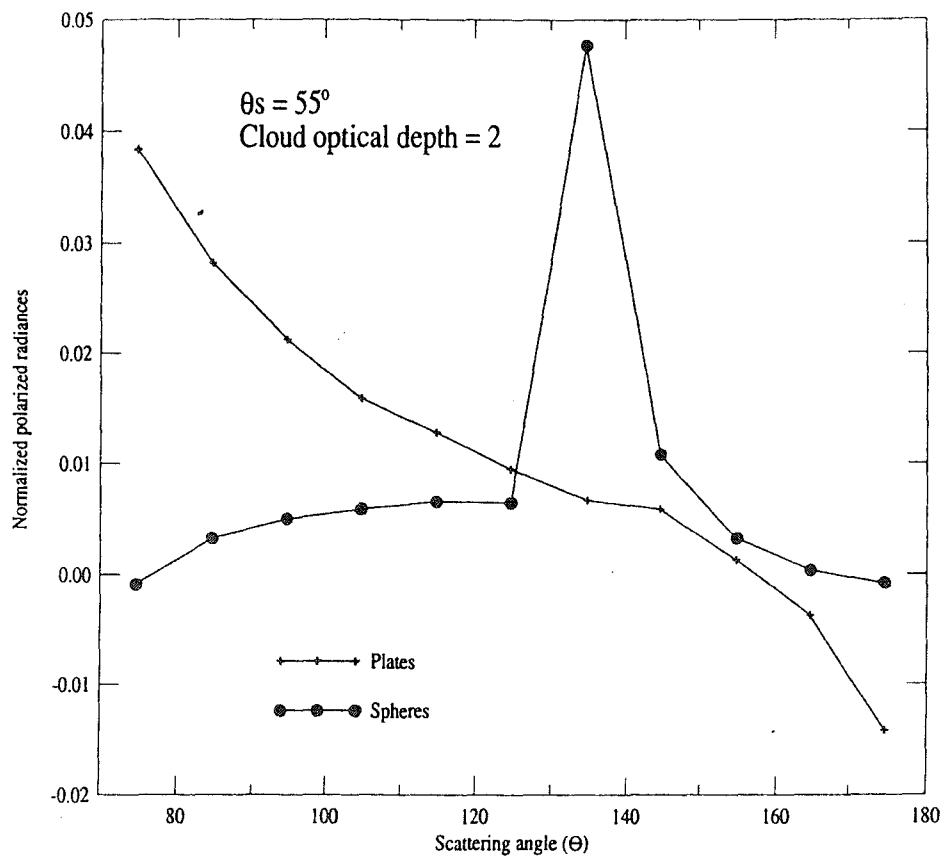


FIG. 1. Bidirectional polarized radiances simulated for a water cloud composed of spherical particles (large dot), and for an ice cloud composed of nonspherical particles (cross). The bidirectional polarized radiances are plotted as a function of the scattering angle.

Hemisphere, and two are in the Southern Hemisphere. The characteristics of the different sites and the parameters of the lidar systems are presented in Table 2. Two of them are devoted to research activities (Palaiseau, Buenos Aires) and are operated at the convenience of the experimenters for the purpose of research work, whereas the other two are new micropulse (MP) lidar systems (Spinhirne et al. 1995). The MP lidar systems operate hands-off and continuously at currently two U.S. Department of Energy Atmospheric Radiation Measurement (ARM) sites in central Oklahoma and Manus Island, Pa-

pua New Guinea. The four lidars probe the atmosphere in the visible at approximately the same wavelength: 532 and 523 nm. The time resolution is better for research lidar than for the MP lidar for which 1-min signal integrations are recorded. In addition, these lidars can penetrate thicker clouds, and one of them has depolarization capability to discriminate between spherical and nonspherical particles. In most cases the lidar depolarization ratio $\Delta = S_p/S_s$ is larger than 0.2 in cirrus clouds, where S_p and S_s are the lidar signals with perpendicular and parallel polarizations, respectively (Sassen 1991).

TABLE 2. Lidar sites and characteristics of four ground-based lidar systems.

	Palaiseau, France	Oklahoma	Manus Island, Papua New Guinea	Buenos Aires, Argentina
Lat	48.43°N	36.61°N	2.06°S	34.60°S
Long	2.15°E	97.41°W	147.44°W	58.50°W
Altitude	115 m	315 m	5 m	0 m
Environment	Continental suburban	Continental Great Plains	Pacific Ocean	Coastal Urban
Lidar type	Research	Micropulse lidar	Micropulse lidar	Research
Wavelength	0.532 μm	0.523 μm	0.523 μm	0.532 μm
Energy per pulse	150 mJ	10 μJ	10 μJ	200 mJ
Divergence	0.3 mrad	0.1 mrad	0.1 mrad	0.3 mrad
PRF	20 Hz	2500 Hz	2500 Hz	10 Hz
Receiver diameter	60 cm	20 cm	20 cm	50 cm
Field of view	2 mrad	0.1 mrad	0.1 mrad	2 mrad
Depolarization capability	Yes	No	No	No
Institution	LMD	ARM	ARM	CEILAP

TABLE 3. Cases selected for validation.

	Palaiseau, France	Oklahoma	Manus Island, Papua New Guinea	Buenos Aires, Argentina
Period of observation	Feb 1997–Jun 1997	Oct 1996–Jun 1997	Apr 1997	Nov 1996–Jan 1997
ADEOS overpass	1000–1100 UTC	1700–1800 UTC	1900–2000 UTC	1400–1500 UTC
No. of cases	6	140	9	1
Single semitransparent cirrus layer	2	21	1	1
Single thick cirrus layer	0	8	1	0
Low-level cloud	4	111	7	0

The different sites include a radiosonde capability and others remote sensors. In the current study the temperature profiles are used to complement the lidar measurements in order to derive the cloud phase (see section 7).

The distribution of the four ground-based lidar stations in the two hemispheres and in different latitude bands allows for some account of the natural geographical variability of cirrus clouds. The optical and structural properties depend on the conditions of formation and maintenance, which in turn depend very much on key meteorological variables, for example, temperature, humidity, wind shear, and seeding by icing cloud nuclei [Sassen et al. 1995; see the special section Subsonic Aircraft: Contrail and Cloud Effects Special Study (SUCCESS 2), in *Geophysical Research Letters*, 1998, Vol. 25, No. 10].

b. Selected cases for validation

The entire lidar network collected 259 periods of observations coinciding with POLDER-1 overpasses (see section 5) from 1 November 1996 until 30 June 1997. From this sample, final case selection for validation purposes was conducted according to the following criteria: (i) the lidar measurements were performed during at least 1 h before and after (± 1 h) the satellite ADEOS overpass time, and (ii) multilayers (i.e., occurrence of broken low clouds and high clouds) and highly heterogeneous cirrus clouds were not considered.

The total number of cases selected for validation at each site varies in large proportion, between operational and research sites, with the ARM sites providing the bulk of the 49 cases out of 156 ultimately used. The cases are divided into three categories: (i) single semitransparent cirrus cloud layer that can be penetrated by any lidar in order to retrieve the cloud boundaries (cloud base and top) at the same time (i.e., an approximate signal-to-noise ratio $SNR > 3$ at cloud top), (ii) single thick high layers such that only the cloud base can be observed by lidar, and (iii) mid- and low-level clouds. Table 3 summarizes the results of the selection process.

c. Inversion methods for lidar data

The lidar measurements collected at the different sites were each processed identically as follows.

- 1) We develop our own algorithm to retrieve the cloud boundaries from the range-corrected lidar signal, that

is, $R^2 S(R)$, where R is the lidar range and S the total lidar signal, using thresholding sets at $SNR > 3$. The cloud-top and -base altitude uncertainty is ± 30 m for the research lidars and ± 150 m for the MP lidars. (Standard MP lidar cloud boundary data are also available from the open ARM data system but do not currently identify the true cloud top.)

- 2) The cloud phase is assessed from cloud-height and temperature profiles recorded by radiosonde. We considered the formation of ice clouds to occur at temperatures less than -40°C . In addition, we used the lidar depolarization ratio (Δ) for measurements collected in Palaiseau.
- 3) The cloud optical depth estimations are obtained in four steps as follow: 1) the lidar signals are normalized to the backscatter signal from molecules assuming a scattering ratio equal to 1.1 or less in clear zones above and/or below the cirrus cloud deck, 2) a mean backscatter-to-extinction ratio k is derived from at least six time samples every 10 to 15 min (Young 1995), 3) a forward solution of the lidar equation allows for determination of a vertical profile of apparent extinction coefficient (Fernald et al. 1972) α_a and so an apparent optical depth δ_a , and 4) this apparent optical depth is corrected for multiple scattering for research lidars; the true optical depth is $\delta = 2\delta_a$ (Nicolas et al. 1997). The correction does not apply to MP lidar data, for they operate with a narrow field-of-view transceiver (see Table 2). The overall uncertainty in optical depth is on the order of 20%–30%. In the case of thick cirrus clouds, when the cloud top cannot be detected in a reliable way, the optical depth is given a minimum value $\delta = 1.5$ for MP lidars and $\delta = 3$ for research lidars (thanks to the multiple scattering effects). It correspond to a minimum measurable value of $T^2 = 0.05$.

5. Implemented procedure for validation

At present, the comparison bears on cloud-middle height and cloud phase for the cirrus cloud cases selected according to section 4. A major source of uncertainty and discrepancy may come from different footprints for POLDER-1 and ground-based lidars. POLDER horizontal resolution for a single pixel is about 6 km \times 7 km at nadir whereas the lidar beam at cirrus cloud level is several meters or tens of meters depending

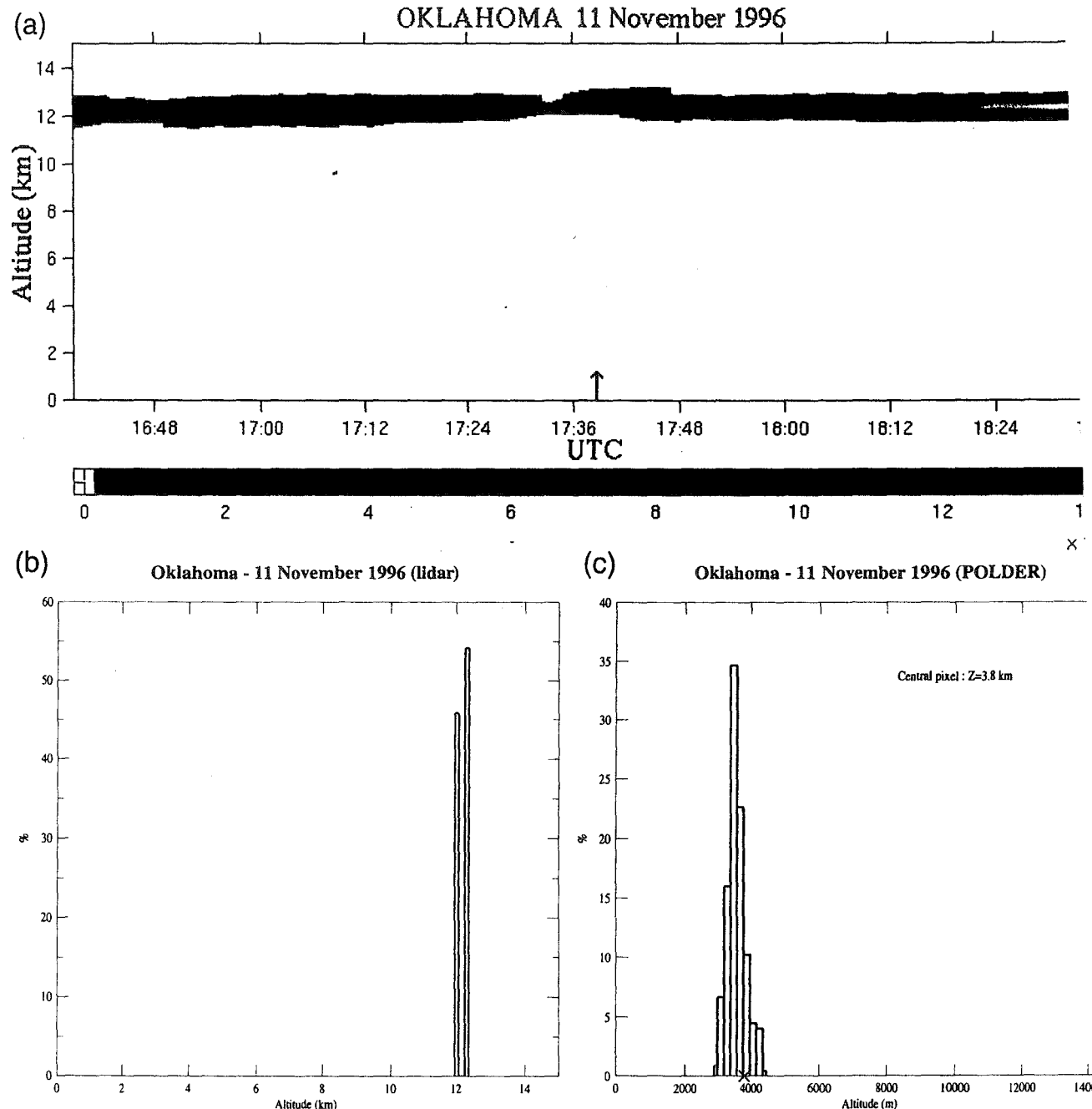


FIG. 2. Cloud altitude for 11 Nov 1996 at the Oklahoma CART site. (a) Cloud altitude deduced from lidar measurements as a function of time. (b) Histogram of cloud altitude inferred from lidar measurements. (c) Histogram of cloud altitude inferred from POLDER data in an area of 15×15 pixels around the lidar site.

on the system. In order to account for such a difference in footprint we proceeded in two steps. (i) First, we take the cloud-top height and cloud phase computed for a single POLDER pixel corresponding to lidar site and compare with the lidar values at the time of satellite overpass. (ii) Second, we compare the POLDER information in a 15×15 (or 125 total) pixel area (at least $100 \text{ km} \times 100 \text{ km}$ at nadir, and more in other configurations) to the values derived by lidar during a 2-h time period ($\pm 1 \text{ h}$) about the time of satellite overpass.

If the lidar time series show a strong variability or when the POLDER-1 histogram indicates a highly dis-

persed dataset, then the cloud case is not accounted in the final result.

6. Results for cirrus cloud altitude

a. Selected examples

Figure 2 shows a comparison between a lidar time series recorded at the Oklahoma Cloud and Radiative Testbed (CART) site on 11 November 1996 (panel a) and lidar histogram for cloud middle height (panel b) with a POLDER-1 histogram for cloud height (panel c).

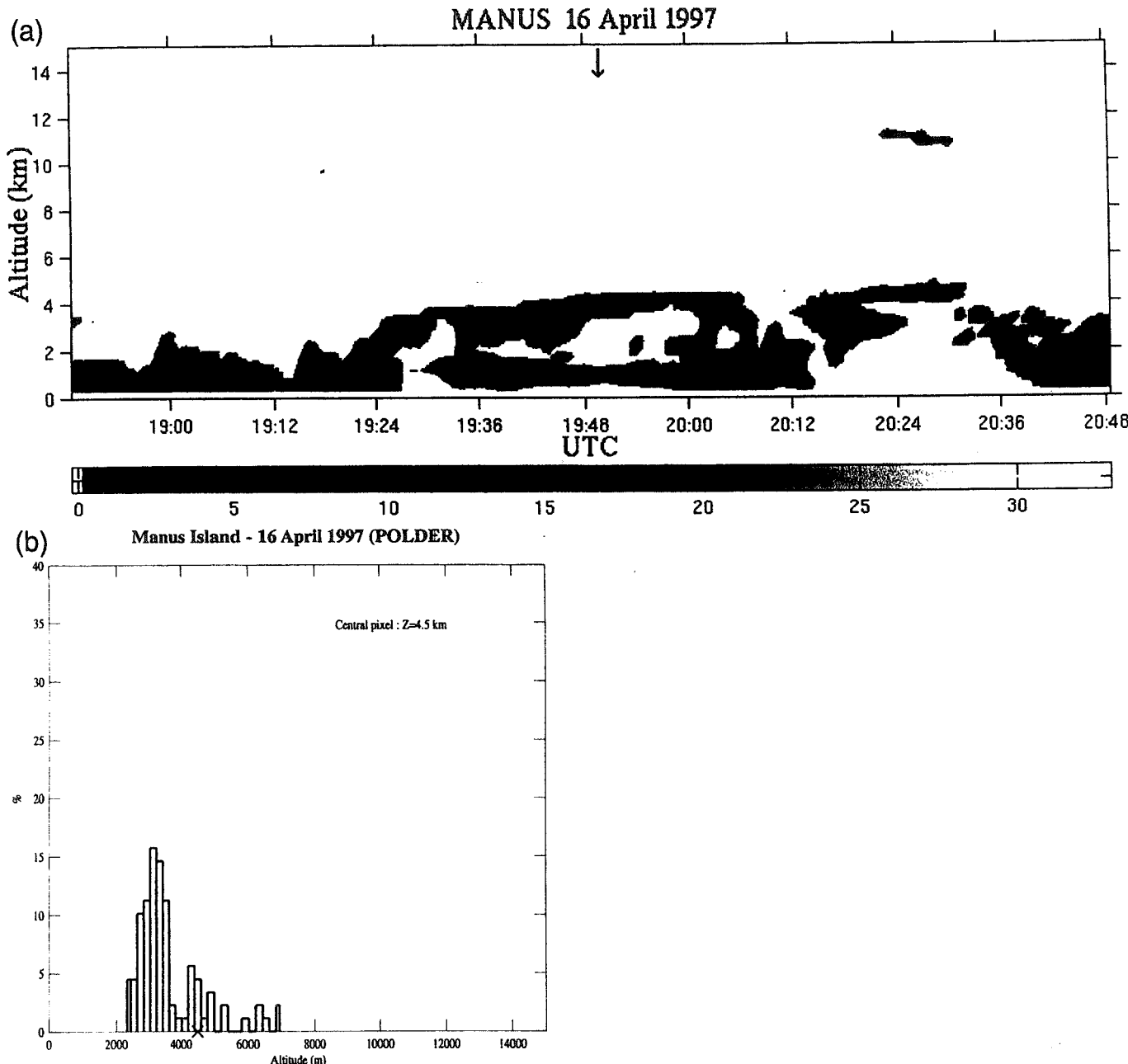


FIG. 3. Cloud altitude for 16 Apr 1997 at the Manus Island site. (a) Cloud altitude deduced from lidar measurements as a function of time. (b) Histogram of cloud altitude inferred from POLDER data in an area of 15×15 pixels around the lidar site.

The time of POLDER-1 overpass, 1738 UTC, is indicated by a vertical arrow in Fig. 2a. The height assigned on the POLDER-1 pixel matching the lidar site is 3.8 km, and it is marked by a cross in Fig. 2c. The cloud height derived from POLDER-1 data makes use of the Rayleigh pressure method (see section 3). The lidar time series shows a single cirrus cloud layer between 11- and 13-km altitude. The layer is stable during two hours as required for a reliable validation (see section 5). The large difference in height may be due to a small optical depth as indicated by lidar measurements ($\delta = 0.2$ at 1738 UTC) (see discussion in section 6c).

Figure 3 shows a comparison from Manus Island data on 16 April 1997. The low-level cloud cannot fully transmit the lidar beam, and the highest cloud layer seen

is 4-km altitude (Fig. 3a). POLDER-1 overpassed Manus Island at 1949 UTC. The altitude inferred from POLDER data using the Rayleigh pressure method (presented in Fig. 3b) ranges between 2.5 and 7 km. The height assigned on the POLDER-1 pixel matching the lidar site is 4.5 km; it is marked by a cross in Fig. 3b. The pixels associated with the highest values of altitude correspond to cloud layers that cannot be detected by the laser beam. From lidar analysis, the cloud optical depth is higher than 1.5.

Figure 4 shows a comparison conducted for data from Oklahoma on 26 January 1997. The cloud bottom is located at 6-km altitude as measured by lidar (Fig. 4a). The MP lidar cannot penetrate such a thick cloud so the cloud top is not determined. POLDER-1 overpassed

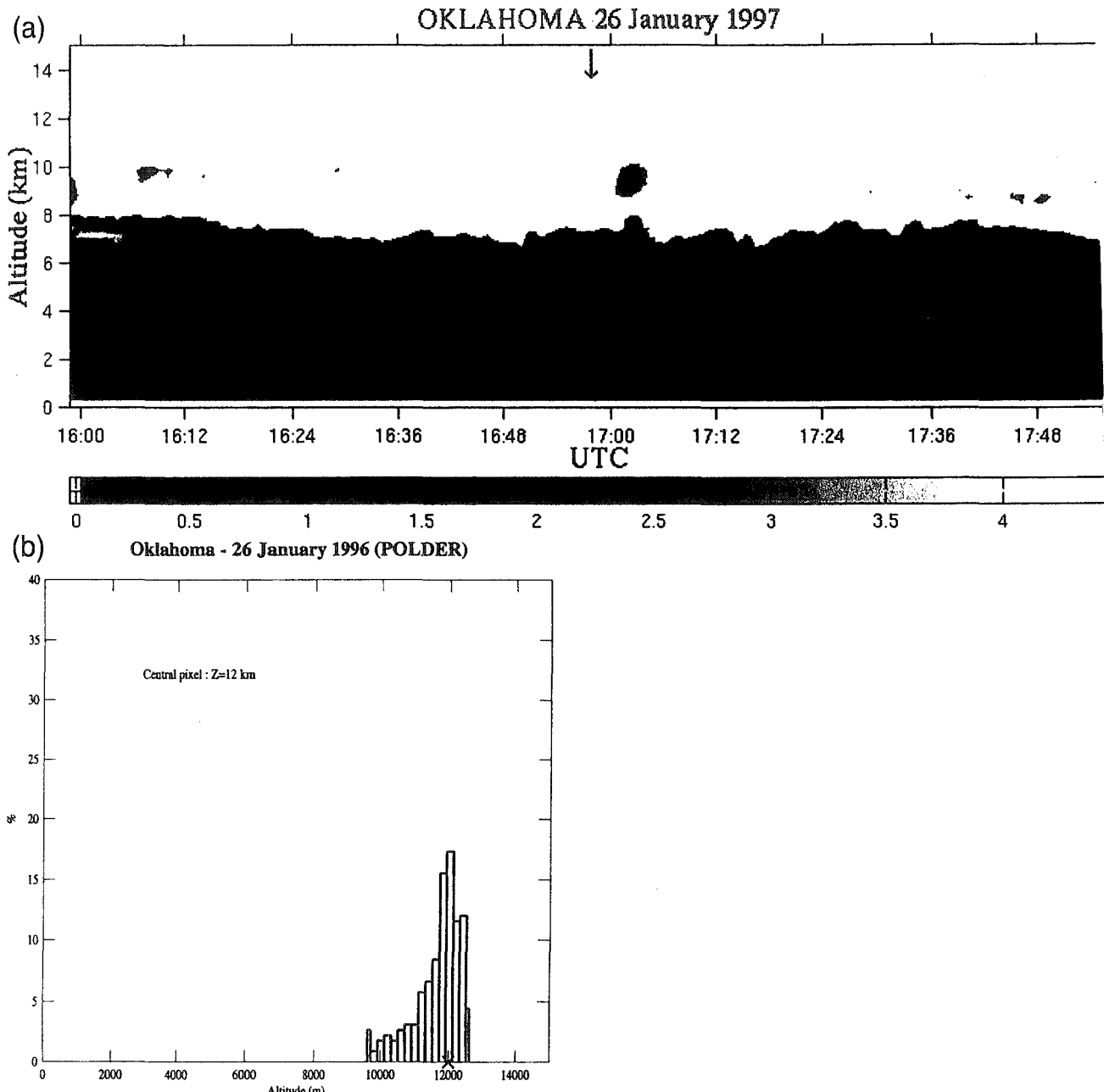


FIG. 4. Cloud altitude for 26 Jan 1997 at the Oklahoma CART site. (a) Cloud altitude deduced from lidar measurements as a function of time. (b) Histogram of cloud altitude inferred from POLDER data in an area of 15×15 pixels around the lidar site.

Oklahoma at 1659 UTC. The altitude inferred from POLDER data using the Rayleigh pressure method is presented in Fig. 4b; it ranges between 10 and 12 km. In this case POLDER-1 provides a cloud altitude higher than the one indicated by the lidar. The difference is due to the presence of an optically thick low-level cloud through which the laser beam cannot pass; hence, the lidar does not see the higher cloud layers detected with POLDER.

b. Analysis of 34 cases

A total of 34 cases of cirrus cloud have been analyzed following the methodology presented above. The height

difference between the cloud-middle altitude measured by lidar and the cloud height inferred from the POLDER-1 data on the pixel corresponding to the lidar site is plotted in Fig. 5 as a function of cloud optical depth derived from lidar measurements. When the lidar cannot reach the cloud top the cloud optical depth has been set equal to 1.5 for MP lidars. No measurements on the cirrus cloud taken by research lidars have been used so far for the validation. Figure 5 clearly shows that the lower the cloud optical depth the bigger the bias. POLDER underestimates the cloud height for low optical depth while the lidar may underestimate the height for large optical depth when POLDER makes a false estimate.

CLOUD ALTITUDE : Rayleigh method (POLDER) / Lidar

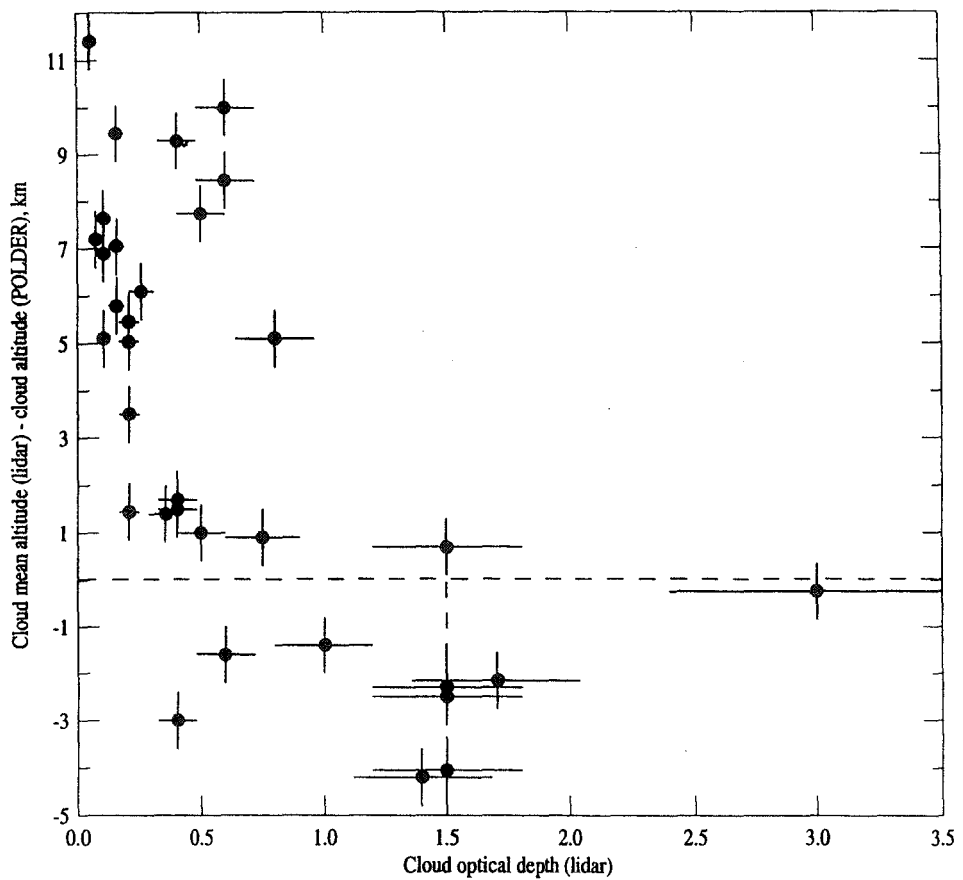


FIG. 5. Differences between cloud altitude inferred from POLDER and cloud-mean altitude measured with lidar as a function of the lidar cloud optical depth. Error bars correspond to the uncertainty on the lidar optical depth ($\pm 20\%$), and to the sum of uncertainties on lidar and POLDER cloud-top altitudes.

c. Discussion of the results

In order to understand the possible limitation of the Rayleigh pressure method used in POLDER inversion to infer cirrus cloud height, it was applied to simulated POLDER polarized radiances at 443 and 864 nm for a prescribed atmosphere. The polarized radiances at the top of the atmosphere are calculated using an adding-doubling code (de Haan et al. 1986). The atmosphere is composed of three layers: (i) air molecules between the surface and 400 hPa, (ii) air molecules and ice particles between 300 and 400 hPa, and (iii) air molecules above 300 hPa. We considered two different types of ice particles: hexagonal plates and polycrystals. A ray tracing code accounting for Fraunhofer diffraction in the forward direction is used to compute the scattering matrix of hexagonal plates (Brogniez 1988; Chepfer 1997), while the scattering matrix for polycrystals is taken from Macke et al. (1996).

The simulations were conducted for different optical depths and various solar zenith angles. Figure 6a displays the retrieved cloud height in pressure units as a function of cloud optical depth, considering a solar zenith angle $\theta_s = 30^\circ$ for plates (solid line), and for poly-

crystals $\theta_s = 30^\circ$ (dashed line with open circle) and $\theta_s = 60^\circ$ (dashed line with cross). In all cases the POLDER polarized radiances are simulated in the principal solar plane for a relative azimuth angle $\Delta\Phi = 0$ (where $\Delta\Phi = \Phi_s - \Phi_v$; Φ_s and Φ_v are, respectively, the azimuth solar angle and the azimuth viewing angle). Figure 6a shows that the height is underestimated for moderate optical depth as the bias is nearly zero when $\delta > 1.5$ –3 for cloud-base height, and when $\delta > 3$ –4 for cloud-top height, depending on the crystal types and experimental conditions. The sensitivity to ice particle shape is more than 100 hPa for solar zenith angle of 30° . The bias is larger at small solar angle for which the transmission is comparatively larger.

Figures 6b and 6c display the cirrus cloud height as a function of $\Delta\Phi$ with values ranging from 0° to 80° . The simulations are conducted for two values of the optical depth equal to 1 (Fig. 6b) and 4 (Fig. 6c), for the two ice crystal shapes used above and the same solar angles. Those figures show that the restitution of the cloud pressure using the Rayleigh pressure method is weakly sensitive to the azimuth viewing angle of POLDER. Figure 6b shows that the results and bias do not

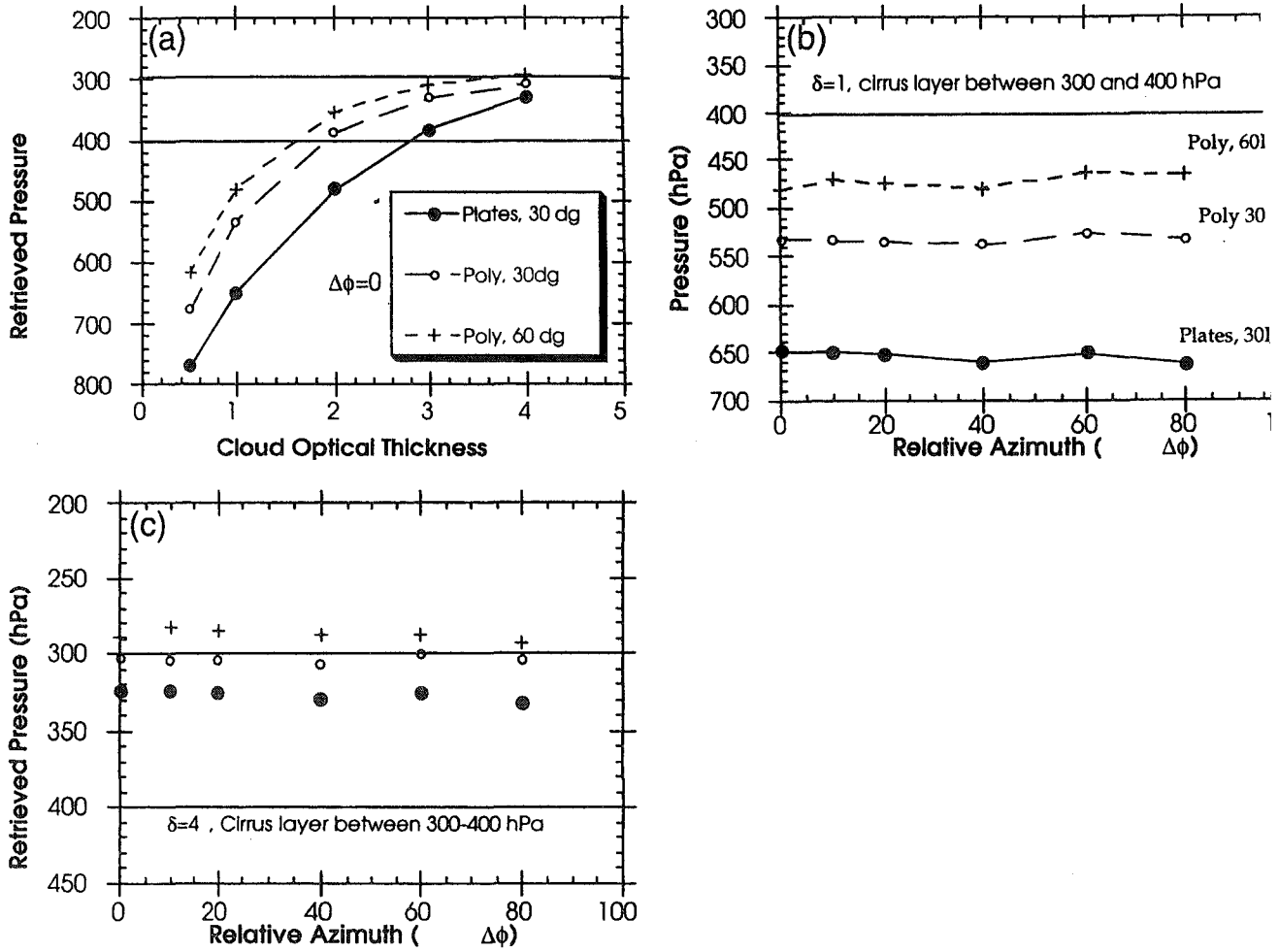


FIG. 6. (a) Simulations of the difference between the altitude of a cloud and the altitude deduced from the polarized bidirectional reflectance in the solar principal plane, as a function of the cloud optical depth for a solar zenith angle $\theta_s = 60^\circ$, and a solar zenith angle $\theta_v = 60^\circ$. Simulations of the cloud pressure retrieved with the Rayleigh pressure method for a cirrus cloud located between 300 and 400 hPa, v an optical depth of (b) $\delta = 1$ and (c) $\delta = 4$, respectively, as a function of the relative azimuth angle ($\Delta\Phi$).

depend on the relative azimuth angle, but rather on the crystal types and solar angle. Figure 6c shows a fair agreement between the input and outputs of the simulation for thick optical depth.

A conclusion drawn from these results is that the Rayleigh pressure method cannot be used for cirrus clouds as it stands and needs to account for actual optical depth. However, a threshold can be set for a reliable application of the method for cloud-top retrieval by considering Figs. 6a and 6b. For cirrus clouds composed of hexagonal plates with an optical depth larger than 4 or for cirrus cloud composed of polycrystals with an optical depth larger than 3, these values correspond to a hemispherical reflectance of 30%. At a later stage, the POLDER algorithm could be improved by an empirical correction accounting for the solar angle and hemispherical reflectance measured by POLDER.

7. Results for cloud phase

The cloud phase inferred from the POLDER-1 polarized radiances is compared with the cloud tempera-

ture assessed by radiosonde and lidar, assuming that only ice particles are present for temperatures lower than -40°C . This threshold value is considered safe for meteorological conditions. Clouds located at temperature ranging between -20° and -40°C can be of mixed phase with liquid and ice particles. We derived the cloud thermodynamical phase inferred from POLDER in a 3×3 pixel (or $20 \text{ km} \times 20 \text{ km}$) area around the lidar site for three ranges of cloud temperatures (i) $T < -40^\circ\text{C}$, (ii) $-40^\circ\text{C} < T < -20^\circ\text{C}$, and (iii) $-20^\circ\text{C} < T < 0^\circ\text{C}$.

a. Selected examples

Figure 7 shows the cloud boundaries derived by lidar and the corresponding temperature range for the case of 28 February observed at Palaiseau. The cloud is located between 9- and 12-km altitude as measured with the lidar (Fig. 7a). ADEOS overpassed Palaiseau at 1022 UTC. The cloud temperature ranges between -45° to -68°C (Fig. 7b). The cloud phase is ice as inferred from an area of 3×3 POLDER-1 pixels around the site. Figure 8 shows a similar example observed at the sam-

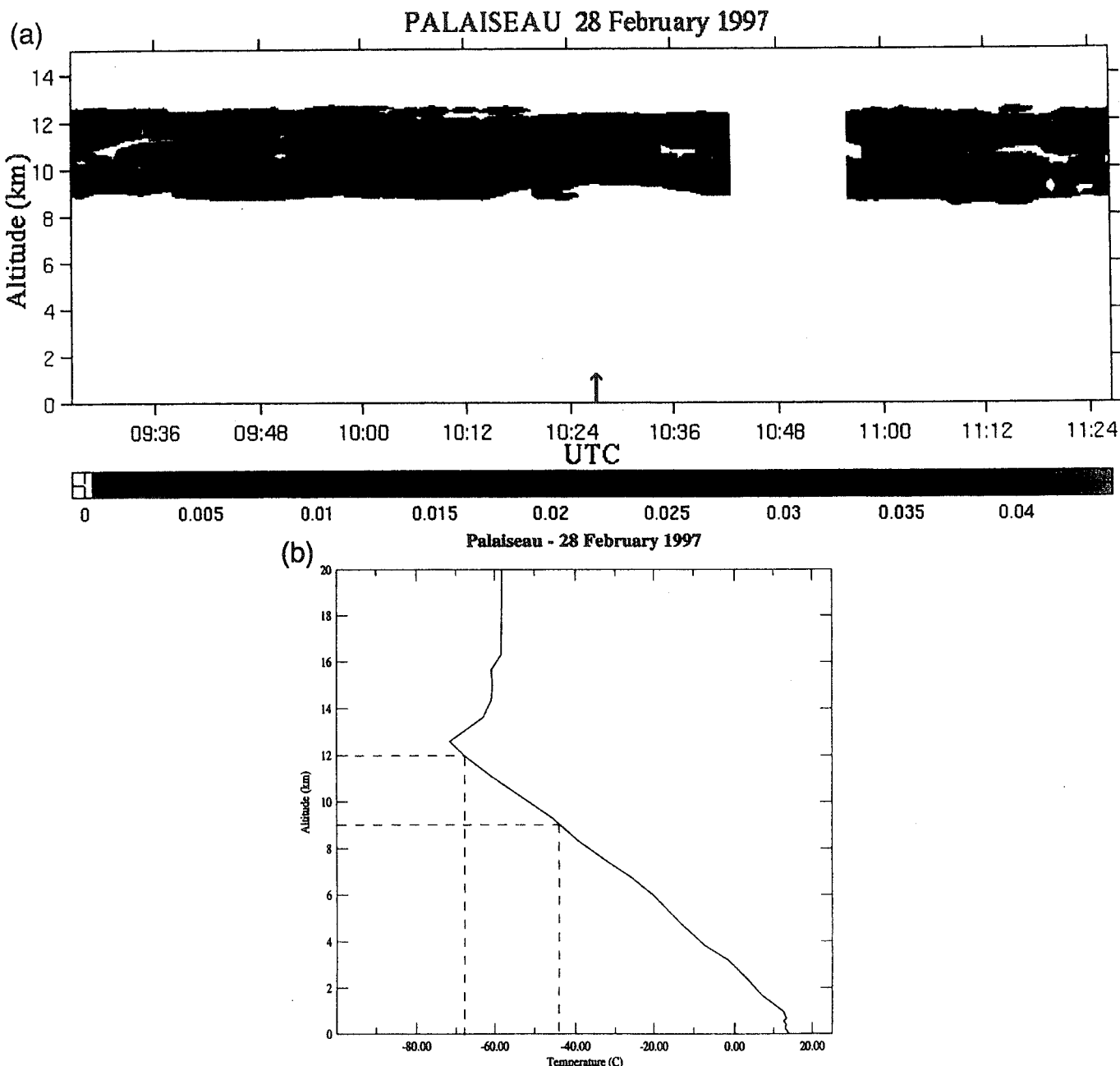


FIG. 7. (a) Lidar signal measured on 28 Feb 1997 at Palaiseau as a function of time. (b) Temperature profile in the atmosphere obtained with radiosonde.

location on 4 June 1997. The cloud is located between 8.5 and 11.8 km as measured with the lidar (Fig. 8a). ADEOS passed over Palaiseau at 1051 UTC. The cloud temperature ranges between -42° and -64°C (Fig. 8b) and the cloud phase is ice as inferred from an area of 3×3 POLDER-1 pixels around the site. Figure 9 shows an example observed at Manus Island on 18 April 1997. The cloud altitude ranges between 6 and 10 km (Fig. 9a). ADEOS overpassed Manus Island at 2049 UTC. The cloud temperature varies between -5° and -32°C , and the cloud phase is liquid as inferred from an area of 3×3 POLDER-1 pixels around the site. Figure 10 presents a cloud observed on 6 December 1996 in Oklahoma. The cloud sample consists of two layers

ranging from 6 to 12 km (Fig. 10a). ADEOS overpassed the Oklahoma site at 1807 UTC. Cloud temperatures range between -18° and -65°C and cloud phase is mixed liquid and ice as inferred from an area of 3×3 POLDER-1 pixels around Oklahoma (seven pixels are identified as ice and two pixels as liquid phase).

b. Analysis of 32 cases

In order to conduct a reliable validation of cirrus cloud thermodynamical phase by POLDER-1 we selected cases where no low clouds were present in the lidar time series, and where the temperature at the cloud lower boundary is lower than -40°C . Accordingly, only

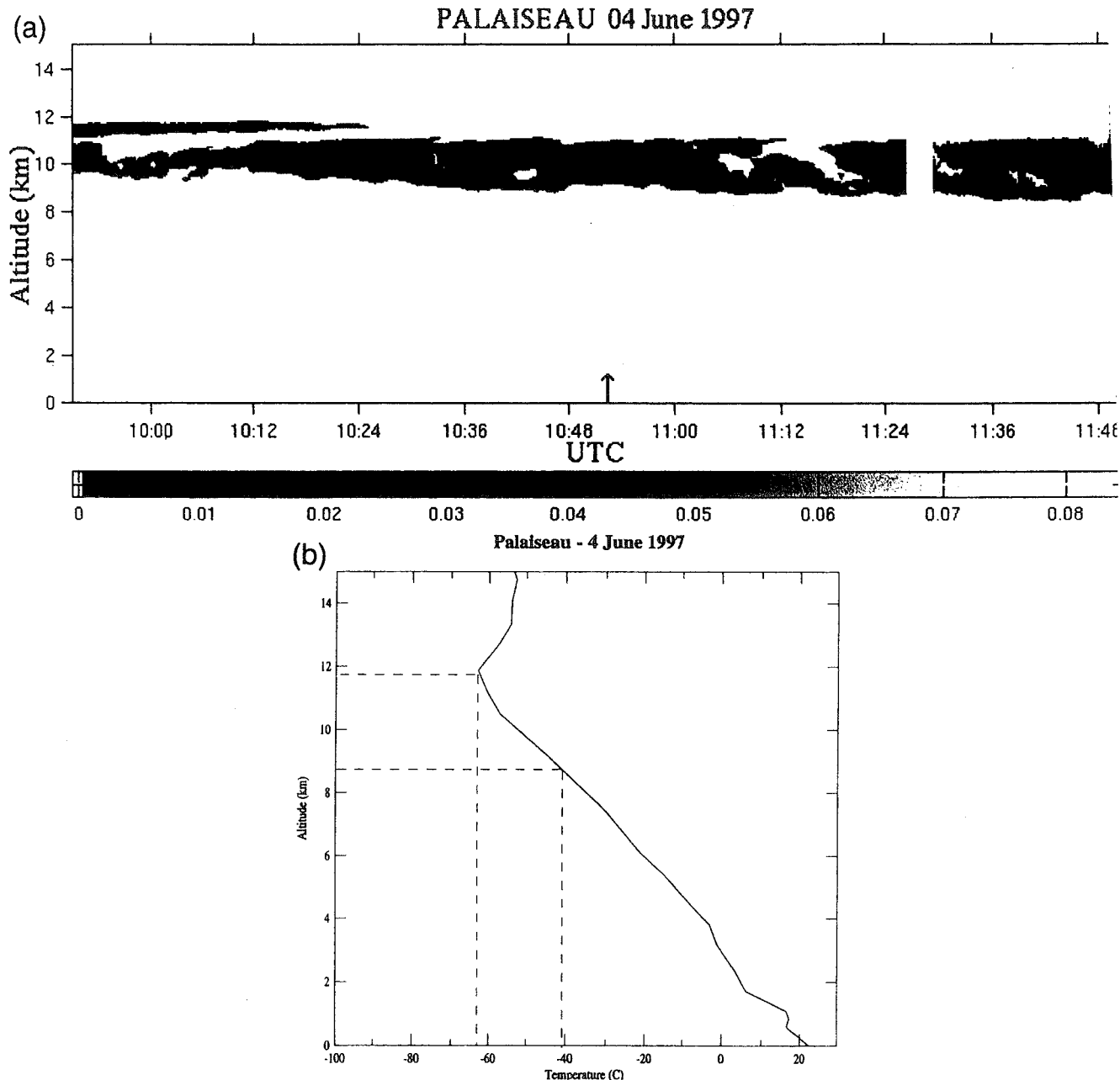


FIG. 8. (a) Lidar signal measured on 4 Jun 1997 at Palaiseau as a function of time. (b) Temperature profile in the atmosphere obtained with radiosonde.

32 cases out of the possible 150 are used in these study where 30 out of 32 are identified as ice (in all nine pixels) by POLDER and two as mixed clouds (ice and liquid water). Ice or liquid water means that all nine pixels identify ice or liquid water, respectively, while a mixed cloud is concluded when a single pixel contains information different from the others. The results are summarized in the first column of Table 4. For high clouds, the discrepancy is 6%.

c. Preliminary climatology derived from POLDER-I

The reliability of the present methodology is illustrated by the various examples presented in Figs. 7, 8,

9, and 10, and the results of the comparison for high clouds, which give a percentage of discrepancy of 6% even if our dataset is limited at present. Since we are interested in a cloud global climatology emphasizing ice/liquid water discrimination, we derive such a climatology using all 150 cases. The results are presented in Table 4. The cloud thermodynamical phase determination with POLDER concerns mainly the higher layers of the cloud, whereas the cloud altitude observed with the lidar mainly detects the cloud base (when the cloud layer is thick or multiple). Nevertheless this preliminary climatology is consistent with other cloud thermodynamical phase determinations inferred from lidar measurements (Sassen et al. 1998; Sassen 1991; Sassen

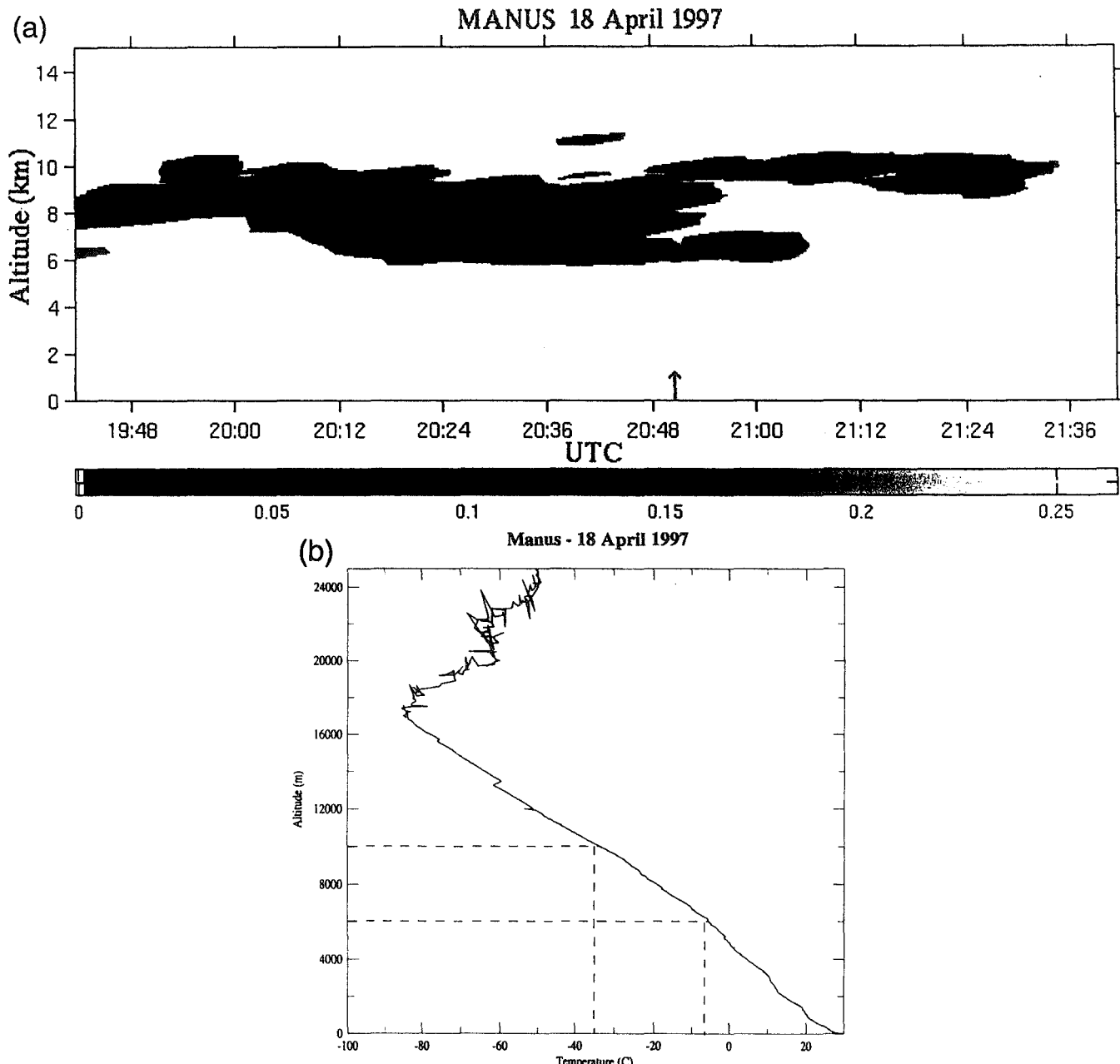


FIG. 9. (a) Lidar signal measured on 18 Apr 1997 at the Manus Island site as a function of time. (b) Temperature profile in the atmosphere obtained with radiosonde.

et al. 1979a,b) or in situ observations collected during intensive field experiments such as First International Satellite Cloud Climatology Project (ISCCP) Regional Experiment (FIRE) I and II (see special issues in *Monthly Weather Review*, 1990, Vol. 118, No. 11 and *Journal of the Atmospheric Sciences*, 1992, Vol. 52, No. 23) and SUCCESS 2.

8. Conclusions and future work

The main purpose of the current study was to conduct a validation of cirrus clouds parameters, that is, height and thermodynamical phase inferred from polarized POLDER-1 data collected from 1 November 1996 until 30 June 1997. The validation makes use of four ground-

based lidar systems geographically distributed in latitude. The validation calls for cloud altitude as measured by lidar and temperature profile by the radiosonde. The methodology proposed is robust and reliable because range measurements by lidar are accurate and reliable. The cloud phase has been assessed using a temperature criterion in which presence of ice is asserted as certain for $T < -40^{\circ}\text{C}$.

A validation of cloud height inferred from POLDER-1 using the so-called Rayleigh method has been conducted for 34 cases. It is shown that POLDER underestimates the cloud height for low values of cloud optical depth. A simulation confirms this result; it has been shown that a fair agreement is obtained when the optical depth is larger than 3, depending on crystal shape and experi-

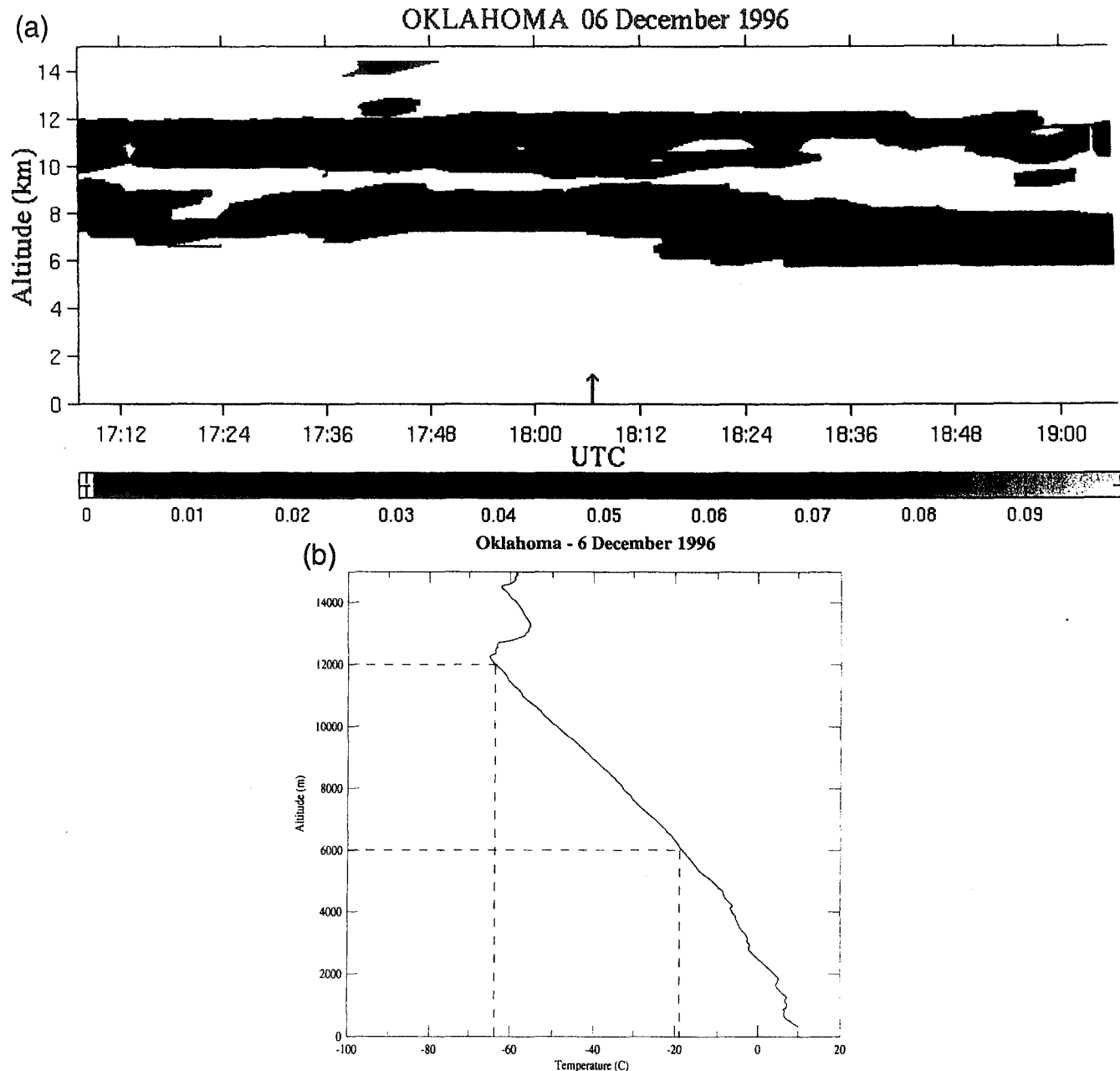


FIG. 10. (a) Lidar signal measured on 6 Dec 1996 at the Oklahoma CART site as a function of time. (b) Temperature profile in the atmosphere obtained with radiosonde.

TABLE 4. Cloud thermodynamical phase derived from POLDER-1 as a function of cloud temperature obtained from radiosonde data and collocated lidar height assignment. The cloud temperature is divided into three bins for temperature ranging from below -40°C , between -40° and -20°C , and above -20°C ; the cloud thermodynamical phase is divided into three categories as ice only, mixed phase or ice and liquid water, and liquid water only. A total of 150 cirrus cloud cases have been selected and analyzed.

Cloud thermodynamical phase	-40°C			Total
	$T < -40^{\circ}\text{C}$	$< T < -20^{\circ}\text{C}$	$T > -20^{\circ}\text{C}$	
Ice	30	22	28	80
Mixed phase	2	8	15	25
Liquid water	0	3	43	45
Total	32	32	86	150

mental condition (i.e., solar angle). Comparisons between POLDER-1 and lidar measurements, and simulations allow us to conclude that the Rayleigh pressure method is satisfactory only for thick clouds. Simulations show that it corresponds to cloud with hemispherical reflectances higher than 30%. In the near future, the Rayleigh pressure method could be improved for thin cirrus clouds using an empirical correction based on radiative transfer calculations, accounting for actual solar angle and hemispherical reflectance measured directly by POLDER. The cloud phase inferred from POLDER-1 data has been compared with the prediction of a combination of temperature and lidar measurements. A validation conducted on 32 cases shows a good agreement.

The current validation relying on a lidar network

could be implemented in the near future for the validation of sensors in the framework of the National Aeronautics and Space Administration Earth Observing Satellite program, and for POLDER-2 to be launched on the *ADEOS-2* satellite in the summer of 2000. It is anticipated that the MP lidar network will be expanded and more research lidar systems could be involved. It is therefore realistic that a total of 20 lidar systems could be involved in a validation effort covering the two hemispheres and all latitude bands.

Starting from the current validation for the cloud phase, future work could be directed to the establishment of a large-scale climatology of particle shape and preferred orientation of ice particles. The sensitivity of polarization measurements to the shape of scatterers will be investigated further to estimate the ice particle shapes. In addition, the bidirectional polarized reflectances will be used to assess a possible preferred horizontal orientation of ice crystals in cirrus clouds.

Acknowledgments. The authors are very grateful to J. Hovenier and J. de Haan from the Free University of Amsterdam who gave us the opportunity to use their doubling-adding radiative transfer code. Thanks are also due to A. Macke for providing us with the polycrystals scattering matrix. This study has been supported by Centre National d'Études Spatiales (CNES). The results presented here were obtained using a subset of the overall dataset collected by the CNES's POLDER radiometer on board the NASA's *ADEOS*. The authors are very grateful to J.-M. Nicolas for the extraction of the useful POLDER data, and to J. Riedi for his participation in the analysis of POLDER cloud thermodynamical phase.

REFERENCES

- Brogniez, G., 1988: Light scattering by finite hexagonal crystals arbitrarily oriented in space. *Proc. Int. Radiation Symp.*, Lille, France, International Association of Meteorology and Atmospheric Physics, 64–67.
- Buriez, J. C., and Coauthors, 1997: Cloud detection and derivation of cloud properties from POLDER. *Int. J. Remote. Sens.*, **18**, 2785–2813.
- Chepfer, H., 1997: Etude théorique et expérimentale des propriétés optiques et radiatives des cirrus. Ph.D. dissertation, Université de Lille-1, 197 pp.
- , —, G. Brogniez, and Y. Fouquart, 1998: Cirrus cloud microphysical properties deduced from POLDER observations. *J. Quant. Spectrosc. Radiat. Transfer*, **30**, 375–390.
- , —, L. Sauvage, P. H. Flamant, V. Trouillet, and J. Pelon, 1999: Remote sensing of cirrus radiative parameters during EUCREX'94. Case study of 17 April 1994. Part II: Microphysical models. *Mon. Wea. Rev.*, **127**, 504–519.
- de Haan, J. F., P. B. Bosma, and J. W. Hovenier, 1986: The adding method for multiple scattering calculations of polarized light. *Astron. Astrophys.*, **183**, 371–391.
- Deschamps, P.-Y., F.-M. Bréon, M. Leroy, A. Podaire, A. Brickaud, J.-C. Buriez, and G. Sèze, 1994: The POLDER mission: Instrument characteristics and scientific objectives. *IEEE Trans. Geosci. Remote Sens.*, **32**, 598–615.
- Fernald, F. G., B. M. Herman, and J. A. Reagan, 1972: Determination of aerosol height distributions by lidar. *J. Appl. Meteor.*, **11**, 482–489.
- Goloub, P., J. L. Deuzé, M. Herman, and Y. Fouquart, 1994: Analysis of the POLDER polarization measurements performed over cloud covers. *IEEE Trans. Geosci. Remote Sens.*, **32**, 78–88.
- Hansen, J. E., 1971: Multiple scattering of polarized light in planetary atmospheres. Part I. The doubling method. *J. Atmos. Sci.*, **28**, 120–125.
- , A. Lacis, D. Rind, G. Russel, P. Stone, I. Fung, R. Ruedy, and J. Lerner, 1984: Climate sensitivity: Analysis of feedback mechanisms. *Climate Processes and Climate Sensitivity*, *Geophys. Monogr.*, No. 29, Amer. Geophys. Union, 130–163.
- Herman, M., J. L. Deuzé, C. Devaux, P. Goloub, F. M. Bréon, and D. Tanré, 1997: Remote sensing of aerosols over land surfaces, including polarization measurements: Application to some airborne POLDER measurements. *J. Geophys. Res.*, **102**, 17 039–17 049.
- Leroy, M., and Coauthors, 1997: Retrieval of atmospheric properties and surface bidirectional reflectances over land from POLDER. *J. Geophys. Res.*, **102**, 17 023–17 037.
- Liou, K. N., 1986: Influence of cirrus clouds on weather and climate processes: A global perspective. *Mon. Wea. Rev.*, **114**, 1167–1199.
- Macke, A., J. Mueller, and E. Raschke, 1996: Single scattering properties of atmospheric ice crystals. *J. Atmos. Sci.*, **53**, 2813–1825.
- Mishchenko, M. I., and L. D. Travis, 1997: Satellite retrieval aerosol properties over the ocean using polarization as well as intensity of reflected sunlight. *J. Geophys. Res.*, **102**, 16 989–17 013.
- Nicolas, F., L. R. Bissonnette, and P. H. Flamant, 1997: Lidar effective multiple-scattering coefficients in cirrus clouds. *Appl. Opt.*, **36**, 3458–3468.
- Sassen, K., 1991: The polarization lidar technique for cloud research: A review and current assessment. *Bull. Amer. Meteor. Soc.*, **72**, 1848–1866.
- , and K. N. Liou, 1979a: Scattering of polarized laser light by water droplet, mixed-phase and ice crystal clouds. Part I: Angular scattering patterns. *J. Atmos. Sci.*, **36**, 838–851.
- , and —, 1979b: Scattering of polarized laser light by water droplet, mixed-phase and ice crystal clouds. Part II: Angular depolarizing and multiple-scattering behavior. *J. Atmos. Sci.*, **36**, 852–861.
- , and Coauthors, 1995: The 5–6 December 1991 FIRE IFO II jet stream cirrus case study: Possible influences of volcanic aerosols. *J. Atmos. Sci.*, **52**, 97–123.
- , J. Campbell, and J. F. Barnett, 1998: Midlatitude cirrus clouds: A climatology from 10-year polarization lidar observation program at FARS. *Proc. 19th Int. Laser Radar Conf.*, Annapolis, MD, NASA, 45–46.
- Sauvage, L., H. Chepfer, V. Trouillet, P. H. Flamant, G. Brogniez, J. Pelon, and F. Albers, 1999: Remote sensing of cirrus radiative parameters during EUCREX'94. Case study of 17 April 1994. Part I: Observations. *Mon. Wea. Rev.*, **127**, 486–503.
- Spinhirne, J. D., A. R. Rall, and V. S. Scott, 1995: Compact eye-safe lidar systems. *Rev. Laser Eng.*, **23**, 112–118.
- van de Hulst, H. C., 1981: *Light Scattering by Small Particles*. Dover Publications, 470 pp.
- Vesperini, M., F. M. Bréon, and D. Tanré, 1999: Atmospheric water vapor content from spaceborne POLDER measurements. *IEEE Trans. Geosci. Remote Sens.*, **37**, 1613–1619.
- Young, S., 1995: Analysis of lidar backscatter profiles in optically thin clouds. *Appl. Opt.*, **34**, 7019–7031.

Comparison of POLDER cloud phase to radar measurements

(submitted to Geophysical Research Letters, april 2000)

Comparison of POLDER phase data to radar measurements

J. Riedi, P. Goloub,

Laboratoire d'Optique Atmosphérique, Université des Sciences et Technologies de Lille, France

R. T. Marchand

The Pacific Northwest National Laboratory, Richland WA, USA

Abstract

A method for cloud top thermodynamical phase determination has been developed using polarimetric data from the spaceborne instrument POLDER. The eight months of data, corresponding to the POLDER/ADEOS operational period, have now been processed. In the present study, data from the Millimeter Wave Cloud Radar (Southern Great Plain - ARM site) which are available for nearly the entire operational POLDER period, are analyzed. The sampling capabilities of the radar (data are acquired every 10 seconds) allow one to compare POLDER cloud top phase with cloud top pressure and temperature, derived from the MMCR data combined with radiosounding measurements.

This approach shows the consistency of the POLDER phase retrieval algorithm but also lead to interesting results concerning (i) the microphysic of cirrus clouds, and (ii) the dependency of cloud phase to pressure and temperature conditions. In particular, a temperature threshold at 240 K appears well defined and could help to predict occurrence of liquid or ice phase in models.

INTRODUCTION

The POLDER (POLarization and Directionality of the Earth Reflectances) instrument proved capabilities in deriving key information needed to improve our knowledge of clouds, radiation and climate interactions. Particularly, the potential of polarization measurements of the upward shortwave radiation to derive clouds information has been clearly demonstrated by spaceborne data analysis [*Bréon and Goloub, 1998*], [*Chepfer et al, 1998*], [*Goloub et al, 2000*]. From November 1996 to the end of June 1997, the satellite version of POLDER provided polarization measurements at the global scale. Thanks to its large field of view, the same pixel can be viewed under up to 14 directions. Cloud observations over a large range of scattering angles make possible the distinction between liquid and ice phase [*Parol et al, 1999*], [*Goloub et al, 2000*]. The eight months of data, corresponding to the POLDER operational period, have now been processed and are fully available to the scientist community.

A first analysis of the POLDER phase product, and comparison with ISCCP data [*Riedi et al, 2000*], have proven the global consistency and quality of the POLDER phase data set. In their studies, *Riedi et al* used a temperature threshold at 240K in order to select ice clouds in the ISCCP dataset, instead of 260K which was currently used [*Rossow et al, 1996*]. This value was retained at that time for consistency with previous analysis [*Hutchison et al, 1997*].

Our present approach consists in analyzing data from the Millimeter Wave Cloud Radar (MMCR instrument - Southern Great Plain - ARM site) for a long period. Nearly each day, POLDER phase information is compared to cloud top pressure and temperature which are derived from the MMCR data combined with radiosounding measurements. The POLDER method of cloud phase determination is based on near-infrared

cloud particles polarization signature, directly linked to cloud particles shape. This method does not require any assumption about relationship between cloud temperature and phase. Thus, it is thought that the joint analysis of radar and POLDER phase data could help in determining temperature and pressure criteria which are needed to establish a realistic parameterization of cloud phase in GCM's.

DATA

The temporal capabilities of the radar, together with the type of information it can provide, make this instrument particularly well adapted for a precise study of the cloud phase product. The operational POLDER phase product is delivered at a spatial resolution of about 60 km x 60 km. The level 1 data set has been processed in order to get the phase index and cloud top pressure at full resolution (6.2 km x 6.2 km) to enable precise comparison to be performed.

The Millimeter Wave Cloud Radar (MMCR) is a zenith-pointing radar that operates at a frequency of 35GHz and its main purpose is to determine cloud boundaries (e.g., cloud bottoms and tops, number of cloud layers). Here, we used the data from the MMCR instrument operating at the Southern Great Plain (SGP) Central Facility ($36^{\circ}37' N$, $97^{\circ}30' W$). Data are acquired every 10s which enables one to match the time of the POLDER observation very precisely. The data have been processed in order to get the cloud top altitude profile. Combined with radiosounding measurements, we obtained the cloud top temperature and pressure profiles. Also the temporal variability of the cloud cover is evaluated by considering data acquired half an hour before and after ADEOS overpass.

We have analyzed 7 months of observations where both MMCR and POLDER data are avail-

able. A total of 201 days of matching observations are available for the SGP site, from December 1996 to June 1997.

The figure 2 shows an example of data available for one particular day. The zone presented is much larger than what is effectively useful for the comparison to radar measurements, but this illustrates how the Rayleigh pressure information can be used for our purpose. The darker region corresponds to high thick clouds associated with low pressure of about 200 hPa. The increase of cloud top pressure from 400hPa up to 700hPa corresponds to a zone covered by thin cirrus (optical depth smaller than 2) for which Rayleigh pressure is known to over estimate the cloud top pressure. Finally, the zone located in the south east is covered by a mixture of cirrus clouds and clear sky, which explains the high pressure variability in that region.

Although the Rayleigh pressure can give useful information about the spatial variability of the cloud cover, the pressure and altitude derived using radar data are thought to be more reliable for our present study. The figure 2 (a) presents the altitude and temperature temporal profile available for that day. These are consistent with the ice phase retrieved by POLDER over the SGP-ARM site (cross on figure 2 (b)).

ANALYSIS

Cloud top phase algorithm accuracy

In order to assess the accuracy of the cloud top phase retrieval algorithm, we analyzed the distribution of cloud phase derived from POLDER data against cloud top temperature provided by the radar/radiosoundings.

Liquid and ice cases are mostly well separated by a threshold at about 240 K, but some of them remained ambiguous. We can distinguish three situations :

- i - Some ice phase cases were associated with temperature greater than 260 K. They have been

identified as low cloud edges. Actually, polarization is not saturated for small optical thickness so that polarization features, on which relies the phase retrieval, are not always well defined for cloud edges and very thin clouds. This is not really a problem when polarization signatures are integrated within 3x3 or 9x9 pixels, but clouds edges tend to be declared as ice clouds when data are processed at full resolution. This is one of the reason why future POLDER phase product should not be delivered at full resolution.

- ii - The second case concerns occurrences of liquid phase below 240 K. A detailed analysis of each case showed that they correspond to multi-layered clouds. A typical situation is shown on figure 3 for a case of thin cirrus overlaying low liquid clouds. On that day, the radar reports two cloud layers and the temperature associated is given for the top layer. Here, the smooth variation of Rayleigh pressure is characteristic of a cirrus with varying optical depth (as mentioned in section 2). The figure 4 presents three typical polarization signatures that can be observed when a cirrus overlays lower liquid clouds. If the cirrus optical depth is greater than 2, the polarization is saturated and the Rayleigh pressure is correctly retrieved (250hPa). Also, the polarization signature presents characteristic features of ice clouds (see figure 4c). As the cirrus optical depth decreases, the Rayleigh pressure increases (500hPa) and underestimates the cloud top altitude as seen by POLDER. At the same time the rainbow at 140°, characteristic of liquid phase (spherical particles), begins to appear due to underlying liquid clouds (Multilayer case on figure 4b). Finally, as the cirrus optical depth decreases further, the polarization signature tends to present only the characteristics features of liquid clouds (4a). Clearly, POLDER sees the liquid clouds through the thin cirrus, but the radar still reports a high and cold cloud layer, hence this apparently surprising result of liquid phase below 240 K.

- iii - The last and most surprising case was the occurrence of liquid phase at 210 K. These cases are not actually associated to liquid clouds, but to cirrus clouds with a particular microphysic. We present on figure 5, two polarization signatures of ice clouds and the associated viewing geometry. Models of ice clouds composed of monocrystalline hexagonal particles (plates, columns) present a positive polarization decreasing with scattering angle, and our initial phase algorithm is partly based on this hypothesis. Thus, if a cirrus exhibits a signature with an increasing polarization, it could be declared as liquid cloud when no other information are available. Typically, models of cirrus composed of polycrystals could produce such a behavior. This problem can be solved using a simple threshold test, but the fact is that this has never been pointed out during the validation process of the POLDER phase algorithm. This is a clear demonstration of the usefulness of radar data to conduct such studies and outlines the fact that these data should be used extensively for the purpose of validation.

Temperature dependency of cloud top phase

The mean hourly cloud top altitude derived from the radar is used to assess the POLDER phase index at the SGP. We will now focus on days which present a rather stable and homogeneous cloud cover so that problems due to cloud edges can be discarded. Also, we reprocessed POLDER data to take into account the microphysic findings previously mentioned.

We have selected cases which presented a cloud cover greater than 90% according to radar data, during a time range of one hour around the POLDER overpass. Then, the cloud top temperature and pressure were averaged during the same period, and the cloud phase index was evaluated on a 3×3 level 1 pixels zone above the SGP site. All cases presented either 100% of ice or liquid phase. The figure 6 shows the results of this analysis. Each of the 98 cases is plotted on a bi-

mensionnal (Temperature/Pressure) diagram.

A temperature threshold of 240 K appears well defined on this figure. Only 3 ambiguous cases remain, with one ice phase case at 270 K (cloud edge) and two liquid cases below 240 K (multi-layered cases).

These results, limited to the SGP site, should not be considered representative for all locations. However, the threshold of 240 K already mentioned in literature [Hutchison et al, 1997] seems to be justified by these results and comparisons of POLDER phase product with ISCCP data [Riedi et al, 2000] tend to confirm this finding. Also, it should be noticed that low and middle clouds associated with a temperature lower than 260K are declared as ice clouds in the present ISCCP dataset [Rossow et al, 1996]. Our present results tend to demonstrate that this threshold should be revised.

CONCLUSION

The comparisons of POLDER phase index to temperature data derived from completely independent radar measurements, show the interest of POLDER phase product to validate parameters which could be used in GCM. Particularly the temperature threshold at 240 K is remarkable.

Of course, the studies presented in this paper will be pursued as soon as more data will be made available. Particularly, the analysis of radar data from instruments located at various latitudes would be very interesting. They could also be used to validate future data which will be acquired and derived from the next POLDER instruments, the first one on ADEOS II, that will be launched at the end of year 2001, and the second one on PARASOL (2003) in conjunction with EOS-PM and Picasso/Cena.

Acknowledgments. The authors are very grateful to NASDA and CNES who provided the POLDER data. Thanks also to the ARM program for providing

ing the radar measurements and to Eugene Clothiaux (Penn State) and Jay Mace (University of Utah) who processed the data.

References

- Bréon, F.M., and P. Goloub, Cloud droplet effective radius from spaceborne polarization measurements, *Geophys. Res. Lett.*, 25, 1879-1882, 1998.
- Chepfer, H., G. Brogniez, and Y. Fouquart, Cirrus clouds microphysical properties deduced from POLDER observations, *J. of Quant. Spectr. and Rad. Transfer*, 30, 375-390, 1998.
- Chepfer, H., P. Goloub, J. Spinhirne, P. H. Flamant, M. Lavorato, L. Sauvage, G. Brogniez and J. Pelon, Cirrus cloud properties derived from POLDER-1/ADEOS polarized radiances : First validation using a ground-based LIDAR network, *J. Applied Meteor.* 39, 154-168, 2000.
- Goloub, P., M. Herman, H. Chepfer, J. Riédi, G. Brogniez, P. Couvert, G. Séze, Cloud thermodynamic phase classification from the POLDER spaceborn instrument, *to appear in J. Geophys. Res.*, 2000.
- Hutchison, K. D., B. J. Etherton, P. C. Topping, and H. L. Huang, Cloud top phase determination from the fusion of signatures in daytime AVHRR imagery and HIRS data, *Int. J. Remote Sensing*, 18, 3245-3262, 1997.
- Parol, F., J. C. Buriez, C. Vanbauce, P. Couvert, G. Sèze, P. Goloub, and S. Cheinet, First results of the POLDER "Earth Radiation Budget and Clouds" operational algorithm. *IEEE/Tran. Geosc. Rem. Sens.*, 1999.
- Riédi, J., M. Doutriaux-Boucher, P. Goloub and P. Couvert, Global distribution of cloud top phase from POLDER/ADEOS I. *Geophys. Res. Lett.*, , XXX, xxx-xxx, 2000.
- Rossow W. B., A. W. Walker, D. E. Beuschel and M. D. Roiter, International Satellite Cloud Climatology Project (ISCCP), Documentation of new cloud datasets, World Climate Research Program (ICSU and WMO), *Tech. Doc. WMO/TD 737*, 115 pp., 1996.

P. Goloub, and
J. Riedi, Laboratoire d'Optique Atmosphérique,
Université des Sciences et Technologies de Lille,
59655 Villeneuve d'Ascq Cedex, France,
Phone: (33) 3 20 33 61 85, Fax: (33) 3 20

43 43 42, (e-mail : riedi@loaser.univ-lille1.fr; goloub@loaser.univ-lille1.fr)

R. T. Marchand, The Pacific Northwest National Laboratory, Richland WA (e-mail : roj@.pnl.gov)

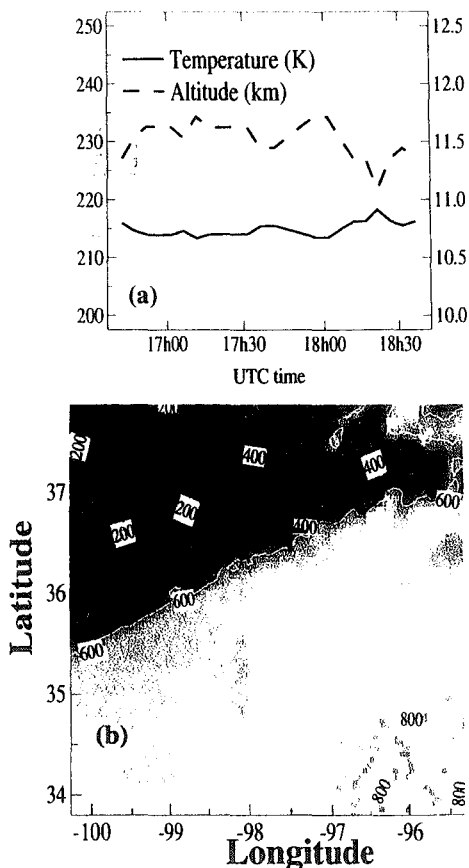


Figure 1. (a) Cloud top altitude and temperature profiles given by the MMCR instrument on 96-12-22
(b) Cloud top Rayleigh pressure (hPa) derived from POLDER data on same day - SGP-ARM site location is marked by the cross

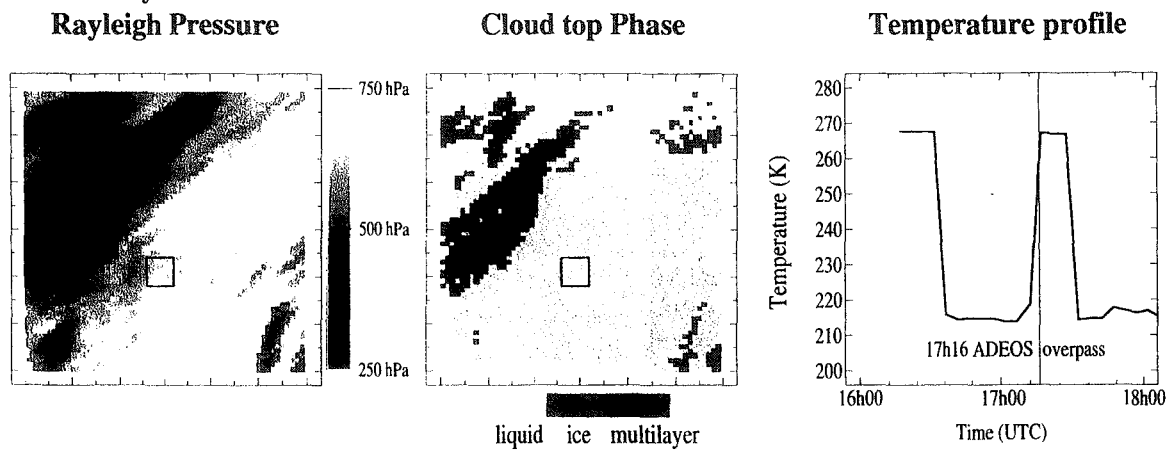


Figure 2. Cloud top Rayleigh pressure and phase derived from POLDER data for a case of cirrus overlaying low liquid clouds (1997-02-13). Associated cloud top temperature profile derived from radar measurements.

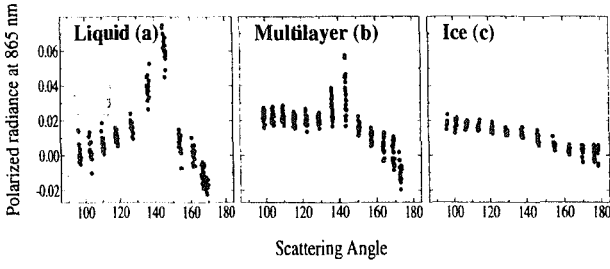


Figure 3. Observed polarized radiance as a function of scattering angle for liquid clouds (a) , thin cirrus overlaying low liquid clouds (b), and thick cirrus (c).

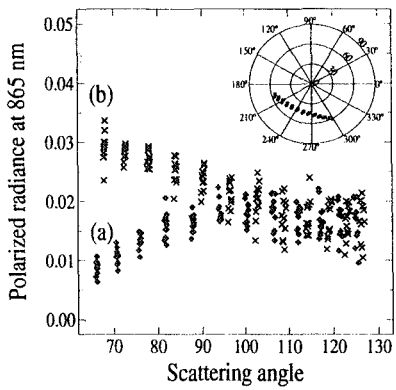


Figure 4. Polarized radiance (corrected from Rayleigh contribution) at 865nm observed by POLDER over two different high thick and cold clouds. One of them (a) present a positive polarization increasing with scattering angle whereas it does usually decrease for most ice clouds models (b). Viewing geometries associated to each case are very similar and presented on top polar diagram.

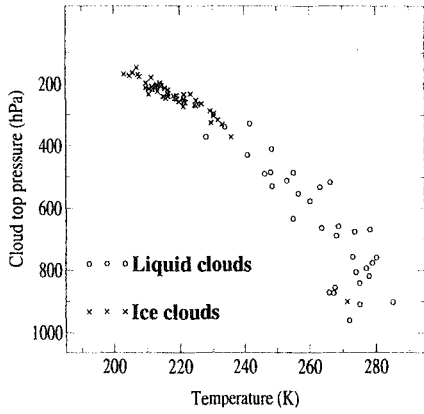


Figure 5. Temperature dependency of cloud top phase for clouds located above the SGP-ARM site ($36^{\circ}37'N, 97^{\circ}30'W$).

Global distribution of cloud top phase from POLDER/ADEOS

Global distribution of cloud top phase from POLDER/ADEOS I.

J. Riedi, M. Doutriaux-Boucher, P. Goloub

Laboratoire d'Optique Atmosphérique, Université des Sciences et Technologies de Lille, France

P. Couvert

Laboratoire des Sciences du Climat et de l'Environnement, Gif-sur-Yvette, France

Abstract. The eight months of data acquired by the POLDER instrument have now been processed. This dataset provides daily information on the global distribution of cloud top phase. We present here the results of a statistical analysis of ice and liquid phase occurrence frequencies at the global scale. Temporal variation of these frequencies above land and ocean are analyzed. These results are compared with ISCCP data and the consistency of the POLDER phase product is demonstrated.

Introduction

Clouds are well known to be crucial modulators of the Earth radiation budget. Their properties (cloud cover, optical thickness, altitude, *phase*, water vapor, microphysical properties) and their variations in space and time, need to be understood if we aim to predict climate change. The POLDER (POLarization and Directionality of the Earth Reflectances) instrument has proven capabilities in deriving key information needed to improve our knowledge of cloud, radiation and climate interactions. Particularly, the potential of polarization measurements of the upward shortwave radiation to derive cloud information has been demonstrated by both airborne and spaceborne data analysis [Bréon and Goloub, 1998]. From November 1996 to the end of June 1997, the satellite version of POLDER provided polarization measurements at the global scale. Thanks to its large field of view, a same location on the surface can be viewed from up to 14 directions. Cloud observations over a large range of scattering angles make possible the distinction between spherical and non spherical particles, in other words, between liquid and ice phase. At first, we will briefly discuss the principle of the cloud phase detection algorithm, and describe the POLDER phase product used in our studies. In a second part, we will expose the results of these analyses, which provide information on zonal and seasonal variation of cloud top phase. POLDER data are then compared with ISCCP data from the D1 dataset. In a last part, the results will be discussed and the quality of POLDER phase product investigated.

Method

Considering a cloudy system observed from satellite, the polarized component of the upward radiance is mainly formed in the upper cloud layer. Around 80% of the single scattered radiation reflected from the cloud layer arises from

the top 100 m of the layer. Calculations have shown that the polarized component, L_p , is saturated for cloud optical depth greater than 2.0. The important quantity for determining cloud phase is the polarized radiance L_p , that is less sensitive than the total radiance¹ L to multiple scattering effects. Thus, the polarization features, which correspond to *single scattering*, are preserved in L_p .

According to both theory and observations [Chepfer *et al.*, 1998], [Goloub *et al.*, 1999], the polarization features of clouds depend strongly on the particle shape. Within the range of scattering angles that can be observed by POLDER, clouds composed of liquid spherical particles, present a strong maximum about 140° from the incoming direction (primary rainbow). Also, a zero of polarization (neutral point) around 90°, and supernumerary bows for angles greater than 145°, make possible the distinction with ice crystals clouds, which show an essentially positive polarization, decreasing as the scattering angle increases (Figure 1). Discrimination between ice crystals and liquid water droplets is made using these differences. In this way, the cloud top phase detection may be considered as a cloud particles shape detection, even if cirrus clouds are unlikely to be composed of spherical ice crystals. A complete description of the algorithm principle has been given by [Parol *et al.*, 1999] and [Goloub *et al.*, (*submitted to J. Geophys. Res.*,) 1999].

The data used in our present studies are the level 2 POLDER phase product, at the resolution of about 60km x 60km which corresponds to a zone of 9x9 full resolution POLDER pixels. All frequencies are calculated using cloudy pixels for which phase has been retrieved successfully. This criteria rejects 14% of the cloudy pixels. Pixels with mixed phase (14%) have also been rejected from the analysis. At this resolution level, they correspond to pixels containing separate ice and liquid clouds, and are not representative of multilayered clouds nor mixed phase single cloud. Hence, the sum of liquid and ice occurrence frequencies is always equal to 1. The next section presents the analysis of eight months of POLDER phase data.

Occurrence frequencies of liquid and ice phase

Only results for ice clouds are presented in this paper. They will be compared with ISCCP high clouds amounts in the next section. The comparisons are limited to the

Copyright 2000 by the American Geophysical Union.

Paper number 1999GL000000.
0094-8276/00/1999GL000000\$05.00

¹Also, the polarization degree, defined as the ratio of L_p over L , is subject to multiple scattering effects since it depends on L .

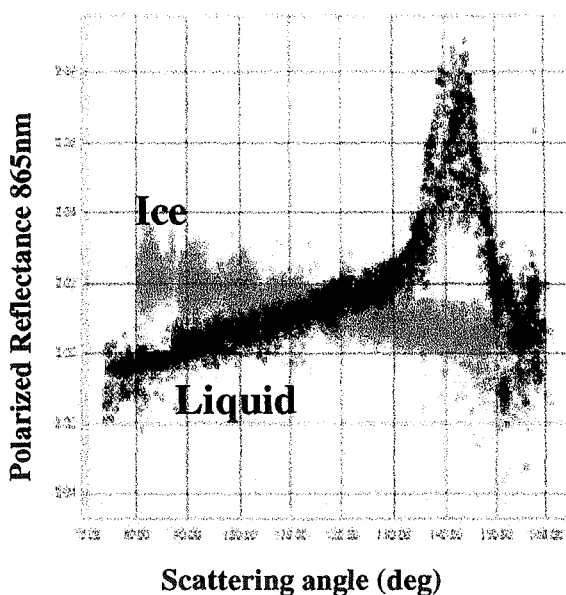


Figure 1. Polarized reflectances observed by POLDER over liquid (black) and ice (grey) clouds at 865 nm.

$\pm 60^{\circ}$ latitude zone, due to difficulties in cloud detection over snow covered surfaces, using visible/near infrared radiometers. Figure 2 shows the occurrence frequencies of ice clouds obtained for the period of November 1996 to June 1997. As expected, the maximum occurrence of ice phase corresponds to the InterTropical Convergence Zone and its variation along the equator. Two minima occur in the tropics at $\pm 20^{\circ}$ latitudes. The maximum of occurrence in the Northern hemisphere appears in February and the minimum during June, respectively associated with boreal winter and summer. Also, June is marked by a maximum of occurrence of ice phase in the Southern hemisphere.

Table 1 summarizes the results of statistics over land and ocean separately. We can observe that the distribution between ice and liquid clouds is rather constant at global scale, with about 30% of ice clouds versus 70% of liquid clouds.

Table 1. Frequency of occurrence (in %) of liquid and ice phase at global scale, over land, ocean, and both.

	Liquid			Ice		
	Land	Ocean	Both	Land	Ocean	Both
Nov	60	75	71	40	25	29
Dec	59	75	71	41	25	29
Jan	60	76	72	40	24	28
Feb	61	73	70	39	27	30
Mar	55	74	69	45	26	31
Apr	57	72	68	43	28	32
May	64	73	70	36	27	30
Jun	68	72	71	32	28	29

But if we look at repartition over land and ocean separately, we observe some differences between land and ocean, and also between the different months. At first, it should be noted that the ice phase is much more frequent over land than over ocean. It is also interesting to observe that liquid and ice phase frequencies of occurrence vary much more over land than over ocean (13% over land, against only 4% over ocean). This could be explained by the fact that ocean have a larger thermal capacity and that deep convection is easier to achieve over land. These variations are amplified in the Northern hemisphere over land, by the large variations of the atmosphere temperature, between local summer and winter.

ISCCP data matching the POLDER operational period are not available at present time. Thus, we have considered the ISCCP-D1 dataset ([Rossow et al., 1996]) from April 1990 to March 1991 which have been analyzed and documented by [M. Doutriaux-Boucher and G. Sèze, 1998].

ISCCP high clouds are classified as clouds with associated pressure lower than 440 hPa. In fact, cloud thermodynamic phase is much more governed by temperature than pressure level. Temperature differences as important as 30K may be found at a given pressure level for different latitudes ranging from 60°N to 60°S . As an example, a temperature of 240 K can be found in June at a pressure level of 410 hPa at 50°N , but one have to go down to 310 hPa to observe the same temperature at the equator. Frequencies of occurrence for clouds above 310 hPa and 440 hPa, have been derived from

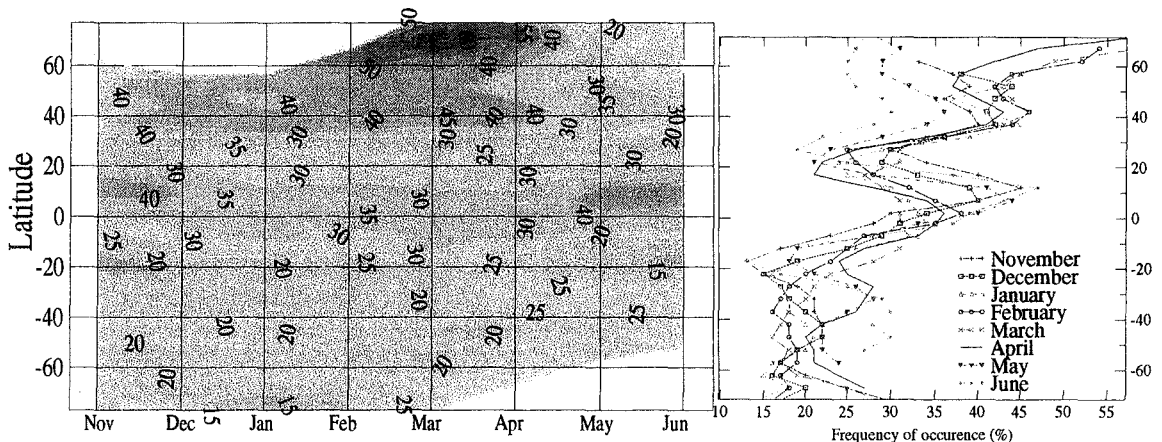


Figure 2. Seasonal variation of ice clouds occurrence frequencies during the POLDER operational period.

ISCCP dataset. In order to select ISCCP high clouds which were colder than 240K (threshold recognized by [Hutchison et al., 1997]), we have used temperature profiles provided with the POLDER dataset. For each latitude L_x , the pressure P_x associated to 240K can be retrieved (see Figure 3). Then, the occurrence frequency F_x of "cold" clouds is derived from the occurrence frequencies of the two classes of ISCCP high clouds (F_{310}, F_{440}), and the previously obtained pressure, using a linear interpolation.

Figure 4 shows the comparisons of POLDER ice clouds with ISCCP "cold" clouds frequency of occurrence as a function of latitude. Clouds detection problems over snow covered surfaces appear clearly in the POLDER results poleward of 60°N for April and May. Very high frequencies occur in this region during winter season, and the frequency falls down suddenly between April and May. In fact this period corresponds to a rapid decrease of snow covered surfaces.

Despite the different periods considered in our studies for POLDER and ISCCP data, the general features are the same for the two datasets. Maxima and minima of occurrence appear at the same location except for December and February, for which the maxima along the equator are shifted. POLDER underestimates frequencies of occurrence in the Southern Hemisphere, particularly between 40°S and the Equator, whereas it tends to overestimate them in the Northern Hemisphere. Once again, the differences occur on the magnitude of the features, but not on the global latitudinal variations. May and June show a rather good agreement however.

Four hypotheses may be advanced to account for these differences between the two datasets. The first reason which could explain these results is that we, unfortunately, have not considered simultaneous ISCCP and POLDER data. This analysis would have to be done again, as the ISCCP data are made available.

The second one, is the different spatial resolution of instruments used to acquire data. According to [Wylie, 1998], both the sensitivity of the sensor and the size of its field of view, have an impact on the cloud amount retrieved using spaceborne radiometers. The bigger the FOV of the sensor is, the larger the total retrieved cloud amount. This is an advantage of the POLDER instrument upon ISCCP, but the spatial resolution of the sensor has also an impact on the detection of small or thin clouds. The POLDER sensor resolution is about 6 km against 2 km for the visible channels of radiometers used to produce the ISCCP cloud products. Preliminary comparisons performed against syn-

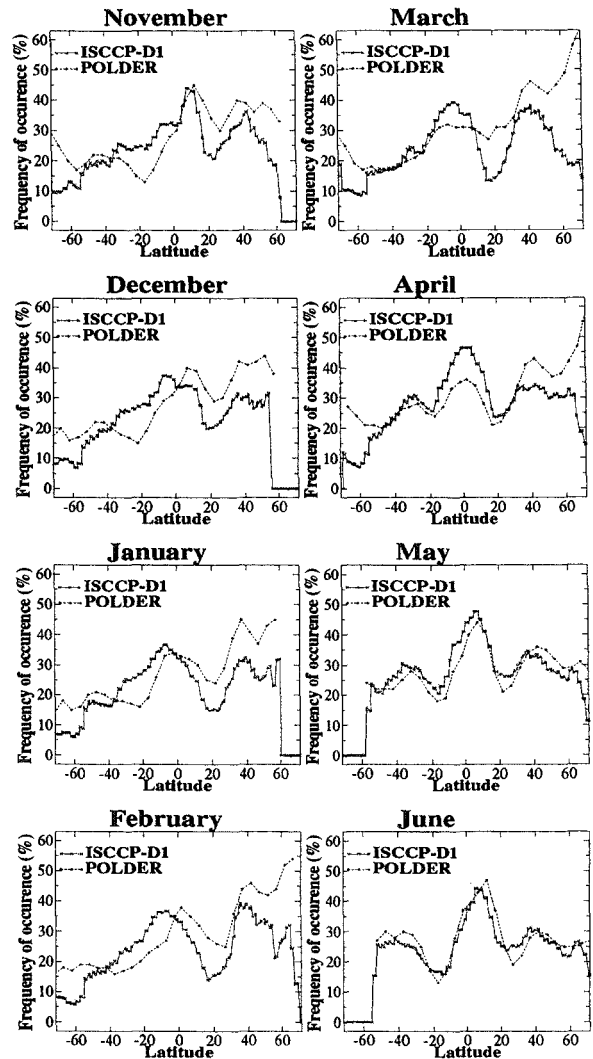


Figure 4. Comparison between ISCCP "cold" clouds fraction (relative to total clouds fraction) and POLDER ice phase frequency of occurrence.

optic weather reports have shown that the relatively low resolution of POLDER level 2 products, reduces by 10% the occurrence of ice clouds when compared with cloud phase analysis done at full resolution.

Concerning the detection of thin cirrus, ISCCP has the advantage of using thermal infrared channels which are more sensitive to that particular type of clouds than visible/near-infrared channels used by POLDER. This could account for the higher occurrence frequencies found by ISCCP in some region.

The last point to consider is the method used for producing the two datasets. ISCCP cloud analysis uses both visible and infrared radiances in order to derive cloud pressure, optical thickness, temperature and cloud types. Our selection of "cold" clouds relies on pressure level and cloud temperature criteria which do not ensure that we are looking at ice clouds only. POLDER cloud analysis is conducted, basically using only visible/near infrared radiances, but the phase retrieval algorithm is based on polarization measurements. This method does not require any assumption about cloud

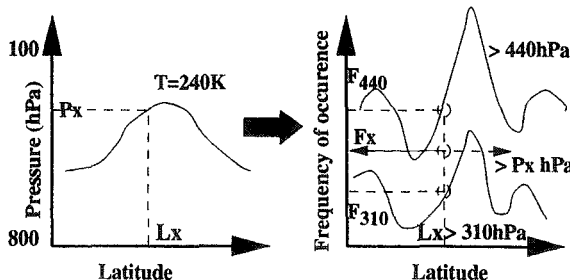


Figure 3. Schematic principle of the method used to select ISCCP "cold" clouds.

temperature or pressure, and lead to informations about microphysical properties of the cloud which is thought to be more reliable for cloud thermodynamic phase analysis.

Conclusions

Cloud phase derived from near-infrared photopolarimetric measurements is a very innovating result. Comparison with ISCCP-D1 dataset shows the global consistency of POLDER phase product, whenever the frequencies of occurrence are not always of same magnitude, very probably due to cloud detection weaknesses of POLDER [Parol *et al.*, 1999]. The analysis of the POLDER phase product is also conducted using comparison against synoptic weather reports, radar and lidar measurements. At the same time, POLDER level 1 data are reanalyzed to produce a phase index at full resolution. Finally, this results will be used to improve and define new algorithms for cloud analysis, for the future instrument POLDER on ADEOS II, which will be launched on the end of year 2000.

Acknowledgments. The authors are very grateful to NASDA and CNES who provided the POLDER data. Special thanks are addressed to F. Hennequart who processed the POLDER level2 data at LOA.

References

- Bréon, F.M., and P. Goloub, Cloud droplet effective radius from spaceborne polarization measurements, *Geophys. Res. Lett.*, **25**, 1879-1882, 1998.
- Chepfer, H., G. Brogniez, and Y. Fouquart, Cirrus clouds microphysical properties deduced from POLDER observations, *J. of Quant. Spectr. and Rad. Transfer*, **30**, 375-390, 1998.
- Doutriaux-Boucher, M., and G. Sèze, Significant changes between the ISCCP C and D cloud climatologies, *Geophys. Res. Lett.*, **25**, 4193-4196, 1998.
- Goloub, P., J. Riedi, M. Doutriaux-Boucher, and P. Couvert, Cloud Thermodynamical Phase from POLDER/ADEOS. Preliminary results, *In Proceedings of the ALPS99 International Conference*, WK2-O-04, 1999.
- Hutchison, K. D., B. J. Etherton, P. C. Topping, and H. L. Huang, Cloud top phase determination from the fusion of signatures in daytime AVHRR imagery and HIRS data, */it Int. J. Remote Sensing*, **18**, 3245-3262, 1997.
- Parol, F., J. C. Buriez, C. Vanbauce, P. Couvert, G. Sèze, P. Goloub, and S. Cheinet, First results of the POLDER "Earth Radiation Budget and Clouds" operational algorithm. *IEEE/Tran. Geosc. Rem. Sens.*, 1999.
- Rossov, W. B., A. W. Walker, D. E. Beuschel, and M. D. Roiter, International Satellite Cloud Climatology Project (ISCCP), World Climate Research Programme (ISCU and WMO), *Tech. Doc. WMO/TD 737*, 115 pp., World Meteorol. Org., Geneva, Switzerland, [Available from ISCCP Global Processing Center, NASA GISS, 2880 Broadway, New York, NY 10025], 1996.
- Wylie, D. P., *Cirrus and Weather: A satellite perspective*, in *Cirrus, OSA Technical Digest (Optical Society of America, Washington DC, 1998)*, 66-69, 1998.
-
- M. Doutriaux-Boucher, P. Goloub, and J. Riedi, Laboratoire d'Optique Atmosphérique, Université des Sciences et Technologies de Lille, 59655 Villeneuve d'Ascq Cedex. France, Phone: (33) 03 20 43 47 66, Fax: (33) 03 20 43 43 42, (e-mail: riedi@loaser.univ-lille1.fr; mdoutri@loaser.univ-lille1.fr; goloub@loaser.univ-lille1.fr)
- P. Couvert, Laboratoire des Sciences du Climat et de l'Environnement, C.E.A, 91191 Gif-sur-Yvette. France (e-mail: couvert@lsce.saclay.cea.fr)

(Received (Received July 13, 1999; revised September 16, 1999; accepted November 8, 1999.)

**Observation of Horizontally Oriented Ice Crystals in Cirrus Clouds with
POLDER/ADEOS**

Figure 2.7

Cloud optical properties



PERGAMON

Journal of Quantitative Spectroscopy &
Radiative Transfer 63 (1999) 521–543

Journal of
Quantitative
Spectroscopy &
Radiative
Transfer

www.elsevier.com/locate/jqst

Observations of horizontally oriented ice crystals in cirrus clouds with POLDER-1/ADEOS-1

Hélène Chepfer^{a,*}, Gérard Brogniez^b, Philippe Goloub^b, François M. Bréon^c,
Pierre H. Flamant^a

^aLaboratoire de Météorologie Dynamique, École Polytechnique, Palaiseau, 91128 Palaiseau Cedex, France

^bLaboratoire d'Optique Atmosphérique, Université des Sciences et Technologies de Lille, Villeneuve d'Ascq, France

^cLaboratoire des Sciences du Climat et de l'Environnement, Commissariat à l'Energie Atomique, Saclay, France

Abstract

Optical and radiative properties of cirrus clouds need to be accurately described at global scale in order to correctly estimate the radiative impact of ice clouds. The orientation of ice crystals in cirrus is capable of having a strong impact on their radiative budget: a cirrus cloud composed of horizontally oriented ice crystals has a larger plane albedo than a cirrus cloud composed of randomly oriented particles. Until recently, space-borne sensors were not adapted to observe ice crystal orientations. The POLDER instrument onboard the ADEOS platform (October 1996–June 1997) enabled us to observe bidirectional polarized radiances. These data are useful to determine the frequency of occurrence of ice crystals horizontally oriented in space within cirrus clouds. This paper describes how the POLDER bidirectional polarized radiances have been analyzed to determine the fraction of ice crystals preferably horizontally oriented. This preferred orientation is identified by observing specular reflection phenomenon above thick ice clouds. Three different periods (January, March and June 1997) of ten days of POLDER/ADEOS data have been processed for this study, and show that at least 40% of the ice pixels exhibit specular reflection peaks that indicate preferred orientation of ice crystals. The intensity and the distribution of specular reflection peaks are presented and discussed as a function of different parameters (solar zenith angle, latitude, cloud reflectance). © 1999 Elsevier Science Ltd. All rights reserved.

1. Introduction

Cirrus clouds have a major influence on the radiative budget of the Earth. This effect is well recognized but still roughly quantified at global scale [1,2]. Over the last two decades intensive

* Corresponding author. Tel.: + 33-169-333606; fax: + 33-169-33005
E-mail address: chepfer@lmd.polytechnique.fr (H. Chepfer)

field experiments like the US program FIRE [3,4], the European programs ICE [5] and EUCRE [6] and more recently CEPEX [7], have allowed to understand more precisely the parameter which significantly influence the radiative budget of cirrus clouds at local scale. Among these parameters, the optical properties of ice crystals composing the cirrus cloud like their size, their shape and their orientation in space seem to have significant influence on the radiative effects of ice clouds. The importance of ice crystal size has been pointed out and quantified by Hansen et al. [8] and Inoue [9], the influence of crystal shape has been studied by Minnis et al. [10], Takano et al. [11,12], and Baran et al. [13]. Furthermore, the presence of ice crystals preferentially horizontally oriented in space has been locally observed with ground-based lidars in USA, Australia and UK [14–20], and with airborne measurements in the USA and Europe [20–24]. The radiative impact of such preferred orientation of ice crystals in cirrus clouds is difficult to quantify because the computation of radiative transfer in an anisotropic media is much more complicated than in an isotropic one. Nevertheless, Takano et al. [25,26], Shanks et al. [23] and Chepfer et al. [24] have estimated the short-wave radiative impact of the horizontal orientation of ice crystals in cirrus clouds, in developing doubling–adding code in anisotropic media, or approximated successive order of scattering code for particles horizontally oriented in space. These different estimations tend to show that cirrus cloud plane albedo is increased when the ice crystals are horizontally oriented compared to the case in which they are randomly oriented in space.

The preferred orientation of ice crystals in cirrus clouds can occur in particular dynamic conditions, for example when the crystal is large enough ($r_e > 15 \mu\text{m}$) to offer a resistance to the air when it falls down [23]. Until recently, few instruments were used to observe horizontal orientation of ice crystals in the atmosphere: (i) scanning lidar pointing at the zenith for which the horizontal orientation can be detected by a strong backscattered signal associated with a low depolarization ratio [27], and (ii) the airborne bidirectional radiance measurements collected with POLDER that allow to identify specular reflection above thick clouds which indicates the presence of horizontally oriented ice crystals. The space-borne version of POLDER instrument onboard ADEOS platform offers a first opportunity to study the frequency of occurrence of such preferred horizontal orientation at global scale. This study is based on the detection of specular reflection phenomena above cirrus clouds. For this detection, it is necessary to observe a single cirrus cloud pixel in different viewing directions within a very short time and to get polarized observations (as discussed in Section 3). Among the different sensors onboard satellite platforms, POLDER is the only one which has the bidirectional and polarized capability. This paper presents a first analysis of ice crystal horizontal orientation based on measurements collected with POLDER/ADEOS. In Section 2 the POLDER instrument capabilities are briefly presented, Section 3 is devoted to the description of the successive tests applied to POLDER data to detect horizontal orientation of ice crystals, in Section 4 the procedure is tested and checked using one day of data (10 November 1996), and Section 5 presents the frequency of occurrence of ice crystal horizontally oriented deduced from the analysis of measurements collected during 3 periods of 10 days in January, March and June 1997.

2. Measurements

The POLDER (POLarization and Directionality of Earth Reflectances [46], instrument has been designed to measure bidirectional reflectances and polarized bidirectional reflectances at the

top of the atmosphere. POLDER-1 instrument on ADEOS-1 performed measurements for 8 months, from 1 October 1996 to 30 June 1997, and the POLDER-2 instrument should be launched on ADEOS-2 in summer 2000. POLDER is a CCD matrix of 242×274 pixels, the pixel resolution in nadir direction is equal to $6.2 \text{ km} \times 6.2 \text{ km}$. Each fixed target is seen several times from different viewing geometries by the POLDER matrix, and one target can be seen from up to 14 different directions during ADEOS overpass (within 4 min). The viewing directions observed with POLDER correspond to scattering angles ranging between 60 and 180° , depending on the solar zenith angle and ADEOS position against the position of the target. POLDER measures bidirectional reflectances in eight different wavelengths and each of those have been dedicated to the study of various atmospheric components like clouds [28], aerosols [29,30], water vapor [31] or ground properties like vegetation [32] or ocean color. Three of those channels (443, 670, 865 nm) present the original feature to be able to measure the state of polarization of the solar light reflected by the atmosphere. The interest of polarization measurements for atmospheric applications has been first pointed out by Hansen [33] and Van de Hulst [34] and more recently from the point of view of the POLDER instrument by Herman et al. [29].

3. Detection of ice crystals horizontally oriented in space

The detection of ice crystals preferentially horizontally oriented in cirrus clouds is based on successive tests on the bidirectional radiances and polarized radiances collected with POLDER. The bidirectional radiance (L) and the bidirectional normalized radiance (L_n) are linked to the bidirectional reflectance (ρ) as follows:

$$\rho = \frac{\pi L}{E_s \mu_s} = \frac{L_n}{\mu_s}, \quad (1)$$

where E_s is the incident solar light.

The first test concerns the cloud detection, the second test concerns the cloud thermodynamical phase and in the present study it is used to select the ice clouds only, the third test concerns the viewing geometry of POLDER/ADEOS and enable us to select the pixels for which the specular direction is observed from one of the multiple measurements, the fourth and last test enables us to identify the specular reflection phenomenon that indicates the horizontal orientation of ice crystals. These different tests are summarized in Table 1 and are precisely described here below:

(a) The first test aims at selecting the cloudy pixels located above oceans or sea surfaces and above land surfaces.

The cloud detection above oceans consists in selecting pixels with bidirectional reflectances higher than a threshold value. This threshold value has to be safe enough to (i) reject clear sky pixels (ii) reject pixels which correspond to optically thin clouds. Actually, as our topic is to detect specular reflection due to ice clouds, we have to avoid ocean sunglint that could be mistaken for cirrus cloud specular reflection if it is optically thin. To determine the value of the reflectance threshold, we have simulated bidirectional reflectances with a radiative transfer code for different values of cloud optical thickness. These simulations were computed at $\lambda = 670 \text{ nm}$ with a successive order of scattering code [35]: the atmosphere contains a cloud composed of spherical particles

Table 1

Summary of the different tests applied to POLDER/ADEOS measurements to detect the specular reflection phenomenon above cirrus clouds

Number	Test purpose	Test	Figs.
1	Detect clouds and avoid sea glitter	Above sea: $\rho(\lambda = 650 \text{ nm}) > 0.4$ Above land surfaces: [37]	1a and t
2	Detect ice clouds	Absence of rainbow ($\Theta = 140^\circ$) Behavior of normalized polarized radiances ($\Theta < 110^\circ$)	2
3	Detect specular reflection direction	Specular reflection direction ($\theta_s = \theta_v$, $\phi_s - \phi_v = 180^\circ$) observed with POLDER	3a
4a	Detect specular reflection peak due to horizontal orientation of ice crystals	$(L_{\text{spec}}^{\text{pol}} - L_{\text{spec}+1}^{\text{pol}}) > 0.0025$ and $(L_{\text{spec}}^{\text{pol}} - L_{\text{spec}+1}^{\text{pol}}) > 0.0025$	4a and b
4b	Detect specular reflection peak due to horizontal orientation of ice crystals	$(L_{\text{spec}}^{\text{pol}} - L_{\text{spec}+1}^{\text{pol}}) > 0.005$ and $(L_{\text{spec}}^{\text{pol}} - L_{\text{spec}+1}^{\text{pol}}) > 0.005$	4a and b

($r_e = 5 \mu\text{m}$), the glitter model has been described as in [36] and the wind speed was taken equal to 2 m s^{-1} so as to simulate a rather unfavorable case of intense glitter. Fig. 1a shows the bidirectional reflectances obtained for different optical thicknesses of cirrus clouds ranging between 1 and 10 and Fig. 1b shows the corresponding polarized radiances. Following these simulations, the signature of the sunglint peak on the polarized radiance (Fig. 1b) vanishes when the clouds optical depth is larger or equal to 5. This corresponds to a minimum value of 0.3 in bidirectional non-polarized reflectance (Fig. 1a). In order to avoid the ocean glitter, the bidirectional reflectance threshold has been fixed at $\rho(\lambda = 0.670 \mu\text{m}) = 0.40$ for pixels located above sea surfaces. This condition is not limited to the specular direction, it must be met by all (up to 14) measurements for the pixel of interest.

For pixels located above land surfaces, the cloud detection is more complex because the ground reflectance is strongly variable depending on the surface type (snow, desert, vegetation, etc.). We used a cloud detection scheme which has been specially developed for POLDER measurements over land surfaces. It is based on the use of four successive tests: (i) a threshold on the $0.443 \mu\text{m}$ reflectance after atmospheric correction, (ii) a smaller value of this threshold applied only over targets with significant spectral variation, (iii) comparisons between the surface pressure and an estimated pressure derived from two POLDER channels centered on an oxygen absorption band, (iv) a detection of rainbow signature in POLDER polarization measurements due to the presence of liquid water cloud. This cloud detection scheme has been developed, tested, and validated by Bréon and Colzy [37]. Its characteristics and validation are safe enough for the study of the orientation of ice crystals in cirrus clouds presented in this paper, despite the fact that some clear pixels are incorrectly declared as cloudy above snow surfaces. In that case, for optically thin clouds,

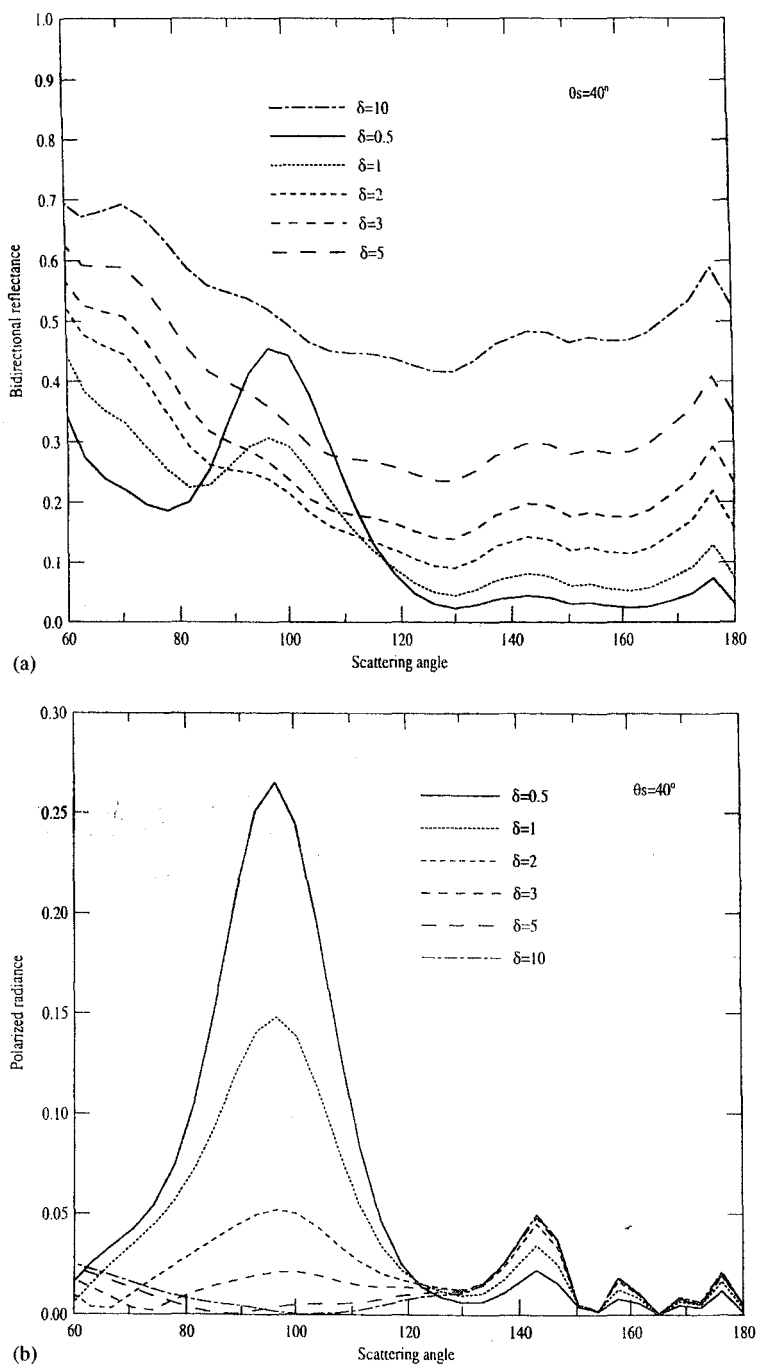


Fig. 1. (a) Bidirectional reflectances and (b) polarized radiances, simulated at 670 nm for an atmosphere composed of a cloud with different values of optical depth. The wind speed is equal to 2 ms^{-1} .

some specular reflection peaks due to very flat snow surfaces could be mistaken for specular reflection peaks due to ice crystals in cirrus clouds.

(b) The second test consists in identifying the cloud thermodynamical phase (ice or liquid water) in order to select ice cloud pixels and reject liquid water cloud pixels (Fig. 2). This test uses POLDER polarized radiances measured at $0.865\text{ }\mu\text{m}$ which enable us to observe (i) the presence (or absence) of rainbow at scattering angles around 140° , and (ii) the behavior of the polarized radiances for scattering angles lower than 110° . Fig. 3 illustrates normalized polarized radiances simulated with an adding-doubling radiative transfer code [38] above a cirrus cloud composed of hexagonal plates [39,40], and above a liquid water cloud composed of spherical particles. The distinction between ice and water cloud can be done in two ranges of scattering angles (Θ): (i) Θ around 140° and (ii) $\Theta < 110^\circ$. This thermodynamical cloud phase test was developed by Goloub et al. [41,42] and the results were compared with lidar measurements [43].

(c) The third test aims at selecting pixels for which the POLDER/ADEOS viewing geometry enables us to observe specular direction. POLDER/ADEOS has observed solar light reflected by a target in 12–14 different directions. To detect specular reflection phenomenon, the 12–14 directions have to include the specular reflection direction itself, which corresponds to a solar viewing angle (θ_v) equal to a solar zenith angle (θ_s) in the solar principal plane ($\phi_s - \phi_v = 180^\circ$). Besides, the procedure requires that this direction is not the first or the last one in time, so that a local maximum can be recognized. Fig. 3 shows a bidirectional polar diagram in which examples of POLDER geometry of observations are plotted, and one of the five sequences c

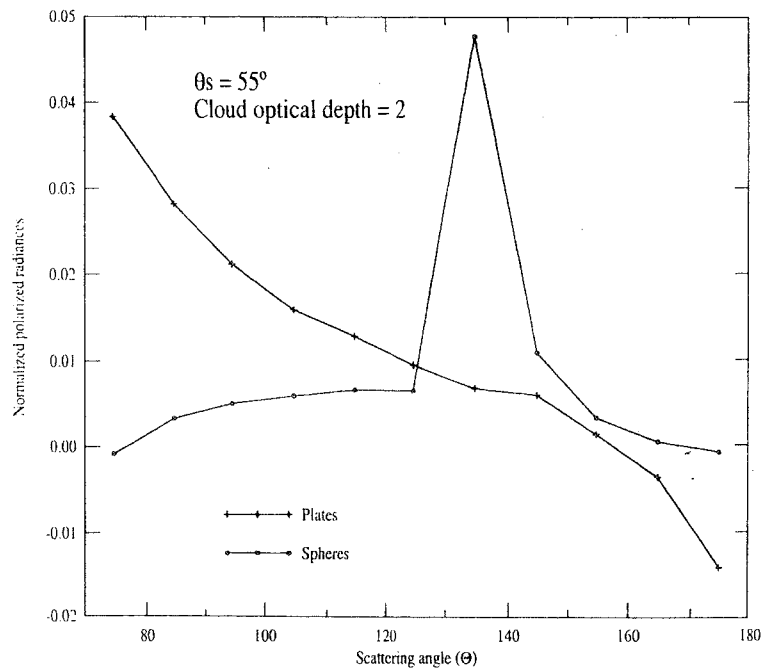


Fig. 2. Normalized polarized bidirectional radiances simulated for a water cloud composed of spherical particles and for an ice cloud composed of non-spherical crystals.

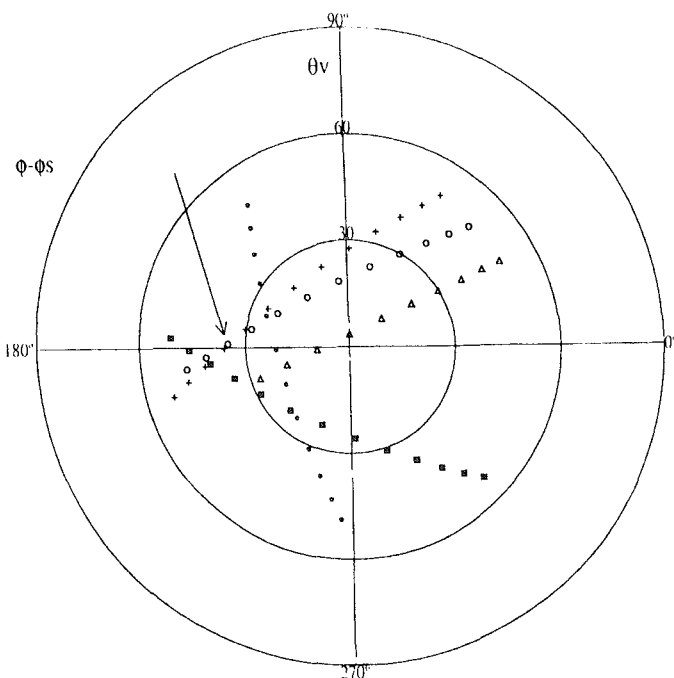


Fig. 3. Polar diagram of bidirectional radiances, the relative azimuth viewing angle ($\phi_{\text{viewing}} - \phi_{\text{sun}}$) ranges between 0 and 360° and the zenith viewing angle ranges between 0 and 90°. The solar zenith angle is equal to 35°, and the specular direction is pointed with an arrow.

POLDER measurements (plotted with circles) enable us to observe the specular direction ($\theta_v = \theta_s$, $\phi_s - \phi_v = 180^\circ$). These geometrical constraints reduce strongly the number of pixels usable for this study.

(d) The fourth test enables us to detect the specular reflection phenomenon itself. It consists in selecting pixels for which the bidirectional polarized normalized radiance shows a peak in the specular direction. The peak is identified when the bidirectional polarized normalized radiance in the specular ($L_{\text{spec}}^{\text{pol}}$) direction ($\pm 2^\circ$) has a greater value than the bidirectional polarized normalized radiance in the following ($L_{\text{spec}+1}^{\text{pol}}$) and previous ($L_{\text{spec}-1}^{\text{pol}}$) directions measured with POLDER. Hence, if

$$(L_{\text{spec}}^{\text{pol}} - L_{\text{spec}-1}^{\text{pol}}) > \text{threshold} \quad \text{and} \quad (L_{\text{spec}}^{\text{pol}} - L_{\text{spec}+1}^{\text{pol}}) > \text{threshold},$$

the specular reflection peak is declared. In order to study the sensitivity of the specular reflection peak intensity to various parameters such as the solar zenith angle, the cloud optical thickness, the latitude, or the ice cloud type, we have defined two thresholds of detection for the specular reflection peak: (i) $\text{threshold_a} = 0.0025$ corresponding typically to an increase of 12.5% of polarized normalized radiance collected above the cirrus cloud ($L^{\text{pol}} = 0.02$). (ii) $\text{threshold_b} = 0.005$ corresponding typically to an increase of 25% of the polarized radiance.

Fig. 4a shows an example of bidirectional normalized radiance collected with POLDER and showing a specular reflection phenomenon. The solar zenith angle is equal to 43.4°, and the two

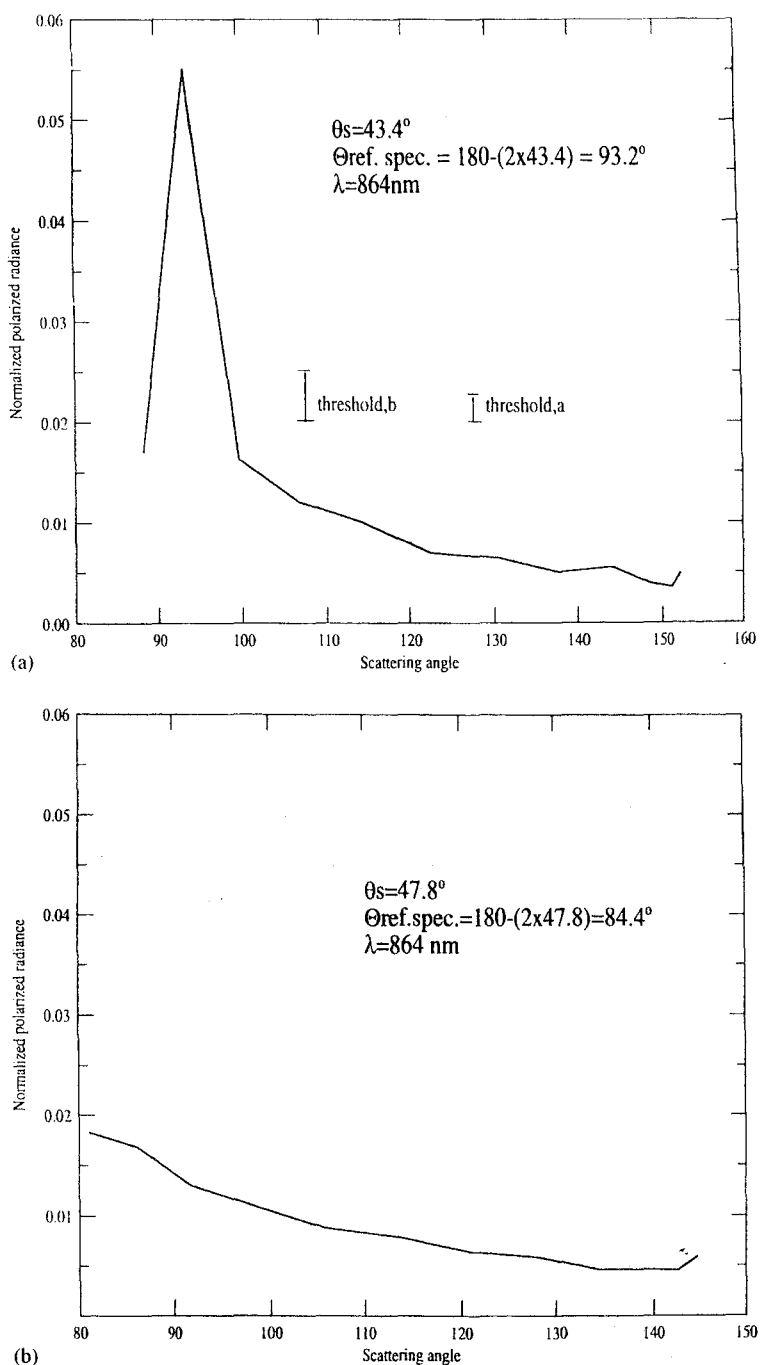


Fig. 4. Bidirectional polarized radiances collected with POLDER/ADEOS above ice clouds (a) showing a reflection peak phenomenon in the direction $\phi_{\text{viewing}} - \phi_{\text{sun}} = 180^\circ$, and $\theta_s = \theta_v = 43.2^\circ$. (The values of the two thresholds used for a systematic detection of reflection peak are reported in the figure.) (b) Showing the absence of the specular reflection peak.

values of thresholds are reported in the same figure. Fig. 4b presents another example of polarized bidirectional radiances as measured with POLDER above an ice cloud. In that case, we do not identify any specular reflection peak, and this typical behavior of polarized radiance can be reproduced with models of particles randomly oriented in space. The typical behavior of polarized radiances simulated for cirrus clouds composed of randomly oriented ice crystals has been presented in [24]. This paper also shows simulations of the single scattering phase function for particles horizontally and randomly oriented in space. These simulations clearly indicate that the specular reflection peak occurs only when the particles are horizontally oriented in space.

As described earlier, the detection of specular reflection peaks is based on polarized bidirectional radiance rather than total bidirectional radiance measurements because:

- (i) The intensity of the specular reflection peak in total radiance decreases with multiple scattering effects. The signature of preferred orientation is then in the ‘noise’ of the total radiance measurements as soon as the cloud is not optically thin.
- (ii) The polarized radiance is mainly governed by single scattering (polarization generated by multiple scattered photons is diversely oriented and the different contributions cancel out). Hence the polarized radiance preserves the specular reflection peak whatever the cloud optical depth.

Hence the polarized radiance is more suitable than the total radiance to detect the signature of preferred orientation.

Fig. 5 shows an example of radiance measured by POLDER matrix on 10 November 1996, over an area of $1700 \times 1500 \text{ km}^2$ over the ocean in the Southern hemisphere. During this sequence of measurements, the solar zenith angle was 43.3° . The grid superimposed on the image indicates the scattering angle with 10° increments. The smaller circle corresponds to a scattering angle $\Theta = 170^\circ$, and the straight line represents the solar principal plane. Fig. 5a corresponds to the non-polarized radiance image and Fig. 5b to the polarized radiance. In the upper right-hand side of Fig. 5a, we can recognize a thick cirrus cloud for which the bidirectional reflectance measured with POLDER is higher than 0.5. This thick cirrus cloud clearly appears in Fig. 5b, and we can identify along the boundary of the cirrus cloud a wide sea glitter [44] that cannot pass through the cloud. The signature of this sea glitter is also present in total radiance, but it is not visible in Fig. 5a because of the color scale chosen. In Fig. 5b, we also observe a thin and intense reflection peak on the cirrus cloud itself at a scattering angle equal to 93.4° . This phenomena corresponds to a specular reflection peak which indicates a preferred horizontal orientation of ice crystals in the observed cirrus cloud. Moreover the prominent bright ring near scattering angles of 140° corresponds to the rainbow phenomena associated with liquid clouds as discussed in Goloub et al. [41] and Bréon and Goloub [45].

4. Ice crystals horizontally oriented: case of 10 November 1996

4.1. Observations during 10 November

The successive tests described in Section 3 have been applied to POLDER/ADEOS measurements collected on 10 November 1996 (Figs. 6–9).

Fig. 6 represents the POLDER/ADEOS data corresponding to thick ice clouds as identified in applying both tests on the cloud detection (test 1) and the cloud thermodynamical phase (test 2).

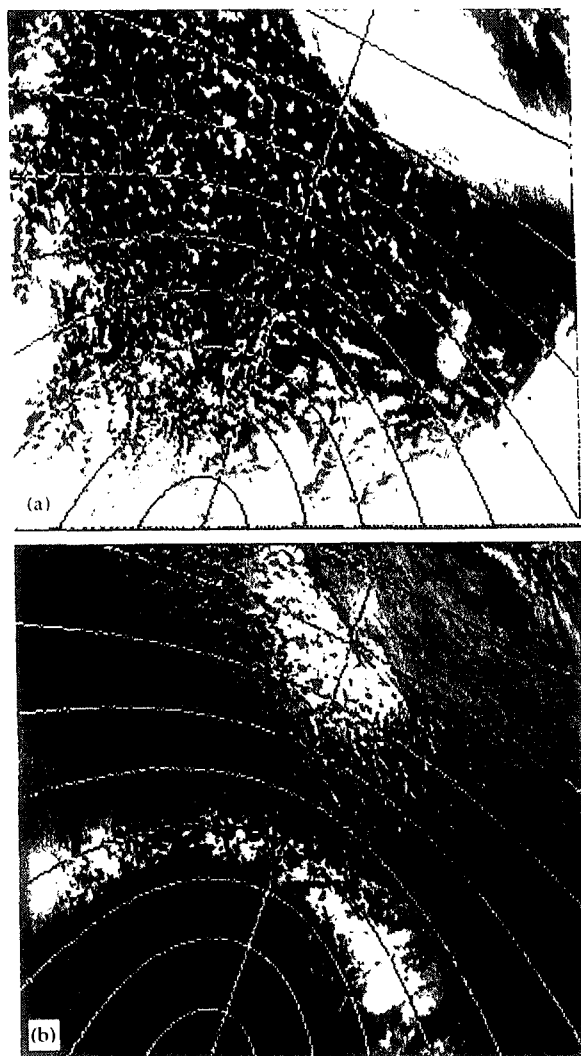


Fig. 5. Images of (a) radiances, (b) polarized radiances measured with POLDER above a cirrus cloud over the ocean. The superimposed grid corresponds to the scattering angle with 10° increment, and the straight line represents the solar principal plane. The solar zenith angle is equal to 43.3° .

The number of pixels for which the specular reflection was capable of being observed on 10 November 1996 relied on POLDER viewing geometry and its position with respect to the solar zenith angle. Fig. 7a is obtained by using test 3 alone, and shows a map of pixels for which the specular direction could be observed. Fig. 7b corresponds to ice cloud pixels, for which the specular direction could be observed (tests 1–3). For 10 November 1996, 2663 pixels correspond to cirrus clouds for which specular direction could be observed.

Fig. 8 corresponds to the specular reflection phenomenon itself observed above cirrus clouds. Fig. 8a is the map of specular reflection peaks deduced from the low threshold value (tests 1–4a),

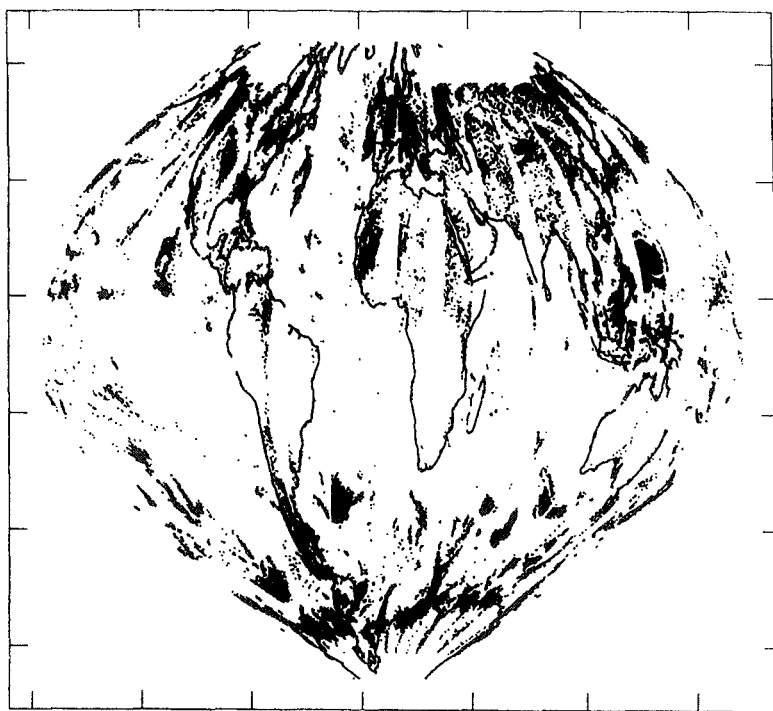


Fig. 6. Map of thick cirrus clouds inferred from POLDER ADEOS data on 10 November 1996 (tests 1 and 2).

and Fig. 8b corresponds to the highest value of threshold (tests 1–4b). The results are quantitatively summarized in Table 2: 39% (1051 pixels on 2663 pixels) of the thick cirrus clouds observed in the viewing geometry allowing the observation of specular reflection phenomenon do present a specular reflection peak following test 4a, and 30% (803 pixels on 2663) following test 4b.

4.2. Analysis

The results presented in Table 2 show that for 10 November 1996, the number of pixels allowing to observe the specular direction above ice clouds is lower over land surfaces than over oceans (we shall see in Section 5 that it is not systematically the case). Results summarized in Table 2 and presented in Fig. 8a and b show that the intensity of the specular reflection peak is variable, but comparing Fig. 8a and b with Fig. 7b enables us to see that specular reflection peaks can be detected in nearly all the groups of pixels for which the specular direction can be observed, i.e. the occurrence of specular reflection phenomenon is not linked to the surface properties. Above land surfaces, the occurrence of the specular reflection peak is not particularly related to the surface type (i.e. snow surfaces, large rivers, desert, mountains) as it is shown in Fig. 8a and b, i.e. the pixels presenting specular reflection peaks are homogeneously distributed in comparison to Fig. 7b.

Fig. 9 show the frequency of occurrence and the amplitude of the specular reflection as a function of different parameters (solar zenith angle, latitude, cloud reflectance):

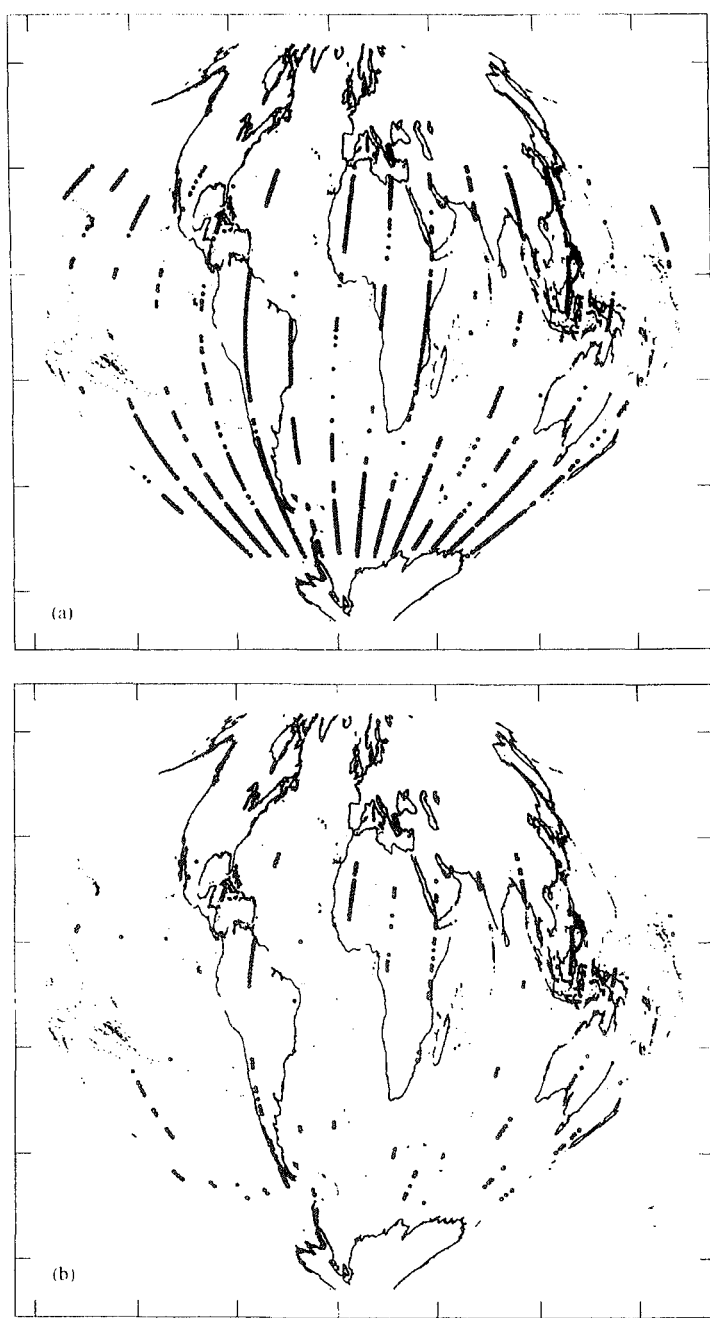


Fig. 7. (a) Map of specular directions observed with POLDER/ADEOS on 10 November 1996. (b) Map of specular directions observed above thick cirrus clouds with POLDER ADEOS on 10 November 1996.

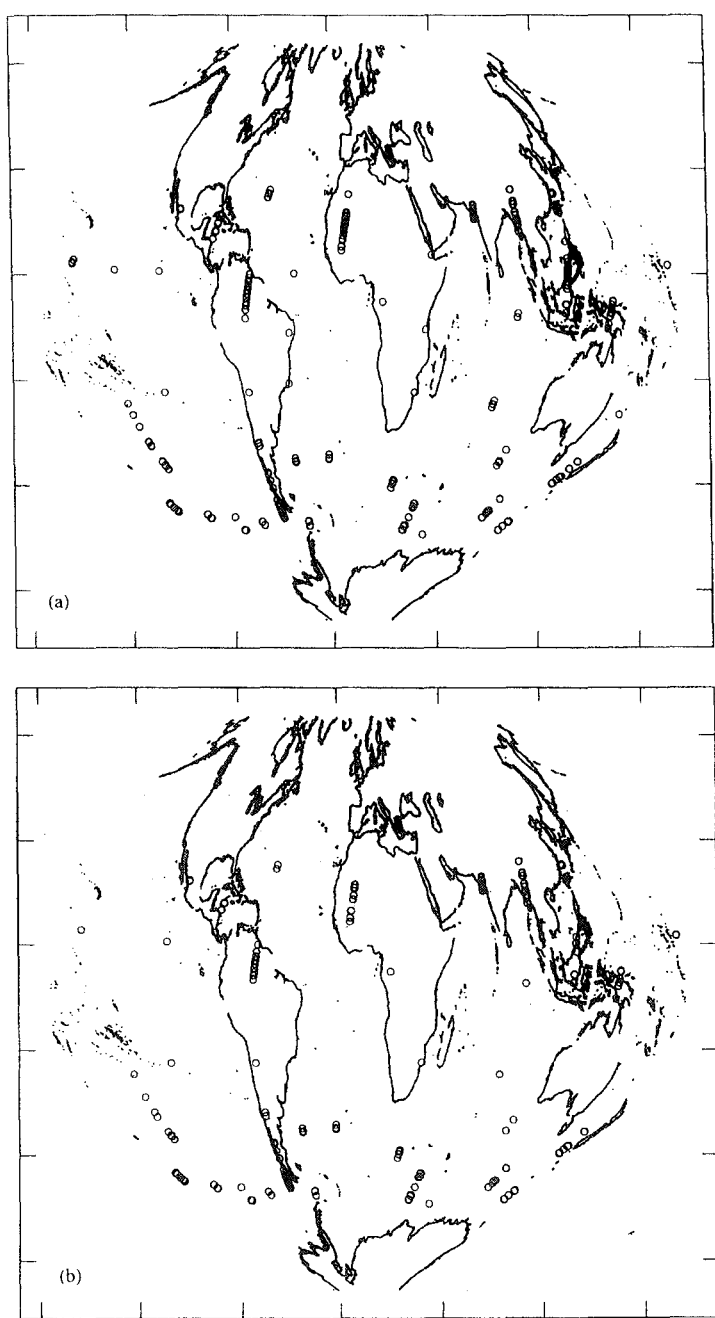


Fig. 8. Map of specular reflection phenomenon observed above ice clouds with POLDER/ADEOS on 10 November 1996 using (a) threshold_a, (b) threshold_b.

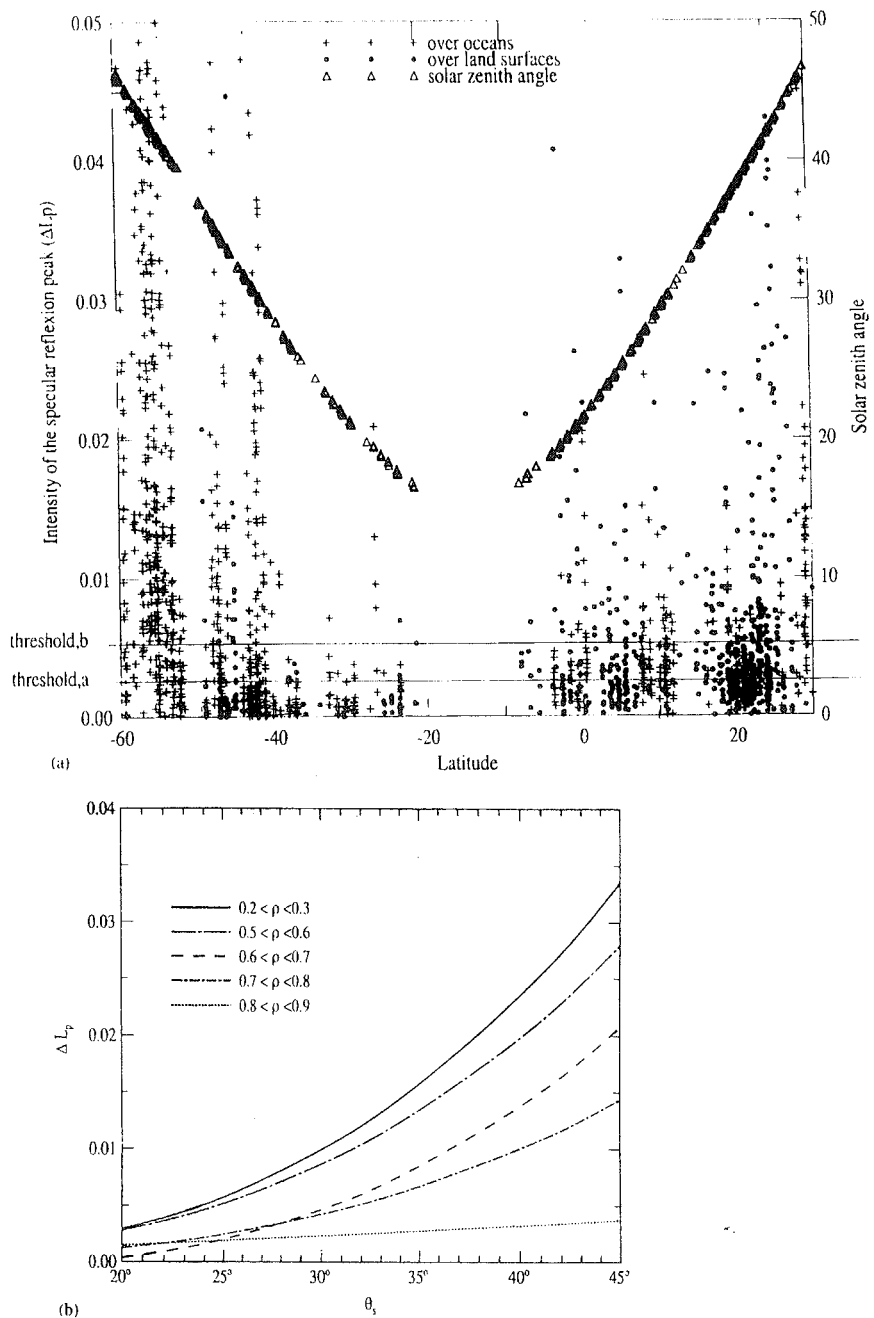


Fig. 9. (a) Intensity of the specular reflection peak and value of the solar zenith angle (θ_s) as a function of the latitude. (b) Intensity of the specular reflection peak as a function of solar zenith angle for different classes of bidirectional reflectances measured at a scattering angle ranging between 100 and 110°.

Table 2
Summary for 10 November 1996 tests (number of pixels)

Test number	Test purpose	Above sea	Above land	Total	Figure
1	Detect clouds and avoid sea glitter				
2	Detect ice clouds				
3	Detect specular reflection direction	1467	1196	2663	7b
4a Threshold_a	Detect specular reflection peak	53% 779	23% 272	39% 1051	8a
4b Threshold_b	Detect specular reflection peak	43% 626	15% 177	30% 803	8b

- Fig. 9a shows the solar zenith angle and the reflection peak intensity as a function of the latitude. The distribution between land surfaces (big dots) and oceans (crosses) is quite homogeneous. This figure shows that weak reflection peaks can be observed whatever the solar zenith angle is, whereas strong reflection peaks are mainly observed at large solar zenith angles which correspond to high values of latitudes. This phenomena is also consistent with the Fresnel's law: the peak amplitude increases strongly with the solar zenith angle, as if the top of the cirrus cloud behaves like a plane dioptric dielectric.
- Fig. 9b shows the intensities of the specular reflection peaks as a function of the solar zenith angle for different classes of cloud bidirectional reflectances. The cloud bidirectional reflectance values correspond to measurements collected at scattering angles ranging between 100 and 110°. Fig. 9b was built on averaging solar zenith angles and bidirectional reflectance values over intervals of 1° and 0.1, respectively. The value of the bidirectional reflection collected above the cloud gives qualitative information on the cloud optical depth: the higher the bidirectional reflectance is, the optically thicker the cloud is. Due to the cloud detection used above oceans (test 1), only pixels corresponding to ice cloud observed above land surfaces are reported in Fig. 9b for bidirectional reflectances lower than 0.3. Fig. 9b shows that the peak intensity is linked to both values of solar zenith angle and bidirectional reflectances. The highest peak amplitudes are observed above optically thin clouds (i.e. low values of bidirectional reflectances) for large zenith angles. The peak amplitude decreases when the cloud optical depth increases. This phenomena can be explained by non-neglecting multiple scattering effects for thick clouds, which tends to remove the specular reflection peak.

Finally, Figs. 6–9 show the self-consistency of the successive tests applied to detect specular reflection peaks due to cirrus cloud ice crystals preferentially horizontally oriented. The main sources of errors that could appear in using these tests are: (i) glitter effects due to snow surfaces or large rivers that may be mistaken with a specular reflection peak due to ice clouds, when the cloud is optically thin or when the cloud detection is incorrect, (ii) a small hole in an heterogeneous

cirrus cloud located above sea, for which the sea glitter could appear through the hole and be mistaken for a specular reflection due to cirrus clouds ice crystals. The variability of the reflectance peak intensity is influenced by the solar zenith angle, but the intrinsic properties of ice crystal also seem to have an impact on it, and even low-intensity peaks can be considered as signatures of preferred orientations. Based on this analysis, the procedure has been applied to several days POLDER data to get the first statistical information on the occurrence of ice crystals horizontal oriented in space in cirrus clouds.

5. Analysis of temporal evolution of horizontal ice crystals

In order to study the variation of occurrence of specular reflection phenomena, we have processed three periods of 10 days of POLDER measurements collected in 1997. The first period does not include 10 successive days for technical processing reasons, it contains 1–6, 14–18 January. The second period goes from 1 to 10 March, and the last period includes 1–June.

The cumulative POLDER observations for January 1997 are presented in Fig. 10. It shows the specular directions observed with POLDER above cirrus clouds. Due to the ADEOS orbit, the latitude area observed with POLDER moves to the North from January to June. Also, during January the specular direction above cirrus clouds is mainly observed above land because of both the important quantity of land surfaces in the Northern hemisphere, and the strongly restrictive threshold applied to avoid glitter and detect clouds over ocean (test 1). In June, a latitude band without observations of specular direction above cirrus clouds occurs in the Northern hemisphere and it is due to POLDER viewing geometry. In this latitude band, the cloud cover is very low, and the solar zenith angle is around 20° , hence the specular direction is around 140° of scattering angle. This range of scattering angle is used for the cloud thermodynamical phase (ice/liquid) determination, and the distinction between specular reflection above ice clouds, and rainbow due to liquid clouds cannot be done. Fig. 10b shows the cumulative specular reflection phenomena observed during the decade in January. Comparisons between Figs. 10a and b confirm what was already noticed for the case of 10 November 1996 (Section 4): each ensemble of ice cloud shows specular reflection phenomenon and contains horizontal ice crystals.

Figs. 11 and 12 present quantitative results and temporal variations of the specular reflection occurrence. Fig. 11a shows the temporal variation of specular directions observed globally with POLDER above cirrus clouds, and Fig. 11b and c present the variation of specular direction above land and sea surfaces, respectively. Globally, the number of pixels considered to detect specular reflection phenomena ranged between 2000 and 6000 each day (Fig. 11a). As shown in Fig. 11b and c, the distribution between land and ocean surfaces is directly linked to the hemisphere covered the most by ADEOS: Southern hemisphere in January (i.e. higher number of ocean pixels in January) and Northern hemisphere in June (i.e. higher number of land pixels in June).

Fig. 12 show the temporal variations of specular reflection occurrence detected with threshold_b: (a) globally, (b) above land surfaces, (c) above oceans.

Considering the global coverage (Fig. 12a), the occurrence of reflection phenomenon does not change strongly with the month, nearly 50% of the cirrus clouds observed contain horizontal ice crystals.

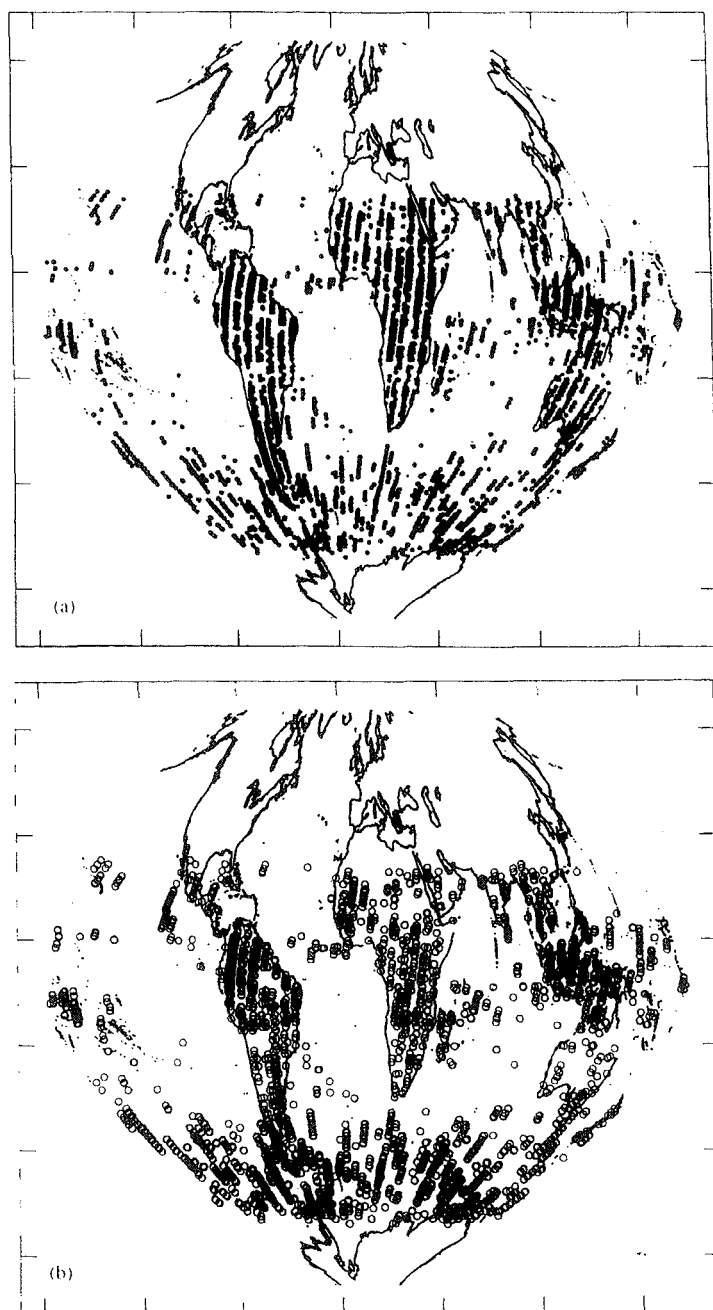


Fig. 10. Cumulative observations collected during 10 days in January 1997. (a) Map of specular directions observed above ice clouds. (b) Map of specular reflection phenomenon observed above ice clouds (using threshold_b).

When we only consider strong amplitude reflection peaks (threshold_b), we can observe the same variations as for low amplitude peaks (threshold_a), but shifted to lower values of occurrence.

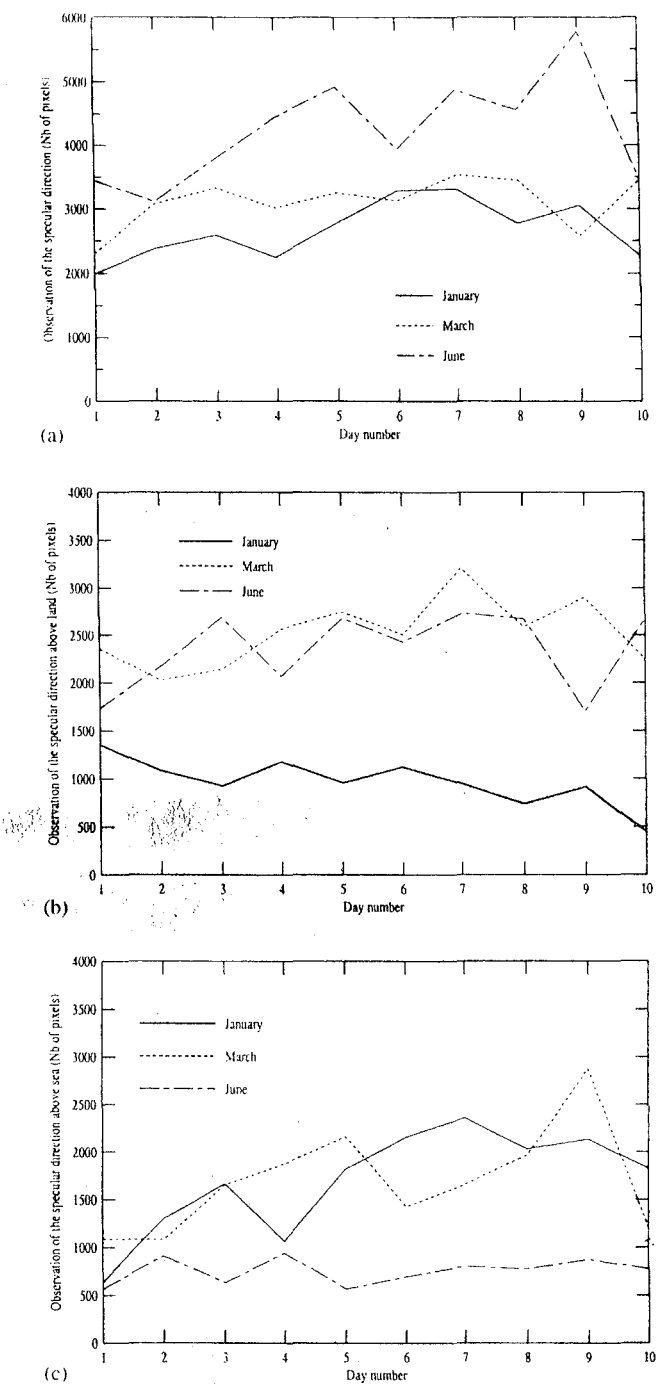


Fig. 11. Number of pixels for which the specular direction can be observed as a function of time: (a) total number of pixels; (b) pixels located above land; (c) pixels located above sea.

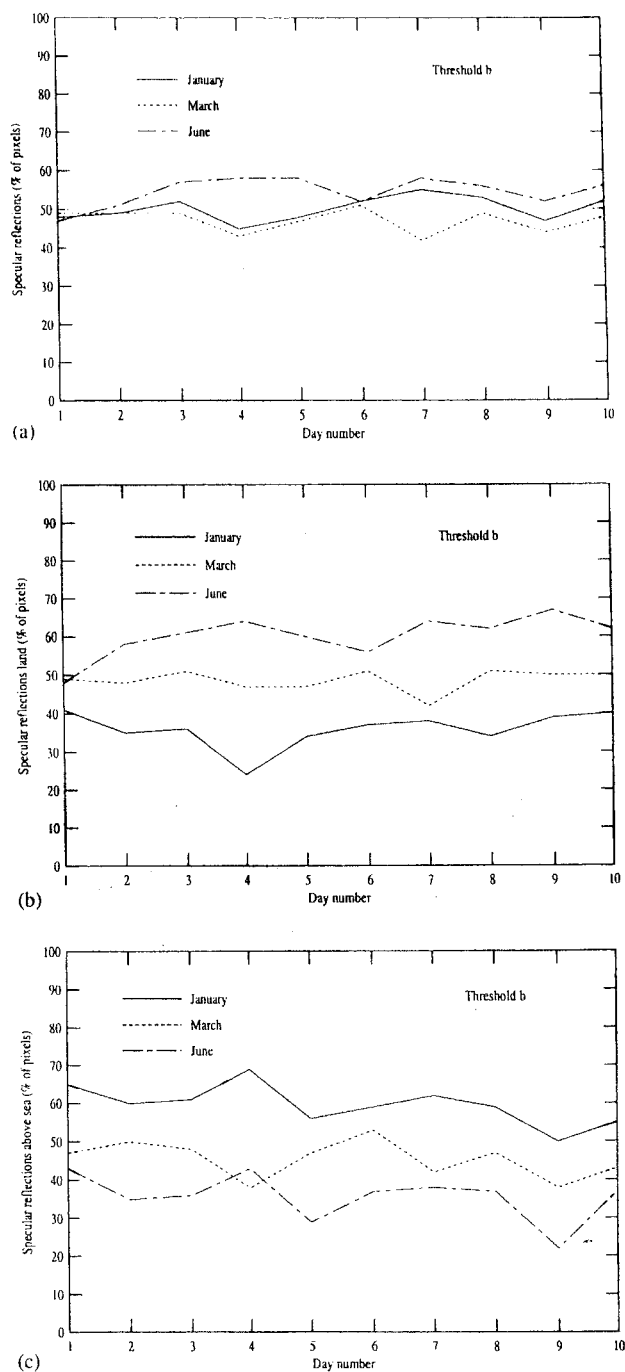


Fig. 12. Variation of the number of specular reflection phenomenon (threshold_b) as a function of the day: (a) global; (b) above land; (c) above sea.

Table 3

Mean frequency of occurrence of specular reflection observed in January, March and June

		January (1–6, 14–16, and 18)	March (12–23)	June (1–10)	Total
Above land (%)	Threshold_a	36	49	60	49
	Threshold_b	24	36	51	40
Above sea (%)	Threshold_a	60	45	36	49
	Threshold_b	45	29	25	34
Total (%)	Threshold_a	50	47	54	50
	Threshold_b	37	33	44	37

The mean frequencies of specular reflection occurrence are summarized in Table 3 for the three time periods (January, March and June), and for the two thresholds used to detect the presence of the specular peaks. This table shows that the global frequency of horizontally oriented ice crystals in cirrus clouds does not depend on the month. Medium intensity peaks appear in 50% of cirrus cloud observations, and strong peaks in 37% of cirrus cloud observations. The different peak intensities may be due to the amplitude of oscillations of ice crystals around the horizontal position, or the internal reflections of light in the crystals, i.e. the geometrical thickness of the crystals which produce these peaks. Moreover, Table 3 shows substantial differences between specular reflections detected over land and sea for a given month depending on the latitude band covered by ADEOS. More specular reflections are detected over sea in January (in the Southern hemisphere), whereas in June it is the contrary: more specular reflection is detected over land in the Northern hemisphere. Consequently, more specular reflection phenomena are detected at high latitudes than at lower ones. This latitudinal variation may be due to the low values of solar zenith angles associated with low latitudes that induced low peaks intensities which cannot be detected with the threshold values used here. But the global mean value obtained using threshold_a do not depend on the surface: 49% over land and over sea. The difference obtained in using threshold_b (34% over sea and 40% over land) may be due to the cloud detection that is different over land and sea: the cloud detection over sea selects only thick clouds (in order to avoid the sea glitter) whereas the cloud detection over land selects both thick and thin clouds.

6. Conclusion

The study of the orientation of cirrus cloud ice crystals is an interesting topic in order to improve our knowledge of microphysical properties of cirrus clouds as well as for better quantifying their radiative impact. Based on this statement, we have developed a method to detect horizontal orientation of ice crystals using bidirectional polarized radiances measured with POL-DER/ADEOS, in order to quantify the frequency of occurrence of ice crystals preferably horizontally oriented at global scale.

This method is based on the detection of specular reflection peak above ice clouds. This specular reflection is a signature of the horizontal orientation of ice crystals, and it has been detected in using several tests concerning: (i) cloud detection above land and ocean surfaces (ii) determination of clouds thermodynamical phase (ice/liquid), (iii) POLDER viewing geometries (iv) intensity of specular reflection peaks. The self-consistency of these successive tests has been carefully checked using data collected on 10 November 1996, and after that, the procedure has been applied to analyze three periods of POLDER/ADEOS measurements collected in January, March and June 1997.

The analysis shows that around 4000 pixels are suitable for the detection of specular reflection peaks every day, i.e. 4000 pixels correspond to ice clouds and include the viewing geometry of specular direction. Among these, 37–50% of the ice cloud pixels present specular reflection phenomenon that indicates the presence of horizontally oriented ice crystals. The percentage depends on the value of the threshold fixed to declare the presence or absence of a peak (depending on the peak amplitude), i.e. 50% of the pixels show a medium peak, and 37% present a peak with amplitude higher or equal to 0.005 in polarized normalized radiance. The occurrence of ice crystals horizontally oriented is distributed above land surfaces and oceans. The results obtained above snow surfaces may be slightly overestimated due to specular reflection of sun light over snow combined with optically thin ice clouds that can hardly be correctly detected.

Considering these analyses of POLDER/ADEOS observations, ice crystals which are horizontally oriented seem to occur quite frequently, at least in the upper layers of ice clouds. These results complete local observations collected with ground-based lidars in Australia, USA and UK, and airborne passive measurements collected in USA and Europe. Following POLDER/ADEOS observations, a large part of ice clouds detected does include horizontally oriented ice crystals, independently of their latitude or conditions of formation.

From a microphysical point of view, all the orientations can be included in an ice cloud, among these different orientations, the preferred horizontal orientation could be associated to the fall of large ice particles with simple shapes like hexagonal shapes larger than 15 μm . From a radiative point of view, the fact that the horizontal orientation of the ice crystals is not a marginal event, has to be further investigated. At present, the radiative impact of horizontally oriented ice crystals in cirrus clouds in the short-wave domain is poorly documented [24–26]. Nevertheless, these papers show that the short-wave plane albedo of a cirrus cloud composed of horizontally oriented particles can be 40% higher than in the case of randomly oriented ice crystals, depending on the solar zenith angle. These computations have to be confirmed to estimate correctly the radiative impact of such preferred orientation. Moreover, there is currently a lack of radiative transfer models suitable for the calculation of polarization in the short-wave domain for particles horizontally oriented in space. A special effort is required for the development of such radiative transfer codes in order to fully understand and interpret polarized observations collected from POLDER instrument. This could lead to a larger understanding of the properties of horizontally oriented ice crystals in cirrus clouds.

Acknowledgements

The results presented in this paper were obtained using data from CNES's POLDER instrument onboard NASDA's ADEOS platform.

References

- [1] Liou KN. Mon Weather Rev 1986;114:1167–99.
- [2] Sassen K. Bull Amer Meteorol Soc 1991;72:1848–66.
- [3] First ISCCP Regional Experiment (FIRE). Special issue, Mon Weather Rev 1990;118:2259–446.
- [4] FIRE IFO II. Special issue, J Atmos Sci 1995;52:4041–392.
- [5] Brogniez G, Buriez JC, Giraud V, Vanbauce C. Mon Weather Rev 1995;123:1025–36.
- [6] Raschke E, Flamant P, Fouquart Y, Hignett P, Isaka H, Jonas PR, Sundquist H, Wendling P. Surv Geophys 1998;19:89–138.
- [7] McFarquhar GM, Heymsfield AJ. J Atmos Sci 1996;52:2401–23.
- [8] Hansen JE, Lacis A, Rind D, Russel G, Stone P, Fung I, Ruedy R, Lerner J. Climate sensitivity: analysis of feedback mechanisms. Climate processes and climate sensitivity. In: Hansen JE, Takahashi, editors. Geophys Monogr S 29. M. Ewing vol. 5. Washington, DC: Amer Geophys Union, 1984:130–63.
- [9] Inoue T. J Meteorol Soc Japan 1985;63:88–98.
- [10] Minnis P, Liou KN, Takano Y. J Atmos Sci 1993;50:1279–304.
- [11] Takano Y, Liou KN, Minnis P. J Atmos Sci 1992;49:1487–93.
- [12] Takano Y, Liou KN. J Atmos Sci 1995;52:818–37.
- [13] Baran AJ, Brown SJ, Foot JS, Mitchell DL, Retrieval of tropical cirrus thermal optical depth, crystal size and shape using a dual view instrument at 3.7 μ m and 10.8 μ m. J Atmos Sci, 1999, accepted.
- [14] Sassen K. J Appl Meteorol 1976;15:292–300.
- [15] Derr VE, Abshire NL, Cupp RE, McNice GT. J Appl Meteorol 1976;15:1200–3.
- [16] Platt CMR. J Appl Meteorol 1978;17:482–8.
- [17] Platt CMR. J Appl Meteorol 1978;17:1220–4.
- [18] Sassen K. J Clim Appl Meteorol 1984;23:568–83.
- [19] Platt CMR, Scott JC, Dilley AC. J Atmos Sci 1987;44:729–46.
- [20] Thomas L, Cartwright JC, Wareng DP. Tellus 1990;42B:211–6.
- [21] Lynch DK, Fraser AB, Gedzelman SD. Appl Opt 1994;33:4580.
- [22] Lynch DK, Shanks JG, Gedzelman SD. Specular scattering and crystal dynamics in cirrus clouds. Proceedings of the SPIE/EOS Symposium on Passive Infrared Remote Sensing of Clouds and the Atmosphere, Rome, 1994. p. 371.
- [23] Shanks JG, Lynch DK. Specular scattering in cirrus cloud. Infrared remote sensing of clouds and atmosphere II 25–27 September, Palais des Congrès, Paris. Proceeding EROPTO Series. SPIE., vol. 2578;1995:227–38.
- [24] Chepfer H, Brogniez G, Fouquart Y. JQSRT 1998;30:375–90.
- [25] Takano Y, Liou KN. J Atmos Sci 1989;46:20–36.
- [26] Y. Takano, K.N. Liou, Effect of ice crystal orientation on cirrus cloud absorption, Proceedings of Conference on Light Scattering by Nonspherical Particles: Theory, Measurements, and Applications, NY Sept 29–Oct 1998:299–300.
- [27] Mishchenko MI, Wieland DJ, Carlson BE. Geophys Res Lett 1997;24:771–4.
- [28] Buriez JC, Vanbauce C, Parol F, Goloub P, Herman M, Bonnel B, Fouquart Y, Couvert P, Sèze G. Int J Remot Sensing 1997;18:2785–813.
- [29] Herman M, Deuzé JL, Devaux C, Goloub P, Bréon FM, Tanré D. J Geophys Res 1997;102:17023–37.
- [30] Deuzé JL, Herman M, Goloub P, Tanré D, Marchand A, Geoph. Res. Lett, 1999, submitted for publication.
- [31] Vesperini M, Bréon FM, Tanré D. Atmospheric water vapor content from spaceborne POLDER measurements IEEE TGARS, 1999, accepted.
- [32] Leroy JL, Deuzé M, Bréon FM, Hautecoeur O, Herman M, Buriez JC, Tanré D, Bouffès S, Chazette P, Roujeau JL. J Geophys Res 1997;102:17023–37.
- [33] Hansen JE. J Atmos Sci 1971;28:120–5.
- [34] Van de Hulst HC. Light scattering by small particles. New-York: Dover Publications, 1981. 470pp.
- [35] Deuzé JL, Herman M, Santer R. JQSRT 1988;41:483–94.
- [36] Cox C, Munck W. J Opt Soc Amer 1954;44:838–50.
- [37] Bréon FM, Colzy, S. Cloud detection from the spaceborne POLDER instrument and validation against synoptic observations. J Appl Meteorol, 1999, in press.

- [38] De Haan JF, Bosma PB, Hovenier JW. *Astron Astrophys* 1986;183:371–91.
- [39] Brogniez G. Light scattering by finite hexagonal crystals arbitrarily oriented in space. Proceeding of the International Radiation Symposium, Lille, France. 18–24 August, 1988:64–7.
- [40] Chepfer H. Etude théorique et expérimentale des propriétés optiques et radiatives des cirrus. PhD thesis, Lille University, 1997. 197 p.
- [41] Goloub P, Deuzé JL, Herman M, Fouquart Y. *IEEE Trans Geosci Remote Sensing* 1994;32:78–88.
- [42] Goloub P, Chepfer H, Herman M, Brogniez G, Parol F. Use of polarization for cloud study. Proceedings of SPIE Conference, vol. 1997;3121:330–41.
- [43] Chepfer H, Goloub P, Sauvage L, Flamant PH, Brogniez G, Spinhirne J, Lavorato M, Sugimoto N. *Phys Chem Earth* 1999;24:203–6.
- [44] Toubbé B, Bailleul T, Deuzé JL, Goloub P, Hagolle O, Herman M. In-flight calibration of the POLDER polarized channels using the sunglint. *IEEE TGARS*. 1999, accepted.
- [45] Bréon FM, Goloub P. *Geophys Res Lett*. 1998;25(11):1879–82.
- [46] Deschamps PY, Bréon FM, Leroy M, Podaire A, Brickaud A, Buriez JC. The POLDER mission: instrument characteristics and scientific objectives. *IEEE* 1994;32:598–615.

Ice crystal shapes in cirrus clouds derived from POLDER-1/ADEOS-1

Ice crystal shapes in cirrus clouds derived from POLDER-I/ADEOS-1

H. Chepfer¹, P. Goloub², J. Riedi², J.F. De Haan³, J.W. Hovenier^{3,4}, P. H. Flamant¹

¹ Laboratoire de Météorologie Dynamique, Palaiseau, France.

² Laboratoire d'Optique Atmosphérique, Villeneuve d'Ascq, France.

³ Department of Physics and Astronomy, Free University of Amsterdam, The Netherlands.

⁴ Astronomical Institute "Anton Pannekoek", University of Amsterdam, The Netherlands.

Submitted to the Journal of Geophysical Research

Revised version March 2000

ABSTRACT

This paper discusses the retrieval of ice crystal shapes of cirrus clouds at a global scale using observations collected with POLDER-1 (Polarization and Directionality of the Earth Reflectance) on board the ADEOS-1 platform. The retrieval is based on polarized bidirectional observations made by POLDER. First, polarized normalized radiances are simulated for cirrus clouds composed of ice crystals that differ in shape and are randomly oriented in space. Different values of cloud optical depths, viewing, geometries, and solar zenith angles are used in the simulations. This sensitivity study shows that the normalized polarized radiance is highly sensitive to the shape of the scatterers for specific viewing geometries, and that it saturates after few scattering- events, which makes it rapidly independent of the optical depth of the cirrus clouds. Next, polarized normalized radiance observations obtained by POLDER have been selected, based on suitable viewing geometries and on the occurrence of thick cirrus clouds composed of particles that are randomly oriented in space. For various ice crystal shapes these observations are compared with calculated values pertaining to the same geometry, in order to determine the shape that best reproduces the measurements. The method is tested fully for the POLDER data collected on January 12, 1997. Thereafter, it is applied to 6 periods of 6 days of observations obtained in January, February, March, April, May and June 1997. This study shows that the particle shape is highly variable with location and season, and that polycrystals and hexagonal columns are dominant at low latitudes, whereas hexagonal plates occur more frequently at high latitudes.

1. Introduction

Cirrus clouds cover permanently more than 20% of the Earth (Warren 1986 and 1988, Liao et al. 1995), and their impact on the Earth-Atmosphere-Ocean radiation balance is still an open question. They affect the radiative budget through two opposite effects, (i) they reflect partly the solar radiation thereby cooling the atmosphere, and (ii) they partly block the terrestrial radiation and this greenhouse effect tends to heat the atmosphere. Currently, neither of these two effects is correctly quantified for all regions of the Earth. Hence, the impact of cirrus clouds on the global radiative budget is still poorly known (Liou 1986, Stephens et al. 1990). Several parameters need to be studied to improve the radiative transfer properties of cirrus clouds in numerical models that are used for climate studies. These parameters are for example: global cirrus cloud cover, cloud height, temperature, geometrical structure, optical depth, ice water content, and microphysical properties (i.e. ice crystal size, shape, and orientation in space).

During the last two decades, several intensive field experiments have been organized to study cirrus cloud properties on a local scale: FIRE I (First ISCCP Regional Experiment FIRE) and II (see the special issues Mon. Wea. Rev. 1990, J. Atmos. Sci. 1995, Amott et al. 1991) took place in the USA in 1986 and 1991, ICE (International Cloud Experiment, Francis et al. 1994, Brooniez et al. 1995) and EUCREX (European Cloud Radiation Experiment, Raschke 1996, Raschke et al. 1998) was performed in Europe in 1991, 1993, and 1994, CEPEX (Central Equatorial Pacific Experiment, McFarquar and Heymsfield 1996) was executed in the Pacific Ocean in 1993, and SUCCES (SUbsonic aircraft: Contrail and Cloud Effects Special Study, special section Geophys. Res. Lett. 1998) took place in the USA in 1996. These experiments increased our understanding of cirrus cloud processes on a mesoscale and they pointed out a strong connection between the microphysical properties and the radiative impact of cirrus cloud.

Based on the results obtained during, those intensive field programs, and work conducted in parallel, several groups have started to consider the retrieval of cirrus cloud properties from space observations. As cirrus cloud properties vary spatially (latitude and longitude), and temporally (life time, and seasons), a complete description of the cirrus properties on a global scale requires satellite observations.

Minnis (1998) has summarized the needs and the state of the art of the retrieval of cirrus cloud parameters from satellite observations. Several authors (Inoue 1985, Parol et al. 1991, Minnis et al. 1993, Giraud et al. 1997, Stubenrauch et al. 1999) have derived ice crystal size using the split window technique applied to IR channels and a *a-priori* ice crystal shape. More recently Baran et al. (1999) deduced the particle size and shape using a dual view instrument, namely ATSR observations at 3.7 μm and 10.8 μm . Moreover, Rolland and Liou (1998) have studied the possibilities of deriving microphysical parameters of cirrus clouds using the MODIS instrument that was recently launched on EOS-AM.

In the present paper, we present results of retrieving ice crystal shapes at a global scale using POLDER-1/ADEOS-1 data. This work is a first attempt to retrieve the particle shape from polarized bidirectional observations in the visible domain. The POLDER instrument characteristics are presented in Sect. 2. In section 3, the ice crystal shapes considered in this study are discussed, as well as the radiative transfer code used to compute the normalized polarized radiance. Section 4 is devoted to the definition of criteria that will be used to select POLDER data suitable for the retrieval of ice crystal shape. In section 5, results of one day of observations are first presented as a test case, and then results of analyzing 6 periods of 6 days of POLDER observations are presented. Section 6 summarizes the results and discusses the limitations of the method used. The conclusions as well as possible future improvements are given in section 7.

2. POLDER instrument

The POLDER instrument (Deschamps et al. 1994) has been designed to measure total normalized radiances (L_n) and polarized normalized radiances ($L_{n,p}$) at the top of the atmosphere. The POLDER-1 instrument on ADEOS-1 performed measurements for 8 months, from November 1, 1996 to June 30, 1997, and the POLDER-2 instrument is scheduled for launch on ADEOS-2 in 2001. POLDER contains a CCD matrix of 242x274 pixels. The pixel resolution in the nadir direction is equal to 6.2 km x 6.2 km. Each fixed target is seen several times in different viewing geometries by the POLDER matrix, and the maximum number of different directions in which one target can be seen during an ADEOS overpass is 14.

The viewing directions observed with POLDER correspond to scattering angles ranging between 60° and 180° , depending on the solar zenith angle and the position of ADEOS with respect to the position of the target. POLDER measures normalized radiances in 8 different wavelength channels, some of which have been dedicated to the study of various atmospheric constituents, such as aerosols (Herman et al. 1997, Deuzé et al. 1998), clouds (Buriez et al. 1997), and water vapor (Vesperini et al. 2000), while others are used for studying ground properties like vegetation (Leroy et al. 1997) and ocean color. The state of polarization of the light reflected by the atmosphere is measured in three different channels (443 nm, 670 nm, and 865 nm). The accuracy of the normalized polarized radiance is 0.001.

The importance of polarization measurements for remote sensing application has been pointed out, among others, by Van de Hulst (1957) and Hansen (1971), and more recently, with regard to the POLDER instrument, by Herman et al (1997). The POLDER instrument provides not only, as do other instruments (Diner et al. 1999), multi-angle observations, but also polarized radiance data. On the other hand, the spatial resolution ($6.2 \times 6.2 \text{ km}^2$) comparatively coarse. Figures 1a and 1b show a POLDER image of a cirrus cloud over the ocean in radiance and polarized radiance, respectively. Studies of cirrus cloud properties using POLDER data started with observations collected with an airborne simulator during intensive field experiments. The first results concerned the discrimination between ice and liquid water clouds by Goloub et al. (1994) and the determination of ice crystal shape and orientation in space (Chepfer et al. 1998). More recently, these studies have been extended to a global scale with POLDER-I/ADEOS-I observations (Goloub et al. 1999 and Chepfer et al. 1999).

3. Simulations of bidirectional polarized reflectances

3.a. Models

In contrast to low level liquid clouds, ice clouds can be composed of particles with shapes much more complex than spheres. In situ observations, collected during intensive field experiments such as FIRE, ICE, EUCREX, CEPEX, SUCCESS, have shown a high variability and sometimes a high complexity of ice crystal shapes (see e.g. Heymsfield 1975, Krupp 1991, Miloshevich and Heymsfield 1996). They also showed that the shape of the crystals depends on latitude, altitude, and on the conditions during formation of the cirrus clouds. These ice crystal shapes are sometimes simple, like plates or columns with a hexagonal base, and sometimes very complicated, like bullet rosettes or dendritic particles. The hexagonal structure is regularly observed, which is consistent with the fact that liquid water naturally solidifies in a hexagonal structure. Based on these local observations, we have selected various typical ice crystal shapes to study the sensitivity of polarized radiance with respect to the particle shape. The selected shapes are: (i) simple ice crystals, like columns and plates, with a shape ratio $Q_{sr} = L/2R$ (L is the length of the crystal, and R the radius of the circumscribed hexagonal base) which ranges from 0.05 to 2.5 (Wendling et al. 1979, Takano and Liou 1989), and (ii) more complex polycrystalline particles (Macke et al. 1996) that were used for ISCCP ice cloud optical depth retrieval.

The complete scattering matrix has been computed for randomly oriented particles having these shapes, by using a ray-tracing method enhanced with Fraunhofer diffraction (cf. Macke et al. 1996 for the polycrystals, Brogniez 1988 and Chepfer 1997 for the hexagonal particles). At the wavelength used (865 nm), the absorption by ice is very low (Warren, 1986 and 1988), hence the single scattering albedo is close to one. The scattering matrix is employed in a doubling-adding radiative transfer code (De Haan et al. 1986) in order to take into account multiple scattering in the atmosphere. These radiative transfer computations yield the Stokes parameters of the emergent light at the top of the plane-parallel atmosphere, (I, Q, U, V). The normalized polarized radiance $L_{n,p}(\theta_v, \phi_v)$ is derived from these Stokes parameters as follows

$$L_{n,p}(\theta_v, \phi_s - \phi_v) = \frac{\pi \sqrt{Q^2 + U^2 + V^2}}{E_s} \quad (1)$$

where E_s is the incident solar flux at 865 nm at the top of the atmosphere, θ_v and ϕ_v are respectively the zenith and the azimuth viewing angles, and ϕ_s is the azimuth angle of the incident sunlight. According to the usual convention,

equals 0° and 180° for forward and backward directions, respectively. The total normalized radiance (L_n) is derived from first element of the Stokes vector (1) in the following manner

$$Ln(\theta_v, \phi_s - \phi_v) = \frac{\pi I}{E_s} \quad (2)$$

The quantities used in this study are the normalized polarized radiances ($L_{n,p}$) and the total normalized radiances (L_n) which are directly measured by POLDER.

3.b. Simulations

In this section, simulated values of normalized polarized radiances at 865 nm are presented for cirrus clouds. Results for various ice crystal shapes, different viewing geometries, and several solar zenith angles are given in order to describe the sensitivity of the polarized signal to these parameters. A wavelength of 865 nm is used because the contribution of scattering by molecules located above cirrus clouds is low at this wavelength. As an example, for a cirrus cloud top located at 530 hPa, the contribution of Rayleigh scattering to the normalized polarized radiance reaches a maximum of 0.0022 for a solar zenith angle equal to 40° . This contribution decreases with the cloud pressure. As we do not have reliable information on the cirrus cloud top pressure observed with POLDER, we have chosen to neglect the contribution of the Rayleigh scattering in our computations, and consider it as uncertainty.

Figure 2 depicts the normalized polarized radiance (cf. Eq. 1) as a function of the scattering angle for cirrus clouds composed of polycrystals. Results for different values of the cloud optical depth, δ , remain between 0.5 and 4, have been plotted. Further, a constant solar zenith angle equal to 60° and a viewing direction in the solar principal plane ($\phi_s - \phi_v = 0^\circ$), have been assumed. Figure 2 shows that the normalized polarized radiance increases with the cloud optical depth until it saturates for optical depths higher than 4. For thicker clouds the polarized radiance is independent of the optical depth.

The normalized polarized radiance has been computed for different particle shapes in order to study the sensitivity of the signal to the particle type. The cloud optical depth was chosen to be five to ensure a saturated signal. Figures 3a to 3e show polar diagrams of the saturated normalized polarized radiance ($L_{n,p}$ (sat)) computed for hexagonal compact crystals with a shape ratio $Q_{sr} = 1$ (Fig. 3a), hexagonal columns with $Q_{sr} = 2.5$ (Fig. 3b), polycrystalline particles (Fig. 3c), hexagonal plates with $Q_{sr} = 0.1$ (Fig. 3d), and hexagonal plates with $Q_{sr} = 0.05$ (Fig. 3e).

These figures illustrate the high sensitivity of the saturated normalized polarized radiance to the ice crystal shape. The high sensitivity of the polarization to the particle shape was also revealed by lidar linear depolarization observations (Sassen 1991). That L_p is much more sensitive to particles shape than the total normalized radiance (L_n) was also found with the airborne version of POLDER during EUCREX'94 (Chepfer et al. 1998). The space-borne version of POLDER measures normalized radiance in viewing directions for which the viewing angles (θ_v) are smaller than 60° . For these viewing angles, Figs. 3a - 3e show that $L_{n,p}$ (sat) is most sensitive to the particle shape for viewing directions comprised in the following angle boxes: $35^\circ < \theta_v < 55^\circ$ and $0^\circ < \phi_v < 50^\circ$ and in the corresponding directions that are symmetric with respect to the solar principal plane: $35^\circ < \theta_v < 55^\circ$ and $310^\circ < \phi_v < 360^\circ$.

Measurements of the normalized polarized radiances in these viewing directions are best suited to discriminate between the shapes of the ice crystals.

Figures 4 show the variation of the saturated normalized polarized radiance with solar zenith angle for the particle shapes considered in this study. Figure 4a, 4b, and 4c pertain to the viewing directions ($\theta_v = 50^\circ$; $\phi_s - \phi_v = 30^\circ$ or 330°), ($\theta_v = 40^\circ$; $\phi_s - \phi_v = 0^\circ$), and ($\theta_v = 40^\circ$; $\phi_s - \phi_v = 50^\circ$ or 310°), respectively. These three examples illustrate that the polarized normalized radiance can be used to discriminate between the different ice crystal shapes in cirrus clouds, and that this discrimination is easier for high values of solar zenith angles ($\theta_v = 60^\circ$) than for low ones ($\theta_v = 20^\circ$). Fig. 4 also shows that the distinction between polycrystalline particles and hexagonal columns ($Q_{sr} = 2.5$) is difficult when we consider the uncertainty induced by ignoring Rayleigh scattering, which yields an error $\Delta L_{n,p} = 0.0022$.

In the following sections the POLDER saturated normalized polarized radiances measured above cirrus clouds are compared to calculated values as to infer a global map of ice crystal shapes. In comparison to the total normalized radiance (L_n), the saturated normalized polarized radiance ($L_{n,p}$) has the advantage of being independent of the cirrus cloud optical depth. As soon as the cloud optical depth is higher than 4, it only depends on the viewing geometry and the solar zenith angle. Consequently, the particle shape obtained by comparing saturated normalized polarized radiance observations and simulated values concerns only the upper layer of the cirrus clouds (i.e. the first few orders of scattering).

4. Selection of POLDER observation

The detection of ice cloud pixels well suited for ice crystal shape determination is based on successive tests on the normalized radiances and normalized polarized radiances collected by POLDER. The first test concerns the cloud detection (cloudy pixels), the second test concerns the cloud thermodynamical phase which in the present study is used to select ice clouds only, the third and fourth tests are applied to select cirrus clouds composed of ice crystals randomly oriented in space. These different tests are briefly described below (for more details, see Chepfer et al. 1999).

- a) The first test aims at selecting cloudy pixels located above oceans or sea surfaces and above land surfaces. Cloud detection above ocean consists in selecting pixels with bidirectional reflectances higher than a threshold value equal to 40%. This threshold value is safe enough to reject clear sky pixels and pixels corresponding to optically thin clouds. For pixels located above land surfaces, cloud detection is more complex because the ground reflectance varies strongly depending on the surface type (snow, desert, vegetation, etc.). We used a cloud detection scheme that has been specially developed for POLDER measurements over land surfaces by Bréon et al. (1998). The use of this scheme for the current application is described in Chepfer et al. (1999).
- b) The second test consists of identifying the cloud thermodynamical phase (ice or liquid water) in order to select ice cloud pixels and reject liquid water cloud pixels. This test was developed by Goloub et al. (1994) who used POLDER polarized radiances measured at 865 nm. It is based on (i) the presence (or absence) of a peak at scattering angles around 140°, and (ii) the behavior of the polarized normalized radiances for scattering angles smaller than 110°. The results of this thermodynamical cloud phase test (Goloub et al. 1994) have been compared with lidar measurements (Chepfer et al. 2000) for validation. Further, Goloub et al. (1999) showed that this test selects ice clouds for which the normalized polarized radiance is saturated.
- c) The third and fourth tests aim at selecting ice clouds composed of particles randomly oriented in space. The third test aims at selecting pixels for which the POLDER views the direction of specular reflection. POLDER observes a given target in 12 to 14 different directions. To detect specular reflection, these directions have to include. (i) the specular reflection direction itself, which corresponds to a viewing zenith angle (θ_v) equal to a solar zenith angle (θ_s) in the solar principal plane ($\phi_s - \phi_v = 180^\circ$), and (ii) neighboring directions to detect the presence of a peak. These geometrical constraints strongly reduce the number of pixels available for this study. The fourth test enables us to detect clouds composed of particles randomly oriented in space. It consists in removing pixels for which the polarized normalized radiance presents a peak in the specular direction. The peak is identified when the bidirectional polarized normalized radiance in the specular ($L_{n,p,spec}$) direction (+/- 2°) has a greater value than the bidirectional polarized normalized radiance in the following

$(L_{n,p,spec+1})$ and previous $(L_{n,p,spec-1})$ directions measured with POLDER. Hence, if:

$$(L_{n,p,spec} - L_{n,p,spec-1}) > 0 \text{ and } (L_{n,p,spec} - L_{n,p,spec+1}) > 0 \quad (2)$$

a specular reflection peak is declared to be present. A previous study has been devoted to the quantity of particles preferentially orientated in space (Chepfer et al. 1999). In contrast, when the inequalities given in Eq. (2) are not satisfied, the cirrus cloud is considered to be composed of particles randomly oriented in space, and the pixel is selected for the particle shape determination.

The various tests described above enable selection of pixels corresponding to thick ice clouds for which the ice crystals can be assumed randomly oriented. For those pixels, the saturated normalized polarized radiances measured with POLDER can be compared with simulated values (cf. Sect. 3) in order to characterize the shape of ice crystals.

5. Results

5.a. Test case

Pixels pertaining to thick ice clouds whose ice crystals are randomly oriented in space have been selected employing the tests described above (Sect. 4) for January 2, 1997. Only 4082 pixels (Chepfer et al. 1999) can be used for crystal shape retrieval. The pixels are classified in boxes of viewing angles and solar zenith angles with 10' bin size in order to be compared with simulations corresponding to the same viewing and solar zenith angle conditions at 5° (Sect. 2b). Then differences between the saturated polarized radiance measured with POLDER and the corresponding simulated values are computed for each of the five ice crystal shapes. Finally, the pixel is flagged with the ice crystal shape for which the difference between the simulated and observed value is minimal. In the case of a minimal difference larger than 0.01, the pixel is rejected.

When the POLDER instrument sees one pixel in 14 different viewing directions, the shape retrieval procedure is

applied to each suitable direction. Next, for a given pixel, a quality indicator (α) is computed for each shape model. We use $\alpha = N_i/N_{tot}$ where N_i is the number of times for which the shape ' i ' has been obtained, and N_{tot} is the total number of shape retrievals for the pixel concerned. Finally, for a given pixel, the retrieved shape is considered reliable if $N_{tot} \geq 2$ and $\alpha > 0.5$. Usually, N_{tot} takes values between 2 and 5, and α is higher than 2/3. This test reduces the number of pixels for which the ice crystal shape is retrieved, but it prevents non reliable shape retrievals. Figure 5a shows an example of comparisons between observations and simulations for one pixel observed on January 2, where $\theta_s = 34^\circ$. The saturated normalized polarized radiance simulated for the appropriate viewing directions is plotted as a function of the scattering angle for the 5 different shapes. In this case the pixel is observed for 3 different directions ($N_{tot} = 3$) corresponding to the big dots in Fig. 5a. Each of these observations is compared to simulations and flagged with the particle shape that agrees best. For example, Fig. 5a shows that all three observations are flagged as "plates $Q_{sr} = 0.1$ ". Further, this retrieval is considered reliable because the quality factor $\alpha = 3/3 = 1$.

Repeating these comparisons for each selected pixel yields a map of ice crystal shapes for January 2, 1997 (Fig. 5b). This map shows that few pixels can be used for the shape retrieval. As shown in Fig. 5b, closely spaced pixels can correspond to different particle shape. The heterogeneous geographical distribution of these pixels is the result of the successive tests applied to the POLDER observations (Sect. 4b), namely: (i) only latitudes between 90°S and 40°N were covered in January (ii) only ice clouds pixels are selected (iii) only pixels corresponding to cirrus cloud composed of particles randomly oriented in space have been used for this study (ie. the specular direction needs to be observed, and the specular reflection peak has to be absent) (iv) only pixels with viewing geometries sensitive to the particle shape (in polarization) have been retained.

5.b. Analyzing 6 periods of 6 days.

To obtain more information about the global distribution of ice crystal shapes, we have processed 6 period pertaining to 6 days collected in January, February, March, April, May and June 1997.

Figure 6 presents the results obtained for the period 1-6 January 1997, and confirms the latitudinal distribution of the pixels used for the particle shape retrieval. This distribution is mainly due to the constraints on POLDER viewing geometry imposed by the selection procedure. In addition, it shows a lack of continuity between pixels located above land and above ocean surfaces, which is probably due to the different cloud detection schemes used above land and sea. A main difference between the schemes is that the cirrus clouds retained for the shape retrieval are very thick above ocean in order to avoid sea glitter and to properly determine the ice crystal orientation in space.

To obtain information about the latitude variation of the particle shape, 30° latitude intervals are considered and a histogram is made of the retrieved shapes in each interval. Figure 7a shows the number of pixel used for the shape retrieval for each latitude interval. Figures 7b to 7e show the percentage of each shape retrieved in each latitude interval. In January, the ITCZ (Inter Tropical Convergence Zone) is located between 0° and 30° South, and the columns dominate there (Fig. 7c). The two histograms corresponding to the adjacent latitude intervals (Figs. 7b and 7d) are highly similar, showing that the dominant particle shape composing cirrus clouds is symmetrical with respect to the ITCZ. Figure 7e shows that at high latitudes the hexagonal plates occur more frequently compared to low latitudes.

The results obtained in the period 1-6 June 1997 are presented in Figure 8 (a to e). In that period, the ITCZ is located in the 0-30° N interval. The dominating ice crystal shape in that interval is the hexagonal compacts ($Q_{sr} = 1$) and the column shape is the second most frequent. In contrast to January, in June the dominant ice crystal shape is not the same in the adjacent latitude bands (Fig. 8c and 8d). The plates are dominant in the 30° to 60° N latitude band, whereas the columns are dominant in the 0° to 30° S band. As in January, the dominant particle shapes at high latitudes (Fig. 8e) are the plates and polycrystals.

The results obtained for 6 different periods of 6 days are presented in Table 1. The polycrystals and hexagonal columns are classified in one single category since their polarization signatures are nearly the same (Sect. 3b). Table 1 shows that the polycrystals and hexagonal columns occur most frequently globally, whereas at high latitudes the hexagonal plates occur more frequently. Table 2 summarizes mean occurrences of the different shapes for all periods considered, and confirms the above results.

6. Discussion

Several points concerning the results mentioned above will be addressed here.

- (a) On one hand, the accuracy of the polarized radiance measured with POLDER is better than 0.001, so that measurement inaccuracies will not affect the shape retrieval significantly. On the other hand, the POLDER spatial resolution is 6x6 km at nadir, which means that the retrieved shape is an average shape corresponding to an area of at least 6x6 km.
- (b) The observations have been compared to several a-priori models. In this respect, two remarks are in order.
- (i) The shape retrieval concerns only cirrus clouds composed of randomly oriented ice crystals, because the radiative

transfer code that we used assumes random orientation of the scattering particles. Selecting pixels with randomly oriented ice crystals strongly reduces the number of pixels available for shape retrieval. In the future, a similar method could be used to retrieve the shape of ice crystals that are horizontally oriented in space, as soon as radiative transfer codes become available that are able to handle such oriented particles.

(ii) Five different models for the ice crystal shape have been considered. We do not pretend to reproduce all the cases encountered in nature. Nevertheless, we have noted that in most cases the polarized signature can be reproduced by one of the models considered. In the future, other shapes based on cloud microphysical models could be taken into account as soon as the complete scattering matrix becomes available) in order to obtain more realistic particle shapes.

c) Several in-situ observations have shown that cirrus clouds are often composed of ice crystals with a mixture of particle shapes. Such cirrus clouds have not been considered in this study, as it would have added an additional degree of freedom to the calculations. Including a particle shape distribution would increase the number of possible solutions. Hence, the retrieved shape is an effective or average particle shape, except, perhaps, for particle shapes corresponding to the extreme curves shown in Fig. 4, i.e. hexagonal plates ($Q_{sr} = 0.05$) and hexagonal compact ($Q_{sr}=1$). For other retrieved particle shapes, the cirrus cloud might actually consist of a mixture of various particle types.

d) The particle shapes retrieved with POLDER have to be validated in the future. The field experiments discussed in Sect. 1 have shown a wide variability of the particle shapes in cirrus clouds, including sometimes ideal shapes like hexagonal plates or columns, and polycrystals. The particle shapes considered in this paper are plausible, as they correspond to particle types that have been observed in nature. Nevertheless, these results are currently difficult to validate rigorously, because no collocated in-situ observations have been done in cirrus cloud during the POLDER-I / ADEOS-1 mission. Hence, future validation is required using two approaches: (i) comparisons with in-situ microphysical samples collected with an aircraft in cirrus clouds during the POLDER-2/ADEOS-2 mission, (ii) comparisons with retrieved shapes deduced from forthcoming space-borne observations, using retrieval techniques that are based on other physical methods.

7. Conclusions

In this paper, normalized polarized radiance observations obtained with POLDER have been used to retrieve the shape of ice crystals that compose cirrus clouds. The method applied in this study is completely new as it uses polarization to retrieve the ice crystal shape. This method has three main advantages in comparison with methods based on total normalized radiance (L_n) observations: (i) the normalized polarized radiance ($L_{n,p}$) is much more sensitive to a change in particle shape than the total normalized radiance, (ii) the polarized normalized radiance ($L_{n,p}$) allows discrimination between ice and liquid clouds, without additional information on the cloud temperature or altitude, and (iii) the polarized normalized radiance is saturated after a few scattering events and therefore independent on the cloud optical depth provided the cirrus cloud is sufficiently thick. Thus, one degree of freedom has been removed from the shape retrieval procedure, as compared to a method based on total normalized radiance (L_n) observations. The main limitation of the method is that the retrieved particle shape pertains to ice crystals contained in the higher sub-layers of the cloud.

This study is based on analyzing observations collected during 6 periods of 6 days in January, February, March, April, May and June 1997. It is shown that the shape of ice crystals varies strongly spatially. Our analysis yielded the following conclusions: (i) the distribution of ice particle shape seems to be symmetric on both sides of the ITCZ (at least in January) (ii) the polycrystals and hexagonal columns seem to dominate at low latitudes, whereas the hexagonal plates seem to occur more frequently at high latitudes. This latitudinal distribution of ice particle shape may be due to the conditions during formation of the cirrus clouds: at low latitude cirrus are often (but not always) the result of convection, whereas at mid and high latitudes they are often associated with fronts but can also be generated by convection. The results obtained at low latitudes are consistent with the study of Baran et al. (1999) who used ATSR observations and concluded that near the top of tropical cirrus clouds columns and polycrystals are most likely to occur.

In a follow-up study the eight months of POLDER observations might be analyzed in order to obtain more data on the natural variability of the shape of ice crystals in cirrus cloud on a global scale. Finally, the next launch of ADEOS-2 and EOS-AM should provide the opportunity to derive global maps of crystal shape simultaneously with different instruments using independent retrieval methods, in order to validate the latitudinal shape distribution obtained in the present study.

Acknowledgments

We are indebted to A. Macke for providing us with the scattering matrix of polycrystals. The results presented here were obtained using, a subset of the overall data set collected by the CNES's POLDER radiometer onboard the NASDA's ADEOS.

References

- Arnott W. P., Y. Dong, and J. Hallet, 1994 : "The role of small ice crystals in radiative properties of cirrus : A case study, FIRE 11, november 22, 1991. " *J Geophys. Res.*, **99**, 1371-1381.
- Baran A. J., S. J. Brown, J. S. Foot, and D. L. Mitchell, 1999 : " Retrieval of tropical cirrus thermal optical depth, crystal size and shape using a dual view instrument at 3.7 μm and 10.8 μm " *J Atm. Sc.*, accepted.
- Bréon, F-M., and S. Colzy, 1999: " Cloud detection from the spaceborne POLDER instrument and validation against synoptic observations " *J Appl. Meteor.*, in press.
- Brogniez G., 1988 : "Light scattering by finite hexagonal crystals arbitrarily oriented in space." *Proceeding of the International Radiation Symposium, Lille, France. 18-24 August*, 64-67.
- Brogniez, G., J. C. Buriez, V. Giraud, and C. Vanbause, 1995 : " Determination of effective emittance and radiatively equivalent microphysical model of cirrus from ground-based and satellite observations during the International Cirrus Experiment : the 18 october 1989 case study " *Mon. Wea. Rev.*, **123**, 1025-1036.
- Buriez, J. C., C. Vanbause, F. Parol, P. Goloub, M. Herman, B. Bonnel, Y. Fouquart, P. Couvert, G. Séze, 1997: " Cloud detection and derivation of cloud properties from POLDER ", *Int. J Rem. Sens.*, **18**, 2785-2813.
- Chepfer H., 1997 : " Etude théorique et expérimentale des propriétés optiques et radiatives des cirrus " PhD thesis, Lille University, 197 pages.
- Chepfer, H., G. Brogniez, and Y. Fouquart, 1998 : " Cirrus clouds microphysical properties deduced from POLDER observations " , *J of Quant. Spectr. and Rad. Transfer*, **30**, 375-390.
- Chepfer H., G. Brogniez, P. Goloub, 1999 : " Cirrus cloud Ice crystals horizontally oriented in space observed with POLDER/ADEOS", *J of Quant. Spectr. and Rad Transfer, accepted*. Chepfer H., Goloub P., J. Spinheimer, P.H. Flamant, M. Lavorato, L. Sauvage, G. Brogniez, and J. Pelon, 2000: " Cirrus clouds properties derived from POLDER-I/ADEOS polarized radiances : First validation using a ground-based lidar network ", *J Appl. Met.*, accepted.
- De Haan J. F., P. B. Bosma, and J. W. Hovenier, 1986 : "The adding method for multiple scattering calculations of polarized light." *Astron. Astrophys.*, **183**, 371-391.
- Deschamps P. Y., F. M. Bréon, M. Leroy, A. Podaire, A. Brickaud, J. C. Buriez, and G. Séze, 1994 : "The POLDER mission : Instrument characteristics and scientific objectives." *IEEE Trans. Geosci. Rem. Sens.*, **32**, 598-615.
- Deuzé, J. L., M. Herman, P. Goloub, D. Tanré, A. Marchand, 1998: " Characterization of aerosols over the ocean from POLDER-I/ADEOS- I " submitted to *Geoph. Res. Let.*
- First ISCCP Regional Experiment (FIRE). Special issue, 1990. *ivion. Wea. Rev.*, **118**, 22592446.
- Dinner D. J., G. P. Asner, R. Davies, Y. Knyazikhin, J. P. Muller, A. W. Nolin, B. Pinty, C. B. Schaaf, and J. Stroeve, 1999 : " New directions in Earth Observing : Scientific Applications of Multiangle Remote Sensing " *BUIL Am. Meteo.*, **80**, 2209-2228. FIRE IFO 11. Special issue, 1995. *J Atmos. Sci.*, **52**, 4041-4392.
- Francis P. N., A. Jones, R. W. Saunders, K. P. Shine, A. Slingo, and Z. Sun, 1994 : "An observational and theoretical study of the radiative properties of cirrus : Some results from ICE'89. " *Quart. J Roy. Meteor. Soc.*, **120**, 809-848.
- Giraud V., J. C. Buriez, Y. Fouquart, and F. Parol, 1997 : "Large scale analysis of cirrus clouds from AVHRR data : Assesment of both a n-ticrophysical index and the cloud top temperature." *J Appl. Meteor.*, **36**, 664-675.
- Goloub P., J. L. Deuzé, M. Herman, and Y. Fouquart, 1994 : "Analysis of the POLDER polarization measurements performed over cloud covers." *IEEE Trans. Geosci. Rem. Sens.*, **32**, 78-88.
- Goloub P., M. Herman, H. Chepfer, J. Riedi, G. Brogniez' P. Couvert, G. Séze, Cloud-Thermodynamical Phase Classification from the POLDER Spaceborne intrument, *J. of Geophys. Res.*, 2000 (to appear).
- Hansen J. E., 1971 : " Multiple scattering of polarized light in planetary atmospheres. Part 1. The Doubling Method " *J Atmos. Sci.*, **28**, 120-125.
- Herman, M., J.L. Deuzé, C. Devaux, P. Goloub, F.M. Bréon, and D. Tanré, 1997 : " Remote sensing of aerosols over land surfaces, including polarization measurements ; application to some airborne POLDER measurements " *J Geophys. Res.*, **102**, 17023-17037.
- Heymsfield A. J., 1975 : "Cirrus uncinus generating cells and the evolution of cirriform clouds. Part I : Aircraft observations of the growth of the ice phase." *J Atm.Sci.*, **32**, 799-807. Inoue T., 1985 : "On the temperature and the effective emissivity determination of semitransparent cirrus clouds by bi-spectral measurements in the 10 μm window region." *J Meteor. Soc. Japan*, **63**, 88-98.
- Krupp C., 1991 : "Holographic measurements of ice crystals in cirrus clouds during the International Cloud Experiment ICE 1989." Report of the 4th ICE/EUCREX Workshop, *Laboratoire d'Optique Atmosphérique, U. S. T L., Lille, France*.
- Leroy. M., J.L. Deuzé, F.M. Bréon, O. Hautecoeur, M. Herman, J.C. Buriez, D. Tanré, S. Bouffiés, P. Chazette, and J.L. Roujean, 1997: " Retrieval of atmospheric properties and surface bidirectional reflectances over the land from POLDER" *J Geophys. Res.*, **102**, 17023-17037.
- Liao X., W. B. Rossow, and D. Rind, 1995: "Comparison between SAGE II and ISCCP hi-hlevel clouds 1. Global and zonal mean cloud amounts." *J Geophys. Res.*, **100**, 1121-1135.
- Liou K. N., 1986 : "Review. Influence of cirrus clouds on weather and climate processes : A global perspective."

Mon. Wea. Rev., **114**, 1167 - 1199.

McFarquhar, G. M., and A. J. Heymsfield, 1996 : " Microphysical characteristics of three cirrus anvils sampled during, the Central Equatorial Pacific Experiment (CEPEX) " *J. Atm. Sci.*, **52**, 2401-2423.

Macke A., J. Mueller, and E. Raschke, 1996 : "Single scattering properties of atmospheric ice cristal." *J Atm. Sci.*, **53**, 2813-1825.

Miloshevich L. M., and A. J. Heymsfield, 1996 : "A balloon-bome cloud particle replicator for measuring vertical profiles of cloud microphysics : Instrument design and performance." *Proc. Int. Conf. on Cl. And precip.*, Zurich.

Minnis P., K-N. Liou, and Y. Takano, 1993 : "Inference of cirrus cloud properties using satellite-observed visible and infrared radiances. Part I : Parametrization of radiance fields." *J Atm.Sci.*, **50**, 1279-1304.

Minnis P., 1998 : " Satellite remote sensing of cirrus : an overview " *Proc. Int. Conf on Cirrus*, Baltimore October 6-8, 94-96.

Parol F., J. C. Buriez, G. Broaniez, and Y. Fouquart, 1991 : "Information content of AVHRR channel 4 and 5 with respect to the effective radius of cirrus cloud particles." *J Appl. Meteor.*, **30**, 973-984.

Raschke E., 1996 : "European Cloud and Radiation EXperiment (EUCREX) " *Final Report on the project, EV5V-CT 92 - 0130 EUCREX-2.*

Raschke E., P. Flamant, Y. Fouquart, P. Hignett, H. Isaka, P. R. Jonas, H. Sundquist, and P. Wendling, 1998 : "Cloud-radiation studies durin- the European Cloud Radiation Experiment (EUCREX) " *Surveys in Geophys.*, **19**, 89-138.

Rolland P. and K. N. Liou, 1998 : " Remote sensing of optical and microphysical properties of cirrus clouds using MODIS channels " *Proc. Int. Conf on Cirrus*, Baltimore October 6-8, 17-19.

Sassen K., 1991 : "The polarization lidar technique for cloud research : A review and current assessment." *Bull Amer. Meteor.Soc.*, **72**, 1848-1866.

Stephens G. L., S. C. Tsay, P. W. Stackhouse, Jr., and P. J. Flateau, 1990 : "The relevance of the microphysical and radiative properties of cirrus clouds to the climate and climatic feedback." *J. Atm.Sci.*, **47**, 1742-1753.

Stubenrauch et al. 1999, JGR, in revision

SUCCESS, 2. Special section, 1998. *Geophys. Res. Lett.*, **25**, 1327-1398.

Takano Y., and K. N Liou, 1989 : "Solar radiative transfer in cirrus clouds. Part I : Singles cattering and optical properties of hexagonal ice crystals." *J. Atm. Sci.*, **46**, 3-19.

Van de Hulst H. C., 1981 : " Light scattering by small particles " Dover Publications, Inc., New-York, 470 pp.

Vesperini, M., F.M. Bréon, D. Tanré: " Atmospheric water vapor content from spaceborne POLDER measurements ", IEEE TGARS, accepted.

Warren S. G., C. J. Hahn, J. London, R. M. Chervin, and R. Jenne, 1986: NCAR Tech. Note TN-273 STR, 212 pp.

Warren S. G., C. J. Hahn, J. London, R. M. Chervin, and R. Jenne, 1988 : NCAR Tech. Note TN-317 STR, 212 pp.

Wendling P., R. Wendling, H. K. Weickmann, 1979 : "Scattering of solar radiation by hexagonal ice crystals. "

Appi. Opt., **18**, 2663 - 2671.

Figure Captions

Figure 1. POLDER image ($1700 \times 1500 \text{ km}^2$) of a cirrus cloud over the North Pacific ocean (9 May 1997) in (a) radiance (b) polarized radiance. The wavelength is 864 nm. The line corresponds to the solar principal plane and the curves denote the scattering angle with a 10° increment between each line. (c) Viewing geometry of the POLDER instrument.

Figure 2 : Simulated values of the normalized polarized radiance reflected by a cirrus cloud as a function of the cloud optical depth, δ . The cloud is composed of polycrystalline particles.

Figure 3a to 3e : Calculated values of the saturated normalized polarized radiance for a cirrus cloud composed various particle shapes: (a) hexagonal compacts ($Q_{sr}=1$), (b) hexagonal columns ($Q_{sr}=2.5$), (c) polycrystalline particles, (d) hexagonal plates ($Q_{sr}=0.1$), (e) hexagonal plates ($Q_{sr}=0.05$). The solar zenith angle is 57.5° .

Figure 4 : The saturated normalized polarized radiance as a function of the solar zenith angle for different ice crystal shapes, and various viewing directions : (a) $\theta_v=50^\circ$; $\phi_s-\phi_v=30^\circ$ or 330° , (b) $\theta_v=40^\circ$; $\phi_s-\phi_v=0^\circ$, (c) $\theta_v=40^\circ$; $\phi_s-\phi_v=50^\circ$ or 310° .

Figure 5 : (a) Comparisons between polarized radiances simulated and observed with POLDER over a thick cirrus cloud. (b) Map of particle shapes randomly oriented in space for January 2, 1997.

Figure 6 : Map of particle shapes for a 6 day period in January 1997.

Figure 7 : Latitudinal variation of the particle shape on a global scale in the period 1-6 January 1997. (a) Number of pixels used for the shape retrieval as a function of latitude. (b) to (e) Histograms showing the relative occurrence (in percent) of the retrieved particle shape. Results for four latitude bands (width 30°) are given.

Figure 8 : Same as Fig. 7, but for the period 1-6 June 1997.

Table 2 : Same as Table 1, but averaged over all periods of six days considered (January , February, March, April, May and June 1997)

Latitude	Number of pixels	Plates Qsr=0.05 (%)	Plate Qsr=0.1 (%)	Columns (Qsr=2.5) and Polycrystals (%)	Compacts Qsr=1 (%)
90-60 N	176	8	40	50	2
60-30 N	3323	4.5	42	47	7
30-0 N	4156	5	39.5	39.5	16
0-30 S	1710	3	18	64.5	14.5
30-60 S	2746	3	30	61	6
60-90 S	360	18	43	39	0

Table 1 : Latitudinal variation of the frequency distribution of retrieved particle shapes. In each latitude band, the dominant shape is listed in bold.

Period	Latitude	Number of pixels	Plates Qsr=0.05 (%)	Plates Qsr=0.1 (%)	Columns (Qsr=2.5) and Polycrystals (%)	Compacts Qsr=1 (%)
January 1-6	90-60 N	0	0	0	0	0
	60-30 N	0	0	0	0	0
	30-0 N	924	1	35	55	9
	0-30 S	509	0	6	82	12
	30-60 S	1423	4	38	50	7
	60-90 S	348	19	42	37	1
February 7-12	90-60 N	0	0	0	0	0
	60-30 N	0	0	0	0	0
	30-0 N	1614	12	61	26	1
	0-30 S	173	4	23	56	17
	30-60 S	821	2	22	72	5
	60-90 S	12	0	67	33	0
March 19-24	90-60 N	0	0	0	0	0
	60-30 N	629	1	24	74	1
	30-0 N	323	2	41	53	4
	0-30 S	882	2	24	60	13
	30-60 S	439	2	21	74	3
	60-90 S	0	0	0	0	0
April 18-23	90-60 N	0	0	0	0	0
	60-30 N	1008	5	47	44	15
	30-0 N	0	0	0	0	0
	0-30 S	1307	3	18	65	15
	30-60 S	63	0	8	89	3
	60-90 S	0	0	0	0	0
May	90-60 N	0	0	0	0	0
	60-30 N	578	5	46	44	6
	30-0 N	214	1	24	40	36
	0-30 S	774	9	21	57	14
	30-60 S	0	0	0	0	0
	60-90 S	0	0	0	0	0
June 1-6	90-60 N	176	8	40	50	2
	60-30 N	1108	6	45	36	13
	30-0 N	1078	1	14	42	43
	0-30 S	1201	1	16	66	16
	30-60 S	0	0	0	0	0
	60-90 S	0	0	0	0	0

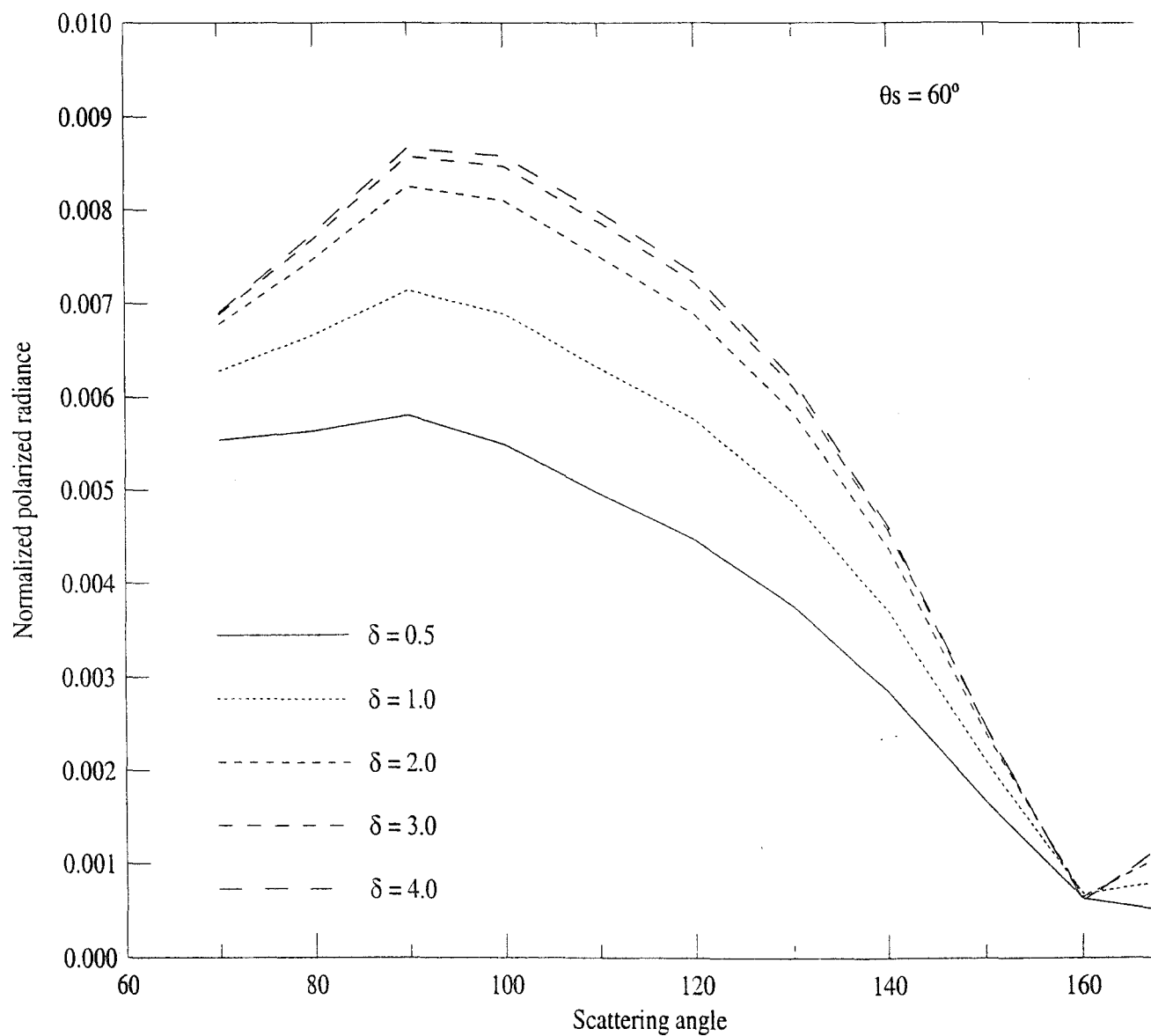


Fig 2

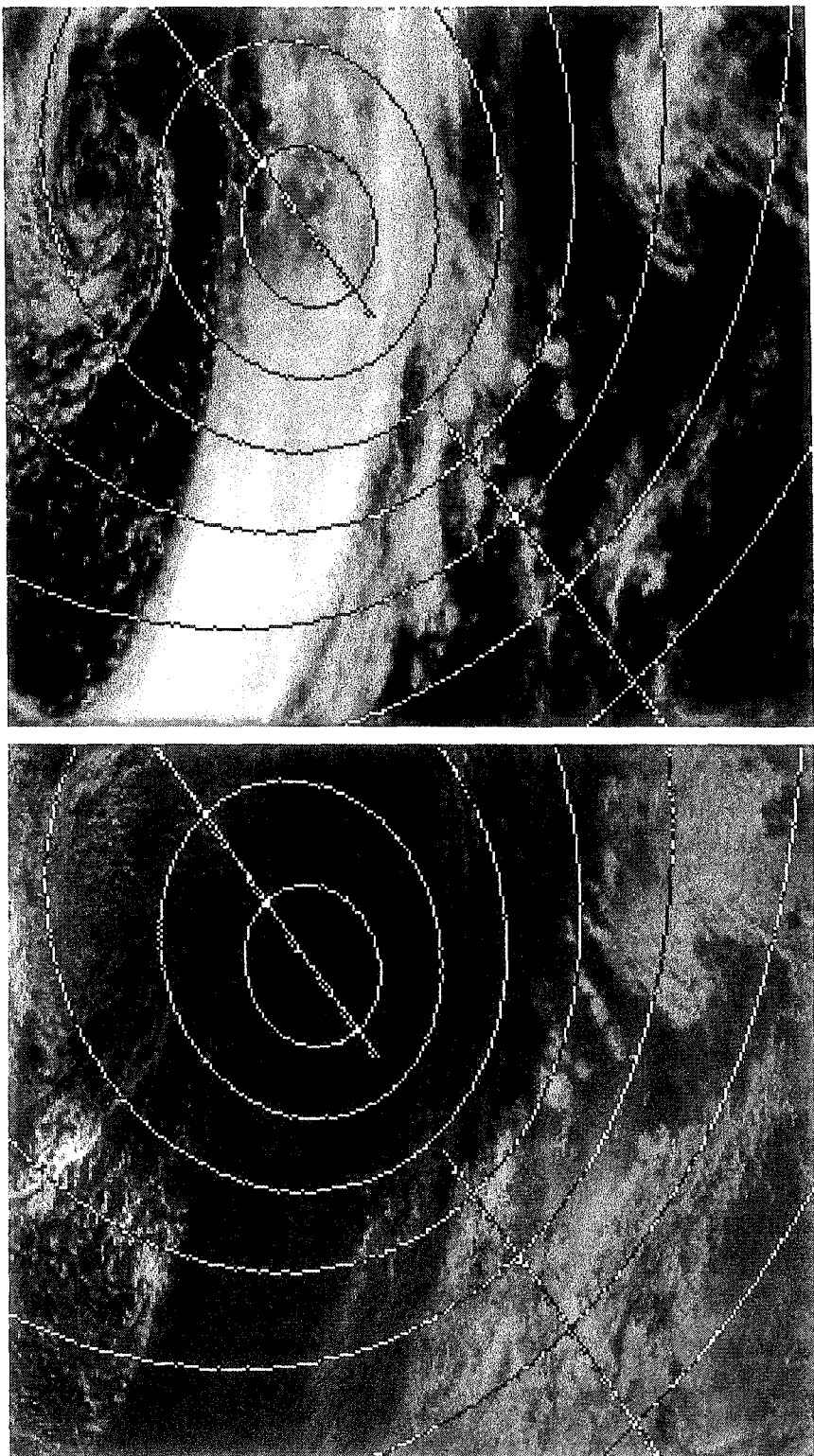
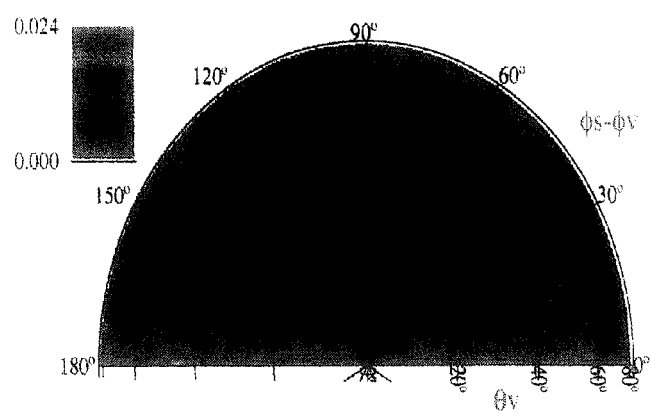
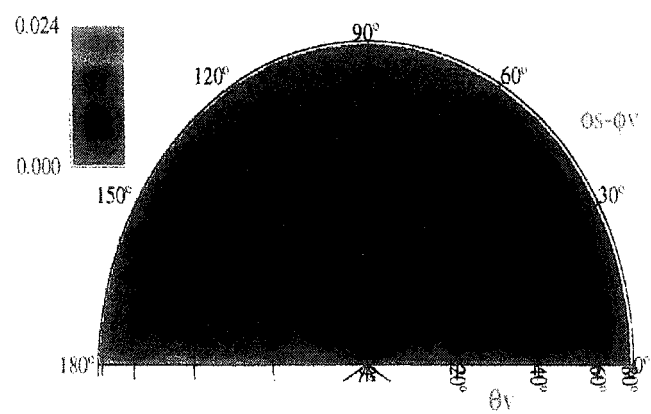


Figure 1

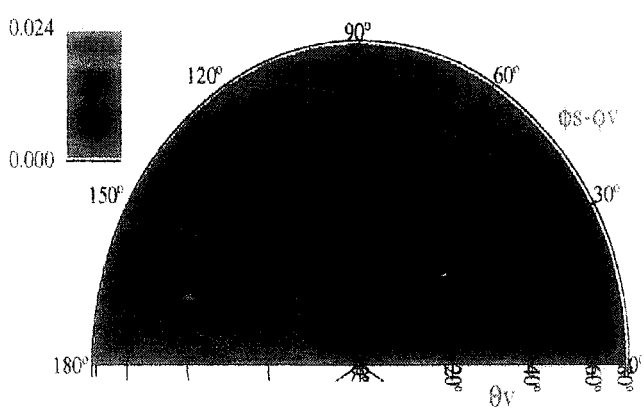
Compact : Q=1



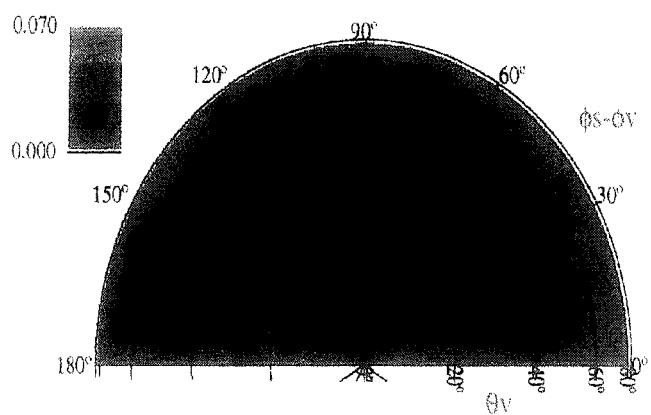
Column : Q=2.5



Polycrystals



Plates : Q=0.1



Plates : Q=0.05

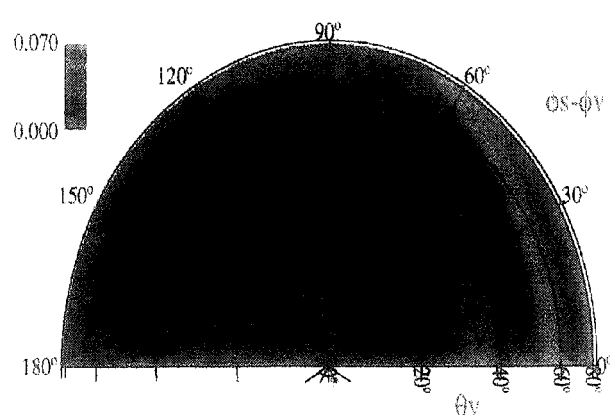


Figure 3

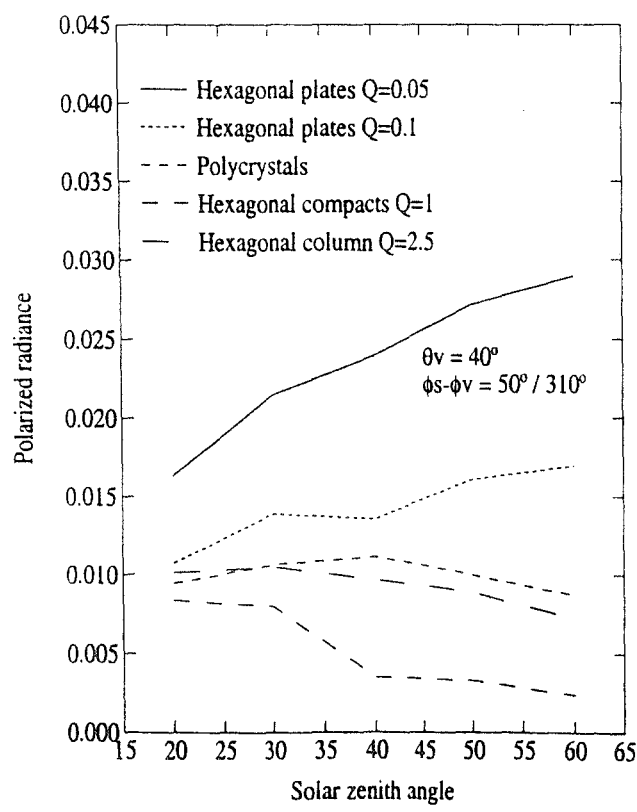
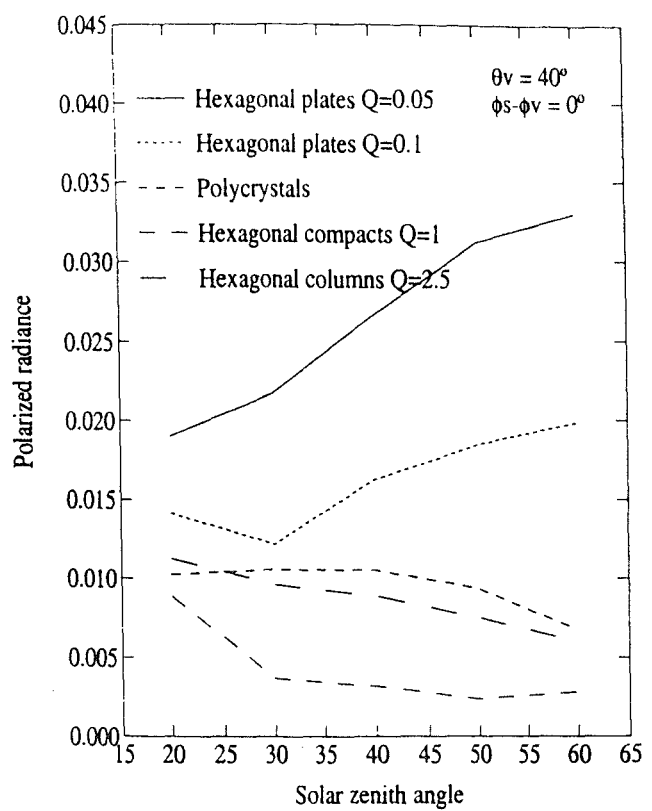
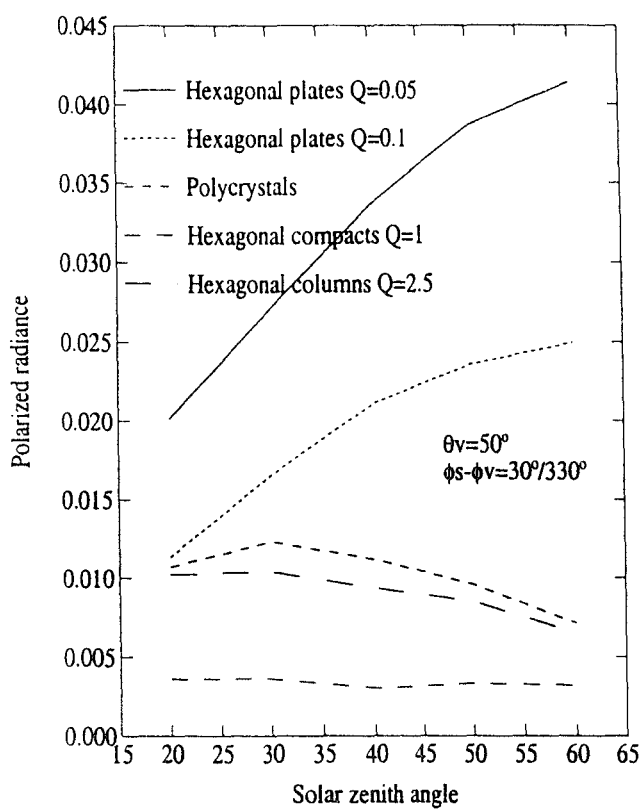


Fig 4

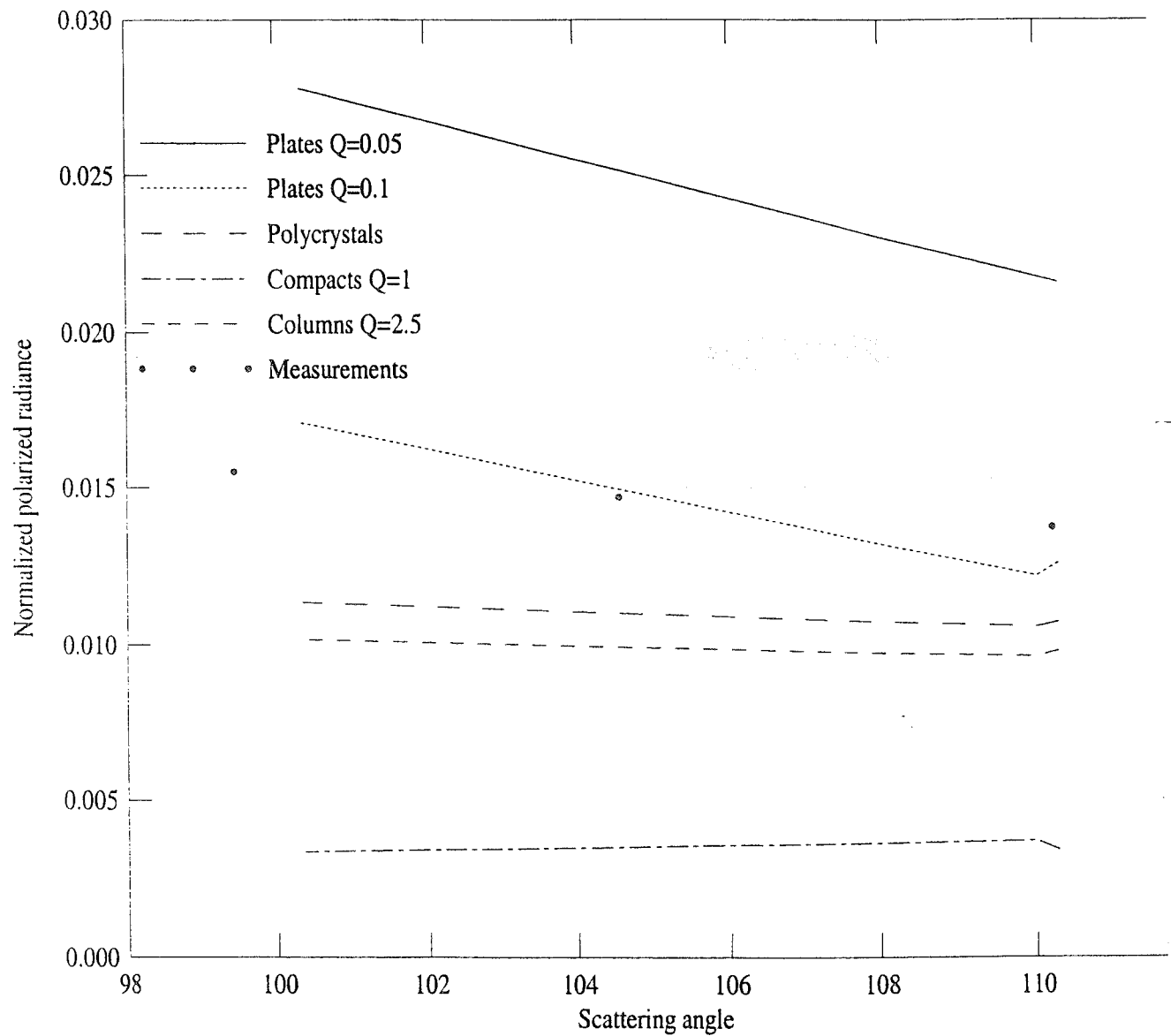


Fig 5a

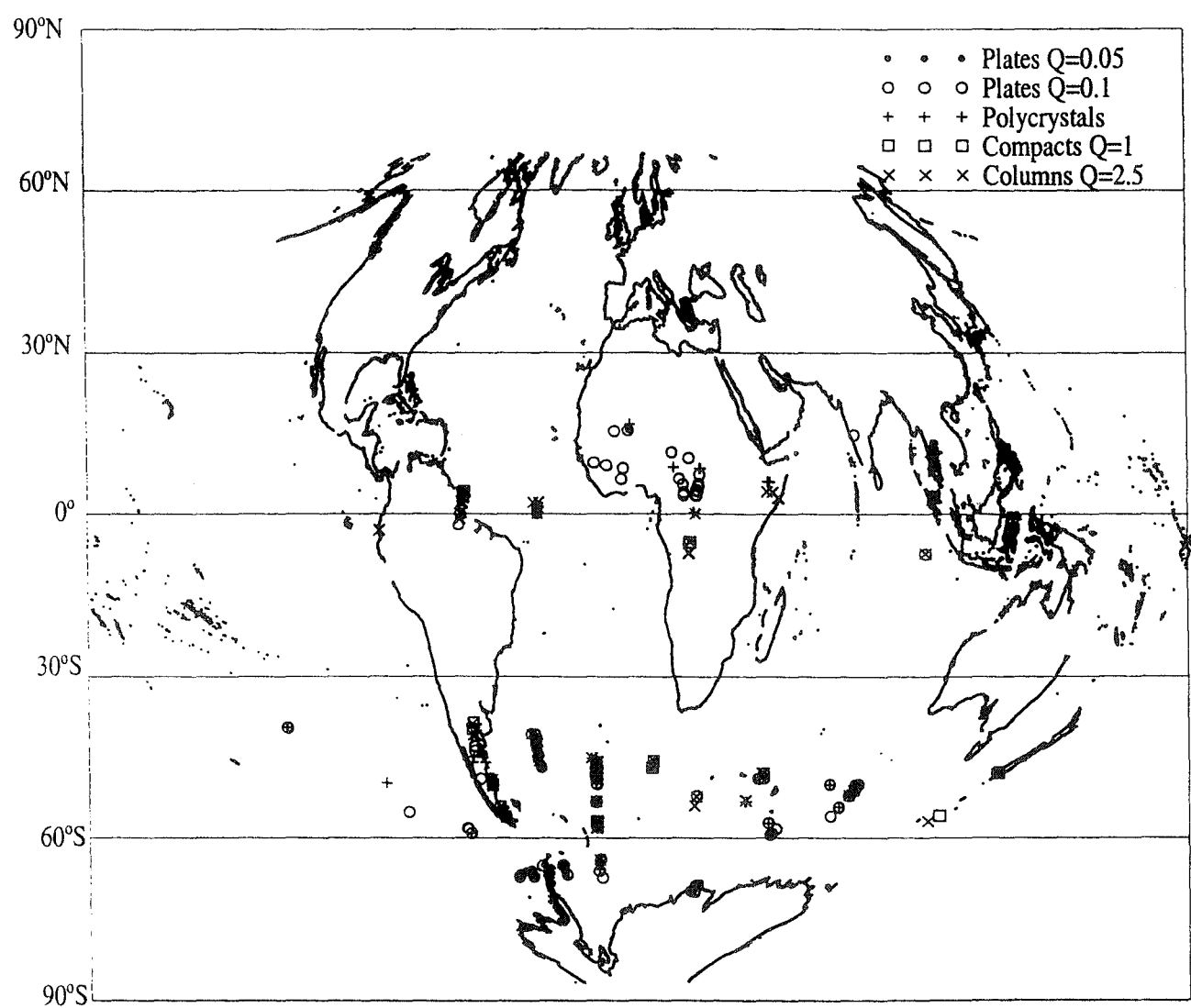


Fig 5b

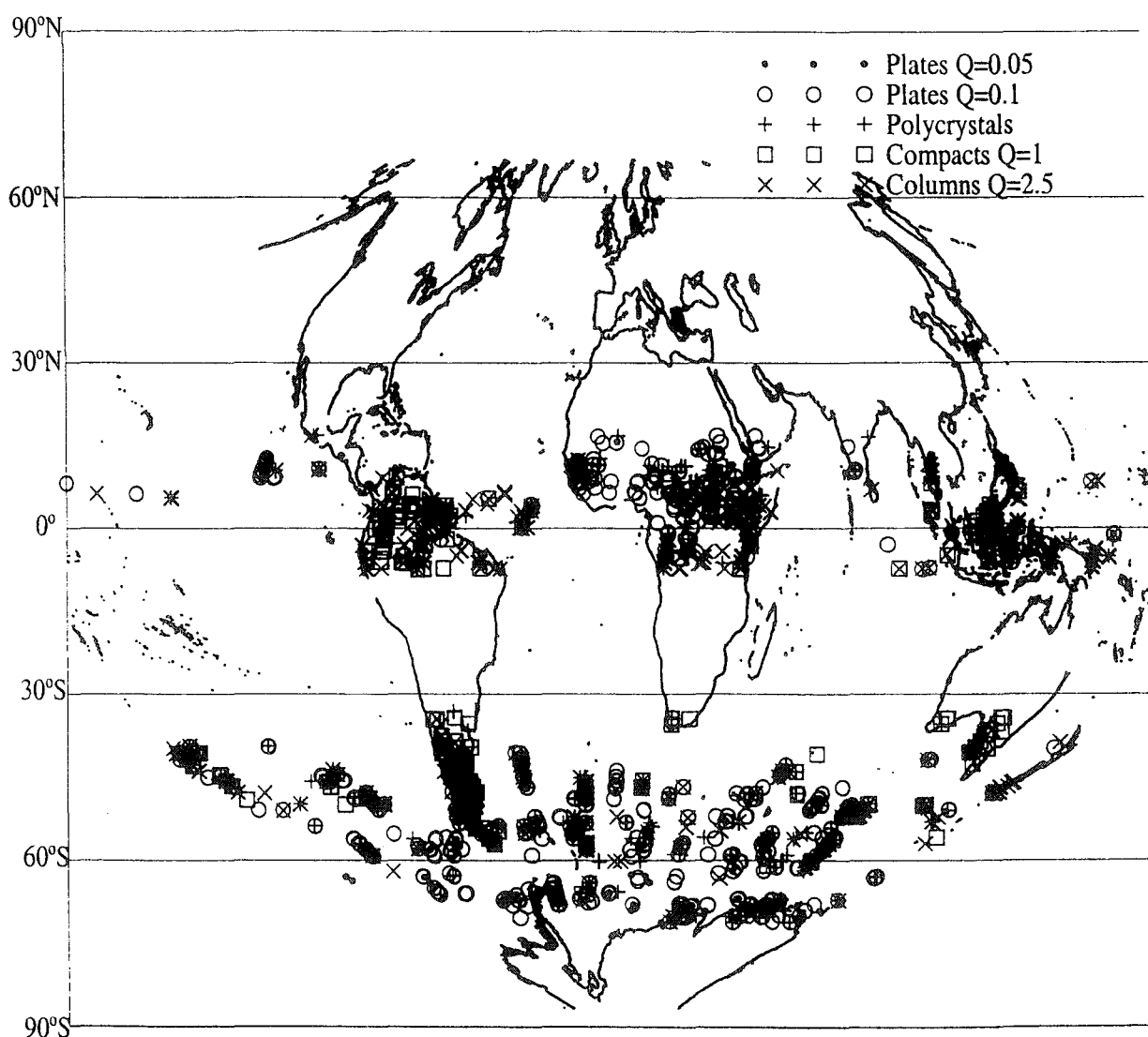
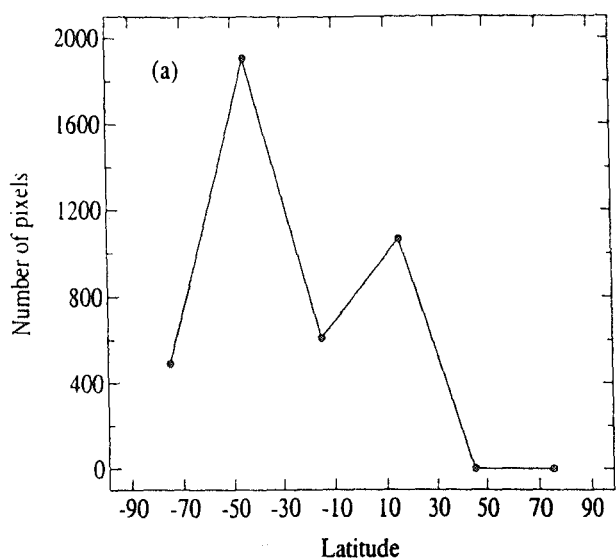


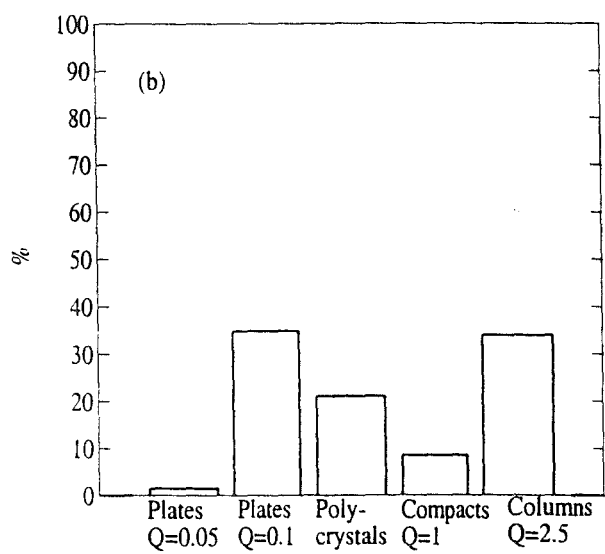
Fig 6

1997 : January 1st to 6th

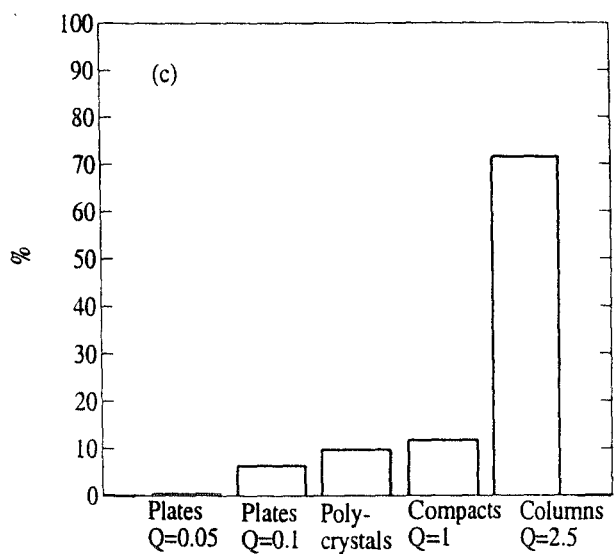
Fig 7



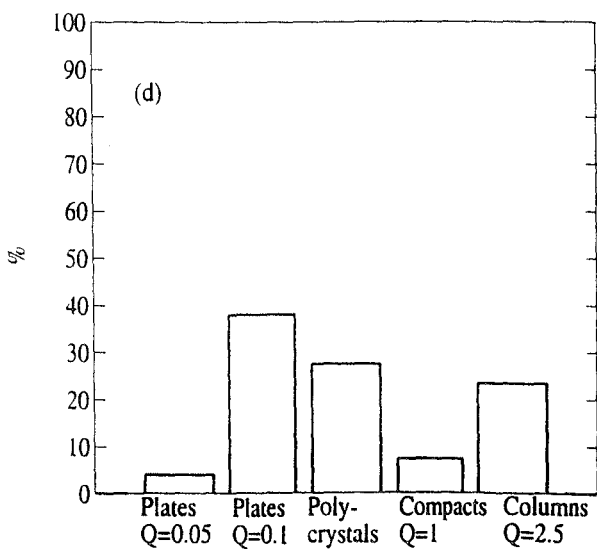
$0^\circ - 30^\circ N$



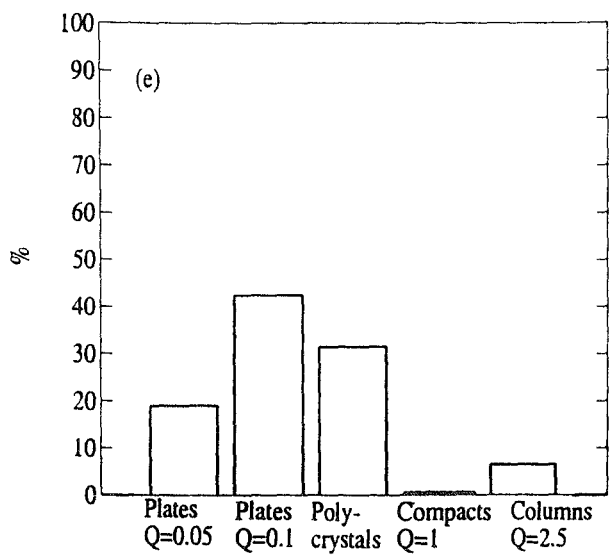
$0^\circ - 30^\circ S$



$30^\circ - 60^\circ S$



$60^\circ - 90^\circ S$



1997 : June 1st to 6th

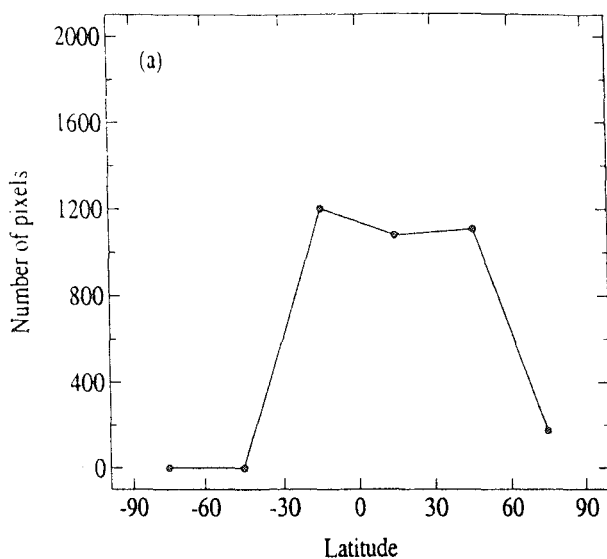
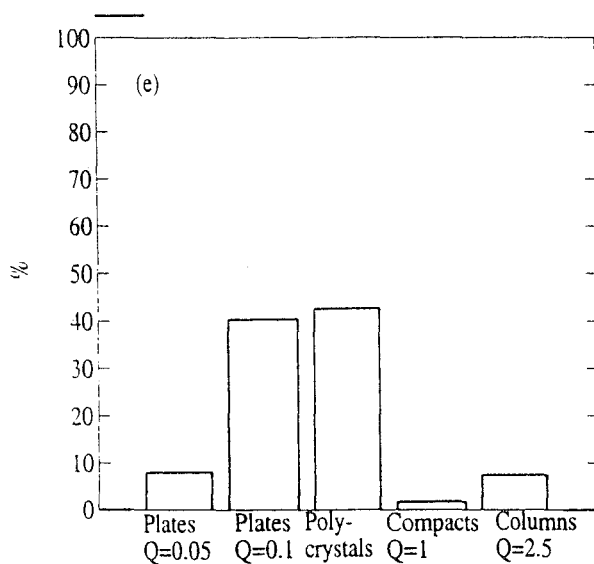
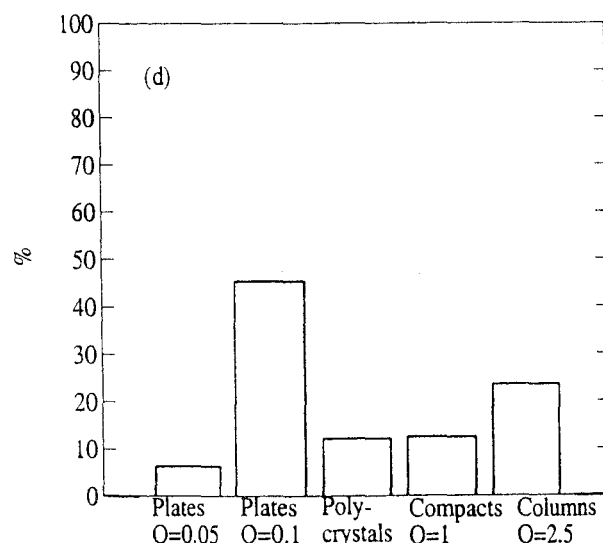


Fig 8

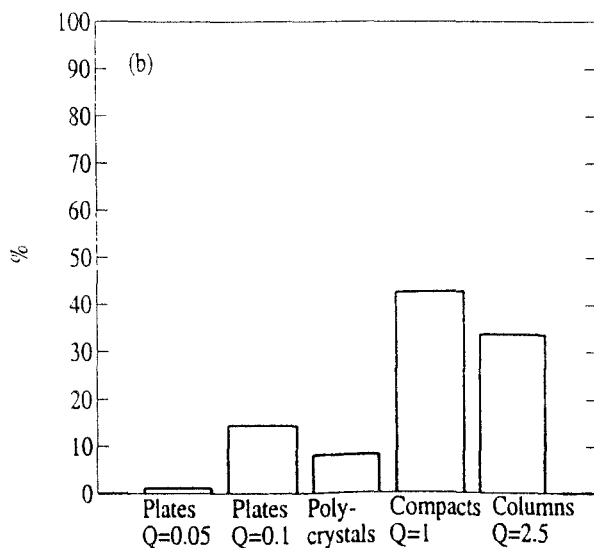
$60^\circ - 90^\circ \text{ N}$



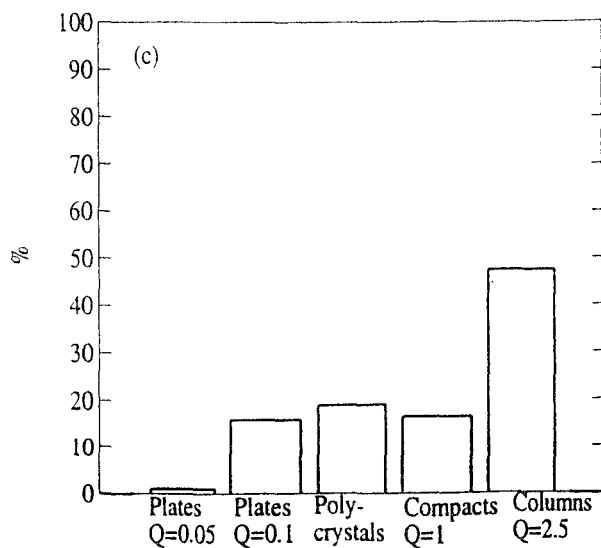
$30^\circ - 60^\circ \text{ N}$



$0^\circ - 30^\circ \text{ N}$



$0^\circ - 30^\circ \text{ S}$



Cloud droplet effective radius from spaceborne polarization measurements.

Cloud droplet effective radius from spaceborne polarization measurements

François-Marie Bréon

Laboratoire de Modélisation du Climat et de l'Environnement, Commissariat à l'Energie Atomique, Gif sur Yvette, France



Philippe Goloub

Laboratoire d'Optique Atmosphérique, Université des Sciences et Techniques de Lille, Villeneuve d'Ascq, France

Abstract. The spaceborne POLDER instrument provided the first quantitative measurements of the Earth reflectance polarization characteristics. Many POLDER images of polarized light show cloudbow type features over cloud fields for scattering angles between 150 and 170°. This unexpected observation is attributed to the polarized radiance generated by single scattering by cloud droplets. It shows that, in many cases, the cloud droplet size distribution is very narrow. The multidirectional polarized radiance measurements can be inverted for an accurate estimate of the cloud droplet radius.

Introduction

The POLDER instrument (Deschamps et al., 1994) was launched on the ADEOS platform in August 1996. Its measurement principle is based on a bidimensional CCD detector, a rotating wheel which carries optical filters and polarisers and a wide field of view optics. At present, POLDER is the only spaceborne instrument which provided quantitative measurements of the reflected sunlight polarization characteristics. Unfortunately, due to electrical failure, the ADEOS platform died on June 30th, 1997. Nevertheless, eight months of measurements have been acquired which allow new investigations on the usefulness of polarization and directionality for Earth remote sensing. In this paper, we show unanticipated observations in polarized light. Further investigation demonstrate that, in favorable conditions, the cloud droplet radius can be retrieved from POLDER measurements with a very high accuracy.

Observation

Figure 1 is a three color composite (Blue : 0.44 μm; Green : 0.67 μm; Red: 0.86 μm) of the radiance measured by the instrument CCD detector over a 1600x2200 km² area located across the west coast of Africa, south of the Equator. The image center location is approximately (20°S, 10°E). The black/white lines overlaid on the figure indicate the scattering angle in 10° increments (angle between the solar incident and the viewing directions) as well as the principal plane. The top figure shows the total radiance and is similar to what would be observed with an instrument without polarization capabilities. On the right side of the image

(East) is the African continent, with more vegetation to the North (top) which is evidenced by the reddish color (larger reflectance at 0.86 μm). A few cloud fields appear as white areas over the land. On the left side of the figure is the Atlantic ocean, which is covered by a variable amount of clouds. This area is well known for a very high occurrence of stratocumulus.

The bottom image corresponds to the exact same area, but displays the perpendicular component of the polarized radiance. In the Stokes vector representation of radiance (I,Q,U,V), it is the second component of the vector (Q) where the reference direction is the plane of scattering (defined by the solar and viewing directions). The white band which follows the 140° line of scattering angle corresponds to a maximum in the polarized radiance around this direction, which is characteristic of water droplets radius larger than the wavelength (Goloub et al., 1994). The intense cloudbow along the 140° scattering angle line is an unambiguous indication of the presence of liquid water droplets at the cloud top. For larger scattering angles, color bands indicate a scattering process which is highly directional and spectrally dependent. This is peculiar since, in the spectral range of interest (0.44-0.86 μm), cloud reflectances are usually expected to be roughly white.

To investigate further this phenomenon, we present in Fig. 2 the same image (only the polarized radiance is shown), but where the three spectral bands have been separated. The same general features are apparent. In the 140-170° range, oscillations of the polarized reflectance as a function of the scattering angle are apparent. Note that the number of oscillations vary with the spectral band. There are about twice as many in the blue band (0.44 μm) than in the near infrared (0.86 μm). The difference in the position of the maxima and minima between the spectral bands explains the "cloudbow" features displayed in Fig. 1.

Interpretation

Radiative transfer simulations show that single scattering provides the main contribution to the polarized radiance. Multiple scattering polarization is very small (Hansen, 1971). Assuming a plane parallel cloud, no absorption, and no other scattering processes, the single scattering contribution to the polarized reflectance is :

$$R_p^{ss} = \frac{1 - \exp[-\tau(1/\mu_s + 1/\mu_v)]}{4(\mu_s + \mu_v)} P_p(\gamma) \quad (1)$$

where τ is the cloud optical thickness, P_p is the polarized

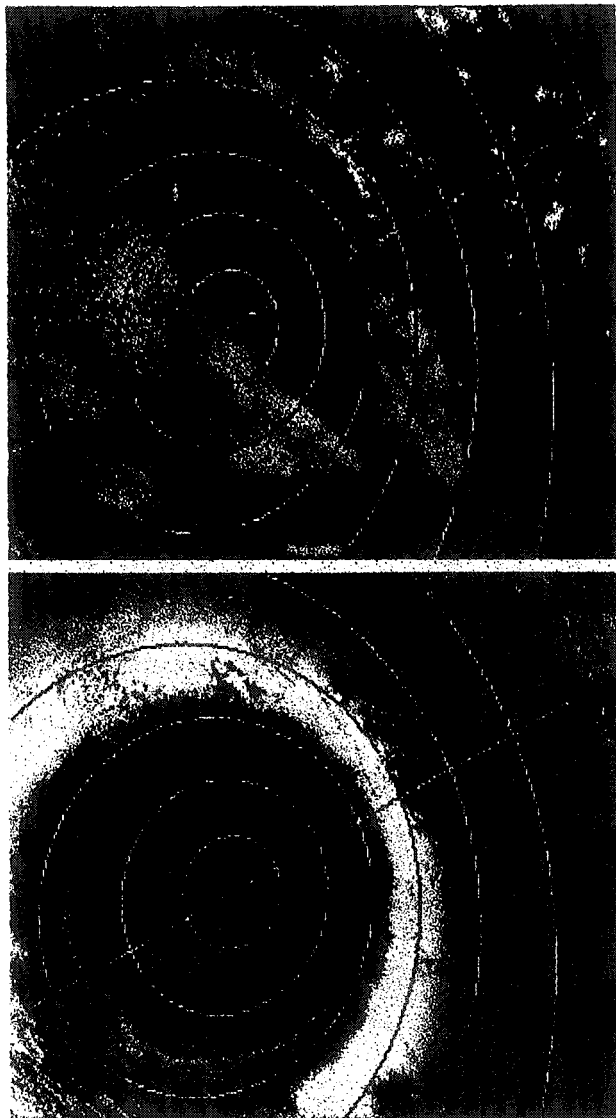


Figure 1. Three color composite (Blue : 0.43 μm , Green : 0.67 μm , Red : 0.86 μm) of POLDER measurements acquired by the CCD matrix over the Atlantic ocean and Southern Africa on Nov. 3rd, 1996. The top figure is for the total reflectance, whereas the bottom figure represents the polarized reflectance. The curved lines indicate the scattering angle in 10° increments (smaller radius line is for 170°). The straight line is the principal plane. For each spectral band, the scale is from 0 to 0.8 in reflectance, and from 0.08 in polarized reflectance.

scattering phase function of the droplets, μ_s and μ_v are the cosines of the solar and zenith angles, respectively, and γ is the scattering angle. In most cases, the cloud optical thickness is such that the exponential takes negligible values. Equation (1) then reduces to :

$$R_p^{ss} = \frac{P_P(\gamma)}{4(\mu_s + \mu_v)} \quad (2)$$

Therefore, the polarized reflectance measurement is directly linked to the polarized phase function. Such functions are calculated using the Mie theory. Fig. 3 shows the polarized phase function $P_P(\gamma)$ computed for several cloud droplet size distributions as (Deirmendjian, 1969) :

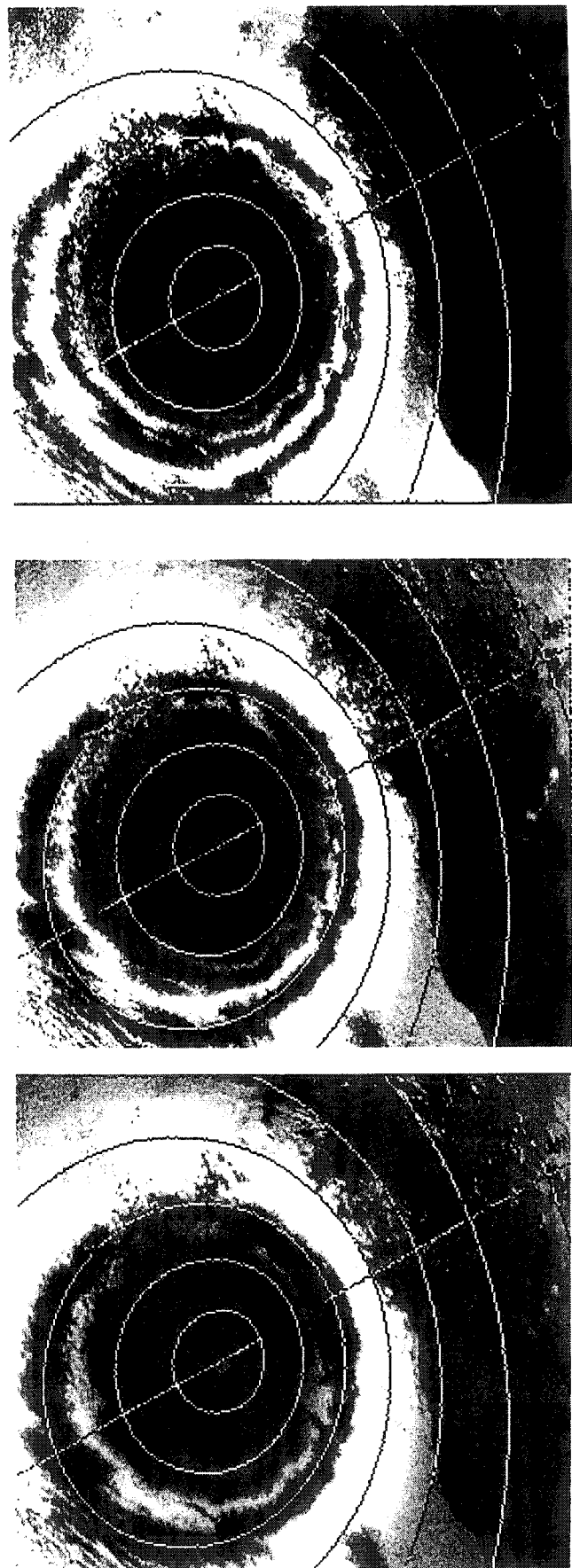


Figure 2. Same as in Fig. 1 but the three bands have been separated and only the polarized reflectance is shown. The spectral band is 0.44, 0.67 and 0.86 μm from top to bottom.

$$n(r) = \left(\frac{r}{r_{\text{eff}}} \right)^{-3} \exp \left[-\frac{1}{\sigma_{\text{eff}}} \left(\ln \left(\frac{r}{r_{\text{eff}}} \right) - \frac{r}{r_{\text{eff}}} + 1 \right) \right] \quad (3)$$

where $n(r)$ is proportional to the droplet number concentration, and r_{eff} (effective radius) and σ_{eff} (effective variance) are two parameters which define the size distribution.

The polarized phase function shows local maxima and minima in the range 150-170°. Note that, as on the POLDER measurements, there are about twice as many oscillations at 0.44 μm than at 0.86 μm (Fig. 3a). As the size distribution broadens (σ_{eff} increases), the amplitude of the oscillations decreases. For effective variances of 0.1, they are smoothed out.

These results provide a simple interpretation of the observed cloudbow features. The observation of similar cloudbows over many large areas indicate that 1) an homogeneous cloud droplet size distribution is a frequent phenomenon, and 2) the size distribution over these areas is relatively narrow ($\sigma_{\text{eff}} \leq 0.05$).

Inversion

To investigate further this phenomenon, and its implication for the remote sensing of cloud droplet radius, we

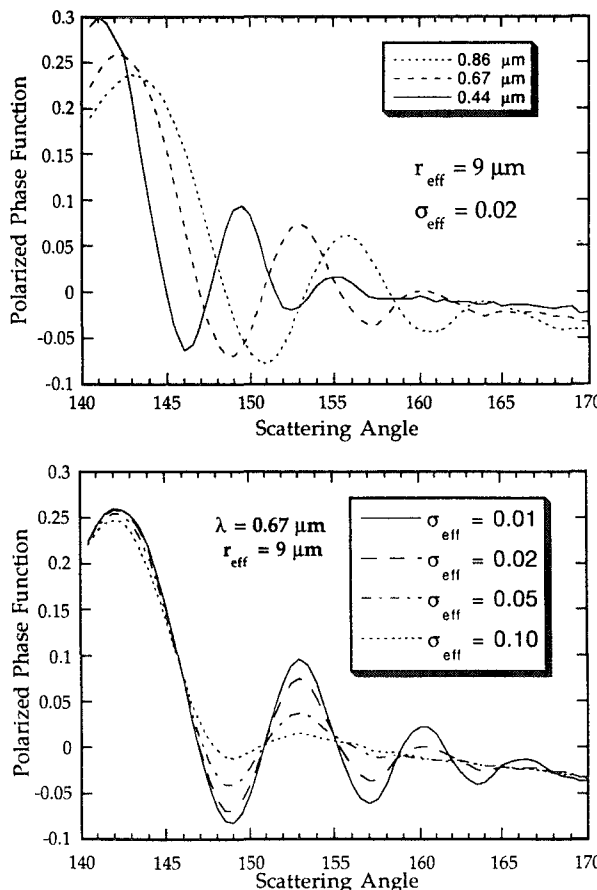


Figure 3. Polarized phase function $P_p(\gamma)$ as a function of scattering angle for cloud droplet size distributions as in eq. (3). In Fig. 3a, we show how $P_p(\gamma)$ varies with the wavelength. Fig. 3b illustrates the variation of $P_p(\gamma)$ with the size distribution variance.

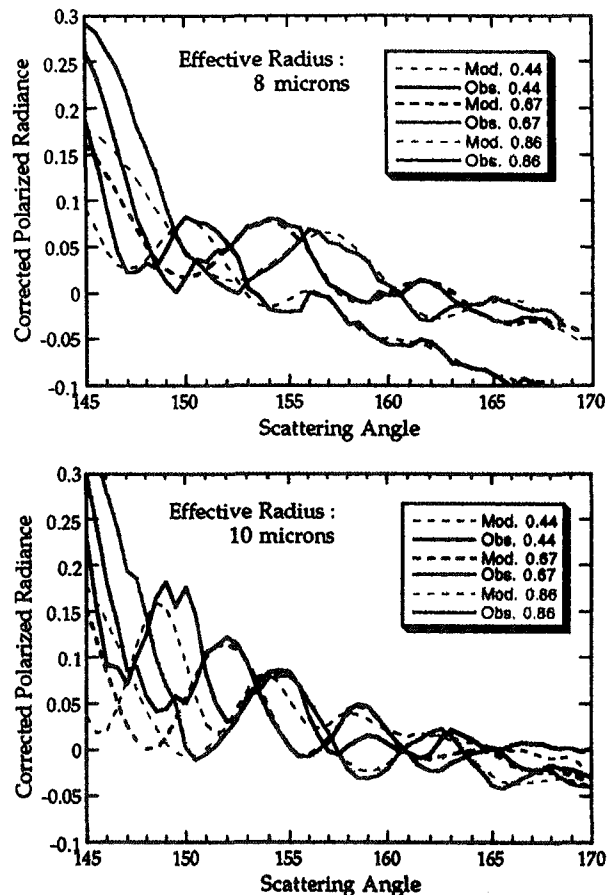


Figure 4. Two examples of model-measurement comparisons after a successful inversion of cloud droplet effective radius from POLDER spaceborne measurements. In both cases, the dispersion σ_{eff} is 0.02.

have separated the POLDER swath into 200x200 km² boxes. For each box, we make use of the directional capabilities of the POLDER instrument (each pixel is viewed from up to fourteen different geometries during a single satellite overpass). For a given pixel, the scattering angle sampling is on the order of 5°, which is not sufficient to observe the oscillations. The spatial aggregation is therefore necessary, assuming homogeneity, because the various pixels in a given box are observed with slightly different viewing angles. A minimum size of 150x150 km² yields an homogeneous sampling of the scattering angles. However, if the cloud droplet distribution is heterogeneous within the area, the measurement variation with scattering angle is noisy, and the inversion is impossible.

The measurements are first corrected for Rayleigh scattering with the assumption that the cloud top height is about 1 km :

$$R_p = R_p^{\text{mes}} \exp \left[-\tau_m \left(\frac{1}{\mu_s} + \frac{1}{\mu_v} \right) \right] - R_p^{\text{mol}} (\tau_m, \mu_s, \mu_v, \phi) \quad (4)$$

where τ_m is the molecular optical thickness above a theoretical 1 km high cloud top, and R_p^{mol} , the result of radiative transfer simulations, is the polarized reflectance generated by molecular scattering in the atmosphere. A normalization for the viewing geometry [i.e. multiplication by $4(\mu_s + \mu_v)$] is then applied. In the single scattering approximation, the normalized measurements are roughly

proportional to the polarized phase function. We then average all corrected measurements within a given box as a function of the scattering angle.

The polarized phase functions P_p have been computed for a large number of size distributions defined by (3). The measurements are fitted by a function $F(\lambda, \gamma)$ where λ is the wavelength :

$$F(\lambda, \gamma) = a P_p(\gamma, \lambda, r_{\text{eff}}, \sigma_{\text{eff}}) + b \gamma + c \quad (5)$$

In eq. (5), a , b and c are three parameters which are inverted through a least square procedure (minimization of the squared difference between the measurements and the function defined in (5), for a given range of scattering angle). "a" accounts for the cloud fractional coverage; $b \gamma + c$ accounts for the polarized radiance generated by aerosol above the cloud, inaccuracies in the molecular scattering correction and contributions from the glitter. The cloud droplet model which best fits the three wavelengths measurements for a range of scattering angle between 150° and 170° is retained. The inversion is successful if "a" is greater than a threshold and the measurement-model RMS error is lower than another threshold.

Fig. 4 shows two examples of results which yield effective radius of $8 \mu\text{m}$ and $10 \mu\text{m}$. Note that position of the maxima and minima are very different for the two cases when the effective radii differ by only two microns. This is an indication of the sensitivity of the method to changes in effective droplet radius. The agreement between model and measurements is excellent. The position of the maxima is accurately reproduced by the model for the three bands. The agreement in Fig. 4b is not as good for the $0.44 \mu\text{m}$ band than for the two others. This may result from an inaccurate correction of the molecular contribution to the polarized light which is much larger at this wavelength than at the others.

The agreement is not as good close to 145° of scattering angle. This angle corresponds to the main cloudbow which shows a larger and wider maximum in the polarized phase function. We have made multiple scattering simulations of polarized light for plane parallel cloud using a code developed by Garcia and Siewert (1986). These simulations show that the single scattering approximation used in the inversion procedure (eq. 2 and eq. 5) is very accurate for local maxima in the range 145 - 170° but underestimates the polarized radiance in the main cloudbow. This underestimation results from photons which are scattered with a scattering angle around 145° and again with a very small angle (forward peak of the phase function), or the opposite. Such photons, which are not accounted for in the single scattering approximation, have a polarization similar to those single scattered and contribute to the polarized radiance around 145° . Because the secondary cloudbows are narrower in term of scattering angle, this double scattering process is smoothed out in the 150 - 170° range.

Discussion

The observation of several cloudbows in the 150 - 170° range of scattering angles is much easier in polarized light

than in total radiance. For most clouds (optical thickness larger than ≈ 2), the total reflected radiance is mostly generated by multiple scattering within the cloud. In such case, single scattering is a small contribution to the radiance and the relative amplitude of the reflectance variations with scattering angle is small (Spinhirne and Nakajima, 1994). On the same scenes as those presented in this paper, we have not been able to measure a variation of the total radiance with a change in scattering angle which is significant with regard to the spatial variation (see Fig. 1a).

The proposed inversion method is applicable only if the droplet size distribution is relatively narrow. For broad size distributions, the phase function maxima and minima are smoothed out and the effective radius retrieval is impossible. Another limitation of the method is that it only probes a cloud layer of optical thickness less than about 1 located at the cloud top. On the other hand, this may be seen as an improvement to other methods based on the spectral signatures of clouds, for which the radius estimate is an indefinite average over the cloud layer. Nevertheless, for favorable conditions, the method is extremely sensitive and yields an unambiguous measurement of the cloud top effective radius. When the inversion is successful, the method also demonstrates that the size distribution is narrow.

The inversion method will now be applied to the full POLDER dataset. We will attempt a comparison of inverted radius with available in-situ measurements. We will also analyze the global distribution of retrieved droplet size in relation to atmospheric parameters such as aerosol loading estimates.

Acknowledgments. The results presented in this paper were obtained using data from CNES/POLDER onboard NASDA/ADEOS.

References

- Deirmendjian, D. Electromagnetic scattering on spherical polydispersions, American Elsevier Publ. Co., New York, 1969.
- Deschamps, P. Y., F. M. Bréon, M. Leroy, A. Podaire, A. Bricaud, J. C. Buriez and G. Seze, The POLDER mission: Instrument characteristics and scientific objectives, *IEEE Transactions on Geoscience and Remote Sensing*, 32, 598-615, 1994.
- Garcia, R.D.M., and C.E. Siewert; A generalized spherical harmonics solution for radiative transfer models that include polarization effects, *J. Quant. Spec. Rad. Transfer*, 36, 401-423, 1986.
- Goloub P., J.L. Deuzé, M. Herman, Y. Foucart, and P.Y. Deschamps, Analysis of the POLDER Airborne Instrument Observations over Cloud Covers, *IEEE Trans. Geosc. Rem. Sens.*, 32, 78-88, 1994.
- Han, Q., W.B. Rossow and A.A. Lacis, Near-global survey of effective droplet radii in liquid water clouds using ISCCP data, *J. Clim.*, 7, 465-497, 1994.
- Hansen, J.E., Multiple scattering of polarized light in planetary atmospheres. Part II. Sunlight reflected by terrestrial water clouds, *J. Atm. Sciences*, 28, 1400-1426, 1971.
- Spinhirne, J.D. and T. Nakajima, Glory of clouds in the near infrared, *Appl. Opt.*, 33, 4652-4662, 1994.

F.M. Bréon, CEA/DSM/LSCE, 91191 Gif sur Yvette, France.
(e-mail : fmbreon@cea.fr)

Ph. Goloub, Laboratoire d'Optique Atmosphérique, bat P5, USTL, 59655 Villeneuve d'Ascq, France.

(Received January 16, 1998, revised March 26, 1998,
accepted April 3, 1998)

Chapitre 4

Caractérisation des aérosols troposphériques

Observation et caractérisation des aérosols troposphériques

Cette dernière partie concerne la télédétection de certaines propriétés optiques et microphysiques des aérosols. Nous montrons comment la mesure de polarisation permet d'améliorer la détection et d'affiner la climatologie des aérosols, notamment au-dessus des continents. Avant de présenter les résultats, nous rappelons brièvement les différents types d'aérosols présents dans la basse atmosphère terrestre.

A) Caractéristiques microphysiques des aérosols troposphériques.

Les aérosols troposphériques sont constitués de particules liquides ou solides (diamètre moyen inférieur à 10 µm). Ils résident pour l'essentiel dans les 2 ou 3 premiers kilomètres de la troposphère. On a coutume de les regrouper en 4 catégories en fonction de leur composition : (i) poussières d'origine minérale, (ii) sulfates et nitrates, (iii) aérosols composés de sel marin, (iv) aérosols carbonés. Les aérosols carbonés sont souvent divisés en aérosols non-absorbants (aérosols d'origine organique, typiquement les fumées) et en aérosols absorbants (suie).

Les aérosols se distinguent également selon leur dimension. Les figures 1a,b et c présentent des exemples de distributions en taille déduites de mesures radiatives (réseau AERONET).

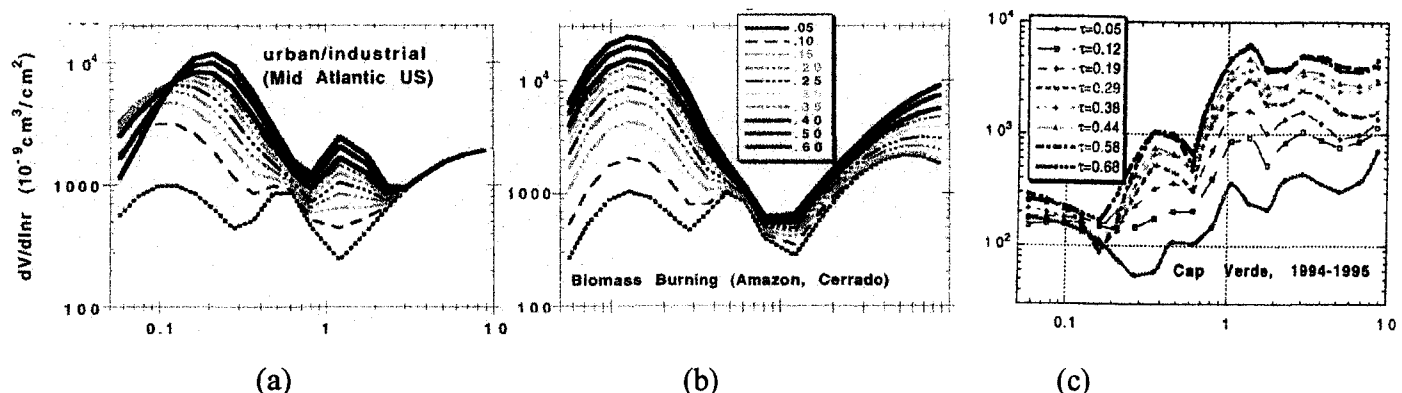


Figure 1 : Exemples de granulométries en volume ($dV/d\ln r$) pour des aérosols urbains et industriels (a), des aérosols de brûlis (b), et des aérosols désertiques (c). Pour chaque type, on a superposé les granulométries associées à des contenus en aérosols (épaisseur optique à 670nm) différents (d'après Kaufman, Remer et Holben). Le rayon est donné en micromètre.

De façon générale, on voit apparaître 4 modes dimensionnels. Le mode d'accumulation ($r < 0.3 \mu\text{m}$), un mode compris entre 0.3 et 0.8µm correspondant aux aérosols de la troposphère libre associés à d'éventuels aérosols stratosphériques et de poussières désertiques, un troisième mode compris entre 0.8 et 2.5 µm, correspondant aux aérosols marins ou désertiques et enfin un mode de grosses particules de rayon supérieur à 2.5 microns.

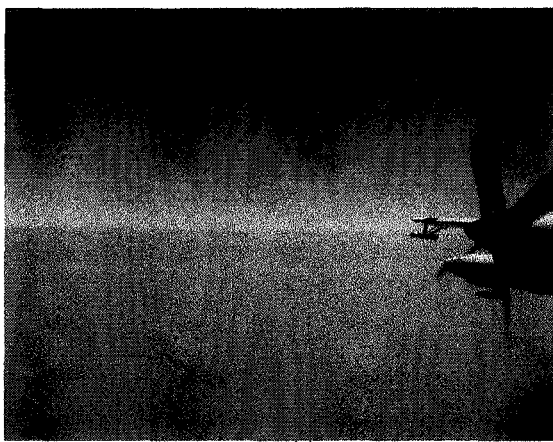
Néanmoins, on a coutume de simplifier cette description à l'aide de deux modes (mode d'accumulation et mode grossier) dépendant du processus de formation des particules.

- Les particules du *gros mode* ont un rayon supérieur à $1 \mu\text{m}$ (figure 1c) et sont constituées de façon majoritaire par les aérosols primaires, c'est-à-dire, des aérosols formés par injection dans l'atmosphère de particules de poussières produites par le vent (figure 2), des aérosols marins produits par embruns océaniques, et des particules de cendre produites par les feux (figure 1a).



Figure 2 :) Soulèvement de poussières désertiques observé pendant l'expérience HAPEX (d'après D. Tanré, LOA).

- Les aérosols du mode d'accumulation ont un rayon inférieur à $1 \mu\text{m}$ et sont majoritairement formés au cours de processus atmosphériques tels que (i) la conversion gaz-particule (ii) la condensation hétérogène, (iii) la coagulation et (iv) après évaporation au sein des nuages. Ces aérosols secondaires sont la plupart du temps des sulfates et des nitrates. Les particules de suie et de fumée, qui sont des aérosols primaires, constituent l'exception car elles sont de taille sub-micrométrique. Les aérosols d'origine anthropique sont essentiellement des particules sub-micrométriques résultant à la fois de processus de formation primaire et secondaire. Ils ont pour origine la combustion de biomasse et de fioul fossile, et constituent la plus grande part des fumées, suies, sulfates et nitrates présents dans la troposphère (figure 3). La formation du smog au-dessus des grandes villes est une manifestation de leur présence. Le bilan en masse des émissions anthropiques est plus faible que celui des poussières minérales ou des aérosols marins, cependant leur taille sub-micrométrique affecte davantage le rayonnement solaire et par suite le bilan radiatif de l'atmosphère.



(a)



(b)

Figure 3 : (a) Photographie d'un nuage de pollution survolé au sud de l'Inde (d'après R. Rocca, Laboratoire de Météorologie Dynamique), dans la région des Maldives (hémisphère Nord), durant l'expérience INDOEX, le 20/03/99. La superficie du nuage est estimée à $500\text{km} \times 500\text{km}$, son épaisseur à 3km . Ce nuage brunâtre est composé d'aérosols soufrés, de suie et de poussières diverses. *(b)* Photographie d'un feux de biomasse en septembre 1992, durant l'expérience BASE-A (Biomass burning Airborne and Spaceborne Experiment) au Brésil (d'après D. Tanré).

B) Caractérisation des aérosols au-dessus des océans à l'aide d'imageurs satellitaires.

La caractérisation fine des aérosols en routine à l'échelle globale à partir de l'imagerie satellitaire, validée par des observations au sol, constitue la seule solution pour réaliser une climatologie des aérosols (contenu, distribution en taille, forme, indice de réfraction, distribution verticale) requise pour étudier leur contribution au changement climatique.

Jusqu'à récemment, on ne pouvait observer en routine les aérosols qu'au-dessus des océans, à partir de l'AVHRR (Advanced Very High Resolution Radiometer). En effet, l'observation des aérosols à partir d'un satellite est basée sur la lumière solaire qu'ils renvoient vers l'espace. Or il s'agit d'un signal faible et, pratiquement, on ne le mesure avec précision qu'au-dessus des surfaces océaniques, à des longueurs d'onde rouge et/ou proche-infrarouge où l'eau est absorbante. Les cartes d'abondance moyenne en aérosols déduites de ces données ont permis de mettre en évidence les principales sources d'injection d'aérosols sur les océans (événements de poussières désertiques, brûlis, pollutions industrielles continentales) et d'en indiquer les variations saisonnières (Husar et al., 1997). On notera que ces résultats sont basés sur une mesure unique (1 seule direction de visée) de l'AVHRR, dans son canal large à 670 nm, ce qui nécessite des hypothèses sur les caractéristiques des aérosols. En effet, la lumière solaire rediffusée par les aérosols dépend de la quantité de particules intégrée sur la colonne atmosphérique mais également de leur probabilité à diffuser la lumière vers le satellite, probabilité (fonction de phase) qui varie largement avec la nature des particules. Puisqu'on ne peut pas préciser le type de particules rencontré, on estime leur abondance en se basant sur un modèle de diffusion moyen a priori; l'incertitude résultante est assez forte. Signalons deux tentatives, récentes, d'utilisation des deux canaux 1 et 2 d'AVHRR pour améliorer les climatologies aérosols (Nakajima et al., 1998 et Mishchenko et al., 1999).

La caractérisation des aérosols au-dessus des océans est réalisée de manière plus complète à l'aide de POLDER. En effet, ses capacités multispectrale, directionnelle et polarisée permettent de mieux contraindre les inversions en fournissant, en plus de l'épaisseur optique τ_a , un indicateur de taille (le coefficient d'Angström α) et l'indice de réfraction. En collaboration avec M. Herman, JL Deuzé, A. Marchand et D. Tanré, j'ai entrepris la validation des résultats obtenus au-dessus des océans (P.3-1). La première version de l'algorithme mis au point par J.L. Deuzé et M. Herman (P. 3-2 et P. 3-3) fait appel à des modèles mono-mode de particules aérosols. En dépit de la « simplicité » restrictive de ce choix et du faible nombre de points de validation disponibles, la restitution de l'épaisseur optique est satisfaisante. Le coefficient α est sous-estimé à hauteur de 30%, ce qui revient à sur-estimer la taille moyenne des particules. Ce travail de validation a montré les limites de l'hypothèse de distribution en taille à un seul mode pour certaines situations géophysiques. La sous-estimation du coefficient d'Angström, constatée avec les modèles à un mode, est due à une sous-estimation du nombre de petites particules. Dans la gamme d'angle de diffusion utilisée (80° - 120°), la polarisation des modèles à un seul mode est inférieure à celle qui est mesurée, ce qui traduit la sous-estimation du nombre de petites particules par les modèles. L'introduction de modèles bimodaux (modes d'accumulation et grossier) avec, pour le gros mode, la prise en compte de particules non sphériques diffusant et polarisant de façon plus isotrope en retrodiffusion, devrait permettre d'améliorer l'interprétation des mesures de luminances et de polarisation.

Dans le même temps, nous avons comparé les produits POLDER et TOMS au-dessus des océans (P. 3-4).

C) Caractérisation des aérosols au-dessus des terres émergées.

Au-dessus des continents, la lumière diffusée par l'atmosphère est généralement noyée dans la lumière beaucoup plus intense réfléchie par les surfaces. Là encore, la méthodologie, tout à fait innovante, utilise la polarisation (Deuzé et al., 1993, Herman et al., 1997 ; Deuzé et al., 2000) a été évaluée à l'aide des données photométriques. La comparaison a montré, sur les points de validation disponibles, une forte surestimation du coefficient d'Angström et, corrélativement, une sous-estimation de l'épaisseur optique (Deuzé et al., 2000). Les résultats témoignent également du faible niveau de polarisation généré par les particules aérosols d'origine désertique, ce qui avait déjà été observé suite à la campagne aéroportée POLDER/HAPEX en 1992. Cependant, dans de vastes régions d'Asie (Inde, Chine, Japon), d'Afrique équatoriale, ou d'Europe de l'est, les observations en lumière polarisée montrent des niveaux de polarisation assez élevés.

Un indice aérosol, noté A_i , défini comme le produit des quantités τ_a et α peut être déduit des mesures de polarisation. On constate, en effet, sur les mesures réalisées au sol que cet indice aérosol est corrélé à la lumière polarisée mesurée (figure 4).

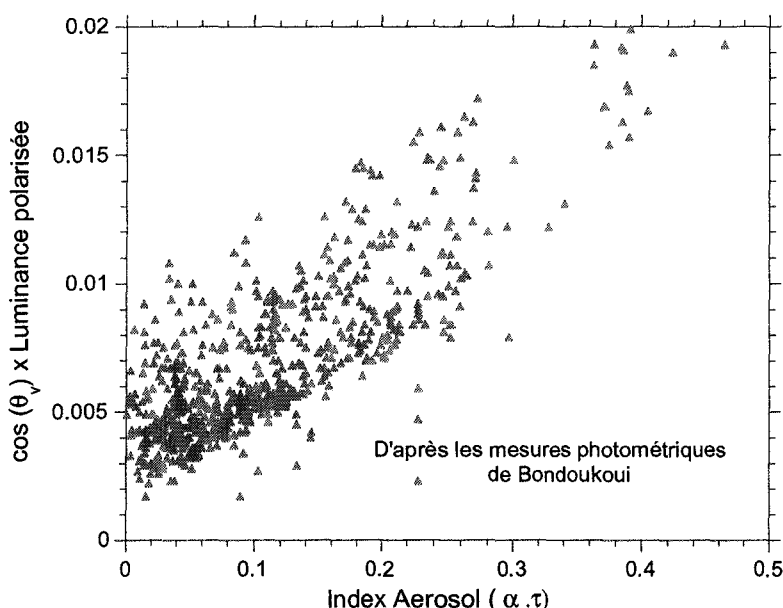


Figure 4 : Luminance polarisée à 60° en fonction de l'index aérosol à 865 nm.

Pour $A_i=0$ (pas d'aérosol), seules les molécules contribuent à la polarisation, ce qui explique que cette dernière ne s'annule pas en ce point. Cet indice sera peu sensible à la présence de grosses particules (mode grossier) ($\alpha=0$) et permettra de remonter à la quantité d'aérosols sub-micrométrique ($\alpha>1$).

La validation, à l'aide des mesures photométriques, de l'index aérosol déduit des mesures POLDER est présentée dans la publication P.3.5. L'accord entre les valeurs sol et satellite est nettement meilleur. D'autre part, la continuité spatiale entre la terre et la mer est mieux respectée. On constate, par ailleurs, que la restitution de l'épaisseur optique s'améliore lorsque les aérosols sont de petite dimension (particules émises par les feux de biomasse, aérosols de pollution).

L'analyse géophysique des cartes moyennes de l'index aérosols POLDER est en cours. On notera par exemple la mise en évidence de très forte pollution dans toute la vallée du Gange, ou encore un déplacement saisonnier de grandes zones de pratique de brûlis de l'Afrique du sud et de Madagascar en novembre, en Amérique centrale en Mai. Nous avons également montré qu'il existait une très bonne corrélation entre l'occurrence et la fréquence des feux de biomasse et l'index aérosols POLDER (**P. 3.6**, **P. 3.7**).

Listes des publications

P. 3.1 Goloub P., D. Tanré, J. L. Deuzé, M. Herman, A. Marchand, and F.-M. Bréon” Validation of the First Algorithm Applied for Deriving the Aerosol Properties Over the Ocean Using the POLDER/ADEOS”, Measurements, *IEEE Trans. Geosci. Remote. Sens.*, May 1999, Vol.37, No. 03, p1586-1596.

P. 3.2 Deuzé, J. L., Herman, M., Goloub, P. ; Tanré, D. , Marchand, A. 1999, Characterization of aerosols over ocean from POLDER/ADEOS-1 *Geophys. Res. Lett.* Vol. 26 , No. 10 , p. 1421

P. 3.3 Deuzé J.L, P. Goloub, M. Herman, A. Marchand, G. Perry, D. Tanré, Estimate of the aerosols properties over the ocean with POLDER, *J. Geophys Res*, 105, 15329-15346, 2000.

P. 3.4 Chiapello I, P. Goloub, D. Tanré, J. Herman, O. Torres, A. Marchand, Aerosol detection by TOMS and POLDER over oceanic regions, *J. Geophys Res*, 105, p 7133-7142, March 2000.

P. 3.5 Deuzé, J.L., F.M. Bréon, C. Devaux, P. Goloub, M. Herman, B. Lafrance, F.Maignan, A. Marchand, F. Nadal, G.Perry, and D. Tanré , « Remote sensing of aerosols over land surfaces from POLDER-ADEOS 1 Polarized measurements, *accepted in Journal of Geophysical Research*, 2000.

P. 3.6 Goloub P., O. Arino. “Verification of the consistency of POLDER aerosol index over land with ASTR-2 fire product”, *Geophys. Res. Lett.*, 27, p. 899-902, 2000.

P. 3.7 Tanré D., JL Deuzé, M. Herman, FM Bréon, P. Goloub, A. Marchand, Global observation of aerosol sources and transport from POLDER on ADEOS. *Submitted to Science*.

Validation of the First Algorithm Applied for Deriving the Aerosol Properties Over the Ocean Using the POLDER/ADEOS Measurements

Validation of the First Algorithm Applied for Deriving the Aerosol Properties Over the Ocean Using the POLDER/ADEOS Measurements

Philippe Goloub, D. Tanré, J. L. Deuzé, M. Herman, A. Marchand, and Francois-Marie Bréon

Reprinted from
IEEE TRANSACTIONS ON GEOSCIENCE AND REMOTE SENSING, Vol 37, No. 3, May 1999

Validation of the First Algorithm Applied for Deriving the Aerosol Properties Over the Ocean Using the POLDER/ADEOS Measurements

Philippe Goloub, D. Tanré, J. L. Deuzé, M. Herman, A. Marchand, and Francois-Marie Bréon

Abstract—Global map of aerosol parameters (optical thickness, Angström exponent, and refractive index) are derived from the POLDER instrument on board the ADEOS-1 platform. This paper focuses on aerosol optical thickness and Angström exponent retrievals that are based on visible and near infrared back scattering measurements. Assessment of the retrieval quality is achieved by means of comparison with AERONET sunphotometer data. The results show that the POLDER measurements can be used to distinguish several aerosol types from their Angström coefficients, in addition to a precise estimate of the aerosol optical thickness.

I. INTRODUCTION

AEROSOLS are suspected to play a major role in climate change by counterbalancing the warming effect due to greenhouse gases, (for review see, e.g., [2] and [7]). There is a need, therefore, for getting more information on their radiative and physical properties at a global scale using satellite remote sensing. The present sensors on board the geostationary satellites (GOES or METEOSAT) or the AVHRR/NOAA instrument can provide the total atmospheric aerosol loading, assuming other aerosol properties such as the size distribution, refractive index, and shape (e.g., [12], [6], [34], [21], [19], [31]) and very recently an estimate of the aerosol size from the two channels of the NOAA/AVHRR instruments [18]. With the new generation of sensors, POLDER (Polarization and Directionality of the Earth's Reflectances), TOMS (Total Ozone Mapping Spectrometer), and OCTS (Ocean Color and Temperature Scanner) on board the ADEOS (Advanced Earth Observing System) launched in August 1996, the planned launch of EOS-AM1 (Earth Observing System) with MISR (Multi-angle Imaging SpectroRadiometer), MODIS (Moderate resolution Imaging Spectro-radiometer), and CERES (Clouds and the Earth's Radiant Energy System) in 1998 and ENVISAT (ENVIRONMENTAL SATELLITE) in 2000, more measurements are available for deriving additional aerosol parameters as reported in [22] and [33].

Manuscript received April 16, 1998; revised October 2, 1998. This work was supported by the Centre National d'Etudes Spatiales (CNES), the Centre National de la Recherche Scientifique (CNRS), the Conseil Régional du Nord-Pas de Calais, the Fonds Européen de Développement Régional (FEDER), and the Délégation Régionale à la Recherche et à la Technologie du Nord-Pas de Calais.

P. Goloub, D. Tanré, J. L. Deuzé, M. Herman, and A. Marchand are with the Laboratoire d'Optique Atmosphérique, UA CNRS 713, Université des Sciences et Techniques de Lille, 59655 Villeneuve d'Ascq, France (e-mail: goloub@univ-lille1.fr).

F. M. Bréon is with the Laboratoire des Sciences du Climat et de l'Environnement, Commissariat à l'Energie Atomique, Gif sur Yvette, France.

Publisher Item Identifier S 0196-2892(99)03578-0.

In the present paper, we analyze the inversion of aerosol optical parameters from the POLDER instrument [50]. The POLDER instrument, launched in August 1996 on board the Japanese heliosynchronous Advanced Earth Satellite System (ADEOS) collected data until end of June 1997. It includes eight narrow-band channels, three of which have polarization capability. The instrument design allows up to 14 directional radiance measurements over the same target during a single satellite overpass which last approximately 4 minutes. It is expected that the use of the spectral, directional, polarization signatures of the reflectance measurement lead to a characterization of the aerosol type, in addition to an accurate estimate of the atmospheric aerosol load. The validation of the aerosol optical thickness and the Angström exponent is achieved against independent ground-based sunphotometer measurements from worldwide station network [3], [20].

In this paper, we first describe the algorithm for the inversion of aerosol parameters from the POLDER measurements over the oceans. The POLDER data as well as the ground-based data acquired during eight months are summarized in Section III and compared in Section IV. Discussion of assumptions, like the selection of the aerosol models and aerosol shape, is given in Section V. Examples of the retrieved aerosol parameters are provided in Section VI.

II. BRIEF DESCRIPTION OF THE ALGORITHM

The retrieval of aerosol properties is based on a lookup table (LUT) approach. The measured Stokes vector (L, Q, U ; see e.g., [46]), in the 670- and 865-nm channels are compared with the results of numerical simulations performed using the successive orders of scattering code [27] for realistic atmosphere (aerosol loading, size, and composition). This code takes into account multiple scattering and the bidirectional surface reflection of the rough ocean. The algorithm consists of retrieving the aerosol optical thickness, the size distribution, and the refractive index that minimize the averaged quadratic difference between measured and simulated radiances, both total and polarized, over the two wavelengths and the available view directions. A full description of the algorithm can be found in [10].

A. Theoretical Background

The solar radiation L_λ reaching a satellite results from photons that are backscattered by molecules and aerosols (respectively noted L_{mol} and L_{aer}) and reflected by the surface.

Over ocean, the ocean reflection includes three contributions, the sunglint reflection L_{SG} due to Fresnel reflection on the waves, the water leaving radiance L_w coming from underwater scattering, and the reflection L_f by foam. Note that L_{aer} includes both tropospheric (L_{aer}^{tropo}) and stratospheric (L_{aer}^{strato}) contributions.

Let us mention that hereinafter, the POLDER measurements as well as the radiative transfer calculations are expressed as normalized radiance L_{norm} defined by

$$L_{\lambda norm} = \frac{\pi L_{\lambda}}{E_{\lambda,s}} \quad (1)$$

where $E_{\lambda,s}$ is the solar irradiance in the spectral band λ .

The gaseous absorption which may occur along any scattering path should formally be computed using a full radiative transfer code. Compared to other optical instruments such as AVHRR, POLDER has narrow filters (between 10 and 40 nm) that have been selected in order to minimize gas absorption (except the 763-, 765-, and 910-nm channels which are used as atmospheric probes). Thus, the POLDER radiances are affected by ozone absorption in the Chappuis band only. Since ozone is an atmospheric gas located at altitudes where molecules and aerosols are sparse, the radiance is computed without accounting for it and corrected for by a simple multiplicative term.

Concerning the reflection on the water surface L_{SG} , it strongly depends on the wind speed [8]. Since the sun glint radiance can be much larger than the aerosol contribution, there is no aerosol retrieval over pixels viewed under directions close to the specular direction. The sunglint mask test consists in selecting direction having pure sunglint contribution (calculated from the actual wind speed derived from the meteorological data) smaller than $0.0005 \times \cos(\theta_s)$ where θ_s is the sun zenith angle, which is of the order of the instrumental noise. Thus in the example shown in Figs. 1 and 2, the threshold used leads to the rejection of direction corresponding to a scattering angle smaller than 98°.

For the surface contribution L_f , the foam reflectance is assumed independent of the wavelength within the POLDER spectral range used in the inversion scheme, i.e., from 670 to 865 nm. The present values are taken from [49] but if new data [13] are confirmed, they can easily be replaced. The percentage of the sea covered by foam depends on the wind speed and is taken from [25]. Finally, the water-leaving radiance L_w is taken equal to zero in both channels, which is justified in open ocean conditions [32]. In coastal zones, the aerosol parameters are also determined but are clearly affected by the uncertainty in the water-leaving radiance at 670 nm due to inorganic particles within the water.

B. Lookup Table (LUT)

The radiative transfer simulations have been performed for five values of the aerosol optical thickness τ_a at 865 nm. $\tau_a = 0.0$ corresponds to a pure molecular atmosphere, $\tau_a = 0.075, 0.15$, and 0.30 are representative of intermediate aerosol loading, and an extreme case ($\tau_a = 0.60$) is used for high aerosol content as observed during dust storms or in smoke plumes resulting from biomass burning. Linear interpolation

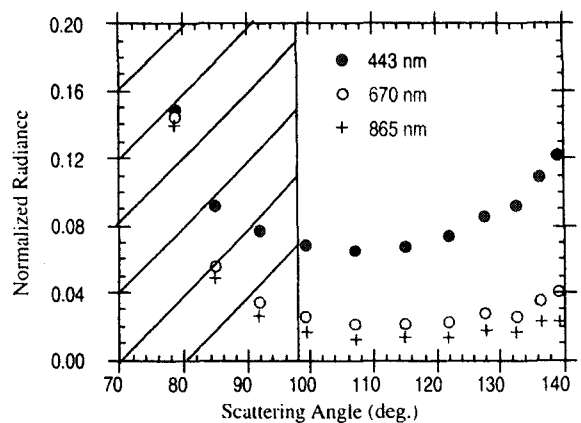


Fig. 1. Normalized radiances measured by POLDER over Crete (25.6W; 35.3N) as a function of the scattering angle [see (5)] in three spectral bands 443, 670, and 865 nm. The shaded area represents the angular range which is not used for the inversion because contaminated by the sun glint.

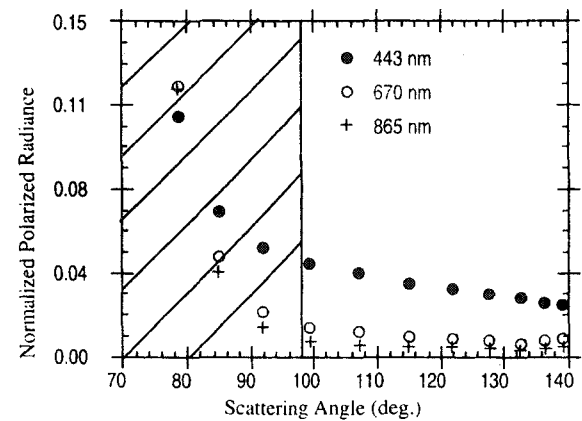


Fig. 2. Same as in Fig. 1 but for the polarized radiances.

is applied to estimate the reflectance for intermediate values of the optical thickness, and linear extrapolation is applied for optical thickness larger than 0.6.

The wind speed is set at 5 m s^{-1} . As said above, the glint contribution to the reflectance varies strongly with the wind speed, and the corresponding measurements are not used. On the other hand, the contribution resulting from the coupling of surface reflection and atmospheric scattering is almost independent of the wind speed, which justifies the choice of a single value for this parameter. Similarly, we assumed a typical scale height value of 8 km for the molecules and 2 km for the aerosols; the actual values of these parameters have a very small influence on the radiative transfer computations.

The top of atmosphere reflectances are computed for a large number of view directions and stored in the LUT with a resolution of 5° in azimuth and 3.7° in zenith angles. Multilinear interpolation is applied between these values which cover the full range of possible azimuth and zenith angles. Computations have been performed for wind speed of 5 m/s only, which is a sufficient assumption far from the specular direction since the sky light reflected by the waves is almost independent on the wind speed [9]. If the actual wind speed is different from the assumed 5 m/s wind speed, the impact on the aerosol optical thickness retrieval is smaller than 1% ($\Delta\tau/\tau < 0.01$). On the contrary, if the only available direction

TABLE I
PARAMETERS OF THE LOG-NORMAL AEROSOL SIZE DISTRIBUTIONS USED IN THE LOOKUP TABLE (LUT)

Aerosol model	Median radius (μm)	Stand. Dev. σ	Angstrom Exponent	Effective Radius (μm)	Refractive index
1	0.27	2.37	0.0	1.74	1.33-0.00i
2	0.14	2.37	0.3	0.89	1.33-0.00i
3	0.07	2.37	0.8	0.45	1.33-0.00i
4	0.03	2.37	1.4	0.19	1.33-0.00i
5	0.22	2.37	0.0	1.41	1.40-0.00i
6	0.12	2.37	0.3	0.77	1.40-0.00i
7	0.06	2.37	0.8	0.38	1.40-0.00i
8	0.02	2.37	1.4	0.19	1.40-0.00i
9	0.18	2.37	0.0	1.15	1.50-0.00i
10	0.10	2.37	0.3	0.64	1.50-0.00i
11	0.05	2.37	0.8	0.32	1.50-0.00i
12	0.02	2.37	1.4	0.13	1.50-0.00i

for inversion is not so far from the specular direction, the assumption of 5 m/s can yield bias on the retrieved optical thickness of the order of 5% for wind speed 10 m/s and even 10% in the extreme case of a 15-m/s wind speed. The impact on the retrieved Angström exponent is, then, of the order of 20%.

C. Aerosol Models

The selection of the aerosol models is a key issue since all aerosol types should be included in the LUT. Aerosol particles originate from different sources (sea-salt, windblown mineral particles, sulfate, organic, combustion material) which yield a large variability in physical properties (size distribution, refractive index, and shape) that are all impossible to consider for computational time reasons.

Generally, an aerosol model is considered as a mixing of several basic aerosol components, each of them defined by its size distribution $n(r)$ and its refractive index m . As shown in the literature where many experimental data are reported [41], [1], [51], [52], we can assume that the aerosol size distribution follows a log-normal law defined by two parameters, the median radius r_m and the geometric standard deviation σ .

$$\frac{dn(r)}{dr} = \frac{N_o}{\sqrt{2\pi \ln \sigma}} \cdot \frac{1}{r} \cdot \exp\left(-\frac{1}{2} \frac{(\ln r - \ln r_m)^2}{(\ln \sigma)^2}\right). \quad (2)$$

The values of the radius (Table I) have been selected for covering the accumulation mode (small particles) as well as the coarse mode representative of maritime particles and dust (larger particles). They have been adjusted for giving the same values of the Angström exponent, i.e., 0.0, 0.3, 0.8, and 1.4, without regard to the assumed refractive indexes. The standard deviation σ is the same ($\sigma = 2.37$) for all models. Aerosols are considered nonabsorbing, i.e., the imaginary part of the refractive index is 0.0 and three values of the real part are selected (Table I). 1.50 is representative of mineral dust, 1.40 of organic particles when 1.33 is the extreme value for high humidity conditions. Since the wavelengths used in the

inversion are close, there is no need for considering a speckle dependence of the refractive indexes.

Let us mention that, although POLDER is measuring spectral radiances, we always refer to the classical Angström exponent α computed from the spectral optical thicknesses

$$\alpha = -\ln\left(\frac{\tau_{670}}{\tau_{865}}\right) / \ln\left(\frac{670}{865}\right).$$

As suggested by Van de Hulst [46] and shown by Har and Hovenier [15], the parameter of the aerosol size distribution which is better retrieved from remote sensing in visible, is the effective radius defined in

$$r_{\text{eff}} = \frac{\int_0^\infty r^3 n(r) dr}{\int_0^\infty r^2 n(r) dr}.$$

The corresponding values are then also reported in Table I and can only be connected with spectral behavior in the case of monomodal size distributions. The computations of the aerosol radiative properties are performed using the Mie theory since particles are assumed spherical.

D. Ancillary Data

There are still three quantities which need to be determined for getting the tropospheric aerosol contribution $L_{\text{aer}}^{\text{tropo}}$, the ozone transmission T_g , the stratospheric aerosol contribution $L_{\text{aer}}^{\text{strato}}$, and the foam radiance L_f .

The ozone column abundance U_{O_3} needed for performing the correction T_g is provided by the total ozone mapping spectrometer (TOMS) instrument also onboard ADEOS along with POLDER. If the simultaneous TOMS/ADEOS measurements are not available, gridded data derived from ECMWF meteorological fields are alternatively used. The transmission of ozone T_{O_3} is expressed as a function of U_{O_3} [28] derived from accurate computations using a line-by-line model [40].

TABLE II

AERONET STATIONS AVAILABLE DURING THE POLDER LIFETIME. (I) MEANS THAT THE STATION IS ON AN ISLAND (C) MEANS THAT THE STATION IS ON THE SHORE

	Country Name	Location	Number of matches	Number of clear matches
Atlantic Ocean (I)	Ascension Islands	14.4 W 8.0 S	24	0
Atlantic Ocean (I)	Barbados	59.5 W 13.2 N	135	5
Atlantic Ocean (I)	Cap Verde	22.9 W 16.7 N	175	27
Atlantic Ocean (C)	Sénégal	16.9 W 14.4 N	116	18
Atlantic Ocean (I)	Guadeloupe	58.5 W 16.0 N	40	0
Atlantic Ocean (I)	Las Cardes	71.3 W 30.2 S	27	0
Pacific Ocean (I)	Hawaii	157.0 W 20.8 N	10	0
Indian Ocean (I)	Maldives	73.5 E 4.2 N	161	0
Mediterranean Sea (I)	Creta	25.6 W 35.3 N	53	17
Mediterranean Sea (C)	Italy	12.5 E 45.3 N	24	5
English Channel (I)	England	4.0 W 50.2 N	20	2

Background stratospheric aerosol contribution ($L_{\text{aer}}^{\text{strato}}$) is corrected using information derived from SAGE-II (Stratospheric Aerosol and Gas Experiment) data [29] for the single scattering assumption and a prescribed aerosol model [28].

Since large aerosol emission, such as those of the El Chichon or the Pinatubo volcanoes, did not occur, the correction remains very small.

Wind speed needed for getting the percentage of foam coverage is also derived from the ECMWF meteorological fields. Then, the foam contribution is easy to consider [5] since its reflectance is assumed lambertian [35].

III. DATA SETS

For validation, the aerosol properties (optical thickness and Angström exponent) derived from satellite are compared with sunphotometer measurements. A large range of aerosol conditions was sampled during the POLDER lifetime, ranging from clean conditions to large aerosol content off the African coast resulting from dust transported from the Sahara over the Tropical Atlantic Ocean. In the next section, POLDER and ground-based sun/sky photometer measurements performed by AERONET (AErosol RObotic Network) are presented.

A. POLDER Data

Due to the unanticipated ADEOS failure, only eight months of POLDER data are available, from October 30, 1996 to June 30, 1997. The global aerosol characterization is performed using the level 1 data stream, i.e., the calibrated Stokes parameters (L, Q, U) projected on a reference earth equal-area grid at 6.2-km resolution. There are no onboard calibration sources and the POLDER in-flight radiometric calibration is based on terrestrial targets [14]. The accuracy of the absolute radiometric calibration, which affects the optical thickness retrieval, is reported to be between 2% up to 4% from the blue to the near-infrared channels. The calibration accuracy of the polarized channels is of same order of magnitude. The relative calibration of the 670- and 865-nm bands, which impacts the retrieval of the aerosol model, is around 1%

[14], which gives us an error in the Angström exponent of 0.04 for spectrally independent radiances and of 0.024 when the Angström exponent is 2.0. The resulting impact on the retrieved size distribution is so very limited.

The spatial resolution of POLDER is 6.2 km after data registration. Cloud detection is achieved at the original resolution. The cloud-free pixels are averaged over a 3×3 -pixel box (19 km), if at least five pixels are found in the box. Spatial averaging is achieved in order to reduce radiometric noise since the horizontal scale of aerosol load is expected to be larger than 20 km in most cases.

The three aerosol level 2 products over ocean are the optical thickness at 865 nm τ_a^{Sat} , the Angström exponent α^{Sat} computed from the 670 and 865 nm channels, and the refractive index. The global processing of the level 1 data for producing the level 2 products is very timeconsuming and for validation purposes, the algorithm is applied on reduced data sets. Extractions of level 1 data over an area of 100×100 km² have been performed near the sun/sky photometer stations (Table II). It allows us to run several times the algorithm for adjusting the threshold values used in the cloud screening and to develop alternative inversion schemes for getting a better match with the ground-based measurements.

Due to the POLDER concept [50], the pixels may be viewed over 14 directions in each spectral band. Due to the glint over the ocean, several directions may be contaminated and rejected. To still benefit from the angular information, which constrains the aerosol model retrieval, 3 of the 14 directions have to be glint free. Figs. 1 and 2 illustrate the concept. The total (Fig. 1) and polarized (Fig. 2) radiances in the three spectral bands (443, 670, and 865 nm) are plotted as a function of the scattering angle γ which is given by

$$\cos(\gamma) = -\cos(\theta_s) \cos(\theta_v - \sin(\theta_s) \sin(\theta_v) \cos(\phi)) \quad (5)$$

where θ_s is the sun zenith angle, θ_v the view zenith angle, and ϕ the relative azimuth angle between both directions. The data are acquired above the sunphotometer in Crete and the sun angle is 60°. At a scattering angle of around 80°,

the spectral behavior clearly shows the contribution of the glint since both radiances in the three channels are equivalent due to the strong spectrally independent surface contribution generated by the specular reflection. The contribution from the glitter is variable and much larger than the aerosol signal. Therefore, all directions which are significantly affected by the glitter are not used in the aerosol inversion. The shaded areas represent the scattering angle range that is rejected in the inversion scheme.

B. Aeronet Data

Simultaneously to the POLDER overpass, ground-based sun/sky radiometers are operating through the AERONET network over the globe [20].

Both satellite and sun-photometers measurements depend on the aerosol optical properties, but they have different sensitivities because the surface contribution and the geometrical conditions are obviously not the same for both observations [3]. Sun-photometers measure the extinction in four channels (443, 670, 865, and 1020 nm) from which the optical thickness and Angström exponent are derived.

In order to validate satellite-derived optical thickness, it is essential to have well calibrated instruments. Typically, the absolute uncertainty in the aerosol optical thickness $\Delta\tau$ from a newly calibrated field instrument under cloud-free conditions is ± 0.01 for $\lambda > 443$ nm and $< \pm 0.02$ for shorter wavelengths [20]. The resulting accuracy on α , based on (3), is between $0.045/\tau_{865}$ for $\alpha = 2$ and $0.055/\tau_{865}$ for $\alpha = 0$.

For validation of a worldwide product, it is important that sun/sky radiometers are located in different aerosol regimes. We would like to have measurements representative of i) urban/industrial aerosols, ii) biomass burning aerosols, iii) marine aerosols, and (iv) mineral dust, i.e., dust coming from the continent and transported over the ocean. During the POLDER lifetime, several oceanic and coastal sun photometer instruments have performed continuous measurements. The location and total amount of operating days are reported in Table II. If the total number of POLDER/sunphotometer matches is significant, about 780, only 72 matches are left after the selection (see Section IV). Due to the early ADEOS end of operation, there is no measurements during the Northern Hemisphere summer season, and no biomass burning or urban/industrial polluted events have coincident satellite and ground-based measurements; most of the data concern Saharan dust plume and marine aerosols.

IV. RESULTS

Evaluation of POLDER aerosol products, optical thickness at 865 nm and Angström exponent calculated from the 670- and 865-nm bands, are achieved by direct comparison of the parameters derived from surface and spaceborne measurements. Since all the parameters cannot be simply matched, we first explain the principle of our comparison. Then, the data processing is described and global comparison is provided.

A. Principle

The total optical thickness τ_a^{S-P} is derived from sun-photometers while it is the scattering optical thickness $\varpi_0 \cdot \tau_a^{\text{Sat}}$

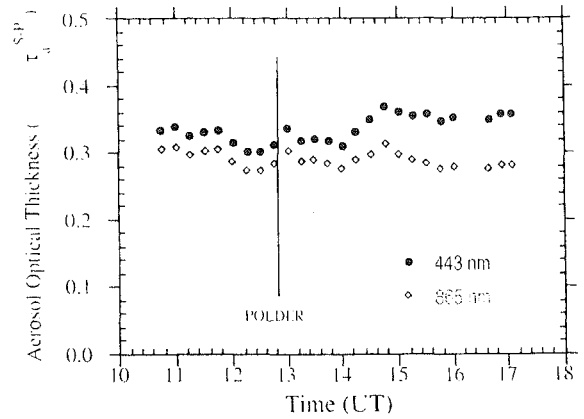


Fig. 3. Aerosol optical thickness measured by the sunphotometer Sal/Cape Verde on March 20, 1997, as a function of the Universal Time spectral bands: 443 and 865 nm. The POLDER time overpass is also repre-

that is derived from POLDER, the comparison is so dependent on the single scattering albedo values ϖ_o assumed in the LUT. There is presently no means for deriving single scattering albedo from satellite over ocean [22] when there are some attempts from ground-based measurements [20], [11]. Nevertheless, since the aerosols included in the LUT are nonabsorbing, it means that some discrepancies may occur. The Angström exponent has the same shortcoming since it is computed from the total optical thicknesses for the ground-based measurement, while it is estimated from the scattered optical thicknesses for satellite measurements. However, according to very recent results [24], dust is shown to have negligible absorption between 670 and 865 nm, which is consistent with the good agreement related here.

B. Screening of Sun-Photometer Data Set

The optical thickness measurements acquired within 1 min of the satellite overpass time are selected and averaged. The sunphotometers acquire about four optical thickness measurements during this time window. Then, only days with a threshold value of 0.10 on the ratio $\sigma(\tau)$ (where σ is the variance and $\langle \tau \rangle$ the averaged optical thickness at 865 nm) are selected. Fig. 3 is a good illustration of the screening capability. It provides the optical thicknesses at 865 and 443 nm measured at Cape Verde on March 20, 1997 as a function of the time. It shows an example of variability with a ratio of 0.05 for this specific day. Only stable days that pass the screening are then considered.

In a second step, to prevent undetected subpixel cloud contamination, systematic analysis of sky radiances measured in the solar principal plane at 865 nm before and after the POLDER overpass are performed. Clear sky provides a uniform and relatively dark background that can be used to detect cloud presence. The downward radiance measured at 865 nm is plotted in Fig. 4 as a function of the scattering angle for the conditions reported in Fig. 3. It clearly shows that, for this specific day, the sky was ideally cloud-free. After both screenings are applied, only 72 days and 72 stations are left (Table II). The representativeness of the sample can be estimated from Fig. 5 where the Angström exponent α^{S-P} is plotted versus the optical thickness τ_a^{S-P} .

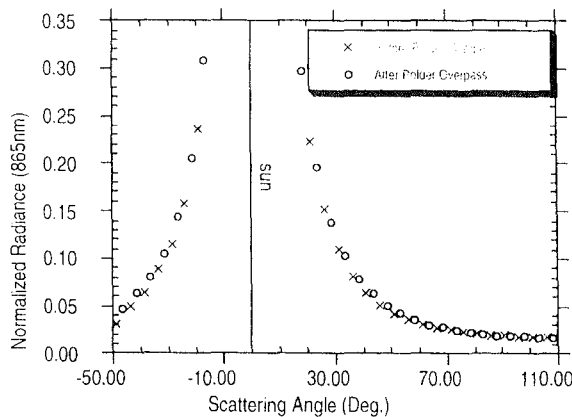


Fig. 4. Normalized downward radiance measured by the sunphotometer put in Sal/Cape Verde on March 20, 1997, as a function of the scattering angle. The two curves correspond to measurements performed at 865 nm before and after the POLDER time overpass. The sun incident angle is 60°.

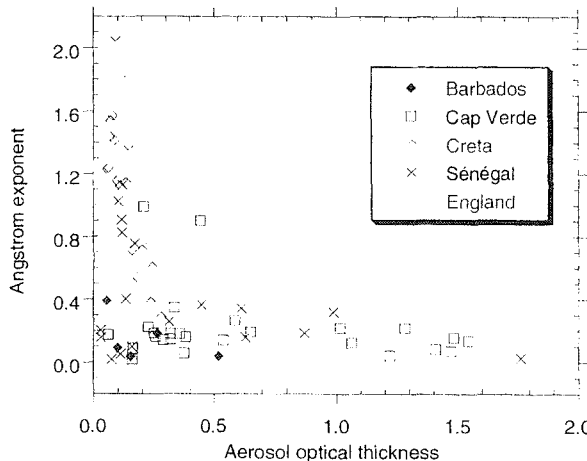


Fig. 5. Aerosol Angström exponent α computed from the 670- and 865-nm spectral bands, as a function of the optical thickness τ measured at 865 nm for the six stations selected in our validation data set.

There is clearly a lack of data for large optical thickness produced by small particles (large Angström exponent) as observed for biomass burning or pollution events. However, to overcome this bias, the aerosol product retrieved over the eastern United States Atlantic region will be compared in Section VI with sunphotometer measurements performed at Goddard Space Flight Center/NASA in Greenbelt, MD, about 100 km upwind.

C. Processing of the POLDER Data

Specific treatments have been applied to Cape Verde and Dakar stations. In the standard cloud screening, one of the cloud detection tests rejects as clouds dust events with optical thickness larger than 0.6 at 865 nm. Since these two sites are often contaminated by dust plumes, the corresponding cloud threshold has been set larger so as to run the aerosol inversion scheme in these turbid conditions.

The POLDER products are averaged over 5×5 boxes of 3×3 individual pixels each, with a resulting spatial resolution of 100×100 km 2 . In case of coastal sites, offshore pixels only are used to prevent as much as possible uncertainties in the water leaving radiance due to the presence of sediments.

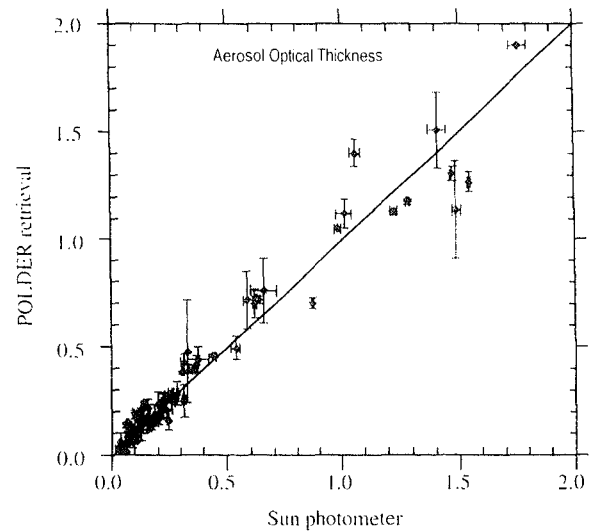


Fig. 6. Aerosol optical thickness τ^{sat} as a function of the optical thickness τ^{sp} measured by the sunphotometers. The comparison is performed at 865 nm. The meaning of the error bars is given in Section IV-D.

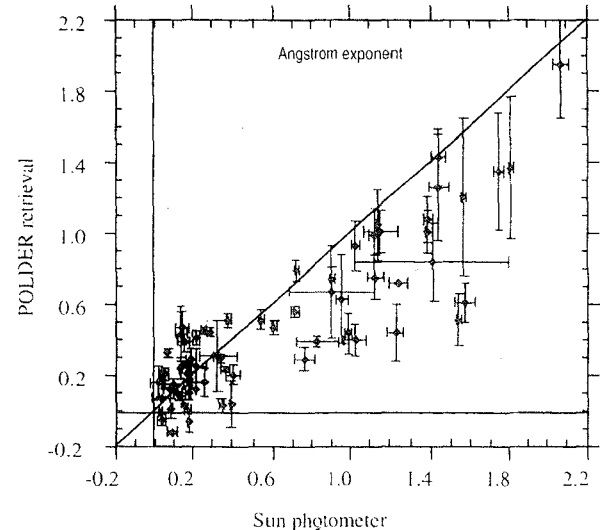


Fig. 7. Same as in Fig. 6 but for the Angström exponent computed from the 670- and 865-nm spectral bands.

D. Results

Comparisons between satellite retrievals and sun photometer measurements are presented in Figs. 6 and 7, respectively, for the aerosol optical thickness and the Angström exponent. The error bars on the x -axis (sunphotometer measurements) correspond to the standard deviation computed over time, i.e., within ± 30 min around the satellite overpass. On the y -axis, error bars correspond to spatial standard deviation over the 5×5 boxes.

A good agreement between the satellite and sunphotometer measurements can be observed in Fig. 6. A linear regression gives

$$\tau^{sat} = 0.96\tau^{sp} + 0.028 \quad (7-a)$$

with a correlation coefficient $R = 0.98$. It can be noticed that, for aerosol content above $\tau > 0.7$, the dispersion is larger. As already mentioned in Section II-B, the largest value included

in the LUT is 0.6, which means that the larger values are linearly extrapolated. Depending on view conditions, a linear interpolation can lead to an underestimate or to an overestimate on the reflectance, which explains the observed dispersion.

Fig. 7 shows a similar comparison for the Angström exponent. A linear fit gives

$$\alpha^{\text{sat}} = 0.65\alpha^{\text{sp}} + 0.08. \quad (7-\text{b})$$

There is clearly a correlation ($R = 0.87$) between the two quantities and no bias (offset is 0.08), but we observe a systematic underestimate of the Angström exponent derived from POLDER for small particles (large α). It can be noticed that the largest value of α included in the LUT (see Table II) is 1.4, but this cannot explain the low value of the slope. This result is discussed in the next section.

V. DISCUSSION

A. Aerosol Optical Thickness

The POLDER retrieval is excellent for optical thickness up to 0.7. The improvement, compared with previous retrievals using NOAA/AVHRR or geostationary satellites, is clearly due to the capability of the instrument to simultaneously derive the aerosol model and the aerosol content. When the LUT is limited to aerosol models with a given refractive index, the slope of the regression is lower, respectively 0.97, 0.77, and 0.6 for 1.33, 1.40, and 1.50 than when we allow the algorithm to derive it from the polarized channels. The operational algorithm gives very frequently a refractive index of 1.33. If such a value is expected in regions where most of the optical thickness is due to condensed water [17], Saharan dust should return more likely 1.40 or 1.50. Although 1.40 is more often retrieved over the Senegal station, we cannot state that the present algorithm works properly regarding the refractive index. Several issues need to be addressed like the selection of the aerosol models in the LUT, and the algorithm itself that should balance the weights of each piece of information with respect to the aerosol parameters.

As noted in Section IV-C, there is a larger dispersion for large optical thicknesses. These cases are observed over the Cap-Verde and Dakar stations and correspond to dust transport. This may result from the extrapolation process, but it can also be connected to the shape since this aerosol type is known to be nonspherical. Nonsphericity affects the aerosol phase function and may generate large errors in the aerosol optical thickness retrieval [30]. However, recent results [24] based both on satellite- and ground-based data indicate dust particles behave like sphere; nonsphericity may impact the phase function by 20% only.

The larger dispersion can also result for subcloudy pixels within the 5×5 boxes since the cloud screening was less severe and the sunphotometer may not observe clouds that are on the edge of the $100 \times 100 \text{ km}^2$ area. A definite statement will be made after the LUT will be modified; a careful analysis of the polarized light will be also performed since it is very sensitive to particle shape.

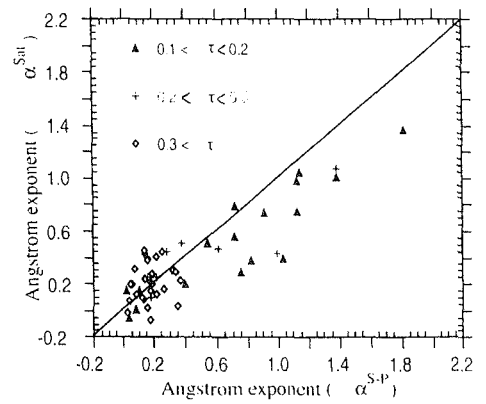


Fig. 8. Same as in Fig. 7 but for optical thickness larger than 0.1.

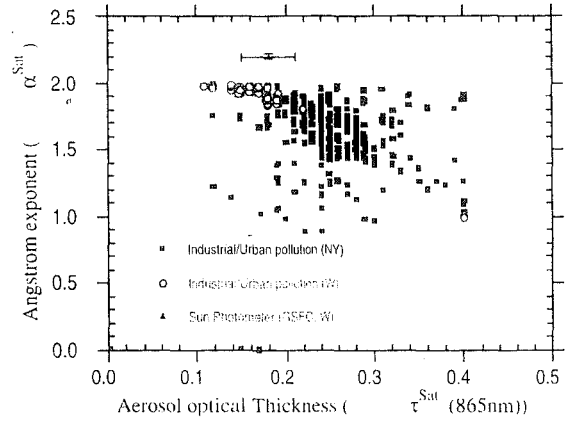


Fig. 9. Scatter diagram of the aerosol Angström exponent α as a function of the optical thickness τ measured at 865 nm on June 21, 1997, for two zones in the eastern United States coast at the latitudes of Washington and New York. Measurements performed at GSFC/NASA, Maryland, are also repre-

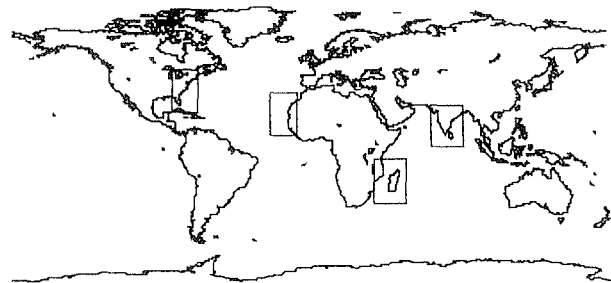


Fig. 10. Location of the selected geographical zones.

B. Angström Exponent

Fig. 8 is the same as Fig. 7 but limited to matches with an aerosol optical thickness larger than 0.1. Obviously, accuracy on the Angström exponent is poor when the aerosol optical thickness is small. Although the slope is not improved (0.63) because of the weight of many small values of α , the comparison is much better for $\alpha > 1$. Nevertheless, the POLDER values are obviously still under-estimated.

Then, to overcome the lack of large aerosol contents associated with small particles in our data set validation, we made a specific study over the eastern United States Atlantic region in the early summer. This region is frequently covered by pollution events coming from the continent [37], [38].

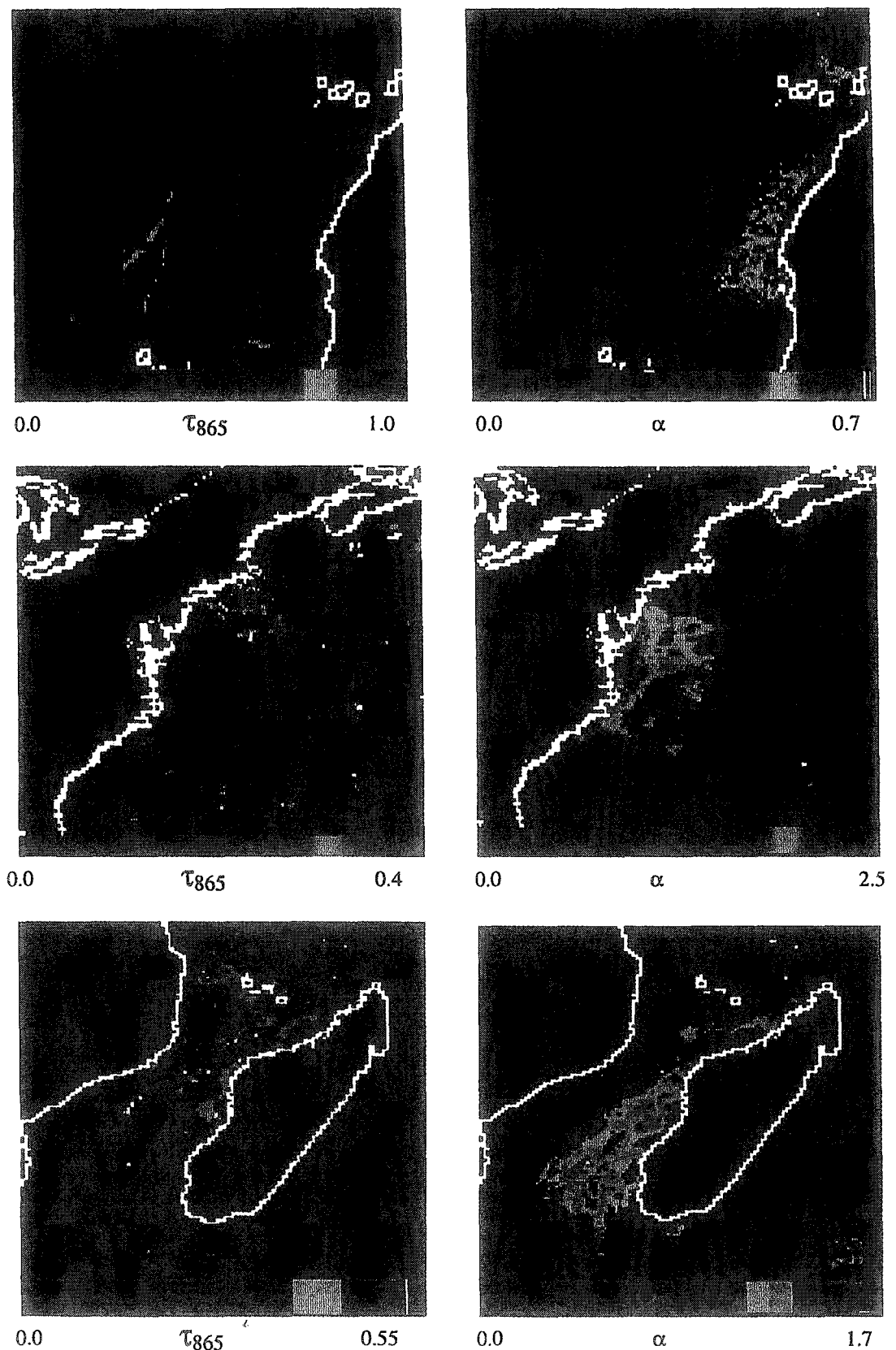


Fig. 11. Maps of the aerosol optical thickness and Angström exponent for the three zones (a) zone off Western Africa, (b) Eastern United States coast, (c) Mozambique Channel between East Africa and Madagascar.

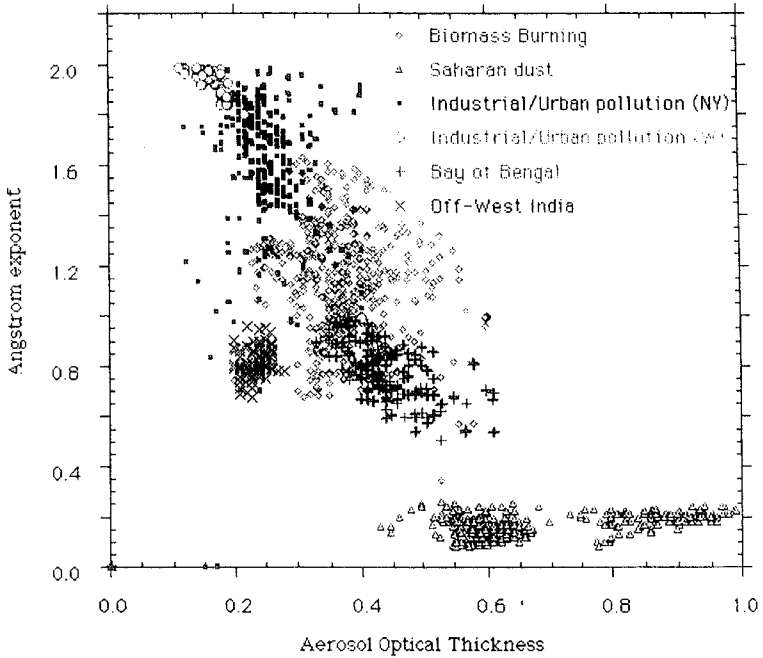


Fig. 12. Scatter diagram of the aerosol Angström exponent α as a function of the optical thickness τ measured at 865 nm for the zones reported in Fig.

In Fig. 9, we plotted the Angström exponent as a function of the optical thickness for two zones off the coast and at the latitudes of Washington and New York City. The images were acquired on June 21, 1997, and the corresponding sunphotometer measurement, performed at GSFC/NASA, is also reported. First of all, POLDER algorithm can produce very large Angström exponent, as large as 2.0, which means the systematic underestimate is not due to a shortcoming in the LUT. Then, the sunphotometer data better fit the scatter diagram for the zone off Washington than for the zone off New York City. This result was anticipated from the wind direction analysis performed from the meteorological data. On the other hand, ground-based measurement, acquired in the region of New York, during TARFOX [39], have shown Angström exponent values up to 1.8 [45], which is compatible with POLDER retrieval.

Nevertheless, the POLDER Angström exponent seems again to be underestimated.

There is clearly, from all the situations we analyzed, a systematic underestimate of α^{sat} . If we examine the obvious assumptions that are questionable in the present version of the algorithm, i.e., the presence of sediments, the updated spectral dependence of the foam, the possible aerosol absorption at 865 nm, they all would result in a smaller value of the slope by decreasing the aerosol contribution at 670 nm or by increasing it at 865 nm. We do not presently have strong evidence of possible physical processes that are missing and would improve the relationship.

VI. FEW EXAMPLES

Several examples of the retrieved aerosol parameters are given in this section. We selected geographical areas (Fig. 10) where different aerosol types are expected: i) a region off the Western Africa on November 4, 1996, ii) the Eastern United

States Atlantic region on June 21, 1996, iii) the Mozambique Channel between East-African and Madagascar on November 20, 1996, and iv) a region in the Bay of Bengal and off West India on November 27, 1996.

Maps of optical thickness and Angström exponent are given in Fig. 11 for the three first zones. A dust event moving over the ocean is detected on the first image [Fig. 11(a)], large optical thicknesses associated with very low Angström exponents can clearly be attributed to Saharan dust [41], [42], [43], [47]. A pollution event, confirmed by analysis of the wind fields, can be seen in Fig. 11(b) with a very high Angström exponent. The aerosol event observed in Fig. 11(c) can be connected to biomass burning activity. November is the fire season in the region [16], and the analysis of the wind fields confirms that the plume originated from inside Madagascar. The range of observed Angström exponent (0.8–1.6) is compatible with spectral extinction measured in the case of Southeast Asian forest fire haze [48] and with similar observations performed off west Mexican coasts during spring 1998.

A scatter diagram of the aerosol Angström exponent α as a function of the optical thickness τ measured at 865 nm is reported on Fig. 12 for the three regions discussed above. The area off the eastern United States coast is split into two zones at the latitudes of Washington and New York City.

The area in the Indian Ocean is also split into two regions, one in the Bay of Bengal and one off Western India. The Western India area exhibits Angström exponent within the range of 0.7–1.0. Sun-photometer data acquired during 1997 in Kaashidhoo Island, indicate Angström exponent varying from 0.5–1.2 [38] which seems to be compatible with the POLDER retrieval. We retrieve the typical signature of Saharan dust; for urban/industrial aerosols (off the Eastern United States), we have a classical behavior with larger partic-

associated with larger optical thickness [36]; for biomass burning aerosols, there is no obvious relationship between the optical thickness and the Angström exponent as well as for the zone off Western India; aerosols over the Bay of Bengal seem to follow the industrial/urban pollution behavior but our analysis is in too early a stage for making a definitive statement. These results show that the POLDER measurements can be used to distinguish several aerosol types from their Angström coefficients, in addition to a precise estimate of the aerosol optical thickness.

VII. CONCLUSION

Spectral, directional, and polarized satellite radiances have been analyzed in terms of aerosol parameters, which are then validated against ground-based measurements widely distributed over the world. From the present study, we can conclude that the present inversion algorithm gives excellent results for the optical thickness. The Angström exponent estimate allows the differentiation of several aerosol types; however, the comparison with sunphotometer measurement indicates a significative underestimate.

Some issues still need to be addressed:

- 1) selection of the aerosol models;
- 2) impact of the number of view directions on the retrieval;
- 3) the sensitivity of the size distribution retrieval to the scattering angle;
- 4) impact of the vertical distribution of the aerosol layer;
- 5) nonsphericity effects;
- 6) absorbing aerosols.

In addition, we did not use the sky radiances measured by the sun-photometers, as well as the polarized channel at 865 nm, for comparison with the POLDER radiance; it will be one of our next priorities.

ACKNOWLEDGMENT

Results presented in this paper were obtained using data from CNES's POLDER onboard NASDA's ADEOS. The authors would like to thank people involved in AERONET (AErosol Robotic Network) for installing, collecting, and processing the Sun/Sky radiometer data, particularly B. Holben, F. Dulac, and G. Zibordi for allowing them to use the sunphotometers measurements at GSFC/NASA, in Crete and Italy. The authors would like to acknowledge A. Lifermann, the POLDER Project Scientist, for her constant support and L. Remer who provided sunphotometer data over Mexico.

Information on POLDER data can be found on the following web site: <http://earth-sciences.cnes.fr:8060/polder/Mission.html>.

REFERENCES

- [1] G. A. d'Almeida, "On the variability of desert aerosol radiative characteristics," *J. Geophys. Res.*, vol. 93, pp. 3017–3026, 1987.
- [2] M. O. Andreae, "Climatic effects of changing atmospheric aerosol levels Ch 10," in *World Survey of Climatology. Vol. 16, Future Climates of the World*, A. Henderson-Sellers, Ed. Amsterdam, The Netherlands: Elsevier, 1995, pp. 341–392.
- [3] F. M. Bréon, J. L. Deuzé, D. Tanré, and M. Herman, "Validation of spaceborne estimates of aerosol loading from sunphotometer measurements, with emphasis on the polarization," *J. Geophys. Res.*, vol. 102, pp. 17 187–17 196, 1997.
- [4] F. M. Bréon and S. Colzy, "Cloud detection from the spaceborne POLDER instrument and validation against surface synoptic observations," *J. Appl. Meteorol.*, to be published.
- [5] S. Chandrasekhar, *Radiative Transfer*. New York: Dover, 1960, p. 393.
- [6] T. N. Carlson, "Atmospheric turbidity in Saharan dust outbreaks as determined by analyses of satellite brightness data," *Mon. Wea. Rev.*, vol. 107, pp. 322–335, 1979.
- [7] Charlson and Heintzenberg, Eds., *Dahlem Workshop Report on Aerosol Forcing of Climate*. London, U.K.: Wiley, 1995, p. 1.
- [8] C. Cox and W. Munk, "Statistics of the sea surface derived from sun glint," *J. Mar. Res.*, vol. 13, pp. 198–208, 1954.
- [9] J. L. Deuzé, M. Herman, and R. Santer, "Fourier series expansion of the transfer equation in the atmosphere-ocean system," *J. Quant. Spectrosc. Radiat. Transf.*, vol. 41, no. 6, pp. 483–494, 1988.
- [10] J. L. Deuzé, G. Perry, A. Marchand, P. Goloub, M. Herman, and D. Tanré, "Estimate of the aerosols properties over the ocean with POLDER," *IEEE Trans. Geosci. Remote Sensing*, to be published.
- [11] O. Dubovik, B. N. Holben, Y. J. Kaufman, M. Yamashita, A. Smirnov, D. Tanré, and I. Slutsker, "Single-scattering albedo of smoke retrieved from the sky-radiance and solar transmittance measured from the ground," *J. Geophys. Res.*, to be published.
- [12] R. S. Fraser, "Satellite measurement of mass of Saharan dust in the atmosphere," *Appl. Opt.*, vol. 15, pp. 2471–2479, 1976.
- [13] R. Frouin, M. Swindling, and P.-Y. Deschamps, "Spectral reflectance of sea foam in the visible and near-infrared: *In situ* measurements and remote sensing implications," *J. Geophys. Res.*, vol. 101, pp. 14 361–14 371, 1996.
- [14] O. Hagolle, P. Goloub, P. Y. Deschamps, H. Cosnefroy, X. Briottet, T. Bailleul, J. M. Nicolas, F. Parol, B. Lafrance, and M. Herman, "Results of POLDER in-flight calibration," this issue, pp. XX–XX.
- [15] J. E. Hansen and J. W. Hovenier, "Interpretation of the polarization of Venus," *J. Atmos. Sci.*, vol. 31, pp. 1137–1160, 1974.
- [16] W. M. Hao and M. Liu, "Spatial and temporal distribution of tropical biomass burning," *Global Biogeochem. Cycles*, vol. 8, pp. 495–503, 1994.
- [17] D. A. Hegg, J. M. Livingston, P. V. Hobbs, T. Novakov, and P. Russell, "Chemical apportionment of aerosol column optical depth off the mid-Atlantic coast of the United States," *J. Geophys. Res.*, vol. 102, pp. 25293–25303, 1997.
- [18] A. Higurashi and T. Nakajima, "Development of a two channel aerosol retrieval algorithm on global scale using NOAA/AVHRR," *J. Atmos. Sci.*, to be published.
- [19] R. B. Husar, J. M. Prospero, and L. Stowe, "Characterization of tropospheric aerosols over the oceans with the NOAA advanced very high resolution radiometer optical thickness operational product," *J. Geo. Res.*, vol. 102, pp. 16 889–16 909, July 27, 1997.
- [20] B. N. Holben, T. F. Eck, I. Slutsker, D. Tanré, J. P. Buis, A. Setzer, E. Vermote, J. A. Reagan, Y. J. Kaufman, T. Nakajima, F. Lavenu, and I. Jankowiak, "Automatic sun and sky radiometer system for network aerosol monitoring," *Remote Sens. Environ.*, vol. 66, pp. 1–16, 1998.
- [21] I. Jankowiak and D. Tanré, "Climatology of Saharan dust events observed from Meteosat imagery over Atlantic Ocean, method and preliminary results," *J. Clim.*, vol. 5, pp. 646–656, 1992.
- [22] Y. J. Kaufman, D. Tanré, H. R. Gordon, T. Nakajima, J. Lenoble, R. Frouin, H. Grassl, B. M. Herman, M. King, and P. M. Teillet, "Passive remote sensing of tropospheric aerosol and atmospheric correction for the aerosols effects," *J. Geophys. Res.*, vol. 102, pp. 16 815–16 830, 1997.
- [23] Y. J. Kaufman, D. Tanré, A. Karniel, and A. Remer, "Re-evaluation of dust radiative forcing using remote measurements of dust absorption," *Geophys. Res. Lett.*, to be published.
- [24] Y. J. Kaufman, D. Tanré, A. Karniel, B. N. Holben, and S. Matto, "Dust size, refractive index and non sphericity derived from remote sensing," in *Conf. Light Scattering by Non Spherical Particles: Theory, Measurements, and Applications*, New York, Sept. 1998, pp. 104–107.
- [25] P. Koepke, "Effective reflectance of oceanic white caps," *Appl. Opt.*, vol. 23, pp. 1816–1824, 1983.
- [26] B. Lafrance and M. Herman, "Correction of the stratospheric aerosol on the POLDER measurements," *IEEE Trans. Geosci. Remote Sensing*, to be published.
- [27] J. Lenoble, *Standard Procedures to Compute Atmospheric Radiative Transfer in a Scattering Atmosphere*. Hampton, VA: Deepak, 1993, p. 532.
- [28] M. Leroy, J. L. Deuzé, F. M. Bréon, O. Hautecoeur, M. Herman, J. C. Buriez, D. Tanré, S. Bouffie, P. Chazette, and J. L. Roujeau, "Retrieval of atmospheric properties and surface bidirectional reflectances over land from POLDER/ADEOS," *J. Geophys. Res.*, pp. 17 023–17 035, 1997.
- [29] M. P. McCormick and R. E. Veiga, "SAGE II measurements of early Pinatubo aerosols," *Geophys. Res. Lett.*, vol. 19, pp. 155–158, 1992.

- [30] M. I. Mishchenko, L. D. Travis, R. A. Kahn, and R. A. West, "Modeling phase function for dustlike tropospheric aerosols using a shape mixture of randomly oriented polydisperse spheroids," *J. Geophys. Res.*, vol. 102, pp. 16 831–16 847, 1997.
- [31] C. Moulin, F. Dulac, C. E. Lambert, P. Chazette, I. Jankowiak, B. Chatenet, and F. Lavenu, "Long-term daily monitoring of Saharan dust load over ocean using Meteosat ISCCP-B2 data. 2. Accuracy of the method and validation using Sun photometer measurements," *J. Geophys. Res.*, pp. 16 959–16 969, 1997.
- [32] A. Morel and L. Prieur, "Analysis of variations in ocean color," *Limnol. Oceanogr.*, vol. 22, pp. 709–722, 1977.
- [33] T. Nakajima, A. Higurashi, A. Kazuma, E. Tatsuo, F. Hajime, M. Toratani, Y. Mitomi, B. G. Mitchell, and R. Frouin, "Early phase analysis of OCTS radiance data for aerosol remote sensing," *IEEE Trans. Geosci. Remote Sensing*, this issue, pp. 1575–1585.
- [34] C. C. Norton, F. R. Mosher, B. Hinton, D. W. Martin, D. Santek, and W. Kuhlow, "A model for calculating desert aerosol turbidity over oceans from geostationary satellite data," *J. Appl. Meteor.*, vol. 19, pp. 633–642, 1980.
- [35] R. E. Payne, "Albedo of the sea surface," *J. Atmos. Sci.*, vol. 29, pp. 959–960, 1972.
- [36] L. A. Remer, S. Gassó, D. Hegg, Y. J. Kaufman, and B. N. Holben, "Urban/industrial aerosol: Ground based sun/sky radiometer and airborne in situ measurements," *J. Geophys. Res.*, vol. 102, pp. 16 849–16 859, 1997.
- [37] L. A. Remer, Y. J. Kaufman, and B. N. Holben, "Interannual variation of ambient aerosol characteristics on the East Coast of the United States," *J. Geophys. Res.*, vol. 104, pp. 2223–2231, 1999.
- [38] S. K. Satheesh, V. Ramanathan, X. Li-Jones, J. M. Lobert, I. A. Podgorny, J. M. Propstero, B. N. Holben, and N. G. Loeb, "A model for the natural and anthropogenic aerosols over the tropical Indian Ocean derived from INDOEX data," *J. Geophys. Res.*, to be published.
- [39] P. B. Russell, P. V. Hobbs, and L. L. Stowe, "Aerosol properties and radiative effects in the US Mid-Atlantic haze plume: An overview of the Tropospheric Aerosol Radiative Forcing Observational Experiment (TARFOX)," *J. Geophys. Res.*, to be published.
- [40] N. A. Scott and A. Chédin, "A fast line-by-line method for atmospheric absorption computations: The automatized atmospheric absorption atlas," *J. Quant. Spectrosc. Radiat. Transf.*, vol. 14, pp. 691–704, 1974.
- [41] E. P. Shettle, "Optical and radiative properties of a desert aerosols model," *IRS'84: Current Problems in Atmospheric Radiation*, G. Fiocco, Ed., Hampton, VA: Deepak, 1984, pp. 243.
- [42] D. Tanré, C. Devaux, M. Herman, R. Santer, and J. Y. Gac, "Radiative properties of desert aerosols by optical ground-based measurements at solar wavelengths," *J. Geophys. Res.*, vol. 83, pp. 14 223–14 231, 1988a.
- [43] D. Tanré, P. Y. Deschamps, C. Devaux, and M. Herman, "Estimation of Saharan aerosol optical thickness from blurring effects in thematic mapper data," *J. Geophys. Res.*, vol. 93, pp. 15 955–15 964, 1988.
- [44] D. Tanré, Y. F. Kaufman, M. Herman, and S. Mattooo, "Remote sensing of aerosol properties over the ocean using MODIS/EOS spectral radiances," *J. Geophys. Res.*, vol. 102, pp. 16 971–16 988, July 27, 1997.
- [45] D. Tanré, L. A. Remer, Y. J. Kaufman, S. Mattooo, P. V. Hobbs, J. M. Livingston, P. B. Russell, and A. Smirnov, "Retrieval of aerosol optical thickness and size distribution over ocean from the MODIS airborne simulator during TARFOX," *J. Geophys. Res.*, to be published.
- [46] H. V. Van de Hulst, *Light Scattering by Small Particles*. New York: Wiley, 1957 (reprinted Mineola, NY: Dover, 1981).
- [47] W. Von Hoyningen-Huene, T. Schmidt, and C. Ah Kee, "Climate-relevant aerosol parameters of South-East-Asian forest fire haze," *J. Atmos. Environ.*, to be published.
- [48] W. Von Hoyningen-Huene, K. Wenzel, and S. Scheinbein, "Radiative properties of desert dust and its effects on radiative balance," *J. Aerosol Sci.*, to be published.
- [49] C. H. Whitlock, D. S. Bartlett, and E. A. Gurganus, "Sea foam reflectance and influence on optimum wavelength for remote sensing of ocean aerosols," *Geophys. Res. Lett.*, vol. 9, pp. 719–722, 1982.
- [50] P. Y. Deschamps, F. M. Bréon, M. Leroy, A. Podaire, A. Bricaud, J. C. Buriez, and G. Sèze, "The POLDER mission: Instrument characteristics and scientific objectives," *IEEE Trans. Geosci. Remote Sensing*, vol. 32, pp. 598–615, 1994.
- [51] Y. J. Kaufman, A. Gilelson, A. Karniekin, E. Garnor, R. S. Fraser, T. Nakajima, S. Mattooo, and B. N. Holben, "Size distribution and phase function of aerosol particles retrieved from sky brightness measurements," *J. Geophys. Res.*, vol. 104, pp. 10 341–10 356, 1994.
- [52] Y. J. Kaufman, D. Tanré, H. R. Gordon, T. Nakajima, J. Lenoble, R. Frouin, H. Grassl, B. M. Herman, M. D. Kong, and P. M. Teillet, "Passive remote sensing of tropospheric aerosol and atmospheric correction for the aerosol effect," *J. Geophys. Res.*, vol. 104, pp. 16 815–16 830, 1997.

Philippe Goloub, for a photograph and biography, see p. 525 of the Jan 1999 issue of this TRANSACTIONS.

D. Tanré received the M.Sc. degree in physics in 1975 and the thesis atmospheres physics, "These de 3ème cycle" and "Doctorat d'Etat," in 1 and 1982, respectively, from University of Lille, France.

Since 1982, he has been with the Laboratoire d'Optique Atmosphérique, Lille, France, as a CNRS (Centre National de Recherche Scientifique) researcher. His activities cover radiative transfer modeling through real atmospheres—both theory and applications. His interests also include remote sensing of the atmospheric properties from satellite- and ground-based observations as well as atmospheric effects in satellite imagery of the earth surface.

J. L. Deuzé received the M.S. degree in physics in 1970 and the Ph.D. de in atmospheric optics in 1974 from the University of Lille, France.

He is currently a Professor of physics at the University of Lille as Researcher at the Laboratoire d'Optique Atmosphérique, Lille. His research activities focus on radiative transfer modeling within the atmosphere the inversion of sky radiance measurements for aerosol monitoring. He also involved in field campaigns to monitor aerosols (Airborne POLI flights) and to estimate the radiance at the sensor level (SPOT calibr atmospheric corrections). One of his main interests is in exploiting polarized data to retrieve aerosol properties for climate investigations. Within POLDER project, he is in charge of the inversion schemes for getting aer characteristics over both ocean and land surfaces.

M. Herman received all degrees in physics in 1962 and the Ph.D. degree physics in 1968 from the University of Lille, France.

He is currently Professor at Université des Sciences et Technologies Lille. His experiment is principally in the area of aerosol remote sensing. research activities concern radiative transfer and atmospheric signal model planetary atmosphere studies from analysis of telescopic observations, ground-based and balloon-borne remote sensing of aerosols, with special emphasis on polarization.

A. Marchand received the engineer computer science degree in 1996 from the Institut de Formation Supérieure en Informatique et Télécommunications de Rennes, France.

Since 1996, she has been a Research Engineer at the Laboratoire d'Optique Atmosphérique of Lille. She is member of the POLDER science team : works on the development of aerosol algorithms.



François-Marie Bréon received the M.S. degree in physics in 1986 and the Ph.D. degree in physics in 1989, both from the Université de Paris, France.

After completing a postgraduate position at Scripps Institution of Oceanography, University California, San Diego, he joined the POLDER science team in 1991. He conducts research in atmospheric radiative transfer, with emphasis on polarization, and develops satellite data inversion algorithms for both the solar and infrared spectral domains. His scientific interests include investigating terrestrial processes and climate change using satellite remote sensing techniques to retrieve important terrestrial parameters. He is currently a project scientist for the POLDER ground segment and a researcher at the Laboratoire des Sciences du Climat et de l'Environnement (CEA Saclay, France).

P. 3.2

Characterization of aerosols over ocean from POLDER/ADEOS-1

Characterization of Aerosols over Ocean from POLDER/ADEOS-1

J.L.Deuzé, M.Herman, P.Goloub, D.Tanré, A.Marchand

Laboratoire d'Optique Atmosphérique, Université des Sciences et Technologies de Lille 1,
Villeneuve d'Ascq.

Abstract. POLDER (POLarization and Directionality of the Earth's Reflectance) is a French instrument, launched in August 1996 onboard the Japanese sun-synchronous Advanced Earth Satellite System (ADEOS). Data were acquired until the loss of the platform June 30th 1997. This paper describes information on the global distribution of tropospheric aerosol over the ocean derived from the POLDER instrument. The aerosol remote sensing algorithm yields the aerosol optical thickness at 0.865 μm , τ and the Angström exponent, α , which allows the retrieval of the aerosol sizes. Monthly synthesis of the global aerosol characteristics over the ocean are presented and described here for three months: November 1996, February, and May 1997. The major and most persistent feature is the Saharan dust outbreaks off West Africa. Biomass burning aerosols are observed during May off the western Mexican Coast and during November in Madagascar. Asian, Indonesian and eastern US pollution are also observed. For some of these areas, statistical distributions of τ and α and their spatial variability are discussed.

1. Introduction

Although minor constituents of the atmosphere, aerosols are suspected to influence the Earth's radiative budget, directly through backscatter and absorption of solar radiation and indirectly through possible modification of the cloud properties. The effect of aerosols, although largely uncertain, might counterbalance global warming due to greenhouse gases (*Charlson et al.* 1992). However, the large variability of the aerosol properties and of their distribution over time and space, makes estimates of their impact quite difficult. Marine aerosols, dust from desert or semi-desert areas, anthropogenic aerosols from urban pollution, smoke from biomass burning, aerosols from chemical reactions differ in their physical and chemical properties and result in different radiative forcing.

Global maps of the aerosol content over the ocean, which are presently derived operationally from NOAA/AVHRR (Husar et al., 1997), clearly display the main aerosol features. The aerosol retrieval, however, is based on the assumption of a single aerosol model, which prevents discrimination of the aerosol type. An improved characterization of the aerosol optical properties is therefore a key issue for new instruments such as POLDER and OCTS (Nakajima et al., 1998) on ADEOS or MODIS (Tanré et al., 1997) on EOS. POLDER is a wide field of view imaging radiometer (Deschamps et al., 1994) that provides the first global systematic measurements of spectral, directional and polarized characteristics of the solar radiation reflected by the Earth/atmosphere system. These innovative observation capabilities open up new perspectives for analyzing tropospheric aerosols. The POLDER data are processed in order to determine global maps of different geophysical products, especially for some properties of the aerosols in order to classify them and study their variability and biogeochemical cycles.

Copyright 1999 by the American Geophysical Union.

Paper number 1999GL900168.
0094-8276/99/1999GL900168\$05.00

Description of the POLDER data and the aerosol retrieval algorithm over the ocean are briefly presented in section 2. Then, monthly mean products of the aerosol content and size variability are shown in section 3, and their behavior over some specific selected regions is discussed. Detailed analysis is not presented in this paper. Here, the main objective is to show POLDER is able to detect aerosol properties and their variability, even if the current algorithm is still being improved.

2. POLDER data and aerosol retrieval over ocean

The aerosol retrieval over the open ocean is mainly based on the radiances measured in the narrow channels centered at 0.570 and 0.865 μm , in the directions where the sunglint contribution is very small. Since the water leaving radiance is negligible at these wavelengths, the measurements depend mainly on the aerosol scattering. The spectral variation from 0.670 to 0.865 μm allows the derivation of the aerosol size and thus their scattering phase function; then, the aerosol optical thickness is derived. Moreover, the polarization provides some information on the aerosol refractive index, which improves the determination of the scattering phase function. The algorithm is based on look up tables (LUT) of the POLDER directional, spectral and polarized measurements for several aerosol models (total content, particle mean dimension, and refractive index). The effects of foam and sea surface reflection are derived respectively from the Koepke (1984) and Cox and Munk (1954) models, according to the wind speed derived from meteorological fields. The inversion scheme is applied to the cloud-free POLDER pixels, according to the cloud-screening algorithm developed by Bréon and Colzy (1998). To reduce the noise level, 3x3 POLDER pixels (i.e. about 20km x 20-km areas) are considered. From the best fit between the LUT and the measurements, the optical thickness at 0.865 μm , τ , the Angström exponent, α , and the refractive index, m , of the aerosols are derived. The level 2 POLDER aerosol products consist in daily maps of τ , α , m at this 20km x 20 km resolution. The level 3 products are gridded and averaged over a 10-day period or over a month. Great attention has been paid to the validation of the τ and α level 2 products. They have been compared with ground-based measurements provided by AERONET (Holben et al., 1998). The retrieved aerosol content and Angstrom exponent are consistent with sun-photometer measurements even in the case of Saharan dust observation when non-sphericity effect may occur. The accuracy on the aerosol optical thickness is 0.05 rms for $\tau < 0.8$. The Angstrom exponent derived from POLDER data well correlated with the AERONET data, although it is systematically underestimated by 30% (Goloub et al., 1999).

3. Results

Examples of global distributions of τ and α are presented on figure 1 for November 1996, February and May 1997. Refractive index is not presented. Figure 1 shows the large heterogeneity of the aerosol distribution over the ocean. As the Angstrom exponent increases when particle size decreases, dark areas correspond to large particles while areas in red represent small particles. When the aerosol optical thickness is lower than 0.1,

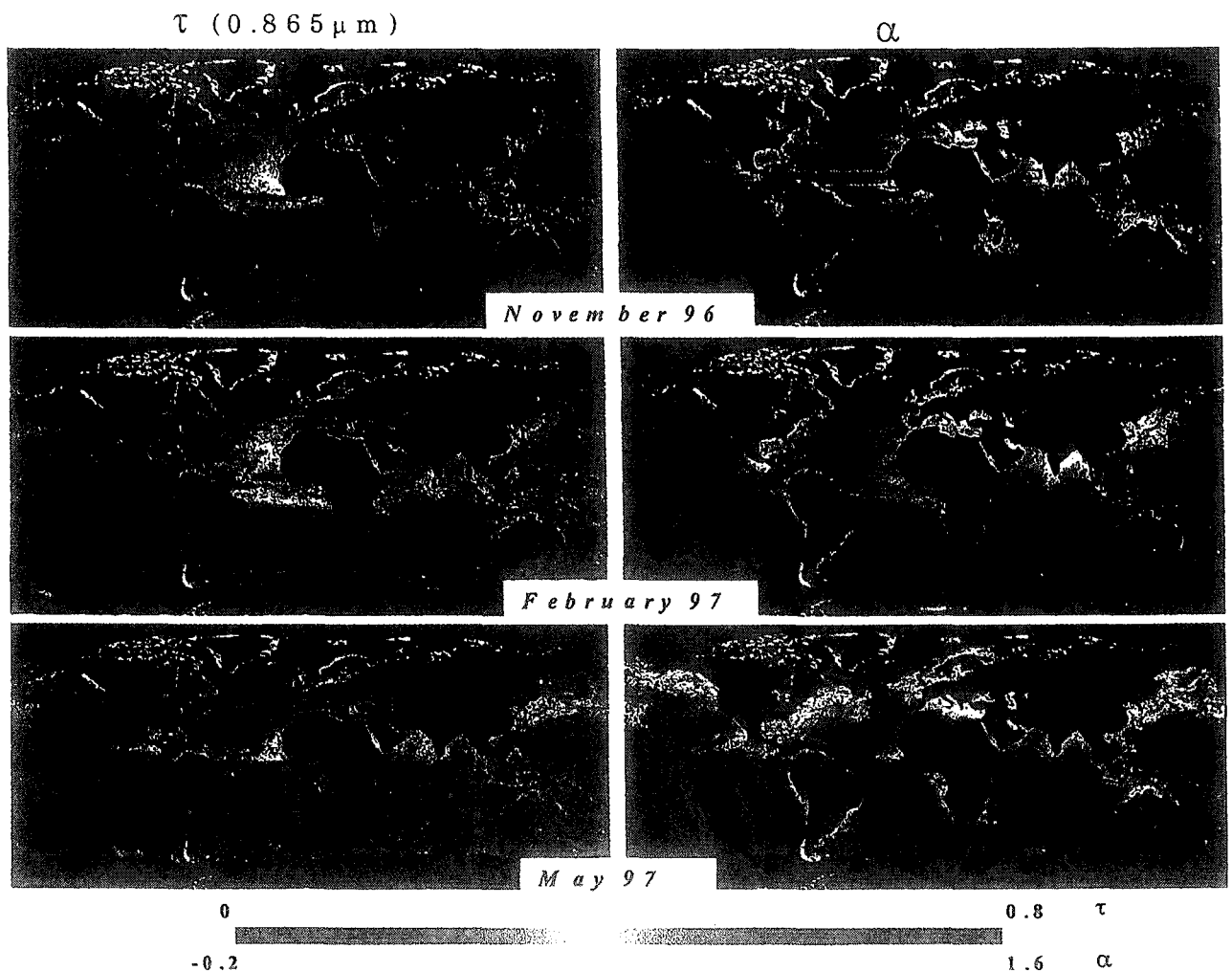


Figure 1 : Monthly composite of aerosol optical thickness ($0.865\mu\text{m}$) and Angström exponent for November 1996, February and May 1997.

the spectral effect between 0.670 and $0.865\mu\text{m}$ channels is too weak to permit the retrieval of the aerosol size. In this case, $\alpha=0$ is prescribed for the calculation of τ . The corresponding data are shown as black areas in the Angstrom exponent charts.

Some major features in figure 1 correspond to well documented aerosol events, which permit assessment of the consistency of the POLDER results, especially the reliability of the Angström exponent. For few regions indicated on figure 1, we have reported in Table 1 the statistical parameters relative to the τ and α distributions corresponding to percentiles 10%, 50% (median) and 90% and their average values over the whole area.

Over the ocean, the major aerosol type is composed of desert mineral matter coming from continents. Figure 1 shows that these areas are characterized by almost persistent large values of τ correlated with small values of α . The most prominent feature is offshore the West African coast. It corresponds to mineral dust generated within the Saharan desert and transported over the Atlantic Ocean up to the American continent. Due to the threshold used in the cloud detection scheme, only dust outbreaks with aerosol optical thickness lower than 0.8 are detected, which may lead to some systematic underestimation of the mean aerosol content. The small values of α (typically 0.25-0.3) are very consistent with coarse particles (D'Almeida, 1987). For West Africa-N area, in Table 1, the largest aerosol loading is observed in February while the mean value of the Angström exponent is small and very stable (0.3). Arabian Sea also exhibits nearly permanent aerosol content associated with small Angström exponent, in agreement with desert aerosols coming from Arabian Peninsula or Thar Desert depending on the wind orientation. Continuous increase of τ is observed from

November to May, as previously observed by Husar et al. (1997). Angström exponent is found to be constant, with α of about 0.3.

Biomass burning is another important source of aerosol particles. In May, an extensive pattern with high Angström exponent associated with moderate τ is observed in Central America, off the west Mexican coast (figure 1). The large Angström exponent (Table 1, Central America region) is very consistent with submicronic smoke particles (Kaufman et al., 1994) and with the sunphotometer measurements performed in the same region in May 1998 (Remer 1998, personal communication). This period corresponds to biomass burning season (forest fires) in this region (Hao and Liu, 1994) and the observations are consistent with dominant westerly winds. Another region where submicronic particles are observed is over the Mozambique Strait (offshore east of Madagascar) in November. Figure 1 shows that smaller particles stand between Africa and Madagascar. They correspond to fire, either in Madagascar or in Africa depending on the wind direction. This is consistent with easterly monthly mean wind direction in November, which corresponds to the end of biomass burning activity period (Hao and Liu, 1994).

Finally, moderate Angström exponent associated to mean (0.1-0.2) aerosol content is measured off west India, mainly in November. Very little fire activity occurs near the Indian West Coast in November and these particles are probably pollution aerosols coming from the India sub-continent, in agreement with wind direction.

Similarly, large pollution plumes with moderate to large Angström exponent, probably linked to anthropogenic aerosols,

Table 1: Statistical parameters relative to τ and α distributions (10%, 50% (median) and 90% percentiles) (lines 1 and 2) and monthly average values over the whole area (line 3).

		November			February			May			November			February			May			
		10%			50%			90%			10%			50%			90%			
		τ	0.04	0.08	0.17	0.03	0.08	0.17	0.16	0.31	0.57	τ	0.03	0.10	0.24	0.08	0.18	0.36	0.10	0.24
W. Mexico (16°N, 99°W) (500 x 500 km ²)	τ	0.04	0.08	0.17	0.03	0.08	0.17	0.16	0.31	0.57	τ	0.03	0.10	0.24	0.08	0.18	0.36	0.10	0.24	0.43
	α	0.0	0.4	0.9	0.2	0.6	1.2	0.7	1.1	1.7	α	-0.1	0.2	0.4	0.0	0.3	0.7	0.0	0.2	0.6
	Average	τ, α	(0.10, 0.4)		(0.10, 0.7)			(0.36, 1.2)			Average	τ, α	(0.13, 0.2)		(0.22, 0.3)			(0.27, 0.3)		
Madagascar (12.5°S, 45°E) (600 x 600 km ²)	τ	0.08	0.18	0.36	0.03	0.09	0.24	0.01	0.05	0.18	τ	0.1	0.17	0.27	0.08	0.18	0.30	0.17	0.25	0.52
	α	0.4	1.1	1.7	0.0	-0.1	0.3	-0.2	0.0	0.5	α	0.4	0.80	1.2	0.1	0.5	1.0	0.1	0.3	0.7
	Average	τ, α	(0.21, 1.1)		(0.13, -0.1)			(0.08, 0.10)			Average	τ, α	(0.20, 0.8)		(0.2, 0.6)			(0.31, 0.4)		
W. Africa N (12°N, 22°W) (600 x 600 km ²)	τ	0.2	0.36	0.60	0.36	0.59	0.86	0.28	0.44	0.67	τ	0.10	0.18	0.29	0.10	0.20	0.33	0.09	0.24	0.43
	α	0.1	0.3	0.6	0.1	0.3	0.5	0.1	0.3	0.5	α	0.2	0.6	1.0	0.4	0.7	1.2	0.2	0.5	0.9
	Average	τ, α	(0.39, 0.3)		(0.61, 0.3)			(0.47, 0.3)			Average	τ, α	(0.20, 0.6)		(0.23, 0.8)			(0.26, 0.5)		
W. Africa S (10°N, 11.5°W) (600 x 600 km ²)	τ	0.27	0.39	0.56	0.50	0.67	0.87	0.21	0.39	0.62	τ	0.02	0.07	0.15	0.05	0.10	0.20	0.05	0.13	0.31
	α	0	0.6	0.9	0.2	0.4	0.6	0.3	0.6	1.0	α	-0.1	0.2	0.7	0.0	0.5	0.9	0.4	1.0	1.6
	Average	τ, α	(0.42, 0.6)		(0.69, 0.4)			(0.43, 0.7)			Average	τ, α	(0.09, 0.24)		(0.13, 0.5)			(0.17, 0.95)		

are observed in May and June over the Midlatitude North Atlantic Ocean, especially along the East Coast of the United States. The corresponding aerosol loading and angstrom exponent are very consistent with in-situ and remote sensing observations performed during TARFOX experiment (Tanré et al., 1998) in the same area. However the pollution peak should occur rather during the summer in the region (Husar et al., 1997). From a careful analysis of the α and τ behaviors, it seems possible to detect mixing between the main aerosol types.

(i) An unusual pattern is the spatial gradient of α observed, offshore Senegal and Guinea coasts (south of Dakar) in November 1996 and May 1997 that can be explained by mixture of mineral dust with smoke particles. Table 1 shows systematically values of α larger for the West Africa-S area than in the West Africa-N one. Larger values of α observed southerly are consistent with ground based measurements performed in Sal Island and in Dakar. Large α (up to 0.8) occur during the last week of November and even during December. Good correlation in temporal evolution is observed between POLDER and in-situ measurements. On the contrary, only a small α mode is observed in February both for POLDER and in-situ data at Cape Verde and at Dakar sites ($\alpha=0.2$).

In May, larger values of α ($\alpha=0.6-0.7$, Table 1) are observed in the West Africa-S area. This result seems to indicate the sensitivity of POLDER to the presence of mixing aerosols. Fires activities are reduced in May, however fires are observed over Senegal according to ERS-2/ATSR-2 3.7 μm channel saturation technique (Arino et al., 1999). These larger values occurred in the West Africa-S area, but only half the previous value ($\alpha=0.3$) is observed very near to Dakar site which is rather consistent with sunphotometer measurements preformed there.

(ii) In the Arabia region, Table 1 (see Arabia region) shows also larger α in February and May 1997, suggesting mixture of desert dusts transported from arid regions with smaller aerosols. Dominant south-westerly winds in May could transport biomass burning aerosols from east Africa while North Easterly dominant winds in February could transport pollution aerosols from the Indian sub-continent (Savoie et al., 1989).

(iii) Another increase of τ correlated with a decrease of α is observed off west India, from November to May. Presumption that smaller α (0.4) is due to mineral dust transported from Arabian peninsula, Thar desert or Northern India peninsula to

West India area is consistent with North Westerly wind. This hypothesis is in a good agreement too with the maximum aerosol loading observed over Arabian region as previously mentioned.

(iv) Finally, the aerosol content observed near Japan (Table 1, Japan) is continuously increasing from November 1996 to May 1997 while the particle size correlative decreases, up to mean Angström exponent 1.0. The maximum of spatial spread out is observed in April-May 1997. Pollution aerosols are expected to be carried from east coast of Asia according to strong westerly flow and transported eastward over Pacific and Japan (Savoie et al., 1989). Sun photometer measurements performed in Japan during April-May-June period (Nakajima et al., 1999) are attesting the presence of small particles (α ranging from 0.5 to 1.7). On the other hand, according to previous regional studies (Tanaka et al., 1989), during the same period, Chinese yellow sand events (larger particles) could occur and be transported over the Japan. However, POLDER observations indicate very frequently the presence of small particles which could be interpreted as a mixing between continuous emission of pollutant with sporadic yellow sand event.

Let us finally consider the characteristics of the Saharan dust aerosol layer as a function of the distance from the African coast. We have considered two identical latitude bands of 3°-latitude wide ranging from 10°W to 60°W centered at 10°N and 18°N. For these bands the monthly mean τ and α are plotted versus African coast distance. The variations of τ and α are shown in Figures 2 a, b, c, d. They show regular decreases both of τ and α away from the African coast. Note that this trend is confirmed by examination of the sun-photometer data acquired at Cape Verde/Dakar and Barbados, although very few data are available for validation.

The general decrease of α could indicate that the dry deposition is not the only process that determines the size distribution. We can also note in Figures 2a,c that the decreasing rate of the aerosol loading is lower in June 1997 than in November 1996 while, correlative, the Angström exponent in June is nearly constant (Figures 2b,d). As the altitude of the transported aerosol layer is known to be higher during spring (Jaenickie and Schütz, 1978; Chiapello et al. 1995), this feature may correspond to weaker interaction of the aerosols with the lower atmosphere in June than during other seasons.

Larger Angstrom exponents observed near the coast and for the

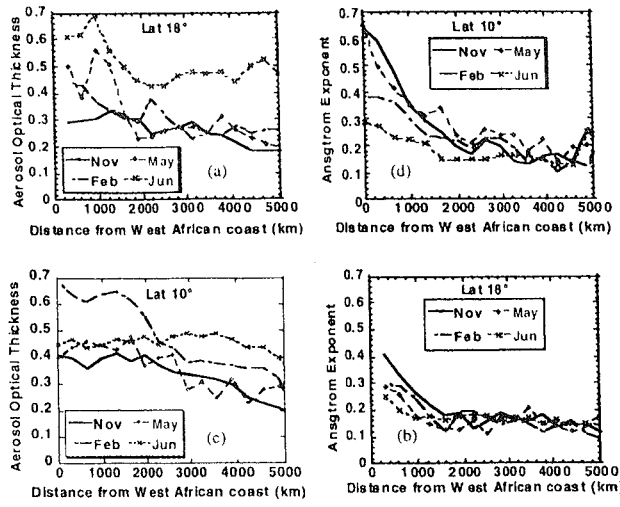


Figure 2 : Evolution of τ and α versus distance to west African coast in 2 latitude bands centered at 18°N (a) and (b) and at 10°N (c) and (d). The 2 bands have a 3° -latitude wide.

souther band (10°) in November and May may indicate the presence of smoke or mixing (co-occurrence) of smoke with dust in the region.

4. Conclusion and Outlook

These early results are the first step showing the capability of POLDER to estimate the particle size. Samples of τ and α spatial and temporal distribution patterns have been presented. Some large Angstrom exponent (small particles) patterns observed in Atlantic Ocean (North America and Europe) and in Asia are associated to pollutant emissions. Other small particles observed in Central America and in Madagascar correspond to biomass burning aerosols. On the other hand, large particles observed off West African coast associated with high aerosol optical thickness are consistent with dust originating from Desert sources. Finally, early evidence of aerosol mixture (biomass burning/mineral dust) and (anthropogenic/mineral dust) have been presented (West Africa-S and West India). Although a complete identification of aerosol types is not performed, this analysis demonstrates that POLDER provides very pertinent global observations that can be used for aerosol remote sensing and associated climate studies (Boucher et al., 1999).

Acknowledgments. Results presented in this paper were obtained using data from CNES POLDER onboard NASDA's ADEOS. This study was funded by the Centre National d'Etudes Spatiales (CNES), the Centre National de la Recherche Scientifique (CNRS), the Conseil Régional du Nord-Pas de Calais, the Fonds Européen de Développement Régional (FEDER) and the Délégation Régionale à la Recherche et à la Technologie du Nord- Pas de Calais. Informations on POLDER data can be found on the following web site: <http://earth.sciences.cnes.fr:8060/polder/Mission.html>. The authors would like to thank people involved in AERONET (AErosol Robotic Network) for installing, collecting and processing the Sun/Sky radiometer data.

References.

- Arino O., J.M Rosaz, P. Goloub, A. Marchand, "1997 World Fire Atlas with ATSR-2 as input to POLDER aerosol product validation", in Reduction of Errors in aerosols forcing of climate, Proceedings of ALPS 1999, Conference, France.
- Boucher O., "The use of model/remote sensing/in situ-measurements to resolve indirect effect", in Reduction of Errors in aerosols forcing of climate, Proceedings of ALPS 1999, Conference, France.
- Bréon, F.M., and S. Colzy, "Cloud detection from the spaceborne POLDER instrument and validation against surface synoptic observations" Submitted to J. Appl. Met..
- Charlson, R. J., S. E. Schwartz, J. M. Hales, R. D. Cess, J. A. Coakley Jr., J. E. Hansen, and D. J. Hoffmann, Climate forcing by anthropogenic aerosols, *Science*, 255, 423-430, 1992.
- Chiapello, I., G. Bergametti, L. Gomes, B. Chatenet, F. Dulac, J. Pimenta, E. Santos Suares, "An additional low layer transport of Sahelian and Saharan dust over the northeastern tropical Atlantic", *Geo. Res. Lett.*, 22(23), 3191-3194, 1995.
- Cox C. and W. Munk, "Measurements of the roughness of the sea surface from photographs of the Sun's glitter" *J. Opt. Soc. Amer.*, 44, 838-850, 1954.
- D'Almeida, G. A., On the variability of desert aerosol radiative characteristics, *J. Geophys. Res.*, 93, 3017-3026, 1987.
- Deschamps, P.Y., F.M.Bréon, M.Leroy, A.Podaire, A.Bricaud, J.C.Buriez and G.Seze, " The POLDER mission: instrument characteristics and scientific objectives" *IEEE Trans. Geosc. Remote Sensing*, 32, 598-615, 1994.
- Durkee, P. A., F. Pfeil, E. Frost, and R. Shema, Global analysis of aerosol particle characteristics, *Atmos. Environ.*, 25A, 2457-2471, 1991.
- Goloub P, D Tanré, J.L Deuzé, M Herman, A Marchand, F.M Bréon, "Validation of aerosol parameters derived from POLDER/ADEOS measurements over the oceans,, to appear in IEEE. TGARS, 1999.
- Holben, B. N., T. F. Eck, I. Slutsker, D. Tanré, J. P. Buis, A. Setzer, E. Vermote, J. A. Reagan, Y. J. Kaufman, T. Nakajima, F. Lavenu, and I. Jankowiak, Automatic sun and sky radiometer system for network aerosol monitoring, *Remote Sens. Environ.*, 66, 1-16, 1998
- Hao W.M. and M. Liu, Spatial and temporal distribution of tropical biomass burning, *Global Biogeochemical Cycles*, 8, 495-503, 1994.
- Herman J. R., P. K. Bhartia, O. Torres, C. Hsu, C. Seftor, E. Celarier, 1997: Global distribution of UV-absorbing aerosols form Nimbus 7/TOMS data.
- Higurashi A., T. Nakajima, Development of a Two Channel Aerosol Retrieval Algorithm on Global Scale Using NOAA/AVHRR, *Journal. Atm. Research*, in press, 1998.
- Husar R. B. J.M. Prospero, Stowe, L., Characterization of tropospheric aerosols over the oceans with the NOAA advanced very high resolution radiometer optical thickness operational product., *Journal. Geo. Research*, VOL 102, 16889-16909, July 27, 1997
- Jaenicke R., and L. Schutz, 1978: "Comprehensive Study of Physical and Chemical Properties of the Surface Aerosols in the Cape Verde Islands Region", *Journal. Geo. Research*, VOL 83, 3585-3601, July 20, 1978.
- Kaufman, Y. J., A. Gitelson, A. Karnieli, E. Ganor, R. S. Fraser, T. Nakajima, S. Mattoo, and B. N. Holben, Size distribution and phase function of aerosol particles retrieved from sky brightness measurements, *J. Geophys. Res.*, 99, 10,341-10,356, 1994.
- Koepke,P., "Effective reflectance of the oceanic whitecaps" *Appl. Opt.*, 23, 1816-1824, 1984.
- Nakajima T., A. Higurashi, A. Kazuma, E. Tatsuo, Fukushima Hajime, M. Toratani, Y. Mitomi, B. Greg Mitchell and R. Frouin, Early phase analysis of OCTS radiance data for aerosol remote sensing, submitted to IEEE Trans. Geosci. Remote Sensing, 1998.
- Tanaka M., T. Nakajima, M. Shiobara, M. Yamano, K. Arao, "Aerosol optical characteristics in the yellow sand events observed in May, 1982 in Nagasaki- Part I Observations "J. Meteor. Soc.Japan, vol. 67, pp267-278, 1989.
- Savoie, D. L., J. M. Prospero, and E. S. Saltzman, Nitrate, non-seasalt sulfate and methanesulfonate over the Pacific Ocean, in *Chemical Oceanography*, vol. 10, edited by J. P. Riley' R. Chester, and R. A. Duce, pp. 219-250, Academic, San Diego, Calif., 1989.
- Tanré D., Y.F Kaufman, M. Herman, S. Mattoo, Remote sensing of aerosol properties over the ocean using MODIS/EOS spectral radiances, *J. Geophys. Res* VOL 102, 16971-16988, July 27, 1997.
- Tanré D., L.A. Remer, Y.J. Kaufman, S. Mattoo, P.V. Hobbs, J.M. Livingston, P.B.. Russell, A. Smirnov, Retrieval of Aerosol Optical Thickness and Distribution over the Ocean from the MODIS Airborne Simulator during TARFOX, *J. Geophys. Res.* To appear, 1999.
- J.L Deuzé, M. Herman, P. Goloub, D. Tanré, A. Marchand, Laboratoire d'Optique Atmosphérique, USTL, Bat P5, 59655 Villeneuve d'Ascq, France.
- (Received November 9, 1998, Revised February 17, 1999, Accepted February 22, 1999)

Estimate of the aerosols properties over the ocean with POLDER

ESTIMATE OF THE AEROSOL PROPERTIES OVER THE OCEAN WITH POLDER

Deuzé J.L.* , P. Goloub*, M. Herman*, A. Marchand*, G. Perry*, S. Susana**, and D. Tanré*.

* Laboratoire d'Optique Atmosphérique, Université de Lille 1, 59655 Villeneuve d'Ascq Cedex, France.

** Laboratoire des Sciences du Climat et de l'Environnement, C.E.A Saclay, L'orme des Merisiers, F-91191 Gif sur Yvette, France.

ABSTRACT

The wide field of view imaging spectroradiometer POLDER (POLarisation and Directionality of the Earth's Reflectance) developed by CNES (Centre National d'Etudes Spatiales) and operated aboard the Japanese heliosynchronous platform ADEOS (ADvanced Earth Observation Satellite) from October 30th 1996 till June 30th 1997, provided the first global systematic measurements of the spectral, directional, and polarized characteristics of the solar radiation reflected by the Earth/atmosphere system. These original observational capabilities offer an opportunity to enhance the characterization of several components of the global environment, especially the oceanic and terrestrial vegetal primary production, the aerosol physical and optical properties, and the tri-dimensional structure and microphysics of clouds. Here we examine the remote sensing of aerosols over the oceans. In a first step, the aerosol optical thickness and Ångström exponent are derived from the radiance measurements. In a second step, the polarization measurements are used for the retrieval of the aerosol refractive index. The inversion algorithm assumes spherical, non-absorbing particles with monomodal log-normal size distribution. The adequacy of this modeling is discussed for a representative set of aerosol observations. Successful retrieval is generally achieved in the presence of small aerosols with Ångström exponent larger than about 1.0. For such particles, polarization may provide information on the particle refractive index. As the Ångström exponent of the particle decreases the data fitting residual errors increase, especially in polarized light, which prevents the retrieval of the aerosol refractive index. The trends of the discrepancies point out two shortcomings of the aerosol modeling. The theoretical results systematically underestimate the contribution of small polarizing particles in the polarization measurements for side-scattering angles ranging from 80° to 120°. This indicates very probably that aerosol models have to follow bimodal size distribution. On the other hand, the systematic trend of the directional behavior of the upward radiance and the lack of significant rainbow effect in the measurements result probably from non-sphericity of some large aerosols. Confirmation of these points requires improved analysis of the POLDER data.

1-INTRODUCTION

Although minor constituent of the atmosphere, aerosols are known to contribute substantially to climate forcing and geochemical cycles (Hansen and Lacis, 1990; Charlson et al., 1992), and there is increasing interest in their global distribution. Many efforts have been devoted to remote sensing of the aerosols from Earth-orbiting satellites (Fraser, 1976; Quenzer and Koepke, 1984; Rao et al. 1989; Higurashi and Nakajima, 1999). Global maps of the aerosol content over the ocean are presently derived routinely from NOAA/AVHRR (Stowe et al., 1992; Husar et al., 1997) by using a one channel algorithm, which needs the choice of a mean aerosol model. Moreover, qualitative monitoring of UV-absorbing aerosols, both over land and ocean, has been achieved recently by using the ultraviolet measurements of TOMS/Nimbus 7 (Herman et al., 1997 ; Torres et al., 1998). Given the large variability of the aerosol physical and chemical properties, improved characterization of the particles is a key issue for new remote sensing instruments, like POLDER and the Ocean Color Temperature Scanner (OCTS) (Nakajima et al., 1999) on the Japanese ADEOS platform, the NASA's Sea-viewing Wide Field-of-view Sensor (SeaWiFS) (Gordon and Wang, 1994) and the Moderate Resolution Imaging Spectroradiometer (MODIS) on the NASA Earth Observing System (EOS) (Tanré et al., 1997).

The wide field of view imaging spectroradiometer POLDER performs multispectral observations of the directionality and polarization of the solar radiation reflected by the Earth. A wide field of view optics and a matrix array detector provide both along and cross track viewing directions, so that the same terrestrial target can be observed from different viewing geometries during the same orbit. A rotating filter wheel provides radiance measurements in 9 channels, ranging from 443 to 910 nm. Moreover, the channels centered at 443, 670 and 865 nm are equipped with polaroids, which permits measurements of the polarized light (Deschamps et al., 1994). These unique capabilities are expected to allow better characterization of different geophysical parameters concerning the terrestrial biosphere, the cloud radiative impact, and the ocean color. Particularly, they should offer new possibilities for characterizing the terrestrial aerosols from space.

POLDER was operating successfully aboard ADEOS from October 30th 1996 till June 30th 1997. The data have been processed by using inversion algorithms which were developed before the POLDER launch and implemented at the POLDER Processing Center, except for minor adjustments after the launch. The various POLDER geophysical products obtained by this way are available from the POLDER Processing Center at CNES. We address here the retrieval of the aerosol properties over the oceans. They consist of the aerosol optical thickness for wavelength $\lambda_0 = 865\text{nm}$, δ_0 , Ångström exponent, α , and refractive index, m , where α and m are column-averaged values. A preliminary validation of the δ_0 and α retrievals has been achieved (Goloub et al, 1999) and preliminary results have been published (Deuzé et al., 1999). The object of this paper is to detail the inversion algorithm, examine its performances and limitations, and discuss the specific problems linked to the polarization analysis.

The main lines of the inversion scheme are described in Section 2. The algorithm assumes spherical, non-absorbing particles with single log-normal size distribution. In a first step, the retrieval of δ_0 and α is achieved using only the radiance measurements in two aerosol channels. In a second step, the refractive index retrieval is attempted from the polarization measurements. The algorithm performances are examined in Section 3. The residuals of the experimental data fitting by the theoretical models are analyzed for a representative sample of aerosol observations. In Section 4, the limitations of the present algorithm with respect to the aerosol modeling are discussed.

2-PRINCIPLE OF THE AEROSOL ALGORITHM

2-1-POLDER data

The processing line starts from the POLDER level 1 data for each POLDER ground pixel. A pixel size of 6kmx6km is obtained after resampling on a latitude-longitude predefined grid. The data are multispectral radiances and polarized radiances at the top of the atmosphere (TOA) measured in 13 or 14 different viewing directions. The POLDER data are normalized radiances, $L_\lambda = \pi L_\lambda^* / E_s$, where E_s is the solar irradiance at TOA and L_λ^* the radiance; λ is the central wavelength of the channel. The aerosol retrieval over the oceans is based on measurements in the two near infrared channels centered at $\lambda_0 = 865\text{nm}$ and $\lambda_1 = 670\text{nm}$, where the water-leaving radiance is negligible. Measurements at shorter wavelengths, especially in the 443nm channel, are discarded because of the possible significant contribution of the water-leaving radiance.

Cloud-free POLDER pixels are firstly selected according to the cloud screening algorithm of Bréon and Colzy (1999), which is based on thresholds on the reflectance in the 443nm channel, examination of the surface pressure derived from the POLDER channels centered in the oxygen absorption band, and seeking for the presence of the rainbow arising from liquid clouds. The O₃ abundance derived from TOMS is used for correcting the 670nm channel data for the ozone absorption. The H₂O content derived from the POLDER measurements in the 910 nm and 865 nm channels (Vesperini et al., 1999) is used for correcting the 865nm channel data for the water vapour absorption. Finally, the data are corrected for the stratospheric aerosol contribution using radiative transfer computations of this effect. The computations were based on a standard modeling of the stratospheric aerosols, with the global distribution of the aerosol optical thickness derived from a two year analysis of SAGE II data (Lafrance and Herman, 1998). Thus, the inputs of the aerosol algorithm are cloud-free pixels corrected for gaseous and stratospheric contaminations. Moreover, 3x3 POLDER pixels (i.e. about 20kmx20km areas) are considered to reduce the noise level. The noise equivalent polarized radiance, $NEDI_{\lambda}^P$, is about $1.25 \cdot 10^{-3}$ in level 1 data (Hagolle et al., 1999 ; Nadal, 1999), that is about $4 \cdot 10^{-4}$ for the 3x3 pixels used here.

Although the algorithm takes into account the reflection from the sea surface, we select measurements in viewing directions where the sunglint contribution is negligible. The POLDER viewing geometry is illustrated in Figures 1a and 1b. Figure 1a is a schematic 3D illustration of the POLDER imaging mode. Figure 1b shows in polar coordinates the sampling of the bidirectional reflectance of the surface target according to the location of the target within the POLDER swath. The corresponding scattering angles are indicated. The radiance of the sunglint is estimated by using the Cox and Munk (1954) modeling of the rough sea surface and measurements are rejected when this radiance is larger than one tenth the molecular radiance at 865nm, which roughly corresponds to an equivalent aerosol optical thickness of 0.01. White and black dots in Figure 1b indicate viewing directions respectively rejected and selected. Figure 1b shows that the number of viewing directions N, selected by this way and the resulting range of scattering angle vary largely through the POLDER swath with the best observational conditions for pixels located west off the orbit.

2-2-Principle of the aerosol retrieval. Aerosol models.

The aerosol retrieval consists in a two-step approach. In the first step, the Ångström exponent and optical thickness of the aerosols are derived by a classic way from the radiance measurements in the two aerosol channels. The polarized radiance measurements, whose the reliability is more questionable and has still to be proved, are only used in the second step for the retrieval of the particle refractive index. The procedure for retrieving δ_0 and α is quite similar to that used by Gordon and Wang (1994) for SeaWiFS and Nakajima et al. (1999) for OCTS. The Ångström exponent of the aerosols (i.e., typically their mean size) is derived from the mean spectral dependence of the radiance. This yields the aerosol model and hence the aerosol phase function, which permits to derive the optical thickness from the radiance level. As the radiance measurements are not sensitive enough to the particle refractive index to provide valuable information on m , the retrieval of m is attempted in a second step from the more sensitive polarization measurements.

The algorithm is based on look up tables (LUT) of the directional, spectral, and polarized radiances calculated for different aerosol models with different optical thicknesses. The choice of the models used to build the LUT is a key issue. According to ground based and airborne observations, many aerosols exhibit multimodal size distributions (e.g. Shettle and Fenn, 1979; Nakajima et al., 1986; Hayasaka et al., 1990; Kaufman et al., 1994; Remer and Kaufman, 1998). Such distributions have been used for the data processings of SeaWiFS (Gordon and Wang, 1994), OCTS (Nakajima et al., 1999), and the future MODIS (Tanner et al, 1997). The present algorithm uses simple monomodal log-normal distributions in the form

$$\frac{dN(r)}{d \ln r} = \frac{1}{\sigma \sqrt{2\pi}} \exp \left[-\frac{1}{2} \left(\frac{\ln r - \ln \bar{r}}{\sigma} \right)^2 \right] \quad (1)$$

Non-absorbing, spherical particles are considered, with three different values of the real refractive index: $m = 1.33$, 1.40 and 1.50. Variation of the refractive index from 670m to 865nm is ignored. The standard deviation of the natural logarithm of the radius is fixed to $\sigma = 0.864$ in equation 1. This gives 0.375 for the standard deviation of the decimal logarithm, which is consistent with the typical values given by Shettle and Fenn (1979). The different models are for values of \bar{r} in equation 1 which yield α ranging from 0.00 to 1.40 (see Section 2.3). Linear

interpolation between, or linear extrapolation from, these data were shown to provide correct estimate of the radiances for Ångström exponents ranging from -0.5 to 2.0.

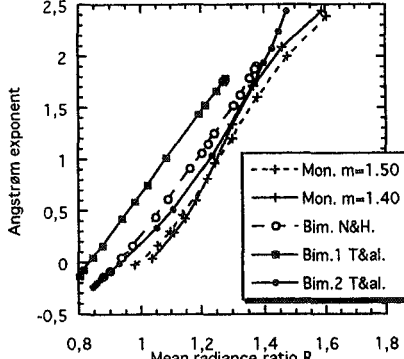


Figure 2

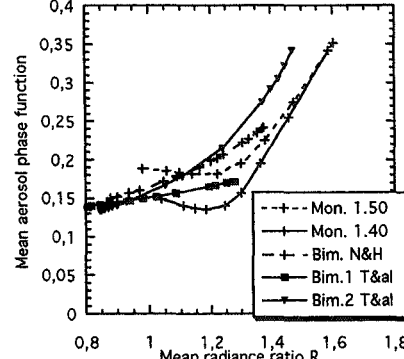


Figure 3

The major improvement expected from the present generation of satellite sensors comes from the estimate of the Ångström exponent

$$\alpha = -\ln(\delta_\lambda / \delta_{\lambda'}) / \ln(\lambda / \lambda'), \quad (2)$$

where δ_λ is the aerosol optical thickness, thanks to the multiple near-infrared channels. The aerosol contribution in the TOA radiance is about $\delta_\lambda p_\lambda(\Theta)$, where $p_\lambda(\Theta)$ the aerosol scattering phase function for scattering angle Θ . Thus, measurements at wavelengths λ_0 and λ_1 provide typically $R = \delta_{\lambda_1} \bar{p}_{\lambda_1} / \delta_{\lambda_0} \bar{p}_{\lambda_0}$ where \bar{p}_λ stands for some mean value of $p_\lambda(\Theta)$.

Figure 2 shows the relationship between α and R and Figure 3 the relationship between \bar{p}_{λ_0} and R for our monomodal models and for bimodal models. The bimodal size distributions are taken from Higurashi and Nakajima (1999) (for the analysis of the NOAA/AVHRR measurements) and from Tanré et al. (1997) (for the analysis of the MODIS measurements over the oceans). For the bimodal models, the parameters r and σ of the two modes are fixed and the relative weight of the modes is varied. The aerosol refractive index varies from 1.40-0.0035i to 150-0.005i depending on the model. For the monomodal models, \bar{r} is varied in equation 1 and results are shown for $m = 1.40$ and 1.50 . Here \bar{p}_λ is defined as the phase function averaged within $100^\circ < \Theta < 160^\circ$.

Bimodal size distributions are more realistic and versatile than monomodal ones, but Figures 2 and 3 show that an inversion scheme based on monomodal models should give significant results in a first approximation. Moreover, Figure 3 shows that uncertainty in the particle refractive index may be as important as the actual shape of the size distribution and impacts also the estimate of the aerosol optical thickness.

2-3-Detailed algorithm

The LUT are built for 12 aerosol models: for the 3 values of m , 4 values of \bar{r} have been adjusted in equation 1 to yield Ångström exponents $\alpha = 0.00, 0.30, 0.80$ and 1.40 . The values for \bar{r} are reported in Table 1. For each aerosol model, the TOA radiances and polarized radiances are calculated for 4 values of the aerosol optical thickness at 865nm, $\delta_0 = 0.075, 0.15, 0.30$, and 0.60 , for a set of observation geometries $(\theta_s, \theta_v, \phi)$, where θ_s is the solar zenith angle, θ_v the viewing zenith angle, and ϕ the relative azimuth angle. We assume linearly polarized light, so that the LUT consist of the Stokes' parameters $(L_\lambda, Q_\lambda, U_\lambda)$.

The computations were made with the successive order of scattering method (Deuzé et al., 1988), taking into account molecular scattering, aerosol scattering, and specular reflection from sea surface. The molecular scattering

is estimated according to a standard atmosphere and the aerosols and molecules are distributed with the altitude according to exponential density profiles, respectively with 2 km and 8 km scale height. In order to test the influence of the vertical structure of the atmosphere, computations were conducted with uniform mixing of aerosols and molecules, i.e. with the same scale height, and the aerosol contributions derived from the two computations by correcting the results for the molecular contribution were compared. For an aerosol optical thickness $\delta_0=0.1$, the largest relative discrepancy was 3% in the radiance and 1% in the polarized radiance at wavelength $\lambda=670\text{nm}$, for $\theta_s=\theta_v=60^\circ$. Because of the small contribution of the molecular scattering at the near-infrared wavelengths here considered the impact of the vertical structure of the atmosphere is not very large. The specular reflection from the rough ocean surface is derived from the model of Cox and Munk (1954) for a fixed wind speed $v=5\text{m/s}$. Calculations show that the results are nearly insensitive to v for the selected viewing directions. In contrast, the glitter mask is estimated according to the prevailing wind speed provided by the French Meteorological Agency. White caps are assumed to exhibit lambertian reflectance, ρ_f , with ρ_f derived from Koepke (1984) as a function of the prevailing wind speed. The contribution of this lambertian reflection at the bottom of the atmosphere is added to the radiance of the LUT by taking into account the diffuse and direct transmissions of the atmosphere, as explained in Tanré et al. (1990). The contributions of the water-leaving radiance is neglected. It is certainly negligible at $\lambda=865\text{nm}$ and is very small at $\lambda=670\text{nm}$ where its reflectance, however, may amount to $\rho_w(670)=0.001$ according to Morel (1983). All of the results reported in this paper have been obtained with $\rho_w(670)=0$, which may lead to slight overestimation of the Ångström exponent for aerosol optical thickness lower than 0.10.

In the first step, for each value of m the radiance measurements are compared with the theoretical radiances of the LUT until a best fit is obtained. This provides the parameters α and δ_0 of a « best » monomodal model.

More precisely, we first derive N estimates of α by fitting the two normalized radiances in the N selected viewing directions. We retain for α the average over these estimates. For this value of α , we derive then N estimates of the optical thickness from the radiances at 865nm. We retain for δ_0 the average over these estimates. Finally, the upward radiances and polarized radiances corresponding to retained values of α and δ_0 are derived from the LUT. All of these calculations are processed by using double linear interpolation (extrapolation) between the four α and four δ_0 values of the LUT.

estimated.

The best models obtained for the three values of m yield to nearly similar values of α and slightly different values of δ_0 , but the residual discrepancies between the radiance measurements and the theoretical results are nearly the same. Therefore, in a second step the polarization measurements at 865nm are compared with the theoretical results. The polarization measurements at 670nm which prove to lead to similar results are not considered. On contrary to the residual discrepancy in the radiances, the residual discrepancy in the polarized radiances differs generally according to m . Interpolation on the refractive index, however, does not seem justified as discussed in section 3-2 and we select the refractive index which leads to minimum residual error in the polarized radiance, with the associated values of α and δ_0 . Finally, the impact of the polarization analysis on δ_0 is typically 20%, corresponding to the typical dependence of the aerosol phase function on m .

Note that another inversion of the POLDER data has been performed through another LUT based on a set of 12 aerosol models of Shettle and Fenn (1979). For each model (i.e. with the value of α fixed), the radiance measurements are compared with the theoretical radiances of the LUT. The best fit now is obtained by adjusting only δ_0 and we just retain this model which leads to the minimum residual error, with the associated value of α and δ_0 . This processing leads to similar order of magnitude of the residual error but, probably because no interpolation here is conducted between the 12 models (hence, between the corresponding values of α), the inverted monomodal model gives quite systematically smaller residual error. Here we will restrict our study to the analysis of the monomodal inversion.

No thresholds were considered in the original algorithm but preliminary processings showed that the retrieved Ångström exponent was systematically small and slightly negative for very clear pixels (typically, with aerosol optical thickness lower than about 0.05). For such conditions, because the uncertainty in the α retrieval is large, α is no longer calculated and instead δ_0 is estimated with $\alpha=0$. These conditions appear principally over the open ocean, and this value of α is consistent with large maritime aerosols.

3-RESULTS

3-1-Examples of level 2 POLDER results

The level 2 POLDER aerosol products, α , δ_0 and m , provided by the CNES POLDER Processing Center are derived according to the previous algorithm. Level 3 products are temporal syntheses (decade or month) of these results at global scale.

Validation of the α and δ_0 retrievals has been examined in Goloub et al. (1999) from comparison with correlative measurements provided by AERONET (Holben et al., 1998). The retrieved aerosol optical thickness proves to be in agreement with ground-based measurements within about 0.05 rms for $\delta_0 < 0.8$. The Ångström exponent derived from POLDER is systematically slightly underestimated but is well correlated with the estimate of α derived from AERONET using the same wavelengths as POLDER. No validation of the aerosol refractive index as a self standing POLDER parameter has been considered. Typical examples of level 3 products of δ_0 and α have been published (Deuzé et al., 1999). The main geographical and seasonal features observed in these global maps are consistent with the properties of the aerosols derived previously from the AVHRR data with respect to their mean content (Stowe et al., 1992; Husar et al., 1997) or size (Higurashi and Nakajima, 1999). Here, we examine the consistency of the inversion scheme by using the multi-directional and polarized capabilities of POLDER to estimate the accuracy of the data fitting depending on the kind of aerosol which we are observing.

The POLDER level 2 aerosol products are detailed here for four aerosol patterns, over areas a few hundred kilometer wide, with aerosol loading large enough to make clear the aerosol signature in the measurements. The scenes have been selected westward of the POLDER swath in order to test the consistency of the results over an extended range of scattering angles (see Figure 1). For eastward pixels at mid-latitudes, the few viewing directions no more exhibit significant directional effect and merge practically into 3 data (radiances at 670 and 865 nm and polarized radiance at 865 nm) that may be fitted with the free parameters of the algorithm. The four cases are representative of the performances, from the best to the worst, obtained by the present inversion scheme according to the aerosol type.

Plate 1 shows an area near Madagascar, on November 20, 1996 (orbit 3248), Plate 2, an area over the Arabian sea, west off the Indian continent, on December 04, 1996 (orbit 3447), Plate 3, an area near China, on April 25, 1997 (orbit 7131), and Plate 4, an area over the Atlantic ocean, west off the African coast, on March 01, 1997 (orbit 5522). The Plates first display images of the δ_0 and α retrievals. The large value of the mean Ångström exponent (about 1.40) in Plate 1 is consistent with biomass burning aerosols between Madagascar and South Africa at the end of the biomass burning period. The moderate value of α (0.60) in Plate 2 corresponds probably to pollution aerosols coming from the Indian continent, according to the prevailing mean wind direction. Large Ångström exponents are observed again over the Chinese area (1.40). Finally, the small Ångström exponent (0.30) in Plate 4 is consistent with desertic particles from the Sahara. The refractive index retrievals are not presented. The retrieved value is nearly the same, $m = 1.33$, all over the areas of Plates 1, 2 and 4, and ranges from 1.33 to 1.40 over the area of Plate 3.

3-2-Radiance analysis

Let us first consider the consistency between the radiance measurements and the theoretical results. For one single pixel of Plates 1 and 2, the measured radiances and the best theoretical results for each value of m have been reported as a function of the scattering angle, respectively in Figures 4 and 5. For comparison, the radiances calculated without aerosols in the atmosphere (molecular terms) have been also reported. Note that different viewing directions may lead to the same scattering angle while the air mass differs, as for the Madagascar case. The three theoretical results are very close in both figures which shows that it is difficult to derive information about the aerosol refractive index from directional and spectral radiance measurements. As outlined in section 2-3 the retrieved Ångström exponent (respectively 1.45 in Figure 4 and 0.39 in Figure 5) is nearly independent on the assumed refractive index and the retrieved optical thickness (respectively 0.33 in Figure 4 and 0.51 in Figure 5) is typically 20% lower (respectively larger) for $m = 1.50$ (respectively $m = 1.33$) than for $m = 1.40$. In any case, Figures 4 and 5 show that the directional feature predicted by the aerosol model which fits the mean bispectral radiances is roughly consistent with the measurements. However, while the results are very good for the Madagascar case, some discrepancies appear in the Indian one.

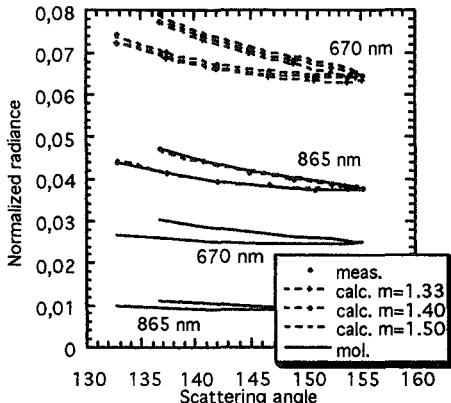


Figure 4

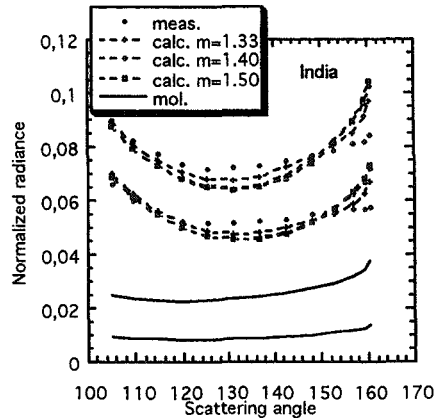


Figure 5

To extend the comparison to the whole scenes, the lower left images (c) in Plates 1 to 4 display the relative residual error in the radiance for each image pixel, i.e. $\bar{\Delta}L/\bar{L}$, where \bar{L} is the radiance averaged over the $2N$ measurements (N selected viewing directions in the 2 aerosol channels), i.e.

$$\bar{L} = \frac{1}{2N} \sum_{i=1}^N \sum_{j=0}^1 L_{\lambda j}^m(\Theta_i)' \quad (3)$$

and $\bar{\Delta}L$ the residual quadratic error

$$\bar{\Delta}L = \sqrt{\frac{1}{2N} \sum_{i=1}^N \sum_{j=0}^1 (L_{\lambda j}^m(\Theta_i) - L_{\lambda j}^c(\Theta_i))^2}; \quad (4)$$

L_{λ}^m and L_{λ}^c stand, respectively, for the measurements and the computations. $\bar{\Delta}L/\bar{L}$ has been calculated for the three values of m and the smallest value is reported.

The results of Plates 1 to 4 are representative of the global results. The directional properties predicted by our monomodal models are in excellent agreement with the measurements for the case of small aerosols with large Ångström exponents, as shown here in Plates 1 and 3. However, as larger particles are present, although the retrieved values of δ_0 and α are still consistent with the ground-based measurements, increasing discrepancies are observed in the directional features : the residual error in the radiance data fitting increases from a few percents as in Plates 1 and 3, up to 5% as in Plate 2 or 10%-15% as in Plate 4.

3-2-Polarization analysis

In the second step, the Stokes' parameters derived from the LUT for the best model associated to each value of m are compared with the measurements. Instead of the Stokes' parameters $(Q_{\lambda}, U_{\lambda})$, let us consider the equivalent and more physical parameters $(L_{\lambda}^P, \psi_{\lambda})$ where L_{λ}^P is the normalized polarized radiance ($L_{\lambda}^P = \sqrt{Q_{\lambda}^2 + U_{\lambda}^2}$), and ψ_{λ} the angle between the polarization direction and the normal to the scattering plane (formed by the solar and observation directions).

Let us first consider the Madagascar pixel. The measured polarized radiance, L_{λ}^P , and the three best theoretical results have been reported in Figure 6a as a function of the scattering angle. For comparison, the polarized radiance calculated without aerosols in the atmosphere have been reported too. Figure 6b shows the same comparison for the polarization angle ψ_{λ} . Note that single scattering within the atmosphere should give a polarized vibration either perpendicular ($\psi_{\lambda}=0^\circ$) or parallel ($\psi_{\lambda}=90^\circ$) to the scattering plane. Figure 6b, however, shows that multiple

scattering and scattering of the polarized light reflected from the sea surface may produce large departures of ψ_λ from 0° or 90° , specially in backscattering directions.

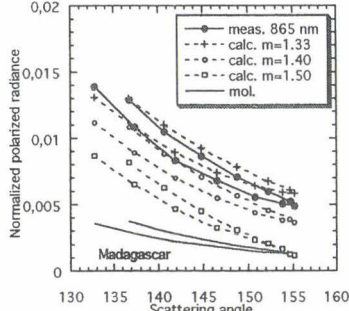


Figure 6a

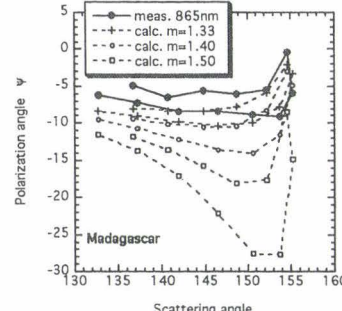


Figure 6b

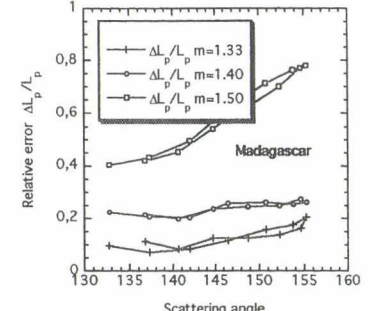


Figure 6c

The large differences between the three theoretical results in Figures 6a and 6b illustrate the sensitivity of polarization to the particle refractive index (Hansen and Travis, 1974). On the other hand, both the amount of polarized light and the polarization direction here are nearly consistent with the theoretical results for $m = 1.33$. The results are summarized in Figure 6c which shows the residual error in the polarized light as a function of the scattering angle, i.e.

$$\Delta L_\lambda^p / L_\lambda^p = \sqrt{(Q_\lambda^m - Q_\lambda^c)^2 + (U_\lambda^m - U_\lambda^c)^2} / L_\lambda^p \quad (5)$$

for the three values of m . Note that the lowest residual error for $m = 1.33$, about 15% that is roughly 0.0015 in terms of normalized polarized radiance, is larger than the $NEDL_\lambda^p$, 0.0004, which suggests that the present retrieval could be improved by using more flexible aerosol models in the algorithm. To extend to the whole scene an estimate of the error, the lower right image (d) in Plate 1 displays the mean residual error in the polarized light

$$\frac{\bar{\Delta}L_\lambda^p}{\bar{L}_\lambda^p} = \frac{\sqrt{\frac{1}{N} \sum_{i=1}^N (Q_{\lambda,0}^m(\Theta_i) - Q_{\lambda,0}^c(\Theta_i))^2 + (U_{\lambda,0}^m(\Theta_i) - U_{\lambda,0}^c(\Theta_i))^2}}{\frac{1}{N} \sum_{i=1}^N \sqrt{Q_{\lambda,0}^m(\Theta_i)^2 + U_{\lambda,0}^m(\Theta_i)^2}} \quad (6)$$

obtained for each image pixel with the best value for m (here, $m = 1.33$ for most pixels of the scene). The results are correct all over the area. Images (c) and (d) in Plate 3 show that similar conclusions are obtained for the aerosols observed near China which correspond to small aerosols as the aerosol type observed near Madagascar.

On the contrary, the matching of the polarization data may be much more questionable or meaningless as illustrated by Figures 7a to 7c for the pixel of the Indian scene of Plate 2.

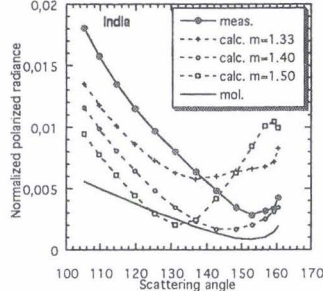


Figure 7a

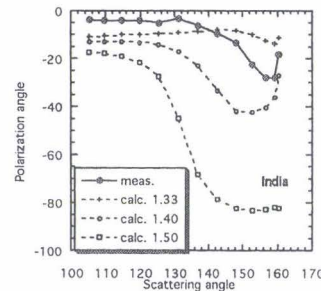


Figure 7b

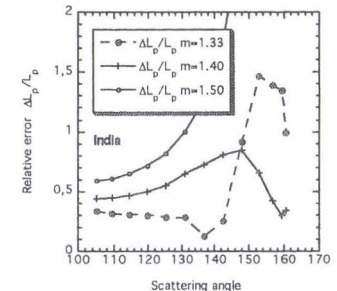


Figure 7c

The agreement here is rather poor for the three values of m . The results are even worse for the African scene as indicated by the large value of $\overline{\Delta L_\lambda^P} / \overline{L_\lambda^P}$ in Plate 4. Clearly, in such cases the analysis of the polarized light fails and the retrieved refractive index is meaningless within the present inversion scheme when larger aerosols are observed.

4-DISCUSSION

4-1-Behavior of the residual errors

As shown in section 3-2, the data fitting achieved with the present algorithm leads to increasing errors in the retrieved polarization and directional radiance when the aerosol dimension increases. Concerning the directional radiance, comparison between observations and calculations clearly shows that our aerosol models tend to overestimate the dissymmetry of the phase function of large aerosols, as seen in Figure 5. On the other hand, comparison between observations and calculations of L_λ^P and Ψ_λ gives no straightforward indication about the defect of the modeling with respect to the polarization.

To clarify, let us discard Ψ_λ and only consider the polarization ratio, L_λ^P / L_λ , which should no longer depend on the aerosol optical thickness and should be controlled by their single scattering properties. More precisely, let us correct the measurements for the molecular contribution and consider the apparent polarization ratio of the light scattered by the aerosols,

$$P_\lambda^m = \frac{\sqrt{(Q_\lambda^m - Q_\lambda^{mol})^2 + (U_\lambda^m - U_\lambda^{mol})^2}}{L_\lambda^m - L_\lambda^{mol}} \quad (7)$$

where L_λ^{mol} , Q_λ^{mol} , U_λ^{mol} stand for computations without aerosols within the atmosphere. Although the multiple scattering and surface reflection effects are not corrected for in equation 7, comparison between P_λ^m and theoretical calculations, say P_λ^c (with L_λ^c , Q_λ^c , U_λ^c in place of L_λ^m , Q_λ^m , U_λ^m in equation 7), should help us to understand the origin of the discrepancies. Figures 8 and 9 compare P_λ^m and P_λ^c for the Madagascar and Indian cases, respectively. Figure 8 shows the same agreement as seen in Figures 6, but Figure 9 clearly displays the origin of the discrepancy for the case of the Indian aerosol. In Figure 9, the measurements exhibit the typical signature of sub-micrometric particles whose the polarization increases regularly when the scattering angle decreases, while the theoretical results exhibit principally the rainbow-like feature of large spherical particles within the range $140^\circ < \Theta < 180^\circ$. In these directions single scattering gives a polarized vibration parallel to the scattering plane (i.e. $\Psi_\lambda = 90^\circ$) (Hansen and Hovenier, 1974), which results in large polarized reflectances with Ψ_{λ_0} far from 0° as illustrated in Figures 7a, 7b and 9. Concerning the polarization, the main shortcoming of our models therefore consists in an underestimation of the polarized light at side-scattering angles, within the range $80^\circ < \Theta < 120^\circ$.

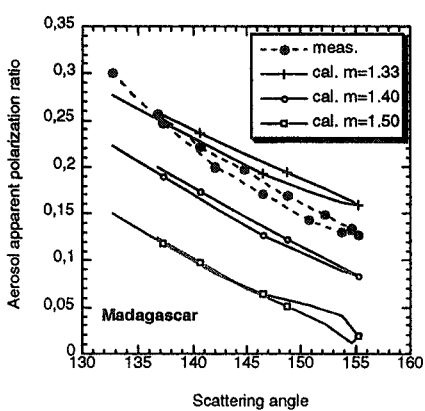


Figure 8

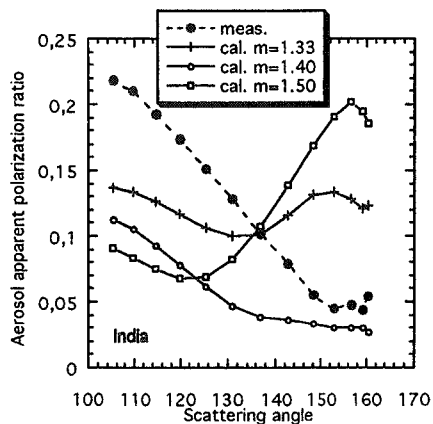


Figure 9

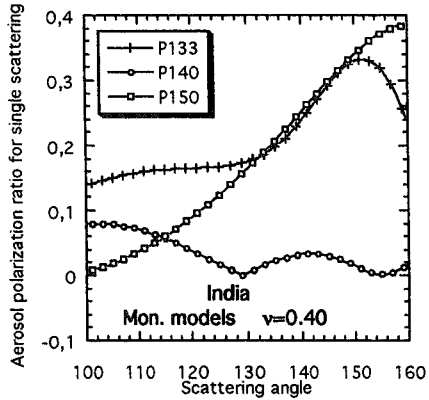


Figure 10

To assess the validity of this comparison, the single scattering polarization ratios corresponding to the theoretical models used in Figure 9 have been reported in Figure 10. Comparison of Figures 9 and 10 confirms that P_λ^c roughly mirrors the single scattering properties of the particles. Note also that if we proceed inversely and search directly for aerosol models consistent with the large values of P_λ^m in Figure 9, the retrieved models yield radiance ratios, L_{670}/L_{865} , about 7% larger than the measured ratios. According to Hagolle et al. (1999), the accuracy of the interband calibration between the two aerosol channels is 2%. Therefore, the 7% departure is not due to measurement errors but must be attributed to the aerosol models.

These trends are persistent features throughout the POLDER data set. The eight months of POLDER data over various areas all over the oceans have been processed and Figure 11 and 12 shows the resulting relationships between the retrieved Ångström exponent and the residual errors $\bar{\Delta}L_\lambda^p/\bar{L}_\lambda^p$ and $\bar{\Delta}L/\bar{L}$, respectively. In these Figures, the results are for ground pixels with $\delta_0 > 0.20$ and with Θ ranging over an interval larger than 30° , which allows valuable control of the data fitting accuracy. The results are shown in the form of normalized frequency of occurrence.

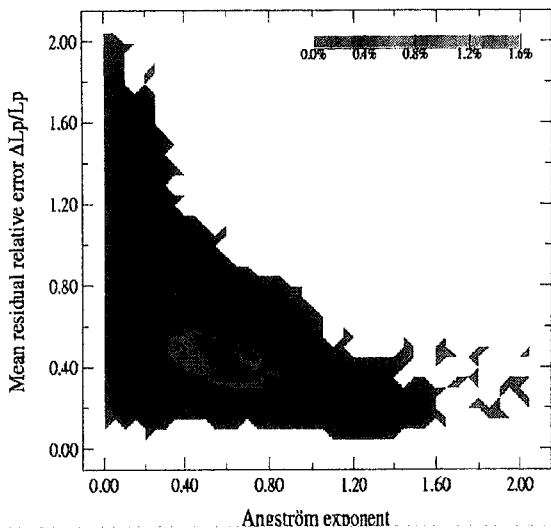


Figure 11

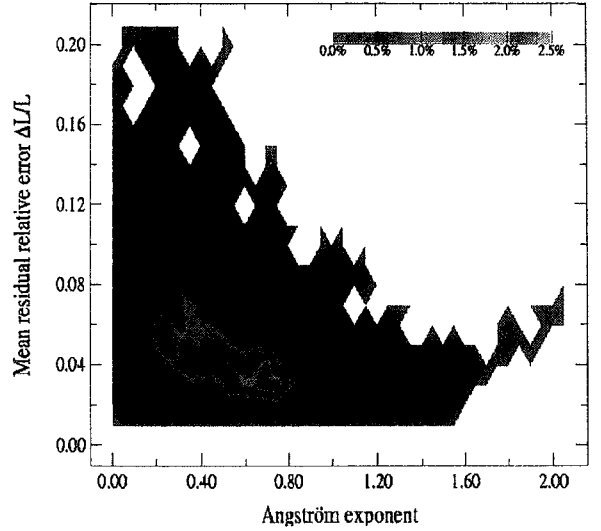


Figure 12

In the presence of small aerosols the theoretical results are consistent with the observations, with $\bar{\Delta}L_\lambda^P / \bar{L}_\lambda^P \approx 0.10$ to 0.30 and $\bar{\Delta}L / \bar{L} \approx 0.01$ to 0.03 for α larger than about 1.0. In the presence of larger particles, the polarization analysis (Figure 11) tends to fail progressively, with $\bar{\Delta}L_\lambda^P / \bar{L}_\lambda^P$ as large as 80% to 100% for large desertic particles ($\alpha < 0.20$). Figure 12 shows that increasing errors in the directional radiances are observed correlative.

4-2-Analysis of the polarization defect

Firstly, let us consider the underestimation of polarized light for side-scattering angles by using our models. As polarization is very sensitive to the properties of the particles many explanations for the failure of the polarization analysis may be suggested, including non-sphericity of the particles which may entail large departures from Mie theory calculations. However, departure from sphericity tends generally to lower the polarized light scattered by the particles (Cai and Liou, 1982 ; J. De Haan, 1987 ; Brogniez, 1992 ; Masuda and Takashima, 1992; Mishchenko and Travis, 1994a and b). Therefore, it may be expected that our spherical models should lead to an overestimation of the polarized light in the presence of non-spherical particles. Moreover, polarization at side-scattering angles is mainly generated by very small particles (Hansen and Travis, 1974) whose the scattering properties are not too sensitive to shape effects (Mishchenko and Travis, 1994a, 1994b). The defect of the present modeling, hence, very likely consists in an underestimation of the sub-micrometric particles in the assumed aerosol size distribution, which seems indicative of bimodality of the aerosols.

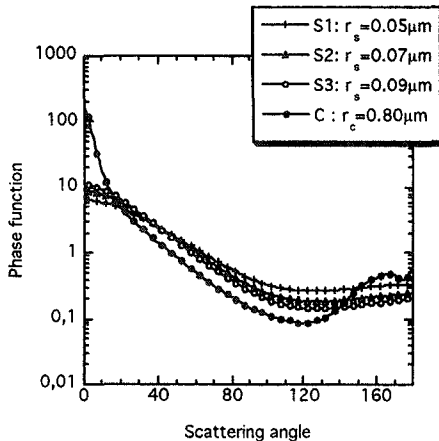


Figure 13

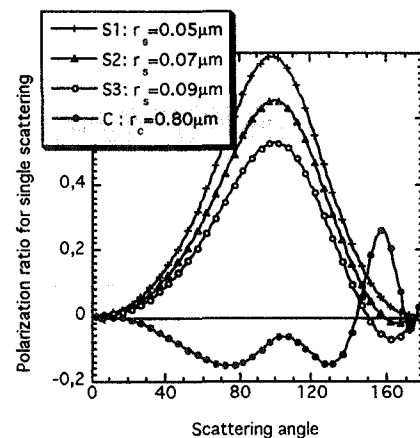


Figure 14

Let us consider bimodal aerosol size distributions drawn from the dynamic models of Remer and Kaufman (Kaufman et al., 1994 ; Remer and Kaufman, 1998) and consisting of a small (S) and a coarse (C) modes of particles, both of the modes being in the form of a log-normal function according to equation 1. In what follows the calculations are for a coarse mode with modal radius $\bar{r}_C = 0.80 \mu m$ and a small mode whose the modal radius \bar{r}_S may range from $0.05 \mu m$ to $0.10 \mu m$, with identical standard deviations $\sigma_C = \sigma_S = 0.60$ for the two modes. All of the calculations are for spherical particles with real refractive index $m = 1.40$. Figures 13 and 14 show the typical phase functions and polarized phase functions of these small and coarse modes for wavelength $\lambda_0 = 865 \text{ nm}$. Calculations (not presented here) show that changing m or changing largely \bar{r}_C does not change the main following statements.

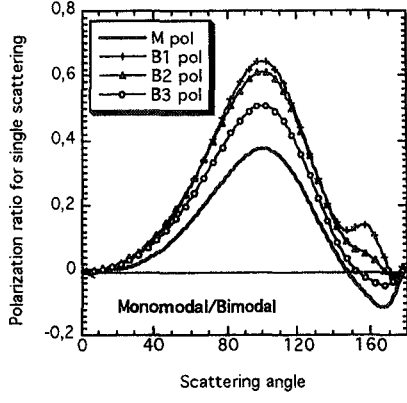


Figure 15

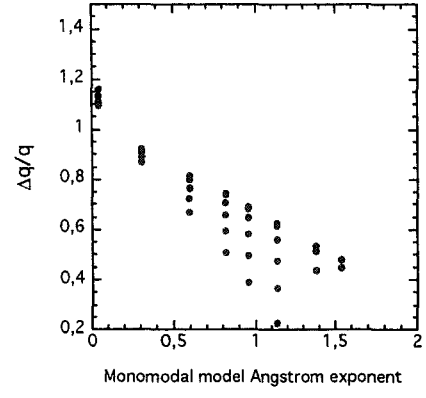


Figure 16

Figure 15 compares the polarization ratios for single scattering computed for the monomodal model $\bar{r} = 0.04 \mu\text{m}$, $\sigma = 0.8635$, and for different bimodal models which were obtained by mixing the previous coarse mode with different small modes, the contributions of the two modes being adjusted to yield the same radiance ratio R as that yielded by the monomodal model (here, $R = 1.27$). The polarization ratio at side-scattering angles is systematically larger for all of these «equivalent» bimodal models than it is for the monomodal model. This is rational. Let us start with very small particles. To adjust R with an assumed monomodal distribution, the size distribution is translated toward larger dimensions which entails vanishing contribution of the small polarizing particles, while with an assumed bimodal distribution, R is changed by increasing the weight of the coarse mode which preserves the polarized light from the small aerosols.

The previous trend is systematic. The polarized phase function for λ_0 and for $\Theta = 110^\circ$ was calculated for various monomodal models (say q_m). In each case, different bimodal models obtained as in Figure 15 were adjusted to yield the same radiance ratio R as yielded by the monomodal model, and the polarized phase functions for λ_0 and $\Theta = 110^\circ$ of these equivalent models were calculated (say q_b). Figure 16 shows the resulting relationship between the Ångström exponent of the monomodal model and the departure between its polarization ratio and that of its equivalent bimodal models

$$\frac{\Delta q}{q} = \frac{q_b - q_m}{q_b} . \quad (8)$$

The order of magnitude of $\Delta q/q$ and its behavior as a function of α in Figure 15 are consistent with the residual error $\bar{\Delta}L_\lambda^p / \bar{L}_\lambda^p$ in Figure 11, which confirms that the observed failure in the polarization retrieval is likely indicative of bimodality of the aerosols, with the parameters of the bimodal models in rough agreement with those of the dynamic models of Remer and Kaufman (1998).

4-3-Analysis of the directional radiance defect

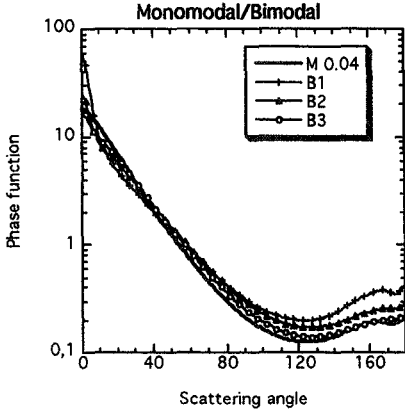


Figure 17

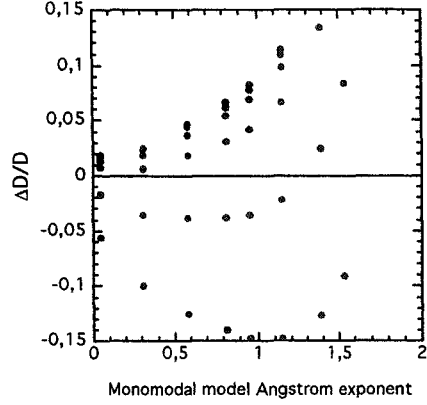


Figure 18

Then let us look at the discrepancy in the directional radiances. It may be thought that bimodality of the aerosol size distribution should explain also this systematic defect by the way of the small particles whose the phase function is nearly isotropic in backscattering directions, as seen in Figure 13. Figure 17 compares the phase functions of the monomodal model and equivalent bimodal models used in Figure 15. Some choices for \bar{r}_S in Figure 17 lead to a phase function of the bimodal model a little bit more isotropic than that of the monomodal model, but this effect is not systematic and, especially, as the mean size of the particles increases the difference between the phase functions of a monomodal model and of an equivalent bimodal model decreases.

Let us estimate the dissymmetry of a phase function by $D = \bar{p}(160^\circ)/\bar{p}(110^\circ)$ where $\bar{p}(110^\circ)$ and $\bar{p}(160^\circ)$ stand for the average value of $p(\Theta)$ over the ranges $100^\circ < \Theta < 120^\circ$ and $150^\circ < \Theta < 170^\circ$ respectively. For the same cases as in Figure 16, Figure 18 shows the relationship between the Ångström exponent of the monomodal model and the departure between its dissymmetry and that of its equivalent bimodal models

$$\frac{\Delta D}{D} = \frac{D_m - D_b}{D_b} \quad (9)$$

where D_m and D_b are the dissymmetries of the monomodal and equivalent bimodal models respectively. As α decreases, the influence of the small mode decreases and $\Delta D/D$ vanishes since the aerosol phase function tends toward that of large spherical particles whether a monomodal or a bimodal model is assumed. The resulting behavior of $\Delta D/D$ as a function of α in Figure 18, therefore, is nearly the opposite of that of $\bar{\Delta L}/\bar{L}$ in Figure 12. Thus, bimodality of the size distribution of spherical particles cannot explain all of the trends of the results.

Therefore, we are faced with polarization measurements at side-scattering angles which require aerosol size distributions with two modes when the particles start to be larger. When α decreases, however, either bimodal or monomodal size distributions of spherical particles lead to directional effects larger than those which are observed. Since the upward radiance is more and more representative of the coarse mode of particles when α decreases, the trend of our directional radiances may be explained by assuming that the phase function of the coarse mode of particles is more isotropic than that of spherical particles.

As shown in Hansen and Travis (1974), the phase function dissymmetry of large enough spherical particles (say, with effective radius $2\pi r_{eff}/\lambda \sim 10$ or more) cannot be changed significantly by changing the size distribution or the refractive index of the particles. On the contrary, it is well known that non-spherical particles tend to exhibit nearly isotropic phase function in side- and backscattering directions (see e.g. Cai and Liou, 1982 ; J. De Haan, 1987 ; Brogniez, 1992 ; Masuda and Takashima, 1992; Mishchenko and Travis, 1994a ; Labonotte et al. , 1998). The observed trend, therefore, may be indicative that the large mode of aerosols consists partly of non-spherical

particles. Note that this should be consistent also with the systematic lack of large rainbow features in the POLDER measurements, within the range $140^\circ < \Theta < 180^\circ$, since non-sphericity is known to remove the rainbow of spherical particles (see e.g. Cai and Liou, 1982 ; J. De Haan, 1987 ; Brogniez, 1992 ; Masuda and Takashima, 1992; Mishchenko and Travis, 1994a)

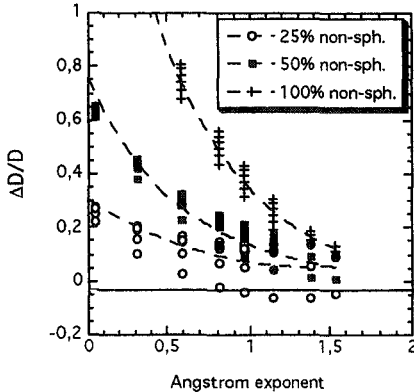


Figure 19

To more quantitatively test this assumption of non-spherical particles, the theoretical behavior of $\Delta D/D$ as a function of α was calculated again but substituting a « non-spherical » coarse mode for the previous coarse model of spherical particles, as suggested by Mishchenko et al.'s (1997) model of polydisperse, equiprobable shape mixture of prolate and oblate spheroids of large enough dimensions. Let $p_c^s(\Theta)$ and $p_c^{ns}(\Theta)$ stand for the phase function of the spherical and non-spherical coarse modes respectively (with $p_c^s(\Theta)$ derived from Mie theory for $\bar{r}_C = 0.80 \mu\text{m}$).

We assumed

$$\begin{aligned} p_c^{ns}(\Theta) &= p_c^s(\Theta) \quad \text{for } \Theta < 80^\circ \\ p_c^{ns}(\Theta) &= p_c^s(80^\circ) \quad \text{for } \Theta > 80^\circ \end{aligned} \quad ; \quad (10)$$

according to the typical trend of the phase functions for polydisperse large spheroids with $2\pi r_{eff}/\lambda_0$ larger than about 10 in Plate 5 of Mishchenko et al. (1997). Moreover, the spectral dependence of the scattering coefficient of this « non-spherical » mode was assumed to be the same as that of the spherical coarse mode, which is a reasonable approximation according to Figure 4 in Mishchenko et al. (1997). The new relationship between $\Delta D/D$ and the Ångström exponent of the monomodal model is shown in Figure 19. The « non-spherical » model (cross symbols in Figure 19) leads to a dramatic modification of the behavior of $\Delta D/D$ whose the trend is now consistent with the results in Figure 12. However, the efficiency of this model (100% non-spherical particle case in Figure 19) is 5 to 10 times larger than the effect observed in Figure 12. So, we have also reported in Figure 19 results obtained by substituting only 25% and 50% of the previous « non-spherical » model of particles to the spherical particles of the coarse mode (i.e. with the coarse mode phase function, p_c , given by $p_c = (1-x)p_c^s + xp_c^{ns}$, with $x = 0.25$ and $x = 0.50$). Despite the crudity of these estimates, the discrepancy in the directional radiance retrieval achieved by the present algorithm could be probably accounted for by assuming an aerosol coarse mode consisting partly, for 10% to 20%, of non-spherical particles. It must be noticed that the pixels corresponding to large values of \bar{L}/\bar{L} in Figure 12, which are principally relevant of the previous analysis, mostly correspond to desertic dust particles transported over the tropical Atlantic ocean, for which the sphericity assumption is questionable.

5- CONCLUSION

The spectral, directional and polarized characteristics of the solar radiation observed by POLDER over the oceans have been processed so far assuming spherical non absorbing aerosols with monomodal log-normal size distributions. As shown previously (Goloub et al., 1999), the optical thickness and Ångström exponent of the particles derived this way, principally from the radiance measurements, are consistent with ground-based

correlative measurements, except for some systematic underestimation of the Ångström exponent by POLDER. The multi-directional and polarized capabilities of POLDER also permit to control the validity of the aerosol models. The present in depth analysis of the measurements over surface target with favorable observation geometries points out the following general trends.

Small aerosols with Ångström exponents larger than about 1.0 exhibit generally directional and polarized effects consistent with the assumption of a single mode of particles. For such cases, improvement in the retrieval of the particle refractive index will be searched for by simply using an extended set of monomodal models.

As larger and larger particles are present, corresponding to smaller Ångström exponents, monomodal models lead to increasing discrepancies both in the directional and polarized features of the aerosols. Compared with the predictions of monomodal models, the data exhibit generally an aerosol phase function slightly more isotropic in backscattering directions and a much larger polarized phase function in side-scattering directions. The underestimation of the polarized light in side-scattering directions by the theoretical models is an indication of the bimodality of the aerosol size distribution, as previously derived from ground-based radiance measurements (Remer and Kaufman, 1998). Bimodality of the size distribution of spherical particles, nevertheless, seems unable to explain the overestimation of the dissymmetry of the directional radiance by the models. This trend, which is principally observed for saharan dust, can be explained by assuming a coarse mode consisting partly of non-spherical particles. The systematic lack of pronounced rainbow feature in the POLDER data would be also consistent with non-sphericity of the large particles. Confirmation of these point requires an improved analysis of the POLDER data and an improved inversion code of the POLDER data based on such bimodal models is presently developed.

Acknowledgments

Results presented in this paper were obtained using data from CNES's POLDER onboard NASDA's ADEOS. This study was funded by the Centre National d'Etudes Spatiales (CNES), the Centre National de la Recherche Scientifique (CNRS), the Conseil Régional du Nord-Pas de Calais, the Fonds Européen de Développement Régional (FEDER) and the Délégation Régionale à la Recherche et à la Technologie du Nord- Pas de Calais. The authors would like to acknowledge A. Lifermann, the POLDER Project Scientist, for her constant support. Informations on POLDER data can be found on the following web site:

<http://polder@www-projet.cnes.fr:8060>

Table 1: modal radius, \bar{r} , of the lognormal aerosol models used in the inversion scheme

	m=1.33	m=1.40	m=1.50
$\alpha=0.00$	0.270 μm	0.220 μm	0.180 μm
$\alpha=0.30$	0.144 μm	0.121 μm	0.100 μm
$\alpha=0.80$	0.071 μm	0.061 μm	0.051 μm
$\alpha=1.40$	0.033 μm	0.029 μm	0.025 μm

REFERENCES

- Bréon,F.M., and S. Colzy, Cloud detection from the spaceborne POLDER instrument and validation against surface synoptic observations, *J. Appl. Met.*, 36, 777-785, 1999.
- Brogniez, G., Contribution à l'étude des propriétés optiques et radiatives des cirrus, Thèse d'Etat, Université des Sciences et Technologies de Lille, 1992.
- Cai, Q., and K. N. Liou, Polarized light scattering by hexagonal ice cristals : theory, *Appl. Opt.*, 21, 3569-3580, 1982
- Charlson, R. J., S. E. Schwartz, J. M. Hales, R. D. Cess, J. A. Coakley, J. E. Hansen and D. H. Hofmann, Climate forcing by anthropogenic aerosols, *Science* 255, 423-430, 1992.
- Cox, C., and W. Munk, Measurements of the roughness of the sea surface from photographs of the Sun's glitter. *J. Opt. Soc. Amer.*, 44, 838-850, 1954.
- De Haan, J., Effects of aerosols on the brightness and polarization of cloudless planetary atmospheres, M.S.Thesis, Fre University of Amsterdam, Holland, The Netherlands, 1987.
- Deschamps, P.Y., F.M.Bréon, M.Leroy, A.Podaire, A.Bricaud, J.C.Buriez and G.Seze, The POLDER mission: instrument characteristics and scientific objectives, *IEEE Trans. Geosc. Remote Sensing*, 32, 598-615, 1994.
- Deuzé J.L., M.Herman, and R.Santer, Fourier series expansion of the transfer equation in the Atmosphere-Ocean system, *J. Quant. Spectrosc. Radiat. Transfer*, 41, 6, 483-494, 1988.

- Deuzé, J.L., M. Herman, P. Goloub, D. Tanré, and A. Marchand, Characterisation of aerosols over ocean from POLDER-ADEOS-1, *Geophys. Res. Lett.*, 26 n°10, 1421-1425, 1999.
- Fraser, R. S., Satellite measurement of mass of Sahara dust in the atmosphere, *Appl. Opt.*, 15, 2471-2479, 1976.
- Goloub, P., D. Tanré, J. L. Deuzé, M. Herman, A. Marchand, and F.-M. Bréon, Validation of the first algorithm applied for deriving the aerosol properties over the ocean using the POLDER/ADEOS measurements, *IEEE Trans. Geosci. Remote Sens.*, 37, n°3, 1586-1596, 1999.
- Gordon, H. R., and M. Wang, Retrieval of water-leaving radiance and aerosol optical thickness over the oceans with SeaWiFS: a preliminary algorithm, *Appl. Opt.*, 33, 443-452, 1994.
- Hagolle, O., P. Goloub, P. Y. Deschamps, H. Cosnefroy, X. Briottet, T. Bailleul, J. M. Nicolas, F. Parol, B. Lafrance, and M. Herman, Results of POLDER in-flight calibration, *IEEE Trans. Geosci. Remote Sens.*, 37, 1550-1566, 1999.
- Hansen, J. E., and Travis, Light scattering in planetary atmospheres, *Space Sci. Rev.*, 16, 527-610, 1974
- Hansen, J. E., and J.W. Hovenier, Interpretation of the polarization of Venus, *J. Atm. Sci.*, 31, 1137-1160, 1974.
- Hansen, J. E., and A. A. Lacis, Sun and dust versus greenhouse gases: an assessment of their relative roles in global climate change, *Nature*, 346, 713-719, 1990.
- Hayasaka, M.T., T. Nakajima, and M. Tanaka, The coarse particle aerosols in the free troposphere around Japan, *J. Geophys. Res.*, 95, 14039-14047, 1990.
- Herman, J. R., P.K. Bhartia, O. Torres, C. Hsu, C. Seftor, and E. Celarier, Global distribution of UV-absorbing aerosols from Nimbus 7/TOMS data, *J. Geophys. Res.*, 102, 16911-16922, 1997.
- Higurashi, A., and T. Nakajima, Development of a two channel aerosol retrieval algorithm on global scale using NOAA/AVHRR, *J. Atmos. Sci.*, 56, 924-941, 1999.
- Husar, R. B., J.M. Prospero, and L. L. Stowe, Characterization of tropospheric aerosols over the oceans with the NOAA advanced very high resolution radiometer optical thickness operational product, *J. Geophys. Res.*, 102, D14, 16889-16909, 1997.
- Holben, B. N., T. E. Eck, I. Slutsker, D. Tanré, J. P. Buis, A. Setzer, E. Vermote, J. A. Reagan, Y. F. Kaufman, T. Nakajima, F. Lavenu, I. Jankowiak, and A. Smirnov, AERONET-A federated instrument network and data archive for aerosol characterization, *Remote Sens. Environ.*, 66, 1-16, 1998.
- Kaufman, Y.J., A. Gitelson, A. Karnieli, E. Ganor, R.S. Fraser, T. Nakajima, S. Mattoo, and B.N. Holben, Size distribution and scattering phase function of aerosol particles retrieved from sky brightness measurements, *J. Geophys. Res.*, 99, 10341-10356, 1994.
- Koepke, P., Effective reflectance of the oceanic whitecaps, *Appl. Opt.*, 23, 1816-1824, 1984.
- Labonotte, L. C., G. Brogniez, M. Doutriaux-Boucher, and J. C. Buriez, Modeling of light scattering in cirrus clouds with inhomogeneous hexagonal monocrystals. Comparison with in-situ and ADEOS-POLDER measurements, to appear in *Geophys. Res. Lett.*, 1999.
- Lafrance, B., and M. Herman, Correction of the stratospheric aerosol radiative influence in the POLDER measurements, *IEEE Trans. Geosci. Remote Sensing*, 36, 1599-1608, 1998.
- Masuda, K., and T. Takashima, Feasability study of derivation of cirrus information using polarimetric measurements from satellite, *Remote Sens. Environ.*, 39, 45-59, 1992.
- Mishchenko, M. I., and L. D. Travis, Light scattering by polydisperse, rotationally symmetric, non spherical particles : linear polarization, *J. Quant. Spectrosc. Radiat. Transfer*, 51, 759-788, 1994a.
- Mishchenko, M. I., and L. D. Travis, Light scattering by polydispersions of randomly oriented spheroids with size comparable to wavelengths of observation, *App. Opt.*, 33, 7206-7225, 1994b.
- Mishchenko, M. I., and L. D. Travis, R. A. Kahn, and R. A. West, Modeling phase functions for dustlike tropospheric aerosols using a shape mixture of randomly oriented polydisperse spheroids, *J. Geophys. Res.*, 102, 16831-16847, 1997.
- Morel, P., Optical modeling of the upper ocean in relation to its biogenous water content (Case I waters), *J. Geophys. Res.*, 93, 10749-10768, 1983.
- Nadal, F., Analyse de la polarisation pour la télédétection de l'atmosphère et des surfaces grâce aux mesures spatiales de POLDER, Doctorat de l'Université de Paris 7, Méthodes Physiques en Télédétection, 1999.
- Nakajima, T., M. Tanaka, T. Hayasaka, Y. Miyake, Y. Nakanishi, and K. Sasamoto, Airborne measurements of the optical stratification of aerosols in turbid atmospheres, *Appl. Opt.*, 25, 4374-4381, 1986.
- Nakajima, T., A. Higurashi, K. Aoki, T. Endoh, H. Fukushima, M. Toratani, Y. Mitomi, B. G. Mitchell and R. Frouin, Early phase analysis of OCTS radiance data for aerosol remote sensing, *IEEE Trans. Geosci. Remote Sensing*, 37, 1575-1585, 1999.
- Quenzel, H., and P. Koepke, Tropospheric aerosol optical depth inverted from upwelling radiances. Aerosols and their climatic impact, *H. E. Gerber and A. Deepak, Eds., A. Deepak Publ.*, 227-240, 1984.
- Remer, L. A., and Y. J. Kaufman, Dynamic aerosol models : Urban industrial aerosols, *J. Geophys. Res.*, 103, 13859-13871, 1998.
- Rao, C. R. N., L. L. Stowe, and E. P. McClain, Remote sensing of aerosols over the oceans using AVHRR data: Theory, practice, and applications, *Int. J. Remote Sens.*, 10, 743-749, 1989.

- Shettle, E. P., and R. W. Fenn, Models for the aerosols of the lower atmosphere and the effect of humidity variations on their optical properties, *Air Force Geophysics Laboratory, Hanscomb AFB, MA 01731, AFGL-TR-79-0214*, 1979
- Stowe, L. L., R. M. Carey, and P. P. Pellegrino, Monitoring the Mt. Pinatubo aerosol layer with NOAA/AVHRR data, *Remote Sens. Environ.*, 60, 22-34, 1992.
- Tanré, D., Y. J. Kaufman, M. Herman, and S. Matoo, Remote sensing of aerosol properties over the oceans using the MODIS/EOS spectral radiances, *J. Geophys. Res.*, 102, 16971-16988, 1997.
- Tanré, D., C. Deroo, P. Duhamel, M. Herman, J. J. Morcrette, J. Perbos, P. Y. Deschamps, Description of a computer code to Simulate the Satellite Signal in the Solar Spectrum, *Int. J. Remote Sensing*, 11, N4, 659-668, 1990.
- Torres, O., P.K. Bhartia, J. R. Herman, Z. Ahmad, and J. Gleason, Derivation of aerosol properties from satellite measurements of backscattered ultraviolet radiation : theoretical basis, *J. Geophys. Res.*, 103, 17099-17110, 1998.
- Vesperini, M., F. M. Bréon, and D. Tanré, Atmospheric water vapor content from space-borne POLDER measurements, *IEEE Trans. Geosci. Remote Sens.*, 37, 1613-1619, 1999.

Figure caption

Figure 1a: Schematic of the POLDER imaging mode. The CCD (Charged Coupled Device) matrix and the positions of the images of the same ground target are shown for two successive snapshots. The target is observed from zenith viewing angle, θ_v , and viewing azimuth angle, ϕ , which change according to the snapshot. A ground target appears in about 13 successive snapshots during the same orbit.

Figure 1b: Typical sampling of the bidirectional properties of the atmosphere from POLDER. The target latitude is 20°N, the solar zenith angle is 38°. The target viewing directions are reported in a (θ_v, ϕ) polar diagram (radius: viewing zenith angle ; angle: viewing azimuth relative to the sun direction). The antisolar direction $(\theta_s, 0)$ is indicated. Each series of about 13 dots indicates the different viewing directions corresponding to the target during the same orbit. The 6 series, from the top to the bottom, are for 6 different positions of the target through the POLDER swath, from west to east respectively. White dots indicate viewing directions within the glitter. Iso-scattering angle curves are indicated for $\Theta = 100^\circ$ to 160° in 20° increments.

Figure 2: Comparison of the relationship between the mean radiance ratio, R (see text), and the Ångström exponent, for monomodal and bimodal aerosol models. Monomodal models (Mon.): lognormal size distribution with standard deviation σ fixed and modal radius \bar{r} varied; results are shown for real refractive index of the particle $m = 1.40$ and 1.50 . Bimodal models (Bim.) : two lognormal size distributions with standard deviations and modal radii fixed, and with the percentages of the two modes varied. Bim. N&H: $\bar{r}_1 = 0.0437 \mu m$; $\bar{r}_2 = 0.3685 \mu m$, $\sigma_1 = 0.673$, $\sigma_2 = 0.863$, $m = 1.50 - 0.005i$ for the two modes (Higurashi and Nakajima, 1999). Bim.1 T&al.: $\bar{r}_1 = 0.040 \mu m$; $\bar{r}_2 = 0.600 \mu m$, $\sigma_1 = 0.600$, $\sigma_2 = 0.800$, $m = 1.45 - 0.0035i$ for the two modes. Bim.2 T&al.: $\bar{r}_1 = 0.080 \mu m$; $\bar{r}_2 = 1.000 \mu m$, $\sigma_1 = 0.600$, $\sigma_2 = 0.600$, $m = 1.50 - 0.0035i$ for the two modes (Tanré et al., 1997). Here R was calculated by using for \bar{p}_{λ_0} the phase function averaged within $100^\circ < \Theta < 160^\circ$.

Figure 3: As in Figure 2, but for the relationship between the mean radiance ratio and the mean aerosol phase function \bar{p}_{λ_0} : $\lambda_0 = 865 nm$.

Plate 1: The observed area is between Madagascar and South Africa. From POLDER orbit 3248: November 20, 1996. Land and cloudy pixels are in white. For each cloud free ocean pixel : the upper left picture (a) gives the derived aerosol optical thickness, δ_0 , the upper right picture (b) gives the Ångström exponent, α , the lower left picture (c) gives the residual relative error in the radiance retrieval, $\bar{\Delta}L/\bar{L}$, and the lower right picture (d) gives the residual relative error in the polarized radiance retrieval, $\bar{\Delta}L_{\lambda}^p/\bar{L}_{\lambda}^p$. The color code is indicated. Increasing values from blue to red.

Plate 2: As for Plate 1, but for an area west off India, on December 04, 1996.

Plate 3: As for Plate 1, but for an area near China, on April 25, 1997.

Plate 4: As for Plate 1, but for an area west off Africa, on March 01, 1997

Figure 4: Normalized radiances as a function of the scattering angle resulting from the viewing geometry, for a pixel near Madagascar (from Plate 1). The POLDER measurements in the 670 and 865nm channels are compared with the theoretical results for the three best models, for the three values of the aerosol refractive index (1.33, 1.40 and 1.50). Retrieval : Ångström exponent 1.40 ; aerosol optical thickness 0.33 at 865nm for $m=1.33$. For comparison, the results for an aerosol-free atmosphere (mol.) are indicated.

Figure 5: As in Figure 4, but for a pixel near Indian continent (from Plate 2). Retrieval: Ångström exponent 0.39 ; aerosol optical thickness 0.51 at 865nm for $m=1.33$.

Figure 6a: Madagascar pixel of Figure 4. Normalized polarized radiance ($\sqrt{Q_{\lambda}^2 + U_{\lambda}^2}$) as a function of the scattering angle. The POLDER measurements in the 865nm channel are compared with the theoretical results for

the three best models, for the three values of the aerosol refractive index (1.33, 1.40 and 1.50). For comparison, the results for an aerosol-free atmosphere (mol.) are indicated.

Figure 6b: Madagascar pixel of Figure 4. As in Figure 6a, but for the angle, ψ_λ , between the polarisation direction and the normal to the scattering plane.

Figure 6c: Madagascar pixel of Figure 4. Residual relative error in the retrieved polarized radiance, $\bar{\Delta}L_\lambda^p / \bar{L}_\lambda^p$, according to the assumed particle refractive index (1.33, 1.40 and 1.50), as a function of the scattering angle Θ .

Figure 7a: As in Figure 6a, but for Indian pixel of Figure 5.

Figure 7b: As in Figure 6b, but for Indian pixel of Figure 5.

Figure 7c: As in Figure 6c, but for Indian pixel of Figure 5.

Figure 8: Madagascar pixel of Figure 4. Aerosol apparent polarization ratio (see text) as a function of the scattering angle. The estimate, P_λ^m , derived from the POLDER measurements in the 865nm channel is compared with the theoretical result, P_λ^C , for the best model obtained for each value of the aerosol refractive index (1.33, 1.40 and 1.50).

Figure 9: As in Figure 8, but for Indian pixel shown in Figure 5.

Figure 10: For the Indian pixel of Figures 5, 7 and 9, the polarization ratio for single scattering, P_λ , for the three best models ($m = 1.33, 1.40, 1.50$) is reported as a function of the scattering angle. Comparison of P_λ with P_λ^C , in Figure 9, confirms that the apparent polarisation ratio reflects the aerosol single scattering features.

Figure 11: For eight months of POLDER aerosol observations over different areas all over the oceans, the residual error in the polarized radiance, $\bar{\Delta}L_\lambda^p / \bar{L}_\lambda^p$, is reported as a function of the retrieved Ångström exponent for each pixel. Color indicates the frequency of occurrence of the result (arbitrary units). The results are for ground pixels with $\delta_0 > 0.20$ and $\Delta\Theta > 30^\circ$ which provides significant test of the model consistency. The retrieval is rather successful for small particles ($\alpha > 1.0$) but the accuracy decreases systematically for larger particles.

Figure 12: As in Figure 11, but for the residual error in the total radiance, $\bar{\Delta}L / \bar{L}$. In the presence of large aerosols, the present aerosol modeling exhibits inadequacy both regarding the phase function and polarized phase function of the particles.

Figure 13: Phase functions at wavelength $\lambda_0 = 865\text{nm}$ for the coarse mode (C) and three different small modes (S) of particles which are used for simulating bimodal aerosol size distributions. The particle refractive index is $m = 1.40$. Note that the dissymmetry of the phase function of the coarse mode is not changed significantly by changing m or r_C .

Figure 14: As in Figure 13, but for the polarized phase functions of the coarse and small modes.

Figure 15: Polarized phase functions at wavelength $\lambda_0 = 865\text{nm}$ for spherical particles with a monomodal size distribution (M: $\bar{r} = 0.04\mu\text{m}$, $\sigma = 0.8635$; $m = 1.40$; $\alpha = 1, 1.15$) and for spherical particles with three different «equivalent» bimodal size distributions (B1: $\bar{r}_S = 0.05\mu\text{m}$, B2: $\bar{r}_S = 0.07\mu\text{m}$, B3: $\bar{r}_S = 0.09\mu\text{m}$; $\bar{r}_C = 0.80\mu\text{m}$, $\sigma_C = \sigma_S = 0.60$; $m = 1.40$). For each bimodal model, the contributions of the two modes have been adjusted to yield the same radiance ratio $R = \delta_{\lambda_1} \bar{p}_{\lambda_1} / \delta_{\lambda_0} \bar{p}_{\lambda_0}$, as that yielded by the monomodal model ($R = 1.27$).

Figure 16: Expected relationship between the Ångström exponent α of the retrieved monomodal model and the discrepancy $\Delta q / q = (q_b - q_m) / q_b$ in the polarized light retrieval near scattering angle $\Theta = 110^\circ$, in the presence of aerosols with bimodal size distribution. For different values of α , q_m and q_b are the polarized phase functions $q_{\lambda_0}(110^\circ)$ for monomodal and «equivalent» bimodal models which yield the same radiance ratio R .

Figure 17: As in Figure 15, but for the phase functions of the monomodal model (M) and of «equivalent» bimodal models (B). Depending on the choice for the small mode, the phase function of an «equivalent» bimodal model may exhibit less dissymmetry than the monomodal model one.

Figure 18: Expected relationship between the Ångström exponent α of the retrieved monomodal model and the discrepancy $\Delta D / D = (D_m - D_b) / D_b$ in the directional radiance retrieval, in the presence of aerosols with bimodal size distribution. For different values of α , D_m and D_b are estimates of the phase function dissymmetries for monomodal and «equivalent» bimodal models which yield the same radiance ratio R , with $D = \bar{p}_{\lambda_0}(160^\circ) / \bar{p}_{\lambda_0}(110^\circ)$ for the estimate of the dissymmetry (see text).

Figure 19: As in Figure 18, but with the coarse mode of the «equivalent» bimodal models. Comparison between the polarized phase function (M) for spherical particles with a monomodal size distribution ($\bar{r} = 0.04\mu m$, $\sigma = 0.8635$ in equation 1 ; $m = 1.40$)

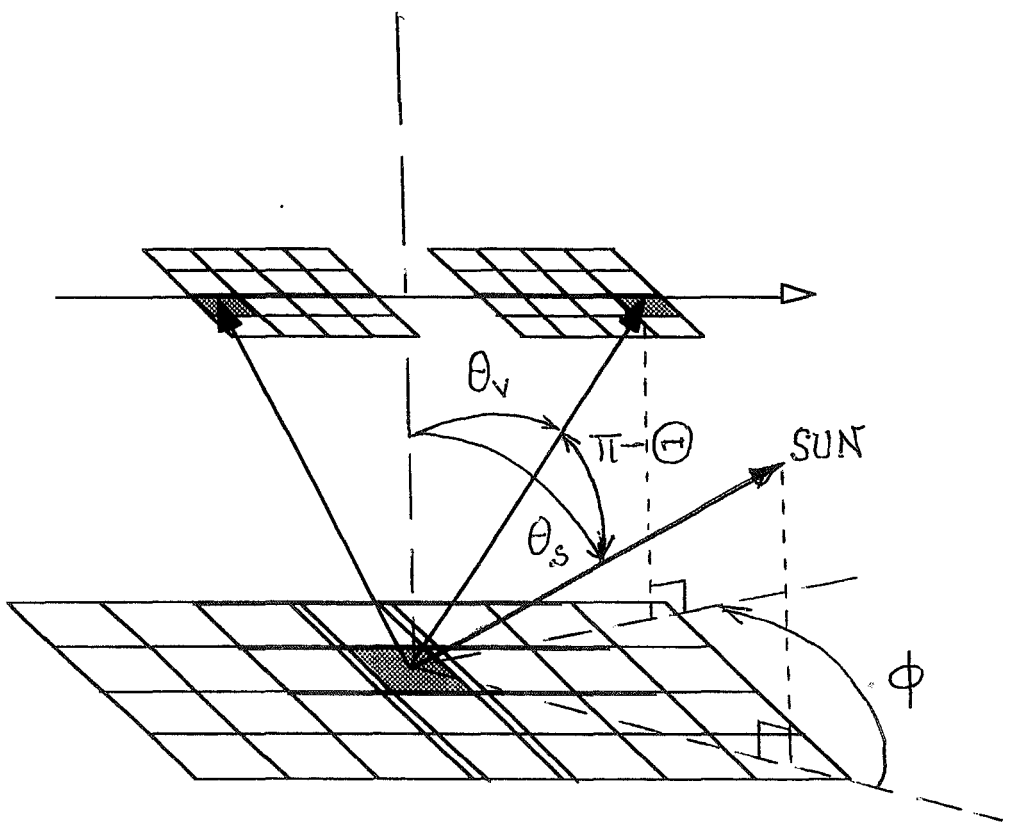


Fig 1a

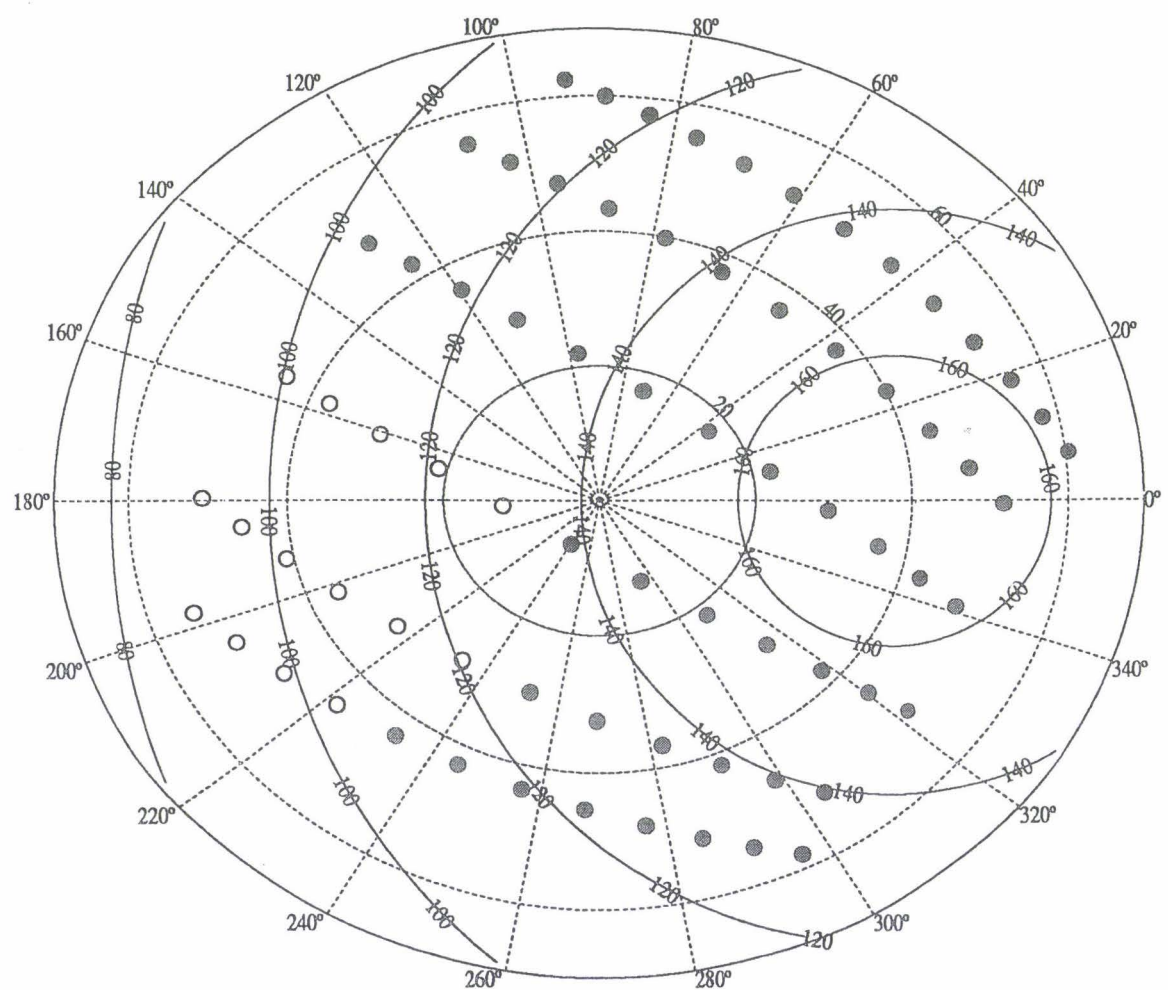
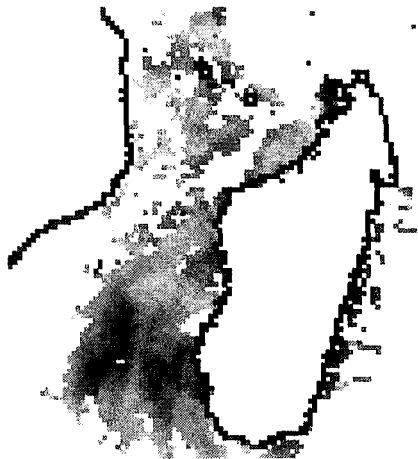


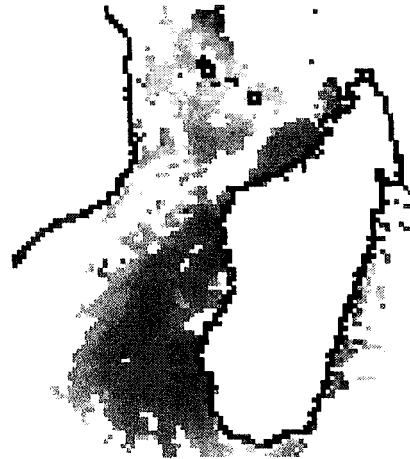
Fig. 1b

MADAGASCAR

(a) Optical thickness



(b) Angström exponent



0.00

0.60

0.00

2.00

(c) Rel. error on radiance



0.00

15%

0.00

100%

(d) Rel. error on pol. Rad.



PLATE 1: The observed area is between Madagascar and South Africa. From POLDER orbit 3248: November 20, 1996. Land and cloudy pixels are in white. For each cloud free ocean pixel : the upper left picture (a) gives the derived aerosol optical thickness, δ_0 , the upper right picture (b) gives the Ångström exponent, α , the lower left picture (c) gives the residual relative error in the radiance retrieval, $\bar{\Delta}L/\bar{L}$, and the lower right picture (d) gives the residual relative error in the polarized radiance retrieval, $\bar{\Delta}L_\lambda^p/\bar{L}_\lambda^p$. The color code is indicated. Increasing values from blue to red.

INDIA

(a) Optical thickness



(b) Angström exponent



0.00

0.60

0.00

2.00

(c) Rel. error on radiance



0.00

15%

0.00

100%

(d) Rel. error on pol. Rad.



PLATE 2: As for Plate 1, but for an area west off India, on December 04, 1996.

CHINA

(a) Optical thickness



(b) Angström exponent



(c) Rel. error on radiance



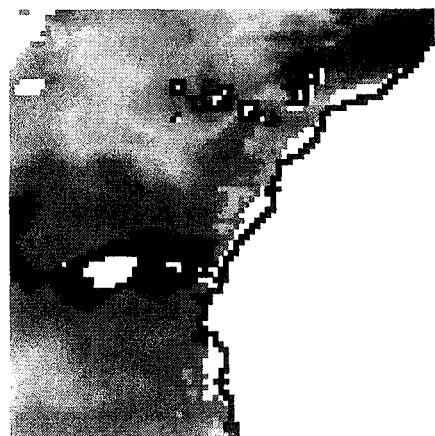
(d) Rel. error on pol. rad.



PLATE 3: As for Plate 1, but for an area near China, on April 25, 1997.

AFRICA

(a) Optical thickness



(b) Angstrøm exponent



0.00

0.60

0.00

2.00

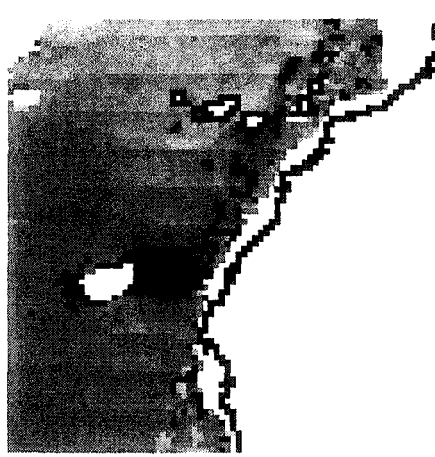
(c) Rel. error on radiance



0.00

15%

(d) Rel. error on pol. Rad.



0.00

100%

PLATE 4 : As for Plate 1, but for an area west off Africa, on March 01, 1997

Aerosol detection by TOMS and POLDER over oceanic regions

Figure 3.4: Comparison of aerosol optical depth derived from TOMS and POLDER over oceanic regions.

Aerosol detection by TOMS and POLDER over oceanic regions

Isabelle Chiapello, Philippe Goloub, Didier Tanré, and Aurelia Marchand

Laboratoire d'Optique Atmosphérique, Université des Sciences et Technologies de Lille, Villeneuve d'Ascq, France

Jay Herman, and Omar Torres

Laboratory for Atmospheres, NASA Goddard Space Flight Center, Greenbelt, Maryland

Abstract. In this paper we investigate the aerosol content retrieved by Earth-Probe Total Ozone Mapping Spectrometer (TOMS) and ADEOS POLDER over oceanic regions for the period November 1996 to June 1997. We combine the aerosol index (AI) derived from TOMS corresponding to UV-absorbing aerosols (desert dust and biomass-burning particles) and the POLDER aerosol optical thickness (AOT) and Angström coefficients. The seasonal composited images from the two sensors show in general consistent spatial distributions of the aerosol over oceans, with the highest aerosol content retrieved over the north tropical and equatorial Atlantic. Over the different oceanic regions investigated (i.e., Atlantic Ocean, Mediterranean Sea, Indian Ocean, and Pacific Ocean), TOMS and POLDER show a good correspondence in the aerosol seasonal variability. At all sites with the exception of the region of the Sea of Japan, we show that during the time periods of maximum aerosol amounts, a linear correlation exists between the TOMS AI and POLDER AOT. For the Sea of Japan the influence of different aerosol types (i.e., desert dust and sulfates) is likely to complicate the TOMS detection. For the other oceanic regions, our results suggest a large variability in the relationship between the TOMS AI and the POLDER AOT, which is likely to be related to changes in aerosol composition and/or altitude.

1. Introduction

Despite its inherent difficulties, remote sensing of tropospheric aerosol from space remains a powerful method to provide good spatial coverage, or in some cases a global view of the atmospheric aerosol system. In recent years, several studies have investigated the retrieval of aerosol spatial distribution and variation with time using sensors such as Meteosat [Jankowiak and Tanré, 1992; Moulin *et al.*, 1997a, 1997b; Moulin *et al.*, 1998], Advanced Very High Resolution Radiometer (AVHRR) [Swap *et al.*, 1996; Husar *et al.*, 1997], and Total Ozone Mapping Spectrometer (TOMS) [Herman *et al.*, 1997; Torres *et al.*, 1998]. The derived information is of first importance to improve the current knowledge of the aerosol system and its effect on climate [Kaufman *et al.*, 1997].

Recently, different original approaches have been developed in order to progress in the field of aerosol monitoring from space. The total ozone mapping spectrometer (TOMS) and polarization and directionality of the Earth's reflectances (POLDER) instruments provide new capabilities for deriving aerosol distributions. TOMS allows the real-time retrieval of the distribution of aerosols in the ultraviolet over both continents and oceans by means of a parameter known as aerosol index (AI), which is generally greater than zero for absorbing aerosols (desert dust, carbonaceous aerosols, and volcanic ash) and less than zero for non-absorbing aerosols (sulfate particles) [Herman *et al.*, 1997; Torres *et al.*, 1998].

From the spectral information contained in AI, aerosol optical depth and single-scattering albedo can be derived [Torres *et al.*, 1998]. POLDER, through multispectral, multiangular, and polarization measurements, improves the estimation of aerosol optical thickness (AOT) and provides additional information on aerosol properties through the Angström coefficient [Goloub *et al.*, 1999; Deuzé *et al.*, 1999].

In this context, it seems important to examine the consistency of the aerosol retrieval from these different approaches. By combining the aerosol observations from different sensors, one should be able to better understand the nature of the information retrieved by each instrument. In the regions where the aerosol load is dominated by UV-absorbing particles (i.e., desert dust and biomass burning) we expect good agreement between the geographical distribution of the aerosol as retrieved by the two sensors and good correlation between the aerosol content retrieved by POLDER and the positive values of the TOMS AI. A more detailed quantitative comparison of TOMS and POLDER optical depths is currently underway and will be published separately.

2. TOMS and POLDER Aerosol Products

Both POLDER and TOMS instruments were aboard the Japanese ADEOS platform (Advanced Earth Observing System) launched in August 1996 and which made measurements until June 29, 1997. Moreover, the TOMS instrument aboard the Earth-Probe platform made measurements at the same time as ADEOS and continues to provide data today.

The POLDER algorithm for the derivation of the aerosol properties is detailed by Goloub *et al.* [1999] and Deuzé *et al.* [1999]. It should be noted that in the present algorithm the

aerosols are considered nonabsorbing, which means that the aerosol optical thickness (AOT) retrieved by POLDER should be considered as a scattering aerosol optical thickness. The POLDER ADEOS aerosol products have been validated against ground-based Sun photometer measurements from the Aerosol Robotic Network (AERONET) [Holben *et al.*, 1998]. The validation of the POLDER derived AOT at 865 nm over the ocean has shown that the POLDER retrieval is excellent for optical thickness up to 0.8. This agreement also suggests a limited contribution of the absorption to the global AOT. The Angström coefficient is well correlated with the AERONET data, although underestimated (30%) [Goloub *et al.*, 1999]. It should be noted that due to the threshold used in the cloud detection scheme, only aerosol events with AOT lower than 1 (at 865 nm) can be detected by POLDER, which may lead to some systematic underestimation of the mean aerosol content [Deuzé *et al.*, 1999].

A detailed description of the TOMS aerosol index (AI) product is given by Herman *et al.* [1997] and Torres *et al.* [1998]. Briefly, the AI is a measure of the wavelength dependent change of Rayleigh scattered radiance resulting from the competing effects of aerosol scattering and absorption relative to a pure Rayleigh atmosphere [Hsu *et al.*, 1999]. For the Earth-Probe TOMS and ADEOS TOMS instruments, the AI is calculated using the ratio of the radiance between the 331- and 360-nm channels. The AI is defined so that positive values generally correspond to UV-absorbing aerosols and negative values to nonabsorbing aerosols. Since the UV surface reflectivity is low over both land and water [Herman and Celarier, 1997], this method allows the detection of aerosols over both kind of surfaces. Because the Earth-Probe TOMS AI measurements have been found to be closely correlated to ground-based measurements of optical depth [Hsu *et al.*, 1999], we choose to use data from Earth-Probe TOMS rather than ADEOS TOMS in this study, even though the difference in equator crossing time between the Earth-Probe and ADEOS spacecrafts is about 35 min. Another advantage of using Earth-Probe TOMS data is that the "footprint" size of the measurement is smaller compared to ADEOS TOMS ($24 \times 24 \text{ km}^2$ instead $40 \times 40 \text{ km}^2$ at nadir). As a consequence, the daily data from Earth-Probe TOMS have better spatial resolution than other TOMS instruments but have gaps between orbits corresponding to 40% of the Earth's surface.

Correlative analysis of the TOMS-derived AI have been performed using both Sun photometer AOT measurements from the AERONET network and measurements of mineral dust concentrations from different aerosol monitoring stations of the North Atlantic Ocean [Hsu *et al.*, 1999; Chiapello *et al.*, 1999]. These comparisons have demonstrated that there is a linear relationship between the AI derived from TOMS and the Sun photometer AOT over regions of biomass burning and African dust, even though the TOMS detection is dependent on the altitude of the aerosol layer and the nature of the aerosol, as predicted by theoretical simulations [Torres *et al.*, 1998].

For this study our comparison between the TOMS and POLDER aerosol products will be limited to the 8-month lifetime of POLDER ADEOS (November 1996 to June 1997). However, it should be noted that additional flights of POLDER instruments are planned over the next decade. Since the POLDER aerosol products have not been validated over

land surfaces, we will limit our comparisons with TOMS oceanic regions. Finally, we will consider only the positive values of the TOMS AI, so that the TOMS data will show mainly the UV-absorbing aerosols, that is, desert dust and carbonaceous aerosols. In some instances this will produce apparent discrepancy between the TOMS data (with sulfate purposely omitted) and the POLDER retrieval that includes both types.

The POLDER aerosol products are delivered over a grid of $\approx 18 \text{ km}^2$, whereas the TOMS data used in this study is uniformly gridded level-3 product (1° latitude $\times 1.25^\circ$ longitude, approximately $110 \times 138 \text{ km}^2$ at low latitudes).

3. Global Aerosol Distributions Over Oceans

Plate 1 shows the global distributions of the absorbing aerosols derived from Earth-Probe TOMS (over both continents and oceans) and of AOT at 865 nm and Angström coefficients (865–670 nm) derived from ADEOS POLDER (over oceans only). The results are presented in four maps of 2-month averaged products, for the 8-month time period of data available for this study (from November 1996 to June 1997). Both POLDER and TOMS images show that over oceanic regions most of the aerosol content is located over the north tropical Atlantic, west of the African coast. Accordingly with observations from other sensors such as AVHRR [Husar *et al.*, 1997], the north tropical Atlantic appears to be the oceanic region where the largest and more persistent aerosol amount are found. POLDER and TOMS show very consistent seasonal shifts of the aerosol plume in this region. The plume is at its maximum extent in May–June, when it reaches into the Caribbean. During the winter (January–February) the plume is located further south due to the seasonal shift of the Intertropical Convergence Zone. In general, the POLDER Angström coefficients show values lower than 0.6 in the north tropical Atlantic region, as expected under the influence of coarse mode particles of Saharan dust. Over the equatorial Atlantic, west of the Gulf of Guinea, the most intense plume appears in January–February and is probably associated with both dust and biomass burning aerosols. Indeed, it has been shown in this region that winter is the season when mineral dust from Sahara and Sahel is transported over the Gulf of Guinea in the low latitudes and toward South America [Morales, 1979; Prospero *et al.*, 1981]. It is remarkable to note that over both equatorial and north tropical Atlantic the aerosol plumes retrieved by POLDER and TOMS have very similar dimensions and show the same seasonal variabilities as that observed by AVHRR [Swap *et al.*, 1996; Husar *et al.*, 1997].

Both TOMS and POLDER show a biomass burning signal over the south tropical Atlantic, west of the coast of Angola. The plume appears in May–June, which corresponds to the beginning of the season of the southern Africa savanna and grassland fires, which occur mostly in July–September [Andreae *et al.*, 1994]. The high Angström coefficients retrieved by POLDER in this region are consistent with submicron fire smoke particles. For the other oceanic regions, both POLDER and TOMS show much more moderate aerosol amounts than over the Atlantic Ocean, with POLDER AOT below 0.4 and TOMS AI below 1. In general, POLDER seems to detect more aerosols than TOMS does, especially

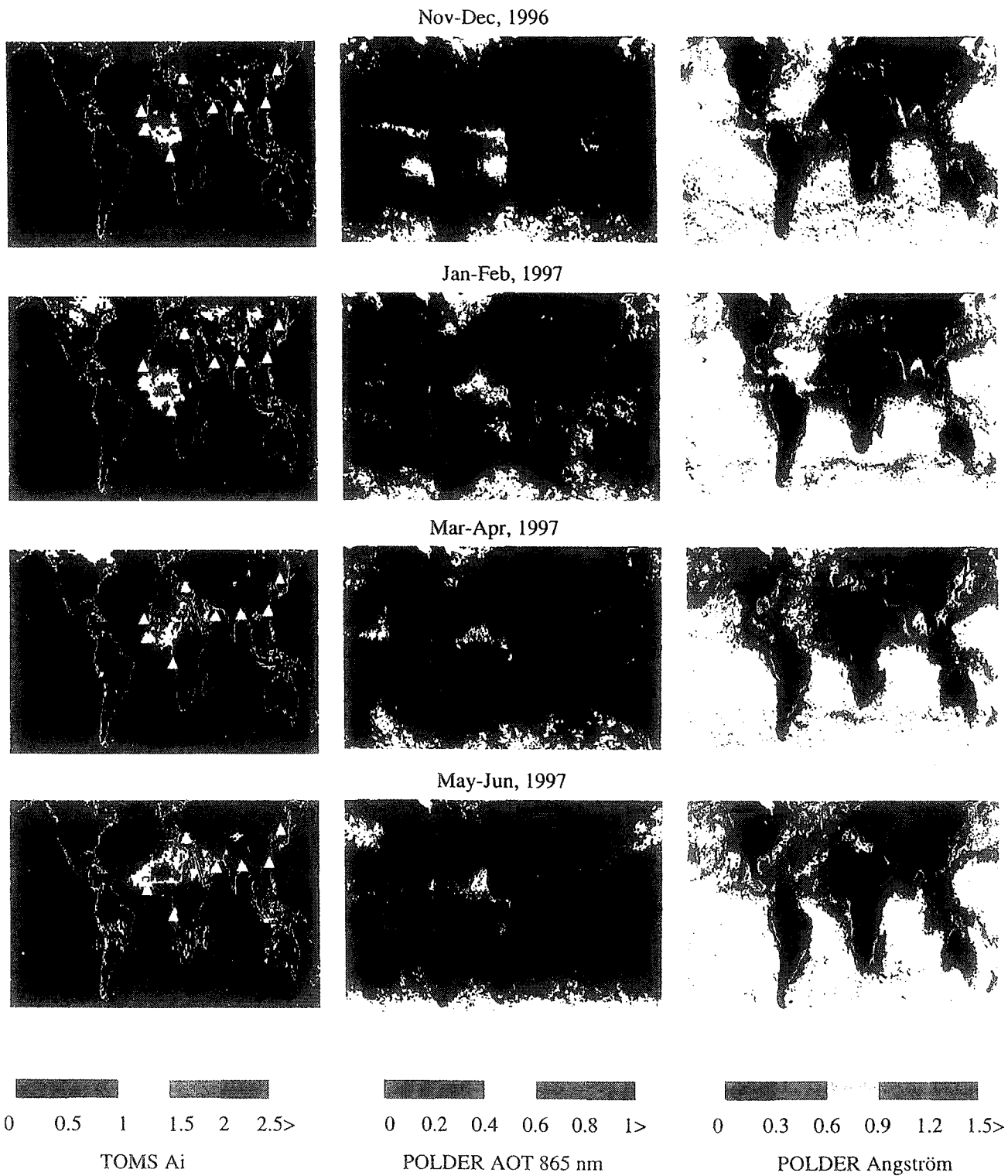


Plate 1. Global distributions of Earth-Probe TOMS-derived absorbing aerosol index, ADEOS POLDER-derived aerosol optical thickness at 865 nm, and Angström coefficient (865–670 nm) for the four 2-month time periods between November 1996 and June 1997. Note that when the POLDER-retrieved aerosol optical thickness is less than 0.1, no retrieval is made for the Angström exponent. These areas corresponding to "no retrieval" are in white on Plate 1. The TOMS aerosol index is retrieved over both oceanic and continental surfaces, whereas the POLDER products are shown over oceanic regions only. The white triangles indicate the regions for which the retrieval of aerosol by TOMS and POLDER are compared.

over the Indian Ocean (off the coast of Arabia and India) and over the Pacific Ocean (off the coast of Asia). These differences may be explained by the presence of non-UV-absorbing aerosols (sulfates particles, not included in the positive AI values) or the lower altitude of the aerosol layer which makes the TOMS retrieval of AI less sensitive to absorbing aerosols. Moreover, the transport of mineral dust particles over the Arabian Sea is known to occur mainly in summer (from July to August) [Husar *et al.*, 1997]. This can explain the rather moderate signal detected by TOMS and POLDER over this region during May-June, which is relatively early in the dusty season. It can be noted that Plate 1 also shows noticeable aerosols over the north tropical Pacific Ocean (just north of the equator) in spring and early summer on the TOMS data, but missing in the POLDER AOT. Interestingly, similar to TOMS data, noticeable aerosols have also been observed by AVHRR in March, April, and May in the same region [Husar *et al.*, 1997]. Since this is a region with less influence from the aerosols originated over land, it is not clear whether this plume is related to a "real" aerosol signal or to other features (as a signal related to the information retrieved by each instrument, for example).

4. Comparison for Selected Sites

Based on the monthly images presented on Plate 1, we select eight oceanic sites under the influence of different aerosol continental sources and for which it is interesting to investigate the consistency of the TOMS and POLDER retrieval. The positions of these sites are indicated on the TOMS images shown in Plate 1 (white triangles). Three sites are located in the Atlantic Ocean (NW Africa, Gulf of Guinea, and Angola), one site is located in the Mediterranean Sea (eastern Mediterranean), two sites in the Indian Ocean (Arabian Sea and Bay of Bengal), and two sites in the Pacific Ocean (East China Sea and Sea of Japan). For this comparison the positive values of the TOMS AI, the POLDER AOT, and Angström coefficients are averaged over a box of 2° in latitude and 2.5° in longitude. The latitude and longitude of the center of each box is given in Table 1. In Table 1 the sites are classified by order of increasing averaged Angström coefficients. Thus the lowest Angström retrieved by POLDER are over NW Africa, Arabian Sea, Gulf of Guinea, and eastern Mediterranean; this is consistent with the location of these regions, relatively close to desert areas. By contrast, the highest POLDER Angström coefficients are retrieved over the Pacific Ocean (Sea of Japan and East China Sea), Bay of Bengal, and Angola. In these regions the aerosol content appears to be dominated by smaller particles, similar to those emitted by biomass burning fires (as in the Angola region).

4.1. Monthly Variations

Figure 1 shows the monthly mean values of the TOMS-derived AI and POLDER AOT at 670 nm for the eight locations described above. Since the TOMS Earth Probe continued to provide data after the POLDER ADEOS failure in late June 1997, the AI is reported until October 1997. Figure 1 shows, in general, a good correspondence between the POLDER and TOMS temporal variability.

Table 1 shows that the NW Africa and the Gulf of Guinea are the regions where the averaged TOMS AI and POLDER AOT are the highest over the period November 1996 to June 1997.

For the NW Africa box, Figure 1 shows that POLDER TOMS present maximum in February and June, in agreement with the Saharan dust transport over this region that occurs both in winter and summer at higher altitude [Chiapello *et al.*, 1995; Prospero and Carlson, 1972]. In the region of Gul Guinea, the largest aerosol amounts are recorded from January to March, in agreement with previous observations from AVHRR in this region [Husar *et al.*, 1997]. This maximum can be related to winter transport of dust over the Gulf Guinea, but biomass-burning products are likely to contribute to the aerosol content as well. For the SW Africa region the coast of Angola, TOMS shows a maximum AI occurring in austral winter (June-September), the dry season in south Africa. This maximum does not appear as intense in variations of the POLDER AOT at least for June. However the mean Angström coefficient derived from POLDER over this region during May-June clearly shows the influence of small particles (see Table 1), as expected under the influence of biomass burning aerosols. The monthly averaged AI derived from AVHRR in this region shows maximum value in austral winter (August-September) [Husar *et al.*, 1997] in agreement with the seasonal variations of the TOMS AI. In the eastern Mediterranean and Arabian Sea, two sites impacted by desert dust, the aerosol contents retrieved by both TOMS and POLDER appear more limited in intensity. Over the Mediterranean region the maximum of POLDER AOT and TOMS AI appear from April to June. This seasonality is in agreement with the dust transport from North Africa which is known to be the greatest during spring and summer [Bergametti *et al.*, 1989a, 1989b; Moulin *et al.*, 1998]. For the Arabian Sea region, the occurrence of maximum in June (from POLDER AOT) and July-August (from TOMS AI) is very consistent with previous observations from AVHRR [Husar *et al.*, 1997]. In the Pacific region (i.e., for the sites East China Sea and Sea of Japan) the seasonal variations of the POLDER AOT and the TOMS AI show maximum during the spring months. Asia is known to be an important source of desert dust, anthropogenic sulfur, and biomass burning products. Aerosol measurements in the North Pacific Ocean have shown that the concentrations of these constituents generally present maximum in spring [Prospero *et al.*, 1989; Savoie *et al.*, 1989; Arimoto *et al.*, 1996; Carmichael *et al.*, 1997], in agreement with the observations of TOMS and POLDER. In the Bay of Bengal both TOMS and POLDER record a peak in March. Considering the rather high values of the POLDER Angström associated to this peak (about 0.8, see Table 1), we can suspect it to be related to biomass burning activities in Bangladesh and northern Burma, which seem to occur during March through May [Hao and Liu, 1994].

4.2. Relations Between the TOMS AI and POLDER AOT

For each of the sites discussed above, Table 2 reports the correlation coefficients and slopes of the relationship obtained between the TOMS AI and the POLDER AOT computed at 440, 670, and 865 nm, along with the number of days available with coincident POLDER and TOMS data for each site. The POLDER AOT at 440 nm is computed from the AOT at 865 nm and the Angström coefficient, which is assumed to be unchanged over the ranges 670-865 and 440-865 nm. The results are reported both over an 8-month time period and over a 2-month timescale. Our results indicate that, depending on the season, the correlation obtained between the TOMS AI and

Table 1. POLDER Mean Angström Coefficients (670–865 nm), POLDER Mean Aerosol Optical Thickness at 670 nm, and TOMS Mean Aerosol Index for Each Oceanic Region

Time Period	POLDER Mean Angström	POLDER Mean AOT 670 nm	TOMS Mean AI
<i>NW Africa, 16°N, 22.5°W</i>			
Global	0.22	0.40	0.78
Nov.-Dec.	0.22	0.28	0.70
Jan.-Feb.	0.20	0.53	0.90
March-April	0.26	0.44	0.58
May-June	0.22	0.50	0.98
<i>Arabian Sea, 18°N, 58.75°E</i>			
Global	0.37	0.27	0.30
Nov.-Dec.	0.31	0.18	0.16
Jan.-Feb.	0.28	0.25	0.25
March-April	0.51	0.28	0.30
May-June	0.31	0.33	0.46
<i>Gulf of Guinea, 5°N, 20°W</i>			
Global	0.40	0.42	0.83
Nov.-Dec.	0.49	0.26	0.74
Jan.-Feb.	0.36	0.62	1.15
March-April	0.41	0.42	0.76
May-June	-	-	-
<i>Eastern Mediterranean, 35°N, 25°E</i>			
Global	0.53	0.19	0.31
Nov.-Dec.	0.48	0.18	0.36
Jan.-Feb.	0.35	0.14	0.24
March-April	0.62	0.19	0.21
May-June	0.65	0.23	0.36
<i>East China Sea, 21°N, 118.75°E</i>			
Global	0.55	0.22	0.29
Nov.-Dec.	-	-	-
Jan.-Feb.	-	-	-
March-April	0.58	0.28	0.50
May-June	0.46	0.17	0.15
<i>Angola, 10°S, 10°E</i>			
Global	0.68	0.25	0.57
Nov.-Dec.	-	-	-
Jan.-Feb.	0.25	0.25	0.77
March-April	-	-	-
May-June	0.83	0.26	0.53
<i>Bay of Bengal, 19°N, 87.5°E</i>			
Global	0.73	0.35	0.43
Nov.-Dec.	0.71	0.29	0.33
Jan.-Feb.	0.76	0.32	0.28
March-April	0.81	0.40	0.76
May-June	0.48	0.45	0.36
<i>Sea of Japan, 40°N, 132.5°E</i>			
Global	0.78	0.25	0.53
Nov.-Dec.	0.53	0.17	0.49
Jan.-Feb.	0.56	0.19	0.54
March-April	1.03	0.31	0.54
May-June	1.09	0.38	0.60

The results are reported for the whole time period (November 1, 1996, to June 29, 1997, designated as "global") and for 2-month time periods. The lines with no data correspond to the lack of coincident days for POLDER and TOMS observations during the period. The latitude and longitude of the center of the box in which the comparison is performed are indicated in the first line. Each box has a size of 2° in latitude and 2.5° in longitude.

the POLDER AOT vary significantly. Figure 2 reports for each site the data from the season giving the best correlation between the TOMS AI and the POLDER AOT at 670 nm. In general, a good correlation is obtained during the period of maximum aerosol content detected by TOMS and POLDER. Thus in the NW Africa region the correlation coefficients are high in January–February and May–June (r above 0.84 at the three wavelengths), which are months associated with the maximum of TOMS AI and POLDER AOT (see Table 1). For the Arabian Sea and eastern Mediterranean regions the best correlation coefficients are obtained in May–June, which

is the period of aerosol peaks associated with maximum dust transport. It is striking to note that in the regions of Gulf of Guinea, East China Sea, and Angola, the correlation coefficients obtained when fitting the TOMS and POLDER data from the whole period are above 0.75 at 670 nm. However, Figure 2 shows that these correlations improve when plotting the data only for the period of the maximum concentrations.

For the Bay of Bengal region a good correlation is obtained between TOMS and POLDER for the March–April time period, corresponding to the aerosol peaks. The Sea of Japan is

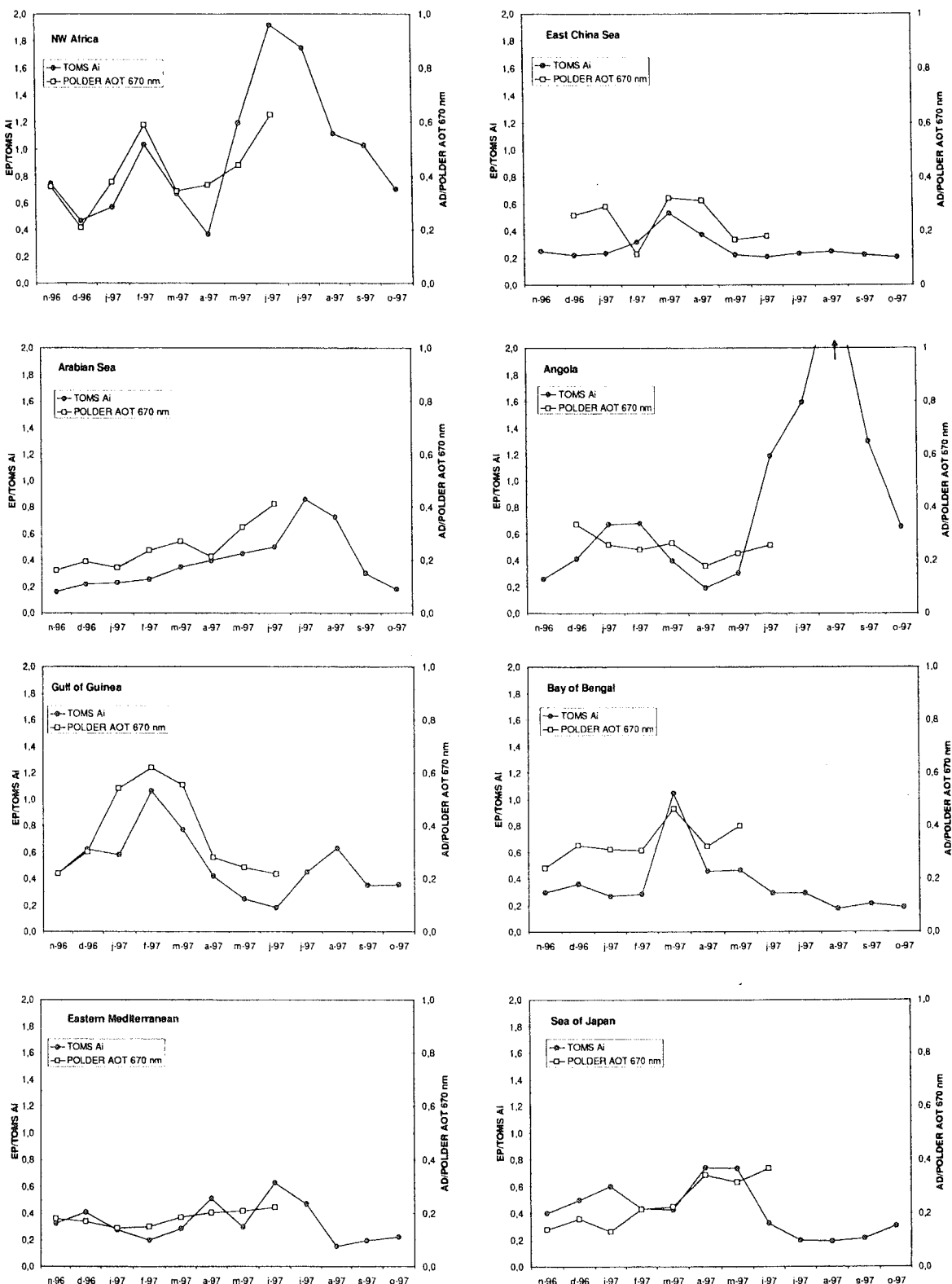


Figure 1. Monthly mean of Earth-Probe TOMS absorbing aerosol index and ADEOS POLDER aerosol optical thickness at 670 nm for various oceanic regions. The locations of the regions are reported in Table 1. Note that the aerosol optical thickness at 670 nm is computed from the POLDER aerosol optical thickness at 865 nm and the POLDER Angström coefficient (865–670 nm).

Table 2. Correlation Coefficients and Slopes of the Relationship Obtained Between the TOMS AI and the POLDER AOT at 865, 670, and 440 nm for Each Oceanic Region

Time Period	Number of Coincident Days	865 nm		670 nm		440 nm	
		Slope	r	Slope	r	Slope	r
<i>NW Africa</i>							
Global	42	1.7	0.67	1.6	0.67	1.5	0.68
Nov.-Dec.	20	1.4	0.48	1.4	0.52	1.3	0.57
Jan.-Feb.	9	2.8	0.86	2.7	0.85	2.4	0.84
March-April	5	0.9	0.66	0.9	0.71	0.8	0.76
May-June	8	2.7	0.86	2.7	0.87	2.7	0.88
<i>Arabian Sea</i>							
Global	62	1.2	0.65	1.1	0.64	0.8	0.59
Nov.-Dec.	13	-0.1	0.05	-0.1	0.09	-0.2	0.15
Jan.-Feb.	14	0.9	0.56	0.8	0.54	0.7	0.49
March-April	19	0.4	0.24	0.3	0.23	0.2	0.19
May-June	16	1.2	0.69	1.2	0.70	1.1	0.69
<i>Gulf of Guinea</i>							
Global	27	1.9	0.74	1.8	0.77	1.6	0.81
Nov.-Dec.	7	6.6	0.91	4.8	0.90	2.7	0.87
Jan.-Feb.	10	2.2	0.86	2.1	0.88	1.9	0.91
March-April	6	1.4	0.48	1.3	0.50	1.2	0.54
May-June	4	-	-	-	-	-	-
<i>Eastern Mediterranean</i>							
Global	67	2.6	0.74	2.2	0.70	1.4	0.56
Nov.-Dec.	18	1.1	0.58	1.1	0.56	0.8	0.47
Jan.-Feb.	16	-0.2	0.05	0.4	0.13	0.6	0.31
March-April	10	2.1	0.81	1.5	0.69	0.6	0.42
May-June	23	4	0.90	3.6	0.86	2.6	0.72
<i>East China Sea</i>							
Global	20	2	0.71	1.8	0.75	1.4	0.79
Nov.-Dec.	2	-	-	-	-	-	-
Jan.-Feb.	1	-	-	-	-	-	-
March-April	8	3	0.97	2.4	0.97	1.6	0.94
May-June	9	0.1	0.08	0.1	0.11	0.1	0.16
<i>Angola</i>							
Global	20	6.4	0.85	5	0.88	2.6	0.84
Nov.-Dec.	3	-	-	-	-	-	-
Jan.-Feb.	6	4.8	0.88	4	0.84	2.4	0.72
March-April	0	-	-	-	-	-	-
May-June	11	6.8	0.85	5	0.91	2.9	0.96
<i>Bay of Bengal</i>							
Global	78	1.6	0.50	1.4	0.55	1	0.57
Nov.-Dec.	22	0.1	0.06	0.1	0.07	0.1	0.08
Jan.-Feb.	27	0.5	0.27	0.4	0.28	0.2	0.29
March-April	21	3.6	0.78	3	0.86	1.8	0.87
May-June	8	1.4	0.71	1.3	0.68	1	0.61
<i>Sea of Japan</i>							
Global	66	1.4	0.37	1	0.40	0.6	0.42
Nov.-Dec.	19	2.3	0.55	2.1	0.58	1.8	0.61
Jan.-Feb.	16	1.8	0.32	1.2	0.27	0.6	0.18
March-April	22	1.4	0.30	1.4	0.43	1	0.58
May-June	9	1.8	0.50	1.2	0.47	0.6	0.42

The number of days available with coincident TOMS and POLDER data is indicated. The results are reported for the whole time period (November 1, 1996, to June 29, 1997) and for 2-month time periods.

the only site for which all the correlation coefficients between POLDER and TOMS are below 0.6. Figure 2 shows that at this site the POLDER retrieved AOT is below 0.35, a rather moderate value. As a possible explanation to the absence of correlation between TOMS and POLDER at this site, several studies of aerosol in the Pacific Ocean have indicated that this region is impacted by aerosols from different sources, especially mineral dust and sulfates from industrial activities, which are likely to be internally mixed [Horai *et al.*, 1993; Parungo *et al.*, 1995; Dentener *et al.*, 1996]. Such a mixture will complicate the use of AI from TOMS in this region.

Figure 2 and Table 2 show that depending on the location and the wavelength we obtain different slopes for the relationship between the TOMS AI and POLDER AOT. At 440 nm the slopes of the best fit obtained for the NW Africa, Gulf of Guinea, and eastern Mediterranean sites range between 1.9 and 2.7 (see Table 2). These values are in the same range as those obtained by Hsu *et al.* [1999] when comparing the TOMS AI to sunphotometer measurements of AOT performed in the Sahel and NW Atlantic regions. For the Arabian Sea region the slope of the fit obtained in May-June is significantly lower (1.1 at 440 nm). For the regions characterized by higher

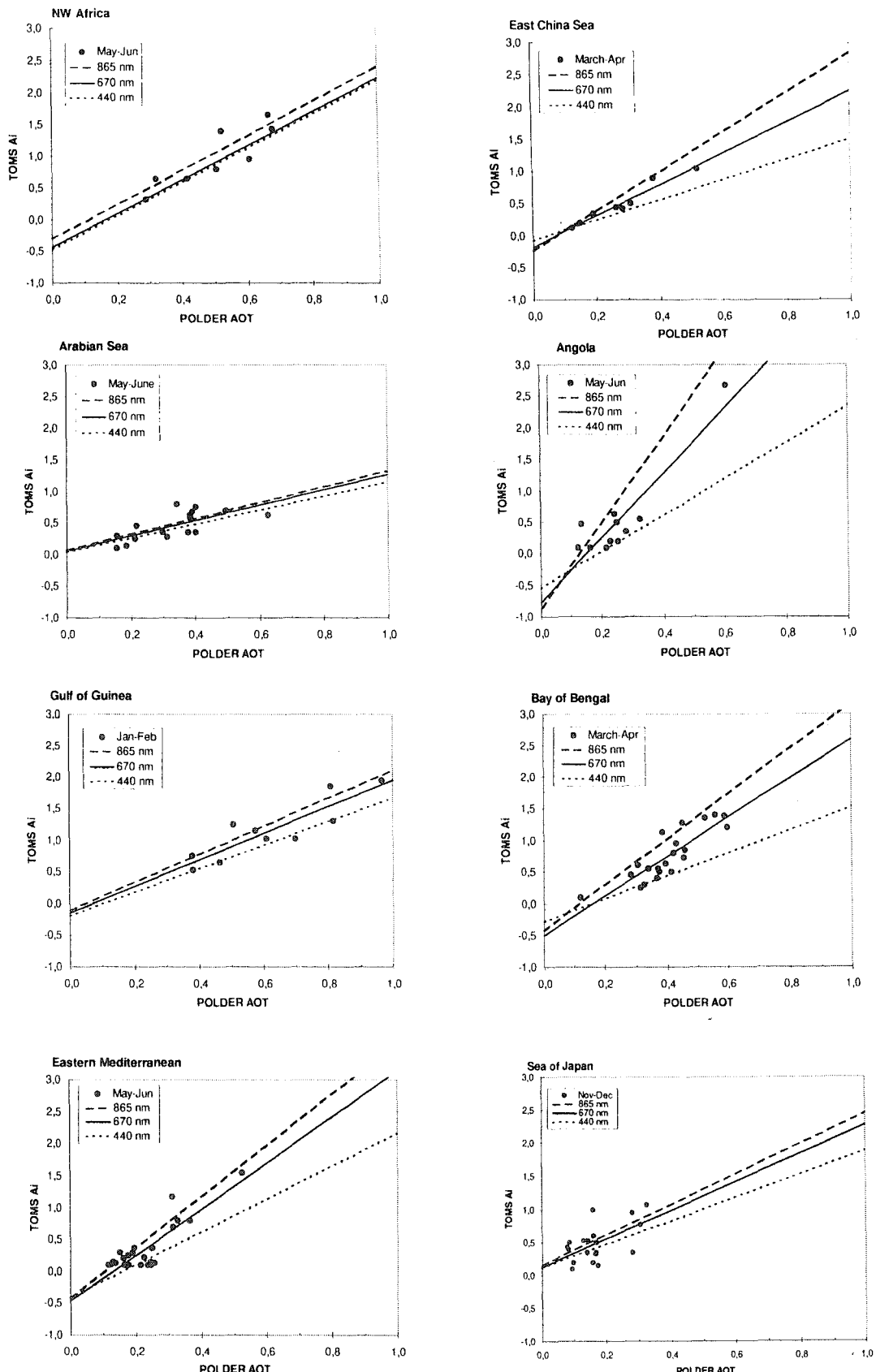


Figure 2. Comparison of Earth-Probe TOMS absorbing aerosol index with ADEOS POLDER aerosol optical thickness at 670 nm for the different oceanic regions described in Table 1 and for the time period which allows the best linear relation (see Table 2). The solid lines represent the regression fits to the data (POLDER AOT at 670 nm). The dotted and dashed lines represent the fits obtained with POLDER AOT at 440 and 865 nm, respectively. The equations and correlation coefficients for the regression lines are reported in Table 2.

Angström coefficients, that is, East China Sea, Angola, and Bay of Bengal, the slopes of the best fit range from 1.6 to 2.9 at 440 nm. The value of 2.9 obtained for the Angola region in May-June is relatively high compared to the one retrieved by *Hsu et al.* [1999] using AOT measured in Zambia during the burning season (June-October). However, the differences in the season and range of AOT (ours are below 0.6) may be sufficient to explain these deviations in the relation between the TOMS AI and the AOT.

Our comparisons suggest that, depending on the geographical situation, a given amount of aerosol optical thickness can lead to a large range of AI (overall the slopes range between 1.1 and 2.9 at 440 nm). The two parameters which are known to play dominant roles in the relationship between the TOMS AI and AOT are the altitude of the aerosol layer and the single-scattering albedo (which depends on the nature of the aerosol) [Torres et al., 1998; *Hsu et al.*, 1999]. These two parameters are likely to be variable from one region to another, which is probably sufficient to explain the variability of the TOMS AI - POLDER AOT relationship.

5. Conclusions

In this paper we investigate the relationship between the TOMS AI and the POLDER derived-AOT over oceans and in particular at eight sites located in the Atlantic Ocean, Mediterranean Sea, Indian Ocean, and Pacific Ocean. In general, the spatial distributions and monthly variations of the aerosol content derived from TOMS and POLDER are very consistent and also in good agreement with other instrument's observations over oceanic regions such as those from AVHRR [*Husar et al.*, 1997]. At all sites, with the exception of the Sea of Japan, our results indicate that, during the time period of maximum aerosol content, a linear correlation exists between the TOMS AI and POLDER AOT. In the region of the Sea of Japan we suspect the occurrence of mixtures of different aerosol types (i.e., mineral dust, soot, and sulfate) as an explanation of the poor correlation observed between TOMS and POLDER. Moreover, it can be noted that among all the sites, the POLDER AOT at the Sea of Japan has the lowest maximum value, and the highest averaged Angström coefficient.

Our results, although limited to an 8-month time period, suggest that TOMS and POLDER aerosol retrievals are very consistent over the oceanic regions under the influence of biomass burning aerosols and desert dust. The good correlation obtained between the POLDER AOT and the TOMS AI are remarkable considering the totally different approaches of the two instruments and the uncertainties inherent to each method. The results of these comparisons confirm that mineral dust and biomass-burning aerosol distributions can be retrieved using different techniques, either in the UV or in the visible range. The main advantage of the TOMS detection in the UV is to offer the retrieval of aerosol distributions over both continents and oceans. The principal limitation of this method is that the aerosol optical thickness of UV-absorbing aerosols cannot be derived without an assumption of the altitude of the aerosol layer. In contrast, POLDER allows the retrieval of physical quantities, that is, aerosol optical thickness and Angström coefficients, but at this point only over oceans. It certainly remains one of the main challenges in the field of aerosol remote sensing from space to retrieve optical thickness of aerosols over both continental and oceanic surfaces.

Acknowledgments. The authors would like to thank the CNRS and the CNES for their financial support. We also thank Olivier Boucher and two anonymous referees for their useful comments.

References

- Andreae, M. et al., Biomass burning in the global environment: First results from the IGAC-BIBEX field campaign STARE/TRACE A/SAFARI 92, in *Global Atmospheric-Biospheric Chemistry*, edited by R.G. Prinn, pp. 83-101, Plenum, New York, 1994.
- Arimoto, R., R.A. Duce, D.L. Savoie, J.M. Prospero, R. Talbot, J.D. Cullen, U. Tomza, N.F. Lewis, and B.J. Ray, Relationships among aerosol constituents from Asia and the North Pacific during PEM-West A, *J. Geophys. Res.*, **101**, 2011-2024, 1996.
- Bergametti, G., A.-L. Dutot, P. Buat-Menard, R. Losno, and E. Remoudaki, Seasonal variability of the elemental composition of atmospheric aerosol particles over the northwestern Mediterranean, *Tellus, Ser. B*, **41**, 353-361, 1989a.
- Bergametti, G., L. Gomes, E. Remoudaki, M. Desbois, D. Martin, and P. Buat-Menard, Present transport and deposition patterns of African dusts to the North Western Mediterranean, in *Paleoclimatology and Paleometeorology: Modern and Past Patterns of Global Atmospheric Transport*, pp. 227-252, Kluwer Acad., Norwell, Mass., 1989b.
- Carmichael, G.R., M.S. Hong, H. Ueda, L.L. Chen, K. Murano, J.K. Park, H. Lee, Y. Kim, and S. Shim, Aerosol composition at Cheju Island, Korea, *J. Geophys. Res.*, **102**, 6047-6061, 1997.
- Chiapello, I., G. Bergametti, L. Gomes, B. Chatenet, F. Dulac, J. Pimenta, and E. Santos Soares, An additional low layer transport of Sahelian and Saharan dust over the northeastern Tropical Atlantic, *Geophys. Res. Lett.*, **22**, 3191-3194, 1995.
- Chiapello, I., J.M. Prospero, J.R. Herman, and N.C. Hsu, Detection of mineral dust over the North Atlantic Ocean and Africa with Nimbus-7/TOMS, *J. Geophys. Res.*, **104**, 9277-9291, 1999.
- Dentener, F.J., G.R. Carmichael, Y. Zhang, J. Lelieveld, and P.J. Crutzen, Role of mineral aerosol as a reactive surface in the global troposphere, *J. Geophys. Res.*, **101**, 22,869-22,889, 1996.
- Deuzé, J.L., M. Herman, P. Goloub, D. Tanré, and A. Marchand, Characterization of aerosols over ocean from POLDER/ADEOS-1, *Geophys. Res. Lett.*, **26**, 1421-1424, 1999.
- Goloub, P., D. Tanré, J.L. Deuzé, M. Herman, A. Marchand, and F.M. Bréon, Validation of the first algorithm applied for deriving the aerosol properties over the ocean using the POLDER/ADEOS measurements, *IEEE Trans. Geosci. Remote Sens.*, **37**, 1586-1596, 1999.
- Hao, W.M., and M.H. Liu, Spatial and temporal distribution of tropical biomass burning, *Global Biogeochem. Cycles*, **8**, 495-503, 1994.
- Herman, J.R., and E. Celarier, Earth's surface reflectivity climatology at 340-380 nm from TOMS data, *J. Geophys. Res.*, **102**, 28,003-28,012, 1997.
- Herman, J.R., P.K. Bhartia, O. Torres, C. Hsu, C. Seftor, and E. Celarier, Global distribution of UV-absorbing aerosols from Nimbus 7/TOMS data, *J. Geophys. Res.*, **102**, 16,911-16,922, 1997.
- Holben, B.N., et al., AERONET-A federated instrument network and data archive for aerosol characterization, *Remote Sens. Environ.*, **66**, 1-16, 1998.
- Horai, S., I. Minari, and Y. Migita, Aerosols composition in Kagoshima, in *Annual Report of the Kagoshima Prefectural Institute*, vol. 9, 1993.
- Hsu, N.C., J.R. Herman, O. Torres, B.N. Holben, D. Tanré, T.F. Eck, A. Smirnov, B. Chatenet, and F. Lavenu, Comparisons of the TOMS aerosol index with Sun-photometer aerosol optical thickness: Results and applications, *J. Geophys. Res.*, **104**, 6269-6279, 1999.
- Husar, R.B., J.M. Prospero, and L.L. Stowe, Characterization of tropospheric aerosols over the oceans with the NOAA advanced very high resolution radiometer optical thickness operational product, *J. Geophys. Res.*, **102**, 16,889-16,909, 1997.
- Jankowiak, I., and D. Tanré, Satellite climatology of Saharan dust outbreaks, *J. Clim.*, **5**, 646-656, 1992.
- Kaufman, Y.J., D. Tanré, H.R. Gordon, T. Nakajima, J. Lenoble, R. Frouin, H. Grassl, B.M. Herman, M.D. King, and P.M. Teillet, Passive remote sensing of tropospheric aerosol and atmospheric correction for the aerosol effect, *J. Geophys. Res.*, **102**, 16,815-16,830, 1997.

- Morales, C. (Ed.), *Saharan Dust: Mobilization, Transport, Deposition*, John Wiley, New York, 1979.
- Moulin, C., F. Guillard, F. Dulac, and C.E. Lambert, Long-term daily monitoring of Saharan dust load over ocean using Meteosat ISCCP-B2 data, 1, Methodology and preliminary results for 1983-1994 in the Mediterranean, *J. Geophys. Res.*, 102, 16,947-16,958, 1997a.
- Moulin, C., F. Dulac, C.E. Lambert, P. Chazette, I. Jankowiak, B. Chatenet, and F. Lavenu, Long-term daily monitoring of Saharan dust load over ocean using Meteosat ISCCP-B2 data, 2, Accuracy of the method and validation using Sun photometer measurements, *J. Geophys. Res.*, 102, 16,959-16,969, 1997b.
- Moulin, C., et al., Satellite climatology of African dust transport in the Mediterranean atmosphere, *J. Geophys. Res.*, 103, 13,137-13,144, 1998.
- Parungo, F., Y. Kim, C.J. Zhu, J. Harris, R. Schnell, X.S. Li, D.Z. Yang, M.Y. Zhou, Z. Chen, and K. Park, Asian dust storms and their effects on radiation and climate, *STC Rep.* 2906, Natl. Oceanic and Atmos. Admin. Air Resour. Lab., Silver Spring, Md., 1995.
- Prospero, J.M., and T.N. Carlson, Vertical and areal distribution of Saharan dust over the western equatorial North Atlantic Ocean, *J. Geophys. Res.*, 77, 5255-5265, 1972.
- Prospero, J.M., R.A. Glaccum, and R.T. Nees, Atmospheric transport of soil dust from Africa to South America, *Nature*, 289, 570-572, 1981.
- Prospero, J.M., M. Uematsu, and D.L. Savoie, Mineral aerosol transport to the Pacific Ocean, in *Chemical Oceanography*, vol. 10, edited by J.P. Riley, R. Chester, and R.A. Duce, pp. 188-210, Academic, San Diego, Calif., 1989.
- Savoie D.L., J.M. Prospero, and E.S. Saltzman, Nitrate, non-sea sulfate and methanesulfonate over the Pacific Ocean, in *Chemical Oceanography*, vol. 10, edited by J.P. Riley, R. Chester, and R.A. Duce, pp. 219-250, Academic, San Diego, Calif., 1989.
- Swap, R., S. Ulanski, M. Cobbett, and M. Garstang, Temporal and spatial characteristics of Saharan dust outbreaks, *J. Geophys. Res.*, 101, 4205-4220, 1996.
- Torres, O., P.K. Bhartia, J.R. Herman, Z. Ahmad, and J. Gleasen, Derivation of aerosol properties from satellite measurements of backscattered ultraviolet radiation: Theoretical basis, *J. Geophys. Res.*, 103, 17,099-17,110, 1998.

I. Chiapello, P. Goloub, A. Marchand, and D. Tanré, Laboratoire d'Optique Atmosphérique, Université des Sciences et Technologies Lille, Bat. P5, 59655 Villeneuve d'Ascq Cedex, France (chiapello@loa.univ-lille1.fr; goloub@loa.univ-lille1.fr; marchand@loa.univ-lille1.fr; tanre@loa.univ-lille1.fr)

J. Herman and O. Torres, Laboratory for Atmospheres, NASA Goddard Space Flight Center, Code 916, Greenbelt, MD 20720 (herman@tparty.gsfc.nasa.gov; torres@tparty.gsfc.nasa.gov)

(Received May 14, 1999; revised September 20, 1999; accepted September 28, 1999.)

Remote sensing of aerosols over land surfaces from POLDER-ADEOS 1 measurements

REMOTE SENSING OF AEROSOLS OVER LAND SURFACES FROM POLDER-ADEOS 1 POLARIZED MEASUREMENTS

Deuzé*, J.L., F.M. Bréon**, C. Devaux*, P. Goloub*, M. Herman*, B. Lafrance***, F. Maignan**, A. Marchand*, F. Nadal*, G. Perry*, and D. Tanré*

*Laboratoire d'Optique Atmosphérique, Université de Lille 1. 59655 Villeneuve d'Ascq Cedex. France.

**L.S.C.E. Gif sur Yvette

***Centre National d'Etudes Spatiales, 18 Avenue E. Belin. 31055 Toulouse Cedex. France.

ABSTRACT

The polarization measurements achieved by the POLDER instrument on ADEOS-1 are used for the remote sensing of aerosols over land surfaces. The key advantage of using polarized observations is their ability to systematically correct for the ground contribution whereas the classical approach using natural light fails. The estimation of land surface polarizing properties from POLDER has been examined in a previous paper. Here we consider how the optical thickness, δ_0 , and Ångström exponent, α , of aerosols are derived from the polarized light backscattered by the particles. The inversion scheme is detailed and illustrative results are presented. Maps of the retrieved optical thickness allow for detection of large aerosol features and, in the case of small aerosols, the δ_0 and α retrievals are consistent with correlative ground-based measurements. However, because polarized light stems mainly from small particles, the results are biased for aerosol distributions containing coarser modes of particles. To overcome this limitation, an aerosol index defined as the product $AI = \delta_0\alpha$ is proposed. Theoretical analysis and comparison with ground-based measurements suggest that AI is approximately the same when using δ_0 and α related to the entire aerosol size distribution or derived from the polarized light originating from the small polarizing particles alone. This invariance is specially assessed by testing the continuity of AI across coastlines, given the unbiased properties of aerosol retrieval over ocean. Although reducing the information concerning the aerosols, this single parameter allows a link between the POLDER aerosol surveys over land and ocean. POLDER aerosol index global maps enable the monitoring of major aerosol sources over continental areas.

1-INTRODUCTION

Recognition of the climatic influence of the aerosols (Hansen and Lacis, 1990; Charlson et al., 1992) has led to large efforts for improving their global monitoring from satellite. Over the ocean, where the aerosol remote sensing is tractable from measurements at near infrared wavelengths, the aerosol survey has been engaged long ago from satellite imagery (Fraser, 1976; Quentzel and Koepke, 1984; Rao et al. 1988; Higurashi and Nakajima, 1999). Presently, aerosol maps are derived routinely from NOAA/AVHRR data (Stowe et al., 1992; Husar et al., 1997), and improved characterization of the aerosols are or should be derived from new remote sensing instruments like OCTS (Ocean Color Temperature Scanner, Nakajima et al., 1999), SeaWiFS (Sea-viewing Wide Field-of-view Sensor, Gordon and Wang, 1994), POLDER (POLarization and Directionality of Earth's Reflectances, Deuzé et al. 1999), MISR (Multiangle Imaging Spectroradiometer, Kahn et al., 1998), or MODIS (Moderate Resolution Imaging Spectroradiometer, Tanré et al., 1997).

By contrast, the aerosol remote sensing over land surfaces, where the main aerosol sources are located, is much less advanced because of the difficulty to discriminate the aerosol contribution from the ground one in TOA (top of the atmosphere) measurements. The problem has been approached by different ways, for example from the reflectance of dark targets (Kaufman and Sendra, 1988), the adjacency effect of the aerosols (Kaufman and Joseph, 1982 ; Tanré et al., 1988), or their effect on the apparent temperature of desertic areas (Legrand et al., 1988). Recently, first monitoring of UV-absorbing aerosols, both over land and ocean, has been achieved by using the ultraviolet measurements of TOMS/Nimbus 7 (Herman J.R. et al., 1997 ; Torres et al., 1998). Here again, the new generation of remote sensing instruments should improve the characterization of the aerosols from dark dense vegetation reflectance (Kaufman et al., 1997a, b), multiangle imagery (Martonchik, 1997) or polarization measurements (Herman et al., 1997). Here we examine the capacity of directional polarization measurements, using the 8 month data acquired by POLDER aboard ADEOS 1. The remote sensing of aerosols is based on the polarized light that they backscatter, by expecting that correction in TOA measurements of the polarized light reflected by surfaces should be more tractable than correction of the total reflected light.

The wide field of view imaging spectroradiometer POLDER on ADEOS-1 provided, from November 1996 to the end of ADEOS, on June 1997, multispectral, multidirectional and polarized measurements of the Earth's reflectances. The wide field of view optics and the matrix array detector of POLDER provide bidimensional pictures of the Earth's surface that allow to observe every day every 6kmx7km ground pixel, from 13 different viewing geometries during the same orbit. A rotating filter wheel provides radiance measurements in 9 channels ranging from 443 to 910 nm. Moreover, the channels centered at 443, 670 and 865 nm, are equipped with polaroids which permits measurements of the polarization (Deschamps et al., 1994).

The aerosol retrieval from these measurements is detailed in Section 2. The polarized light scattered by the aerosols is firstly estimated by correcting the molecular and surface influences, which needs convenient modeling of the POLDER measurements and surface BPDF (Bidirectional Polarization Distribution Function). By processing multitemporal series of

POLDER data, Nadal and Bréon (1999) have developed BPDF models of the land surfaces which have been entered in the inversion scheme. Presently, the 443 nm data are not used. At this wavelength, the molecular contribution dominates largely the measurements so that, because of the uncertainty in the calibration factor of the blue channel, there is too little accuracy in the remaining aerosol contribution to use in an aerosol inversion scheme. Finally, comparison of the aerosol polarization measurements in the 670 and 865 nm channels with calculations for a set of aerosol models provides the optical thickness of the particles at the wavelength $\lambda_0=865$ nm, δ_0 , and their Ångström exponent, α , such that $\delta_1 = \delta_0 (\lambda_1 / \lambda_0)^{-\alpha}$ between wavelengths $\lambda_0=865$ nm and $\lambda_1=670$ nm.

The applicability of the method is examined in Section 3 and examples of level 2 aerosol products, α and δ_0 , over land are shown. Some large aerosol features are recognizable in daily maps of the retrieved optical thickness. Section 4 present comparisons of the POLDER results with correlative ground-based measurements. The retrieved parameters α and δ_0 are significant in the case of small aerosols, like biomass burning events, but are generally biased. Because polarized light is mainly sensitive to scattering by small particles and cannot detect coarser modes of aerosols, α and δ_0 are probably related to the small mode of particles, leading to an overestimation of the Ångström exponent and underestimation of the optical thickness in the case of bimodal size distribution of the particles. In a first approach it is proposed, in Section 5, to combine the two parameters into a simple aerosol index, $AI = \alpha\delta_0$, which should be almost the same when using for α and δ_0 either the biased parameters derived from polarization or those corresponding to the whole size distribution. This aerosol index makes possible to link the two different aerosol surveys performed by POLDER over land and over the ocean, and global maps of AI provide a new monitoring of the major aerosol sources over continental areas, including desertic particles.

2-AEROSOL RETRIEVAL FROM POLARIZED LIGHT

2-1- Scheme of the aerosol retrieval.

The principle of the method has been discussed previously (Herman et al., 1997). Ground-based measurements suggest that the polarized light reflected by ground targets is small and stable enough to allow correction in TOA measurements, and we assume that these surface BPDF have been determined. Then, the POLDER data can provide at several wavelengths λ , and for several scattering angles Θ , the polarized light scattered by the aerosols, that is about $\delta_a q_a(\Theta)$ where δ_a is the optical thickness of the aerosols and $q_a(\Theta)$ their polarized phase function, i.e.

$$q_a(\Theta) = p_a(\Theta)P_a(\Theta) \quad (1)$$

where $p_a(\Theta)$ is the phase function and $P_a(\Theta)$ the polarization ratio for single scattering of the aerosols. The derivation of $\delta_a q_a(\Theta)$ from the measurements is detailed in Section 2-2. We examine here how the aerosol retrieval may be achieved from $\delta_a q_a(\Theta)$, instead of $\delta_a p_a(\Theta)$ in the classical approach from total radiance measurements.

The inversion seems more delicate because the polarized phase function $q_a(\Theta)$ is more versatile than the normalized phase function $p_a(\Theta)$. Ground-based measurements, however,

suggest that at near infrared wavelengths ($\lambda = 850\text{nm}$ to $\lambda = 1650\text{nm}$) $q_a(\Theta)$ is reasonably definite for many terrestrial aerosols (Vermeulen et al., 1999). Figure 1 shows examples of $q_a(\Theta)$ functions measured from the ground for different kinds of aerosols. Most aerosols exhibit rather stable polarized phase functions, except desertic particles whose polarization is typically 5 to 10 times lower. The POLDER measurements over ocean now will allow to enlarge estimations of $q_a(\Theta)$ to a broader class of terrestrial aerosols. The present scheme is based on monomodal aerosol models whose polarization mimics the main behavior of the data set in Fig. 1. Log-normal size distributions have been retained (see Section 2-3), with fixed value of the standard deviation σ , and several values of the modal radius \bar{r} , and refractive index m , of the aerosols. Figure 2 shows examples of the resulting polarized phase functions, for $m=1.40$. They agree reasonably with observations.

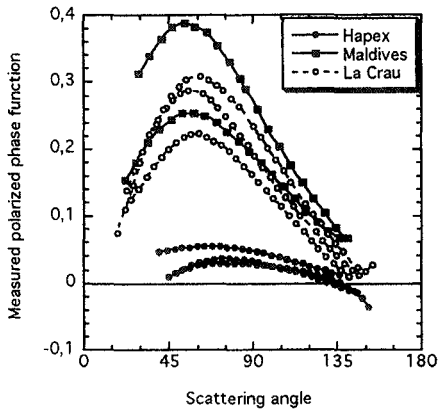


Figure 1

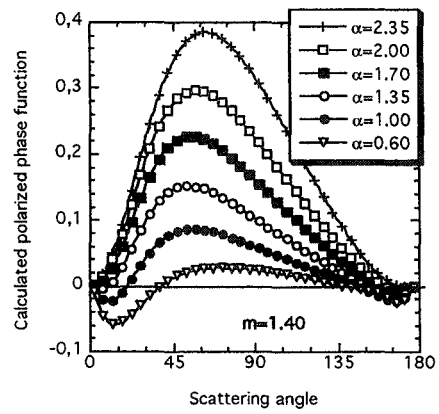


Figure 2

To select the best model from the measurements, one may look at the directional behavior of $q_a(\Theta)$ within the different viewing directions of POLDER, or/and to the spectral behavior of $\delta_a q_a(\Theta)$ in the 3 polarized channels. The interval of scattering angles varies from a few degrees to more than 80° depending on the target latitude and localization within the POLDER swath (Bréon et al., 1997). As explained previously, the present results are obtained by using only the 670 and 865 nm data. (The measurements at 443 nm are not retained because of the difficulty to perform correction of the large molecular contribution in this channel). In these conditions, Figs. 3 and 4 show that retrieval of the aerosol model is rather delicate.

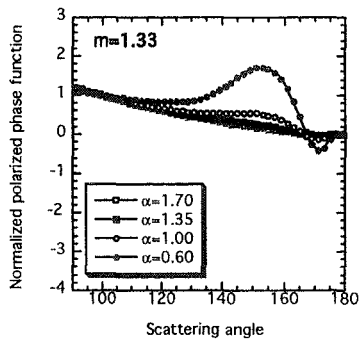


Figure 3a

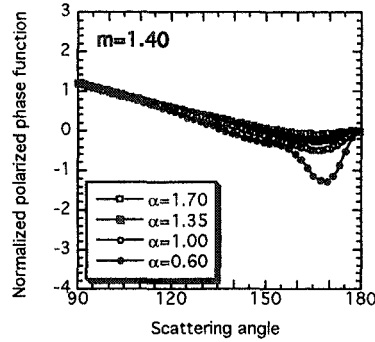


Figure 3b

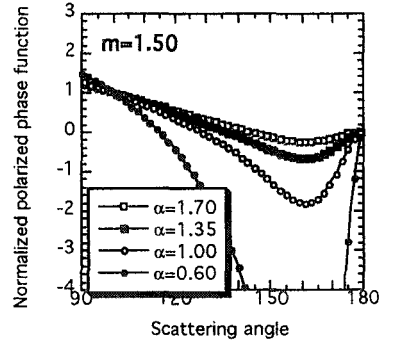


Figure 3c

For a few models, Figs. 3 shows how $q_a(\Theta)/q_a(100^\circ)$ varies according to the particle refractive index and Ångström exponent (or particle mean dimension). Except for large particles which exhibit characteristic polarization features in backscattering directions, the expected directional effects are quite small. Practically, for α larger than 1.35, the $q_a(\Theta)$ functions in Fig.3 differ only by a multiplicative factor.

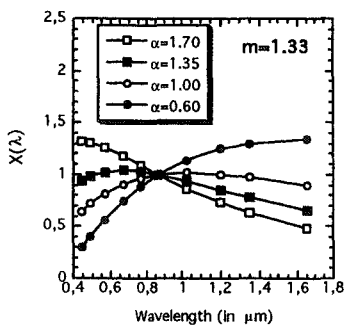


Figure 4a

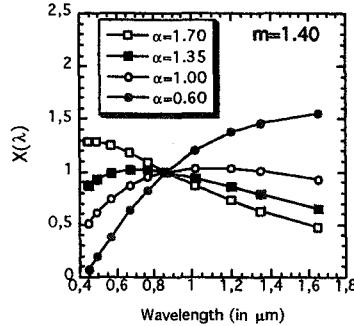


Figure 4b

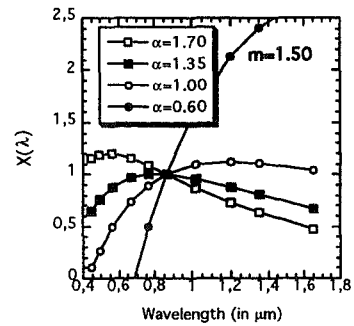


Figure 4c

On the other hand, for the same aerosol models, Figs. 4 show how the polarized light varies as a function of the observation wavelength. The spectral dependence of the polarized light is estimated here by

$$X(\lambda) = \delta_a(\lambda) q_a(\lambda, \Theta_0) / \delta_a(\lambda_0) q_a(\lambda_0, \Theta_0) \quad (2)$$

with $\Theta_0 = 100^\circ$ and $\lambda_0 = 850\text{nm}$. The spectral information is much more reliable than the directional one, although restricting to channels at 670 and 865 nm limits the sensitivity of the method.

2-2-Modeling of the measurements

We consider cloud free POLDER pixels, selected according to the cloud screening algorithm of Bréon and Colzy (1999). Preliminary correction of the influences of the gaseous absorption (Hagolle et al., 1999; Vesperini et al., 1999) and of the stratospheric aerosol contribution (Lafrance and Herman, 1998) is performed. To reduce the noise level, the aerosol algorithm is applied to 3x3 POLDER pixels (i.e. about 20 x 20 km areas). Moreover viewing directions corresponding to specular reflection within 3° are eliminated in order to avoid contamination by the sunglint from sub-pixel water surfaces (lakes, bogs...).

The partially polarized light at TOA is assumed to be linearly polarized, and the 3 measurements performed in a POLDER polarized channel are converted (Hagolle et al., 1996) into the Stokes' parameters (I_0, Q_0, U_0) with

$$I_0 = L, \quad Q_0 = L_p \cos(2\psi_0), \quad U_0 = L_p \sin(2\psi_0) \quad (3)$$

where L and L_p are the normalized radiance and polarized radiance, i.e. $L(L_p) = \pi L^*(L_p^*) / E$ where E is the solar irradiance at TOA and $L^*(L_p^*)$ the radiance (polarized radiance). Here, the Stokes' parameters are referred to axes linked to the meridian plane which contains the viewing direction ; in eq.(3), ψ_0 is therefore the angle between the polarisation direction and the meridian plane ($-\pi/2 < \psi_0 < +\pi/2$). The accuracy of the polarization measurements have been controled by using observations of the sunglint over the ocean (Toubb   et al., 1999) and is estimated as about ± 2 percent polarization (Hagolle et al., 1999).

Given the uncertainties, the measurements are modeled in a simplified way by considering only the polarized light corresponding to single scattering by aerosols, single scattering by molecules, and direct reflection on the surface. Because primary scattering largely dominates the polarized light this approximation is sufficient to take into account most of the polarized light in channels centered at 670 and 865 nm, where molecular scattering is small, and for aerosol optical thickness smaller than about 0.25 (Br  on et al., 1997, Lafrance 1997). Single scattering by molecules or disordered particles gives polarized light perpendicular or parallel to the scattering plane, which contains the solar and viewing directions. Similarly, BPDF are modeled by assuming that the polarized light comes from specular reflection on surface elements whose the normal bissects the solar and viewing directions. The resulting polarization, therefore, is perpendicular to the scattering plane also. Thus, by referring the Stokes' parameters to axes perpendicular and parallel to the scattering plane (i.e. with $\psi=0$ or $\pi/2$ for the angle between the polarisation direction and the normal to the scattering plane), each polarized term reduces into its Q parameter, $Q = L_p \cos(2\psi) = \pm L_p$, with

$$Q_a = \delta_a q_a(\Theta) / (4 \cos \theta_v), \quad (4a)$$

$$Q_m = \delta_m(z) q_m(\Theta) / (4 \cos \theta_v), \quad (4b)$$

$$Q_g = L_p^g. \quad (4c)$$

where θ_v (θ_s) is the zenith viewing (solar) angle and Ω the sun incident angle on the surface element (i.e. $(\pi - \Theta)/2$); the molecular polarized phase function, $q_m(\Theta)$, is positive while the aerosol polarized phase function, $q_a(\Theta)$, may be positive or negative for polarization direction respectively perpendicular or parallel to the scattering plane; the BPDF modeling gives L_p^g positive ; note that the molecular optical thickness, $\delta_m(z)$, is scaled according to the altitude of the target. Finally, the normalized polarized radiance at TOA, referred by this way, is written

$$Q_{cal} = Q_m + e^{-M\delta_m} (Q_a + e^{-M\beta\delta_a} Q_g) \quad (5)$$

where the exponential transmission terms account for the screening effects of the upper molecular layer and aerosol layer on the polarized light from lower layers ; β accounts for the large forward scattering of the aerosols which reduces their screening effect on the polarized light from the ground (Br  on et al., 1995; Lafrance, 1997). For typical surface BPDF and aerosol models, simulations of the TOA polarized radiance have been performed with vertical mixing of the molecules and aerosols. The aerosol and molecule number densities were given exponential profiles with respective scale heights 2km and 8km. The results show that, with $\beta \approx 0.50$, eq.(5) is accurate within about 0.0001 at 865nm and 0.0002 at 670 nm for aerosol

optical thickness smaller than 0.25 and viewing angles smaller than 60° (Lafrance, 1997).). The accuracy of eq.(5) decreases for larger aerosol optical thicknesses.

On the other hand, given (Q_0, U_0) and the observation geometry, the angle ψ_{meas} between the observed polarization direction and the normal to the scattering plane is evaluated. Of course, because of the multiple scattering, scattering/reflection processes, and measurement errors, ψ_{meas} is not exactly 0 or $\pi/2$. Numerical simulations, however, show that for the 865 and 670 nm wavelengths, ψ_{meas} should depart significantly from 0 or $\pi/2$ only when the polarized light is nearly null. To be consistent with the simplified modeling, given $L_p^{meas} = \sqrt{Q_0^2 + U_0^2}$ and ψ_{meas} , the measured Stokes' parameters referred to the scattering plane are approximated into the form

$$Q_{meas} = \varepsilon_{meas} \sqrt{Q_0^2 + U_0^2} \quad \begin{aligned} \varepsilon_{meas} &= +1 \text{ for } |\psi_{meas}| < 45^\circ \\ \varepsilon_{meas} &= -1 \text{ for } |\psi_{meas}| > 45^\circ \end{aligned} \quad (6)$$

Given L_p^g and the known molecular term, the algorithm consists finally in fitting Q_{meas} by adjusting the aerosol parameters in

$$Q_{meas} = \frac{\delta_m q_m}{4 \cos \theta_v} + e^{-M\delta_m} \left(\frac{\delta_a q_a}{4 \cos \theta_v} + e^{-M\beta\delta_a} L_p^g \right) \quad (7)$$

2-3-Aerosol inversion

Crude modelings only of surface BPDFs were known before the POLDER launch (Vanderbilt et al., 1990 ; Rondeaux and Herman, 1991; Bréon et al., 1995). From a preliminary analysis of time series measurements of the polarized radiance in the 865nm POLDER channel, Nadal and Bréon (1999) have developed improved BPDF models with L_p^g in the form

$$L_p^g = \alpha \cos \theta_s \{1 - \exp[\beta R_p(\Omega) / (\cos \theta_s + \cos \theta_v)]\} \quad (8)$$

where $R_p(\Omega)$ is the Fresnel reflection coefficient for polarized light, calculated for refractive index m=1.50. α and β are empiric coefficients adjusted for the different classes of land surface according to the main IGBP biotypes and the NDVI (Nadal and Bréon, 1999). Equation (8) gives values of L_p^g similar to the expected polarized radiance scattered by the aerosols, which explains why remote sensing of the aerosols in polarized light should be feasible. We assume that the polarized light reflected by surfaces is independent on the wavelength (Vanderbilt et al., 1990 ; Rondeaux and Herman, 1991; Bréon et al., 1995) and so the same BPDF is used in the 670 nm channel.

The aerosol modeling consists of tabulations of the $q_a(\lambda, \Theta)$ functions and scattering coefficient $s_a(\lambda)$ of the aerosols at 670 and 865 nm. We consider spherical non absorbing particles with monomodal size distributions in the form

$$\frac{dN(r)}{d \ln r} = \frac{1}{\sigma \sqrt{2\pi}} \exp \left[-\frac{1}{2} \left(\frac{\ln r - \ln \bar{r}}{\sigma} \right)^2 \right] \quad (9)$$

Following Shettle and Fenn (1979), a value of 0.864 is used for σ . Three values of the aerosol real refractive index are considered, $m = 1.33, 1.40$ and 1.50 , because of possible different behaviors of $q_a(\Theta)$ in backscattering directions depending on m (see Figs. 3). For each value of m , 12 values of \bar{r} are adjusted to provide Ångström exponents ranging from 0.30 to 2.50.

Given the $2N$ (2 wavelengths, N viewing directions) measurements, for each aerosol model the error

$$\eta = \sqrt{\frac{1}{2N} \sum_{\lambda_0, \lambda_1} \sum_j [Q_{cal}(\lambda, \Theta_j) - Q_{meas}(\lambda, \Theta_j)]^2} \quad (10)$$

is minimized by adjusting δ_0 . The retrieved aerosol parameters are the Ångström exponent α and optical thickness δ_0 corresponding to the model which gives the smallest residual error η . Examination of the measurements shows that we never observe the large polarization features corresponding to the rainbow of large particles, in Figs. 2 and 3, which could provide valuable information on the particle refractive index. Therefore, the refractive index corresponding to the selected model is not expected to be significant and will not be examined.

3-RESULTS

3-1-Preliminary qualitative results

The ability to control the land surface contribution from satellite is a key point of the method. A qualitative illustration of this problem is shown in Plate 1. For each ground pixel of a large geographic area, pictures A and B display the maximum and minimum values, over a 30 day period, of the polarized radiance measured in the 865 nm channel in the viewing direction corresponding to a constant scattering angle, $\Theta=120^\circ$. The measurements are corrected from the molecular term according to eq.(4b). By selecting constant Θ , thus constant Ω , variations of the surface BPDF should be minimized. Scattering angle $\Theta=120^\circ$ provides good repetitivity of the measurements at the considered latitudes and is far enough from the cloud rainbow direction (about 140° ; Goloub et al., 1994) to prevent contamination of the polarized light by residual liquid clouds.

Plate 1

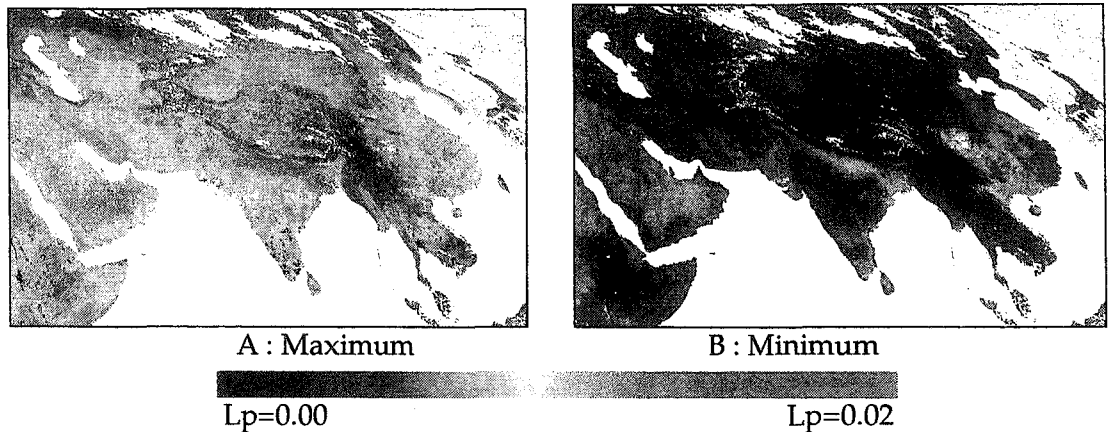
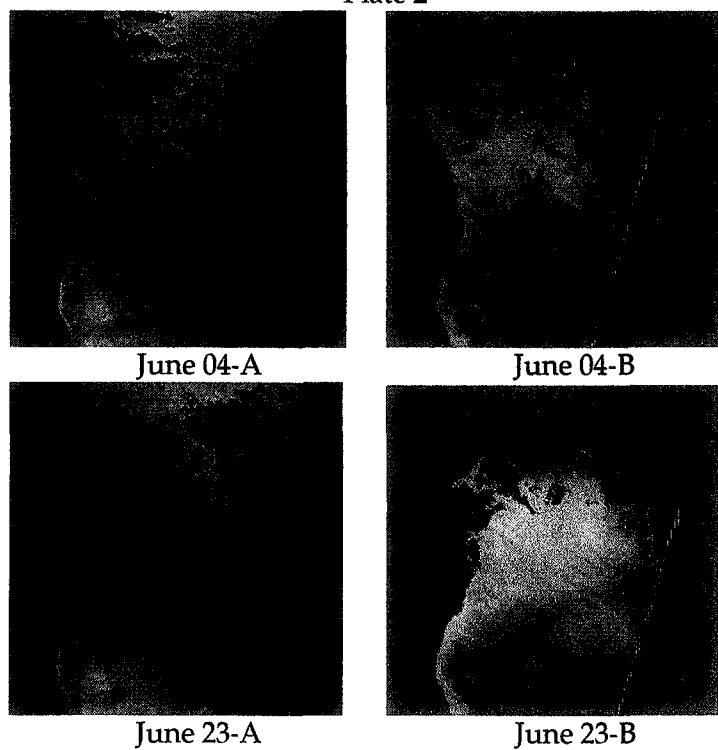


Plate 2



The noiseless behaviors of the pictures give confidence in the results and the mean levels are consistent with the expected orders of magnitude. In picture A, with $\delta_a \cong 4 \cos \theta_v L_p / q_a (120^\circ)$ and $q_a (120^\circ) \cong 0.06$ to 0.12 according to Fig. 1, the maximum values, $L_p \cong 0.0175$, correspond to $\delta_a \cong 0.35$ to 0.70. In picture B, minimum values ranging from $L_p \cong 0.002$ to 0.006 are consistent with previous ground-based measurements of vegetation and bare soil polarizations (Vanderbilt et al., 1990; Rondeaux and Herman, 1991; Bréon et al., 1995), and show that land surface polarization is generally no larger than the aerosol one. Moreover, the smoothness of the minimum picture confirms that land surface polarization exhibits lower spatial variability than land surface reflectance, which makes the correction of the measurements easier.

On the other hand, comparison of pictures A and B shows that very clear conditions probably never prevail over polluted areas like China or Ganga basin, which prevents estimation of the surface polarization by a simple minimum technique. The applicability of the method clearly needs some general modeling of the land surface BPDF according to the land surface geotype, as achieved in Nadal and Bréon (1999).

Another qualitative example is provided by Plate 2 which shows composites of POLDER pictures acquired over occidental south Africa on June 4 and June 23, 1997, respectively at the very beginning and at the height of the biomass burning activity as confirmed by the ATSR-2 fire products (Goloub and Arino, 1999).

The viewing direction selected for each pixel corresponds again to a constant scattering angle (here, $\Theta = 110^\circ$). Moreover, the two orbits differ from a few POLDER sub-cycles (about 4 days) so that the viewing geometries, and thus the surface contribution, should be nearly the same in the two pictures. For each day, images A and B display in true color the radiances and polarized radiances measured in the 3 channels. Because of the importance of the molecular polarization at 443 nm, the molecular contribution has been subtracted from the polarization data. Clearly, from June 4 to June 23, the large increase of the extended plume of biomass burning aerosols is more discernible in the polarized radiance picture than in the radiance one. Note that the yellow color of the polarized picture is a quite persistent feature which shows that most aerosols scatter less polarized light at short wavelengths.

3-2-Level 2 aerosol products

Let us first illustrate the algorithm functioning on typical measurements. Figure 5 shows the case of a pixel in the Ganga valley, near New Delhi. Rather than level 1 data (Q_0, U_0), Fig. 5 display the polarization angle and polarized radiance, (χ, L_p) as a function of the scattering angle. Figure 5a confirms that the polarization direction, as expected, is nearly orthogonal to the scattering plane except in backscattering directions where the polarized light becomes very small. In these directions, the aerosol single scattering contribution vanishes and multiple scattering processes make the polarization behavior more involved. In the present case, the aerosols exhibit probably negative polarization (parallel to the scattering plane) in a small angular range near $\Theta = 170^\circ$, but analysis of such effects is out the scope of our simplified treatment

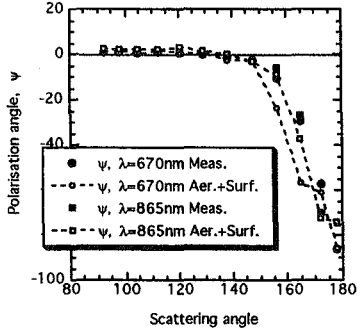


Figure 5a

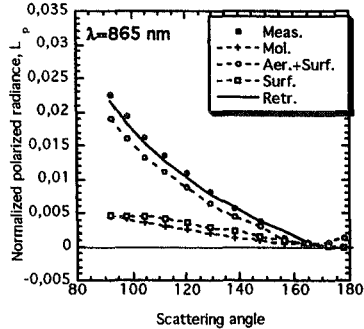


Figure 5b

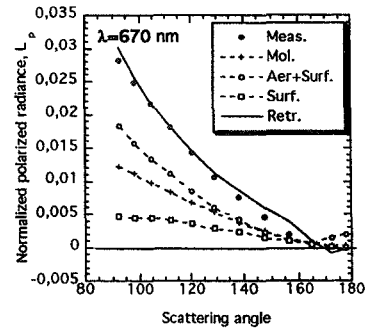


Figure 5c

Figures 5b and 5c show the normalized polarized radiances. Different labels indicate respectively the raw measurements ($L_p^{meas} = \sqrt{Q_0^2 + U_0^2}$), the molecular contribution ($L_p^m = Q_m$), the measurements corrected from the molecular effect ($(L_p^{meas} - L_p^m)e^{\delta_m M}$), the ground contribution (L_p^g), and the retrieved signal ($|Q_{cal}|$). The retrieved optical thickness here is $\delta_0 = 0.44$, with $\alpha = 1.38$. Over this highly polluted pixel the aerosol contribution is well above the molecular and ground ones and the inversion scheme allows to fit correctly the measurements.

Plate 3
India, Nov. 14, 1996

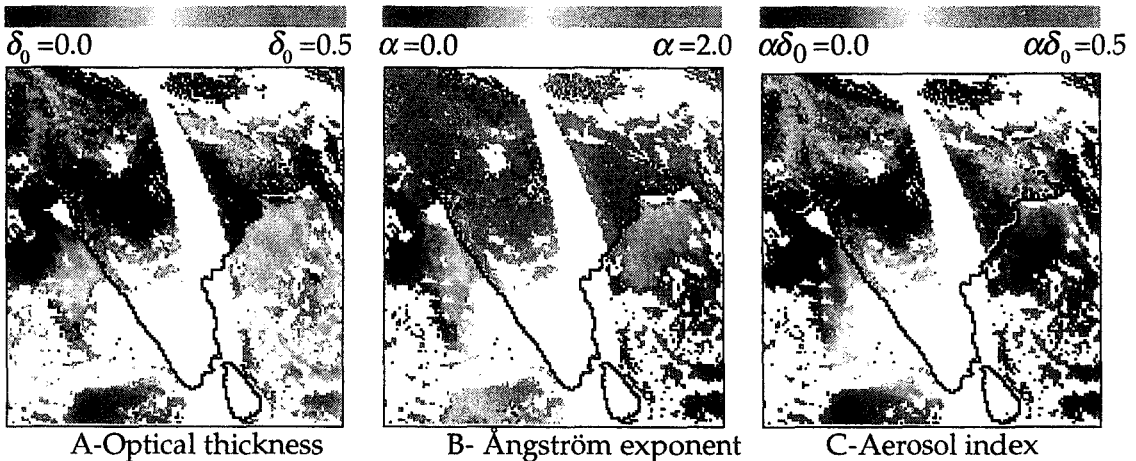
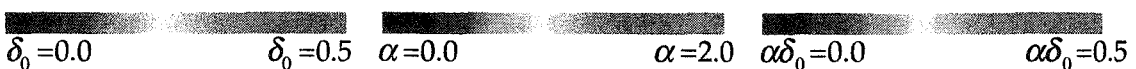
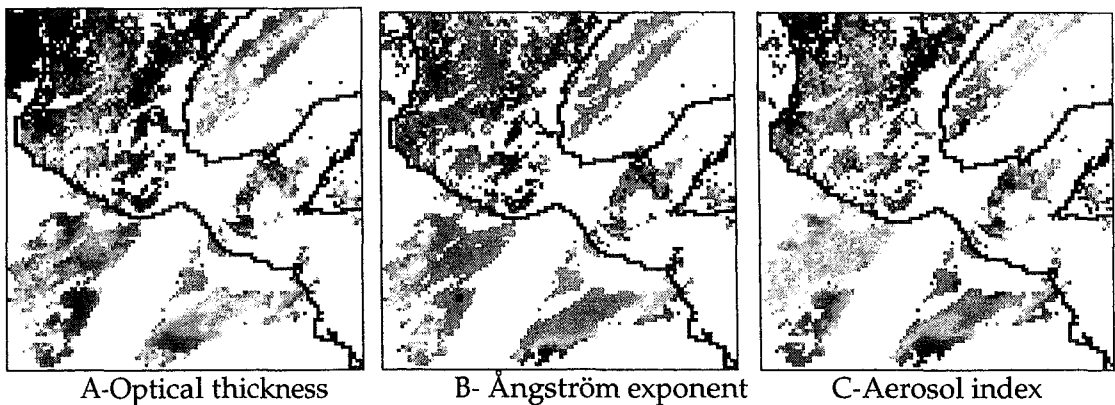


Plate 4
Mexico, May 27, 1997





Examples of global results derived by this way are shown in Plates 3 and 4 as maps of the retrieved aerosol optical thickness (picture A) and Ångström exponent (picture B). Plate 3 is for measurements over the whole Indian sub-continent on November 14, 1996 (2 consecutive orbits), Plate 4, for measurements over Mexico on May 27, 1997. For comparison, the results obtained over ocean by a very different way (Deuzé et al., 1999) are reported also. As these last results are derived from more confident radiance data and compare well with correlative ground-based measurements (Goloub et al., 1999), comparison allows an indirect validation of the land products.

The global distribution of the aerosol optical thickness over lands is not unrealistic. In Plate 3 for example, the known pollution prevailing within the Ganga basin contrasts with lower loading over the main Indian continent and the orders of magnitude of δ_0 and α are reasonable. In Plate 4, the large aerosol loading of small particles with large Ångström exponent is consistent with biomass burning activity in this region in May. However, while the results obtained over land and over the ocean are rather consistent in Plate 4, they differ markedly in Plate 3. Such discrepancy between the results of the two processing lines over coastlines is a common feature of similar comparisons. Except when the results over the ocean indicate very small particles with high Ångström exponent, the inversion scheme over land generally underestimates the optical thickness while it overestimates the Ångström exponent, which suggests some systematic bias in the aerosol products over lands.

4-COMPARISON WITH GROUND-BASED MEASUREMENTS

The reliability of the results has been assessed more directly from comparison with direct measurements of δ_0 and α achieved by ground-based Sun-photometers. Data obtained during the POLDER overpass, with clear sky conditions according to the POLDER cloud mask, have been selected in the data bank of AERONET (Aerosol RObotic NETwork, Holben et al., 1998) or provided independently by T. Nakajima, R. Santer and V. Soufflet. Table 1 lists the stations where these correlative measurements were performed. Note that a lot of data concern desertic sites.

The methodology of the comparison is explained in Goloub et al. (1999). Filtering of the sun-photometer data was performed in order to select measurements simultaneous to the satellite overpass within half an hour, corresponding to stable atmospheric conditions, specially controlled to prevent undetected sub-pixel clouds, and with large enough aerosol content ; only

observations with $\delta_0 > 0.05$ were retained. The POLDER results are averaged over a 100x100km² area around the ground station (average of 5x5 boxes of 3x3 pixel each).

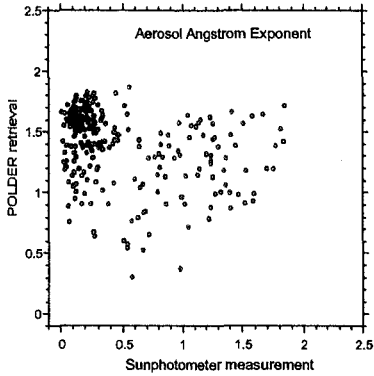


Figure 6

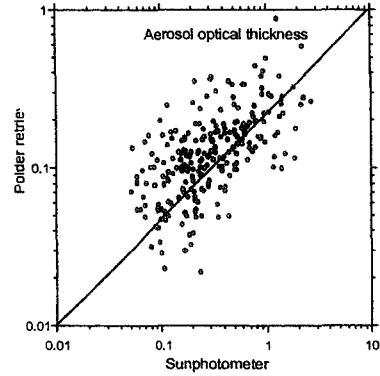


Figure 7

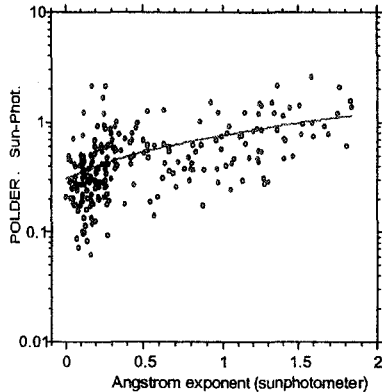


Figure 8

Comparison between the POLDER and Sun-photometer results is shown in Figs. 6 and 7, respectively, for α and δ_0 . Both results are extremely noisy as shown in Plates 3 and 4 by the very different qualities of the over land and over ocean products. This is not too surprising. The uncertainty on the surface contribution, typically $\Delta L_p^S \approx 0.001$ to 0.002 according to Nadal and Bréon (1999) is noticeable compared with the aerosol contribution, generally about $L_p^a \approx 0.010$. But the outstanding feature in Figs. 6 and 7 is the systematic bias in the α and δ_0 retrievals which confirms the previous results over coastlines. In most cases the retrieved Ångström exponent is overestimated while comparatively the aerosol optical thickness is underestimated. For all measurements, Fig. 8 shows how the optical thickness ratio $\delta_0^{POLDER} / \delta_0^{SUNPH}$ varies as a function of α . The linear fit is indicated. The aerosol optical thickness derived from POLDER is largely underestimated for large aerosols and tends progressively toward consistent figures for very small aerosols as outlined previously.

5-DISCUSSION - AEROSOL INDEX

5-1-Biases of the results and bimodality of the aerosols

Let us focus on the polarized light scattered in side-scattering directions, say in the range $80^\circ < \Theta < 120^\circ$, where polarization is large (see Figs. 5). Polarization features like the rainbow should deserve a specific study. In side-scattering directions, it is well known that the polarizing efficiency of scattering increases when the particle dimension decreases (Hansen and Travis, 1974) so that polarization measurements allow to detect only the small particles of the aerosol size distribution. Therefore, the bias in the optical thickness retrieval indicates that the implicit relationship between [large/non polarizing] and [small/polarizing] particles entailed by our aerosol modeling is wrong. Two simple possibilities can be examined in a first approach. A first obvious explanation is that some particles, because they are non-spherical, provide less polarized light than expected according to Mie theory, which should explain the underestimation of the optical thickness. Another simple possibility is that by assuming monomodal size distribution we underestimate the number of [large/non polarizing] particles linked to the [small/polarizing] ones. This defect may appear for pronounced bimodality of the size distribution and ground-based observations have shown that many aerosols exhibit significant bimodality (Shettle and Fenn, 1979; Nakajima et al., 1996 ; Remer and Kaufman, 1998).

Let us consider the POLDER observations over the ocean, which provide both the total and polarized light scattered by the aerosols. As explained in Deuzé et al. (1999b), these observations are also analyzed with monomodal aerosol models but the inversion starts with the total radiance in the 670 and 865nm channels. These theoretical monomodal models allow to fit the radiance and lead to values of δ_0 and α consistent with ground-based observations (Goloub et al., 1999), but they tend to underestimate the polarized light measured in side-scattering directions (Deuzé et al., 1999b). This trend is inconsistent with the hypothesis of non-polarizing particles but is very understandable in the presence of bimodal size distribution of the aerosols. Let us consider according to Remer and Kaufman (1998) a size distribution consisting of a small accumulation mode and a large coarse mode. Mie calculations show that the coarse mode gives negligible polarized light in the range $80^\circ < \Theta < 120^\circ$ while its contribution in the total light is noticeable. Then, as shown qualitatively in Fig.9a and confirmed by numerical simulations (Deuzé et al., 1999b), because the monomodal model has to take into account the contribution of the coarse mode in the total radiance, its adjustment is at the expense of the small particles which leads to underestimation of the polarized light. Conversely, we can understand that in the present algorithm where the monomodal model only accounts for polarized light, it adjusts on the accumulation mode as shown qualitatively in Fig. 9b, at the expense of the large particles and of their contribution in δ_0 and α , thus leading to larger α and smaller δ_0 .

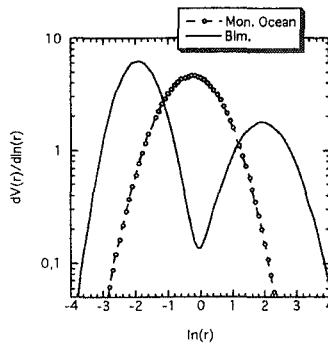


Figure 9a

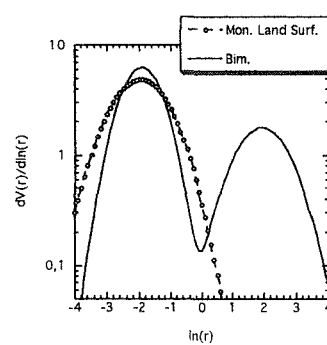


Figure 9b

5-2-Aerosol index

The discussion suggests that δ_0 and α derived from polarization are characteristics of the small mode of aerosols and correspond to the aerosol global properties only when the size distribution reduces to this mode. More precise assessment of the physical significance of δ_0 and α requires further analysis of the POLDER data but the previous analysis may be supported indirectly by examination of the reduced parameter

$$AI = \alpha\delta_0 \quad (11)$$

which, moreover, could provide a convenient aerosol indicator.

Let (α_A, δ_A) and (α_C, δ_C) stand for the parameters of the accumulation and coarse modes of a bimodal model respectively. According to the previous considerations, let us assume crudely that the coarse mode corresponds to $\alpha_C \approx 0$ and gives negligible polarized light, so that our inversion leads to (α_A, δ_A) . As the Ångström exponents are derived from nearby channels λ_0 and λ_1 , with $\delta_{\lambda_1} \approx \delta_{\lambda_0}(1 + \alpha\Delta\lambda/\bar{\lambda})$ the Ångström exponent of the bimodal model is approximately

$$\alpha = \frac{\delta_A\alpha_A + \delta_C\alpha_C}{\delta_A + \delta_C} = \frac{\delta_A\alpha_A + \delta_C\alpha_C}{\delta} \quad (12)$$

so that, with $\alpha_C = 0$

$$AI = \delta\alpha = \delta_A\alpha_A. \quad (13)$$

As shown in Appendix, the crude previous derivation may be supported by a more refined analysis. Therefore, equation (13) suggests that simple comparison of AI values based on the true aerosol parameters with AI estimates derived only from polarization measurements allows to check the «bimodal» explanation of the observed biases in δ_0 and α . If this explanation is correct, the aerosol index AI should provide partial characterization of the whole aerosol size distribution from data related only to the small polarizing particles.

5-3-Validation-Aerosol survey over lands and ocean

The δ_0 and α parameters reported in Figs. 6 and 7 have been combined according to eq.(11) in order to compare aerosol indices derived from direct Sun-photometer measurements with those derived from the correlative POLDER data. Figure 10 shows that the results are reasonably consistent and that the systematic biases in δ_0 and α are reduced in the resulting AI .

The same transformation has been applied to the aerosol parameters δ_0 and α reported in images A and B of Plates 3 and 4, and the resulting aerosol indices are reported in images C of the Plates. The systematic discrepancies between the POLDER aerosol results of the two independent processing lines disappear largely when expressed in terms of aerosol index.

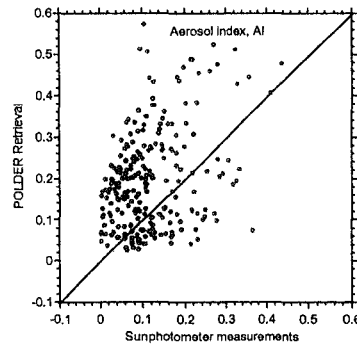


Figure 10

Therefore, these comparisons support the possibility of combining the present POLDER aerosol results over land in a single aerosol indicator, AI , which, despite providing only a reduced information about the particles, is related to the entire aerosol distribution.

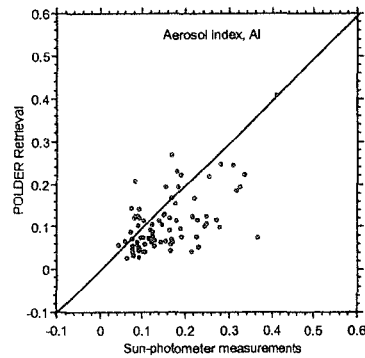


Figure 11a

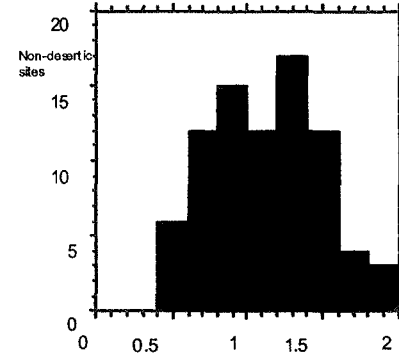


Figure 11b

It is worthwhile to examine the behavior of the AI for the particular case of desertic particles. These aerosols are known to consist partly of non-spherical and slightly polarizing particles, so that the ability of polarization measurements to detect this important component is questionable. The results of Fig. 10 have been dispatched in Figs. 11a and 12a according to the Ångström exponent of the particles. Figures 11a and 12a correspond, respectively, to $\alpha > 0.50$ and $\alpha < 0.50$ according to the ground-based values. Most values of $\alpha < 0.50$ correspond to the 3 African stations of AERONET and are very likely associated to large dust events as suggested by the histograms of the Angstrom exponent in Figs. 11b and 12b.

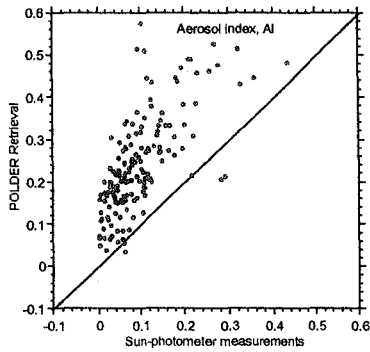


Figure 12a

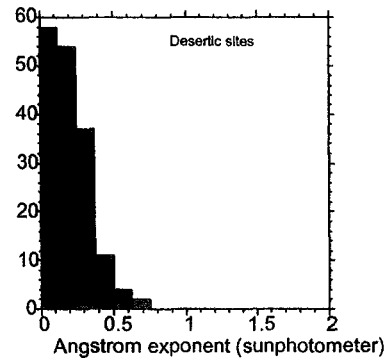
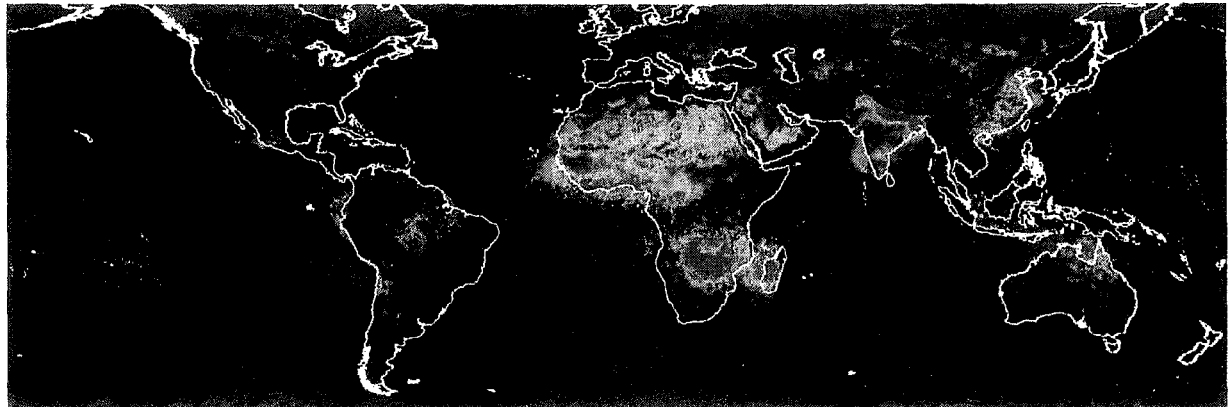


Figure 12b

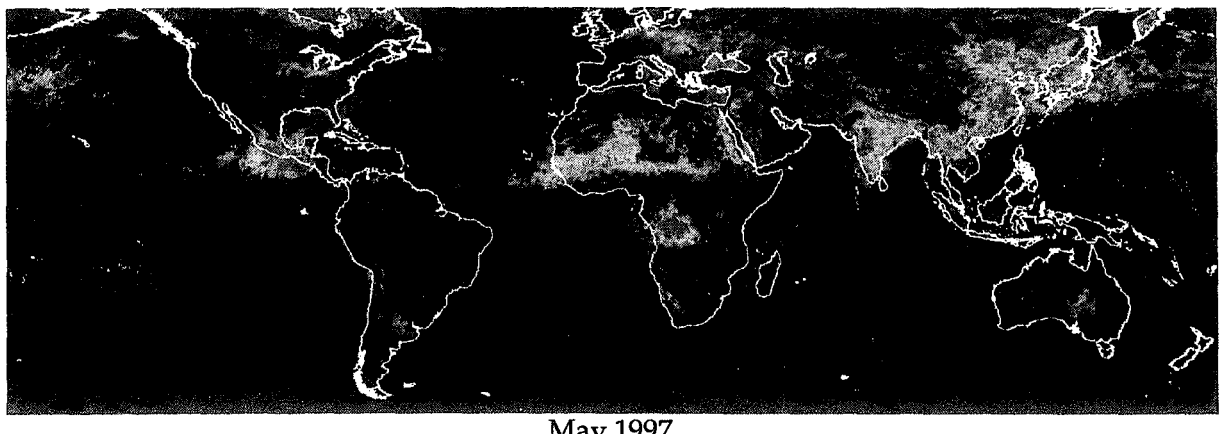
Strikingly, Fig. 12a shows that the aerosol index is sensitive to desertic particles, with a lot of events showing significant values of AI , larger than 0.05 to 0.10. Despite the systematic bias in Fig. 12a between the POLDER and Sun-photometer results, which may be indicative of the inadequacy of Mie theory for such particles, the aerosol index derived from polarized light allows qualitative detection of desertic particles.

Finally, Plate 5 shows global maps of the aerosol index derived from the two aerosol processing lines, over land and over ocean respectively. The results are average values of AI over one month, for November 1996 and May 1997. The consistency between the two kinds of results is impressive. More extensive and in depth analysis of these results should be developed in another paper, but Plate 5 shows that AI evidences some large and well known pollution sources over lands, such as the Indian continent, Sahara and China. Major areas of biomass burning activity are particularly well detected, over Madagascar and South Africa in November and over Mexico and China in May.

Plate 5



November 1996



$\alpha = 0.00$

$\alpha = 0.50$

A dedicated analysis of these specific aerosols (Goloub and Arino, 1999) highlights good correlation between times series of AI with fire occurrences derived from the ATSR infrared channels, which provides independent confirmation of the AI reliability. Moreover, the main geographical and seasonal aerosol features derived from the POLDER data over the oceans (Deuzé et al, 1999) are consistent with the properties of the aerosols derived previously from the NOAA/AVHRR data with respect to their mean content (Stowe et al., 1992; Husar et al., 1997) or size (Higurashi and Nakajima, 1999). Although a reduced information about the aerosols, AI appears as a powerful key to achieve an unified global survey of aerosols both over land and ocean.

6-CONCLUSION

Remote sensing of aerosol over land surfaces is examined by using the polarized light measured by POLDER at near infrared wavelengths, after due correction for the surface contribution. The polarized light scattered by the aerosols is analysed through monomodal models of spherical non absorbing particles to derive their Ångström exponent α , and optical thickness δ_0 .

Comparisons with in-situ measurements show that the retrieved parameters are meaningful for small aerosols, specially biomass burning aerosols, but otherwise are generally biased, with systematic overestimation of α and correlative underestimation of δ_0 . Since polarized light is mainly sensitive to scattering by small particles, the biases are probably linked to bimodality of the aerosol size distribution, with the retrieved parameters related to the smaller accumulation mode of particles.

POLDER measurements over ocean, which allow more in depth analysis, will be processed with a bimodal inversion scheme. Further examination of these improved results near coastlines should allow to assess more precisely the significance of the individual parameters α and δ_0 retrieved over land. In a first approach, an aerosol index $AI = \alpha\delta_0$ is proposed. It permits to link the POLDER aerosol surveys over land and over ocean so that global maps of AI allows some monitoring of the main aerosol sources over continental areas, including desertic particles.

Acknowledgments

Results presented in this paper were obtained using data from CNES's POLDER onboard NASDA's ADEOS. The authors would like to acknowledge A. Lifermann, the POLDER Project Scientist, for her constant support and helpful comments. The authors are grateful to Prof. T. Nakajima of the University of Tokyo, Japan, and to Prof. R. Santer and V. Soufflet for the Université du Littoral, France, who kindly provided ground-based measurements. This study was funded by the Centre National d'Etudes Spatiales (CNES), the Centre National de la Recherche Scientifique (CNRS), the Conseil Régional du Nord-Pas de Calais, the Fonds Européen de Développement Régional (FEDER) and the Délégation Régionale à la Recherche et à la Technologie du Nord-Pas de Calais. Informations on POLDER data can be found on the following web site:

<http://polder@www-projet.cnes.fr:8060>

Appendix

Equation (13) may be supported by a more refined analysis. In order to estimate more precisely how the present algorithm performs with bimodal aerosols, we have computed the Ångström exponents, α , and polarized phase functions, $q_a(\lambda, \Theta)$, for various monomodal and bimodal size distributions. Given the lack of directional information (see Figs.3), we have just calculated $q_a(\lambda)$ for the fixed scattering angle $\Theta = 100^\circ$.

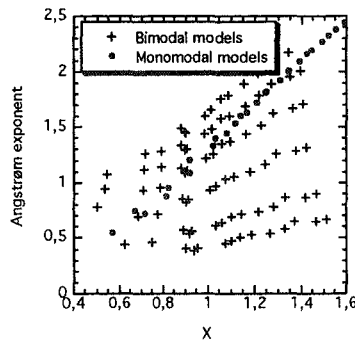


Figure A-1

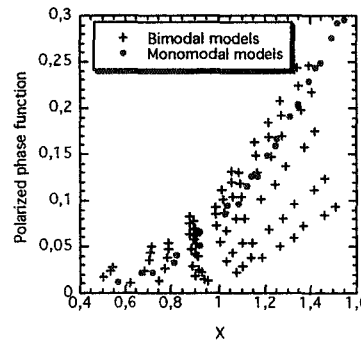


Figure A-2

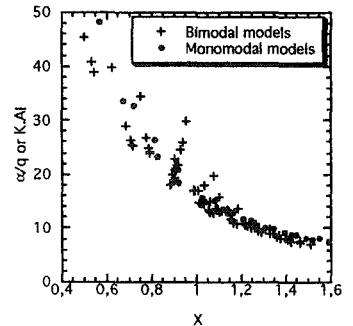


Figure A-3

Since the algorithm operates mainly with the ratio of polarized light

$$X = \frac{L_p^a(\lambda_1)}{L_p^a(\lambda_0)} = \frac{\delta_a(\lambda_1)q_a(\lambda_1)}{\delta_a(\lambda_0)q_a(\lambda_0)},$$

Figure A-1 firstly displays the relationship between X and α for monomodal and bimodal models respectively. According to Figure A-1, by fitting with a monomodal model the X ratio corresponding to bimodal aerosols will generally lead to overestimation of the Ångström exponent, which is the general trend of the present algorithm. Then, Fig. A-2 compares the relationship between X and $q_a(\lambda_0)$ for the two kinds of models. Figure A-2 shows that $q_a(\lambda_0)$ is generally smaller for bimodal than for monomodal models. Thus, given the polarized light $L_p^a(\lambda_0)$ scattered by bimodal aerosols, the optical thickness, $\delta_0 \approx L_p^a(\lambda_0)/q_a(\lambda_0)$, will be underestimated when assuming monomodal models. Finally, as $AI = \alpha\delta_0 \approx (\alpha/q(\lambda_0))L_p^a(\lambda_0)$, Fig. A-3 displays the direct relationships between X and $\alpha/q_a(\lambda_0)$ for monomodal and bimodal models. Figure A-3 confirms that, given X , the biases in α and δ_0 compensate partly in the product $\alpha\delta_0$ so that the aerosol index AI derived from the monomodal algorithm will not differ significantly from its true value.

REFERENCES

- Bréon F.M., D.Tanré, P.Lecomte P., M.Herman, Polarized reflectance of bare soils and vegetation; measurements and models. *IEEE Trans. Geosc. Remote Sens.*, 33, 2, 487-499, 1995.
- Bréon, F. M., J.L. Deuzé, D. Tanré, and M. Herman, Validation of spaceborne estimates of aerosol loading from Sun photometer measurements with emphasis on polarization, *J. Geophys. Res.* 102, D14, 17187-17195, 1997.
- Bréon,F.M., and S. Colzy, Cloud detection from the spaceborne POLDER instrument and validation against surface synoptic observations, *J. Appl. Met.*, 36, 777-785, 1999.
- Charlson, R. J., S. E. Schwartz, J. M. Hales, R. D. Cess, J. A. Coakley, J. E. Hansen and D. H. Hofmann, Climate forcing by anthropogenic aerosols, *Science* 255, 423-430, 1992.
- Deschamps, P.Y., F.M.Bréon, M.Leroy, A.Podaire, A.Bricaud, J.C.Buriez and G.Seze, The POLDER mission: instrument characteristics and scientific objectives, *IEEE Trans. Geosc. Remote Sensing*, 32, 598-615, 1994.
- Deuzé, J.L., M. Herman, P. Goloub, D. Tanré, and A. Marchand, Characterization of aerosols over ocean from POLDER-ADEOS-1. *Geophys. Res. Lett.*, 26, 1421-1425, 1999.
- Deuzé, J.L., P. Goloub, M. Herman, A. Marchand, G. Perry, S. Susanna, and D. Tanré, Estimate of the aerosol properties over the ocean with POLDER. Submitted to *Geophys. Res. Lett.*, 1999b.
- Fraser, R. S., Satellite measurement of mass of Sahara dust in the atmosphere, *Appl. Opt.*, 15, 2471-2479, 1976.
- Goloub P., J.L.Deuzé, M.Herman, Y.Fouquart, Analysis of the POLDER polarization measurements performed over cloud covers. *IEEE Trans. Geosc. Remote Sens.*, 32, 78-88, 1994.
- Goloub, P., D. Tanré, J. L. Deuzé, M. Herman, A. Marchand, and F.-M. Bréon, Validation of the first algorithm applied for deriving the aerosol properties over the ocean using the POLDER/ADEOS measurements, *IEEE Trans. Geosc. Remote Sens.*, 37, n°3, 1586-1596, 1999.
- Goloub, P., and O. Arino, Verification of the consistency of the POLDER aerosol index over land with ATSR-2/ERS-2 fire products, *accepted in GRL*, 1999.
- Gordon, H. R., and M.Wang, Retrieval of water-leaving radiance and aerosol optical thickness over the oceans with SeaWiFS: a preliminary algorithm, *Appl. Opt.*, 33, 443-452, 1994.
- Hagolle, O., A. Guerry, L. Cunin, B. Millet, J. Perbos, J. M. Laherrere, T. Bret-Dibah, and L. Poutier, POLDER level 1 processing algorithms, *SPIE Proc., Orlando*, Vol 2758, 308-319, 1996.
- Hagolle, O., P. Goloub, P. Y. Deschamps, H. Cosnefroy, X. Briottet, T. Bailleul, J. M. Nicolas, F. Parol, B. Lafrance, and M. Herman, Results of POLDER in-flight calibration, *IEEE Trans. Geosci. Remote Sens.*, 37, 1550-1566, 1999.
- Hansen, J. E., and Travis, Light scattering in planetary atmospheres, *Space Sci. Rev.*, 16, 527-610, 1974
- Hansen, J. E., and A. A. Lacis, Sun and dust versus greenhouse gases: an assessment of their relative roles in global climate change, *Nature*, 346, 713-719, 1990.
- Herman, J. R., P. K. Bhartia, O. Torres, C. Hsu, C. Seftor, and E. Celarier, Global distribution of UV-absorbing aerosols from Nimbus 7/TOMS data, *J. Geophys. Res.* 102, 16911-16922, 1997.
- Herman M., J.L. Deuzé, C. Devaux, P. Goloub, F.M. Bréon and D. Tanré, Remote sensing of aerosols over land surfaces including polarization measurements and application to POLDER measurements, *J. Geophys. Res.* 102, D14, 17039-17049, 1997.
- Higurashi, A., and T. Nakajima, Development of a two channel aerosol retrieval algorithm on global scale using NOAA/AVHRR, *J. Atmos. Sci.*, 56, 924-941, 1999.
- Holben, B. N., T. E. Eck, I. Slutsker, D. Tanré, J. P. Buis, A. Setzer, E. Vermote, J. A. Reagan, Y. F. Kaufman, T. Nakajima, F. Lavenu, I. Jankowiak, and A. Smirnov, AERONET-A federated

- instrument network and data archive for aerosol characterization, *Remote Sens. Environ.* 66, 1-16, 1998.
- Husar, R. B., J.M. Prospero, and L. L. Stowe, Characterization of tropospheric aerosols over the oceans with the NOAA advanced very high resolution radiometer optical thickness operational product, *J. Geophys. Res.*, 102, 16889-16909, 1997.
- Kahn, R., P. Banerjee, D. McDonald, and D. J. Diner, Sensitivity of multiangle imaging to aerosol optical depth and to pure-particle size distribution and composition over ocean, *J. Geophys. Res.*, 103, 32195-32213, 1998.
- Kaufman, Y. J. and J. H. Joseph, Determination of surface albedo and aerosol extinction characteristics from satellite imagery, *J. Geophys. Res.*, 87, 1287-1299, 1982.
- Kaufman, Y. J. and C. Sende, Algorithm for automatic atmospheric corrections to visible and near-IR satellite imagery, *Int. J. Remote Sens.*, 9, 1357-1381, 1988.
- Kaufman, Y. J., A. Wald, L. A. Remer, B. C. Gao, R. R. Li, and L. Flynn, Remote sensing of aerosol over the continents with the aid of a 2.2 μm channel, *IEEE Trans. Geosc. Remote Sens.*, 36, 1286-1298, 1997a.
- Kaufman, Y. J., D. Tanré, L. A. Remer, E. F. Vermote, A. Chu, and B. N. Holben, Operational remote sensing of tropospheric aerosol over land from EOS-Moderate Resolution Imaging Spectroradiometer, *J. Geophys. Res.*, 102, 17051-17067, 1997b.
- Lafrance, B., Modélisation simplifiée de la lumière polarisée émergeant de l'atmosphère. Correction de l'impact des aérosols stratosphériques sur les mesures de POLDER. *Thèse de Spécialité. Université des Sciences et Technologies de Lille*, 59655 Villeneuve d'Ascq, France, 1997
- Lafrance, B., and M. Herman, Correction of the stratospheric aerosol radiative influence in the POLDER measurements, *IEEE Trans. Geosci. Remote Sensing*, 36, 1599-1608, 1998.
- Legrand, M., M. Desbois, and K. Vovor, Satellite detection of Saharan dust : Optimized imaging during nighttime, *J. Climate*, 1, 256-264, 1988.
- Martonchik, J. V., Determination of aerosol optical depth and land surface directional reflectance using multiangle imagery, *J. Geophys. Res.* 102, 17015-17022, 1997.
- Nadal, F., and F. M. Bréon, Parameterization of surface polarized reflectance derived from POLDER spaceborne measurements, *IEEE Trans. Geosci. Remote Sens.*, 37, 1709-1718, 1999.
- Nakajima, T., G. Tonna, R. Rao, P. Boi, Y. Kaufman, and B. Holben, Use of sky brightness measurements from ground for remote sensing of particulate polydispersions, *App. Opt.*, 36, 15, 2672-2686, 1996.
- Nakajima, T., A. Higurashi, K. Aoki, T. Endoh, H. Fukushima, M. Toratani, Y. Mitomi, B. G. Mitchell and R. Frouin, Early phase analysis of OCTS radiance data for aerosol remote sensing, *IEEE Trans. Geosci. Remote Sensing*, 37, 3, 1575-1585, 1999.
- Nakajima, T., and A. Higurashi, A use of a two-channel radiances for an aerosol characterization from space, *Geophys. Res. Lett.*, 25, 29, 3815-3818, 1998.
- Quenzel, H., and P. Koepke, Tropospheric aerosol optical depth inverted from upwelling radiances. Aerosols and their climatic impact, *H. E. Gerber and A. Deepak, Eds., A. Deepak Publ.*, 227-240, 1984.
- Rao, C. R. N., L. L. Stowe, and E. P. McClain, Remote sensing of aerosols over the oceans using AVHRR data: Theory, practice, and applications, *Int. J. Remote Sens.*, 10, 743-749, 1989.
- Remer, L. A., and Y. J. Kaufman, Dynamic aerosol models : Urban industrial aerosols, *J. Geophys. Res.*, 103, 13859-13871, 1998.
- Rondeaux, G., and M. Herman, Polarization of light reflected by crop canopies, *Remote Sens. Environ.*, 38, 63-75, 1991.
- Shettle, E. P., and R. W. Fenn, Models for the aerosols of the lower atmosphere and the effect of humidity variations on their optical properties, *Air Force Geophysics Laboratory, Hanscomb AFB, MA 01731, AFGL-TR-79-0214*, 1979

- Stowe, L. L., R. M. Carey, and P. P. Pellegrino, Monitoring the Mt. Pinatubo aerosol layer with NOAA/AVHRR data, *Remote Sens. Environ.*, 60, 22-34, 1992.
- Tanré D., C.Devaux, M.Herman, R.Santer, J.Y.Gac, Radiative properties of desert aerosols by optical ground-based measurements at solar wavelengths. *J. Geophys. Res.*, 93, D11, 14223-14231, 1988.
- Tanré, D., Y. J. Kaufman, M. Herman, and S. Mattoo, Remote sensing of aerosol properties over the oceans using the MODIS/EOS spectral radiances, *J. Geophys. Res.*, 102, 16971-16988, 1997.
- Torres, O., P.K. Bhartia, J. R. Herman, Z. Ahmad, and J. Gleason, Derivation of aerosol properties from satellite measurements of backscattered ultraviolet radiation : theoretical basis, *J. Geophys. Res.*, 103, 17099-17110, 1998.**
- Toubbé B., T. Bailleul, J.L. Deuzé, P. Goloub, O. Hagolle, and M. Herman, In-flight calibration of the POLDER polarized channels using the sun's glitter. *IEEE Trans. Geosc. Remote Sens.*, 37 n°1, 513-525, 1999
- Vanderbilt, V. C., L. Grant and S.L. Ustin, Polarization of light by vegetation, In *Photon-Vegetation Interactions, Applications in Optical Remote Sensing and Plant Ecology*, R. Myneni and J. Ross, Editors, Springer Verlag, 1990.
- Vermeulen, A., C. Devaux, and M. Herman, Retrieval of the aerosol scattering characteristics from ground-based measurements; correction for the parasitic effects. Submitted to *IEEE Trans. Geosci. Remote Sens.*, 1999.
- Vespérini, M., F. M. Bréon, and D. Tanré, Atmospheric water vapor content from space-borne POLDER measurements, Submitted to *IEEE Trans. Geosci. Remote Sens.*, 1999.

Table 1 : List of the stations where the correlative aerosol measurements used for the POLDER validation have been performed, with the number of observations available according to the different filterings.

	<i>Site Name</i>	<i>Location</i>	<i>Number of filtered data</i>
North Europ/ France	Aire/ Adour	43.7°N, 0.2°E	24
North Europ / France	Lille	50.5°N, 3°E	5
North Europ/France	Wimereux	50.7°N, 1.6°E	30
Asia / Japan	Niigata	38°N, 139E	21
Africa / Senegal	Dakar	14.4° N, 16.9° W	40
Africa / Burkina Faso	Bidibahn	14°N, 0.5°W	27
Africa / Burkina Faso	Bondoukoui	11.8°N, 3.75°W	39
Africa / Niger	Banizoumbou	3.5°N, 2.6°E	57

Figure captions

Figure 1: Observed polarized phase functions $q_a(\Theta)$, for different kinds of aerosols as a function of the scattering angle Θ ; $q_a(\Theta)$ is derived from ground-based measurements of the polarized skylight at wavelength $\lambda = 865\text{nm}$ (Vermeulen et al., 1999). Results are shown for desertic dusts (Hapex campaign), aerosols from the Indian continent (Indoex campaign), and urban-industrial aerosols (La Crau campaign).

Figure 2: Calculated polarized phase functions $q_a(\Theta)$ at $\lambda = 865\text{nm}$ for the monomodal models used in the inversion scheme, according to the corresponding modal radius, \bar{r} , or the corresponding Ångström exponent, α . The assumed refractive index of the particles is $m=1.40$.

Figure 3a: Directional dependence of the polarized light. Behavior of $q_a(\Theta)/q_a(100^\circ)$ as a function of Θ for monomodal models with refractive index $m=1.33$. Large particles exhibit characteristic polarization features but for small particles ($\alpha > 1.35$) no information on \bar{r} and m (see Figs. 3b and 3c), hence on $q_a(\Theta)$, can be derived from the angular dependence of polarized light.

Figure 3b: Same as Fig.3a, but for particle refractive index $m=1.40$.

Figure 3c: Same as Fig.3a, but for particle refractive index $m=1.50$.

Figure 4a: Spectral dependence of the polarized light. Behavior of $(\delta_a q_a)_\lambda / (\delta_a q_a)_{\lambda_0}$ as a function of λ for the monomodal models of Fig.3a. The scattering angle is fixed ($\Theta=100^\circ$) and $\lambda_0 = 850\text{nm}$. The spectral behavior of polarized light is mainly linked to the behavior of $\delta_{a,\lambda} / \delta_{a,\lambda_0}$ and allows retrieval of the particle dimension or Ångström exponent.

Figure 4b: Same as Fig.4a, but for particle refractive index $m=1.40$.

Figure 4c: Same as Fig.4a, but for particle refractive index $m=1.50$.

Figure 5a: POLDER observations over a pixel in the Ganga basin, near New Delhi. Measurements and calculations of the angle between the polarization direction and the perpendicular to the scattering plane, ψ , as a function of the scattering angle corresponding to the viewing direction. Full dots and squares: measurements at 670 and 865 nm respectively. White dots and squares: calculations at 670 and 865 nm. The polarized vibration is perpendicular to the scattering plane, except in backward directions where multiple scattering and/or changes in the aerosol polarization direction make the polarization behavior more complex.

Figure 5b: As Fig.5a, but for the polarized light at wavelength $\lambda = 850\text{nm}$. Measurements (full dots) compare well with calculations for the retrieved aerosol model (full line). The surface and molecular contributions are indicated.

Figure 5c: As Fig.5b, but for wavelength $\lambda = 670\text{nm}$.

Figure 6: Comparison of the aerosol Ångström exponent derived from POLDER with that derived from Sun-photometer measurements. Polarized light leads quite systematically to overestimation of α .

Figure 7: As Fig.6, but for the aerosol optical thickness at 865 nm. Polarized light leads quite systematically to underestimation of δ_0 .

Figure 8: The ratio $\delta_0^{\text{Polder}} / \delta_0^{\text{Sun-Phot}}$ of the aerosol optical thicknesses derived from POLDER and Sun-photometers is reported as a function of the Ångström exponent of the particles. The solid line corresponds to linear regression. The POLDER results tend to consistent values for small particles with large Ångström exponent.

Figure 9a and 9b: In order to fit the radiance from bimodal aerosols, the monomodal model of the ocean processing line has to take into account the coarse mode of aerosols, at the expense of a lot of small polarizing particles (Fig. 9a). Inversely, in order to fit the polarized radiance, the monomodal model of the land surface processing line has mainly to take into account the accumulation mode of particles, at the expense of the large particles (Fig. 9b).

Figure 10: Comparison of the aerosol index, AI , derived from POLDER with that derived from Sun-photometer measurements. The biases in δ_0 and α derived from POLDER (see Figs. 6 and 7) are reduced in $AI = \alpha\delta_0$.

Figure 11a: As Fig.10, but the comparison between the POLDER and Sun-photometer AI is shown for the case of rather small particles; $\alpha > 0.50$ according to the ground-based values.

Figure 11b: Histogram of the Ångström exponent (from ground-based measurements) for observations reported in Fig.11a.

Figure 12a: As Fig.10, but the comparison between the POLDER and Sun-photometer AI is shown for the case of large particles; $\alpha < 0.50$ according to the ground-based values. Most results are from AERONET stations in Africa and correspond to saharan dusts. The POLDER AI estimates, while slightly overestimated, are significant which shows that detection of desertic particles from polarized light is possible.

Figure 12b: Histogram of the Ångström exponent (from ground-based measurements) for observations reported in Fig.12a.

Plate 1: For each ground pixel of the area, images A and B display the maximum and minimum value, respectively, of the polarized radiance L_p observed over a one month period with cloudless conditions. In order to minimize variations in surface reflection and air mass effects, L_p corresponds to a viewing direction providing constant scattering angle ($\Theta = 120^\circ$). Qualitatively, images A and B are expected to display the land surface and the largest aerosol contributions in polarized light. Image A confirms that the land surface contribution does not exhibit large spatial variability, and comparison with image B shows that the aerosol contribution may be well above the surface one.

Plate2: True color composites (443nm : blue ; 670nm : green ; 865nm :red) of POLDER pictures over occidental south Africa, on June 4, 1997 (upper) and June 23, 1997 lower), for radiance (images A) and polarized radiance (images B) ; polarized radiances are corrected for molecular scattering. The large plume of biomass burning aerosols, which appears on June 23, is more discernible in polarized light.

Plate 3: Aerosol parameters derived from POLDER. Comparison between the results over land, derived from polarized light (present paper), with the more confident results over ocean, derived principally from total light (Deuzé et al., 1999b). The observed area is over India; POLDER orbits 3161 and 3162 , on November 14, 1996. For each cloud free pixel, image A displays the retrieved optical thickness, δ_0 , image B, the retrieved Ångström exponent, α , and image C, the product $\delta_0\alpha$. The color codes are indicated; increasing values from blue to red. For these urban-industrial aerosols, the results over land and over ocean contrast over coastlines, indicating overestimation of α and underestimation of δ_0 over land. Image C indicates compensation of the biases in the aerosol index $AI = \delta_0\alpha$.

Plate 4: As Plate 3, but for an area over Mexico; POLDER orbits 8012 and 8013 on May 27, 1997. For these small biomass burning aerosols, the results agree reasonably on either sides of coastlines, indicating that POLDER results over land are consistent.

Plate 5: One month average values of the aerosol index, $AI = \delta_0\alpha$. Upper map: November 1996; lower: May 1997. While the POLDER aerosol processing lines over land and ocean lead to δ_0 and α results which may differ largely though coastlines, the aerosol index exhibits good continuity and allows to detect large pollution sources (Indian continent, China), areas of biomass burning activity (Madagascar and South Africa in November, Mexico in May), and saharan dusts.

Figure A-1: For monomodal and bimodal aerosol models, typical relationship between the Ångström exponent, α , and the ratio of polarized light, X (see text), which is the main information on the aerosols. Given X corresponding to bimodal aerosols, the estimate of α according to monomodal models leads generally to overestimation of α . Monomodal models: lognormal size distribution with the modal radius \bar{r} varied and standard deviation fixed ($\sigma=0.8735$). Bimodal models (adapted from Tanré et al, 1997): two lognormal size distributions with the percentages of the two modes varied; mode 1: different modal radius ($\bar{\eta}_1 = 0.050, (0.015), 0.11\mu m$), standard deviation fixed ($\sigma_1=0.6$); mode 2: modal radius and standard deviation fixed ($\bar{\eta}_2 = 1.0\mu m$, $\sigma_2=0.8$). For the two kinds of models : spherical non absorbing particles, with refractive index $m=1.33, 1.40$ and 1.50

Figure A-2: As Fig.10, but for the relationship between the aerosol polarized phase function, $q_a(\lambda_0)$, and X ; $q_a(\lambda_0)$ is calculated for 100° scattering angle. Given X corresponding to bimodal aerosols, the estimate of $q_a(\lambda_0)$ according to monomodal models leads generally to overestimation of $q_a(\lambda_0)$, therefore to underestimation of the optical thickness $\delta_0 \approx L_p^a(\lambda_0)/q_a(\lambda_0)$, where $L_p^a(\lambda_0)$ is the polarized light.

Figure A-3: As Fig.10, but for the relationship between X and $\alpha/q_a(\lambda_0)$, similar to the relationship between X and AI ($AI = \alpha\delta_0 \approx (\alpha/q(\lambda_0))L_p^a(\lambda_0)$). Given X for bimodal aerosols, the estimate of AI according to monomodal models does not differ largely from the true value.

Validation of POLDER aerosol index over land using ATSR-2 fires maps

Verification of the consistency of POLDER Aerosol Index over land with ATSR-2/ERS-2 fire product

Philippe Goloub

LOA, Université des Sciences et Technologies de Lille, Villeneuve d'Ascq, France

Olivier Arino

ESA/ESRIN, Remote Sensing Exploitation Department, Earth Observation Project and Engineering Division, 00044 Frascati, Italy

Abstract.

The remote sensing of aerosol over land remains a difficult task. Global distribution of polarizing aerosols (urban, industrial, smoke particles) are obtained, over land, from POLDER/ADEOS-1 visible and near-infrared measurements. In the paper, we study the correlation between POLDER aerosol index retrieved over land from polarimetric measurements and fire products derived from ATSR-2/ERS-2 3.7 μm channel. At global scale, fire patterns and aerosol index distributions agree well. A selection of 9 continental sites distributed in Africa, America and Asia have been studied. Monthly variations of aerosol index as well as fire occurrence are presented. A good correlation is observed, in traditional biomass burning regions, between aerosol index monthly average and fire count. These results clearly demonstrate POLDER capability to monitor biomass burning aerosol and also suggests polarizing aerosol presence in countries such as India or China.

Introduction

Aerosols have a large effect on the Earth Radiative Budget both directly through backscatter and absorption of solar radiation and indirectly by playing an important role in the formation of cloud condensation nuclei. Aerosols sources, transport in the atmosphere and sinks characterization are of interest for biogeochemical cycles studies and require global mapping of aerosol both over ocean and land. Although quantitative assessment is required, qualitative evidence of aerosol presence is the first step. Global monitoring of aerosol over land remains a challenge since aerosol contribution is generally smaller than the surface one. In this paper, we compare POLDER aerosol index [Deuzé *et al.*, (submitted to *J. Geophys. Res.*, 1999)] and ATSR-2 fire count [Arino *et al.*, 1995]. Examples of global aerosol index and fire maps are presented as well as preliminary analysis performed over $3^\circ \times 3^\circ$ zones selected in Africa,

Asia and America. This early approach is not actually a validation, since it is not a quantitative comparison. However, correlations observed over biomass burning regions show the consistency of the aerosol index over such regions.

POLDER Aerosol Index and ATSR fire detection

Aerosol Index over land.

Airborne POLDER experiments have shown previously polarization capability for aerosols monitoring over the continents [Herman *et al.*, 1997]. The principle of this approach is that the main contribution to the top of atmosphere polarized radiance is due to the atmosphere. Surface contribution to polarization is low but not negligible and parametrization of land surface polarization properties has been achieved by Nadal and Bréon, (1999) from analysis of two months of POLDER data. Basically, the algorithm makes use of 670 and 865 nm polarized channels. Corrections from surface and molecular contributions are then performed to extract aerosol spectral polarized contributions which are used to retrieve aerosol content and model [Leroy *et al.*, 1997]. Since the difference between the two spectral bands is weak, only an aerosol index which is nearly the optical thickness at 865 nm corresponding to a standard monomodal aerosol model with an Angstrom exponent $\alpha \approx 1$, is provided. This aerosol index must be interpreted as an indicator of polarizing aerosols. Some validations against sunphotometric data have been attempted, mainly in urban (European/North American) and desertic sites. Unfortunately, no data were available in biomass burning regions during ADEOS lifetime. However, limited in-situ sky-polarized radiances measurements have been performed, during SCAR-B experiment in Brazil in 1995 [Tanré, personal communication]. These data sets clearly indicated that smoke particles strongly polarize light.

Fire detection with ATSR-2/ERS-2.

To assess POLDER biomass burning aerosols detection capability, we can take advantage of global daily

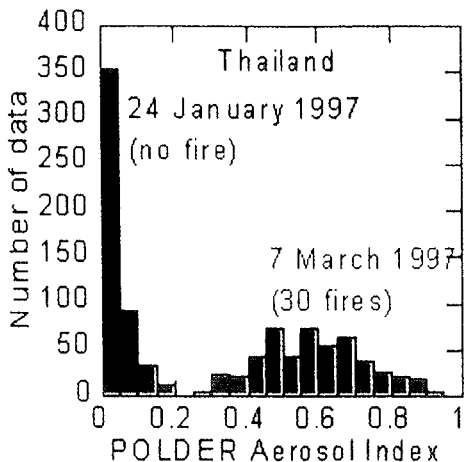


Figure 1. Histogram of POLDER Aerosol Index for 2 distinct days over Thailand region.

fire maps provided by ATSR-2. The nighttime (10pm) fire detection algorithm is based on ATSR-2 3.7 μm channel data. Spatial resolution of the sensor is 1km. A fixed threshold, 312K (sensor temperature saturation), on the 3.7 μm brightness temperature is used to flag high temperature surfaces indicating fire presence. The use of nighttime data prevents from sunlight reflection contamination but can bias the daily comparison with POLDER morning overpass (10.30am). Nighttime overpasses have been processed over land surfaces for the whole POLDER dataset.

Methodology, results and discussion

Methodology

Figure 1 shows aerosol index histograms over a $3^\circ \times 3^\circ$ zone selected in Thailand ($20^\circ\text{N}, 98^\circ\text{E}$) for two distinct days in term of aerosol content. We can clearly observe that high aerosol index ($\simeq 0.6$) is retrieved when fire activity is detected ($\simeq 30$ fires). On the contrary, aerosol index is almost one order of magnitude lower

when no fire is detected. However, comparison on such a daily basis is not suitable because of the differences between POLDER and ATSR overpass times (10.30am and 10pm respectively) as well as in swath width (2400km and 500km respectively) that can bias correlation between fire count and aerosol index. Hence, comparisons, limited to nine $3^\circ \times 3^\circ$ zones, are performed on a monthly average basis that should minimize the overpass time shift and difference in satellite swath width biases.

Results and Discussion

Comparison is, first, presented at the global scale (Figure 2). Global monthly aerosol index average as well as fire count maps are presented for March 1997. The main patterns consist in substantial amount of polarizing aerosols over India, Bengal, South East Asia, Sub-Saharan and China. Most of them are well correlated with fires occurrence, except, for example China exhibiting a large aerosol index without any fire detected by ATSR-2. This can be explained by fire associated to surface temperatures lower than 312K. Fuel wood use, coal burning, industrial pollution generate also large amount of aerosols in these regions but are not necessarily associated with detectable infrared emission. On the reverse, infrared emission of continuous oil-refinery activity around Persian Gulf is detected by ATSR. According to POLDER, this oil-refinery activity does not generate noticeable amount of polarizing aerosols. Moreover, frequent dust particles presence can yield complex aerosol mixing in this regions.

Low aerosol index as well as very limited fire activity are observed in Argentina and Brazil. In these regions the biomass burning period occurs later in July-September. In addition, one can note that in most places, a good ocean-land continuity is observed, which is an other indicator of coherence. Finally, some bias in the aerosol index retrieval are observed, mainly in Canada, Siberia and Himalayan regions that can be attributed to miss-detection of snow.

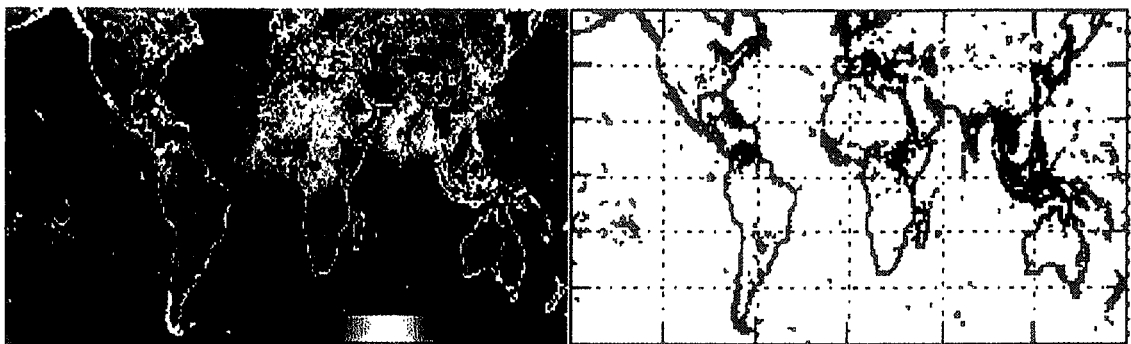


Figure 2. Global distribution of POLDER Aerosol Index (left) and ATSR-2 fire count (right) in March 1997. Aerosol index color scale ranges from 0 (in blue) to 0.5 (in red).

Let us, now, focus our comparisons on limited zones. In Figure 3, we present the monthly variation of aerosol index as well as fire count for 9 small zones in Africa, Asia and America.

(i) Savanna and forest burning in Guinea region ($10^{\circ}\text{N}, 11^{\circ}\text{W}$) reach their maximum in February, as reported by *Hao and Liu, (1994)*, and confirmed by fire counts derived from ATSR. This is consistent with POLDER aerosol index that exhibits a broad peak centered in February. Three other zones have been considered in the Southern Hemisphere. In Zaire ($7^{\circ}\text{S}, 24^{\circ}\text{E}$) maximum aerosol index observed in June is also consistent with fire occurrence. However, another peak occurs in February when fire count is close to zero. This interesting feature can be explained by transport of smoke particles coming from Sub Saharan regions that exhibit their maximum of burning activity in February as mentioned previously or by another local aerosol sources. Another good correlation is observed in November in

Zimbabwe ($18^{\circ}\text{S}, 29^{\circ}\text{E}$) and Madagascar ($17^{\circ}\text{S}, 47.5^{\circ}\text{E}$) where fire counts decrease and vanish within one month. Fire count is roughly the same for these two regions, however, the aerosol index is larger in Zimbabwe than in Madagascar, which can be explained by differences in fire efficiency and particles size. For both Zimbabwe and Madagascar, November corresponds to the end of the forest and savanna burning period *Hao and Liu, (1994)*.

(ii) In Asian zones, biomass burning peak period is March-April according to fire occurrence depicted in Figures 3 both for North East India (Orissa district, $20.5^{\circ}\text{N}, 84^{\circ}\text{E}$) and Thailand ($20^{\circ}\text{N}, 98^{\circ}\text{E}$). This fire activity are likely related to pre-monsoon agricultural burning. For these two regions fire count and aerosol index maxima are in phase. Magnitude of these maxima are roughly the same for Orissa district and Thailand though the fires occurrence is almost double for the latter. Interpretation relies upon fire efficiency, smoke par-

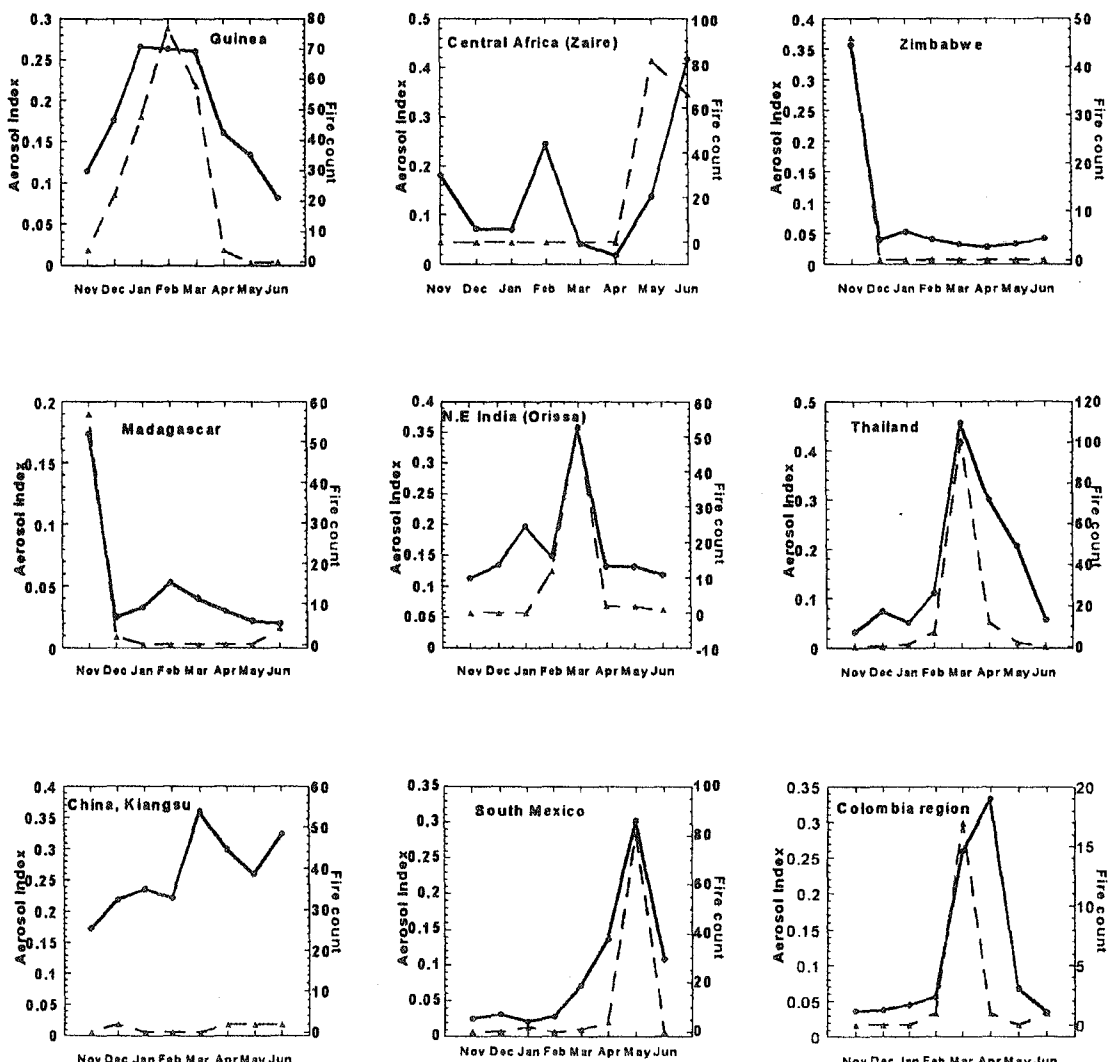


Figure 3. Monthly variations of POLDER Aerosol Index (solid line) and ATSR-2 fire count (dashed line) over 9 representative zones.

ticles size. One can also notes that background aerosol index (0.10-0.15) is larger over Orissa region. Continuous intensive use of fuel wood as well as increasing industrial pollution can explain this background aerosol component.

The last Asian zone studied is in China, more precisely in the Kiangsu district ($33^{\circ}\text{N}, 119.7^{\circ}\text{E}$), where increasing amount of aerosols is observed from November to June, with a maximum in March. However, surprisingly, no nighttime fire is detected. In this region, permanent polarizing aerosols emission is linked to large consumption of coal as well as fuel wood that generate undetectable surface heating with ATSR $3.7\ \mu\text{m}$ channel.

(iii) In Central America zone, located South of Mexico ($16.8^{\circ}\text{N}, 98.3^{\circ}\text{W}$), maximum of aerosol index occurs in May and is also clearly connected to the forest burning peak as indicated by fire count reaching also its maximum in May. Beside this noticeable period, fire count is close to zero in this area. The broader peak can be interpreted by the transport of smoke particles coming from neighboring regions where burning period is slightly shifted. The last zone studied in the American continent is in Colombia ($8.7^{\circ}\text{N}, 75.5^{\circ}\text{W}$), where, according to Hao and Liu (1994), forest and savanna burning season occurs in March-April. In this region again, a rather good correlation is observed between aerosol index and fire count.

Conclusions

Global scale comparison as well as local studies clearly indicate a good accordance between diurnal POLDER aerosol index and smoke particles presence traced by nighttime fire count derived from ATSR-2. Furthermore, the absence of correlation, for example in China, suggests the presence of other polarizing aerosols, originating from fuel wood use and industrial emissions, undetectable with ATSR $3.7\ \mu\text{m}$ channel detection. The main result of this study show that when fires occur in traditional biomass burning regions, then POLDER aerosol index is high. The improvement of the aerosol retrieval over land is currently under investigation. More-

over, missing in snow cover detection as well as overestimation for dust particles yield artificial high aerosol index in some regions.

Acknowledgments.

Aurélia Marchand, from LOA, is acknowledged for her help in processing part of the POLDER data and Jean-Michel Rosaz, from ESA/ESRIN for processing of ATSR fires atlas "<http://shark1.esrin.esa.it/ATLAS>". Results presented in this paper were obtained using data from CNES's POLDER onboard NASDA's ADEOS. More information on POLDER instrument and products can be found at URL:<http://polder@www-project.cnes.fr:8060/>".

References

- Arino O. and J.-M. Melinotte, Fire Index Atlas, Earth Observation Quarterly, 50, December 1995, edited by T.D. Guyenne, ESA Publications, 1995
- Hao, W. M., and M.-H. Liu. 1994. Spatial and Temporal Distribution of Tropical Biomass Burning. Global Biogeochemical Cycles, 8, pp.495-503.
- Herman, M., J.-L. Deuzé, C. Devaux, P. Goloub, F.-M. Bréon, and D. Tanré, Remote sensing of aerosols over land surfaces including polarization measurements and application to POLDER measurements, *J. Geophys. Res.*, 102, 17,039-17,049, 1997.
- Leroy M., J.L. Deuzé, F.M. Bréon, O. Hautecoeur, M. Herman, J.C. Buriez, D. Tanré, S. Bouffé, P. Chazette, J.L. Roujean, Retrieval of atmospheric properties and surface bidirectional reflectances over land from POLDER/ADEOS, *J. Geophys. Res.*, 102, 17,023-17,038, 1997.
- Nadal, F., F.-M. Bréon, Parameterization of Surface Polarized Reflectance Derived from POLDER Spaceborne Measurements, *IEEE Trans. Geosciences Remote Sensing*, Vol.37, No. 03, 1698-1709, 1999.
- Tanré D., personal communication., 1999.

P. Goloub, Laboratoire d'Optique Atmosphérique, U.F.R. de Physique, Université des Sciences et Technologies de Lille, 59655 Villeneuve d'Ascq Cedex, France. (e-mail: goloub@loa.univ-lille1.fr, olivier.arino@esrin.esa.it)

O. Arino,
ESA/ESRIN, Remote Sensing Exploitation Department, Earth Observation Project and Engineering Division, 00044 Frascati, Italy (e-mail: olivier.arino@esrin.esa.it)

(Received July 9, 1999; revised September 24, 1999; accepted December 7, 1999.)

**Global observation of aerosol sources and transport from POLDER on
ADEOS**

(submitted to Science, June 2000)

Global observation of anthropogenic aerosol sources and transport.

D. Tanré*, F.M. Bréon†, J.L. Deuze*, M. Herman*, P. Goloub*, F. Nadal†, A. Marchand*

* Laboratoire d'Optique Atmosphérique, CNRS, U.S.T. de Lille, 59655 - Villeneuve d'Ascq Cedex, France

† Laboratoire des Sciences du Climat et de l'Environnement, Commissariat à l'Energie Atomique, 91191 - Gif sur Yvette, France

This paper provides the first climatology of anthropogenic aerosol loading at the near global scale, both over land and oceanic surfaces. Our results indicate that biomass burning is the main source of small particles in the atmosphere and that, at the regional scale, other anthropogenic activity has a significant impact limited to China and India. Our aerosol index maps may be used to adjust the aerosol sources in atmospheric transport and climate models and to estimate the human impact on climate or in geochemical cycles.

Sources and transport of anthropogenic aerosols in the atmosphere are an essential component of the geochemical cycles¹, atmospheric chemistry² (both tropospheric and stratospheric) and in climate modelling³. The largest uncertainty of the anthropogenic radiative forcing⁴ on climate results from the impact of atmospheric aerosols both through direct and indirect effects⁵. There is a lack of measurements on the aerosol sources, their transport and their radiative properties. Global distribution of aerosol optical thickness is as yet limited to oceanic areas, with limited information on aerosol type⁶. Measurements in the ultraviolet spectrum by the Total Ozone Mapping Spectrometer (TOMS) instrument allow an estimate of aerosol loading both over land and oceans⁷. However, the derived aerosol index is very much function of the particle absorption and the altitude of the aerosol layer⁸. Although dust transport is well depicted from the TOMS data and some of the aerosol events due to biomass burning activities are detected, several regions which are known to be highly polluted do not show high aerosol indices⁹.

The POLDER instrument¹⁰ (POLarization and Directionnality of Earth's Reflectances) onboard the Advanced Earth Observing Satellite (ADEOS) provides a new opportunity to identify aerosol presence both over land and oceanic areas thank to its polarisation capabilities¹¹. Aerosol loading is retrieved using a new remote sensing technique based on the polarisation signature of scattered solar radiances and sensitive to the particles that are smaller than • 0.5µm. A rough identification of aerosol origin is obtained from the concomitant detection of fires from ATSR2/ERS2 (Along-Track Scanning Radiometer/ Earth Remote sensing Satellite) space-borne observations. The eight months of POLDER data, from November 1996 to June 1997, acquired before the failure of the ADEOS solar panel, have been processed to derive global maps of aerosol index which are used hereafter to discuss sources and transport of aerosol.

In this paper, our analysis is focused on aerosols of anthropogenic origins such as biomass burning and industrial emissions. These particles have a size distribution with a significant fraction in the accumulation mode (around a few tenths of microns) when dust generated by eolian friction presents generally much larger sizes.

Methods

Over land, the contribution of the surface to the top of atmosphere reflected radiance is generally much larger than that of the aerosol, which makes such measurements difficult to use for their monitoring. The polarisation capabilities of POLDER provide an attractive alternative since the polarisation of most aerosol types is much larger than that of natural land surfaces¹². The polarised radiance is mostly generated

by small particles. Therefore, the optical thickness derived from POLDER measurements over land is directly related to the accumulation mode of the aerosol loading. Inversion of optical thickness from polarised light measurements is based on a fixed aerosol model of small particles, similarly to algorithms widely used for the aerosol monitoring over the oceans from AVHRR or METEOSAT¹³. This model represents a typical accumulation mode size distribution with an effective radius of 0.18 μm and a refractive index of 1.4, resulting in an Ångström exponent of 1.4. These values are in good agreement with the urban¹⁴ and smoke¹⁵ aerosol models previously derived from sunphotometer measurements. The effective radius and the Angstrom exponent of the accumulation mode are respectively between 0.12 and 0.19 μm and between 0.8 and 1.5 for industrial regions, depending on the pollution level and around 0.18 μm and 1.6 for smoke aerosol produced by biomass burning activities.

Over oceanic areas, the directional and spectral signatures of the reflected radiances measured by the POLDER instrument allow the characterisation of the aerosol type and optical thickness¹⁶. The size of the particles is roughly quantified by the Ångström exponent α , which is close to 0 for large particles such as the coarse mode of dust, and close to 1 for the accumulation mode. Therefore, we compute an aerosol index, representative of small particle loading, as the product of the retrieved τ and α . This product yields small values in the presence of marine and dust type aerosols. Another advantage of this product for the analysis of aerosol transport over the oceans is the absence of cloud contamination (cloud contamination is mostly white), a problem apparent on most maps of aerosol load derived from optical remote sensing.

The inversion algorithm is clearly different over land and oceanic surfaces. As explained above, both methods aim at quantifying roughly the accumulation fraction of the aerosol loading, but the continuity of the index at the land/sea boundaries is not granted. Nevertheless, the analysis of global maps of the aerosol index indicates that such continuity is obtained in most regions. Therefore, although our index cannot be claimed as fully quantitative, the numerical values have similar meanings over land and ocean and can be used to estimate the strengths of the sources and the resulting transport over the oceans.

All cloud free POLDER observations have been processed. The eight monthly means have been computed with a spatial resolution of roughly 20 km, and binned at 0.5 degree resolution (Fig. 1). Although POLDER provides a daily monitoring of most of the Earth, cloud cover may strongly reduce the temporal coverage, in which case the monthly mean is based on a limited number of retrievals, representative of cloud free conditions only. Note that, such cloud free averages are those to be considered when computing the aerosol direct radiative effect. When no clear sky measurement was available during the month, the corresponding areas are shown in grey.

One identified shortcoming of our aerosol index is related to snow covered pixels. Snow generates more polarised light than vegetation that may be wrongly attributed to the presence of aerosol. Therefore, caution is necessary when interpreting POLDER aerosol index over area/month when snow may cover the surface.

Sources

Since smoke and urban/industrial aerosol models have optical properties that are not distinguishable from the POLDER data, it is difficult to identify the aerosol type from POLDER maps only. A fire atlas coupled with our aerosol index maps can partly remove the ambiguity since the smoke aerosols are obviously related to the presence of fires. We have reported also in Fig.1 the fire activity detected by the ATSR-2/ERS-2 instrument¹⁷ as white ellipsis. These ellipsis are centred on the barycentre of the fires located within the area, their orientation is adjusted on the main location of the fires and their surface is proportional to the total number of detected fires. An ellipse is shown if at least 50 fires have been detected during the month in the area of interest. In the tropical regions, there is a strong relationship between the aerosol index and the presence of fires. The largest aerosol indices are clearly related to biomass burning activity¹⁸. The synergy of the two satellite based products allow a rough identification of the aerosol sources.

signal observed from January through March over the Eastern Europe as well as over Canada, may result from pollution, but the index is here unreliable because the presence of snow contaminates the signal. This effect is difficult to correct for in the data processing.

Transport.

Over the oceans, aerosol loading as quantified by the POLDER aerosol index is clearly influenced by the sources described in the previous section. Significant values are observed downwind of the continents. Our results are analysed separately for the ocean basins.

Atlantic Ocean: The North Atlantic appears very clear during the winter. Starting in April and increasing towards June, the influence of North and Central America is apparent. In the Gulf of Mexico, a very strong loading is observed during April and May, in coincidence with the sources of biomass burning in Central America. The aerosol originating from Central and North America hardly never reach the European continent. Aerosol loading appears small in the Eastern part of the basin, a result of the dominant winds from the West. Tropical Atlantic is affected by both dust from Sahara and Sahel and biomass burning from Sahelian regions. The later is apparent in coincidence with the sources activity, i.e. in January and February. Note that the size distribution of the dust is shifted towards smaller particles during the transport. Therefore, our aerosol index, which is little sensitive to dust close to the sources, may be more sensitive, for a given mass load, after long range transport. Our results confirm that of other studies indicating that dust crosses the Atlantic and reaches the Caribbean and Brazil. On the other hand, the high aerosol contents observed in winter time offshore of West Africa, that are generally attributed to the presence of dust, are also clearly related to aerosol resulting from biomass burning. Our present study does not demonstrate that dust is not present at all, but indicates that smoke is a major contributor to the high aerosol loading in the area in winter. The main source of aerosol loading over the South Atlantic appears to be biomass burning in South and Central Africa. It is in coincidence with the sources discussed in the previous section. Note however that the transport is of shorter range than that of dust in the tropical North Atlantic. The November sources of Madagascar and Mozambique do not reach the Atlantic Ocean

Indian Ocean: The South Indian Ocean is not influenced by African sources, except in the immediate South and East vicinity of Madagascar in November. This absence of contamination results from the direction of the trade winds in this region that blow towards the continent. In the Eastern part of the Indian ocean, the influence of Australia is apparent in November, which corresponds to the end of the biomass burning season in the Northern part of this Island. North Indian Ocean and the Bay of Bengal are widely affected by the sources in India. This influence is maximal in March, large from November to May, and decreases in June, in conjunction with the monsoon.

Pacific Ocean: The open Pacific ocean appears mostly clear all year long. Nevertheless, three regions are affected by continental influence :

- (i) North of Australia and Southern Indonesia in November and June, which correspond to the months when the fire activity is maximum. In addition, a stable aerosol layer can be observed over the Eastern part of Indonesia, during the eight months which may reflect anthropogenic activity other than biomass burning.
- (ii) the oceanic regions surrounding Central America in May et April due to biomass burning. The oceanic area that borders the South Western part of Mexico is always affected by the presence of aerosol plume that can be attributed to pollution since no fire is reported in the vicinity
- (iii) The North Pacific, East of Asia. Long range aerosol transport affects the region from March to June. It even can reach the shores of North America in April and May.

Biomass Burning Aerosol:

The affected areas vary with the season, as it is clearly apparent, for example, over Africa: Madagascar and Tanzania show large values in November. Then, from December to February, the largest aerosol index values are found in Western Africa, North of the equator. In May and June, the maximum has moved south of the equator. These temporal evolutions are consistent with the fire product as well as previous observations of biomass burning activity¹⁹. During July to September, a period with no POLDER measurements, the potential area of biomass burning activity in Africa shifts from West to East, South of the equator. The fires observed in Libya as well as around the Persian Gulf are due to oil industry and do not result in large smoke emissions.

In Central America, a strong signal is apparent in April and May, whereas it is one month earlier in the Northern part of South America. The strongest period of biomass activity in South America occurs during late August and September²⁰, which are months missing from our dataset. Nevertheless, one can depict some activity in November and December in North Brazil, again consistent with the period of activity in this region¹³.

Biomass burning also occurs in south-east Asia and Eastern India in early spring with a maximum in March, which is clearly apparent on the aerosol index maps. In April, May and June, there are large aerosol indices over China and the south-western part of the Japan Islands. Previous observations²¹ show that yellow sand coming from the Eastern Asian desert can affect the region at that time of the year. However, several factors²² indicate that dust is not a major contributor to the large aerosol index values observed over this region: (i) dust is composed of large non spherical particles that have little effect on the polarisation, and therefore on the POLDER aerosol index; and (ii) off the coast of East Asia, the Angstrom coefficient measured by POLDER indicates the presence of anthropogenic aerosol rather than dust particles. The TOMS aerosol index, which is sensitive to dust, indicates also rather small, if any, aerosol loading in this region. The aerosol index may result from a mixing between urban/industrial aerosols and smoke but we can argue that the large aerosol index values over East Asia should be attributed, in a large extend to aerosol of anthropogenic origin¹¹.

In Northern Australia, smoke aerosols are present in November and December. For the other months, the smoke emission is low compared to that of other regions and do not result in large aerosol index values.

Urban/Industrial Aerosol:

The strongest signal that can be attributed to pollution is observed over the Ganges valley, from November until February with a maximum in December and January. In spring, the pollution is less severe because of the scavenging by monsoon rain but some aerosol traces can still be observed all year long. In March, the aerosol loading results from a mixing of both aerosol types. In June, the aerosol index is strong again, with no detected fire, which indicates a pollution origin. Over the Eastern part of China, in February and March, our measurements indicate a high load of urban/industrial aerosol, since the fire activity is limited, although a contribution of smoke aerosol cannot be totally ruled out. In April, the aerosol loading is shifted northwards and, according to the prevailing wind in the area, results from the fires depicted from ATSR data.

The Western part of North America does not show any significant aerosol loading during our eight months of measurements. A small signal can be observed on the Eastern part in June but much weaker than over the Asia continent. Again, due to the unexpected failure of ADEOS, the July and August months are missing in our data set when the pollution level is expected to be maximal in this region. Central Europe is also affected by pollution events with a maximum in April and May. The large aerosol

Conclusion and final comments

At the global scale, it appears that biomass burning activity is the major source of anthropogenic aerosols. At the regional scale, pollution aerosol type appears significant in China and India and, at a lower level, over Central Europe, the northern part of Central America and Eastern United States. These conclusions are based on eight months of measurements that exclude the summer period when pollution may become more significant in Eastern United States and Western Europe. Besides, our study does not quantify the possible anthropogenic fraction of dust load.

Our study brings a very innovative aerosol data set. The aerosol index derived from POLDER measurements provides a sound description of the global aerosol load needed in aerosol sources and transport models. The monthly maps can be also used to assess the radiative impact of aerosol at the global scale.

Acknowledgments. The results presented in this paper were obtained using data from POLDER onboard ADEOS; the instrument was developed by the Centre National d'Etudes Spatiales (CNES), the French Space Agency, and the platform by NASDA, the Japanese Space Agency. The fire index is based on the ATSR-2/ERS-2 data managed by the European Space Agency (ESA). The authors would like to acknowledge Anne Lifermann, the POLDER project scientist for her constant support and the ESA for providing the ATSR World Fire Atlas. This study was funded by the Centre National d'Etudes Spatiales (CNES) and the Centre National de la Recherche Scientifique (CNRS). Information on POLDER data can be found on the following web site: <http://earth-sciences.cnes.fr:8060/polder>. More information on the fire Atlas can be found on the following web site: http://shark1.esrin.esa.it/ATLAS_ATSR.

Correspondence and requests for materials should be addressed to D. Tanré (e-mail: tanre@loa.univ-lille1.fr)

Figure 1: Maps of the monthly mean aerosol index derived from POLDER space-borne measurements. Grey pixels over land indicate areas where permanent cloud cover prevented an estimate of the aerosol parameters. The fire activity is reported by the use of white ellipsis. They are centred on the barycentre of the fires located within the area, their orientation is adjusted on the main location of the fires and their size is related to the total number of fires and their spatial extension. An ellipsis is drawn when more than 50 fires have been detected during the month.

¹ Langner, J., Rodhe, H., Crutzen, P.J., Zimmermann, P., Anthropogenic influence on the distribution of tropospheric sulfate aerosols, *Nature*, **359**, 712-715, (1992).

² Andreae, M.O., Crutzen, P.J., Atmospheric aerosols: biogeochemical sources and role in atmospheric chemistry, *Science* , **276**, 1052-1058, (1997).

³ Kiehl, J.T., Briegleb, B.P., The relative roles of sulfate aerosols and greenhouse gases in climate forcing, *Science*, **260**, 311-314, (1993).

⁴ Charlson, R.J., Schwartz, S.E., Hales, J.M., Cess, R.D., Coackley, Jr., J.A., Hansen, J.E., Hofman, D.J., Climate forcing by anthropogenic aerosols, *Science*, **255**, 423-430, (1992).

⁵ *IPCC Science of Climate Change*, Eds J.T. Houghton et al., Cambridge University Press, UK, (1996).

⁶ Husar, R.B., Prospero, J., Stowe, L.L., Characterization of tropospheric aerosols over the ocean with the NOAA/AVHRR optical thickness operational product, *J. Geophys. Res.*, **102**, 16889-16909, (1997).

⁷ Herman, J.R., Bhartia, P.K., Torres, O., Hsu, C., Seftor, C., Seralier, E., Global distribution of UV-absorbing aerosols from Nimbus 7/TOMS data, *J. Geophys. Res.*, **102**, 16911-16922, (1997).

⁸ Torres, O., Bhartia, P.K., Herman, J., Ahmad, Z., Gleason, J., Determination of aerosol properties from satellite measurements of backscattered ultraviolet radiation: theoretical basis, *J. Geophys. Res.*, **103**, 17099-17110, (1998).

⁹ Chiapello, I., Goloub, P., Tanré, D., Herman, J., Torres, O., Marchand, A., Aerosol detection by TOMS and POLDER over oceanic regions, *J. Geophys. Res.*, **in press**, (2000).

¹⁰ Deschamps, P.Y, Bréon, F.M., Leroy, M., Podaire, A., Bricaud, A., Buriez, J.C., Sèze, G., The POLDER mission: instrument characteristics and scientific objectives, *IEEE Transactions on Geoscience and Remote Sensing*, **32**, 598-615, (1994).

¹¹ Deuzé, J.L., Bréon, F.M., Devaux, C., Goloub, P., Herman, M., Lafrance, B., Maignan, F., Marchand, A., Perry, G., Tanré, D., Remote Sensing of aerosols over land surfaces from POLDER/ADEOS-1 polarized measurements, *J. Geophys. Res.*, **submitted**, (2000).

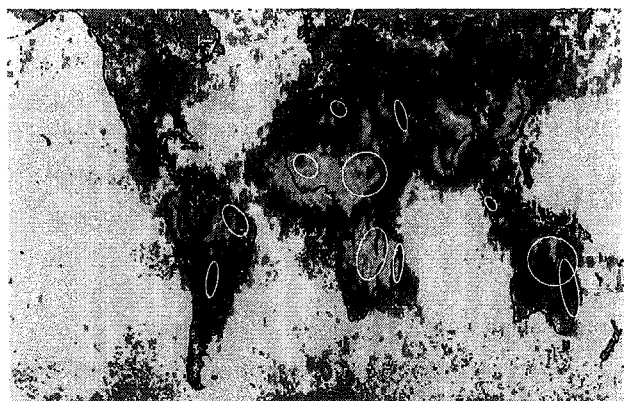
¹² Herman, M., Deuzé, J.L., Devaux, C., Goloub, P., Bréon, F.M., Tanré, D., Remote sensing of aerosols over land surfaces including polarization measurements and applications to POLDER measurements, *J. Geophys. Res.*, **102**, 17039-17050, (1997).

¹³ Moulin, C., Dulac, F., Lambert, C.E., Chazette, P., Jankowiak, I., Chatenet, B., Lavenu, F., Long-term daily monitoring of Saharan dust load over ocean using Meteosat ISCCP-B2 data, *J. Geophys. Res.*, **102**, 16959-16970, (1997).

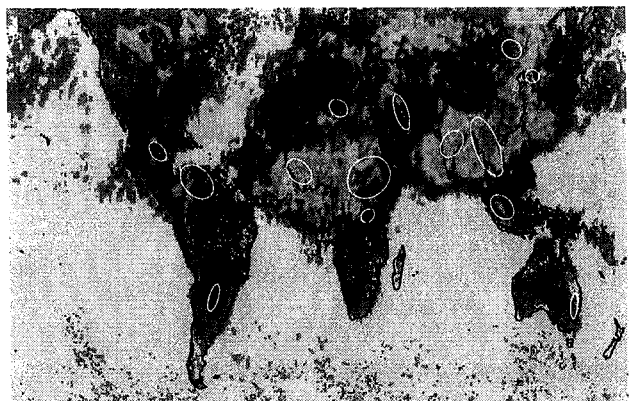
¹⁴ Remer, L.A., Kaufman, Y.J., Dynamic aerosol model: urban/industrial aerosol, *J. Geophys. Res.*, **103**, 13859-13871, (1998).

-
- ¹⁵ Remer, L.A., Kaufman, Y.J., Holben, B.N., Thompson, A.M., McNamara, D., Biomass burning aerosol size distribution and modeled optical properties, *J. Geophys. Res.*, **103**, 31879-31891, (1998).
- ¹⁶ Deuzé, J.L., Herman, M., Goloub, P., Tanré, D., Marchand, A., Characterization of aerosols over ocean from POLDER/ADEOS-1, *Geophys. Res. Lett.*, **26**, 1421-1424, (1999).
- ¹⁷ Arino, O., Melinotte, J.M., Fire Index Atlas, *Earth Observation Quarterly*, **50**, ESA publications, T.D Guyenne eds., (1995).
- ¹⁸ Goloub, P., Arino, O., Verification of the consistency of the POLDER aerosol index over land with ATSR-2/ERS-2 fires count, *Geophys. Res. Lett.*, **in press**, (2000).
- ¹⁹ Hao, W.M., Liu, M.-H., Spatial and temporal distribution of tropical biomass burning, *Global Biochemical Cycles*, **8**, 495-503, (1994).
- ²⁰ Kaufman Y.J. et al., Smoke, clouds, and radiation-brazil (SCAR-B) experiment, *J. Geophys. Res.*, **103**, 31783-31808, (1998).
- ²¹ Tanaka, M., Nakajima, T., Shiobara, M., Yamano, M., Arao, K., Aerosol optical characteristics in the yellow sand events observed in may, 1982 at Nagasaki – Part I Observations, *J. Meteor. Soc. Japan*, **67**, 267-278, (1989).
- ²² Nakajima, T., Tanaka, M., Shiobara, M. Yamano, M., Arao, K., Nakanishi, Y., Aerosol optical characteristics in the yellow sand events observed in may, 1982 at Nagasaki – Part II Models, *J. Meteor. Soc. Japan*, **67**, 279-291, (1989).

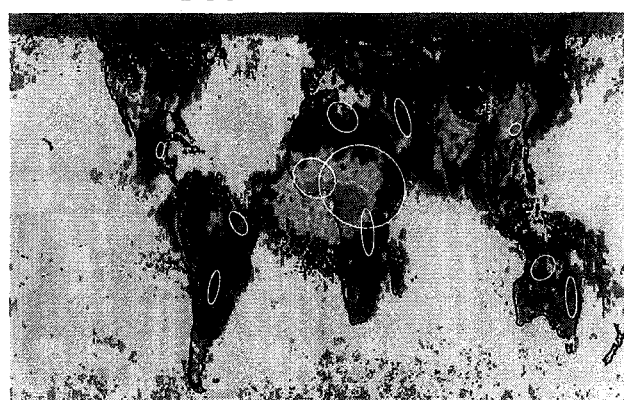
November 1996



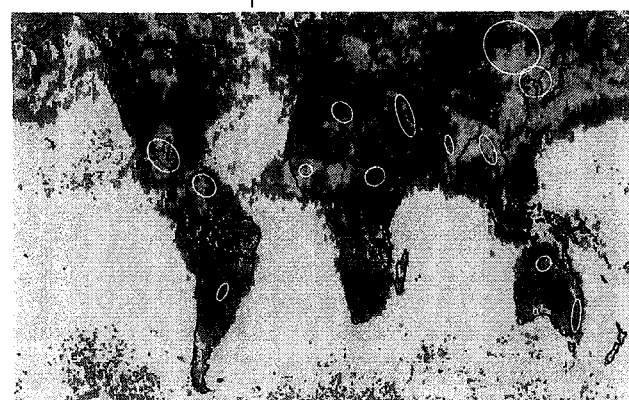
March 1997



December 1996



April 1997



January 1997



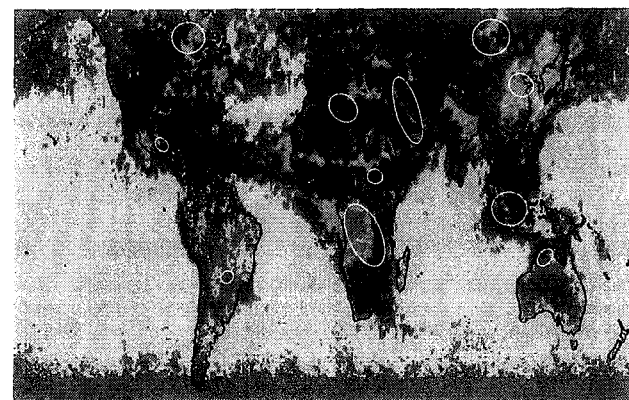
May 1997



February 1997



June 1997



0.00 0.05 0.10 0.15 0.20 0.25 0.30 0.35

Chapitre 5

Conclusions et perspectives

Conclusions et perspectives.

Depuis plus d'une dizaine d'années, le laboratoire est fortement impliqué dans l'expérience POLDER. En dépit de la durée limitée de la mission, des données d'une grande richesse ont pu être acquises. Aujourd'hui, même si l'ensemble des données n'a pas encore été analysé en détail, les résultats obtenus indiquent que le bilan de cette expérience est très positif. Après une phase de mise en route difficile, du fait de la nouveauté de l'instrument et des problèmes à résoudre tant sur le plan technique, algorithmique, que scientifique, plusieurs résultats originaux ont été obtenus.

Ma contribution à l'expérience a essentiellement porté sur « l'aspect » polarisation de cette expérience. Dans un premier temps, j'ai travaillé sur la version aéroportée de l'instrument et participé à l'élaboration de techniques d'étalonnage en vol. Ensuite, je me suis impliqué dans l'analyse des observations relatives aux nuages et aux aérosols. Les résultats obtenus ont permis des avancés sensibles dans la connaissance de leurs certaines propriétés optiques et microphysiques.

La phase thermodynamique des nuages (liquide ou glace) au sens de POLDER, c'est-à-dire déterminée indépendamment de la température ou de toute mesure infrarouge, constitue un produit original, validé à l'aide de lidars et radar au sol ainsi qu'à l'aide de données synoptiques. La limite intrinsèque de la détection de phase apparaît dans les systèmes nuageux multicouches pour lesquels le nuage de glace coiffant l'ensemble des nuages bas et moyens est très fin. L'autre limitation est due à la qualité de la détection nuageuse, notamment au-dessus des continents, que l'on peut obtenir à l'aide d'imageurs tels que POLDER ne fonctionnant que dans le visible et le proche infrarouge.

La caractérisation des propriétés microphysiques des nuages de glace (forme de cristaux) présentée dans ce document pourra, à l'avenir, être affinée. Depuis la publication de ces premiers résultats, la détection nuageuse et la détection de phase ont été nettement améliorées. De plus, les progrès récents dans la modélisation des propriétés optiques de cristaux, notamment en polarisation, devraient permettre d'introduire des modèles de cristaux plus réalistes (Labonne et al., 2000).

Si l'on considère les particules aérosols au-dessus des océans, les mesures directionnelle et polarisée réalisées à 0.670 et 0.865 μm permettent de caractériser plus finement les aérosols. L'utilisation initiale de modèles granulométriques d'aérosols à un seul mode a permis, dans certaines situations, d'interpréter correctement les observations. Néanmoins, la validation photométrique a montré les limites de ce type de modèle. La sous-estimation du coefficient d'Angström constatée avec les modèles de type mono-mode est due à une sous-estimation du nombre des petites particules. Dans la gamme d'angle de diffusion utilisée (80°-120°), la polarisation des modèles à un mode est inférieure à celle qui est mesurée, ce qui traduit la sous-estimation du nombre de petites particules par les modèles.

L'introduction de modèles bimodaux (modes d'accumulation et grossier) avec, pour le gros mode, la prise en compte de particules non sphériques devrait permettre d'améliorer l'interprétation des mesures de luminances et de polarisation.

Au niveau des continents, l'index aérosol POLDER, même s'il n'est qu'un produit préliminaire correspondant à la fraction de l'épaisseur optique associée au petit mode, permet de repérer depuis l'espace certaines sources d'aérosols (anthropique et les feux de biomasse). L'apport de l'indice aérosol pour la mise en évidence des aérosols de pollution est indéniable, comme le montre les premiers résultats obtenus sur l'Inde. Cependant, peu de mesures optiques sont disponibles dans cette région du monde et, par conséquent, il apparaît nécessaire de caractériser les aérosols sur le sous-continent indien en préparant une campagne de caractérisation optique des aérosols dans la vallée du Gange.

Le travail de validation ainsi que l'analyse des produits POLDER réalisés à ce jour ont fait apparaître certaines limitations du concept POLDER et suggèrent des pistes pour l'avenir.

(i) Au-dessus des continents, des limitations apparaissent très clairement dans la détection des aérosols. La première est liée à la contribution du sol, la seconde aux bandes spectrales polarisées trop proches pour rendre compte correctement des propriétés spectrales des aérosols. Il semble aujourd'hui nécessaire d'étendre les mesures de polarisation vers l'infrarouge moyen, c'est-à-dire jusqu'à $2.2\text{ }\mu\text{m}$. A cette longueur d'onde, l'atmosphère devient transparente ce qui permettra de mesurer la polarisation intrinsèque de la surface et de la corriger instantanément aux longueurs d'onde plus courtes, obtenant ainsi beaucoup plus précisément qu'avec POLDER-1, la polarisation de l'atmosphère de 0.490 à $1.6\text{ }\mu\text{m}$. La réalisation de l'instrument « microPOL », version unidirectionnelle de POLDER, mais étendue jusqu'à $2.2\text{ }\mu\text{m}$ est en cours. Des campagnes aéroportées légères ont déjà été réalisées sur une version prototype étendue jusqu'à $1.6\mu\text{m}$ et nous permettent de caractériser spectralement la polarisation des surfaces afin de vérifier leur neutralité du visible à $2.2\mu\text{m}$, neutralité qui est fondamentale pour éliminer très précisément la contribution du sol dans l'inversion des aérosols sur terre.

(ii) Pour l'étude des nuages, la présence de canaux polarisés supplémentaires entre $0.865\text{ }\mu\text{m}$ et $2.2\text{ }\mu\text{m}$ permettrait, d'une part d'améliorer la détection de phase, notamment pour les nuages bas dans certaines conditions de visée pour lesquelles la contribution moléculaire peut biaiser la détection et, d'autre part, de contraindre davantage les procédures de restitutions des propriétés microphysiques (taille des gouttes, dimension et forme de particules de glace) en utilisant la réflectance et la polarisation directionnelle.

Les confrontations, réalisées dans ce travail, entre les mesures et/ou les produits provenant de différents instruments en orbite, POLDER, TOMS et ATSR-2 pour l'étude des aérosols, ou au sol (réseau de lidars, radar, photomètres), démontrent l'intérêt de développer de telles synergies pour mieux discerner les différentes facettes des objets que nous observons. Très récemment, la combinaison de la phase POLDER et des résultats des classifications nuageuses déduites des canaux infrarouges d'ATSR-2 a permis de préciser certaines limites de ce type de classification et de mettre en évidence la relation entre la température et la phase (Giraud et al., 2000, soumis), confirmant les résultats obtenus, localement, en combinant les mesures de POLDER, d'un radar et de radiosondages.

Vers 2004, de nombreux instruments complémentaires d'observation de l'atmosphère seront en orbite et, pour certains comme PARASOL, PICASSO-CENA, MODIS-Aqua et CLOUDSAT, sur des orbites très proches. Ce regroupement de moyens d'observations spatiaux sera unique. Par ailleurs, les réseaux sol de photomètres (AERONET) et de lidars (EARLINET) devraient, alors, être pleinement opérationnels. Ce jeu de données unique permettra de réaliser des comparaisons, de nombreuses mesures et produits satellitaux. Les profils verticaux de dépolarisation fournis par le lidar spatial donneront accès à la forme des

particules nuageuses ou aérosols. Dans le cas des nuages, il sera très intéressant de comparer la forme des diffusants au sommet des nuages avec le produit phase déduit par différentes méthodes (infrarouge multispectrale, polarisation proche infrarouge). Il en sera de même pour les propriétés microphysiques des nuages de glace. La combinaison de la phase POLDER et de la température radiative déduite des mesures infrarouges de MODIS ou IIR permettra d'approfondir les résultats obtenus avec ATSR-2.

En situation de ciel clair, la dépolarisation lidar sera également très utile en fournissant un indicateur de la sphéricité des aérosols. Cette information sur la forme des particules aérosols aidera à l'interprétation des mesures satellitaires comme dans le cas des aérosols désertiques par exemple. D'autre part, les profils d'extinction obtenus à 0.532 et 1.064 µm donneront accès à l'épaisseur optique intégrée sur la colonne atmosphérique ainsi qu'à la répartition verticale du coefficient d'Angström, tous deux utilisables pour la validation des produits aérosols POLDER ou MODIS, sur terre comme sur mer. Une expérience préparatoire (SHADE) devrait se dérouler en septembre 2000, au large des îles du Cap Vert. Elle mettra en œuvre le simulateur aéroporté POLDER, le lidar aéroporté LEANDRE, des photomètres au sol conjointement aux observations de MODIS-Terra. Elle permettra de constituer une première base de données regroupant des mesures directionnelles, spectrales et polarisées avec POLDER, moyen-infrarouges et infrarouges avec MODIS, et de profils de dépolarisation avec le lidar.

Bibliographie sommaire.

Arino O., JM. Melinotte, 1995, Fire Index Atlas, Earth Obs. Quart., 50, pp11-16.

Baran A. J., S. J. Brown, J. S. Foot, and D. L. Mitchell, : "Retrieval of tropical cirrus thermal optical depth, crystal size and shape using a dual view instrument at 3.7 μm and 10.8 μm " *J. Atm. Sci.*, 56, 92-110, 1999.

Baran A. J., S. J. Brown, J. S. Foot, and D. L. Mitchell, : "Retrieval of tropical cirrus thermal optical depth, crystal size and shape using a dual view instrument at 3.7 μm and 10.8 μm " *J. Atm. Sci.*, 56, 92-110, 1999.

Baran A.J., P.D Watts, P.N. Francis, Testing the coherence of cirrus microphysical and bulk properties retrieved from dual-viewing multispectral satellite radiance measurements, *J. Geophys. Res.*, 104, D24, p 31673-31683, 1999.

Baum B. A, P. F. Soulen, K. I. Strabala, M.D. King, S. A. Ackerman, W. P. Menzel, P. Yang, "Remote sensing of cloud properties using MODIS Airborne simulator Imagery during SUCCESS. II. Cloud Thermodynamic Phase. To appear in *Geophys. Res. Letts.*

Bréon, F.M., and P. Goloub, "Cloud droplet effective radius from spaceborne polarization measurements", *Geophys. Res. Letts*, Vol. 25, N 11, PAGES 1879-1882, 1998.

Bréon FM, S. Colzy, P. Goloub « Global distribution of cloud droplet radius from POLDER polarization measurements », Proceedings of ALPS'99 symposium, 1999.

Buriez J.C, C. Vanbause, F. Parol, P. Goloub, M. Herman, B. Bonnel, Y Fouquart, P Couvert, G. Seze 1997: Cloud detection and derivation of cloud properties from POLDER. *Int. J. of Remote Sensing*, Vol 18, N. 13, 2785-2813.

Chepfer H., 1997 : " Etude théorique et expérimentale des propriétés optiques et radiatives des cirrus " PhD thesis, Lille University, 197 pages.

Chepfer H., P. Goloub, J. Spinhirne, P. H. Flamant, M Lavorato, L. Sauvage, Brogniez, and J. Pelon, "Cirrus Cloud properties deived from POLDER-1/ADEOS Polarized Radiances: First Validation using a Ground based Lidar Network", *J. Applied. Meteor*, VOL 39, Pages 154-168, 2000.

Chepfer H., G. Brogniez, P. Goloub, F. M. Bréon, P. H. Flamant, "Observation of Horizontally Oriented Ice Crystals in Cirrus Clouds with POLDER/ADEOS ", *J. Quant. Spec. Rad. Transfer, Special Issue, Light Scattering by nonspherical particles'98*, Vol. 63, 521-543, Sept/Dec 1999.

Chepfer H., P. Goloub, J. Riedi, J.F. De Haan, J.W. Hovenier, P.H Flamant, Ice crystal shapes in cirrus clouds derived from POLDER-1/ADEOS-1, to appear in *Journal of Geophysical Research*, 2000.

Chiapello I, P. Goloub, D. Tanré, J. Herman, O. Torres, A. Marchand, Aerosol detection by TOMS and POLDER over oceanic regions, *Journal of Geophysical Research*, VOL 105, D6, p 7133-7142, March 2000.

Coffeen D.L, "Polarization and scattering characteristics in the atmospheres of Earth, Venus, Jupiter", *J. Opt. Soc. Am*, 69, 1051-1064, 1979.

De Haan J. F., P. B. Bosma, and J. W. Hovenier, 1986 : "The adding method for multiple scattering calculations of polarized light." *Astron. Astrophys.*, 183, 371-391.

Deschamps, P.Y., F.M.Bréon, M.Leroy, A.Podaire, A.Bricaud, J.C.Buriez and G.Seze, The POLDER mission: instrument characteristics and scientific objectives, *IEEE Trans. Geosc. Remote Sensing*, 32, 598-615, 1994.

Deuzé JL, C. Devaux, M. Herman, R. Santer, JY. Balois, L. Gonzalez, P. Lecomte, C. Verwaerde, Photopolarimetric Observations of Aerosols and Clouds from Balloon., *Rem. Sens. Environ.*, 29, 03-109, 1989.

Deuzé J.L , Goloub P., Herman M., Frouin R., 1992: "Retrieval of aerosols over the Gerlache Strait from photopolarimetric observations". *Antarctic Journal of United States*, Vol 27, p 197-199.

Deuzé JL., FM Bréon, PY Deschamps, C. Devaux, M. Herman, A Podaire, JL Rougean, Analysis of POLDER Airborne Instrument Observations over Land surfaces, *Em. Sens. Environ.*, 45, 137-154, 1993.

Deuzé, J. L., Herman, M., Goloub, P. ; Tanré, D. , Marchand, A. 1999 Characterization of aerosols over ocean from POLDER/ADEOS-1 *Geophys. Res. Lett.* Vol. 26 , No. 10 , p. 1421

Deuzé J.L, P. Goloub, M. Herman, A. Marchand, G. Perry, D. Tanré, Estimate of the aerosols properties over the ocean with POLDER, to appear in *Journal of Geophysical Research*, 2000.

Deuzé, J.L., F.M. Bréon, C. Devaux, P. Goloub, M. Herman, B. Lafrance, F.Maignan, A. Marchand, F. Nadal, G.Perry, and D. Tanré , « Remote sensing of aerosols over land surfaces from POLDER-ADEOS 1 Polarized measurements, accepted in *Journal of Geophysical Research*, 2000

Egan. WG, WR Johnson, V.S Whitehead, Terrestrial polarisation imagery from Space Shuttle: characterization and interpretation. *Appl. Opt.* 30, 435-442, 1991.

Elias T, C. Devaux, P. Goloub, M. Herman, « Polarising propertis of aerosols in the North-Eastern Tropical Atlantic Ocean, with emphasis on the ACE-2 period », *Tellus*, 52B, 2000, p 620-635.

Hagolle O. , P. Goloub , P.Y. Deschamps, T.Bailleul, J.L. Deuzé, M. Herman, J.C.. Buriez, X. Briottet. "POLDER in-flight calibration results", *IEEE Transactions on Geosci. Em.Sensing*, Vol 37, N 3, May 1999, pp 1550-1566.

Giraud. V, O. Thouron, J. Riedi, P. Goloub, "Cloud top temperature and infrared split window signature in relation with thermodynamic phase", submitted to Geophys. Res. Letts, 2000.

Goloub P., Deuzé J.L., Herman M, "Etude du modèle radiométrique de POLDER". Rapport contrat CNES n° 833-2-91-0094, 1992.

Goloub P., Deuzé J.L., Herman M., "POLDER interband calibration, using the sunglint". Rapport de contrat CNES n° 833-2-91-0151, 1992.

Goloub P., Herman M., Deuzé J.L., Frouin R. 1992: "Contrast between polarization properties of snow/ice and clouds". Antarctic Journal of United States, Vol 27, p 199-202.

Goloub P, JL Deuzé, M Herman and Y Fouquart "Analysis of the POLDER Airborne Polarization Measurements Performed over Clouds Covers", IEEE Transactions on Geoscience and Remote Sensing, Vol 32, N 1, January 1994, p78-87.

Goloub P, M Herman, O Hagolle, 1996: "Etalonnage en vol de l'instrument POLDER. Suivi de la polarisation". Rapport contrat CNES n° 95/1956/00., 1996.

Goloub P, H. Chepfer, M. Herman, G. Brogniez, F. Parol, "The use of polarization for clouds study", SPIE's 1997, San Diego, July, California, in the Polarization measurements, analysis and remote sensing session. Vol 3121. p330-341.

Goloub P., D. Tanré, J. L. Deuzé, M. Herman, A. Marchand, and F.-M. Bréon" Validation of the First Algorithm Applied for Deriving the Aerosol Properties Over the Ocean Using the POLDER/ADEOS", Measurements, *IEEE Trans. Geosci. Remote. Sens*, May 1999, Vol.37, No. 03, p1586-1596.

Goloub P., M. Herman, H. Chepfer, J. Riedi, G. Brogniez' P. Couvert, G. Séze, Cloud Thermodynamic Phase Classification from the POLDER Spaceborne intrument, *Journal of Geophysical Research*, 105., D11, p14747-14759, 2000.

Goloub P., O. Arino. "Validation of POLDER aerosol index over land using ASTR-2 fires maps", *Geophys. Res. Lett.* Vol. 27 , No. 6 , p. 899-902, 2000.

Goloub P., I. Chiapello, Comparaison POLDER/TOMS/ATSR dans les régions de biomass burning. Note interne. Laboratoire d'Optique Atmosphérique. Mai 2000.

Han, Q., W.B. Rossow, and A.A. Lacis, 1994: "Near-gloabl survey of effective droplet radii in liqui water clouds using ISCCP data", *J. Climate*, 7, 465-497.

Hansen, J.E. and L.D.Travis, 1974. Light scattering in planetary atmospheres. *Space Science Reviews*, 16, 527-610.

Hansen J. E., 1971 : " Multiple scattering of polarized light in planetary atmospheres. Part 1. The Doubling Method " *J Atmos. Sci.*, 28, 120-125.

Herman, M. Balois JY., Gonzalez L, L. Lecomte, P. Lenoble, J., Santer R., Verwaerde C., Stratospheric aerosol observations from a balloon-borne polarimetric experiment, *App. Opt.*, 15, 3573-3584, 1986.

Herman, J. R., P. K. Bhartia, O. Torres, C. Hsu, C. Seftor, and E. Celarier, Global distribution of UV-absorbing aerosols from Nimbus 7/TOMS data, *J. Geophys. Res.* 102, D14, 16911-16922, 1997.

Herman M, Deuzé JL, Devaux C, Goloub P, Bréon FM, Tanré D, "Remote sensing of aerosols over land surfaces, including polarisation measurements". Application to Polder Measurements". *Journal of Geophysical Research*, Vol 102, D14, 17039-17049, July 1997.

Hsu, N.C., J.R. Herman, O. Torres, B.N. Holben, D. Tanré, T.F. Eck, A. Smirnov, B. Chatenet, and F. Lavenu, Comparisons of the TOMS Aerosol Index with Sun-Photometer Aerosol Optical Thickness: Results and Applications, *J. Geophys. Res.*, 104, 6269-6279, 1999.

Higurashi, A., and T. Nakajima, Development of a two channel aerosol retrieval algorithm on global scale using NOAA/AVHRR, *J. Atmos. Sci.*, 56, 924-941, 1999.

Husar, R. B., J.M. Prospero, and L. L. Stowe, Characterization of tropospheric aerosols over the oceans with the NOAA advanced very high resolution radiometer optical thickness operational product, *J. Geophys. Res.*, 102, D14, 16889-16909, 1997.

Hutchinson K. D., B.J. Etherton, P.C. Topping, H.L. Huang, Cloud top phase determination from fusion of signatures in daytime AVHRR imagery and HIRS data, *Int. J. Em. Sensing*, 18, N 15, 3245-3262, 1997.

Holben, B. N., T. E. Eck, I. Slutsker, D. Tanré, J. P. Buis, A. Setzer, E. Vermote, J. A. Reagan, Y. F. Kaufman, T. Nakajima, F. Lavenu, I. Jankowiak, and A. Smirnov, AERONET-A federated instrument network and data archive for aerosol characterization, *Remote Sens. Environ.* 66, 1-16, 1998.

Jin, Y., W.B. Rossow, D.P. Wylie, 1996: Comparison of the climatologies of high level clouds from HIRS and ISCCP., *J. Climate*, 9, 2850-2879.

Kaufman, Y.J., A. Gitelson, A. Karniely, E. Ganor, R.S. Fraser, T. Nakajima, S. Mattoo, and B.N. Holben, Size distribution and scattering phase function of aerosol particles retrieved from sky brightness measurements, *J. Geophys. Res.*, 99, 10341-10356, 1994.

Kaufman, Y. J. and C. Sendra, Algorithm for automatic atmospheric corrections to visible and near-IR satellite imagery, *Int. J. Remote Sens.*, 9, 1357-1381, 1988.

Key J.R, J. M. Intrieri, Cloud Particle Phase Determination with the AVHRR, *J. Applied Meteorology*, to appear, 2000.

King M.D, Y. Kaufman, W.P. Menzel, D. Tanré, 1992, Remote sensing of Cloud, Aerosol, and Water vapour properties from Moderate Resolution Imaging Spectrometer (MODIS), *IEEE Transactions on Geoscience and Remote sensing*, Vol 30., N 1, January 1992.

Knap W.H., M. Hes, P. Stammes, R.B.A. Koelemeijer, P.D. Watts, Cirrus optical thickness and crystals size retrieval from ATRS-2 data using phase functions of imperfect hexagonal ice crytslas, *J. Geophys. Res.*, 104, D24, 31721-31730, 1999.

Knibbe, W.J.J, J.F. de Haan, J.W. Hovenier, L.D. Travis, Derivation of cloud properties from bi-wavelength polarization measurements, Proc. Soc. Photo. Opt. Instrum. Eng., 2582, 244-252, 1995.

Knibbe, W.J.J, Analysis of Satellite Polarization Observations of Cloudy Atmospheres, PhD Thesis, Octobre 1997. Free University of Amsterdam, The Netherlands.

Labonne, L. C., G. Brogniez, M. Doutriaux-Boucher, and J. C. Buriez, Modeling of light scattering in cirrus clouds with inhomogeneous hexagonal monocrystals. Comparison with in-situ and ADEOS-POLDER measurements, *Geophys. Res. Lett.*, Vol 27, NO 1, PAGES 113-116, 2000.

Labonne, L. G. Brogniez, JC. Buriez, M Doutriaux-Boucher, JF Gayet, A. Macke, "Polarized Light scattering by inhomogeneous hexagonal monocrystals. Validation with ADEOS-POLDER measurements. Submitted to *Geophys. Res. Lett.*, 2000.

Legrand M., JJ Bertrand, M. Desbois, L. Menenger, Y. Fouquart, The potential of infrared satellite data for the retrieval of Saharan dust optical depth over Africa. *J. Appl. Meteorol*, 28, 309-318.

Leroux C., JL Deuzé, P Goloub, C Sergeant, E. Pougatch, M. Fily. "Ground measurements of polarized bidirectional reflectance of snow in the middle infrared. Comparisons with model results", *Journal of Geophysical Research*, Vol 103, D16, 19721-19732, August 1998.

Leroy M., J.C Buriez, P.Y Deschamps, J.L Deuzé, M. Herman, P. Goloub, D. Tanré, M. Vesprini, F.M. Bréon, G. Séze, A. Bricaud, A. Liferman, « Les premiers résultats scientifiques de POLDER sur ADEOS ». Contribution au rapport quadriennal 1995-1998 du Comité National Français de Géodésie et Géophysique, p241-250.

Mishchenko, M. I., and L. D. Travis, Light scattering by polydisperse, rotationally symmetric, non spherical particles : linear polarization, *J. Quant. Spectrosc. Radiat. Transfer*, 51, 759-788, 1994a.

Mishchenko, M. I., and L. D. Travis, Light scattering by polydispersions of randomly oriented spheroids with size comparable to wavelengths of observation, *App. Opt.*, 33, 7206-7225, 1994b.

Mishchenko, M. I., and L. D. Travis, R. A. Kahn, and R. A. West, Modeling phase functions for dustlike tropospheric aerosols using a shape mixture of randomly oriented polydisperse spheroids, *J. Geophys. Res.*, 102, 16831-16847, 1997.

Mishchenko M.I, I.V. Geogdzhayev, B. Cairns, W.B. Rossow, A. Lacis, « Aerosol retrieval over ocean by use of channels 1 and 2 AVHRR data : sensitivity analysis and preliminary results », *Applied Optics*. Vol 38, N 36, pp 7325-7341, December 1999.

Nadal, F., Analyse de la polarisation pour la télédétection de l'atmosphère et des surfaces grâce aux mesures spatiales de POLDER, Doctorat de l'Université de Paris 7, Méthodes Physiques en Télédétection, 1999.

Nakajima, T., M. Tanaka, T. Hayasaka, Y. Miyake, Y. Nakanishi, and K. Sasamoto, Airborne measurements of the optical stratification of aerosols in turbid atmospheres, *Appl. Opt.* 25, 4374-4381, 1986.

Nakajima, T., A. Higurashi, K. Aoki, T. Endoh, H. Fukushima, M. Toratani, Y. Mitomi, B. G. Mitchell and R. Frouin, Early phase analysis of OCTS radiance data for aerosol remote sensing, *IEEE Trans. Geosci. Remote Sensing*, 37, 1575-1585, 1999.

Nakajima, T., G. Tonna, R. Rao, P. Boi, Y. Kaufman, and B. Holben, Use of sky brightness measurements from ground for remote sensing of particulate polydispersions, *App. Opt.*, 36, 15, 2672-2686, 1996.

Nakajima, T., and A. Higurashi, A use of a two-channel radiances for an aerosol characterization from space, *Geophys. Res. Lett.*, 25, 29, 3815-3818, 1998.

Parol F., J.C Buriez, C. Vanbause, P. Couvert, G. Sèze, P. Goloub, and S. Cheinet, "First Results of the POLDER « Earth Radiative Budget and Clouds » Operational Algorithms. POLDER-ADEOS ", *IEEE Trans. Geosci. and Rem. Sensing*, vol. 37, pp. 1597-1612, 1999.

Riedi J., P., Goloub, R. Marchand, 2000, « Comparison of POLDER phase to radar measurements », submitted to *Geophys. Res. Lett.* 2000.

Riedi J., M. Doutriaux-Boucher, P., Goloub, P., Couvert, 1999, « Global distribution of cloud top phase from POLDER/ADEOS 1 », *Geophys. Res. Lett.*, VOL 27, N 12, Pages 1707-1710, 2000.

Remer, L. A., and Y. J. Kaufman, Dynamic aerosol models : Urban industrial aerosols, *J. Geophys. Res.*, 103, 13859-13871, 1998.

Roger JC., R. Santer, M. Herman, JL Deuzé, Polarization of the solar light scattered by the Earth-Atmosphere system as observed from the US Shuttle, *Rem. Sens. Environ.*, 48, 275-290, 1994.

Stowe, L. L., R. M. Carey, and P. P. Pellegrino, Monitoring the Mt. Pinatubo aerosol layer with NOAA/AVHRR data, *Remote Sens. Environ.*, 60, 22-34, 1992.

Tanré, D., Y. J. Kaufman, M. Herman, and S. Matoo, Remote sensing of aerosol properties over the oceans using the MODIS/EOS spectral radiances, *J. Geophys. Res.*, 102, 16971-16988, 1997.

Tanré D., JL Deuzé, M. Herman, FM Bréon, P. Goloub, A. Marchand, Global observation of aerosol sources and transport from POLDER on ADEOS. Submitted to *Science*. 2000

Torres, O., P.K. Bhartia, J. R. Herman, Z. Ahmad, and J. Gleason, Derivation of aerosol properties from satellite measurements of backscattered ultraviolet radiation : theoretical basis, *J. Geophys. Res.*, 103, 17099-17110, 1998.

Toubbé B., T Bailleul, JL Deuzé, P Goloub, O. Hagolle and M. Herman "In-flight calibration of the POLDER polarized channels using the sunglint", *IEEE Transactions on Geosci Rem. Sensing*, Vol 37, N 1, January 1999, pp 513-525.

Wylie D.P., P. Wang, 1997: Comparison of cloud frequency data from HIRS and SAGE II. J. Geophys. Res, 102, 29893-29900.

Wylie D.P, 1998: "Cirrus and Weather: A satellite Perspective", in *Cirrus*, OSA Technical Digest (Optical Society of America, Washington DC, 1998), pp.66-69.

Some Web sites

POLDER

<http://www-projet.cnes.fr:8060/POLDER/index.html>

TOMS

<http://toms.gsfc.nasa.gov/>

ATSR-2 Atlas

<http://shark1.erin.esa.it/ATLAS/>

PICASSO-CENA

<http://www-picasso-cena.larc.nasa.gov/picasso.html>

MODIS

<http://modarch.gsfc.nasa.gov/MODIS/ATM/index.html>

Clouds:

<http://www.arm.gov/docs/sites/sgp/sgp.html> (ARM Southern Great Plains CART Site)

<http://www-loa.univ-lille1.fr/~riedi/> (*Information of cloud top retrieval from POLDER data*).

<http://www.gewex.com> (*GEWEX*)

<http://asd-www.larc.nasa.gov/fire/index.html> (*First ISCCP Regional Experiment (FIRE)*)

Aerosols:

<http://www.lrz-muenchen.de/~uh234an/www/radaer/gads.html> (*Global Aerosol data Set*).

<http://aeronet.gsfc.nasa.gov:8080/> (*AERONET*)

<http://capita.wustl.edu/CAPITA/DataSets/GlobalAerosol/globaer.html> (*GlobalAerosol Information Network*).

<http://acd.ucar/~zchu/data/> (*IGAC Atmospheric-Biospheric Chemistry*).

<http://gacp.giss.nasa.gov/> (*GACP*)

http://www.giss.nasa.gov/data/rsp_air/ (*RSP, US Radiometer Scanning Polarimeter*)

http://www.iap-kborn.de/optik/aer_trop/EARLINET.htm (*EARLINET*)

